SPACE NUCLEAR POWER SYSTEMS

Digitized by the Internet Archive
in 2024

https://archive.org/details/spacenuclearpowe0000symp_o6o8

Please Return to
Dr. Mark D. Hoover

SPACE NUCLEAR POWER SYSTEMS 1984

Proceedings of the
First Symposium on Space Nuclear Power Systems
held in Albuquerque, New Mexico, January 11–13, 1984

(IN TWO VOLUMES)

Edited by

Mohamed S. El-Genk
Institute for Space Nuclear
Power Studies
University of New Mexico

Mark D. Hoover
Lovelace Inhalation Toxicology
Research Institute
Albuquerque, New Mexico

VOLUME 2

ORBIT BOOK COMPANY, INC.
MALABAR, FLORIDA
1985

Original Edition 1985

Printed and Published by
ORBIT BOOK COMPANY, INC.
2005 Township Road
Malabar, Florida 32950

Copyright © 1985 by
ORBIT BOOK COMPANY, INC.

All rights reserved except for the use of material produced by employees of the United States government whose work is available to the U.S. government on a non-exclusive royalty free license to publish those parts authored under Government auspices.

No liability is assumed with respect to the use of the information contained herein.

Printed in the United States of America

This material is listed in the Department of Energy Technical Information Center as
CONF-840113

Library of Congress Cataloging in Publication Data
Main entry under title:

Space nuclear power systems 1984.

Includes index.
1. Space vehicles—Nuclear power plants—Congresses.
I. El-Genk, Mohamed S. II. Hoover, Mark D.
TL1102.N8S66 1985 629.47′53 84-16634
ISBN 0-89464-004-6 (set)

10 9 8 7 6 5 4 3 2

PREFACE

Early in 1983 a number of researchers at the University of New Mexico, the Air Force Weapons Laboratory, Sandia National Laboratories, and Los Alamos National Laboratory, all located in New Mexico, assembled to discuss the need for a national technical forum for the space nuclear power community. The result of that meeting was the formation of an organizing committee to plan the 1st Symposium on Space Nuclear Power Systems. This symposium was held in Albuquerque, New Mexico, January 11–13, 1984, and was highly successful in assembling both the scientists and engineers involved in research and development and the potential users of space nuclear power technology. There were over 375 registered attendees.

The Symposium was sponsored by the Department of Chemical and Nuclear Engineering of the University of New Mexico and was co-sponsored by a number of federal agencies and industrial concerns. Individuals who were instrumental in the early organization of the Symposium include Prof. Mohamed S. El-Genk from the University of New Mexico, Lt. Col. James Lee, Jr., Lt. Col. Robert E. Smith, and Dr. Robert Wick (on leave from Texas A&M University) from the Air Force Weapons Laboratory, Dr. Patrick McDaniel and Mr. Louis Cropp from Sandia National Laboratories, Dr. Gerald Leigh from the New Mexico Engineering Research Institute, and Mr. David Buden and Mr. John Hanson from Los Alamos National Laboratory. Industrial participants for the organizational efforts included Mr. Hal Snyder of GA Technologies, Mr. Bruno Katz of Rockwell International, and Dr. Steven Seiffert of the BDM Corporation.

Major financial support for the 1st Symposium was obtained from the U.S. Department of Energy, the Air Force Space Technology Center, the Air Force Office of Scientific Research, and the Wright Aeronautical Laboratory. Financial support was also provided by a number of industrial sponsors, including Gilbert Commonwealth, The BDM Corporation, GA Technologies, Inc., The General Electric Company, and Westinghouse Electric Corporation.

The Department of Chemical and Nuclear Engineering at the University of New Mexico formed the Institute for Space Nuclear Power Studies to support the Symposium organizationally, as well as to offer MS and Ph.D. degrees in nuclear engineering with a space power option, and to offer a series of short courses at the graduate level in this technology area. The first of these short courses was offered during the two days preceding the 1st Symposium and covered the Status of Space Nuclear Power Technology. The featured lecturers were Dr. Joseph Angelo, Jr., Chief, Electro-Optics Branch, Advanced Technology Division, Patrick Air Force Base, Florida, and Mr. David Buden, who was at that time Manager, Special Energy Conversion Projects, National Aeronautics and Space Administration, Washington, DC. These gentlemen have a combined technical experience of over thirty years in advanced nuclear and space technology and have co-authored a book in this area, *Space Nuclear Power* (Orbit Book Company, Malabar, FL, 1985). The short course was attended by 110 individuals including a large number of "old hands", many recent entrants into this technical field, and a large number of undergraduate and graduate engineering students. It was an excellent warmup to the 1st Symposium.

The Symposium was able to attract outstanding speakers, contributing a large measure to its success. A special thanks is due to Lt. Gen. Ernest C. Hardin, Jr. (USAF, Ret.) of the U.S. Department of Energy for chairing the Plenary Session and serving as master of ceremonies at the banquet. He was also instrumental in obtaining Dr. Dixie Lee Ray as our banquet speaker. Her talk was, as always, timely and exceptionally enlightening. Our luncheon speaker was Congressman Manuel Lujan, Jr. (R-NM), who gave us a valuable insight into the importance of high technology developments to our state and to the entire country.

Our Plenary Session gave an outstanding opening to the Symposium, emphasizing the importance of technology developments in space. Featured speakers included Dean Gerald W. May of the University of New Mexico College of Engineering, Mr. Gordon L. Chipman of the U.S. Department of Energy, Congressman

Robert A. Young (D-MO), Dr. Hans Mark of the National Aeronautics and Space Administration, Col. Gerald M. May of the United States Air Force Space Command, Dr. George P. Dix, consultant, and Mr. Duane C. Sewell, Chairman of the SP-100 Safety Advisory Committee.

General guidance for the direction and content of the Symposium were provided by the Symposium Steering Committee, which consisted of a number of highly respected members of the technical community, both from government and industry. That committee included Robert R. Barthelemy of the Air Force Wright Aeronautical Laboratory, Richard C. Dahlberg of GA Technologies, Inc., Col. Bob L. Francis of the USAF Space Technology Center, Steven Lanes of the U.S. Department of Energy, Kaye D. Lathrop of Los Alamos National Laboratory, Jerome Mullin of the National Aeronautics and Space Administration Space Energy Systems Office, and Duane C. Sewell of the SP-100 Safety Advisory Committee.

The Symposium Organizing Committee was responsible for the local planning and execution of the Symposium. The Honorary Chairman was Harold M. Agnew, President, GA Technologies, Inc., to whom we owe a debt of gratitude for his support and encouragement. The Technical Program Committee was co-chaired by Prof. Mohamed S. El-Genk of the University of New Mexico and Mr. John E. Hanson of Los Alamos National Laboratory. Those gentlemen are largely responsible for the most important aspect of the Symposium, the technical papers presented.

Two members of our Organizing Committee who were in a large measure responsible for the competence with which we handled local details were our Administrative Chairwoman and Co-Chairwoman. Carlota R. Klimas of the New Mexico Engineering Research Institute served as the Administrative Chairwoman. Her expertise in conference organization was largely responsible for the smooth operation which we achieved. She was assisted by Patricia A. Quinn of the University of New Mexico, who co-chaired administrative activities and was generally available for crisis management during the Symposium.

Other members of the Organizing Committee to whom we owe special thanks include Dr. Mark D. Hoover of the Lovelace Inhalation Toxicology Research Institute, who ably handled the publication interface for the Symposium; Capt. William J. Barattino of the United States Air Force Institute of Technology and the University of New Mexico, who performed remarkably as Finance Chairman for the Symposium, obtaining the bulk of the external financial support; and Capt. Douglas E. Zimmerman of the United States Air Force Weapons Laboratory who organized the industrial exhibits.

A final thanks are to the Symposium participants for their attendance and for their active and enthusiastic involvement. Among these attendees were a large number of undergraduate and graduate engineering students. Perhaps the most valuable service provided by the Symposium was the interest which it generated among the faculty and students of engineering education institutions across the country. That impact will be felt in years to come as more trained professionals join the ranks of those who are developing this exciting technology.

David M. Woodall, P.E.
General Chairman

INTRODUCTION

These two volumes contain the peer reviewed and edited versions of many of the papers presented at the 1st Symposium on Space Nuclear Power Systems held in Albuquerque, New Mexico, January 11–13, 1984. The objective of the symposium, and hence these volumes, was to summarize the state of knowledge in the area of space nuclear power systems and to provide a forum at which the most recent findings and important new developments could be presented. The Symposium succeeded largely because it attracted leading experts in the field at a time when there was a renewed national interest in nuclear power systems for applications in space.

These volumes include a total of 65 papers prepared by 117 authors from more than 40 organizations. We are grateful to the authors for their cooperation, enthusiasm, and sincere desire to contribute to a clear, useful, and technically sound publication.

For the purpose of organizing the material, the Symposium papers are divided into 8 parts. Parts 1 through 5 are contained in Volume 1. Parts 6 through 8 are contained in Volume 2. Part 1 provides a historical perspective on the U.S. space nuclear power program, addresses some of the promises and challenges of both civilian and military applications of nuclear power in space, and discusses the critical area of safety considerations. Part 2 goes into more detail on the plans, requirements, and costs of space nuclear power programs. Part 3 deals with the critical issues of integrating space nuclear power systems. Part 4 presents a methodology for selecting appropriate space reactor systems and reviews several candidate systems. Part 5 reviews the status of a number of nuclear reactor concepts in detail. Part 6 gives an update on the technologies for nuclear fuels, advanced refractory alloys, and energy conversion systems for space applications. Part 7 reviews the critical issues and options for thermal management and heat rejection in space. Part 8 covers the history, concerns, and methods for providing a safe and reliable use of nuclear reactors in space.

The preparation of these volumes has been accomplished through the encouragement, support, and diligence of many individuals. The chairpersons of the technical sessions at the Symposium were a fundamental part of the network we established for conducting the peer review process. We gratefully acknowledge their contributions in selecting appropriate technical experts to review manuscripts and in providing us with their composite reviews. The chairpersons of the Symposium sessions were; **Plenary**, Lt. Gen. Ernest C. Hardin, Jr. (USAF, Ret.) of the U.S. Department of Energy; **Programmatics and Applications I**, Vincent Truscello of the Jet Propulsion Laboratory, and Judith Ambrus of the National Aeronautics and Space Administration; **Programmatics and Applications II**, Richard Dahlberg of GA Technologies, Inc., and Richard Katucki of the General Electric Company; **Systems Concepts**, Lt. Col. James Lee, Jr. of the Defense Nuclear Agency, and David Buden of Science Applications International Corporation; **Reactors**, William Ranken of Los Alamos National Laboratory, and Hal Snyder of GA Technologies, Inc.; **Safety and Reliability**, Louis Cropp of Sandia National Laboratories, and Gary Bennett of the U.S. Department of Energy; **Thermal Management**, Robert Wick of the Air Force Weapons Laboratory (on leave from Texas A&M University), and Tom Mahefkey of Wright-Patterson Air Force Base; **Materials**, Roy Cooper of Oak Ridge National Laboratory, and Bill Buckman of Westinghouse Electric Corporation; **Power Conversion and Conditioning**, Gerry Stapfer of the Jet Propulsion Laboratory, and T. S. Jayadev of Lockheed Missiles & Space Company; **Power Systems Integration and Control**, Gail Klein of the Jet Propulsion Laboratory, and James Masson of Martin Marietta Denver Aerospace Company; and **Technical Exchange**, Patrick McDaniel of Sandia National Laboratories.

We wish to acknowledge the individual technical reviewers whose names were provided to us by the session chairpersons: August W. Cronenberg of Engineering Science and Analysis; Robert J. Campana, C. R. Fisher, and Stanley L. Koutz of GA Technologies, Inc.; D. Todd Newell, Wayne Phillips, and Richard A. Wallace of the Jet Propulsion Laboratory; Thomas A. Butler, Kenneth C. Cooper, Donald L. Hanson, William L. Kirk,

and Daniel R. Koenig of Los Alamos National Laboratory; Bruce B. Boecker and Richard G. Cuddihy of the Lovelace Inhalation Toxicology Research Institute; G. Martin Hudson, J. A. Navarro, and L. K. Rudolph of Martin Marietta Denver Aerospace; R. L. Heestand, F. J. Homan, James A. Horak, C. T. Liu, and M. M. Martin of Oak Ridge National Laboratory; Edward J. Britt of Rasor Associates, Inc.; R. V. Anderson and Richard B. Harty of Rockwell International; H. A. Bennett, Kathie Hubert Dodd, Dennis Engi, John P. Long, R. E. Pepping, Suzanne L. K. Roundtree, Dallas W. Sasser, and Robert G. Spulak, Jr. of Sandia National Laboratories; Massoud T. Simnad of the University of California, San Diego; and Bill L. Pierce of Westinghouse Advanced Energy Systems Division. We also express our gratitude to the many other individuals, whose names we do not have, who contributed to the peer review process at various stages of the preparation and revision of the Symposium papers.

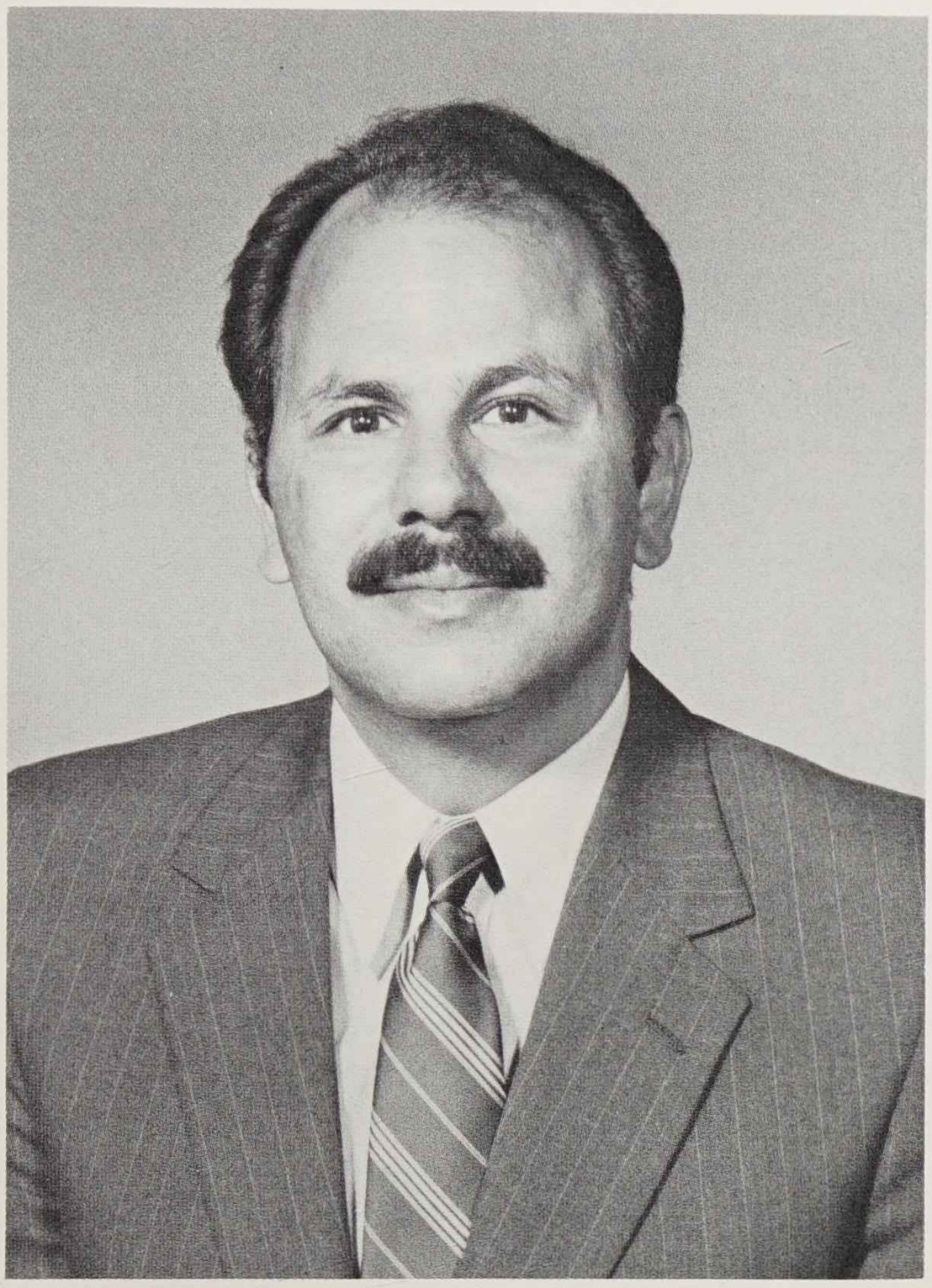
In the preparation of these volumes for publication, we gratefully acknowledge the guidance and support of Mr. Robert E. Krieger, President, The Orbit Book Company, and of Marie Bowles and the other enthusiastic and competent members of his staff. We are also grateful to the management and staff, especially Patricia Post, of Genesis Typography, Ltd. for their excellent skill. We thank Dr. Katherine Brogan of the University of New Mexico and Mr. Lynn Beyers of the Lovelace Inhalation Toxicology Research Institute for very useful discussions and editorial assistance. For the encouragement to tackle and complete this task, we are grateful to Prof. Glenn A. Whan, Chairman, Department of Chemical and Nuclear Engineering, University of New Mexico, to Prof. David M. Woodall, General Chairman of the 1st Symposium, and to Drs. Hsu-Chi Yeh, Bruce B. Boecker, and Roger O. McClellan of the Lovelace Inhalation Toxicology Research Institute.

Our final and most heartfelt thanks go to our wives Martha Hoover and Irene El-Genk, and to our children Alison Hoover and Ryan Hoover and Hussein El-Genk for their understanding, patience, and encouragement through all the phases of preparing these volumes.

Mohamed S. El-Genk, Ph.D.
Technical Chairman

Mark D. Hoover, Ph.D.
Publications Chairman

EDITORS





Mohamed S. El-Genk is an associate professor of Chemical and Nuclear Engineering and is the Director of the Institute for Space Nuclear Power Studies at the University of New Mexico. Dr. El-Genk holds BS (1968) and MS (1975) degrees from the University of Alexandria, Egypt, and a Ph.D. degree (1978) from the University of New Mexico, all in nuclear engineering. From 1978 to 1981 he was an engineering specialist doing light water reactor fuel behavior research at the Idaho National Engineering Laboratory. In 1981 he joined the Faculty at the University of New Mexico. Dr. El-Genk has produced numerous technical articles and reports on light water reactor and liquid metal fast breeder reactor safety, heat transfer with change of phase, steam explosion, post-accident heat removal, thermal hydraulics, nuclear fuel irradiation behavior, fission gas release, and space nuclear power. He is a member of the Honor Society of Phi Kappa Phi, the American Nuclear Society, the American Society of Mechanical Engineers, and the American Institute of Chemical Engineers.

Mark D. Hoover is a research scientist at the Lovelace Inhalation Toxicology Research Institute in Albuquerque, New Mexico. Dr. Hoover holds a BS degree (1970) in mathematics and English from Carnegie-Mellon University and MS (1975) and Ph.D. (1980) degrees from the University of New Mexico in nuclear engineering. His research focuses on the inhalation hazards associated with nuclear fuel cycles. Dr. Hoover has published in the open literature on aerosols from fusion energy systems, aerosols from fabrication of mixed-oxide reactor fuels, instrumentation for characterizing airborne particles, and on the inhalation hazards of plutonium recycle, use of thorium-uranium fuels, use of beryllium in reactor systems, and decommissioning of radioactively contaminated facilities. He is a member of the Honor Societies of Phi Kappa Phi and Tau Beta Pi, and the American Association for Aerosol Research. He is Chairman-elect of the New Mexico Section of American Nuclear Society (ANS) and Program Chairman of the ANS Environmental Sciences Division.

ABOUT THE SYMPOSIUM LOGO



The four corners of the logo represent the points of a compass and symbolize the role space nuclear power can play in the exploration of new frontiers; the large and small circles represent the integrated space system with a nuclear power plant at its center; the radiating spirals, also resembling a stylized atomic nucleus, symbolize the transfer of thermal and electric energy to support the space mission; and the logo's overall appearance of simplicity reflects the emphasis on space nuclear power systems that can operate without failure and provide reliable power for the duration of their mission.

TABLE OF CONTENTS

VOLUME 1

Preface iii
Introduction v
Editors vii
The Symposium Logo viii

Part 1
PLENARY

Chapter

1. THE ROLE OF THE UNIVERSITY IN THE DEVELOPMENT OF NEW TECHNOLOGIES
   Gerald W. May 3
2. CIVILIAN AND MILITARY APPLICATIONS OF SPACE NUCLEAR POWER: A CONGRESSIONAL PERSPECTIVE
   Manual Lujan, Jr. 7
3. THE CHALLENGES OF A JOINT CIVILIAN/DEFENSE PROGRAM TO DEVELOP SPACE NUCLEAR POWER SYSTEMS: A CONGRESSIONAL VIEWPOINT
   Robert A. Young 11
4. SPACE NUCLEAR POWER PROGRAMS: PRESENT AND FUTURE
   Gordon L. Chipman, Jr. 15
5. SPACE SYSTEMS ARCHITECTURE
   Gerald M. May 19
6. THE PIED PIPER: A HISTORICAL OVERVIEW OF THE U.S. SPACE POWER REACTOR PROGRAM
   George P. Dix and Susan S. Voss 23
7. SAFETY CONSIDERATIONS FOR THE USE OF NUCLEAR POWER IN SPACE
   Duane C. Sewell 31

Part 2
PROGRAMMATICS

8. ACCOMPLISHMENTS AND PLANS OF THE SP-100 PROGRAM
   William E. Wright 37
9. EMERGING SPACE NUCLEAR POWER NEEDS
   Frank J. Redd and Efren V. Fornoles 41
10. POTENTIAL CIVIL MISSION APPLICATIONS FOR SPACE NUCLEAR POWER SYSTEMS
    Judith H. Ambrus and Richard G. Beatty 43
11. SPACE REACTOR SYSTEMS AND SAFETY STRATEGIES
    Delbert F. Bunch 53

12. PROJECTED COSTS FOR SPACE NUCLEAR ELECTRIC POWER SYSTEMS
W. R. Determan, R. B. Harty, and A. F. Lillie 57
13. SPACE NUCLEAR POWER SYSTEM CONCEPTS AND THE TEST FACILITY NEEDS/PROGRAMMATIC REQUIREMENTS
Dennis Ferrigno and Larry J. Vachon 71

Part 3

POWER SYSTEMS INTEGRATION AND CONTROL

14. SPACE POWER SYSTEMS PRELAUNCH INTEGRATION
A. F. Lillie and J. W. Patrick 79
15. SPACE SHUTTLE INTEGRATION CONSIDERATIONS FOR NUCLEAR POWER SYSTEMS
Arthur L. Major and Alexander A. Vivona, Jr. 87
16. REACTOR POWER SYSTEM DEPLOYMENT AND STARTUP
J. R. Wetch, C. J. Nelin, E. J. Britt, and G. Klein 93
17. INSTRUMENTATION AND CONTROLS EVALUATION FOR SPACE NUCLEAR POWER SYSTEMS
J. L. Anderson and L. C. Oakes 109
18. AUTONOMOUS CONTROL DESIGN CONSIDERATIONS FOR SPACE NUCLEAR POWER SYSTEMS
M. S. Imamura and J. H. Masson 115
19. REACTOR POWER SYSTEM/SPACECRAFT INTEGRATION
Richard V. Elms 127

Part 4

SYSTEMS CONCEPTS

20. AN APPROACH TO SPACE REACTOR SYSTEM SELECTION AND DESIGN
David Buden and James H. Lee, Jr. 139
21. EVOLUTION OF SYSTEMS CONCEPTS FOR A 100 KWE CLASS SPACE NUCLEAR POWER SYSTEM
R. Katucki, A. Josloff, A. Kirpich, and F. Florio 149
22. THE ROCKWELL SR-100G REACTOR TURBOELECTRIC SPACE POWER SYSTEM
R. V. Anderson 165
23. REVIEW OF THE DESIGN STATUS OF THE SP-100 NUCLEAR POWER SYSTEM
Mohamed S. El-Genk, David M. Woodall, Virginia F. Dean, and David L. Y. Louie 177

Part 5

REACTORS

24. GAS COOLED REACTOR CONCEPTS FOR SPACE APPLICATION
Bill L. Pierce 191
25. THERMIONIC REACTORS FOR SPACE NUCLEAR POWER
W. G. Homeyer, M. H. Merrill, J. W. Holland, C. R. Fisher, and D. T. Allen 197
26. LIQUID METAL COOLED REACTORS FOR SPACE POWER APPLICATIONS
Sterling Bailey, Sam Vaidyanathan, and John Van Hoomissen 207
27. HEAT PIPE REACTOR DESIGNS FOR SPACE POWER
Daniel R. Koenig 217
28. SPACE NUCLEAR POWER REACTOR DESIGN BASED ON COMBINED NEUTRONIC AND THERMAL-FLUID ANALYSIS
D. R. Koenig, R. G. Gido, and D. I. Brandon 229
29. SNUG: A COMPACT PARTICLE BED REACTOR FOR THE 400 TO 4000 KWT POWER RANGE
J. R. Powell, T. E. Botts, F. L. Horn, O. W. Lazareth, and J. Usher 239
30. MULTIMEGAWATT SPACE NUCLEAR POWER CONCEPT
J. E. Jones, Jr., R. E. MacPherson, and J. P. Nichols 249

31. A BIMODAL REACTOR FOR HIGH AND LOW SPACE POWER
T. E. Botts, J. R. Powell, F. L. Horn, and O. W. Lazareth 257
32. ON THE EXPANSION EXPONENT FOR GAS-SOLID FLUIDIZED BEDS RELATIVE TO THE ROTATING FLUIDIZED BED REACTOR
Owen C. Jones, Jr. and Tai Sung Shin 265
33. THERMAL HYDRAULIC-NEUTRONIC INTERACTION IN THE ROTATING FLUIDIZED BED REACTOR: THE SEMI-INFINITE ONE-DIMENSIONAL REACTOR
C. C. Lee, M. Becker, and O. C. Jones, Jr. 273
34. THERMAL STRESS IN THE ROTATING FLUIDIZED BED REACTOR END PLATES
Jen-Tai Lin and Owen C. Jones, Jr. 281
35. CYCLIC GASEOUS CORE REACTORS FOR SPACE NUCLEAR POWER APPLICATIONS
E. T. Dugan and N. J. Diaz 291

Author Index A1
Key Word List A3

VOLUME 2

Preface iii
Introduction v
Editors vii
The Symposium Logo viii

Part 6
MATERIALS AND ENERGY CONVERSION

36. FUEL SYSTEMS FOR COMPACT FAST SPACE REACTORS
C. M. Cox, Dale S. Dutt, and R. A. Karnesky 301
37. IRRADIATION EFFECTS ON FUELS FOR SPACE REACTORS
August W. Cronenberg and William A. Ranken 307
38. THE BEHAVIOR OF MIXED-OXIDE FUEL SUBJECTED TO MULTIPLE THERMAL TRANSIENTS
G. R. Fenske, G. L. Hofman, L. A. Neimark, and R. B. Poeppel 317
39. REVIEW OF PREVIOUS SHIELD ANALYSIS FOR SPACE REACTORS
William J. Barattino, Mohamed S. El-Genk, and Susan S. Voss 329
40. THE FORMING OF METAL COMPONENTS FOR RADIOISOTOPE HEAT SOURCES
Ernest W. Johnson 341
41. TECHNOLOGY STATUS OF TANTALUM ALLOYS FOR SPACE NUCLEAR POWER APPLICATIONS
Eugene E. Hoffman 349
42. TECHNOLOGY STATUS OF MOLYBDENUM AND TUNGSTEN ALLOYS
William D. Klopp 359
43. THERMIONIC FUEL ELEMENT TECHNOLOGY STATUS
J. W. Holland, M. H. Horner, and L. Yang 371
44. STATIC CONVERSION SYSTEMS
Richard Ewell and Jack F. Mondt 385
45. ALKALI METAL THERMOELECTRIC CONVERSION (AMTEC) FOR SPACE NUCLEAR POWER SYSTEMS
C. P. Bankston, T. Cole, S. K. Khanna, and A. P. Thakoor 393

Part 7
THERMAL MANAGEMENT

46. OVERVIEW OF THERMAL MANAGEMENT ISSUES FOR ADVANCED MILITARY SPACE NUCLEAR REACTOR POWER SYSTEMS
Tom Mahefkey 405
47. LIQUID METAL HEAT TRANSFER ISSUES
H. W. Hoffman and G. L. Yoder, Jr. 409
48. HEAT PIPE TECHNOLOGY ISSUES
Michael A. Merrigan 419
49. LIQUID DROPLET RADIATOR TECHNOLOGY ISSUES
A. T. Mattick and A. Hertzberg 427
50. MAGNETIC DROPLET RADIATOR COLLECTORS
T. E. Botts, J. R. Powell, and F. L. Horn 437
51. ROTARY RADIATORS FOR REDUCED SPACE POWERPLANT TEMPERATURES
David G. Elliott 447
52. THERMAL ANALYSIS OF RADIATION SHIELDS FOR SPACE REACTORS USING ANALYTICAL AND FINITE ELEMENT METHODS
William J. Barattino and Mohamed S. El-Genk 455

53. THERMAL MANAGEMENT OF HIGH POWER SPACE BASED SYSTEMS
Han Hwangbo and William S. McEver 465
54. MULTI-MEGAWATT SPACE POWER THERMAL MANAGEMENT SYSTEM REQUIREMENTS
Robert T. Taussig 473
55. RADIATOR CONCEPTS FOR HIGH POWER SYSTEMS IN SPACE
Jason R. Feig 483

Part 8
SAFETY AND RELIABILITY

56. SPACE NUCLEAR SAFETY REVIEW PROCESS
Marvin P. Norin 493
57. MECHANICS OF SPACE NUCLEAR SAFETY
Richard W. Englehart 497
58. SNAP-10A AEROSPACE NUCLEAR SAFETY: A GOOD FOUNDATION FOR THE SP-100 PROGRAM
R. B. Harty and J. A. Hartung 505
59. SPACE NUCLEAR SAFETY FROM A USER'S VIEWPOINT
Robert W. Campbell 515
60. FISSION GAS AND VOLATILE RELEASE-VENTING MODEL FOR SPACE NUCLEAR REACTORS
David L. Y. Louie, Mohamed S. El-Genk, and Steven Wright 525
61. OVERVIEW OF THE HAZARDS OF USING LITHIUM IN SPACE NUCLEAR REACTOR SYSTEMS
Mark D. Hoover, Michael D. Allen, Bernard J. Greenspan, Simon J. Rothenberg, and Fritz A. Seiler 535
62. STATE VARIABLE METHOD OF FAULT TREE ANALYSIS
Robert J. Bartholomew, Harold K. Knudsen, and Glenn A. Whan 545
63. RELIABILITY ANALYSIS USING NETWORK SIMULATION
Dennis Engi 557
64. ARTIFICIAL INTELLIGENCE APPLICATIONS TO DESIGN VALIDATION AND SNEAK FUNCTION ANALYSIS
Rex C. Stratton 567
65. TRANSFERENCE OF ADVANCED LIQUID METAL FAST BREEDER REACTOR CONTROL TECHNOLOGY TO THE AEROSPACE POWER SYSTEM PROGRAM
Gregory H. Chisholm 577

Author Index A1
Key Word List A3

Part 6

MATERIALS AND ENERGY CONVERSION

Space Nuclear Power Systems 1984
Edited by M. S. El-Genk and M. D. Hoover
© Orbit Book Company, Malabar, FL, 1985

Chapter 36

Fuel Systems for Compact Fast Space Reactors

C. M. Cox, D. S. Dutt, and R. A. Karnesky

Westinghouse Hanford Company
P. O. Box 1970
Richland, WA 99352

About 200 refractory metal clad ceramic fuel pins have been irradiated in thermal reactors under the 1200 K to 1550 K cladding temperature conditions of primary relevance to space reactors. This paper reviews fuel performance with respect to fissile atom density, operating temperatures, fuel swelling, fission gas release, fuel-cladding compatibility, and consequences of failure. The UO_2 and UN fuels show approximately equal potential for acceptable performance; UC fuel has lesser potential. The W/Re alloys have performed quite well as cladding materials; and Ta, Nb, and Mo/Re alloys, in conjunction with W diffusion barriers, show good promise. Significant issues to be addressed in the future include high burnup swelling of UN, effects of UO_2-Li coolant reaction in the event of fuel pin failure, and development of an irradiation performance data base with prototypically configured fuel pins irradiated in a fast neutron flux.

Introduction

A substantial program was conducted in the 1960s to develop fuel elements for space nuclear reactors. Much of the program emphasized refractory metal clad UN, UC, and UO_2. This paper reviews the state of development of these fuel systems and discusses their technical feasibility as they relate to the current interest in space reactors. Previous reviews were provided by Weaver and Scott (1965) and by Gluyas and Watson (1975).

Design Considerations

The fundamental requirements for a space nuclear reactor are relatively low weight, small size, and long lifetime. For the reactor core, this has been translated to a compact liquid metal-cooled fast reactor with fuel goal burnups of 3 to 5 at. percent and fast neutron fluences of 2 to 3×10^{22} n/cm^2. Specific powers are modest by comparison with terrestrial reactors, but coolant temperatures are much higher, up to 1500 K versus about 800 K. High operating temperatures are required to increase thermal efficiency and minimize the size and weight of the heat rejection system. This has a significant effect on the reactor design: Li rather than the more conventional Na or NaK must be used as the liquid metal coolant, because of its lower vapor pressure; refractory metals must be used as fuel pin cladding, rather than more conventional ferrous alloys; and fuel melting temperatures must be high, forcing use of ceramic fuel material. There are several considerations that must be addressed in selecting a fuel system: fissile atom density, fuel operating temperature, fuel swelling, fission gas release, fuel-cladding compatibility, and the consequences of cladding failure.

Irradiation Data

The relevance of data is largely controlled by the operating environment, namely the linear heat rate (or fuel temperature), fuel burnup, cladding temperature, and fast neutron fluence. Irradiation data were compiled from multiple reports, primarily from National Aeronautics and Space Administration (NASA); Oak Ridge National Laboratory (ORNL); and Battelle Memorial Institute (BMI). Mayer et al. (1973) provide a good source of references. Earlier work on a Pratt and Whitney/ORNL Program was summarized by Weaver et al. (1969).

The irradiation data base of interest, defined here as fuel pins having a cladding temperature range of 1200 K to 1550 K, is shown in Figure 1. This figure shows the cladding temperature and burnup for each fuel pin. Fuel pin failures identified on this plot were determined primarily from visual examinations after irradiation. The data shown here represent 124 UN, 61 UC, and 9 UO_2 fuel pins. All these data suffer the nonprototypic feature of having been irradiated in a thermal rather than a fast reactor; thus, the effects of fast neutrons on cladding properties were not simulated, and the fission rate distribution across the fuel diameter had a marked depression in the center of the fuel.

Many of the early experiments had fuel columns of an inch or less in length. This complicates heat transfer analyses and magnifies the effects of power peaking at the ends of the fuel columns. Thus, the local burnup,

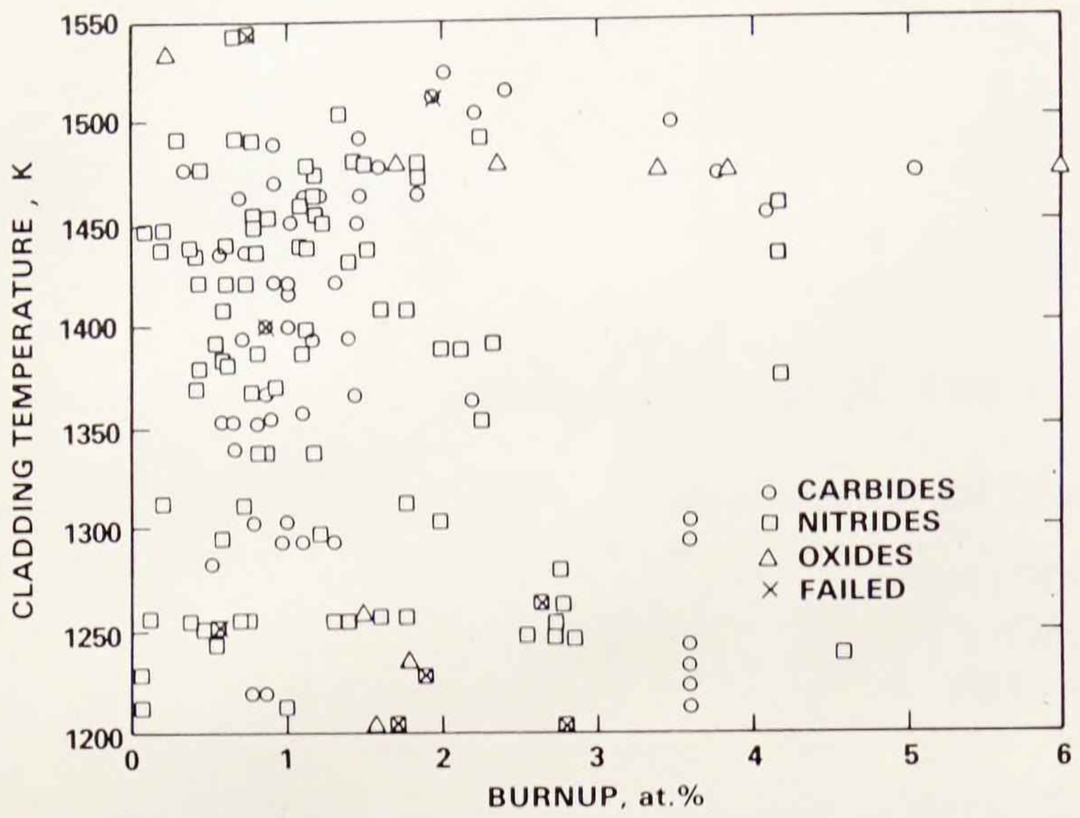


Figure 1 *Temperature and Burnup Experience with Refractory Metal Clad Fuel Pins which support SP-100 Fuel System Selection.*

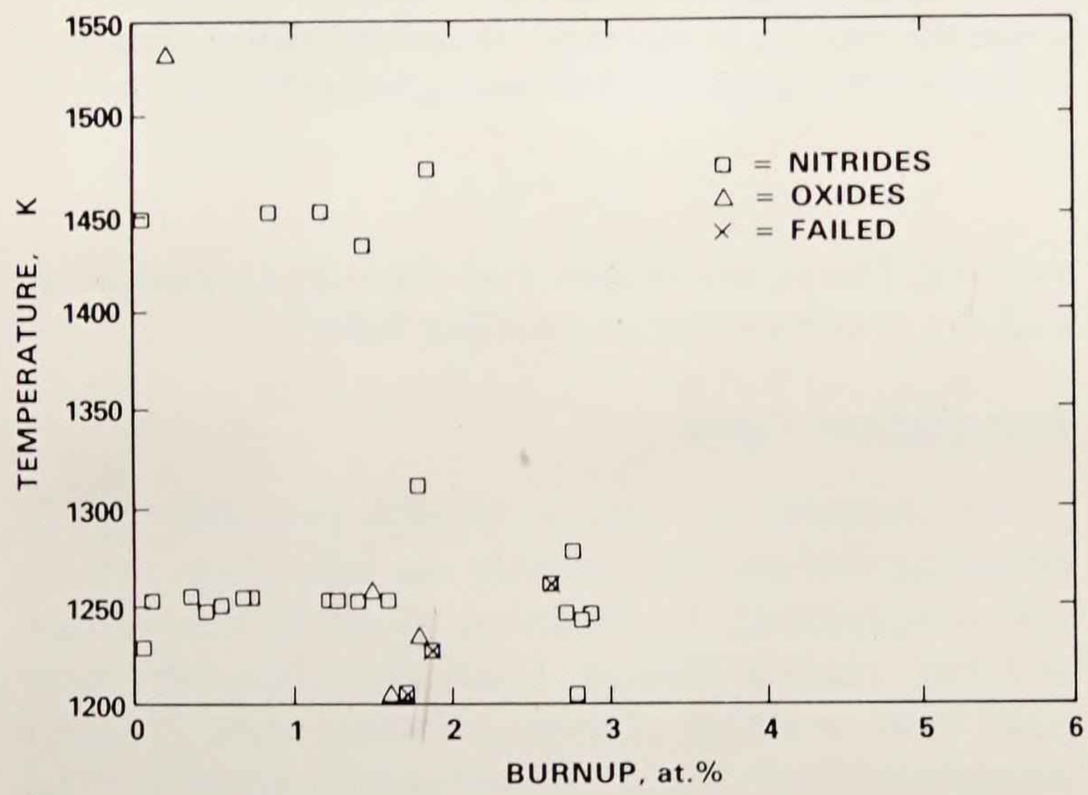


Figure 2 *Temperature and Burnup Experience of Refractory Metal Clad Fuel Pins which have a Length-To-Diameter Ratio greater than 4.*

thermal gradients, and calculated cladding temperatures have considerable uncertainty. To obtain a relatively reliable set of data with respect to operating power and temperatures, it is desirable to have the length-to-diameter ratio ($1/d$) greater than 4 to minimize these effects. The data field with an $1/d$ greater than 4 is shown in Figure 2. The irradiation data fields shown in Figures 1 and 2 supplemented by reviews of relevant laboratory and theoretical studies form the bases for the discussion of fuel selection issues which follows.

Fissile Atom Density

The high fissile atom densities of theoretically dense UN and UC make these materials good candidates for space reactor fuels. UO_2 is less attractive because of its

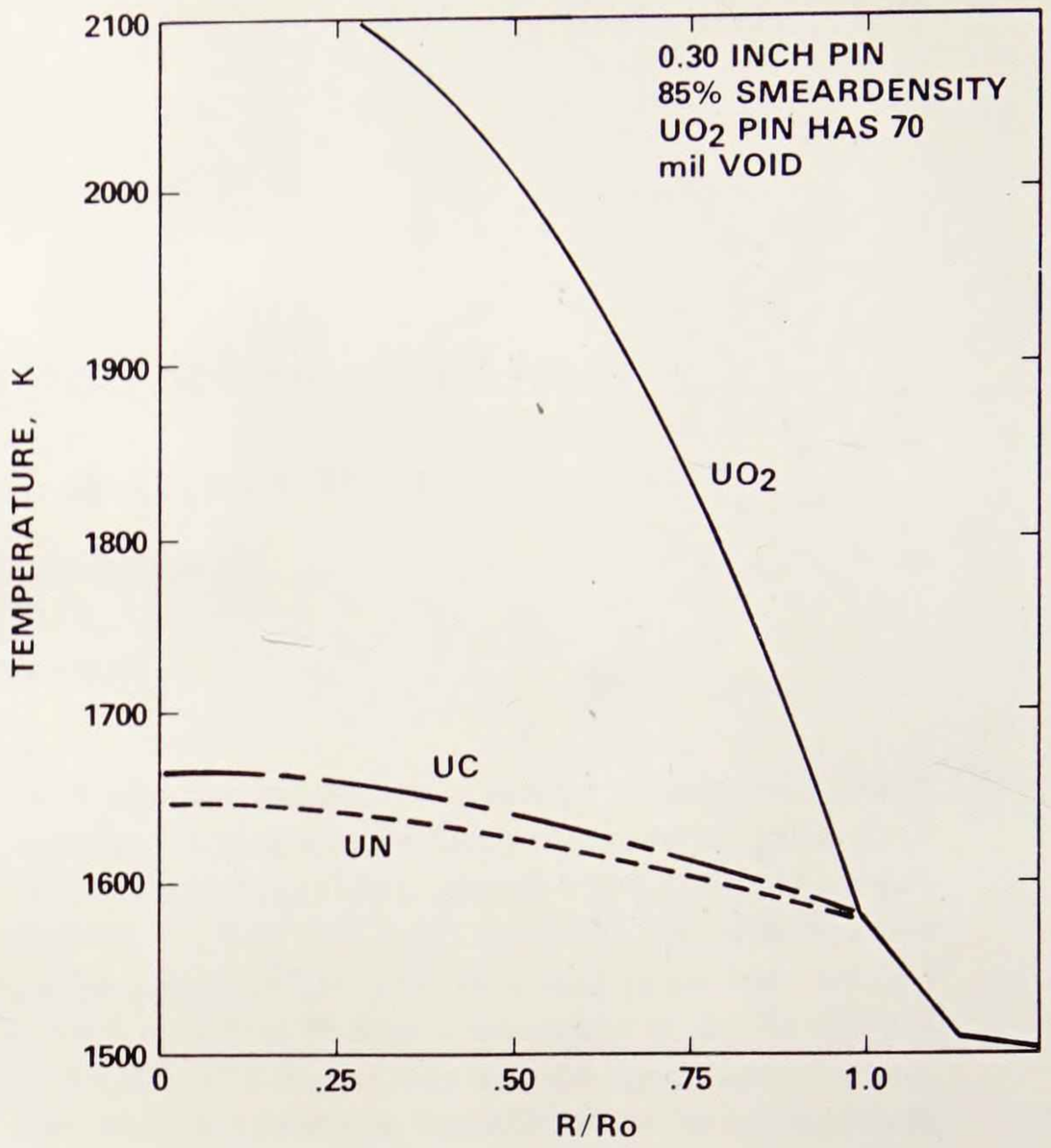


Figure 3 *Calculated Fuel Temperature Distribution at a Linear Power of 200 W/cm to compare the Expected Peak Temperatures for UC, UN, and UO_2 Fuel under SP-100 Conditions.*

30 percent lower theoretical fissile atom density. Cermet fuels are probably unacceptable because of large core volume requirements due to their rather dilute fissile material density. Part of the advantage of reduced reactor core size for the higher fissile density fuels is offset by use of somewhat higher smear density UO_2 fuel.

Fuel Operating Temperatures

Figure 3 displays typical operating temperatures of the three fuels at a linear heat rate of 200 W/cm (6 kW/ft) and with 1500 K cladding temperature. UN, UC, and UO_2 under such conditions operate at 54, 60, and 67 percent of their respective melting temperatures. These temperatures are relatively independent of fuel pin diameter.

Fuel Swelling

Figure 4 compares fuel swelling estimates as a function of temperature at a burnup of 1 at. pct. for UN, UO_2, and UC based on the work of Chubb, Storhok, and Keller (1973). The data, largely "unconstrained," show considerable scatter reflecting experimental difficulties and the effects of compositional variables. Fuel swelling, and the related gas release are dependent on stoichiometry of UC and UN and, to a lesser degree, the O_2 content of UN. Experiments reported by Zim-

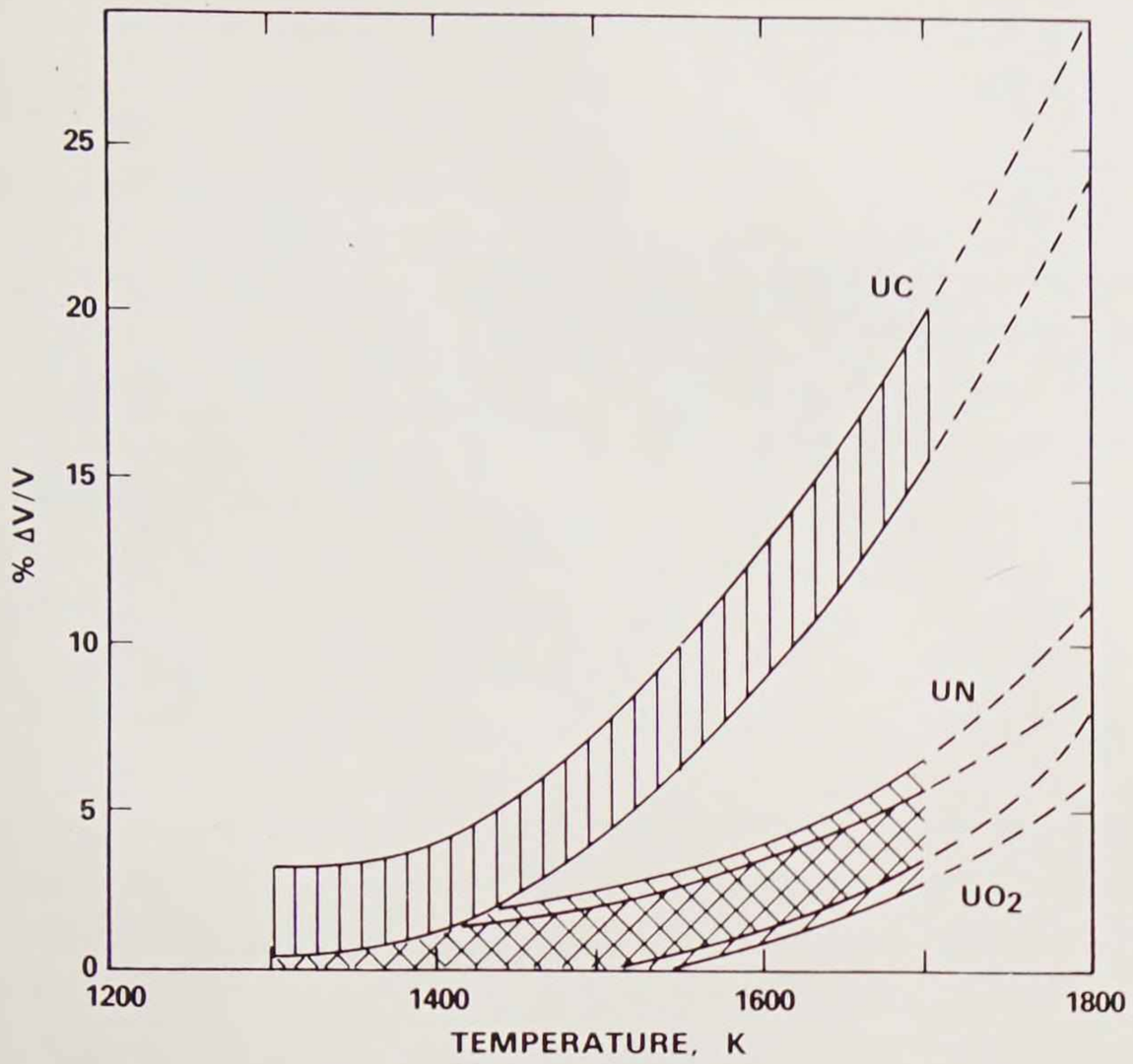


Figure 4 *Unconstrained Fuel Swelling of UC, UN, and UO_2 Fuel as a Function of Average Fuel Temperature at 1 Atom% Burnup as Inferred from Specimens Irradiated by Battelle Memorial Institute.*

mermann (1978) have been conducted to higher burnups with UO_2 and show (Figure 5) that the swelling rate decreases with burnup. Comparable high burnup data were not found for UN and UC. However, limited work reported by Zimmermann and Dienst (1974) with high oxygen content UN indicates the swelling rate may increase with burnup. Considering these uncertainties under space reactor conditions, comparable fuel swelling is expected from UO_2 and low oxygen content UN; significantly greater swelling is expected from UC.

Although UO_2 has a much higher creep rate than UN and UC below 1100 K, the creep rate of all three fuels increases very significantly and may be comparable above 1400 K. Thus, high unconstrained swelling at temperatures above, say, 1600 K is of little technical significance because it is apparently limited in fuel pins by cladding restraint or restraint of the colder fuel regions (Dienst et al. 1979).

In summary, fuel swelling considerations favor UO_2 over UN because the UO_2 operates at higher temperatures and is thus more plastic, leading to lower cladding stresses. UC is expected to exhibit the greatest fuel swelling.

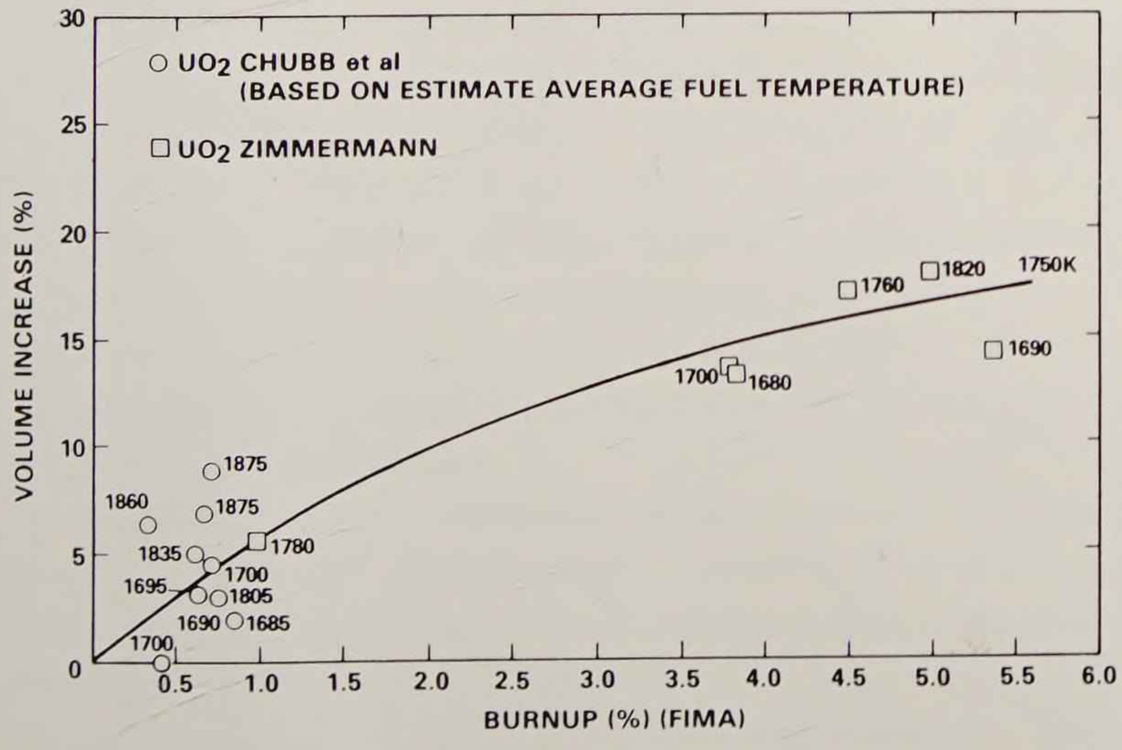


Figure 5 *High Burnup UO_2 Data at 1750 K Showing a Saturation of Unconstrained Fuel Swelling.*

Fission Gas Release

Fission gases released from the fuel form a major loading on the fuel pin cladding. Figure 6 compares the fission gas releases at 4 at. pct. burnup in the operating temperature range of interest. This figure was derived from data compilation plus the work of Dollins and Nichols (1977), Weaver and Scott (1965), and Grando et al. (1971). UC and UO_2 are shown to have comparable fission gas release. UN demonstrates significantly less fission gas release; thus, unless fuel pins are vented, fission gas release considerations favor UN.

Fuel-Cladding Compatibility

Figure 7 summarizes the understanding of fuel-cladding chemical compatibility based on the earlier summary by Weaver and Scott (1965), the irradiation data base summarized for this paper, and a review of several laboratory experiments.

Relevant irradiation data for UO_2 are limited. These data, in conjunction with laboratory experiments, show

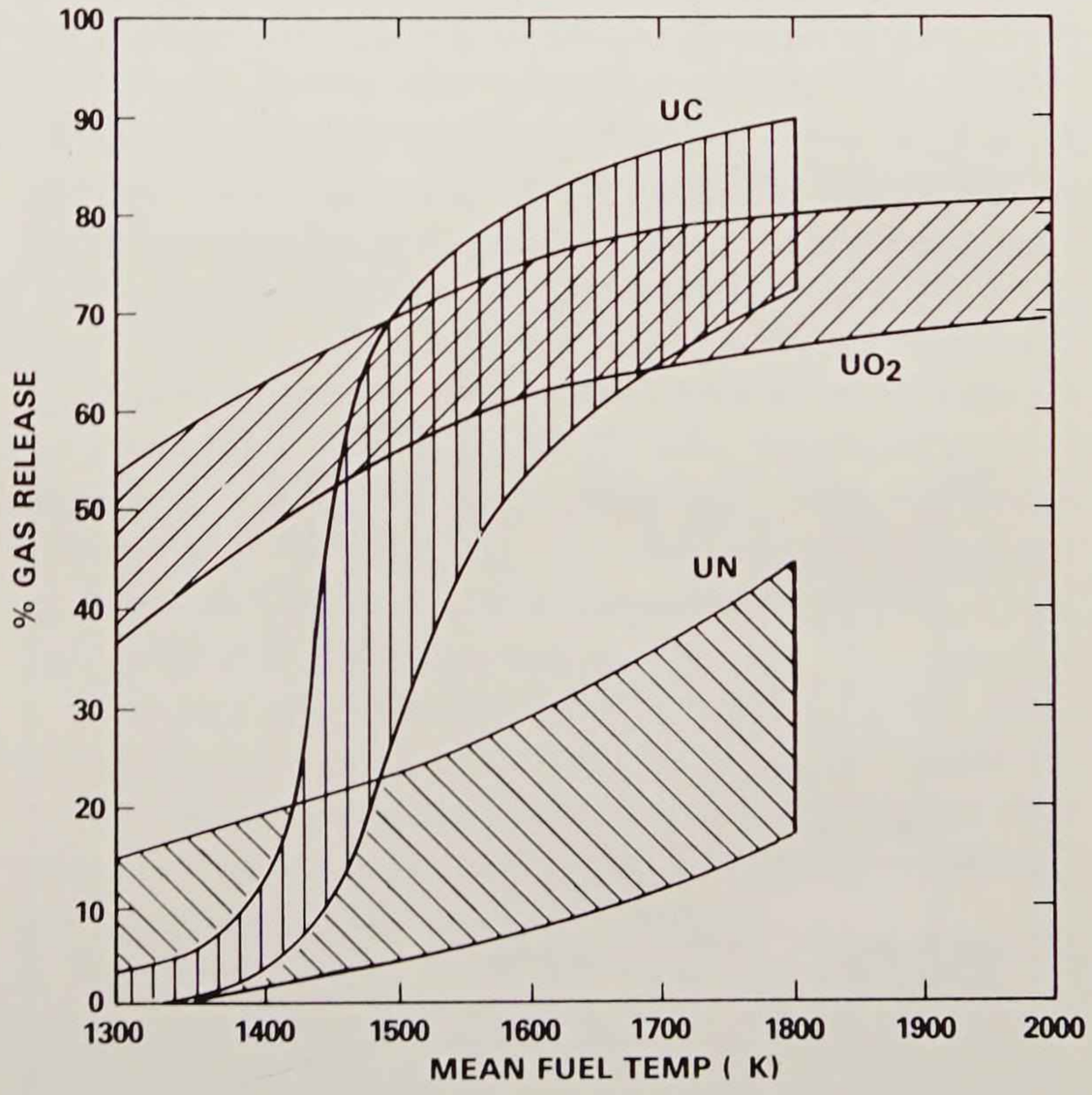


Figure 6 *Estimated Fission Gas Release of UC, UN, and UO_2 Fuel at 4 Atom% Burnup showing the Lower Release of UN compared to UC and UO_2.*

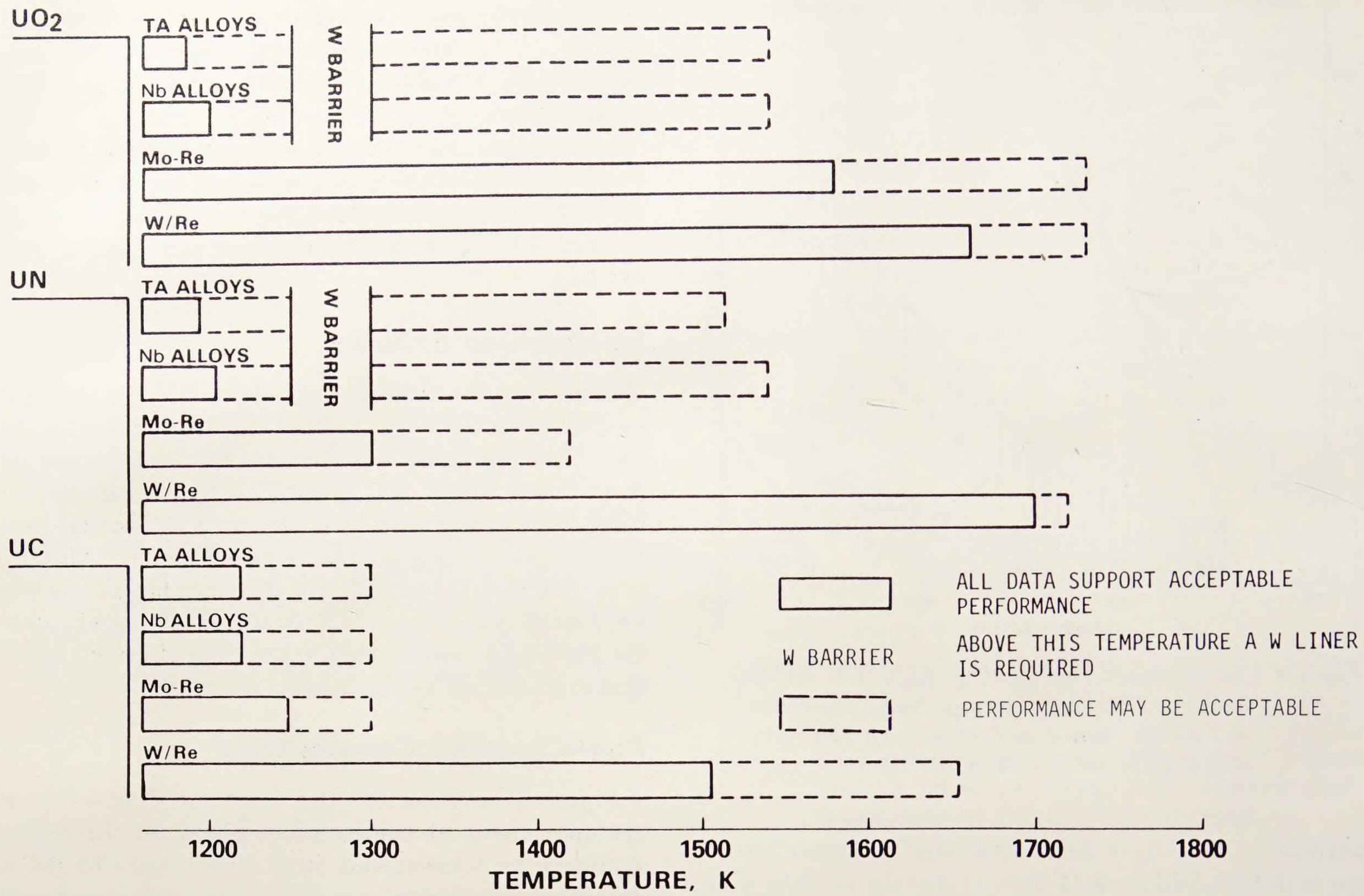


Figure 7 *Summary of Irradiation and Laboratory Fuel/Cladding Chemical Compatibility Data showing Temperatures where Fuel/Cladding Combinations are expected to be Compatible and the Temperature above which a Chemical Diffusion Barrier (W) is Required.*

UO_2 to be compatible with W/Re alloys for temperatures well in excess of 1500 K. Ta and Nb alloys were found to be incompatible with UO_2 above 1250 K but have been used successfully with a W diffusion barrier at temperatures above 1300 K. Mo/Re alloys have not been used under relevant reactor experiment conditions. Laboratory studies and in-reactor fuel pin irradiations using other Mo alloys indicate compatibility should be adequate at temperatures above 1500 K; however, O_2 and Mo transport issues remain unanswered. W diffusion barriers may thus also be required with Mo alloys. Compatibility considerations for UO_2 thus indicate

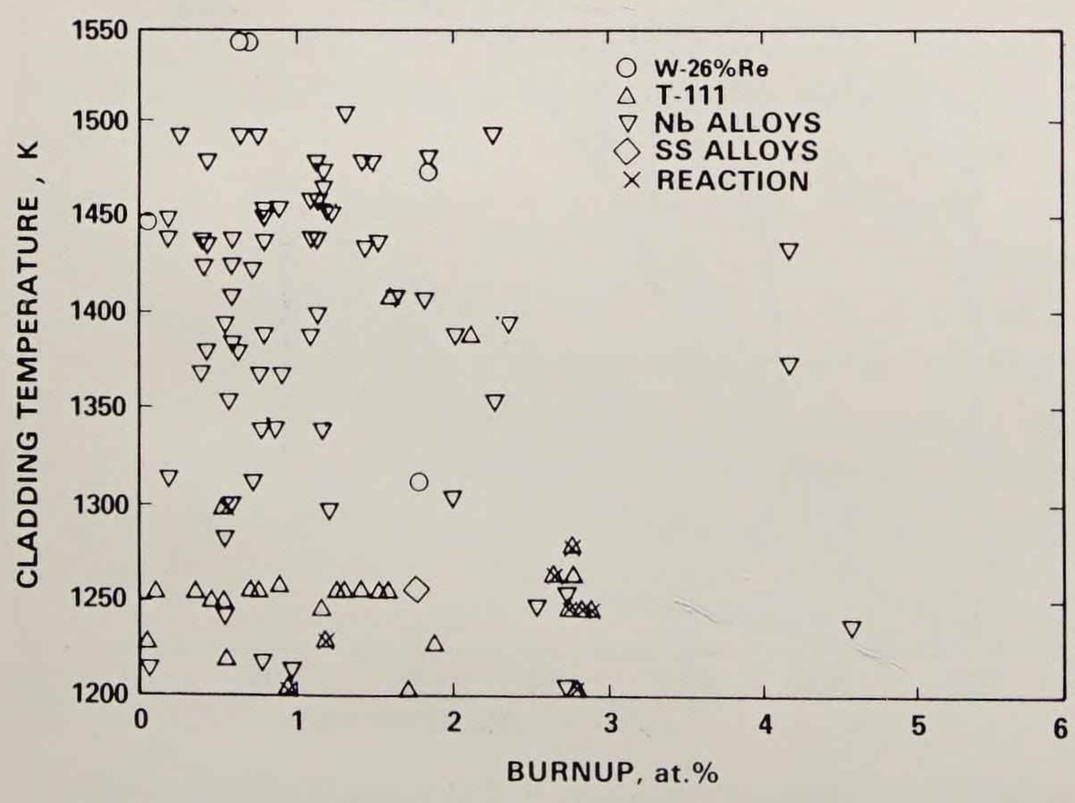


Figure 8 *Observed Fuel/Cladding Chemical Reaction on Refractory Clad UN Fuel Pins after Irradiation.*

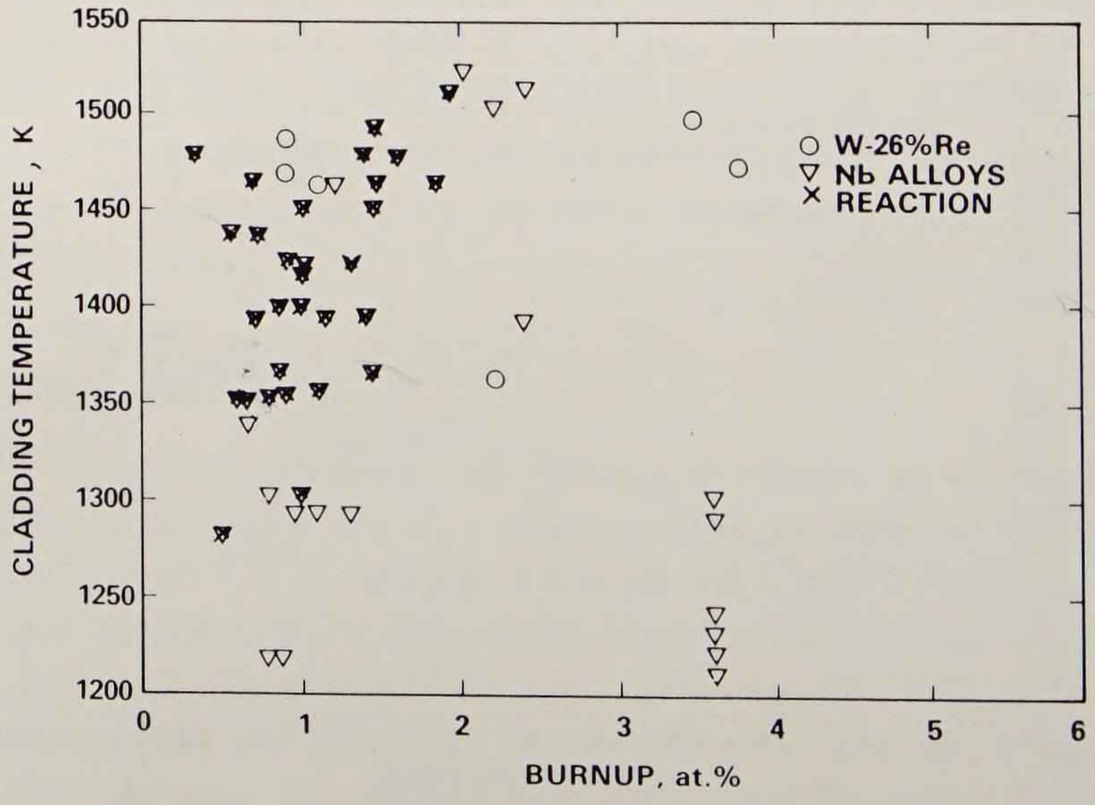


Figure 9 *Observed Fuel/Cladding Chemical Reaction on Refractory Clad UC Fuel Pins after Irradiation.*

preference in decreasing order for W/Re, Mo/Re, and Nb or Ta alloys, with use of W diffusion barriers probably required for the latter three.

Relevant irradiation data for UN are more abundant (Figure 8). Again, W/Re alloys are compatible with UN at cladding temperatures above 1500 K. Ta and Nb alloys clearly require a W barrier above 1250 K. Compatibility of Mo/Re alloys is in doubt above 1300 K.

Relevant irradiation data for UC are limited to W/Re and Nb alloys (Figure 9). These plus laboratory studies indicate that UC, in particular hyperstoichiometric UC, is incompatible with all refractory metals other than W alloys above 1300 K. W/Re alloys have been found to be compatible with uranium carbide to at least 1500 K.

Low ductilities have been observed in many refractory alloys, notably T-111 and to a lesser extent Nb-1Zr, after fuel pin irradiation. This has been primarily attributed to hydrogen embrittlement from handling during post-irradiation examination or to poor fabrication practices but other sources have been postulated, such as (n, p) reaction, experimental anomalies, and carbon pickup.

Consequences of Failure

Three issues related to fuel pin failure are: fuel-Li reactions, the potential for fuel dissociation, and fuel-refractory metal reactions resulting from the formation of a lithium diffusion path.

Thermochemical data at temperatures ranging from 1000 K to 2000 K indicate that reactions between UN and Li are not thermodynamically feasible. Compatibility experiments conducted with UN pellets immersed in a pool of Li and a defected UN fuel pin in a Li loop (Weaver and Scott 1965 and Gluyas and Watson 1975) showed good compatibility of UN with Li, although some pellet spalling and washout were reported. Stoichiometric UC is also compatible with Li; however, excess carbon is readily soluble in liquid Li and will react with cladding and structural materials. A significant potential problem has been identified for failed UO_2 fuel pins. Laboratory experiments have shown UO_2 to react readily with Li at temperatures of 1400 K to 1500 K, Kangilaski et al. (1965). The reaction yields free U and consequently low melting, ~1300 K, eutectics with cladding and structural materials. Thus, use of UO_2 fuel pins in Li systems requires either a very reliable fuel pin design or accommodation of the effects of the UO_2-Li reaction.

Although all three fuels will disassociate at low pressures, UN has the highest vapor pressure. The primary concern is formation of free U which could react with cladding and structural materials and N_2 which also might react with cladding and structural materials. This does not appear to be a problem in the temperature range of interest since the equilibrium nitrogen pressure for the reaction $UN(s) = U(1) + 1/2N_2$ is only $\sim 10^{-10}$ atmosphere (Kubaschewski, Evans, and Alcock 1967, Inouye and Leitnaker 1968, and Oetting and Leitnaker 1972).

If Li enters a failed fuel pin, it will form a diffusion path between the fuel and cladding. When this happens, at some point the fuel will react with the cladding by diffusion of excess interstitial atoms through the Li. For example, nitriding was reported of T-111 cladding in a defected UN pin in a Li loop (Gluyas and Watson 1975).

Summary

Results from irradiation of about 200 fuel pins at prototypic space reactor temperatures indicate refractory metal clad ceramic fuel pins can perform adequately. However, there are few data with both prototypic temperatures and prototypic configurations. Furthermore, all relevant irradiations have been conducted in thermal reactors, whereas the more likely application is a fast reactor. Thus, the achievable operating temperature/lifetime envelope of such fuel pins cannot be defined.

UN and UO_2 show comparable performance potential. UC appears of less promise since it has the highest fuel swelling, the least compatibility with refractory metal claddings, and relatively high release of fission gases.

Fuel swelling appears to favor UO_2 since the low burnup unconstrained swelling rates of UO_2 and UN are similar, UO_2 is more plastic at its operating temperature, and the UO_2 swelling rate appears to decrease with burnup. High burnup swelling of UN is not well defined but the swelling rate may increase with burnup. Fission gas release considerations favor UN. Use of UO_2 with its higher fission gas release might require stronger cladding, larger fission gas plena, or venting of fission gases.

W/Re cladding appears chemically compatible with both UO_2 and UN to at least 1500 K. Mo/Re cladding has not been used in irradiation tests but is expected to be compatible with UO_2 to 1500 K, based on performance of other Mo alloys; however, a W diffusion barrier may be required. Ta and Nb alloys appear usable with UO_2 and UN to greater than 1300 K when used with a W diffusion barrier.

There is a potential problem for failed UO_2 fuel pins, namely reaction with Li to form free U. This may result in low melting eutectics with refractory metals and thus requires either a very reliable fuel pin design or accommodation of the effects of this reaction.

Significant issues to be addressed in the future include high burnup swelling of UN, effects of UO_2-Li coolant reaction in the event of a fuel pin failure, and development of an irradiation performance data base with prototypically configured fuel pins irradiated in a fast neutron flux.

Acknowledgments

The authors gratefully acknowledge the help of J. W. Jost and W. A. Briggs in processing and plotting data, of D. A. Himes in compiling irradiation test data and reviewing fuel swelling, and of R. E. Woodley in providing thermochemical evaluations. This work for the SP-100 Program was sponsored by the US Department of Energy.

References

Chubb, W., V. W. Storhok, and D. L. Keller (June 1973) "Factors Affecting the Swelling of Nuclear Fuels at High Temperatures," *Nuclear Technology* 18:231–256.

Dienst, W., I. Mueller-Lyda, and H. Zimmermann (1979) "Swelling, Densification, and Creep of Oxide and Carbide Fuels Under Irradiation," in *Proc. of International Conference Fast Breeder Reactor Fuel Performance*, March 1979, American Nuclear Society Press, LaGrange, IL, pp. 166–175.

Dollins, C. C. and F. A. Nichols (1977) "Swelling and Gas Release in UO_2 at Low and Intermediate Temperatures," *J. Nucl. Mater.* 66:143.

Gluyas, R. E. and G. K. Watson (1975) *Materials Technology for An Advanced Space Power Nuclear Reactor Concept: Program Summary*, NASA-TN-D-7909.

Grando, C., M. Montgomery, and A. Strasser (1971) "Unrestrained Swelling and Fission Gas Release of Fast Reactor Fuels," in *Proc. Fast Reactor Fuel Element Tech.*, April 1971, American Nuclear Society Press, LaGrange, IL, p. 771.

Inouye, H. and J. M. Leitnaker (1968) "Equilibrium Nitrogen Pressures and Thermodynamic Properties of UN," *J. Am. Ceram. Soc.* 51:6.

Kangilaski, M., E. O. Fromm, D. H. Lozier, V. W. Storhok, and J. E. Gates (1965) *High Temperature Irradiation of Niobium—1 w/o Zirconium Clad UO_2*, BMI-1730, Battelle Memorial Institute, Columbus, OH.

Kubaschewski, O., E. L. Evans, and C. B. Alcock (1967) *Metallurgical Thermochemistry*, 4th Edition, Pergamon Press, London.

Mayer, J. T., R. L. Smith, M. B. Weinstein, and H. W. Davison (1973) *EXFILE: A Program for Compiling Irradiation Data on UN and UC Fuel Pins*, NASA TM X-68226.

Oetting, F. L. and J. M. Leitnaker (1972) "The Chemical Thermodynamic Properties of Nuclear Materials. I. Uranium Mononitride," *J. Chem. Thermodynamics* 4:199.

Weaver, S. C., J. L. Scott, R. L. Senn, and B. H. Montgomery (1969) *Effects of Irradiation of Uranium Nitride Under Space-Reactor Conditions*, ORNL-4461, Oak Ridge National Laboratory, October 1969.

Weaver, S. C. and J. L. Scott (1965) *Comparison of Reactor Fuels for High Temperature Applications*, ORNL-TM-1360, Oak Ridge National Laboratory, December 1965.

Zimmermann, H. and W. Dienst (1974) *Irradiation Behavior of Uranium Nitride*, KFK-EXT-6/74-1, Kernforschungzentrum, Karlsruhe, FRG, February 1974.

Zimmermann, H. (1978) "Swelling in Mixed-Oxide Fuel Pins," *Nuclear Technology* 41:408–410.

Space Nuclear Power Systems 1984
Edited by M. S. El-Genk and M. D. Hoover
© Orbit Book Company, Malabar, FL, 1985

Chapter 37

Irradiation Effects on Fuels for Space Reactors

August W. Cronenberg
Engineering Science and Analysis
836 Claire View Street
Idaho Falls, ID 83402

William A. Ranken
Los Alamos National Laboratory
P.O. Box 1663
Los Alamos, New Mexico 87545

Because of high-temperature/high-burnup requirements for efficient space reactor operation, fission gas induced fuel swelling and attendant gas release are important concerns in the evaluation of an optimum fuel choice and in-core design considerations. A review of irradiation induced swelling and gas release experience is presented here for the three principal fuels; UO_2, UC, and UN. The primary advantage of UC and UN over UO_2 is higher thermal conductivity and attendant lower fuel temperature at equivalent pellet diameter and power density, while UO_2 offers the distinct benefit of well-known irradiation performance. Irradiation test results indicate that at equivalent burnup, temperature, and porosity conditions, UC experiences higher swelling than UO_2 or UN. Fission gas swelling becomes important at fuel temperatures above $\simeq$ 1430 K for UC, and at somewhat higher temperatures for UO_2 and UN. Evidence exists that at equivalent fuel temperatures and burnups, high density UO_2 and UN experience comparable swelling behavior; however, differences in thermal conductivity influence overall irradiation performance. The low conductivity of UO_2 results in higher thermal gradients which contribute to fuel microcracking and gas release. As a result UO_2 exhibits higher fractional gas release than UN, at least for burnups up to about 3%.

Introduction

Forthcoming missions of planetary exploration, earth surveillance, communications, and human presence in space require the development of a highly reliable energy source capable of providing large amounts of electrical power. Nuclear reactors offer many advantages for space applications due to their weight/power superiority and proven base technology. Nevertheless, because of long lifetime and high operating temperature requirements, potential fuel behavior problems arise with respect to thermal stability, fuel-cladding compatability, and fission gas induced swelling and release phenomena. The subject of this paper is the latter concern, where fission gas release and swelling effects are evaluated for the primary fuel candidates, namely UO_2, UC and UN.

Although the choice of reactor design will influence fuel requirements, the following criteria appear common to most reactor design concepts:

- High fuel temperatures (in the range of 1500–2000 K, so as to make possible high reject heat radiator temperatures) and
- High fuel burnup (in the range of 3–10 atom percent, so as to accommodate a relatively long core lifetime of 7–10 years).

For such high-temperature/high-burnup conditions, significant fission gas induced fuel swelling and attendant gas release can be expected.

Swelling and gas release will not only impact the ultimate choice of fuel, but it will also alter parameters such as the as-manufactured stoichiometry, porosity, grain size, gap-thickness, and gas plenum volume. Swelling adversely affects fuel performance because it promotes fuel-cladding contact, which not only can cause cladding strain, but which can result in cladding contamination and alteration of mechanical properties that may shorten fuel element lifetime. Irradiation induced pore formation also decreases fuel conductivity, leading to temperatures higher than exhibited by fully dense fuel, at the same heating rate. High gas release requires either retention in a plenum which adds to reactor weight and overall dimensions, or venting of released gas to space, which complicates design considerations.

Table 1 presents an overview of properties affecting fuel performance. Although UO_2 offers the advantage of a large body of experience, its low thermal conductivity and fissile density can be a drawback where weight considerations and high temperatures are of primary importance. UC and UN in comparison offer distinct advantages with respect to thermal performance and weight characteristics. The principal drawbacks with regard to physical and chemical properties are that the carbides are more reactive with potential cladding materials and both UC and porous UN are subject to attack by water vapor in the air and hence have to be handled in protective gas environments. UN also has a relatively high vapor pressure. Because the vapor species is mainly N_2, free uranium formation will occur at high temperature unless a nitrogen overpressure is maintained.

Table 1 *Comparison of UO_2, UC, and UN Properties and Parameters Affecting Fission Gas Induced Fuel Swelling and Gas Release Behavior.*

Property	UO_2	UC	UN
Theoretical density, g/cm^3	10.97	13.63	14.32
Uranium density, g/cm^3	9.67	12.97	13.52
Melting Point, K	3120	2660	3030
Thermal conductivity at 1300 K, W/cm-K	0.03	0.25	0.23
Crystal Structure	Cubic-CaF_2	Cubic-NaCl	Cubic-NaCl
Lattice Constant	5.47Å	4.96Å	4.89Å
Vapor Pressure, Pa (Stoichiometric Compound)			
1600 K	1.5×10^{-6}	$\sim 10^{-9}$	2×10^{-5}
1800 K	2.0×10^{-4}	$\sim 2 \times 10^{-7}$	2×10^{-3}

Swelling/Gas Release Trends

Variable	Fuel Swelling	Fission Gas Release
Increased Microcracking	(↓)	(↑)
Increased Burnup	(↑)	(↑)
Increased Temperature	(↑)	(↑)
Increased Dislocation Density	(↓)	(↓)
Increased Grain Size	(↓)	(↓)
Increased Porosity	(↓)	(↑↓)[a]

(↑) Denotes direct proportionality
(↓) Denotes inverse proportionality
[a] Medium initial porosity traps gas bubbles in fuel matrix, high initial porosity vents gas to pellet surface.

Table 1 also presents a comparison of parameters affecting swelling/gas release performance, which is discussed in the following section.

Overview of Fission Gas Behavior

Figure 1 illustrates the general nature of fission gas ($\simeq$25 percent of fission yield) behavior in polycrystalline fuel. Atoms of fission gas, particularly Xe and Kr, migrate to the grain boundaries of the fuel microstructure, either individually or in the form of small *intra*granular bubbles. At these boundaries they form larger *inter*granular bubbles. In as much as the gas density is lower than that of a solid, atoms residing in gas bubbles occupy more volume than the solid fissile atoms they replace. Bubble precipitation and growth thus lead to fuel swelling.

Pileup of bubbles at grain boundaries stresses the grain structure, resulting in grain boundary separation that eventually interlinks to form an interconnected network of pores. If such porosity is open to the fuel-cladding gap, fission gas is effectively vented to the pellet free surface. The fraction of gas released from the pellet gives rise to a cladding overpressure during its lifetime.

At high fuel temperature, the movement of pores formed by thermal cycling induced fuel cracking will occur by a fuel evaporation-condensation process in a temperature gradient. As discussed by Barnes (1963) and Olander (1976), such pores will migrate to the

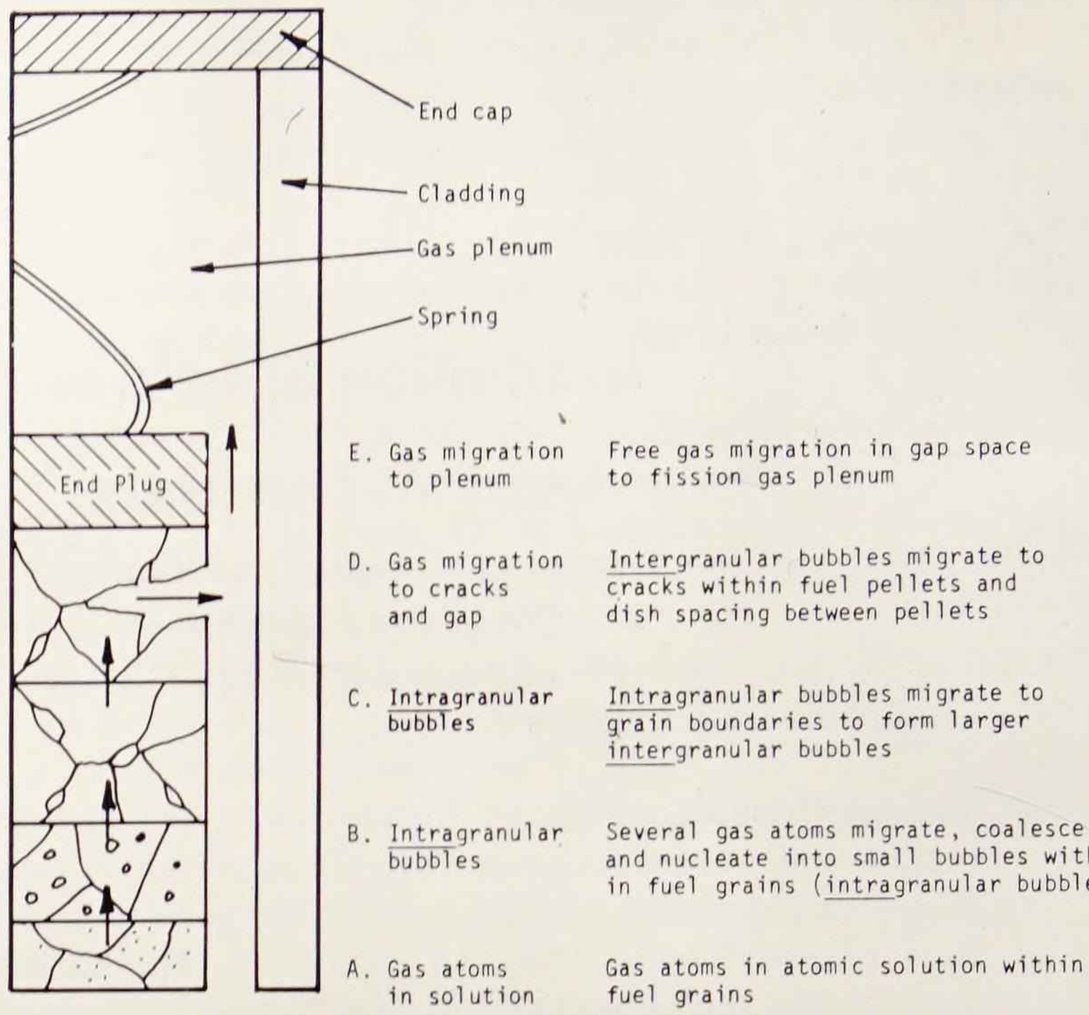


Figure 1 *Illustration of Fission Gas Behavior in Solid Fuel.*

center of a cylindrical fuel body, sweeping up fission gas along the way and depositing it in a central void. This mechanism thus provides an additional means of releasing fission gases from the fuel microstructure. It is principally operative for UO_2 at temperatures above 2000 K.

Knowledge of fuel swelling/gas release behavior is of importance for designs that require high burnups, since the necessary margin required in the rod pressure to failure is reduced. The challenge to the designer is to ensure the maximum fuel rod reliability and to optimize gas retention/fuel swelling characteristics versus that for gas release and rod pressurization. It should be noted that such a competing tradeoff is not particularly restrictive if one has the option of venting gas to a large plenum or completely from the rod. Venting introduces severe complications in the design of a fuel pin reactor, however, and hence most space reactor designs call for a limited plenum volume and no gas-venting; thus, swelling and gas release phenomena are of primary concern.

Table 1 also lists some of the principal factors affecting fission gas behavior in polycrystalline fuel. Given the number of variables involved, the complexity of the problem becomes apparent; nevertheless, general trends have been determined from well established empirical findings and analysis of controlling phenomena. Such trends are as illustrated, where the symbol (↑) denotes a direct relationship between the variable under consideration and its effect on swelling/gas release, while the symbol (↓) denotes an inverse relationship. For example, the trend for increasing burnup is toward both increased swelling and gas release, while a larger grain size results in decreased swelling and gas release. In the following section specific findings with respect to UO_2, UC and UN fuels are reviewed.

Fuel Pellet Swelling/Gas Release Experience

Swelling and gas release are complimentary processes. Retention of fission gases in the fuel matrix as burnup proceeds is usually accompanied by increased swelling. Conversely, fuel that releases a large fraction of its fission gas generally exhibits low swelling. However, some swelling almost always precedes gas release due to the buildup of *inter*granular bubbles with increased burnup. This induces matrix fuel swelling and stressing of the grain boundaries, causing grain boundary separation, interlinkage, and ultimately venting of gases from the fuel interior.

Although a large body of swelling/gas release data exists, this review centers primarily on a consideration of UO_2, UC, and UN samples tested under similar irradiation conditions. Such an approach was deemed appropriate in order to obtain as accurate a ranking of UO_2, UC, and UN fuel swelling/gas release characteristics as possible, without the introduction of large differences in exposure conditions.

Battelle-Columbus Data

One of the more consistent sets of data with respect to similar UO_2, UC and UN test conditions is from the experiments of Hilbert et al. (1971). Each cylindrical fuel specimen was clad with W-25Re alloy having a diameter to thickness ratio of 12.5. The irradiation data was correlated to cladding surface temperatures. Figure 2 presents a comparison of the high temperature swelling behavior for UN, UC, and UO_2 fuel samples, at burnups of $\simeq 0.6$ to 0.8 atom-percent. As indicated, UC experienced the greatest amount of swelling, while UN swelled the least. The data also indicates that at increased temperatures, differences in extent of swelling for the three fuel types is reduced. The lower limits of the curves in Figure 2 represent the approximate points where a strong dependence of swelling on temperature begins, that is where fission gas induced swelling first becomes a factor (at a swelling rate of 1.0% per 10^{20} fissions/cm^3). The cladding temperatures associated with this phenomenon are ~1430 K for UC, 1530 K for UO_2, and 1670 K for UN. As discussed by Hilbert et al. (1971), at equivalent cladding temperatures the average temperature of UO_2 is $\simeq 100$ K higher than that of the carbide and nitride samples; thus, the UO_2 data would be shifted to the right accordingly. On a fuel temperature basis, the swelling rate of UO_2 would thus be nearly the same as that of UN. Clearly UC has a significantly higher swelling rate than either UO_2 or UN.

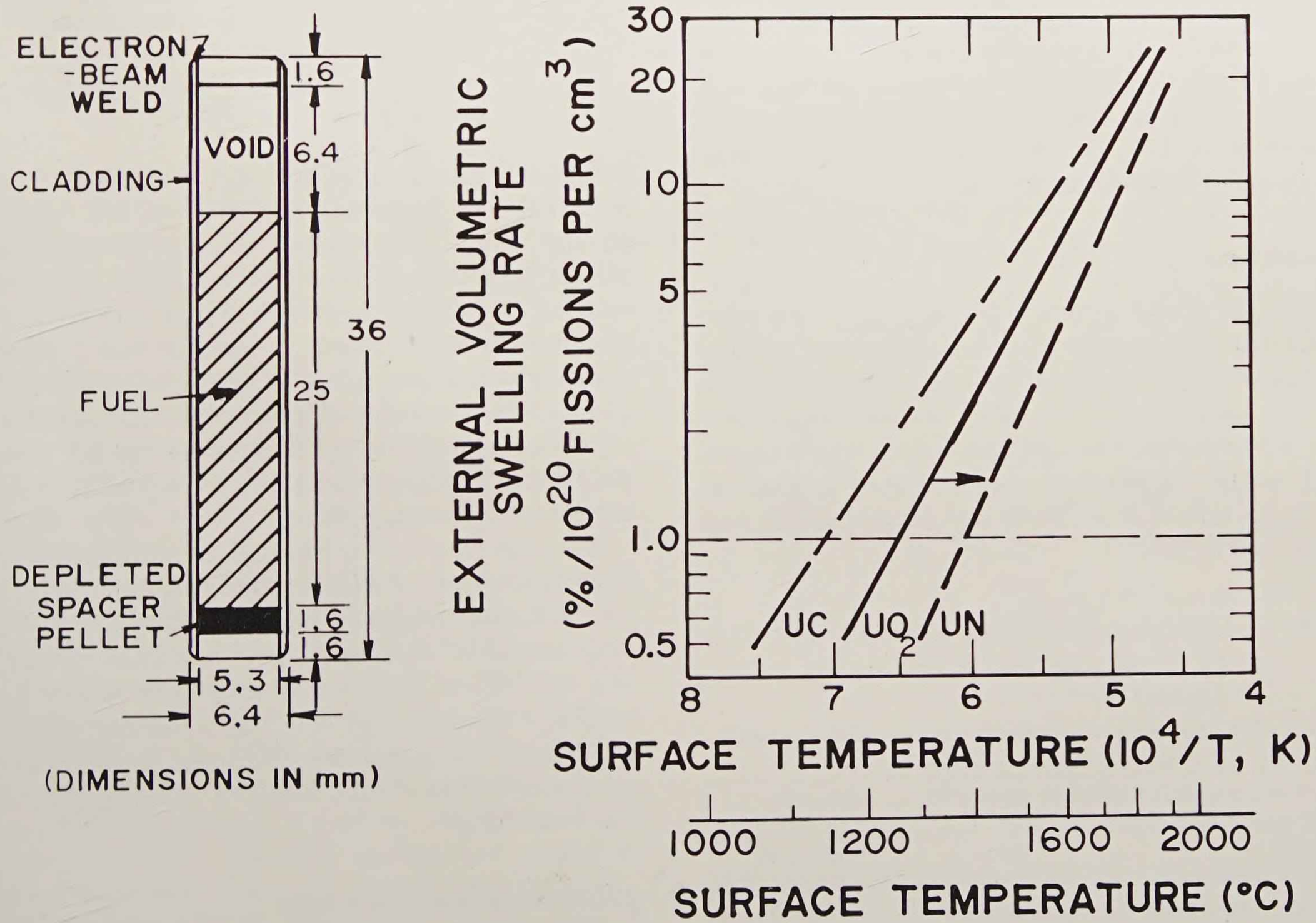


Figure 2 *Irradiation Geometry and Associated Swelling Data as a Function of Cladding Surface Temperature, at a Burnup of 2.0 (10^{20}) fiss/cm^3 ($\simeq 0.6$ atom-% for UN and UC, $\simeq 0.77$ atom-% for UO_2). The Arrow on the UO_2 Curve indicates the Amount of Relative Curve Shift that occurs if Average Fuel Temperature is used instead of Cladding Surface Temperature. (Data from Hilbert et al. 1971.)*

Table 2 *Fission Gas Release Data for Fuel Samples Irradiated to a Burnup Level of $2(10^{20})$ Fissions/cm^3 at a Cladding Surface Temperature of $\simeq 2000$ K*[a,b].

Fuel	Percent Gas Release: High-Density Fuel (98-99 TD)	Percent Gas Release: Porous Fuel (60-70 TD)
UN	<5 percent	$\simeq 20$ percent
UC	$\simeq 40$ percent	$\simeq 90$ percent

[a] Data from Hilbert et al. 1971.
[b] To convert MW-d/ton-U into fiss/cm^3, the burnup in MW-d/ton-U is multiplied by $2.68(10^{15})$ and the uranium density (g/cm^3) of the fuel. Thus, $2(20^{20})$ fiss/cm$^3 \simeq 0.6(10^4)$MW-d/ton-U $\simeq 0.6$ atom-percent burnup.
[c] TD is percent Theoretical Density.

Fission gas release data for the UC and UN samples are compared in Table 2. The data show that UC releases more gas than UN, and, as would be expected, highly porous fuel releases more gas than high density fuel. However, since UC swelled more than UN, it is apparent that higher gas release does not necessarily mean low swelling. To the contrary, the post-test microstructure suggest that a large proportion of the gas release was preceded by swelling. Although such parameters as initial porosity, stoichiometry, impurity content, and grain size were not well documented in the references cited and could have influenced fuel swelling/gas release conditions, the fact remains that for similarity in test conditions significant differences in swelling and gas release behavior were noted for the UC samples versus those for UO_2 or UN, at the low burnup conditions employed in these tests.

SNAP-50 Data

Under the SNAP program UC and UN fuels were investigated with respect to compatibility and irradiation characteristics. A tungsten lined Nb-Zr cladding alloy was used, while W-Re alloy thermocouples measured fuel centerline and cladding surface temperatures. Details of the test conditions are described by DeCrescente et al. (1965a and 1965b) and Huegel (1965) and summarized in Table 3.

Table 3 *Fuel and Irradiation Parameters for the SNAP-50 UN and UC Comparative Study of Fuel Swelling and Gas Release Characteristics*[a].

Property	UC	UN
Fuel Density, percent TD	80–97	90–96.4
U-235 enrichment, percent	9.6–11.6	10–93
Rod OD, cm	0.75	0.75–0.79
Fuel stoichiometry	0.94–1.14	not specified
Burnup, atom-percent	0.31–1.84	0.31–1.94
Clad surface Temp., K	1340–1530	1240–1520
Fuel center Temp., K	1480–1870	1370–1840

[a] Data from DeCrescente, Freed, and Caplow 1965a and 1965b, and Huegel 1965.

Figure 3 presents a comparison of the swelling and gas release data. As indicated, UN experienced significantly less swelling at an equivalent burnup than hyperstoichiometric UC. The superior swelling behavior of UN over UC, was primarily ascribed to a lower rate of bubble migration and agglomeration at grain boundaries in UN than UC.

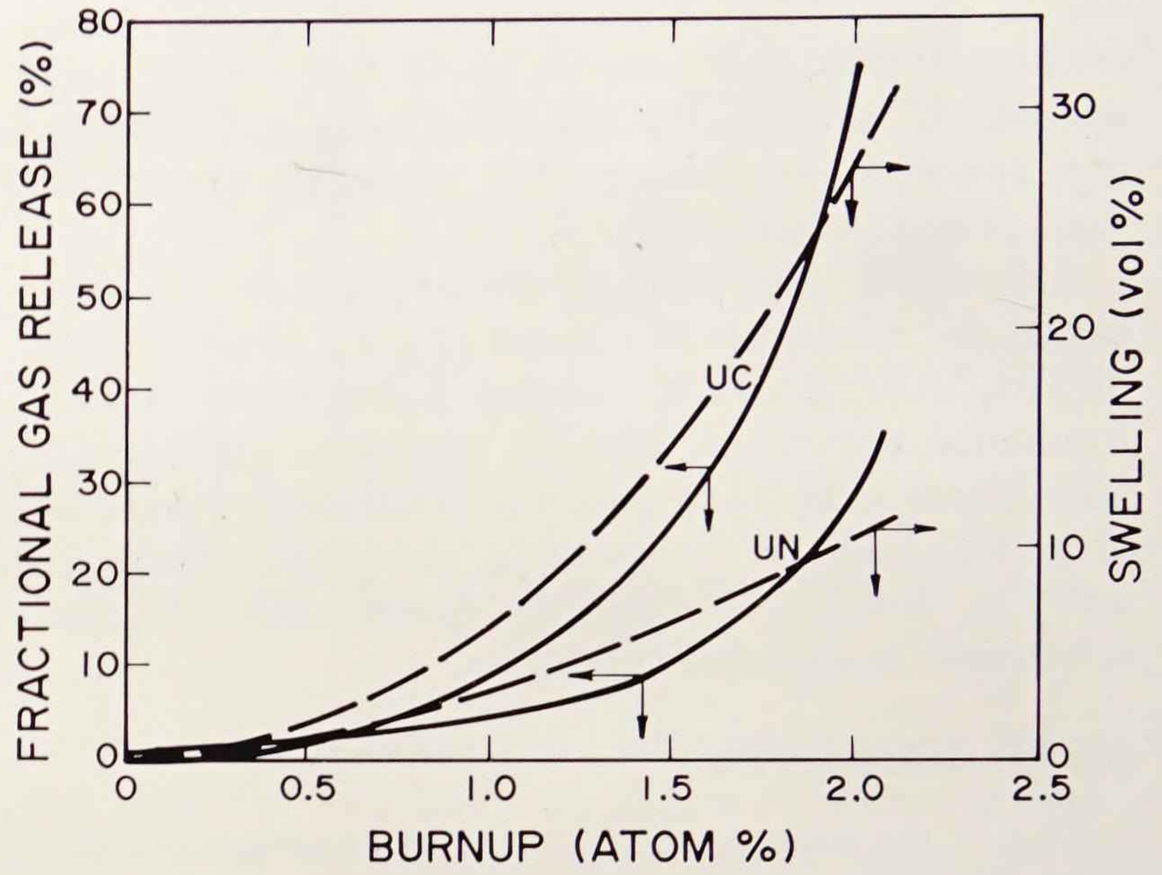


Figure 3 *Comparison of SNAP-50 UN and UC Swelling and Gas Release Data at a Fuel Centerline Temperature of $\simeq 1670$ K. (Data from DeCrescente, Freed, and Caplow 1965a and 1965b and Huegel 1965.)*

Figure 3 also compares fission gas release data. As indicated, the fractional release from UC at higher burnup levels (>0.5 atom percent) is significantly greater than that observed for UN. For UN less gas reached the boundaries (more gas was retained as *intra*granular bubbles) resulting in less buildup of *inter*granular bubbles, less stressing of grains, less swelling, and less attendant gas release. It was concluded that the UN crystal structure must be inherently more gas retentive than the UC structure, with UN having lower diffusivities for microbubble diffusion.

Although results must be qualified with respect to the important effects of as-fabricated properties (for example, initial stoichiometry, porosity, grain size, and cladding restraint), the fission gas data indicate that, in general, UN experiences superior gas retention and swelling behavior than UC under similar irradiation conditions. The remaining discussion therefore centers on a comparison of UO_2 and UN swelling/gas release characteristics.

Zimmermann and Dienst Data

Zimmermann and Dienst (1975) and Zimmerman (1978) performed irradiation experiments with UO_2 and UN annular pellets. In the oxide tests an alternating arrangement of UO_2 and Mo pellets ensured a low

temperature gradient in the fuel. Because of the fabrication technique employed, the UN samples contained approximately 5-10 volume percent UO_2, generally in the form of inclusions at grain edges. Fuel temperatures in both experiments were measured via a thermocouple mounted in the mid-position between the inner and outer annular dimensions. Table 4 presents pertinent fuel characterisitics and irradiation conditions.

Table 4 *UO_2 and UN Fuel Characteristics and Irradiation Data at a Fuel Mean Temperature $\simeq$ 1500 K*[a].

Property	Unrestrained UO_2 Samples	Unrestrained UN Samples
Fuel density, percent TD	98	95
U-235 enrichment, percent	15	8
Mean grain diameter, μm	10	15
Fuel stoichiometry	$2.00 < 0/U < 2.005$	5–10 vol.– % UO_2
Pellet annular diameters, mm	5.1/2.2	9.87/2.9
Pellet height, mm	1	4.5–8.5
Burnup, atom-percent	0.4–12	1.0–3.0
Mean fuel temperature, K	1300–2020	1450–2070

Irradiation Results

Burnup, atom-percent	Volume Swelling, percent		Gas Release, percent	
	UO_2	UN	UO_2	UN
1	1	1	10	0.4
2	3	2	27	0.1
3	5	7	40	29

[a] Data from Zimmerman 1978 and Zimmerman and Dienst 1975.

Figure 4 presents the UO_2 swelling and gas release data as a function of burnup and temperature. The burnup dependence shows a linear increase in swelling at low and medium burnup values. However, at elevated burnup levels, the swelling rate diminishes, particularly for higher irradiation temperatures, which can be interpreted as due to the saturation of fission gas retention. Figure 4 also illustrates fission gas release results, showing the release fraction increasing with both temperature and burnup. The release fraction increases markedly with burnup in the region of one atom-percent.

Zimmerman's irradiation tests of annular UN fuel pellets were conducted to three burnup levels of 10, 20, and 30 MWd/kg-U. (As a rule-of-thumb 10^4 megawatt-days of thermal energy released per metric ton (10^3 kg) of heavy metal corresponds to 1.0 atom-percent burnup; that is 10 MWd/kg-U $\simeq$ 1.0 atom-percent burnup.) The effects of swelling were assessed via measurement of the change in fuel volume from its as-fabricated condition. Figure 5 presents the change in sample volume as a function of burnup for a mean fuel temperature of $\simeq$ 1520 K. The volume change, effect of sintering, and estimated fission gas induced swelling are plotted. As discussed by Zimmermann (1975), a decrease in initial volume due to radiation-induced sintering was noted, which concludes at a burnup of $\simeq$ 10

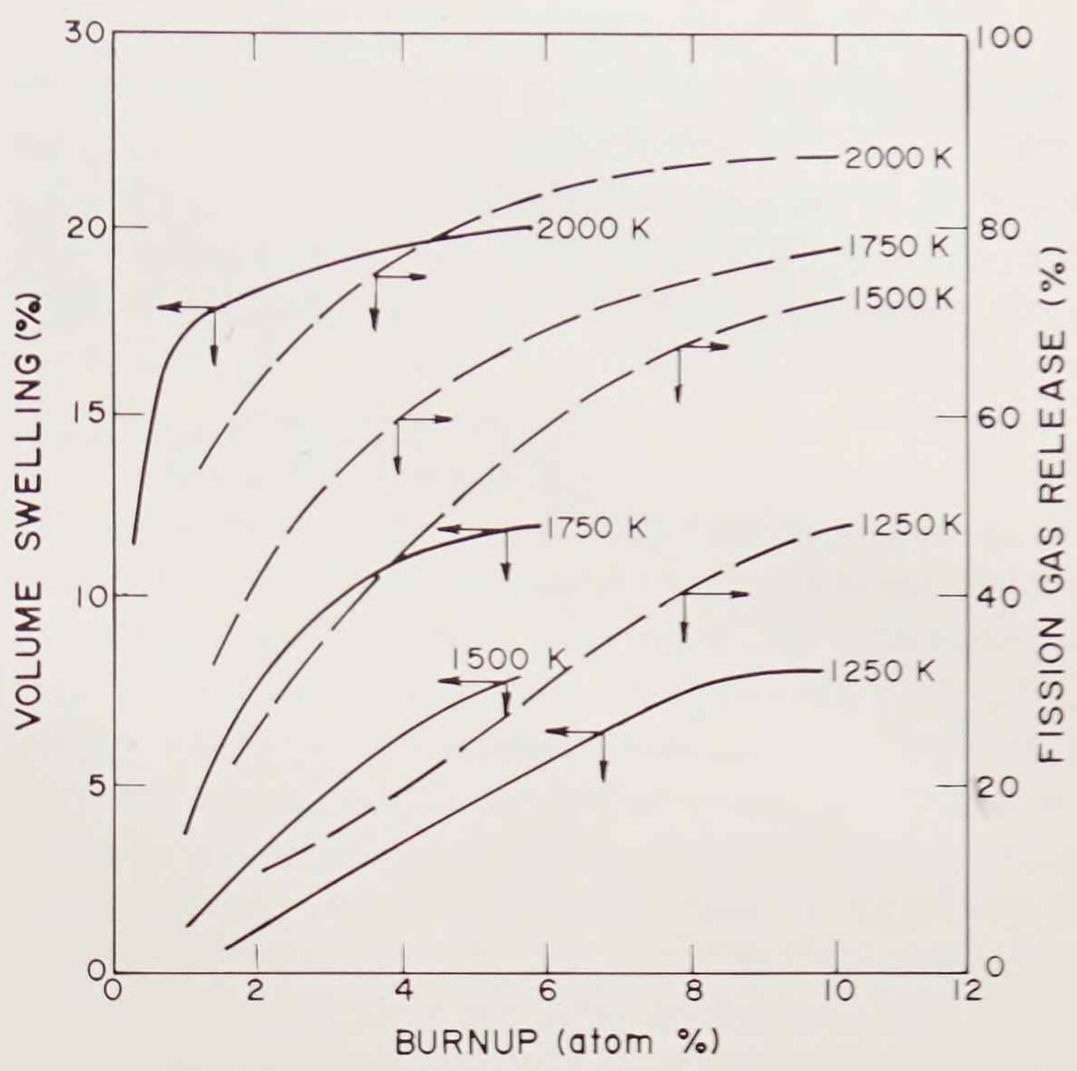


Figure 4 *UO_2 Volumetric Swelling and Fractional Gas Release as a Function of Burnup and Fuel Mean Temperature (Full Density $\simeq$ 98% TD). (Data from Zimmerman 1978.)*

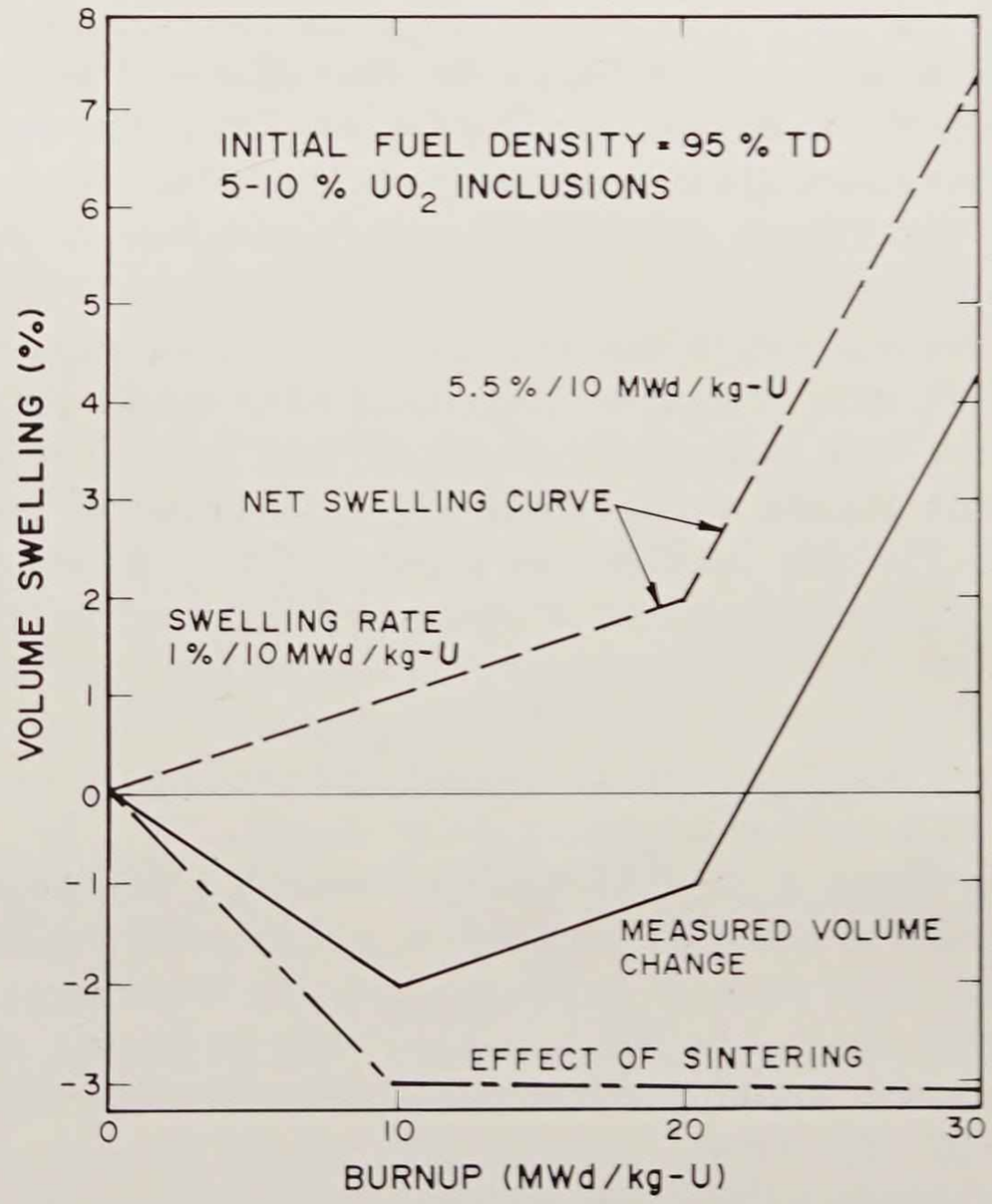


Figure 5 *UN Volume Change as a Function of Burnup at a Mean Fuel Temperature of $\simeq$ 1520 K. (Data from Zimmerman and Dienst 1975.)*

MWd/kg-U. The effect of sintering and the associated enlargement of the fuel-clad gap explains the observed drop in heat transfer coefficient noted at the beginning of irradiation. Subtracting out the effect of sintering from the measured value of volume change, Zimmermann obtained the fission gas swelling curve as indi-

cated. Below 20 MWd/kg-U the swelling rate is about one percent per 10 MWd/kg-U, while above 20 MWd/kg-U approximately 5.5 percent per 10 MWd/kg-U. It should be noted however, that the contamination of the UN samples with UO_2 inclusions may have influenced initial sintering and subsequent swelling characteristics.

A comparison of the UO_2 and UN swelling and gas release data is presented in Table 4. For the same mean fuel temperatures ($\simeq$ 1520 K) the data indicate similar volumetric swelling at low burnup levels. The UN sample however was more gas retentive than UO_2. Although caution must be used in extrapolation of this limited data, such a comparison illustrates that at equivalent fuel temperatures, the swelling of UO_2 and UN may be similar, which also corresponds to the trend observed by Hilbert et al. (1971). One can interpret such results as indicating that at equivalent burnup and temperature conditions the UO_2 must release more gas from the fuel matrix than UN, for a similar increase in volumetric swelling. Considering the combined advantages of limited swelling and gas release, UN may exhibit somewhat better irradiation performance characteristics than high density UO_2. The one caution in this interpretation is the rather sudden increase in swelling and gas release occurring for UN above 20 MWd/kg-U burnup (Figure 5). This behavior is similar to the breakaway swelling observed for UC at about 2% burnup for a cladding temperature of 1425 K (Weaver and Scott 1965).

In recent work by Rest (1983a and 1983b), the UO_2 fission gas release and swelling data of Zimmermann (1978) were analyzed using the FASTGRASS code, which is a mechanistic model for the prediction of fission gas and volatile behavior in stoichometric UO_2 fuel. The code calculates gas production from fissioning nuclei, bubble nucleation and re-solution, bubble migration, bubble coalescence, gas-bubble/channel formation of grain faces, interlinked porosity on grain edges, microcracking, gas release and swelling for steady-state and transient thermal conditions.

In Figure 6, the FASTGRASS calculated UO_2 swelling, due to retained fission gas, as a function of irradiation temperature is compared with the experimental results obtained by Zimmermann (1978). In general, the predicted swelling agrees quite well with the data trends. The results show a very strong temperature dependence of the swelling rate at low burnups. With increased burnup, the swelling rate and the temperature dependence diminish, which can be attributed to the predicted interlinked grain boundary porosity and attendant gas venting from the fuel matrix. A comparison of gas release results is presented in Figure 7. Grain diameters between 1 and 10 microns were used for the code calculations, for average fuel temperatures between 1250 and 2000 K. Good agreement is evident within the range of probable grain size. Such agreement

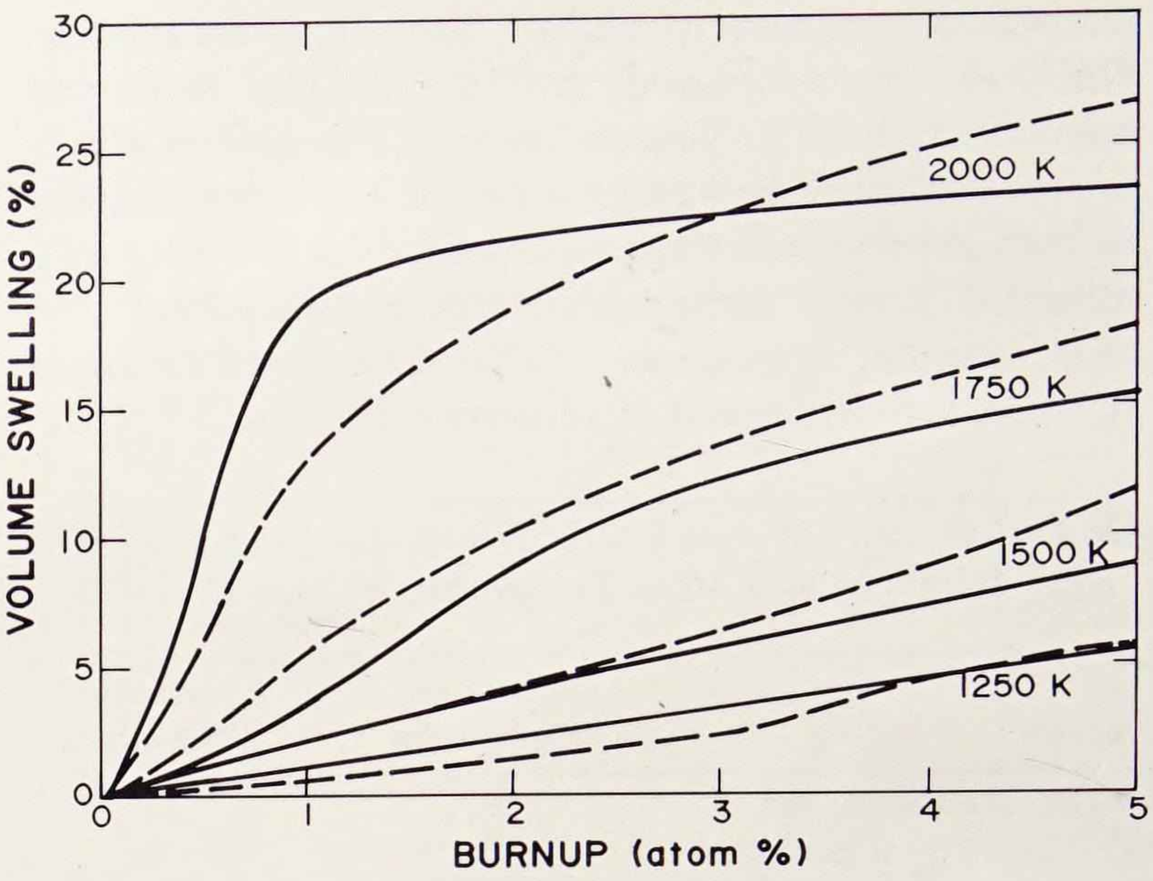


Figure 6 *Predicted Swelling of UO_2 (from Rest 1983a and 1983b) (Dotted Curves) as a Function of Fuel Temperature and Burnup compared with the Data of Zimmermann (1978) (Solid Curves).*

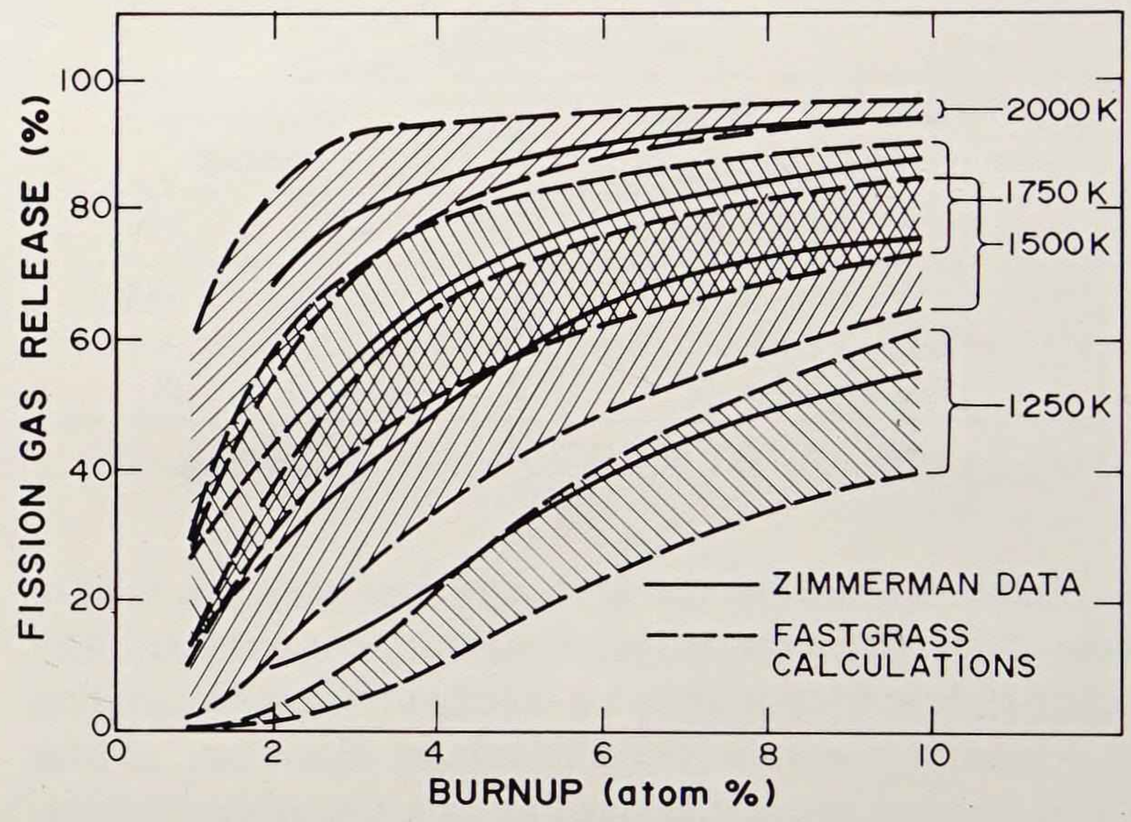


Figure 7 *FASTGRASS Predicted Fractional Fission Gas Release from UO_2 at 1250, 1500, 1750, and 2000 K (from Rest 1983a and 1983b) (Dotted Curves) compared with the Data of Zimmermann (1978) (Solid Curves).*

indicates to the present reviewers, that consideration should be given to the use of the FASTGRASS code for a preliminary evaluation of UO_2 fission gas release and swelling under SP-100 fuel conditions. Besides the Zimmermann data, Bowles and Gluyas (1975) also studied UO_2 and UN swelling/gas release phenomena under similar irradiation conditions. Their results are reviewed next.

Bowles and Gluyas Data

Bowles and Gluyas (1975) compared the irradiation performance of low and high density UN with high density UO_2 for space reactor applications. The variables studied were UN density (85 and 95 percent dense), fuel type (UN and UO_2), and cladding alloy

(Ta-8W-2Hf and Nb-Zr) (the numbers refer to the weight percent of constituents added to the base metal). The reason for varying initial UN density was to assess the effect of interconnnected-open porosity (low density fuel) versus closed porosity (high density fuel) on fission gas release and swelling phenomena. Pertinent initial conditions and swelling/gas release results are presented in Table 5. The data indicate that low-density/high-porosity UN experiences less swelling than high density UO_2, although at these burnup levels ($\leqslant$ 3-atom-percent) high density UN exhibits markedly higher swelling than UO_2, at equivalent density/porosity conditions.

Limited fission gas release data are given in Table 5. The fission gas release from the 95 percent dense UO_2 was six to eight times greater than the gas released from the 85 percent dense UN sample.

Metallographic examination of the UO_2 pellets indicated severe pellet cracking and weakening of the grain boundaries due to fission gas bubble pileup at grain interfaces. In comparing the 95 and 85 percent dense UN fuel samples, it was found that the fission gas induced diametral increase was more readily accommodated in the high-porosity/low-density specimen, as would be expected. The greater fission gas release fraction of the low-density UN may be a factor in this difference. Another factor may be the lower creep strength of the porous fuel, ameliorating its potential to strain the cladding. (The volumetric increase of these low density UN specimens may have been as much as 5%.) Of the three types of fuel, the 85 percent dense UN exhibited superior diametral stability and gas release characteristics.

Table 5 *UO_2 and UN Characteristics and Irradiation Data*[a].

Property	UO_2	UN
Cladding	Nb-Zr/T-111[b]	T-111[b]
Cladding liner	Tungsten (W)	Tungsten (W)
U-235 enrichment, percent	8.0–10.0	10.96–19.86
Fuel Density, percent TD	95	85/95
Pellet OD, cm	0.78	0.78
Burnup, atom-percent	1.67–2.04	2.64–2.87

Swelling Data (at cladding surface temperature $\simeq$ 1260 K)

Clad	Fuel Density, percent	Burnup, atom-percent	Cladding Diametral Change, percent
T-111	85-UN	2.87	0.2
T-111	85-UN	2.83	0.3
T-111	85-UN	2.79	0.2
T-111	85-UN	2.72	0.4
T-111	95-UN	2.74	1.5 (Cracked Cladding)
T-111	95-UN	2.64	3.7 (Cracked Cladding)
Nb-Zr	95-UO_2	1.67	0.5
T-111	95-UO_2	1.76	0.5
Nb-Zr	95-UO_2	2.04	1.0

Gas Release Data

Clad	Fuel Density, percent	Fission Gas Release, percent
T-111	85-UN	4.3
T-111	95-UO_2	34.9
Nb-Zr	95-UO_2	26.4

[a] Data from Bowles and Gluyas 1975.
[b] T-111 signifies Ta-8W-2Hf.

Interdata Comparison

In the previous sections swelling and gas release data were compared for different fuels irradiated under similar test conditions. Here such data are presented in composite graphs to illustrate UO_2 versus UN irradiation performance for a wide range of test conditions. Figure 8 illustrates swelling data from a number of sources. Several important features are first noted upon inspection of this figure, notably that all high burnup data for high density UO_2 are from Zimmermann, while no data are indicated for UN at burnup levels in excess of 3-atom-percent. Nevertheless, the fact remains that one cannot definitively conclude, based upon available data, an overriding superiority in swelling characteristics for UN over UO_2. Indeed at all burnup levels the UO_2 data generally show somewhat better swelling performance than UN, at equivalent fuel temperature. However, it is noted that because of a lower thermal conductance, UO_2 will exhibit higher fuel temperatures at an equivalent power rating than UN, which will induce somewhat greater swelling in UO_2 over that for UN, at least at low burnups.

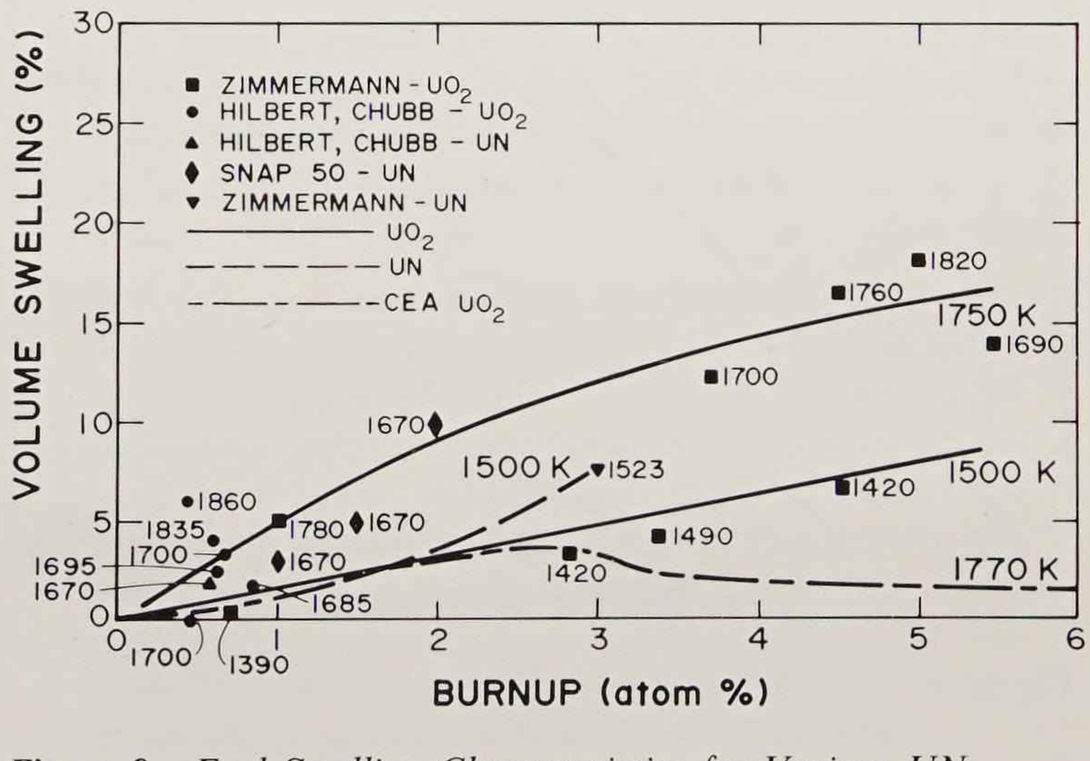


Figure 8 *Fuel Swelling Characteristics for Various UN and UO_2 Data as a Function of Burnup and Fuel Temperature. (Data from Zimmerman 1978, Hilbert et al. 1971, DeCrescente, Freed, and Caplow 1965a and 1965b, Huegel 1965, and Kauffman et al. 1980.)*

The practical effect of this observation is the tilt it gives towards using small diameter (and hence lower temperature drop) fuel rods with UO_2 or using molybdenum or tungsten fins for augmenting the thermal conductivity of the UO_2 when the resulting fuel volume fraction reduction can be tolerated.

These conclusions are based on comparative irradiation testing between UN and UO_2 where the specimen geometry and irradiation conditions were rather closely equivalent. In the one instance where lower density UO_2—fabricated with the use of pore formers—was irradiated under relatively isothermal, as well as unrestrained, conditions, the conclusions are substantially different. The lowermost curve in Figure 8 shows the swelling observed for 93% dense UO_2 irradiated in the form of 1-mm diameter spheres to burnups of approximately 2%, 4%, and 6% at an average fuel temperature of 1770 K (Kauffmann et al. 1980). The shape of the curve suggests that above 2% burnup fuel sintering forces counterbalanced residual fission gas swelling forces. As a result the swelling at 1770 K and 6% burnup was just slightly more than 1%.

Figure 9 illustrates a comparison of gas release behavior between UN and UO_2, where again it is noted that the data for UN are limited to burnup levels less than 3-atom-percent. Comparing the low burnup data, it can be seen that for equivalent fuel temperatures, the UN data indicate less gas release than from UO_2. Unfortunately the UN data are too limited to extrapolate to high burnup conditions. However, the trend is toward high fractional gas release for burnups greater than 3%.

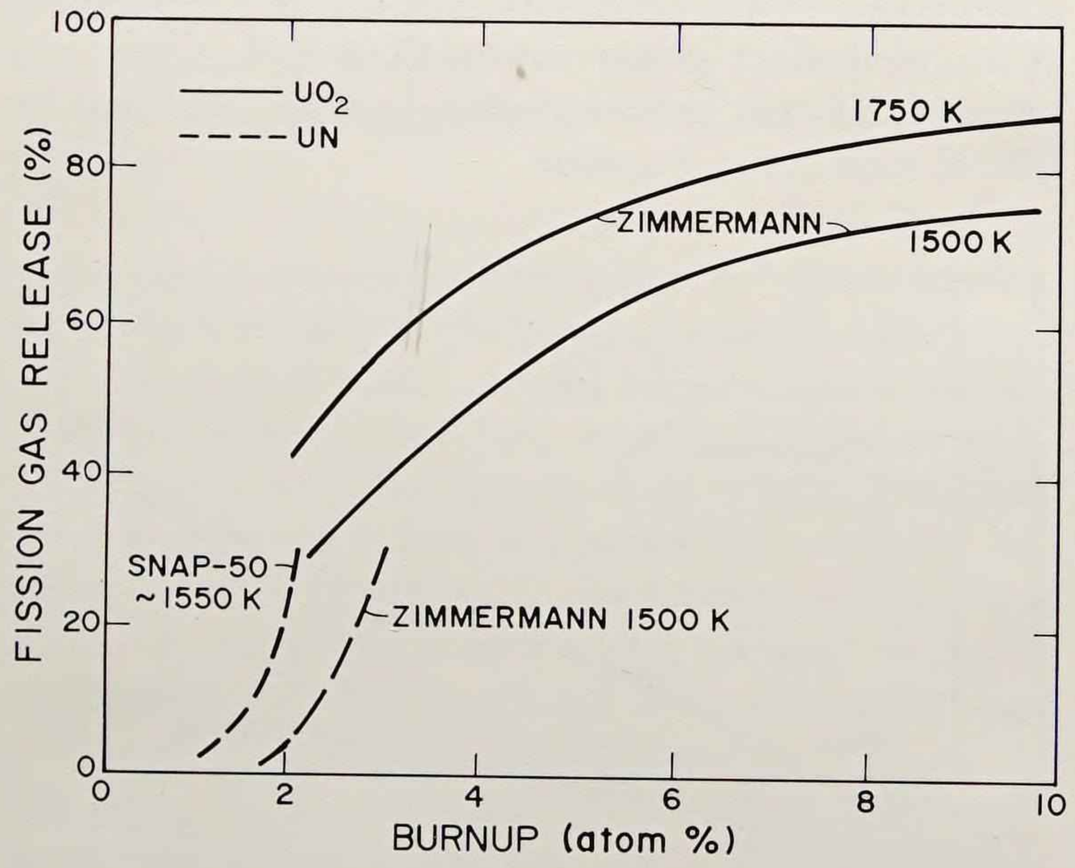


Figure 9 *Fission Gas Release Characteristics for Various UN and UO_2 Data as a Function of Burnup and Fuel Mean Temperature. (Data from Zimmerman and Dienst 1975, Zimmerman 1978, and DeCrescente, Freed and Caplow 1965a and 1965b.)*

Coated Particle Fuels

An alternative type of fuel configuration is the coated particle concept used successfully in gas cooled reactor design. In this concept the idea is to retain the fission gases in an impervious shell of high strength carbide. To date most irradiation experience has been with UC_2 or UO_2 kernels of fuel coated with a succession of graphite and SiC layers. For these particles the ratio of fuel volume to total particle volume has been low—on the order of 10%—so that they are of little interest for high performance space reactor design. However, a small amount of data consists for UO_2 kernels coated with sufficiently thin pyrocarbon and ZrC so that fuel volume fractions of 68 to 72% were obtained (Bullock and Kaae 1982). This data suggests that, for burnups on the order of 5% and coated particles surface temperatures of 1475 K, it may be possible to contain the fission gases within the particle. If such containment could be obtained with similarly coated UC particles it could eliminate the need for either a fission gas plenum or venting of the fuel rods and do so with relatively little penalty in fuel density compared to UO_2 fuel.

Fuel Swelling Effects in the In-Core Thermionic Converters

The fuel form for in-core thermionic reactors consists of relatively thin-walled cylindrical refractory metal cups filled with nuclear fuel. These cups are the fueled emitters which, when heated in cesium vapor to temperatures above about 1700 K by the fission process, produce the electron emission current upon which the thermionic conversion process is based. For reactor power levels of 100 kWe the optimum fuel emitter diameter is somewhat above two centimeters and the average emitter temperature is on the order of 1750–1800 K. The need for good electron emission properties and for fuel and clad stability at these temperatures has led to the selection of chemically vapor deposited tungsten as the cladding (high strength and excellent emission properties) and to UO_2 as the fuel. UC has been tested for this application but has been found to cause deterioration of the tungsten emission properties with time and has been observed to exhibit breakaway swelling at about 0.2% burnup at 1860 K (Fitzpatrick, Yates, and Schwarzen 1973). This behavior is shown in Figure 10 for both 1940 K and 1860 K. The initial density of this fuel was about 75% of theoretical. Associated with the sudden diametral increase of the tungsten cladding and fuel was a very pronounced fall-off of the surface area of the interconnected porosity, caused either by a coarsening of the initial porosity or a change from open to closed porosity.

Irradiation tests of tungsten clad UO_2 also show diametral increase. In this case it is roughly linear with burnup and amounts to about 4.3% increase in diameter for each 1% burnup in 28-mm diameter specimens with 1.0-mm tungsten cladding at 1780 K. Doubling the cladding thickness reduced the rate of diametral increase to approximately 2.4% per 1% burnup. A diametral increase of about 2% will cause the fueled emitter to short out to the collector that surrounds it in the typical thermionic fuel element design. It should be emphasized, however, that these dimensional increase rates represent initial values for data limited to about 0.3%

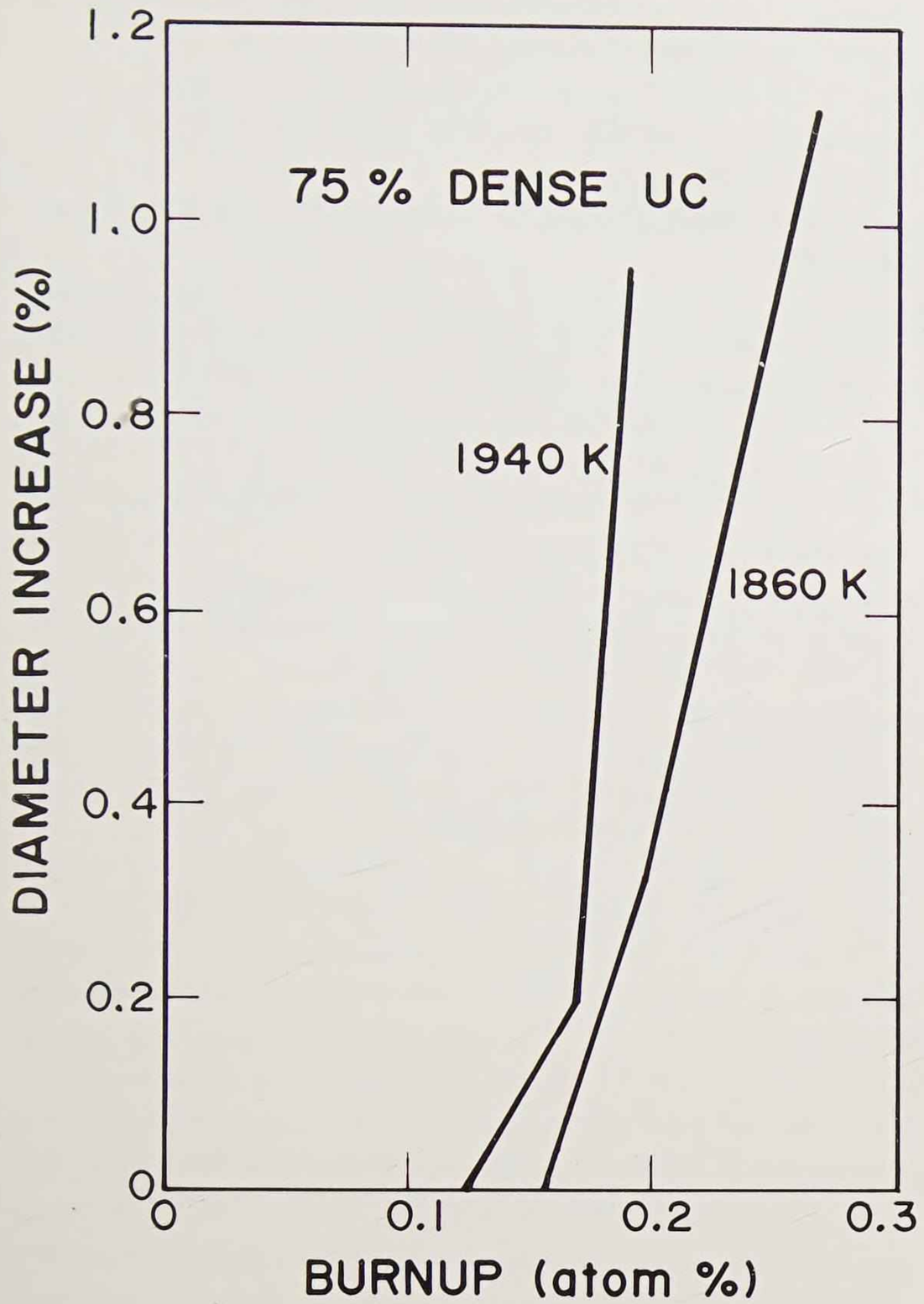


Figure 10 *Diametral Increase of Tungsten Clad versus Burnup for 75% Dense UC. (Data from General Atomic 1973.)*

burnup and it is likely that a linear extrapolation of these results will overpredict swelling at higher burnup values due to saturation-of-swelling effects. The lack of high-burnup experience for thermionic fuels, however, makes lifetime prediction tenuous.

The high disassociation pressure of UN (see Table 1) at thermionic emitter temperatures as well as unfavorable high temperature irradiation data in W-25Re cladding (severe cladding-fuel reaction and swelling) (Keller 1970) has discouraged the use of this fuel for the thermionic application. Further discussions of thermionic fuel element design and irradiation performance have been presented by General Atomic (1973) and Yang et al. (1972).

Summary/Conclusions

From the foregoing comparison of irradiation data, the following conclusions are drawn with respect to fission gas induced swelling and attendant gas release behavior.

Swelling Phenomena

- The predominant factors affecting fuel swelling are burnup level and temperature, where an increase in both results in increased swelling.
- Fission gas induced fuel swelling is caused primarily by the growth of *inter*granular bubbles entrapped at grain boundaries prior to the development of interlinked grain boundary porosity. Once such interlinked porosity has developed, fission gas release via 'tunneling' to the pellet exterior occurs, resulting in a saturation of swelling.
- For equivalent burnup, temperature, and fabricated porosity conditions, UC fuel experiences significantly more swelling than either UO_2 or UN. Enhanced swelling caused by fission gas has been observed for temperatures above about 1430 K for UC and at somewhat higher temperatures for UO_2 and UN.
- Fuel stoichiometry condition and impurity content can have a pronounced effect on swelling. Other factors being equal, *hyper*stoichiometric (nitrogen-rich) UN exhibits less swelling than *hypo*stoichiometric (nitrogen-deficient) UN, which is also true for UC. However, in general *hyper*stoichiometric UO_{2+x} experiences greater swelling than oxygen deficient UO_2, due to enhanced gas diffusivities in oxygen-rich UO_2.
- Although evidence exists that at equivalent fuel temperatures and burnup levels, UO_2 and UN experience comparable swelling behavior, differences in thermal conductivity influence overall irradiation performance. The low conductivity of UO_2 results in higher thermal gradients which contribute to fuel microcracking and gas release. As a result UO_2 exhibits higher gas release fraction than UN, at least for burnups up to about 3%.

Gas Release Phenomena

- The three predominant factors affecting fission gas release are porosity, burnup, and fuel temperature. Interconnected porosity in the fuel enhances gas release as do higher temperature and burnup conditions.
- The effect of as-manufactured fuel porosity is twofold. Closed porosity can serve as a collection vessel for fission gas so that fuel of this type can actually be more gas retentive than fully dense fuel where gas collects at grain boundaries and generates its own, eventually interconnected, porosity. Duplicating this self-generated interconnected porosity in the initial fuel may produce a fuel has inherently high gas release properties and consequently low swelling characteristics.
- Microcracking, due to fission gas pileup at grain boundaries and elevated temperatures, exerts a strong influence of gas release. Because UO_2 exhibits lower thermal performance, microcracking and attendant enhanced gas release can be expected to somewhat greater UO_2 than UN, other factors being equal.
- Venting of released fission gas into space may be a viable alternative to plenum containment. This is readily accomplished for reactor designs in the fuel surrounding the coolant channels, but introduces considerable design complexity for fuel pin type reactors. In addition, condensation of non-noble gas

volatile fission products such as iodine, cesium, strontium and tellurium and/or their associated compounds (for example, CsI and various tellurides) can introduce potential fission product induced corrosion and plugging of vent lines.

Acknowledgments

This work was performed at Engineering Science and Analysis and at Los Alamos National Laboratory under funding from the U.S. Department of Energy.

References

Barnes, R. S. and D. J. Mazey (1963) "The Migration and Coalescence of Inert Gas Bubbles in Metals," *Proc. Roy. Soc. A275*:47.

Bowles, K. J. and R. E. Gluyas (1975) *Evaluation of Refractory-Metal-Clad Uranium Nitride and Uranium Dioxide Fuel Pins After Irradiation for Times Up to 10,450 Hours at 990° C*, Report NASA-TND-7891.

Bullock, R. E. and J. L. Kaae (1982) *Performance of Coated Oxide Particles Gettered with ZrC*, Report GA-A16624.

DeCrescente, M. A., M. S. Freed, and S. D. Caplow (1965a) *Uranium Nitride Fuel Development: SNAP-50*, Report PWAC-488.

DeCrescente, M. A., M. S. Freed, and S. D. Caplow (1965b) *Uranium Carbide Fuel Development: SNAP-50*, Report PWAC-489.

General Atomic (1973) *Final Report on Thermionic Reactor Program*, Report Gulf-GA-12608.

Hilbert, R. F., W. Chubb, V. W. Storhok, and D. L. Keller (1971) "Swelling of UC and UN at High Temperatures," *Proc. Conf. Fast Reactor Fuel Element Technology*, New Orleans, LA.

Hilbert, R. F., V. W. Storhok, W. Chubb, and D. L. Keller (1971) "Mechanisms of Swelling and Gas Release in UO_2," *J. Nucl. Mater.* 38:26–34.

Huegel, F. J. (1965) *Swelling of Irradiated UC and UN*, Report PWAC-482.

Kauffman, Y., J. P. Morlevat, J. C. Janvier, and M. Bruett (1980) "Unconstrained Swelling of UO_2," *Proc. Fuel Element Performance Computer Modelling Specialists' Conference*, Blackpool, UK.

Keller, D. L. (1970) *Progress on Development of Fuels and Technology for Advanced Reactors*, Report BMI 1886.

Olander, D. (1976) *Fundamental Aspects of Nuclear Reactor Fuel Elements*, ERDA Publication, TID-26711-P1.

Rest, J. (1983a) "Evaluation of Volatile and Gaseous Fission Product Behavior in Water Reactor Fuel Under Normal and Severe Core Accident Conditions," *Nucl. Tech.* 61:33–48.

Rest, J. (1983b) "An Improved Model for Fission Product Behavior in Nuclear Fuel During Normal and Accident Conditions: Comparison with Experimental Data and Identification of Key Uncertainties," *J. Nucl. Mater.* (submitted).

Weaver, S. C. and J. L. Scott (1965) *Comparison of Reactor Fuels for High Temperature Applications*, Report ORNL-TM-1360.

Yang, L. et al. (1972) "Development Status of Thermionic Materials," in *Proc. 7th Intersociety Energy Conversion Engineering Conference*, September 25, 1972.

Zimmermann, H. and W. Dienst (1975) *Irradiation Behavior of UN*, Report LA-TR-75-22.

Zimmermann, H. (1978) "Investigations on Swelling and Fission Gas Behavior in Uranium Dioxide," *J. Nucl. Mater.* 75:154–161.

Space Nuclear Power Systems 1984
Edited by M. S. El-Genk and M. D. Hoover
© Orbit Book Company, Malabar, FL, 1985

Chapter 38

The Behavior of Mixed-Oxide Fuel Subjected to Multiple Thermal Transients

G. R. Fenske, L. A. Neimark, and R. B. Poeppel
Materials Science and Technology Division
Argonne National Laboratory
Argonne, Illinois 60439

G. L. Hofman
EBR-II Project
Argonne National Laboratory
Argonne, Illinois 60439

The microstructural behavior of irradiated mixed-oxide fuel subjected to multiple, mild thermal transients was investigated using direct electrical heating. The results demonstrate that significant intergranular porosity, accompanied by large-scale ($>90\%$) release of the retained fission gas, developed as a result of the cyclic heating. Microstructural examination of the fuel indicated that thermal-shock-induced cracking of the fuel contributed significantly to the increased swelling and gas release.

Introduction

Commercial and defense-related activities in space are projected to have power requirements in the range from 100 kW to 10–100 MW, and, depending on the application, the power requirements may fluctuate with time by several orders of magnitude. Two schemes currently under consideration to meet load fluctuation requirements involve the use of nuclear reactors. In one scheme, a relatively low-power steady-state reactor would be used to charge an energy storage system (such as batteries or fuel cells). Low-power requirements would be met by steady-state operation of the reactor/storage system, while temporary high-power requirements would be met by discharging the storage system. In the other scheme, the load-following power requirements would be met by operating the reactor at different power levels. However, reactor load following has a potential disadvantage: The system reliability may be impaired by fuel swelling and microcracking phenomena caused by the thermal transients that occur during the power cycles. This is of particular concern for fuel/cladding concepts that use fuels with high fission gas retention (such as carbides and nitrides).

In this paper, we analyze the results of a series of direct electrical heating (DEH) experiments (Bandyopadhyay, Buzzell, and Hofman 1980a and Hofman et al. 1979) that investigated the microstructural changes (and associated swelling) and fission gas behavior of irradiated mixed-oxide fuel subjected to single and multiple mild thermal transients similar to those that might occur in a pulsed duty-cycle reactor. These experiments were performed to investigate the behavior of oxide fuel elements that would act as driver fuel for a transient test reactor. The results suggest that during thermal transients (particularly cyclic transient conditions), thermal-shock-induced cracking of grain boundaries and grain edges contributes significantly to fuel swelling and fission gas release phenomena, both of which are important in cladding failure mechanisms.

The DEH technique and the transient thermal histories of the tests are described in this paper along with the post-test experimental results on the fuel swelling, microcracking, and gas release behavior. The analysis by Bandyopadhyay and his coworkers (1980a) of the phenomena that can account for the observed trends is also presented. Finally, we discuss the relevance of these results to alternative ceramic fuels such as carbides and nitrides.

Experimental Technique

The basic concept of DEH is to use ohmic heating to simulate the nuclear heating during a reactor transient, by passing an electrical current through a stack of fuel pellets or a segment of an irradiated fuel element. This technique was originally utilized at Argonne National Laboratory (ANL) by Wrona and coworkers (1976 and 1977) to investigate the transient behavior of unirradiated UO_2. Later applications with irradiated fuel were developed by Bandyopadhyay and coworkers (1977, 1978a, 1978b, 1979, and 1980b) and Fenske and Bandyopadhyay (1981) to simulate hypothetical fast reactor transients, and by Gehl (1979 and 1982) to simulate hypothetical light water (LWR) accidents.

A schematic of the DEH system used in these experiments is shown in Figure 1. A segment (~25 mm long) of irradiated fuel was placed between two tungsten electrodes. To prevent the electrical current from short-circuiting through the stainless steel cladding surround-

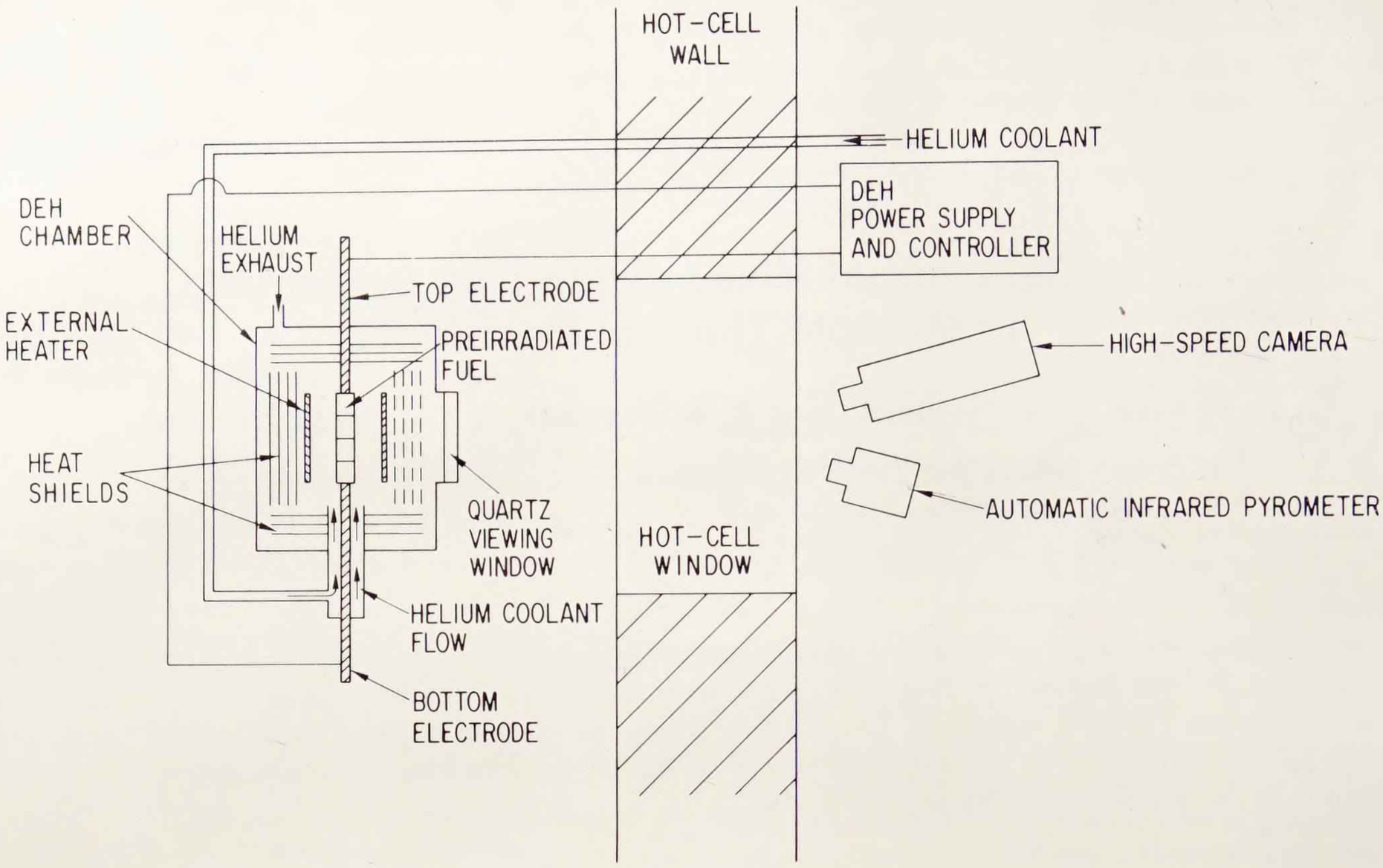


Figure 1 *Schematic of the DEH System Used to Investigate the Transient Behavior of Irradiated Fuel.*

ing the fuel, the fuel was extruded into appropriately sized quartz tubes. The external tungsten wire mesh heater and heat shield assembly that surround the fuel stack are used in conjunction with the DEH to control the temperature gradients and heating rates. During each test, the current flowing through and the voltage drop across the fuel segment, together with measurements of the surface temperature, were recorded for subsequent calculations of the transient temperature profile using the DIPHASE code (Das et al. 1983). A high-speed camera was also used to record the macroscopic behavior of the fuel; however, because the present work involved mild transients, the high-speed movies were not analyzed, but rather served as a check on the uniformity of the heating.

Description of Thermal Transients

After a flat radial temperature profile (with a surface temperature of ~925°C) was established by use of the external heater, the segments of fuel were subjected to transients 5–10 s in duration at surface heating rates of 80–100°C/s. The external heater remained on during the transient. Power to the fuel and heater were shut off when the surface temperature reached 1400°C, at which time a gas flow of helium over the sample was increased to a maximum to aid in cooling the surface. The maximum centerline temperature under such conditions was typically ~2600°C; nevertheless, in one test (E-20), the fuel did experience ~4% melting (by area). However, this level of melting did not significantly influence the results.

A number of single- and multiple-cycle transients were performed on segments of fuel from low-(P-15-55c) and medium-(PNL 9-13) burnup fuel pins irradiated in EBR-II at 18 kW/m to peak axial burnups of 0.5 and 5 at.%, respectively. Table 1 summarizes the following variables for each test: fuel burnup, fabricated fuel density and grain size, number of heating cycles, maximum surface and centerline temperatures for each cycle, average surface and centerline heating rates for each cycle, the energy absorbed (J/g) during each cycle and the average heating rate (J/g · s) during each cycle. Note that the average energy input rate during the transients was ~24 – 45 J/g · s. Assuming a heat capacity of ~1/2 J/g · °C, the heating rate (volume averaged) ranged from ~50 to 90°C/s.

Post-Test Characterization

The local fuel swelling that occurred during irradiation and during the transients was calculated based on the radial porosity distributions and the as-fabricated porosity as determined by standard ceramographic examination of as-irradiated and DEH-tested fuel segments. (Percent local swelling = 100 × (final pore volume fraction)/(1 – final pore volume fraction) where final pore volume fraction = measured porosity – fabricated porosity.) The volume-averaged swelling was determined by normalizing the sum of the local swelling and the volume exhibiting that swelling over the entire volume of the specimen. The swelling measured by this technique is only representative of the intergranular swelling and not of the intragranular swelling.

Table 1 *Description of the Direct Electrical Heating (DEH) Experiments.*

Test No.	Fuel Burnup (atom percent)	Fuel Density[a] (%T.D.)	Grain Size[b] (μm)	No. of cycles	Maximum Surface Temperatures (°C)	Avg. Surface Heating Rate (°C/s)	Maximum Centerline Temperature (°C)	Average Centerline Heating Rate (°C/s)	Energy Absorbed[d] (J/g)	Average Energy Input Rate (J/g · s)
E10	0.5	89.8	10	1	1410	88	1960	184	244	45
E11	0.5	89.8	10	4	1405	62	2500	193	331	42
					1390	116	1750	190	206	52
					1400	35	2030	77	250	19
					1410	74	2350	209	299	46
E12	0.5	89.8	10	2	1410	44	2650	147	358	32
					1410	57	2430	168	319	37
	0.5	89.8	10	8	1410	91	2030	196	251	47
					1400	106	1840	189	221	49
					1420	68	2470	203	325	45
					1420	89	2000	188	247	46
					1415	87	2020	182	248	44
					1410	46	2640	158	360	34
					1390	99	1650	143	193	41
					1410	71	2260	185	287	42
E17	5.0	90.1	10	1	c	c	c	c	c	c
E18	5.0	90.1	10	2	1300	101	1630	192	176	48
					1230	35	2440	173	282	32
E20	5.0	90.1	10	8	1350	38	2660	150	347	31
					1350	47	1810	91	197	22
					1350	56	2516	197	296	39
					1340	26	1400	27	140	11
					1350	40	2780	164	357	33
					1340	39	2700	158	345	32
					c	c	c	c	c	c
					1345	36	1530	49	160	14
E25	5.0	90.1	10	4	1355	48	2430	164	308	35
					1355	44	2665	172	341	35
					1340	115	1660	191	184	51
					1355	39	2820	166	367	33

[a] As-fabricated fuel density (percent of theoretical density); data on as-irradiated density/porosity is presented in the text.
[b] As-fabricated grain size (assumed).
[c] Data for these cycles were not available.
[d] The thermal histories originally presented (Bandyopadhyay 1980a) were recalculated using an improved version of the DIPHASE code. The original values differ from those presented above; however the analysis and conclusions are not changed.

Fracture surfaces of as-irradiated and DEH-tested segments were examined by scanning electron microscopy (SEM) to evaluate how changes that occurred in the inter- and intragranular fission gas bubble morphology may have contributed to the observed fuel swelling and gas release behavior. Detection of fission gas bubbles was limited by the resolution of the SEM (~700-Å detection limit).

One of the as-irradiated fuel segments and one DEH-tested segment were analyzed using a laser microsampling technique (Graczyk et al. 1979). This technique is capable of measuring the radial distribution of the inter- and intragranular ^{85}Kr gas, which when properly normalized provides information on the transient fission gas release.

Fuel Swelling

Ceramographic cross sections of as-irradiated P-15-55c and PNL9-3 fuel are shown in Figures 2a and b, respectively. Both types of fuel were fabricated with ~10% porosity. The P-15-55c fuel (0.5 at.% burnup) showed no significant change in the radial distribution of the porosity due to irradiation. In the PNL9-3 fuel, however, grain boundary swelling due to irradiation near the center of the fuel produced local porosities of ~20%. Near the edge, the porosity remained at ~10%.

Ceramographic examination of the DEH-tested segments indicated that significant swelling occurred during the thermal transients. Most of the porosity oc-

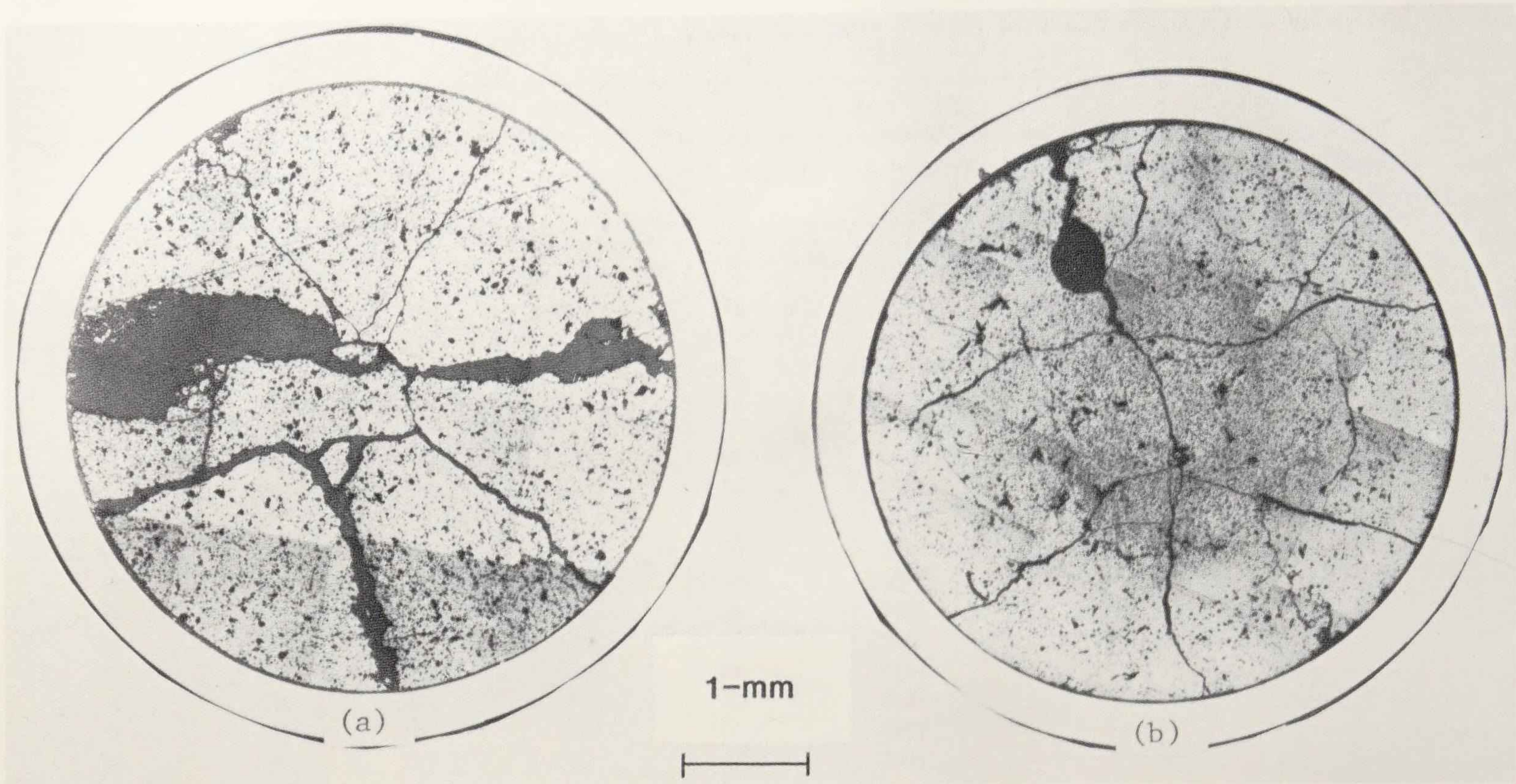


Figure 2 *Ceramographic Cross Sections of As-irradiated Fuel Used in the Cyclic DEH Experiments (a) P-15-55c (0.5 a/o burnup) Fuel and (b) PNL9-3 (5.0 a/o burnup).*

curred at the grain boundaries or grain edges. The maximum porosity observed was ~25%, which is in agreement with previous DEH tests on mixed-oxide fuel (Bandyopadhyay and coworkers 1977, 1978a, 1978b, 1979, and 1980b). Examples of the porosity that occurred at three different radial locations (defined as fractions of R_0, the radius that corresponds to the fuel outer surface) are shown in Figure 3 for PNL9-3 fuel subjected to eight cycles (test E20). Near the center of the fuel (Figure 3c), where the higher temperatures occurred, the porosity is extensive and surrounds entire grains. However, near the outer regions (Figures 3a and b), the grain boundary porosity (or separation) is not as severe, and is characterized by "microcracks," which, as discussed later, are a result of thermal-shock-induced cracking and are particularly prevalent under cyclic heating conditions in the presence of grain boundary fission gas.

SEM examination of fracture surfaces of DEH-tested segments of fuel provided further information on the character of the observed fuel swelling. Both intra- and intergranular fission gas bubbles were observed, as shown in Figures 4 and 5, respectively. Figure 4 illustrates the type of intragranular swelling that occurred in

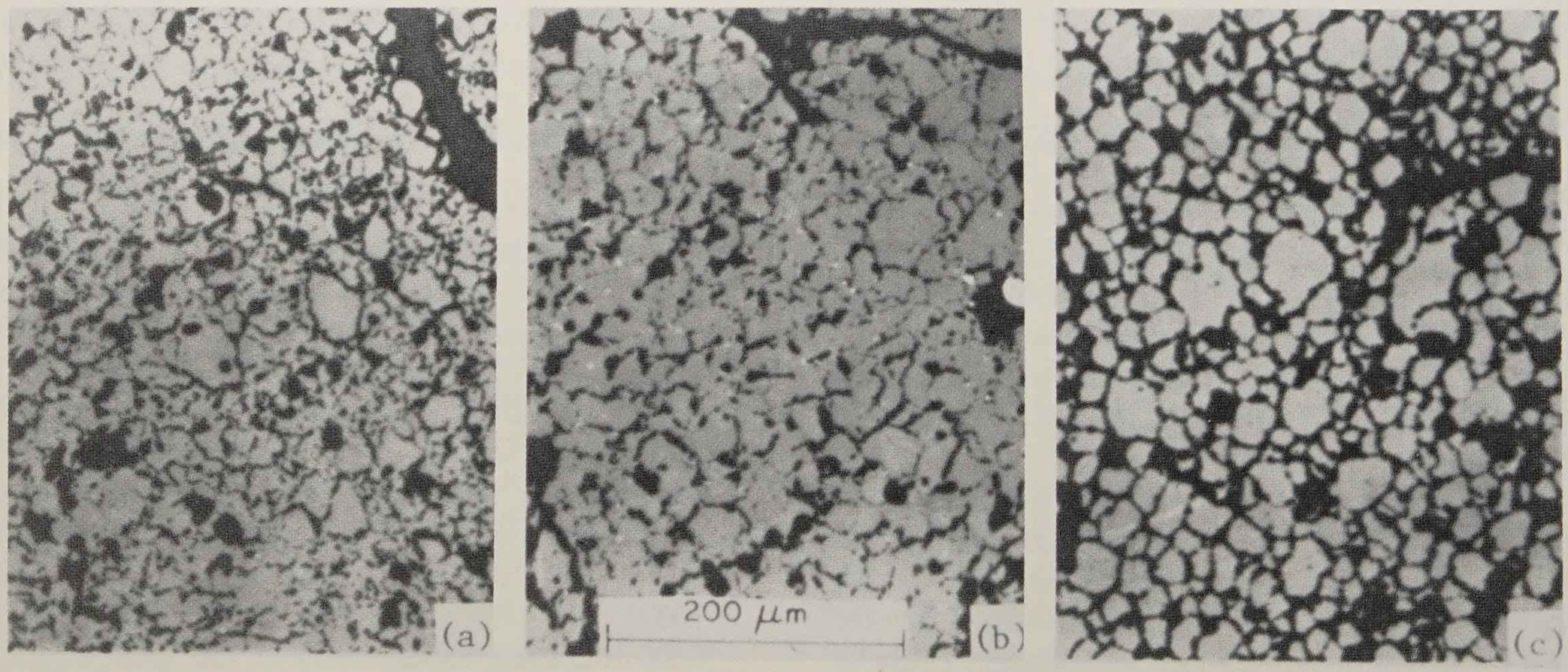


Figure 3 *Ceramographic Sections of PNL9-3 (5 a/o burnup) Fuel Segment Subjected to Eight Heating Cycles. The Photographs Illustrate the Grain Boundary Porosity Generated at Radial Positions of (a) 0.95 R_0, (b) 0.7 R_0, and (c) 0.2 R_0, where R_0 is the Fuel Radius.*

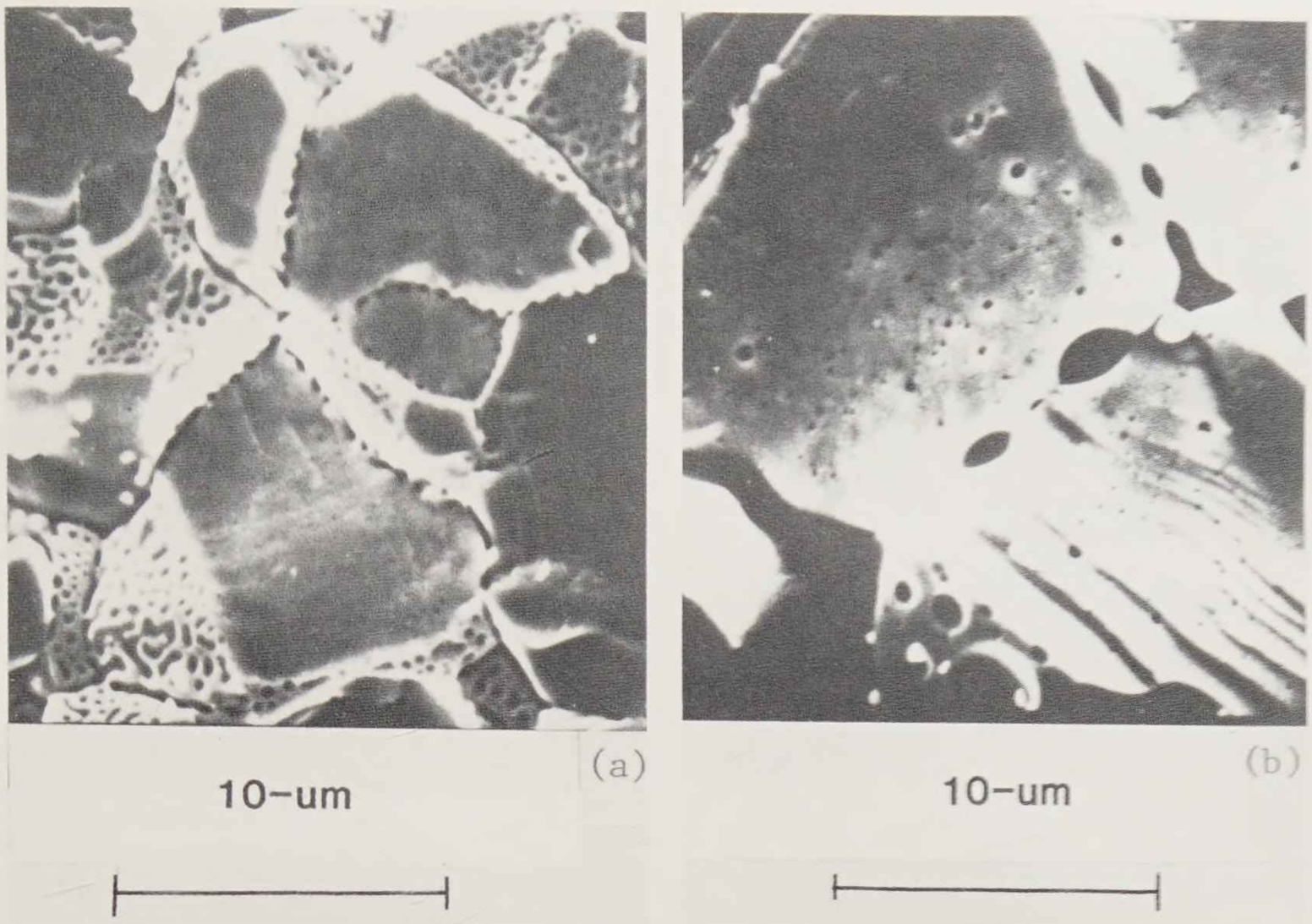


Figure 4 *Scanning Electron Micrographs of Fuel after Four DEH Cycles, Illustrating Intragranular Fission Gas Bubbles in (a) P-15-55c (0.5 a/o burnup) Fuel after Test E11 at 0.8 R_0, and (b) PNL9-3 (5.0 a/o burnup) Fuel after Test E25 at 0.6 Ro.*

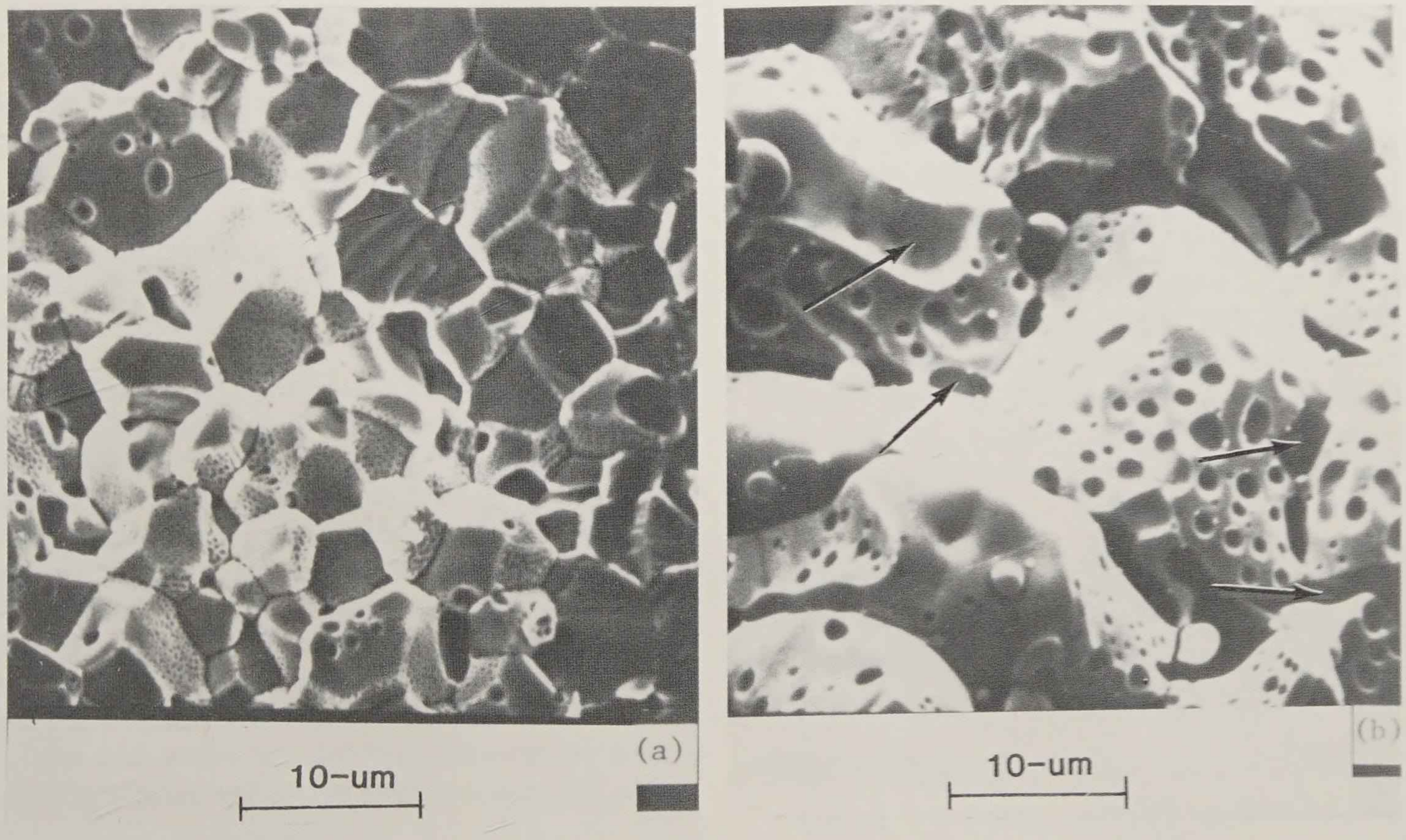


Figure 5 *Scanning Electron Micrographs Illustrating Intergranular Fission Gas Bubbles in (a) P-15-55c (0.5 a/o burnup) Fuel after Test E-25 at 0.5 R_0. The Arrows in (b) Illustrate Grain Boundary Tunnels.*

the P-15-55c and PNL9-3 fuel. The intragranular bubbles ranged in size from ~900 to 2000 Å, with densities between 0.5 and 4×10^{19} bubbles/m^3. The intragranular swelling was small in magnitude (less than about 1 vol.%) compared to the intergranular swelling determined by quantitative analysis of the ceramographic samples (Figure 3); therefore, the intragranular swelling was not included in the total swelling calculations.

Several distinct types of intergranular gas bubble networks were observed, as seen in Figure 5a and b. The intergranular bubble network (for unrestructured

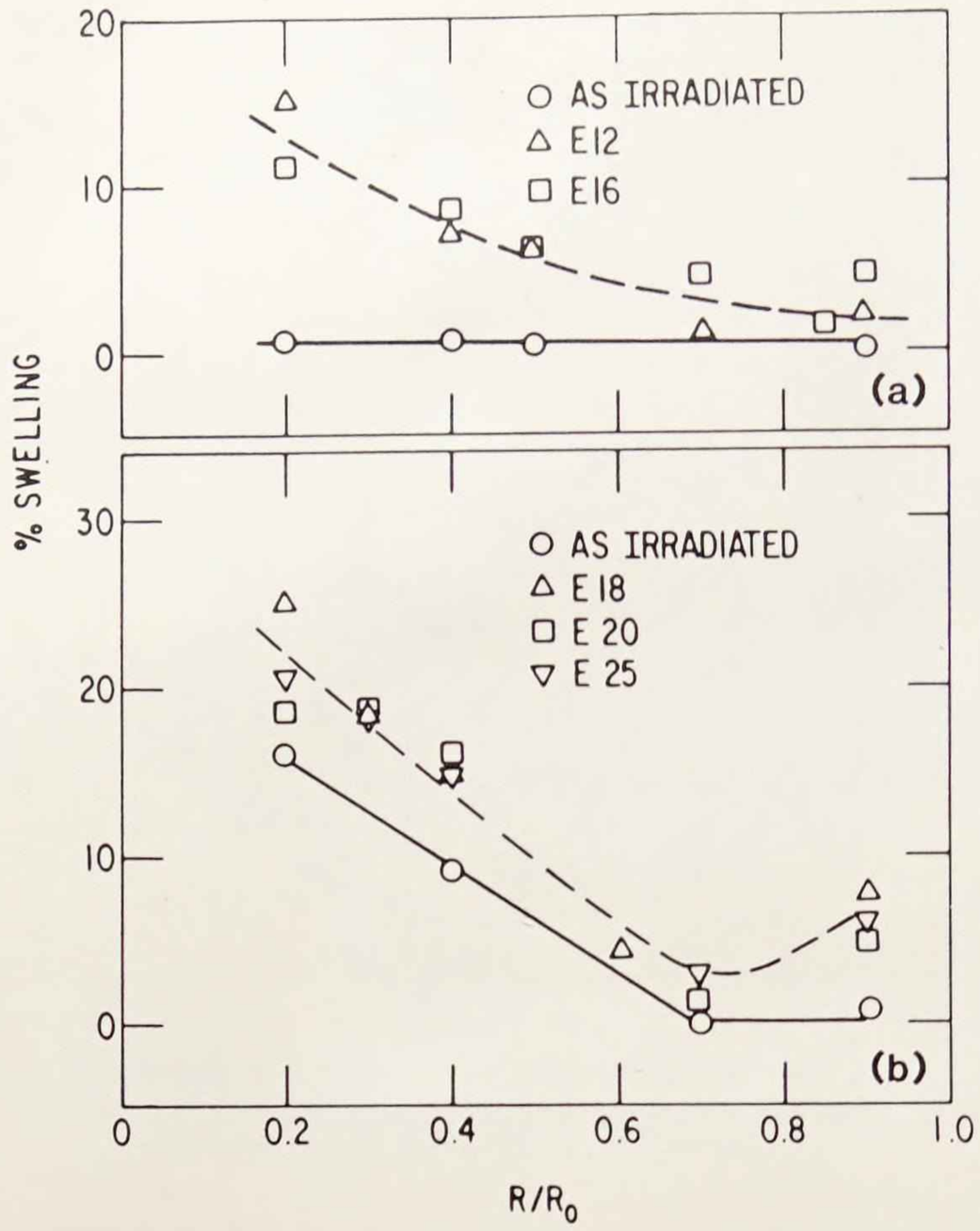


Figure 6 *Measured Swelling as a Function of Radial Position for As-irradiated and Transient-tested Fuel (a) P-15-55c (0.5 a/o burnup), and (b) PNL9-3 (5.0 a/o burnup). The Dashed Lines Show Approximate Trends for the Transient-tested Fuel.*

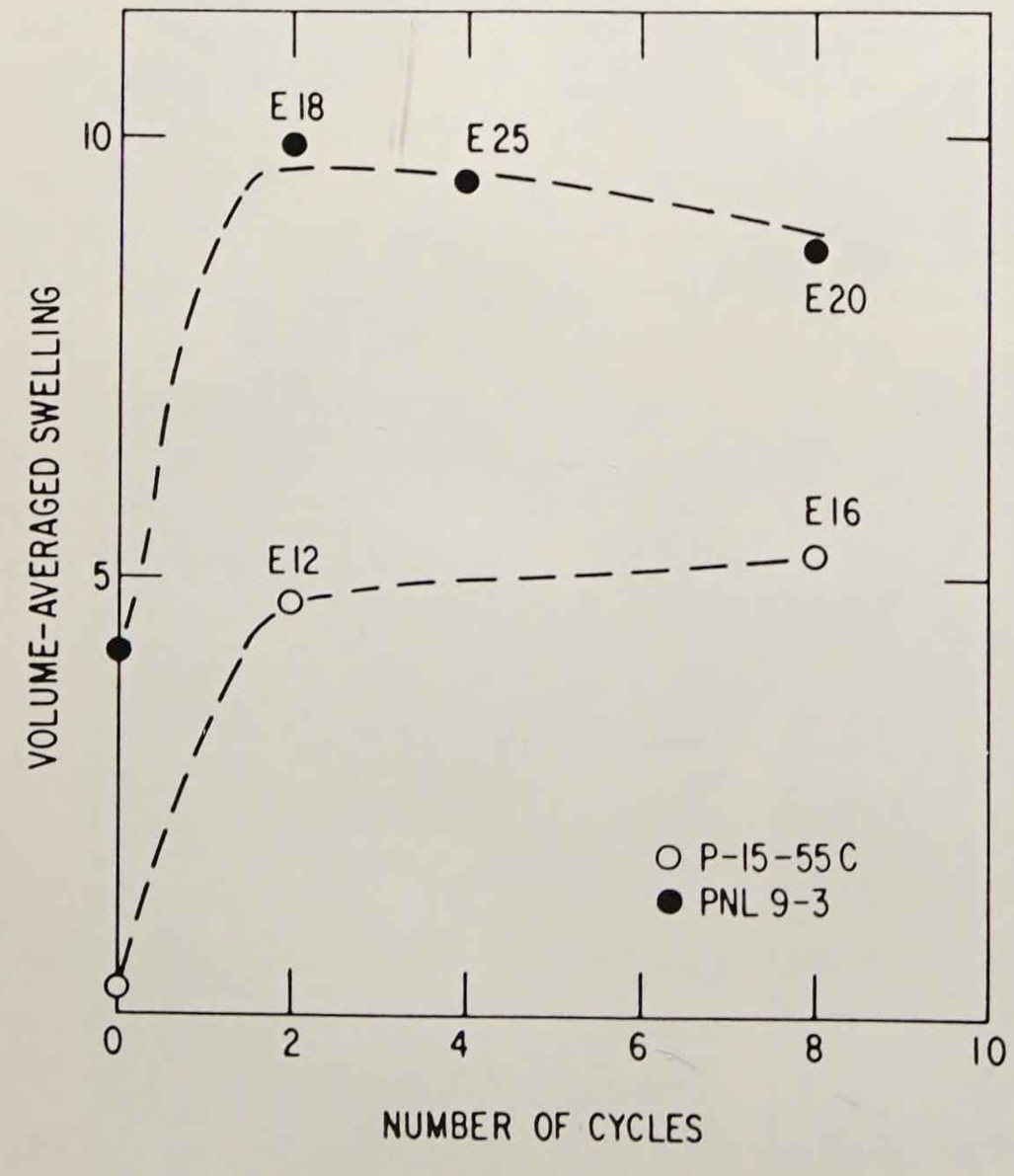


Figure 7 *Volume-averaged Swelling of As-irradiated and DEH-tested P-15-55c (0.5 a/o burnup) and PNL9-3 (5.0 a/o burnup) Fuel as a Function of the Number of Heating Cycles.*

P-15-55c fuel subjected to two heating cycles) seen in Figure 5a shows an early stage of bubble coalescence occurring on the grain faces. The network seen in Figure 5b (PNL9-3 fuel subjected to four heating cycles) shows evidence of extensive interlinkage (larger bubble sizes and lower densities) of grain boundary bubbles and the development of grain edge tunnels.

Figure 6 shows the measured swelling of as-irradiated and a select number of DEH tested segments of P-15-55c and PNL9-3 fuel as a function of radial position. The maximum uncertainty in the swelling data shown in Figure 6 is $< 5\%$. The dashed lines show approximations to the radial variation in the swelling. The volume-averaged swelling of P-15-55c and PNL9-3 fuel segments is shown in Figure 7 as a function of the number of heating cycles. As seen in Figures 6 and 7, the swelling of P-15-55c fuel due to steady-state irradiation in EBR-II was small ($\sim$0.3%); it was also independent of radial position (Figure 6). For the PNL9-3 fuel, the steady-state swelling was dependent on radial position, with $\sim$15% swelling near the center and near-zero swelling at the surface for a volume-averaged swelling of $\sim$4%. Figures 6 and 7 also demonstrate that the cyclic thermal transients resulted in additional swelling for all radial positions, resulting in an additional 4–6% volume-averaged swelling for the PNL9-3 fuel, and an additional $\sim$5% swelling for the P-15-55c fuel. Also as seen in Figure 7 the swelling ceased and essentially remained constant (within the 5% uncertainty of the swelling data) after the second heating cycle. (Since quantitative swelling measurements were not made after the first cycle, the swelling may have reached a maximum and ceased after only the first cycle.)

Fission Gas Release

Laser microsampling (Graczyk et al. 1979) was performed on as-irradiated and DEH-tested (four cycles) segments of PNL9-3 fuel to determine the radial distribution of inter- and intragranular ^{85}Kr and thus obtain data on the gas release due to the transient. This technique distinguishes inter- and intragranular gas components by performing sequential ^{85}Kr sampling of the same region. (The test region consists of a volume that undergoes fuel melting surrounded by a larger volume that undergoes grain boundary cracking.) The first sampling provides data on the total (inter- plus intragranular) ^{85}Kr concentration while the second sampling of the same region provides data only on the intragranular component because the intergranular component was previously released during the first sampling. The intergranular component is then deduced from the total- and intragranular concentrations. Figure 8 shows the results of this gas release analysis for the as-irradiated and DEH-tested (E25) fuel segments. The total ^{85}Kr content of the as-irradiated fuel shows a peak concentration in the unrestructured region at a location of

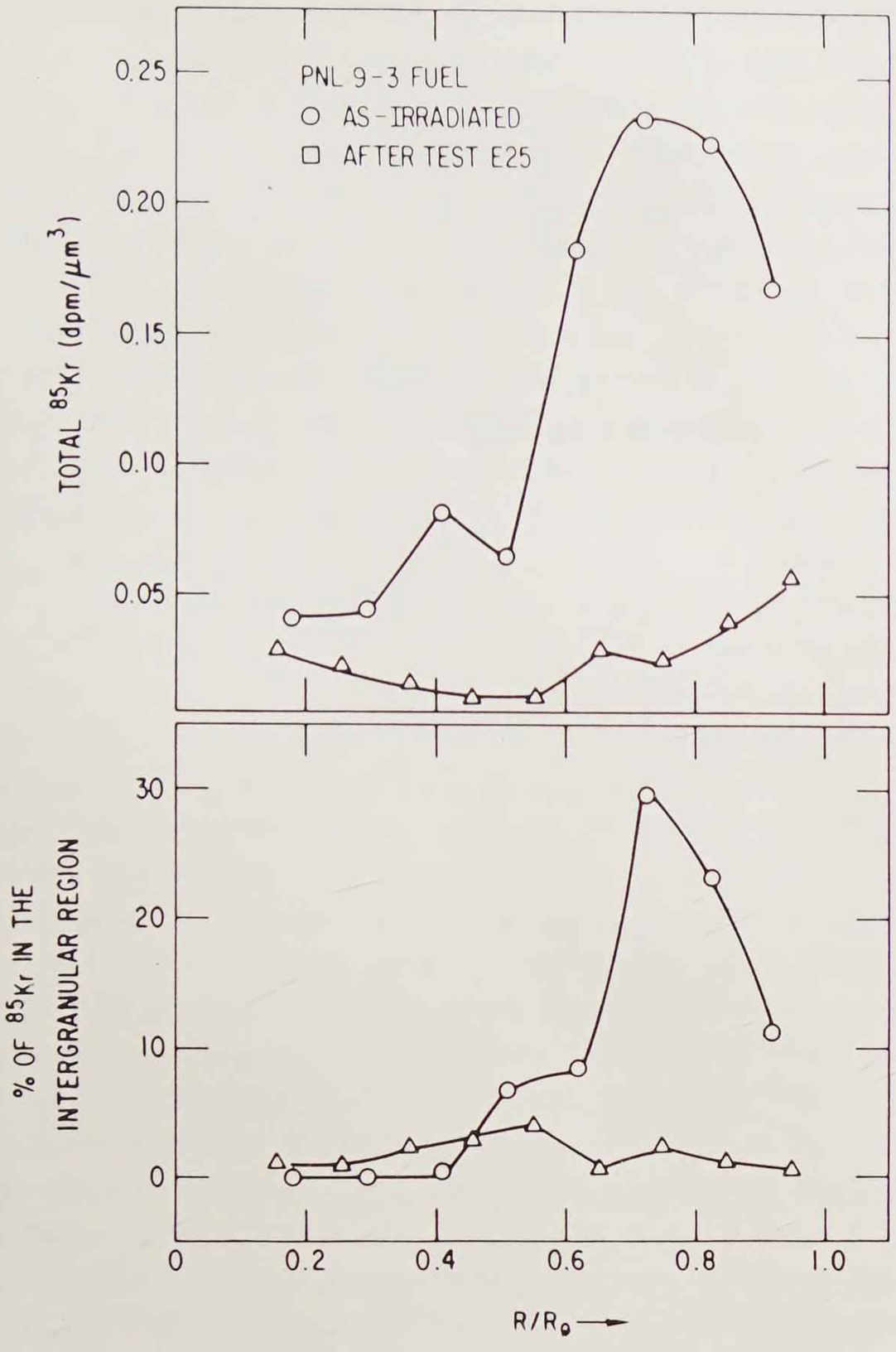


Figure 8 *Laser Microsampling Data on the Retained Fission Gas in Intra- and Intergranular Regions of As-irradiated and DEH-tested (E25) PNL9-3 (5.0 a/o burnup) Fuel as a Function of Radial Position.*

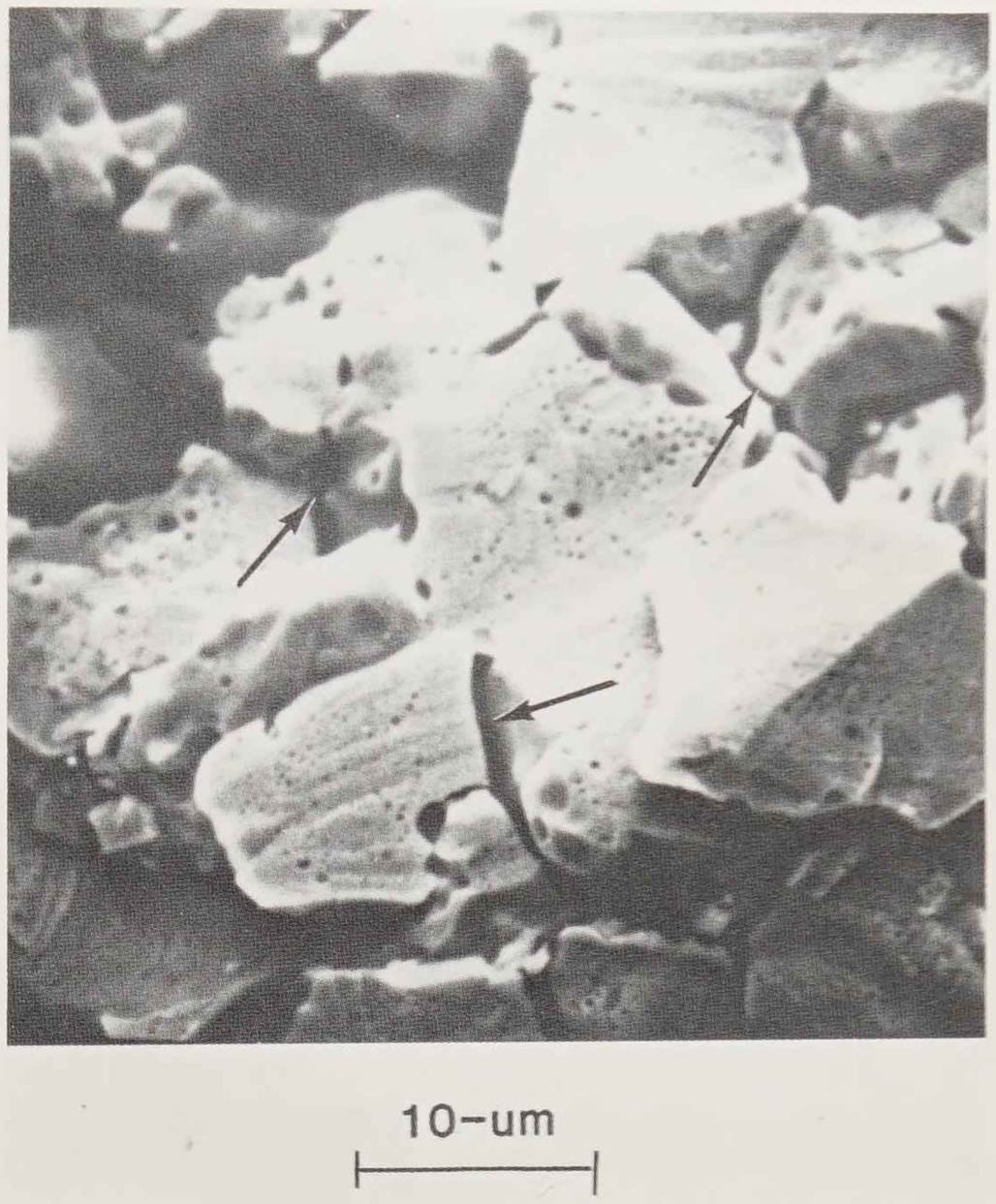


Figure 9 *Scanning Electron Micrograph of a Region near the Outer Surface of PNL9-3 (5.0 a/o burnup) Fuel after Test E25 Illustrating (arrows) Open Grain Boundaries due to Thermal-shock-induced Cracking.*

~0.8 R_0. A comparison of the volume-averaged ^{85}Kr content for the as-irradiated and DEH-tested data shown in Figure 8 indicates that ~90% of the gas in the as-irradiated fuel was released during the four heating cycles that comprised test E25. This value when compared to the 40–50% release data for single-cycle DEH tests on LWR fuel (Gehl 1982) and mixed-oxides (Fenske 1983) indicates the multiple heating cycles significantly increased the transient gas release behavior, especially when one considers the DEH transients by Gehl (1982) and Fenske (1983) were more severe in nature (higher temperatures).

Also shown in Figure 8 is the fraction (percentage) of ^{85}Kr retained as intragranular gas. Prior to the transients of E25, the as-irradiated fuel had as much as 30% of the ^{85}Kr trapped in intergranular regions (grain boundaries/edges). After the four heating cycles in E25, however, the fraction of the gas retained in the sample as intergranular gas was practically nil, thus indicating a highly interconnected network of grain boundaries developed that released all of the grain boundary gas, such as those illustrated in Figure 5b at 0.5 Ro for E25. Another example of the open grain boundaries that provided escape paths for fission gas release during test E25 is shown in Figure 9 at a near-surface radial position of ~0.8 R_0. In this case, however, the morphology is prototypical of a microcracked region similar to that shown in Figure 3a. The difference between the morphologies seen in Figures 5b and 9 is that the gas release path in Figure 5b is an outgrowth of grain boundary bubble precipitation, growth, coalescence, and tunnel formation (as evidenced by the tunnels in Figure 5b), while the gas release path shown in Figure 9 is a result of opened grain boundaries due to thermal-shock-induced cracking.

Discussion

Analysis by Bandyopadhyay, Buzzell, and Hofman (1980a) of the data presented above indicates that the fuel swelling and gas release characteristics of the tested fuels were determined by both diffusion-controlled mass-transport and thermal-shock-induced cracking (or microcracking) phenomena. Microcracking was particularly important in these tests because of their cyclic nature and the fact that most of the pretransient retained fission gas was located in unrestructured fuel

regions that did not achieve temperatures sufficient for mass-transport processes to significantly affect the fuel behavior. Because of the strong impact of microcracking on the fuel behavior, the discussion presented below focuses on microcracking and its relationship to fuel swelling and gas release phenomena. Also, the discussion concentrates only on the intergranular nature of the swelling, gas release, and microcracking. Intragranular bubbles (as seen, for example, in Figure 4b) contributed little to the overall swelling. This is in agreement with previous DEH studies as well as with code predictions from several models (Gruber, DiMelfi, and Bandyopadhyay 1979 and Gruber and Randklev 1979) (GRASS and FRAS) which indicate that the intragranular swelling should not exceed ~1.5%. Furthermore, once the gas is released from intragranular regions, its eventual release is controlled by the intergranular behavior of the gas. As a result, the present discussion analyzes the microcracking, fuel swelling, and gas release in terms of the intergranular behavior of fission gas bubbles.

The transient swelling, gas release, and microcracking phenomena observed in these tests can be explained by considering the physical processes that occur under steady-state (Olander 1976 and Tucker and Turnbull 1975) and transient (Rest and Gehl 1980 and Gruber and Randklev 1979) conditions. During steady-state conditions, stable networks of intergranular porosity develop in columnar and equiaxed zones of oxide fuel, particularly during high-temperature irradiations. This porosity is open in nature and connected to an exterior surface via pellet interfaces and/or macrocracks that extend deep into the pellet. The presence of such open porosity essentially reduces the effective diffusion length required for fission gas release from a distance comparable to the pellet radius to a distance comparable to the grain radius. As a result, fuel regions with high levels of interconnected porosity will have greatly enhanced fission gas release during steady-state conditions; this was observed for PNL9-3 fuel used in test E25 (Figure 8).

Near the center of the fuel, where a high-porosity interconnected network developed, the observed retention of ^{85}Kr was low (relative to the near-surface gas content in Figure 8) indicative of high gas release. In the unrestructured region, the interconnected porosity was low and thus the ^{85}Kr gas retention was high, indicative of low gas release. Note that although the gas release from unrestructured fuel was low, this does not mean that the steady-state release of intragranular gas to intergranular regions (grain boundaries) was low; it only implies that an interconnected gas release path had not developed. In fact, as seen in Figure 8, the intergranular gas in the unrestructured region was ~30% of the local ^{85}Kr gas. Thus, although the release of gas from the overall unrestructured region was minimal, a significant quantity of gas that was originally intragranular was released to intergranular regions. This latter aspect is important because, as discussed later, the propensity for fuel to microcrack under transient conditions is strongly enhanced by the presence of grain boundary fission gas in the form of bubbles, and the data in Figure 8 demonstrate that this gas is already present as a result of steady-state operation.

The same physical processes that result in gas release and swelling during steady state can also occur under transient heating conditions, but at an accelerated rate, owing to higher temperatures incurred during the heating cycle. Precipitation and growth of intragranular bubbles contribute to intragranular swelling, but the magnitude of this is small compared to the intergranular swelling component and can be disregarded. Intragranular gas, in excess of that already present on the grain boundaries, is released to grain boundaries by transport of gas atoms and/or biased migration of gas bubbles. With continued gas migration to boundaries, grain boundary bubbles continue to precipitate, grow, and coalesce in excess of the level present at the end of steady state. When the bubbles are sufficiently close to one another, channels begin to form on grain surfaces, as seen in Figures 4a and 5a. These channels eventually interlink and vent their gas to grain edge tunnels. In a similar manner, the grain edge tunnels interlink to form a path for the release of gas. In the process of forming the channels for gas release, the intergranular regions (particularly in high-temperature regions) undergo a significant increase in volume which results in fuel swelling such as that seen in Figure 3c.

Figure 10 (Gehl 1982) illustrates the sequence of events that can lead to gas release and the associated swelling. The central path in Figure 10 is strongly dependent on diffusional processes and thus is greatly enhanced by high temperatures. An alternative gas release process (and to some extent volume swelling process) illustrated in Figure 10 that can effectively short-circuit the diffusion-controlled release path is thermal-shock-induced cracking or microcracking of grain boundaries (Gehl 1982 and DiMelfi and Deitrich 1979). In contrast to the diffusion-controlled gas release path, which involves thermally activated phenomena, the microcracking process is enhanced at low temperatures where the grain boundary bubbles act as crack nuclei, leading to brittle failure of the grain boundaries. Resintering is another process shown in Figure 10 that hinders gas release and swelling. While resintering was not a significant process in the tests described above, because of their short duration, it may be significant in pulsed reactors that operate for long periods at low power levels between pulses.

Recently, DiMelfi and Deitrich (1979) developed a model ("D-D" model) to determine whether microcracking or diffusion-controlled processes will dominate the gas release and swelling behavior of irradiated fuel. Their model is based on the premise that

GAS RELEASE PROCESSES ON GRAIN SURFACES

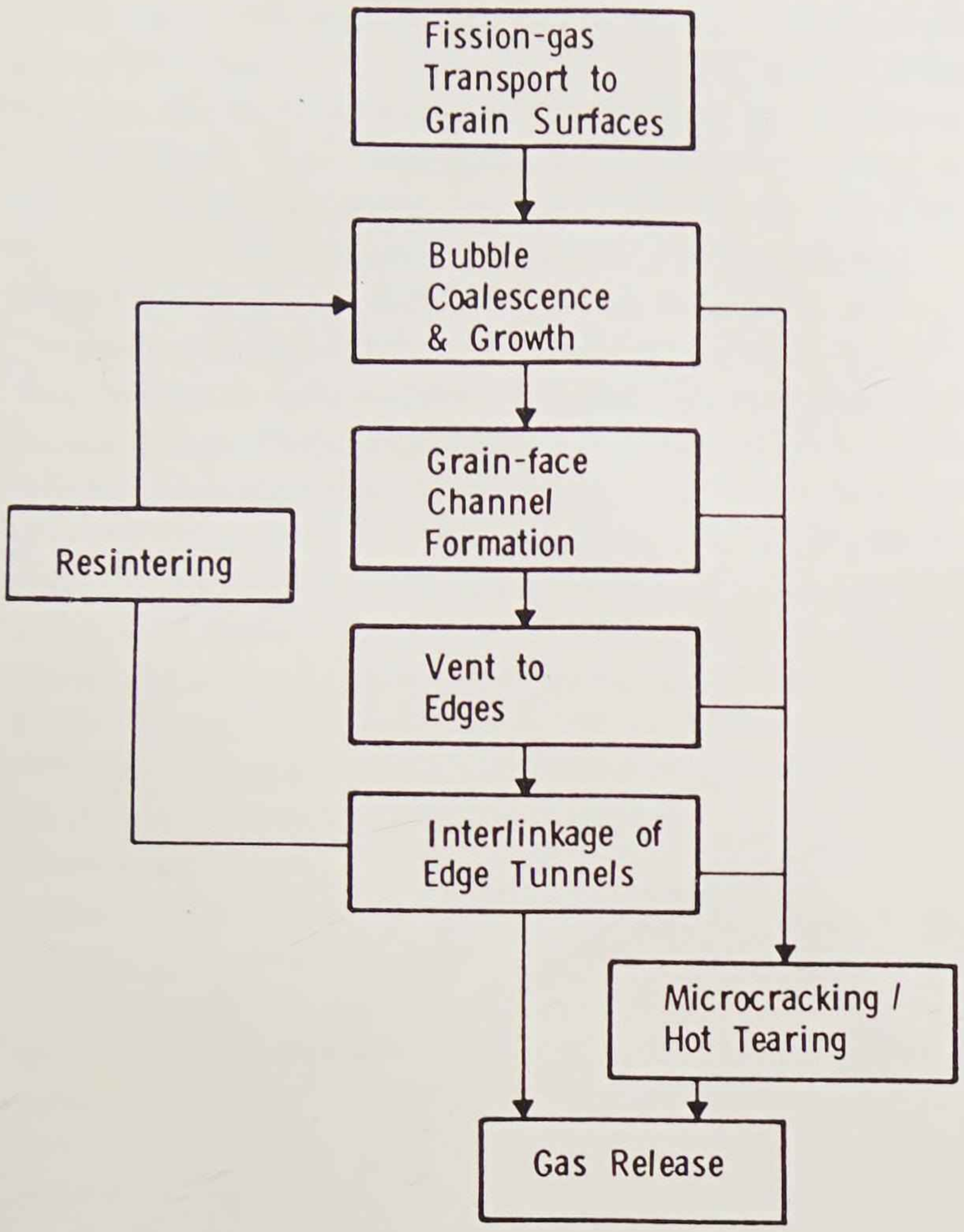


Figure 10 *Interrelationships among the Mechanisms Responsible for the Release of Grain Boundary Gas (Gehl 1982).*

grain boundary gas bubbles can act as crack nuclei. It can be shown that such a crack will propagate unstably if the internal gas pressure exceeds that required for bubble equilibrium:

$$p > \frac{\delta_s}{\rho} - \sigma, \qquad (1)$$

where p, δ_s, ρ, and σ are the internal pressure, fuel-gas surface energy, radius of curvature of the bubble, and the applied tensile stress normal to the grain boundary.

During a thermal transient, the internal gas pressure will increase above the equilibrium value owing to the gas transport to the grain boundary and gas heating. (Overpressurization can also occur if the applied stress σ is suddenly removed. As discussed later, this apparently occurs during spallation of irradiated mixed-oxide fuel, and upon cladding breach during transient over power (TOP) transients on irradiated carbide fuel.) Under these conditions, crack propagation will occur unless diffusional growth of the bubble occurs sufficiently fast to maintain equilibrium. Thus the dominant gas release (and swelling) mode will depend on the quantity of gas on the grain boundaries, the fuel temperature, and the heating rate. Gas release and swelling via diffusion-controlled processes are favored by high temperatures and/or slow heating rates, while microcracking is favored by low temperatures and high heating rates.

A comparison of the microstructures in the DEH-tested segments indicates that the dominant gas release/swelling process (diffusion-controlled or microcracking) depended on the radial location. Near the center of the fuel (Figures 3c, 4b, and 5b) where high temperatures were reached, the gas release and swelling were due mainly to diffusion-controlled processes. In the outer regions (Figures 3a and 9) where temperatures were lower, the gas release and swelling were due mainly to microcracking.

Consideration of both processes accounts for the swelling saturation observed in Figure 7. During the first two heating cycles, the fuel swelled and released gas by diffusion-controlled and microcracking processes. The onset of pore and tunnel interlinkage during the first two cycles provided an open path for gas release. Thus, any gas released to the grain boundaries during subsequent cycles would be vented and would not contribute to further swelling. This rationale is supported by the laser microsampling data in Figure 8, which demonstrates that the grain boundaries did not retain any fission gas after four heating cycles; this indicates that an interconnected path for gas release was created.

The saturation of the swelling observed in Figure 7 after two cycles was, in part, due to the fact that gas production, release, and resintering did not occur between the cycles. In a transient reactor, gas production and release and resintering will occur during the low-power steady-state cycles between pulses, thus regenerating the potential for microcracking (and swelling) to continue during subsequent heating cycles.

Additional evidence of microcracking phenomena and their impact on transient fuel and cladding behavior has been obtained in out-of-reactor (Fenske and Bandyopadhyay 1981a and Gehl 1979 and 1982) and in-reactor (Argonne 1980 and Gehl 1982) tests on irradiated fuel. An extensive microstructural examination by Gehl (1979 and 1982) of LWR fuel subjected to single-cycle DEH transients indicated that the gas release was controlled by the amount of interconnected grain boundary porosity that developed via diffusion-controlled and microcracking processes. The relative importance of these modes in determining the amount of interconnected porosity was found to be dependent not only on the heating rate but also on whether or not the fuel was radially constrained. At low heating rates, the observed gas release was primarily a result of diffusion-controlled processes that produced an interconnected path of grain edge tunnels. At high heating rates ($\lesssim$50°C/s), microcrack-induced interlinkage of grain

boundaries was the dominant factor influencing the swelling and gas release. Restraining the fuel in a radial direction strongly influenced the gas release behavior by limiting the amount of swelling (and hence, interconnected porosity) that developed during the transients. In restrained fuel, the swelling in unrestructured regions was significantly diminished (by a factor of ~2–4), reducing the gas release by a factor of ~4.

The effect of mechanically restraining fuel during in-reactor thermal cycling of LWR fuel was also reported by Gehl (1982). In this instance, LWR fuel near the fabricated disk volume at pellet-pellet interfaces readily expanded to fill the disk volume by microcracking while fuel near the cladding which was mechanically restrained failed to undergo microcracking.

While a radial restraint such as that imposed by cladding can mitigate transient gas release and swelling induced by diffusion-controlled and microcracking phenomena, under certain conditions the cladding will be damaged as a result of strong fuel-cladding mechanical interactions. For example, Figure 11 shows a cross section of an irradiated mixed-carbide fuel pin ramped to 520% overpower (maximum fuel temperature 1850°C) within 3 s in the transient reactor test (TREAT) facility (test SC-4, Argonne 1980). The large (comparable in size to the cladding thickness in Figure 11) gap between the fuel and cladding that existed in the as-irradiated condition before the transient was largely eliminated due to microcracking-induced swelling of the fuel that resulted in a large permanent strain of ~0.36% in the cladding.

If cladding strains, sufficiently large to breach the cladding, occur, then additional, more extensive microcracking can occur due to the sudden overpres-

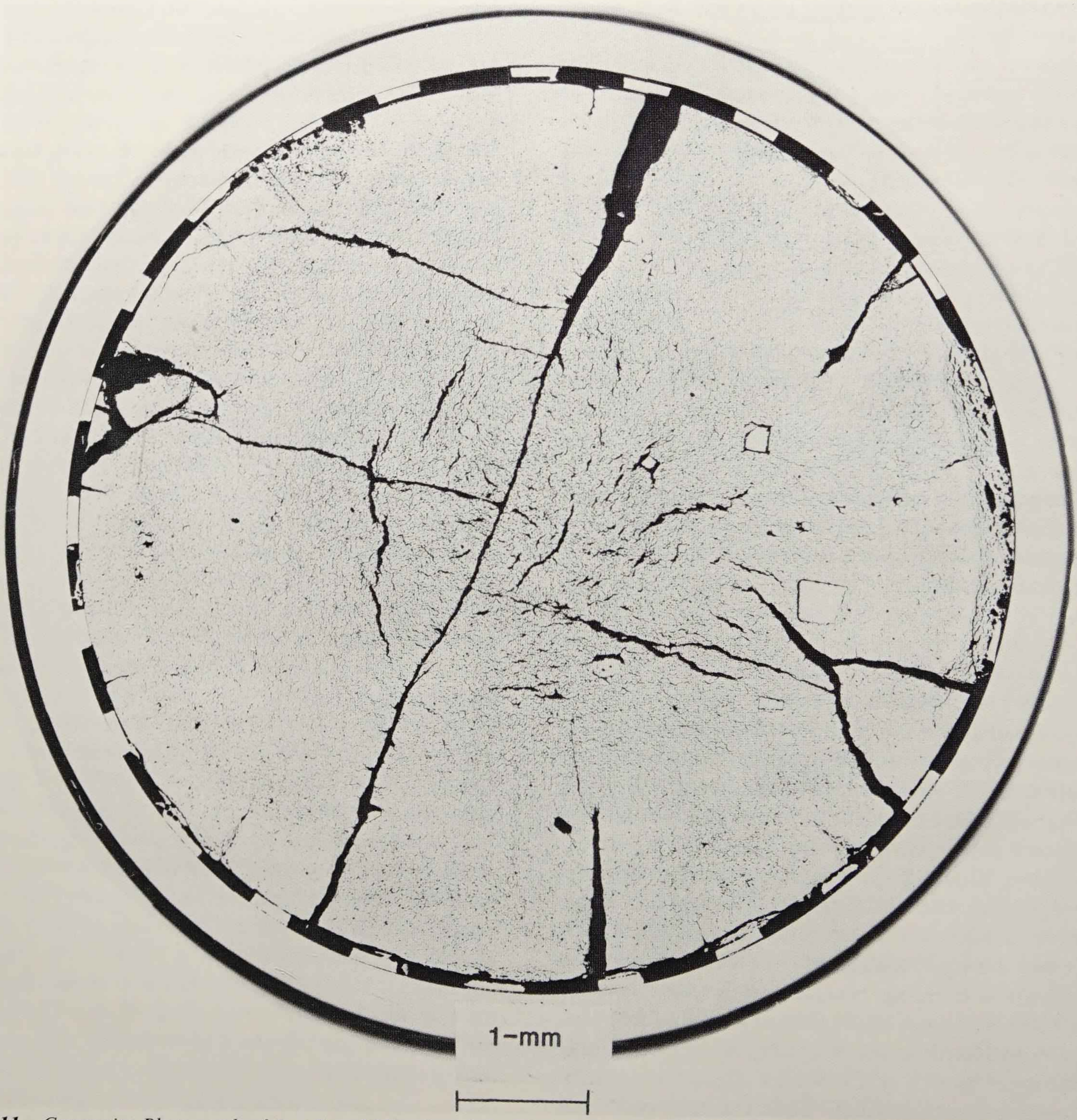


Figure 11 *Composite Photograph of Irradiated Mixed-carbide Fuel Illustrating Microcracking in the Central Region after a 520% Overpower Transient (from Argonne National Laboratory 1980).*

surization of the grain boundaries as the applied compressive stresses (σ in Equation 1) imposed by the cladding are relaxed. Evidence of this occurring have been reported for in-pile tests (HC-3, Argonne 1980) on mixed-carbides and out-of-pile tests (Fenske and Bandyopadhyay 1981) on irradiated mixed-oxides. In the out-of-pile tests, the depressurization and microcracking occurred as the cladding melted off of the pellets. As the cladding melted, the fuel underwent "spallation," a process characterized by the energetic ejection of solid particles of fuel. Both experimental (Fenske 1983 and Fenske and Bandyopadhyay 1981) and analytical (DiMelfi and Kramer 1983) studies of this behavior indicate its occurrence and extent are strongly dependent on the quantity of gas trapped within the fuel.

The experimental and analytical studies discussed above demonstrate that the role of fuel microcracking must be considered in assessing the reliability of reactor systems operated in a pulsed duty-cycle mode. The increased fuel swelling and gas release behavior noted above can impact on fuel pin (cladding) integrity in several ways. First, the increased gas release due to transient microcracking will lead to increased plenum pressures and hence cladding stresses. In a similar manner, the increased swelling due to transient microcracking may also lead to higher cladding stresses when the fuel comes in contact with the cladding. This last aspect may be circumvented by incorporating a larger initial gap between the fuel and cladding to accommodate the fuel swelling; however, a larger gap increases the likelihood for fuel particles (dislodged by microcracking) to relocate between the fuel and cladding, resulting in high local cladding stresses during subsequent transients (Cole and Wood 1976). The larger gap is also undesirable from a thermal performance standpoint because of the attendant higher fuel operating temperatures. Degradation of gap thermal performance will also result from the additional fission gases that are released during each thermal transient.

Analytical (DiMelfi and Deitrich 1979, DiMelfi and Kramer 1976, and Rest 1982) and experimental studies (Fenske and Bandyopadhyay 1981 and Gehl 1982) indicate that the severity and occurrence of microcracking phenomena are strongly dependent on the quantity of fission gas retained in the fuel (or, more specifically, on the quantity of gas retained on the grain boundary). As a result, fuels with high gas retention may show an increased tendency toward microcracking, and the associated increased swelling and gas release. Figure 12 shows the steady-state gas release behavior (Fenske 1983, Petty and Latimer 1981a and b, and Bauer, Cybalskis, and Green 1977) as a function of burnup for mixed-oxide, -nitride, and -carbide fuel pins irradiated in EBR-II. A range of values are shown for the oxides and carbides to cover different power levels for the oxides and different bonding (helium or sodium) techniques for the carbides. Of the three fuel types shown in

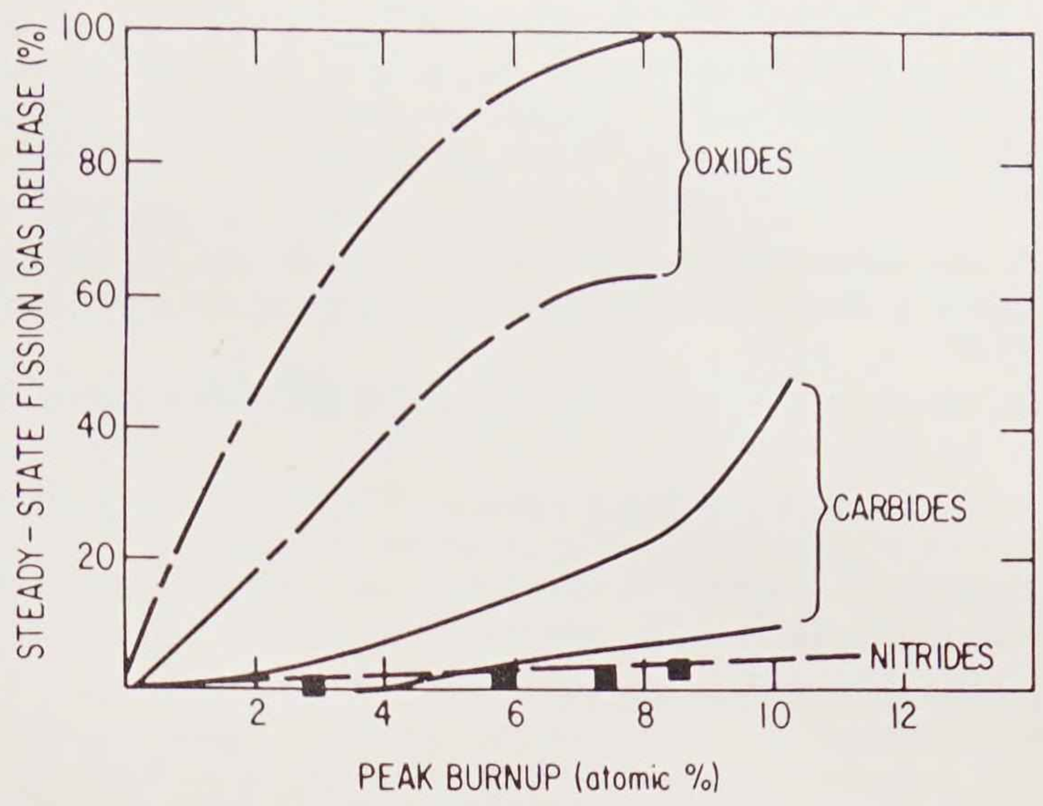


Figure 12 *Steady State Fission Gas Release of Mixed-oxide, -carbide, and -nitride Fuel Pins Irradiated in EBR-II.*

Figure 12, the oxides have the largest steady-state release, with carbides second, and nitrides releasing the smallest amount of gas (less than 4%) at 8.5 at.% burnup. The relative propensity of these fuels to undergo transient microcracking will further depend on resintering, gas production, and gas release processes during subsequent intermittent steady-state cycles. Nevertheless, the high inventories of gas in the carbides and nitrides that would be available for release to grain boundaries may result in more severe microcracking and thus lead to cladding failure.

Conclusion

Experimental and analytical studies have demonstrated that thermal-shock-induced microcracking can increase the swelling and gas release of irradiated fuel subjected to thermal transients, especially the gas release during multiple-cycle transients. Since fuels such as mixed-carbides and -nitrides (which are attractive for space reactor applications because of their high fissile density) show high gas retention, they may be more susceptible to microcracking. Consequently, the role of fuel microcracking (both analytically and experimentally) should be addressed in evaluating the potential fuel failure mechanisms of a particular reactor concept.

Acknowledgments

The authors wish to express their gratitude to S. G. Das for performing the temperature calculations, W. S. Mosevich for preparing the technical drawings, and E. M. Stefanski for editing the manuscript. Work supported by the U.S. Department of Energy.

References

Argonne National Laboratory (1980) *Advanced Fuels Development Program Quarterly Report for the Period April–June 1980*, Argonne National Laboratory Report ANL-AFP-89.

Bandyopadhyay, G. and J. A. Buzzell (1977) "Microstructural Investigation of Mixed-Oxide Fuels Subjected to Simulated Thermal Transient Conditions," in *Ceramic Microstructures '76*, R. M. Fulrath and J. A. Parks, Eds., Westview Press, Boulder, CO., p. 835.

Bandyopadhyay, G. (1978a) "Fuel and Fission Gas Response to Simulated Thermal Transients: Experimental Results and Correlation with Fission-Gas Release and Swelling Model," *Nucl. Technol.* 40:62.

Bandyopadhyay, G. (1978b) "Response of Oxide Fuel to Simulated Thermal Transients," *Nucl. Technol.* 41:349.

Bandyopadhyay, G. and J. A. Buzzell (1979) "Cladding and Fuel Motion of Irradiated Stainless Steel-Clad Mixed-Oxide Fuels in Response to Simulated Thermal Transients," in *Proc. Intl. Mtg. on Fast Reactor Safety Technology*, Seattle, WA, August 1979, Vol. IV, American Nuclear Society, La Grange Park, IL, p. 1745.

Bandyopadhyay, G., J. A. Buzzell, and G. L. Hofman (1980a) "Microstructural Studies of Irradiated Mixed-Oxide Fuels Subjected to Multiple, Mild Thermal Transients," *J. Nucl. Mater.* 92:51.

Bandyopadhyay, G., and J. A. Buzzell (1980b) "The Role of Fission Gas and Fuel Melting in Fuel Response During Simulated Hypothetical Loss-of-Flow Transients," *Nucl. Technol.* 47:91.

Bauer, A. A., P. Cybalskis, and J. L. Green (1977) "Mixed-Nitride Fuel Performance in EBR-II," in *Proc. Topical Meeting on Advanced LMFBR Fuels*, Tucson, AZ, 1977, p. 299.

Cole, J. T. and R. E. Wood (1976) "Power Burst Facility Fuel Studies," *Nucl. Technol.* 28:9.

Das, S. G., G. K. Leak, M. Minkoff, and R. B. Poeppel (1983) *Numerical Calculation of the Thermal Response of a Cylinder of UO_2 Heated by an Axial Electrical Current*, Argonne National Laboratory Report ANL-82-77, February 1983.

DiMelfi, R. J. and L. W. Deitrich (1979) "The Effects of Grain Boundary Fission Gas on Transient Fuel Behavior," *Nucl. Technol.* 43:328.

DiMelfi, R. J. and J. M. Kramer (1983) "Modeling Fragmentation and Spallation of Oxide Reactor Fuel During Transient Heating Including the Effects of Burnup and Fission Product Distribution," *Nucl. Technol.* 62:51.

Fenske, G. R. and G. Bandyopadhyay (1981) "The Effect of Burnup on the Response of Stainless Steel-Clad Mixed-Oxide Fuels to Simulated Thermal Transients," *J. Am. Ceram. Soc.* 64(7):375.

Fenske, G. R. (1983) Unpublished Results, Argonne National Laboratory, Argonne, IL.

Gehl, S. M. (1976) *Comparison of Fission Gas Release and Mechanical Behavior During Transient Nuclear and Electrical Heating of Light Water Reactor Fuel*, U.S. Nuclear Regulatory Commission Report NUREG/CR-1001, and Argonne National Laboratory Report ANL-78-60, June 1979.

Gehl, S. M. (1982) *The Release of Fission Gas During Transient Heating of LWR Fuel*, U.S. Nuclear Regulatory Commission Report NUREG/CR-2777, and Argonne National Laboratory Report ANL-80-108, May 1982.

Graczyk, D. G., G. Bandyopadhyay, S. M. Gehl, J. P. Hughes, and H. T. Goodspeed (1979) *A Laser Microsampling Method for Determination of Retained Fission Gas in Irradiated Nuclear Fuels*, Argonne National Laboratory Report ANL-79-86, October 1979.

Gruber, E. E., R. J. DiMelfi, and G. Bandyopadhyay (1979) "Analysis of Fuel Dispersal in Direct Electrical Heating Experiments," in *Proc. Specialists' Workshop on Predictive Analysis of Materials Dynamics in LMFBR Safety Experiments*, Los Alamos, NM, p. 269.

Gruber, E. E. and E. H. Randklev (1979) "Comparison of Fission Gas Effects in a Transient Overpower Test (HUT-5-7A) to FRAS3 Code Predictions," in *Proc. Intl. Mtg. on Fast Reactor Safety Technology*, Seattle, WA, August 1979, Vol. IV, American Nuclear Society, La Grange Park, IL, p. 2050.

Hofman, G. L., G. Bandyopadhyay, F. L. Brown, and J. L. Buzzell (1979) "Behavior of Irradiated UO_2-PuO_2 Under Simulated Cyclic Overpower Transients," in *Proc. Intl. Conf. on Fast Breeder Reactor Fuel Performance*, Monterey, CA, 1979, p. 327.

Olander, D. R. (1976) *Fundamental Aspects of Nuclear Reactor Fuel Elements*, TID-26711-PI, National Technical Information Service, Springfield, VA, 1976, Chapters 13 and 15.

Petty, R. L. and T. W. Latimer (1981a) "The Behavior of Helium-Bonded Carbide Fuel Elements Irradiated to Goal Burnups," *Trans. Am. Nucl. Soc.* 39:413.

Petty, R. L. and T. W. Latimer (1981b) "The Behavior of Sodium-Bonded Carbide Fuel Elements Irradiated to Goal Burnups," *Trans. Am. Nucl. Soc.* 39:418.

Rest, J. and S. M. Gehl (1980) "The Mechanistic Prediction of Transient Fission-Gas Release from LWR Fuel," *Nucl. Eng. Des.* 56:233.

Rest, J. (1982) "The Prediction of Transient Fission Gas Release and Fuel Microcracking Under Severe Core-Accident Conditions," *Nucl. Technol.* 56:553.

Tucker, M. O. and J. A. Turnbull (1975) "The Morphology of Interlinked Porosity in Nuclear Fuels," in *Proc. Roy. Soc.* (London) A343:299.

Wang, W. L., J. Rest, and G. Bandyopadhyay (1978) "Transient Fission Gas Behavior: Experimental and Analytical Results," *Trans. Am. Nucl. Soc.* 28:240.

Wrona, B. J. and E. Johanson (1976) "Development of Direct Electrical Heating Apparatus to Study the Response of Nuclear Fuels to Applied Transients," *Nucl. Technol.* 29:433.

Wrona, B. J., J. T. A. Roberts, M. Galvin, and G. T. Higgins (1977) "Mechanical Response of UO_2 Subjected to Transient Heating," *Nucl. Technol.* 32:276.

Space Nuclear Power Systems 1984
Edited by M. S. El-Genk and M. D. Hoover
© Orbit Book Company, Malabar, FL, 1985

Chapter 39

Review of Previous Shield Analysis for Space Reactors

William J. Barattino
Air Force Institute of Technology
University of New Mexico
Albuquerque, NM 87131

Mohamed S. El-Genk
Dept. of Chemical and Nuclear Engineering
University of New Mexico
Albuquerque, NM 87131

Susan S. Voss
Air Force Weapons Laboratory
Kirtland Air Force Base
Albuquerque, NM 87117

In the ten years that have elapsed since serious space shielding work was conducted, major changes in the external environment have occurred. The stronger need for conducting civilian and military operations in space will require both higher power and greater radiation shielding. The concomitant need for weight optimization as well as thermal and stress analysis will offer a significant challenge at today's higher power requirements (100 kWe to multi-MW). This paper reviews previous shielding work for space reactors, focuses on neutronic analysis, thermal and stress analysis, and assesses the performance of lithium hydride and tungsten shields.

Introduction

Because of renewed interest in conducting military and civilian operations in space, developing a large power source with high power density has re-emerged as a national priority. The organization of the tri-agency office, comprised of the National Aeronautics and Space Administration (NASA), Department of Energy (DOE), and Department of Defense (DOD) personnel, indicates the growing commitment to the development of space nuclear power systems.

Although high power density requirements (40 to 50 W/kg) can easily be accomplished by using nuclear power systems, such systems require an adequate radiation shield to attenuate core radiation to acceptable dose levels at the prescribed dose plane. The dose plane limits are a function of the mission for which the power is being supplied. At the time of the SNAP program closeout, extensive experimental testing of candidate shielding materials had been performed. This testing also investigated the application of numerous neutron transport codes to insure that the dose requirements were met at the dose plane. However, as the operating power levels reached the multi-kilowatt range, the need to study the thermal performance of the shield became apparent. Unfortunately, SNAP program funding was terminated before many significant questions concerning shield thermal analyses were answered.

This paper discusses previous shielding work pertinent to space nuclear reactors; it focuses on neutronic analysis, thermal and stress analysis, and major issues regarding the performance of tungsten and lithium hydride shields. The discussion begins by reviewing previous shielding work for space reactors. The review is separated into the following areas: space shield neutronics analysis, space shield thermal analysis, lithium hydride shield and experimental results of shields using lithium hydride for neutron attenuation.

Review of Previous Shield Design for Space Reactors

In the 1960s and early 1970s, much work was done on the development of radiation shields for space reactors. Table 1 is a composite picture of the major reactor shields developed during the SNAP program. Although other space reactors reached some level of design and testing, those listed in Table 1 represent the space reactors with the best documentation currently available. Tracing the development of space reactor shields shows the increasing sophistication of neutronic analysis and design from the SNAP 10A shield that had no gamma attenuation to the potassium heat pipe reactor shield that is layered and optimized for weight (Engle et al. 1971). Figure 1 shows an example of a layered shield. The table also implies the increasing concern with the need for thermal and structural analysis as the reactor power level increases (Keshishian et al. 1973).

Space Shield Neutronic Analysis

The selection of radiation shielding materials is based on the shield's ability for attenuating core radiation to acceptable dose levels at the prescribed dose plane. The dose plane limits are functions of the mission for which the power is being supplied. For instance, the SNAP missions were primarily unmanned and, therefore, required only 2π shields. Table 2 lists the dose criteria specified for electrical component shielding in the SNAP 10A.

Table 1 *Summary of Radiation Shield Design for Space Reactors.*

Reactor	Power Level	Time Frame	Gamma Shield	Neutron Shield	Dosage Requirements[a]	Status	Remarks
SNAP 10A (Engle et al. 1971)	0.5 kWe (39 kWt)	Early '60s	None	LiH	γ's: 10^7 RAD @100 ft n's: 10^{12} nvt @100 ft Over 1 year	Built, tested and flown	Only reactor flown. Fast neutron flux, higher than predicted due to scattering around shield.
SNAP 50/SPUR (Pratt and Whitney 1964)	300–1200 kWe	1964	None mentioned	Li^7H LiH	Shadow shield: γ's: 5 mR/hr A 40 m n's: $5 \times 10''$–10^{13} nvt @12.8 m	Paper studies	For unmanned mission, preliminary design. Two region shield.
SNAP 8 (Masora 1973)	30 kWe	1960s-early '70s	W	LiH	None mentioned	Built developmental shields	Higher power level led to enrichment of Li-7 in LiH to reduce internal heating.
Advanced hydride/ 5 kWe (Keshishian et. al 1973)	5 kWe	Early '70s	Borated Stainless Steel	LiH	γ's: 10^6 rad @100 ft n's: 10^{12} nvt @100 ft Over 5 years	Paper studies	At program closeout, need for additional thermal analysis was documented.
Potassium heat pipe reactor (ORNL 1971)	450 kWt 1780 kWt	Early '70s	W	LiH	3 mrem/hr @100 ft, Within shadow 300 mrem/hr @100 ft, Outside shadow	Paper studies	Shielding materials layered to optimize for weight, without consideration to varying thermal expansion coefficients.
40-kWe thermionic (Gietzen et al. 1974)	40 kWe	Early 70s	W	LiH	Side shield: 100R/hr @ 30.5 m	Paper studies	Reactor designed for manned missions. Shield layered to minimize weight
SP-100 reactor (Los Alamos 1982 and JPL 1982)	100 kWe (1.6 MWt)	Early '80s	W	LiH	γ's: 10^6 rad @25 m n's: 10^{12} nvt @25 m Over 7 years	Paper studies	Consideration being given to the need for active cooling of shield.

[a] γ's: Gamma absorbed dose.
n's: Neutron fluence.

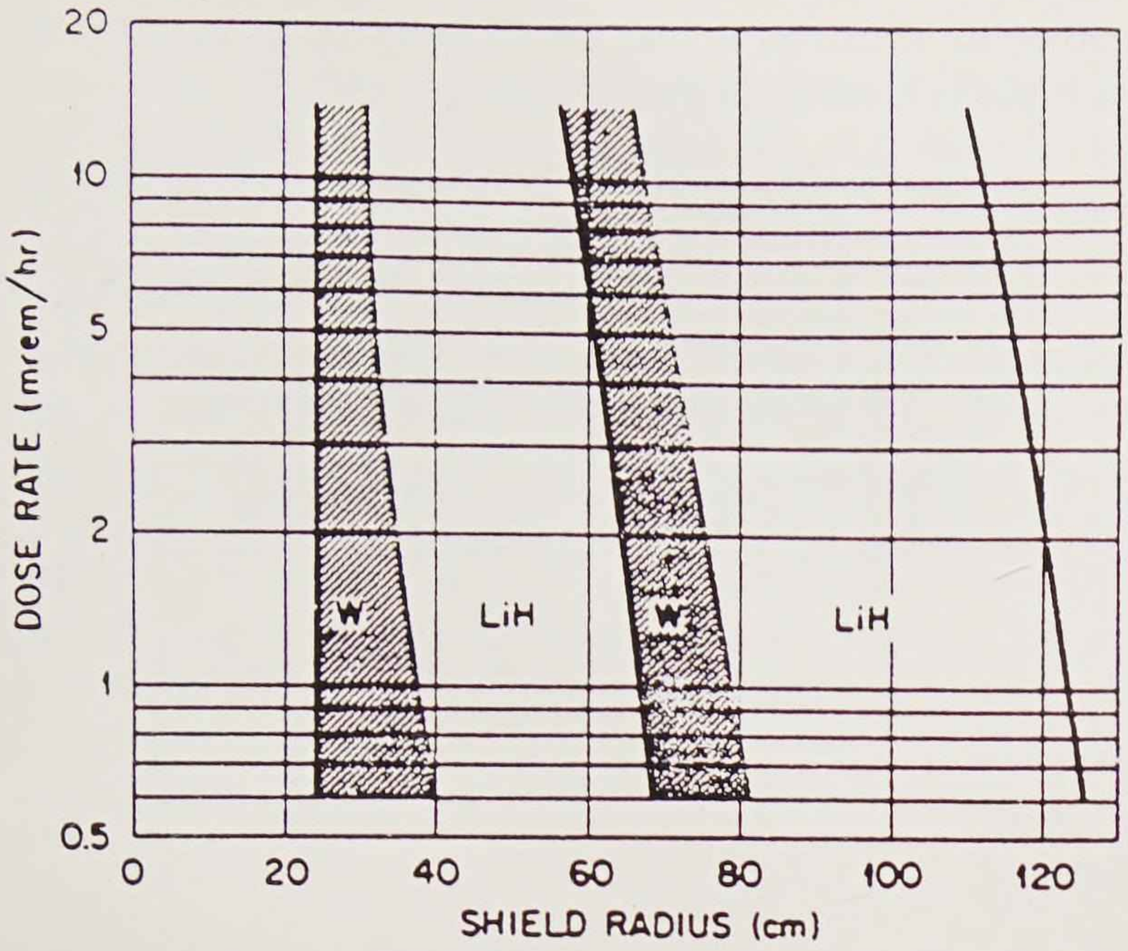


Figure 1 *Thickness of W and LiH Layers in a Two-Cycle Shield Configuration for a Dose Constraint of 1.2 rem/hr at a Distance of 45.71 m (1780 kWt) (from Engle et al. 1971).*

Table 2 *Dose Criteria for SNAP 10A for Five Year Lifetime.*[a]

Radiation Source	Dose Limit (20 m from core center)
Neutrons fluence ($E_n > 0.1$ MeV)	10^{12} nvt
Gamma rays absorbed dose	10^6 rad

[a] From Keshishian et al. 1973.

SNAP 10A Shield

The SNAP 10A was a 0.5 kWe reactor, thermoelectric system launched on April 3, 1965. Neutron attenuation for the SNAP 10A was accomplished using a lithium hydride shield. No gamma shielding material was included in the shield design because of the low power level of the core.

Although expected to operate for at least 6 months, the reactor shut down after only 43 days of operation due to an apparent failure of a voltage regulator. Post-flight shield analysis revealed that the fast neutron flux densities were underestimated by a factor of 6.5 to 7.8, while the gamma fluxes were within 10 percent of pre-flight projections. On-board measurements were made with a Np-237 fission chamber for fast neutron fluxes, U-235 fission chambers (one cadmium wrapped) for thermal neutron fluxes, and a CO_2-filled ion chamber for gamma detection. The higher than expected fast neutron fluxes were caused by scattering from the control drums, and from the sides of the reactor; and by streaming though the NaK coolant piping which came out from the core and curved around the shield.

The use of NaK served as a source of secondary gammas by the following reactions:

$$_{11}Na^{23} + n \longrightarrow {}_{11}Na^{24} \xrightarrow[14.8\ hr]{\beta-} {}_{12}Mg^{24} + 2\gamma$$

$$(E_\gamma = 2.75\ \text{MeV}, 1.37\ \text{MeV})$$

$$_{19}K^{41} + n \longrightarrow {}_{19}K^{42} \xrightarrow[12.4\ hr]{\beta-} {}_{20}Ca^{42} + \gamma\ (18\%)$$

$$(E_\gamma = 1.52\ \text{MeV}).$$

SNAP 8 Reactor Shield

The SNAP 8 reactor program began in the early 1960s and continued into the early 1970s. The reactor was intended to provide 30 kWe of power for both manned and unmanned missions. The two SNAP 8 reactors that were built were never taken beyond the ground test stage. The radiation shield consisted of tungsten for gamma radiation, and lithium hydride enriched to 99.99 wt.% Li-7 for fast neutrons. The enrichment of Li-7, 92.6 at% natural abundance, was done to reduce the internal heat generation within the shield caused by the (n, α) reaction with Li-6, 7.4 at% natural abundance (Masora 1973).

When the SNAP reactor developmental programs were stopped, unresolved concerns regarding the thermal and stress analysis as well as the prolonged performance of the radiation shield (for 3 to 7 years in space environment) remained.

Thermionic Reactor Shield

In the early 1970s, the use of in-core thermionic conversion for space was introduced. Two examples are the Atomics International 5 kWe thermionic reactor (Keshishian et al. 1973), an auxiliary power supply for unmanned space applications, and the Gulf General Atomic design of a 40 kWe power system for a manned space laboratory (Grietzen et al. 1971).

Shield design for the 5 kWe thermionic reactor included borated stainless steel and lithium hydride. The selection of borated stainless steel over stainless steel and a tungsten alloy was based on 1-D calculations showing less weight for the same gamma attenuation. However, this result apparently is the only time that tungsten did not emerge as the gamma attenuation material. Tungsten, although costly, is regarded as the most efficient (from a minimum-shield weight standpoint) material for gamma radiation attenuation.

Table 3 is a listing of the materials considered for gamma attenuation in the 5 kWe thermionic reactor.

The following codes were used in the analysis of the

Table 3 *Materials considered for Gamma Attenuation Shield Design of the 5 KWe Thermionic Reactor System.*[a]

Material	Comment
Lead	*Rejected*, because of its low melting point (600 K)
Ta-W (10 wt%)	*Rejected*, because of the secondary gammas from Ta
U-Mo (10 wt% U and 80 wt% Mo)	*Rejected*, in spite of its low mass, because of its high internal heating and temperature instability.
W alloy (95 wt% W)	*Evaluated*, based on 1-D calculations
Stainless steel	*Evaluated*, based on 1-D calculations
Natural and enriched B_4C	*Evaluated*, based on 1-D calculations
Borated stainless steel	*Evaluated*, based on 1-D calculations

[a] From Keshishian et al. 1973.

5 kWe reactor shield:

1D ANISN Transport Code,
QAD for gamma fluxes,
DOT/SPACETRAN Code, and
DDM (DOT-DOMINO-MORSE) Code.

No single neutronic code is used as an industry average and selection of a particular code generally depends on the application. Thermal analysis information of the shield was also reported and will be discussed in a later section.

The 40 kWe thermionic power system (Gietzen et al. 1971) was designated to be launched by the space shuttle in two loads because of its large mass (12,000 kg); most of which was the shielding necessary for the manned space station. In a second design, the power system was designed to be tethered 2 miles away from the space station, reducing the shielding requirements and the total mass of the system by one-half.

NASA-Lewis Shield Design

In September 1969, NASA-LeRC published a comparison of tungsten-LiH and depleted uranium-LiH shields for a 2.2 MWt reactor output. The analysis apparently was for a manned mission because the reference dose requirement was 2 mrem/hr at a distance 20 m from the core, RBE = 7 for fast neutrons (Lahti and Herrman 1969).

The contributions of radiation sources to the 2.0 mrem/hr dose rate were as follows: 15 percent from core neutrons, 1 percent from neutrons generated in depleted U, secondary gammas from reflector and shield accounted for 70 percent of dose for W and 55 percent of dose for U, remaining 15 percent of dose are from inelastic scatter gammas and fission gammas for U. Although the radiation source contributions will differ for each reactor, the contribution of secondary gammas must be considered in the thermal analysis of radiation shield. The neutronic analysis of the shield was performed using the following codes:

GAM II and GATHER II programs for 26 group cross sections (P_3 approx),
ANISN program for radiation transport (S_{16}-P_3 approx in 1-D), and
OPEX II for optimization of shield thickness.

The effects on dose rates of perturbing the thickness of a given region of the shield was determined as:

$$D_i = C_i \exp\left(-\sum \mu_{ij} t_j\right),$$

$$D = \sum_i D_i ,$$

where

D_i = the ith component of the dose rate

D = the total absorbed dose rate

C_i = a constant determined from perturbing the thickness

μ_{ij} = the ith component attenuation of the jth region

t_j = the thickness of the jth region

The depleted uranium-LiH shield had a mass of 25,300 kg; the W-LiH shield had a mass of 28,500 kg. However, these results may be misleading since using uranium near the reactor core is not desirable because excessive fissioning of uranium can cause an appreciable increase in heat generation and introduce intolerable swelling of the uranium shield (Kaszubinski 1973).

ORNL Shield Design

In 1971, ORNL published an optimized shield design for a stainless steel, potassium heat pipe reactor, fueled with uranium nitride fuel and operating at either 450 kWt or 1600 kWt. The dose constraints were 3 mrem/hr within the shield shadow and 300 mrem/hr outside the shadow at 32.81 m radii (Engle et al. 1971). The neutronic model used in the analysis was the ASOP code (ANISN Shield Optimization Program) using 1-D discrete ordinates transport theory and 3-D weight functions. The optimization technique calculates the dose rate for a given geometry and the first and second derivatives of the dose rate with a design variable (for example, mass) when the thickness of material is perturbed. The constraints were then the prescribed dose rate at the 32.81 m dose plane and a selected tolerable range of d(dose)/d(mass).

The heat pipes were assumed to protrude through the shield, as with the SP-100 reactor (Los Alamos 1982 and JPL 1982). However, the ORNL approach assumed

that the temperature near the heat pipe would be above the LiH melting point (960 K) and Be0 was used in this region instead. For a given dose rate (1.2 rem/hr at 45.71 m), the thickness of Be0 required was 1.5 m, or 0.57 m thicker than the equivalent LiH thickness of 0.93 m.

Results of required thicknesses of W, LiH, and BeO for an operating power level of 1600 kWt are included in Figure 1. As shown in this figure, changing the dose rate requirement changes only the thicknesses of the first layers of W and LiH. The optimization of the material thickness in the shield for minimizing mass is based on the need to layer the gamma and neutron attenuating materials to minimize the effects of secondary gamma production on the dose plane.

SP-100 Reactor Shield Design

Figure 2 is a side view of the radiation shield for the Los Alamos heat pipe reactor, SP-100 reactor (Los Alamos 1982 and JPL 1982). Gamma attenuation is achieved with a layer of tungsten and neutron attenuation with lithium hydride shield. The characteristics of the shield (which are tentative at this stage) are included in Table 4.

Figure 3 is a plot of contours of neutron fluence over a seven-year lifetime for a 1.33 MWt average power level. The current SP-100 design calls for the reactor to operate at a slightly larger thermal output of 1.66 MW. As seen from Figure 3, the total neutron dose must be attenuated by five orders of magnitude in order to meet the dose plane requirement of 1×10^{12} nvt at 20 m. Using the Monte Carlo code (MCNP), Los Alamos researchers have determined that 0.80 m of LiH are necessary to achieve the desired dose rate. The heat pipes, which transfer the reactor power to the thermoelectric conversion system, subtend part of the radiation shield as shown in Figure 2. This pathway through the shield is a source of concern because of heat transfer from the heat pipe to the shield (somewhat offset with multi-foil insulation wrapped around the heat pipe), thermal expansion compatibility with shield materials, and radiation streaming through these ducts.

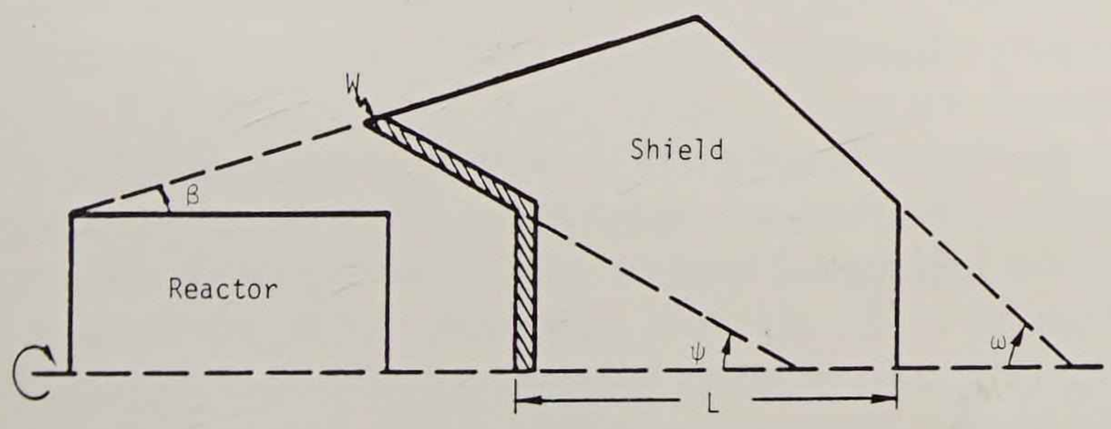


Figure 2 *SP-100 Lithium Hydride-Stainless Steel Neutron Shield Baseline Design Configuration (from JPL 1982).*

Table 4 *SP-100 Radiation Shield Characteristics.*[a]

Neutron fluence	10^{12} nvt
Gamma dose	10^{6} Rad/Si
Cone half-angle	15 deg
Axial thickness	0.80 m
Side length	0.80 m
Maximum diameter	1.05 m
Component mass	
LiH and container	485 kg
Tungsten	305 kg
Total shield	790 kg
Internal thermal power generated	to be determined

[a] From JPL 1982.

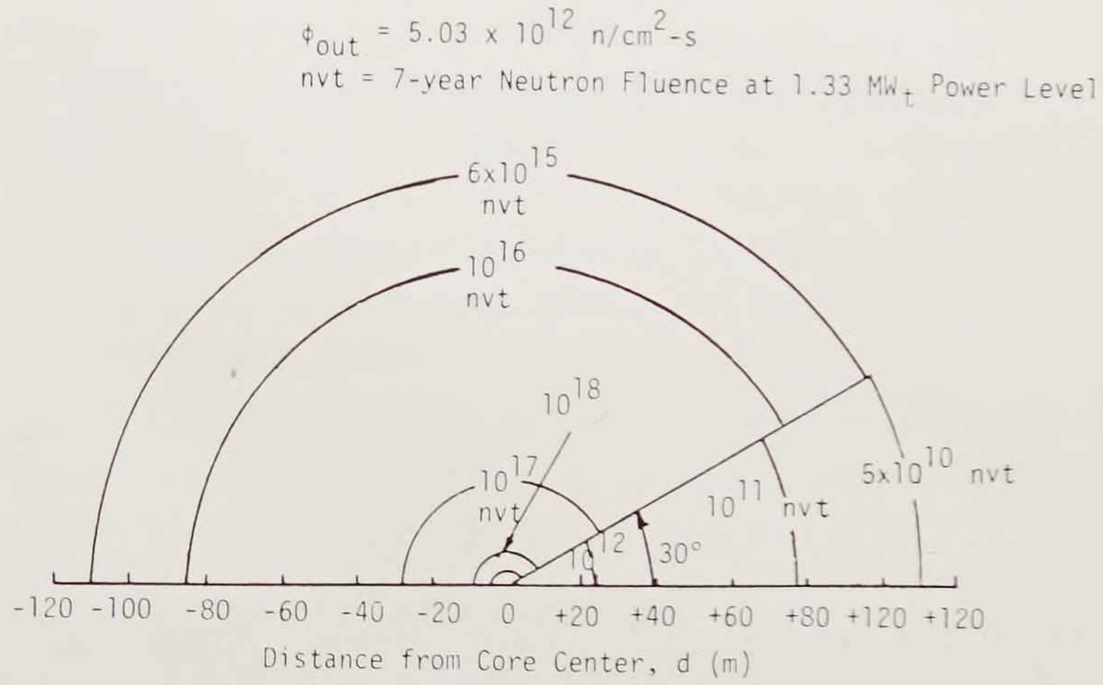


Figure 3 *SP-100 Contours of Neutron Fluence over 7-year Period, 1.33 MW Average Power Level. Neutron flux at Reactor External Surface (from JPL 1982).*

Space Shield Thermal Analysis

The area of thermal analysis of a space reactor's shield has not been covered extensively in the literature. Recent NASA-funded research has focused on thermal analyses of heat shield performance upon reentry into the earth's atmosphere, with particular emphasis on the space shuttle.

Keshishian et al. (1973) in their work on the shield design of the ZrH_2 reactor were concerned with the applied stresses on the W-LiH shield during lift-off. They were particularly concerned with the accompanying displacements in the shield and the effect on the structural support components and coolant pipes through the shield.

An area which remained unresolved at program closeout in 1973 was the determination of stresses induced in the shield outer casing, internal structure, and piping ducts. These stresses are caused by large differences in thermal expansion coefficients of LiH and stainless steel, particularly in the presence of thermal gradients during the shield casting cycle and during system transient and steady state operation. The shield temperatures were calculated using a computer code

called "DEAF"; internal heating was not considered due to the low core operating power level (5 kWe). Even at such low power level, it was concluded that " . . . passive control of shield temperature within a band smaller than 150°F is not considered a realistic objective" (Kehishian et al. 1973).of all radiating surfaces was 0.8. For the Pb-W-LiH shield, the maximum temperature of the LiH was 972°F (795 K) at 600 kWt, and 1019°F (821 K) at 1200 kWt. The W-LiH temperature analyses were not reported since the melting temperature of the LiH was exceeded.

- Refinement of the meteoroid equation to determine the probability of holes in the shield;
- Formulation of a model to describe the hydrogen migration in the shield as a function of both temperature and geometry;
- Determination of the temperature profile of the LiH shield under most probable (steady-state) operating conditions; and
- Determination of the rate of plugging of punctures by LiH (assuming condensation at the hole) as a function of temperature and meteoride hole size.

The Keshishian et al. work (1973) was the latest of the publications dealing specifically with space shielding. Earlier works which included some thermal analysis of radiation shield are those of Beiriger (1968) and Thompson and Schwab (1969). Beiriger (1968) conducted a thermal analysis of Pb-W-LiH shield and a W-LiH shield, with the LiH separated by insulation from the Pb-W-LiH case. The steady state operating powers of the reactor were 600 and 1200 kWt, and the heat generated in the shield was radiated to the reactor vessel (top and bottom at 1300°F) and then to space (at 100°F). The emissivity of all radiating surfaces was 0.8. For the Pb-W-LiH shield, the maximum temperature of the LiH was 972°F (795 K) at 600 kWt, and 1019°F (821 K) at 1200 kWt. The W-LiH temperature analyses were not reported since the melting temperature of the LiH was exceeded.

Thompson and Schwab (1969) examined the accuracy of several neutronic models in comparing the nuclear heating within the ZrH_2 reactor shield (Keshishian et al. 1973). The results indicated that the QAD (point kernel) code and the ANISN code overestimated the heating in the shield due to primary and secondary gammas by a factor of 2, when compared to the DOT (discrete ordinates) code. This overestimation was corrected by "tuning down" the fluxes until agreement with DOT fluxes was reached. However, it was not clear how the DOT code results were calibrated to serve as the benchmark.

Lithium Hydride Shield

Lithium hydride, although brittle at elevated temperature, has been recommended as the material for space power nuclear reactors because of its high hydrogen

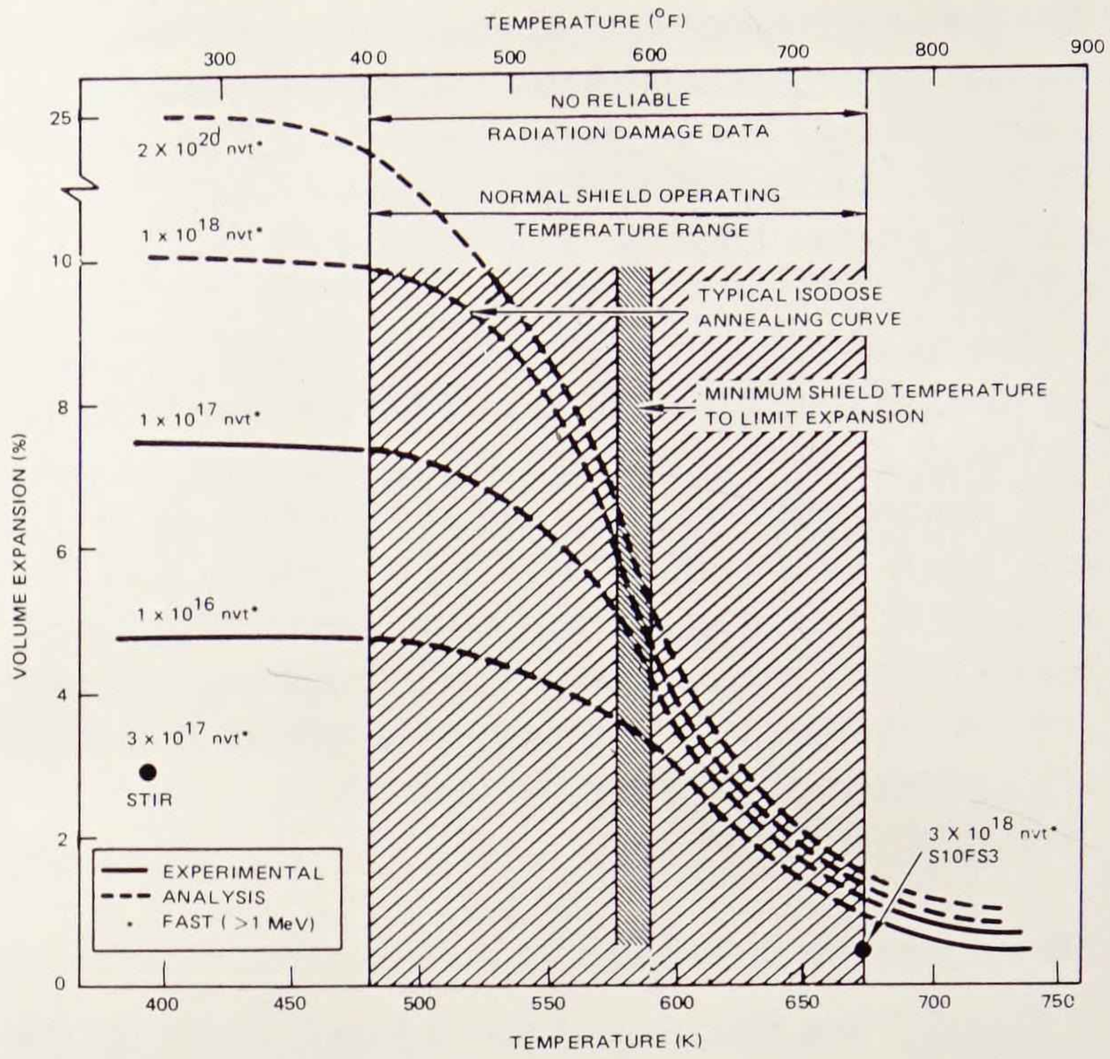


Figure 4 *Radiation-Induced Expansion in LiH (Natural) (from Welch 1967a).*

content, low density (0.72 gm/cc), high melting point (960 K), relatively low dissociation pressure, very high effective neutron attenuation coefficient, and its ability to capture neutrons without releasing gamma rays. The major thermal concerns are the very low thermal conductivity and the need to maintain the temperature of lithium hydride between 600 and 680 K (Welch 1967a).

The widely accepted temperature range of 600 K (620°F) to 680 K (769°F) for the LiH is based primarily on the data of Figures 4 and 5. From Figure 4, the volume expansion of LiH is less than 6 percent for fast neutron fluence levels of 2×10^{20} nvt or less at LiH temperatures of 600 K (620°F) or greater.

Since natural LiH is generally less than 94 percent of theoretical density, the volume expansion due to irradiation at temperatures in excess of 600 K can be handled without any structural damage. Typical shield casing thickness designs (Type 316 stainless steel) in the SNAP program were 0.15 to 0.25 cm (0.06 to 0.10 in). From Figure 5, for a typical shield casing, the dose rate at the back shield surface should remain constant for temperatures below 680 K during prolonged exposure (10,000 hours) to meteoroid bombardment. (Dose rate increase is proportional to hydrogen loss through the puncture holes.)

Based on these figures, many engineering issues were raised. The first was whether the dissociated hydrogen in the LiH would migrate quickly to the cooler regions because of the expected steep temperature gradients in the LiH, thus escaping faster than assumed in Figure 5. To answer this question, a slab of LiH 0.66 m thick was subjected to a temperature difference of 550 K (500°F) to 866 K (110°F) for periods of 1000 and 2000 h. The results showed that the maximum migration of hydro-

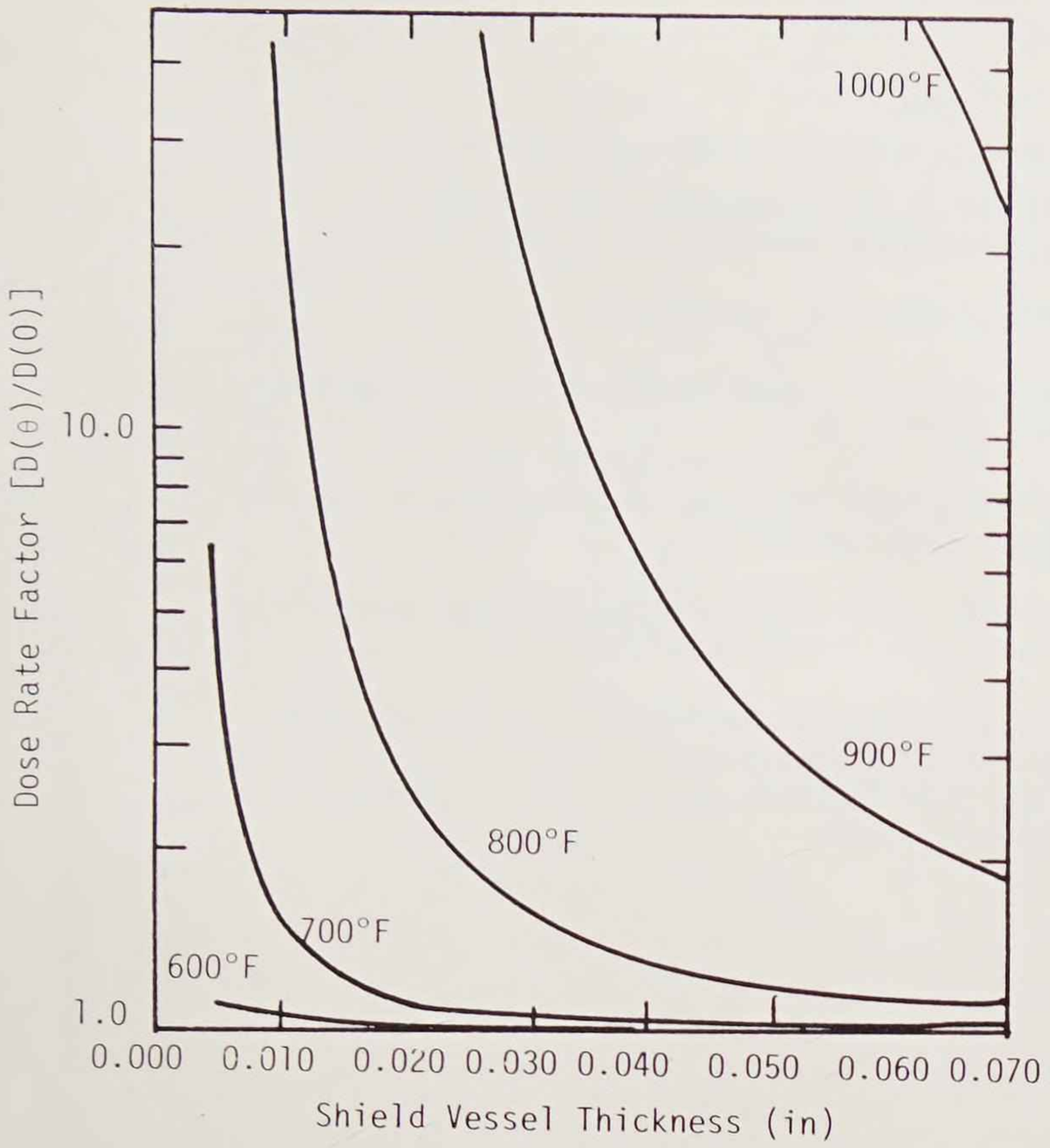


Figure 5 *Increase in Dose Rate after 10,000 Hours Due to Meteroid Puncture of the S8DS Shield as a Function of Shield Vessel Thickness with Lithium Hydride Temperature as a Parameter (from Keshishian et al. 1973).*

gen, (ave H content-min H content)/ave H content, was 3.3 percent. This value was probably too high because of leaks detected in the system; the migration occuring in the gas phase concomitantly increases with an increased surface area and path size. In turn, this increase is controlled by the rate of diffusion of H_2 to the surface of the LiH crystal.

The second issue was whether the interaction of molten LiH and stainless steel would affect the H_2 diffusion rate through the stainless steel casing. (The later LiH shields were manufactured by casting molten LiH into a stainless steel matrix and heating the shield to 1200° F to outgas any LiOH impurities.) The results of an experiment measuring this effect showed that the surface action of LiH and stainless steel did not have any impact on the H_2 diffusion rate. However, surfaces of LiH (both external boundaries and internal along cracks and crystal boundaries) will dehydride and metallic Li will form, while the LiH remains crystalline. The H_2 diffuses more slowly through the LiH crystal than through the capsule wall. The effects of hydrogen diffusion on the heat transfer properties and on the overall shielding performance were not reported.

Fabrication of LiH Shield

During the casting of the LiH into the stainless steel matrix, approximately 3 to 6 percent volume voids remained after solidification. The void problem was overcome by backfilling with metallic Li. This, in turn, reduced the number of cracks and added structural integrity during lift-off. (An unanticipated advantage of an increase of 15–30% in the thermal conductivity of the Li-LiH shield above those recorded in Figure 6 was also realized.) There was concern that the Li would interact with LiH at operating temperatures. A summary of Li-LiH interaction at various temperatures and periods of time is shown in Table 5. At temperatures near 588 K (600°F), very little interaction after 4000 h occurred; however above 810 K (1000°F) substantial interaction after 4000 h took place. Hence, if a portion of the LiH shield is subjected to the higher temperatures over long periods, the effects on thermal and neutronic properties (as well as stresses due to volume increases) would have to be accounted for. Once normal operation of the reactor in space begins, some additional cracking of the LiH can be anticipated.

These results imply that maintaining the shield above the Li melting point (453 K) may allow for self-sealing of cracks within the LiH by molten Li present in the shield. These findings also support justification of keeping the upper temperature limit of the LiH shield near 600 K. In general, one observes that cast LiH exhibits less creep under compressive loading than cold-pressed LiH. At 530 K, LiH behaves as a plastic; at 730 K, LiH becomes quite brittle. Some data regarding the compressive creep of LiH are shown in Figure 7. Hence, cast LiH is better from both a thermal conductivity and time-dependent structural performance standpoint.

Emissivity Coating

To increase the emissivity of radiating surfaces, coatings are applied to the surface either before or after the casting process. A variety of coating materials and application methods was tested; after the tests, the coating was exposed to a vacuum (10^6 torr) at 800 K for 14 days to check for deterioration in emissivity. A second test was performed with the emissivity checked after the coating was subjected to hydrogen gas at 1300°F for five days. This test simulated the application of the coating prior to the LiH casting. Both chrome oxide and titanium oxide retained high emissivities (0.87 to 0.90) in the vacuum, with the TiO_2 preferred if applied before casting, and the Cr_2O_3 preferred if applied after casting. However, a range of 0.85 to 0.90 for shield emissivities over the lifetime of the reactor system may not be reasonable because:

- One cannot necessarily extrapolate from 5–14 days tests to the lifetime of the reactor (3–7 years), and
- Testing has not been conducted to determine the stability of the coating in a high radiation field during prolonged operation.

In studies conducted to date, many of the material properties of lithium hydride in a space shielding envi-

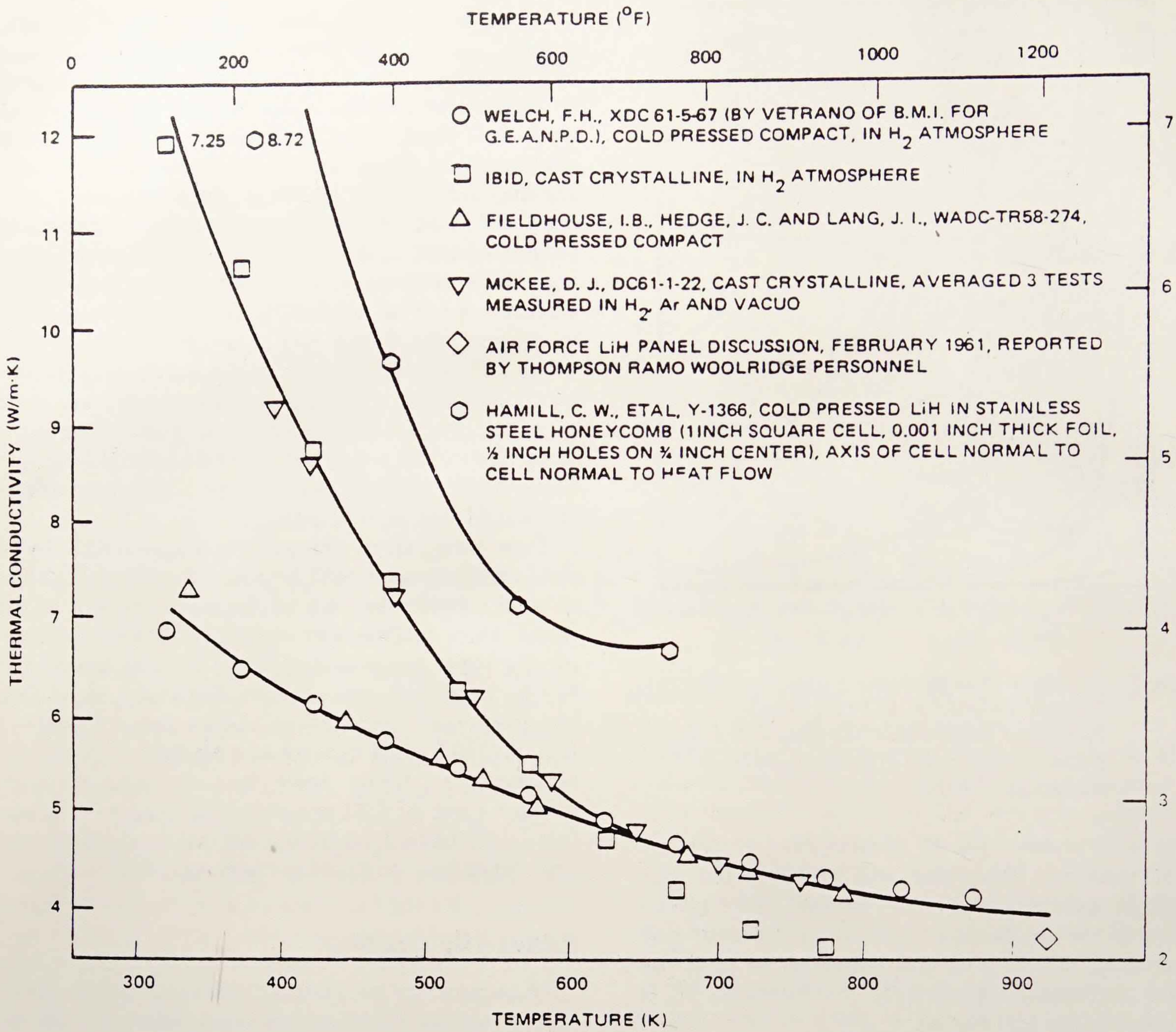


Figure 6 *Thermal Conductivity of LiH (from Keshishian et al. 1973).*

ronment have been determined through experimental analysis. In particular, the interaction of lithium, lithium hydride and stainless steel at elevated temperatures has been examined closely. These results support the previously stated requirement to maintain the maximum temperature of the LiH to the upper 600 K range.

Summary and Conclusions

Previous shielding work for space reactors is reviewed focusing on the areas of neutronic analysis, thermal and stress analysis, and the performance of lithium hydride and tungsten shields. In the 1960s and early 1970s, much work was done on the development of radiation shields for space reactors. The major reactor shields were developed during the SNAP program. Tracing the development of space reactor shields in Figure 9, one observes the increasing sophistication of neutronic analysis and design from the SNAP 10A shield that had no gamma attenuation to the potassium heat pipe reactor shield that is layered and optimized for mass. There is an increasing concern with the need for thermal and structural analysis as the reactor power level increases.

Lithium hydride, although brittle at elevated temperature, has been recommended as the material for space power nuclear reactors because of its high hydrogen content, low density (0.72 gm/cc), high melting point (960 K), relatively low dissociation pressure, very high effective neutron attenuation coefficient, and its ability to capture neutrons while minimizing secondary gamma production.

The major thermal concerns are the very low thermal conductivity and the need to maintain the lithium hydride between temperature limits of 600 and 680 K during steady state operation. A minimum temperature of 600 K is recommended to minimize radiolytically induced hydrogen dissociation from the Li metal, and the accompanying swelling of the shield.

Table 5 *Observations on the Interaction of Lithium-Lithium-Hydride at 600, 900, and 1200° F for 500, 1000, and 4000 Hours.*[a]

Temperature	Heating Time			
	500 hr	1000 hr	2000 hr	4000 hr
600° F (589 K)	Li metal drained clean when capsule was inverted at 600°F. LiH appeared unchanged, although stuck to capsule.	Li metal drained from LiH sample. Apparently no change in the LiH pellet.	Li did not drain completely from LiH sample at 600°F.	Li did not drain completely from the LiH sample at 600°F. LiH crystals were observed in the Li at the bottom of the capsule.
900°F (755 K)	Li did not drain from LiH sample when inverted at 900°F. Surface of LiH appeared unchanged.	Same as 500-hr test, although capsule was kept inverted at 900°F for 3 days.	Capsule leaked air at pinchoff tube at edge of lower pinch. The walls of the capsule were coated with a 1/8-in thick layer of hard material.	Li did not drain completely at 900°F. Material at top and bottom both appeared metallic, but upper part had evidence of crystalline LiH.
1200°F (922 K)	The Li-LiH apparently interacted to form a liquid which flowed when the capsule was inverted and drained at 1200°F.	The Li did not drain when inverted at 1200°F. LiH sample completely interacted, except for a small trace adhering to the capsule walls.	Only small flecks of LiH could be found in the Li matrix. Material did not drain at 1200°F	Very small amount of liquid drained when inverted at 1200°F. Remainder of material appeared metallic with no evidence of crystalline LiH.

[a] From Welch 1967c.

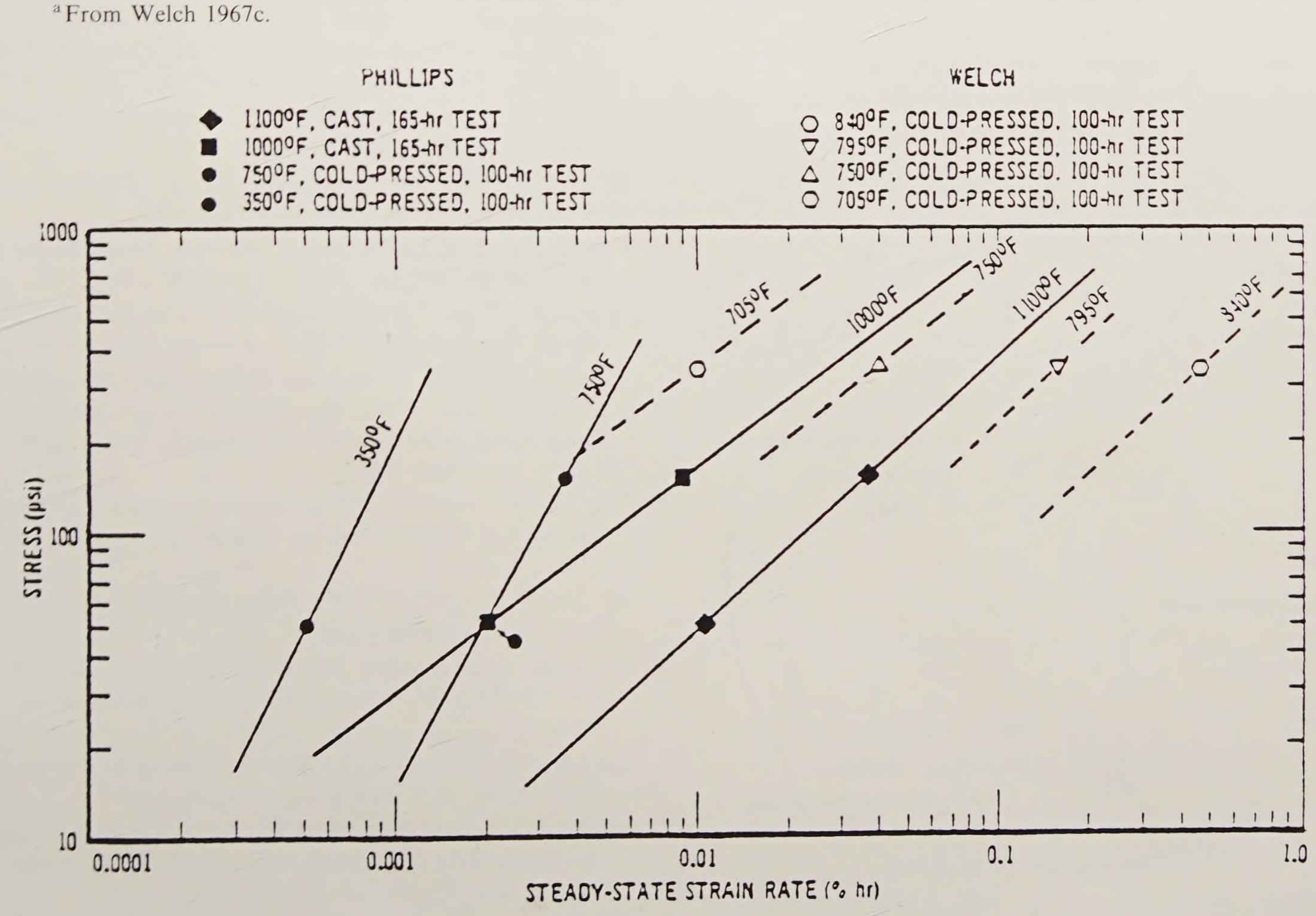


Figure 7 *Compressive Creep of Lithium Hydride (from Welch 1967a).*

Above 600 K, the volume expansion of the LiH remains below 6 percent for a wide range of fast neutron fluences (10^{16} to 10^{20} nvt). Since the density of LiH after being cast into stainless steel matrix remains below 94 percent of theoretical density, this volume expansion does not cause structural deformation to the shield.

The upper operating temperature of LiH is limited to 680 K to reduce the effect of losing the dissociated hydrogen from the shield through the punctures caused by meteoriod impact. For typical shield outer casing thicknesses (0.15 to 0.25 cm), the dose rate at the dose plane will not change due to hydrogen loss if the LiH remains below 680 K.

Tungsten, although costly, is regarded as the most efficient material (from a minimum-shield mass standpoint) for gamma radiation attenuation. Depleted uranium's efficiency as a gamma attenuation material is similar to that of tungsten; and it is much less expensive because it is available as tailing from fuel enrichment plants. However, using uranium near the reactor may not be desirable because excessive fissioning of uranium may cause an appreciable increase in heat generation and introduce intolerable swelling of the uranium shield.

There is considerable literature about the neutronic analysis of previous shield designs. The evolution to mass optimized layered shields credits the advances in capabilities within the radiation transport community. However, a number of significant issues regarding thermal analysis of the shield remained at the time of the SNAP program closeout. Improvements in the skills and tools currently available to the nuclear and thermal sciences communities, allows for more efficient designs in subsystems such as the radiation shield. Advances such as more accurate cross section data, better numerical analysis methods, as well as increased capacities of digital computers encourage re-examination of designs completed before these tools were fully implemented.

Major unresolved thermal issues like the temperature range limitation of LiH, the need for active cooling of the shield, and the induced thermal stresses resulting in excessive cracking of the neutron shield are worthy of further study.

Another major environmental change is the need for more stringent allowable dosages due to the increased sensitivity of modern electronics equipment. Off-the-shelf shield designs coupled with increased limitations of allowable payloads in the space shuttle (in place of rocket delivery systems), will not prove acceptable.

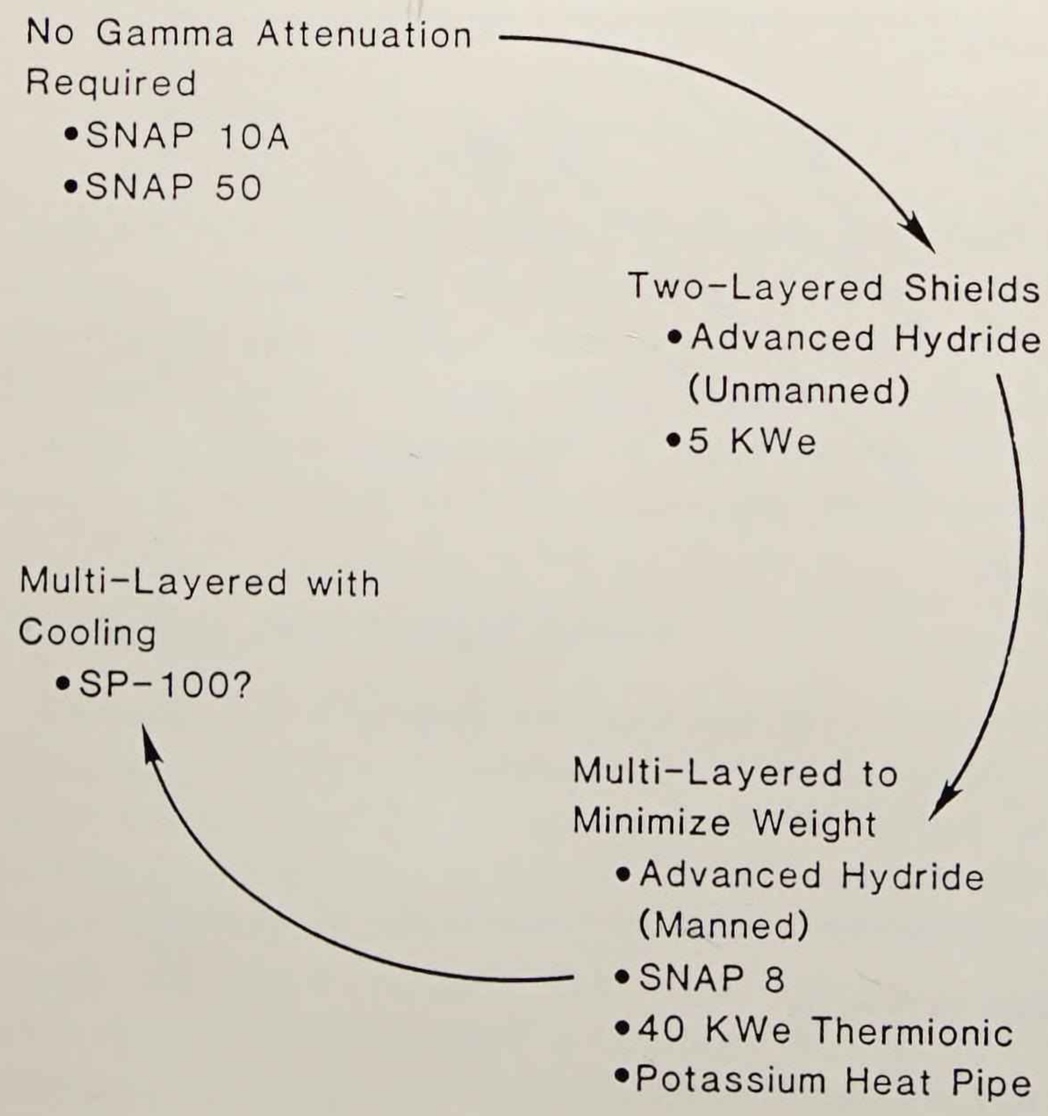


Figure 9 *Evolution of Neutronics Analysis and Design of Space Reactor Shields during SNAP Program.*

Acknowledgments

This research was conducted at the University of New Mexico under the sponsorship of the Air Force Institute of Technology, Wright-Patterson Air Force Base, Ohio.

References

Beiriger, F., Jr. (1968) *Thermal Analysis-Advanced ZrH_2 Reactor*, TI-696-20-001, Atomics International, May 1968.

Engle, W. W., Jr., R. L. Childs, F. R. Mynatt, and L. S. Abbott (1971) *Optimization of a Shield for a Heat Pipe Cooled Fast Reactor Designed as a Nuclear Electric Space Power Plant*, ORNL-TM-3449, Oak Ridge National Laboratory, June 1971.

Gietzen, A. J. et al. (1971) *A 40 kWe Thermionic Power System for a Manned Space Laboratory*, Gulf-GA-A10535.

JPL (1982) *SP-100 Conceptual Design Description No. 1.*, NASA-Jet Propulsion Laboratory, June 1982.

Kaszubinski, L. J. (1973) *Shield Materials Recommended for Space Power Nuclear Reactors*, NASA TM X-2835, July 1973.

Keshishian, F. et al. (1973) *Radiation Shielding for Zirconium Hydride Reactor Systems*, AI-AEC-13081, Atomics International Division.

Lahti, G. P. and P. F. Herrman (1969) *Comparison of Tungsten and Deplete Uranium in Minimum Weight Layered Shields for a Space Based Power Reactor*, NASA TM-X-1874, NASA Lewis Research Center, September 1969.

Los Alamos (1982) *SP-100 Project Semi-annual Technical Progress Review*, Los Alamos National Laboratory, New Mexico, October 1982.

Masora, D. G. (1973) *SNAP 8 Design Description*, NAA-SR-MEMO-8740, Atomic International.

Pratt and Whitney (1964) *SNAP 50/SPUR Program Summary*, Report CNLM-5889, Pratt and Whitney Co., Middletown, CN, Sept. 1964.

Schaeffer, N. M. (Ed.) (1973) *Reactor Shielding for Nuclear Engineers*, KIP-2595, U. S. Atomic Energy Commission.

Stidler, J. T. and R. W. Weiss (1976) *A Thermal Analysis Evaluation of the Viking RTG Heat Shell*, ANSP-M-12, Johns Hopkins University, Applied Physics Lab, March 1976.

Thompson and Schwab (1969) *Nuclear Heating in Reference ZrH_2 Shield*, TI-696-23-040, Atomics International, December 1969.

Voss, S. S. (1984) *SNAP: Reactor Overview*, AFWL-TN-84-14, Air Force Weapons Laboratory, Kirtland AFB, NM, August 1984.

Welch, F. H. (1967a) *Lithium Hydride Technology: III. Properties of Lithium Hydride for SNAP Shielding Applications*, NAA-SR-9400, Vol. III, Atomics International, August 1967.

Welch, F. H. (1967b) *Lithium Hydride Technology: IV. A Novel Neutron-Gamma Material for SNAP Applications*, NAA-SR-9400, Vol. IV, Atomics International, August 1967.

Welch, F. H. (1967c) *Lithium Hydride Technology: V. Testing and Examiniation of SNAP Shadow Shields*, NAA-SR-9400, Vol. V, Atomics International, August 1967.

Space Nuclear Power Systems 1984
Edited by M. S. El-Genk and M. D. Hoover
© Orbit Book Company, Malabar, FL, 1985

Chapter 40

The Forming of Metal Components for Radioisotope Heat Sources

Ernest W. Johnson

Monsanto Research Corporation (MRC)
Mound
Miamisburg, Ohio 45342

Use of refractory and noble metals to encapsulate the plutonium-238 fuel used to power radioisotope thermoelectric generators (RTGs) presents a series of problems for the fabricator. These alloys (Ta-10 W, T-111, Mo-Re, Pt-Rh, and Ir-0.3 W) permit a high RTG operating temperature, which increases the efficiency, and minimizes the risk of releasing plutonium dioxide in an accident. The choice of materials for heat source construction has evolved from superalloys and refractory metal systems to iridium/carbon. This paper describes techniques employed at Monsanto Research Corporation (MRC) to develop flight-quality iridium Clad Vent Sets (CVSs) to support production of the General Purpose Heat Source (GPHS). Techniques of forming, welding, and heat treating are addressed, as are the quality requirements necessary to justify employing the "DOP-26" iridium alloy parts as a primary encapsulation for $^{238}PuO_2$ fuel. The methods employed have enabled MRC to meet the DOE-defined requirements to support the CVS requirements for the Galileo and International Solar-Polar Missions.

Introduction

The General Purpose Heat Source Radioisotopic Thermoelectric Generator (GPHS RTG) has been defined as the power generating system to be employed for the Galileo and International Solar Polar spacecraft. This RTG is shown schematically in Figure 1. Figure 2 illustrates its heat source.

Earlier, MRC, which operates Mound for the Department of Energy, had been charged with the production of primary containment components for plutonium-238 fuel used in various space missions. For the Viking and Pioneer Missions, molydenum-47% rhenium, tantalum-10% tungsten, T-111, and platinum-10% rhodium parts were produced (Wendeln et al. 1972). The next

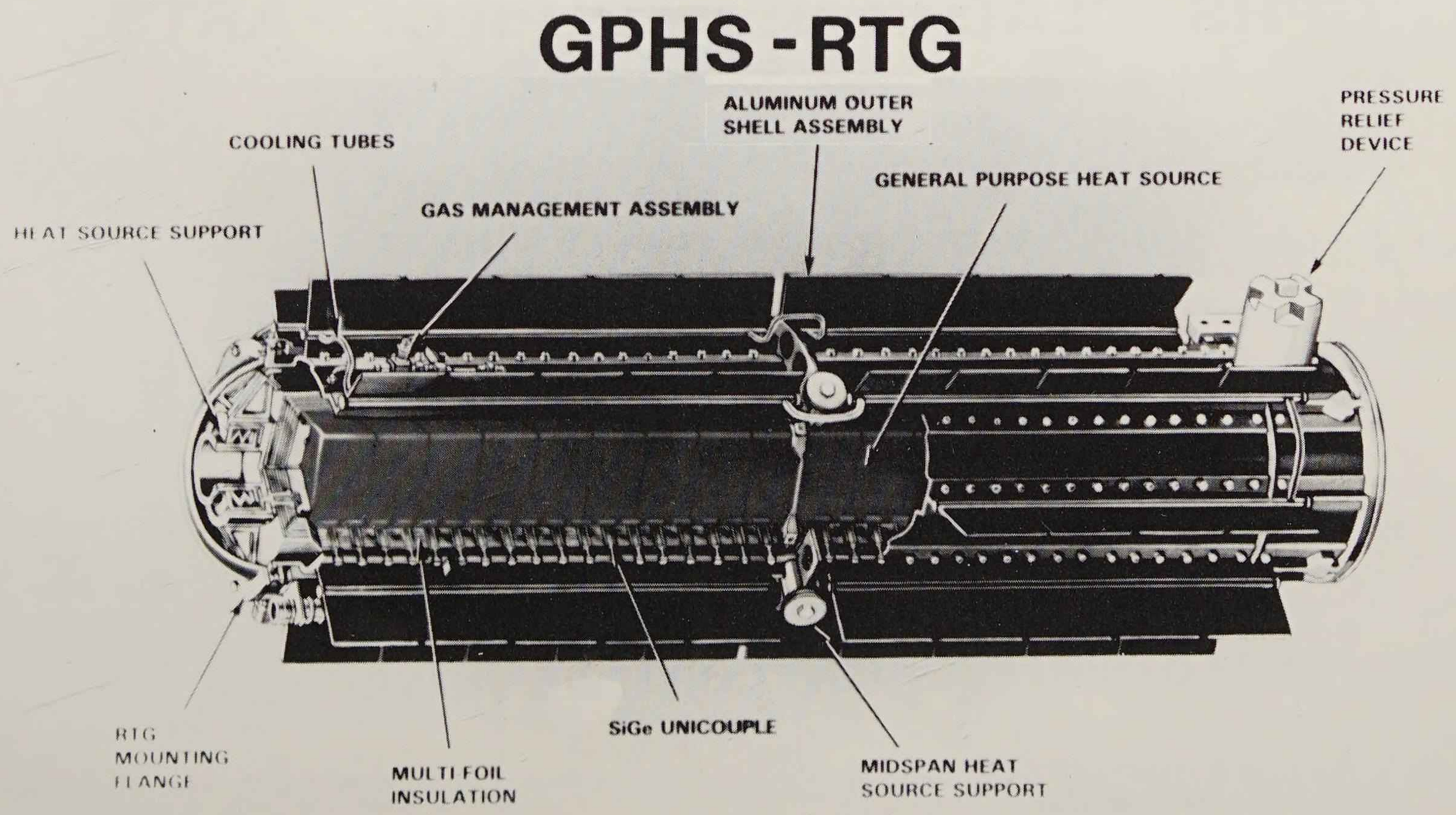


Figure 1 *The GPHS RTG is Assembled using 18 250-W Heat Source Modules.*

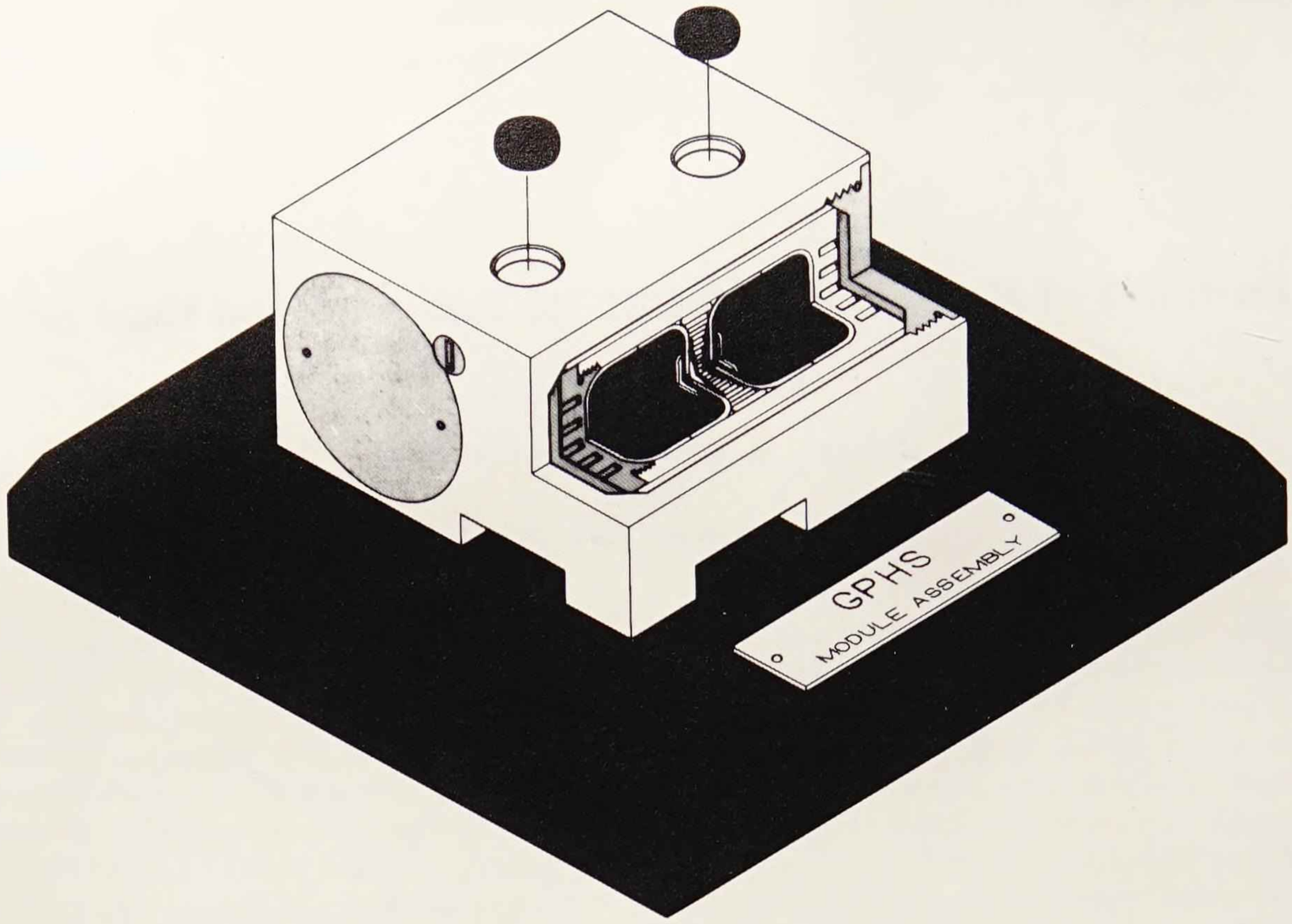


Figure 2 *One GPHS Module contains Four Fueled Clads.*

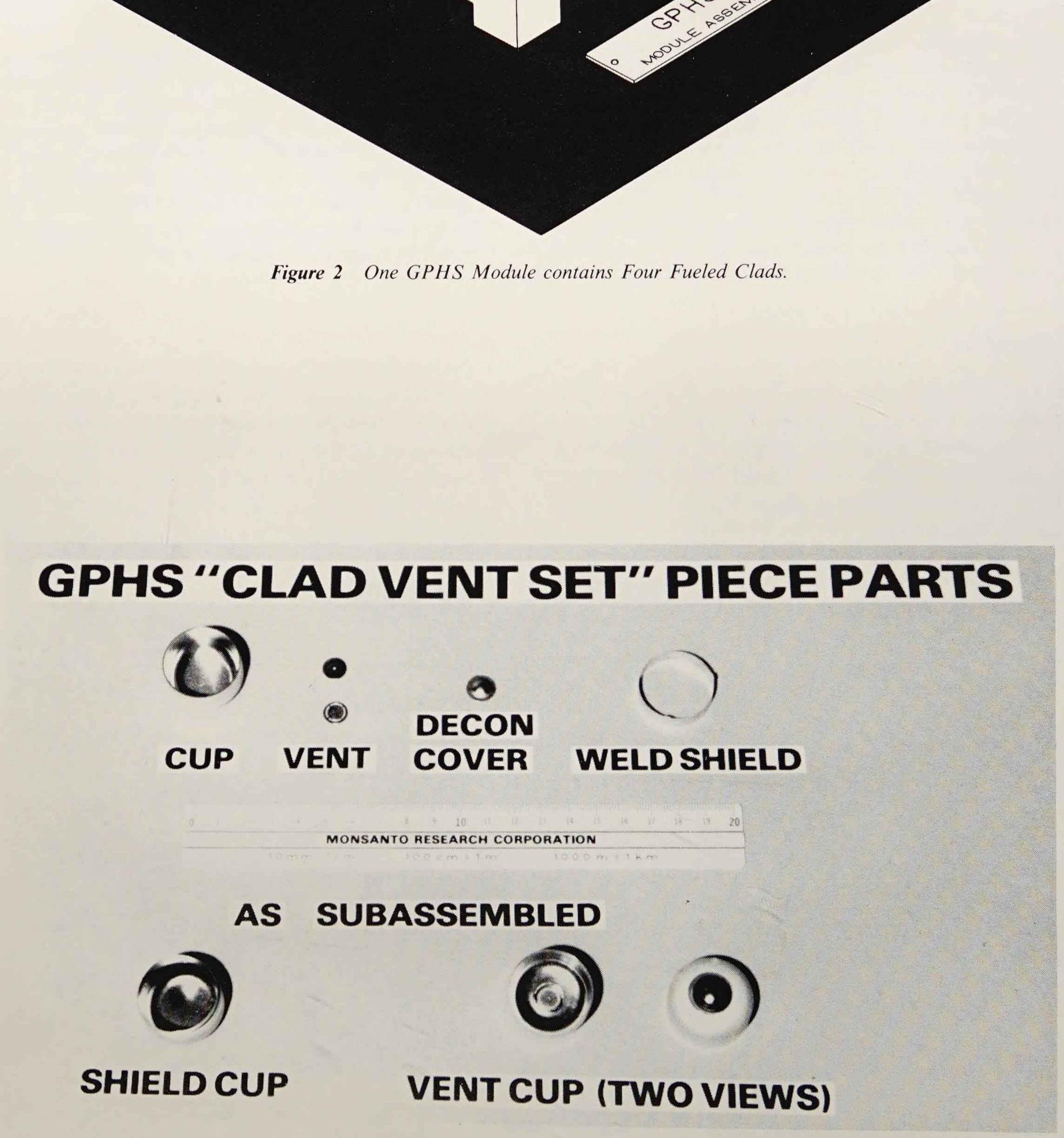


Figure 3 *Production of Iridium GPHS CVS Hardware includes the Electron Beam (EB) Subassembly of the Vent, Decon Cover and Weld Shield to the Cups.*

generator system, the Multi-Hundred Watt (MHW) RTG, featured a clad manufactured from iridium-0.3% tungsten. The technology incorporated in the fabrication of these components is described elsewhere (Wyder 1974 and 1976).

As in the MHW program, the supplier for the iridium alloy starting blanks and foil for the GPHS program was the Oak Ridge National Laboratory (ORNL). ORNL had developed the original iridium-0.3% tungsten alloy, which was used in the MHW program (Liu and Inouye 1977). Further behavioral enhancement (better high-temperature impact ductility and reduced grain growth rate) was realized by the addition of ~50 ppm of aluminum and ~60 ppm of thorium. This alloy was designated DOP-26 (Liu and David 1982). Components in various stages of production are shown in Figure 3.

Methods

The fabrication processes for the various components are described as follows:

Cup

The blank is sandwiched between two 0.08-mm tantalum barrier sheets and electron beam welded into Type 304 stainless steel waster sheets. The rolling direction of the waster sheet is oriented to ±45° with the final rolling direction of the iridium blank. This minimizes forming anisotropy. A two-step, deep-draw process employing heated tooling is performed at 925→650°C to transform the metal blank into a cup (Figure 4). The heated tooling is shown schematically in Figure 5.

There are several advantages to this process:

1. Lubrication is Controlled—Graphite foil washers provide good lubrication virtually without tooling wear.
2. Dimensions are Controlled—Compensation inserts correct for wall thickening; final precision sizing is only a minor correction step.
3. Environment is Shielded—Electron beam welded packet prevents unwanted compatibility problems.
4. Earring is Neutralized—Waster sheets permit virtual elimination of nonuniform deformation due to sheet rolling processes.
5. Thermal Losses are Minimized—Warm-forming temperature is retained by the blank due to the waster sheet insulating properties.

After forming, the barrier and waster sheets are removed, the cup recrystallized and lapped to length, rounded up, and grit blasted to an 0.8–3.2 μm finish. Dimensional and dye penetrant inspection are the principal quality requisites for this component.

The early cup production effort was plagued by the incidence of extremely small surface defects, which were found by the ultrasensitive fluorescent dye penetrant inspection technique being employed. To ascertain whether or not this effect could be eliminated, tests

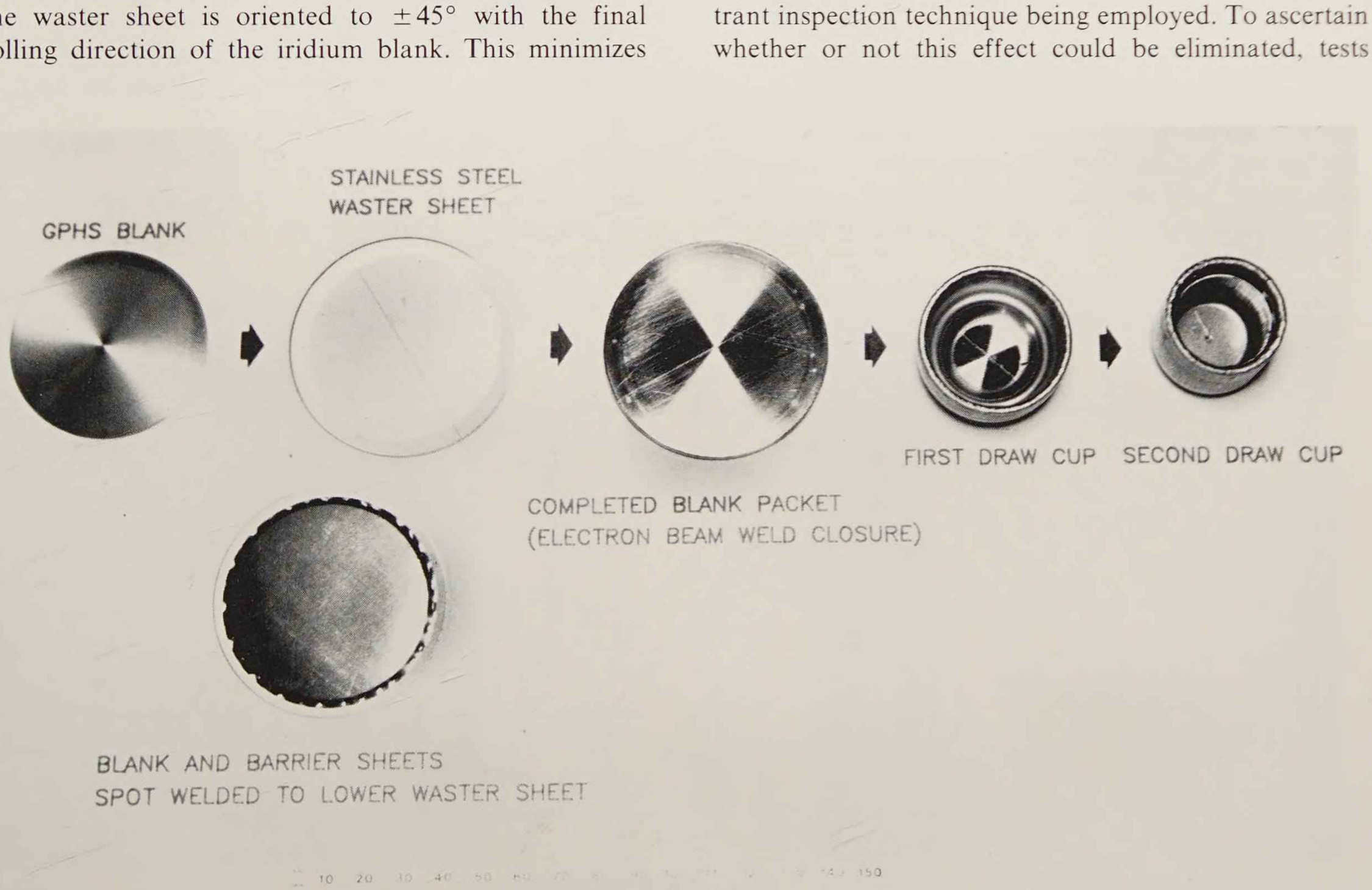


Figure 4 *Prior to Forming GPHS Cups from DOP-26 Iridium the Blanks are sealed in a Waster Sheet Packet.*

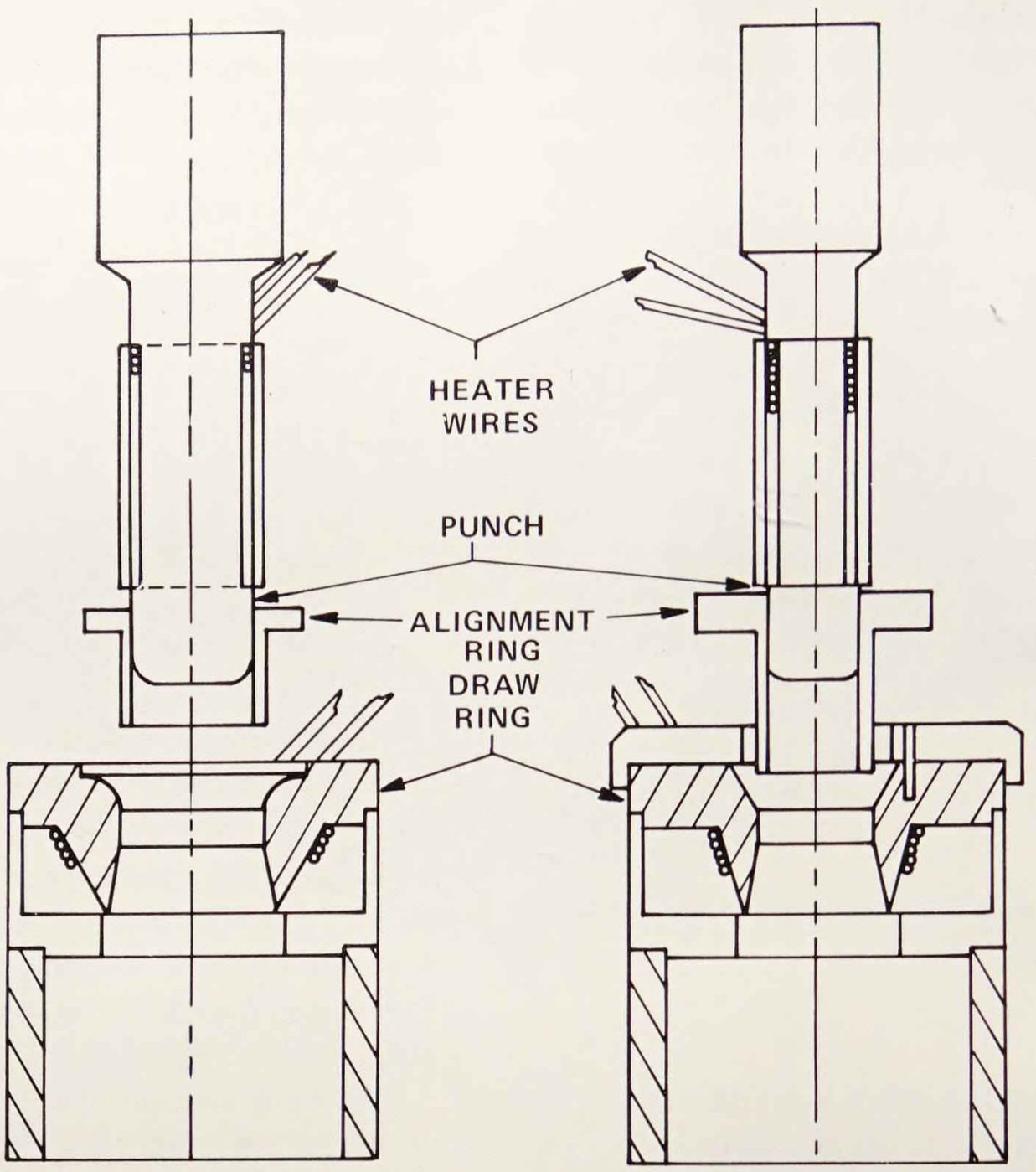


Figure 5 *Heated GPHS Cup Drawing Tooling results in Quality Parts after a Two-Step Operation.*

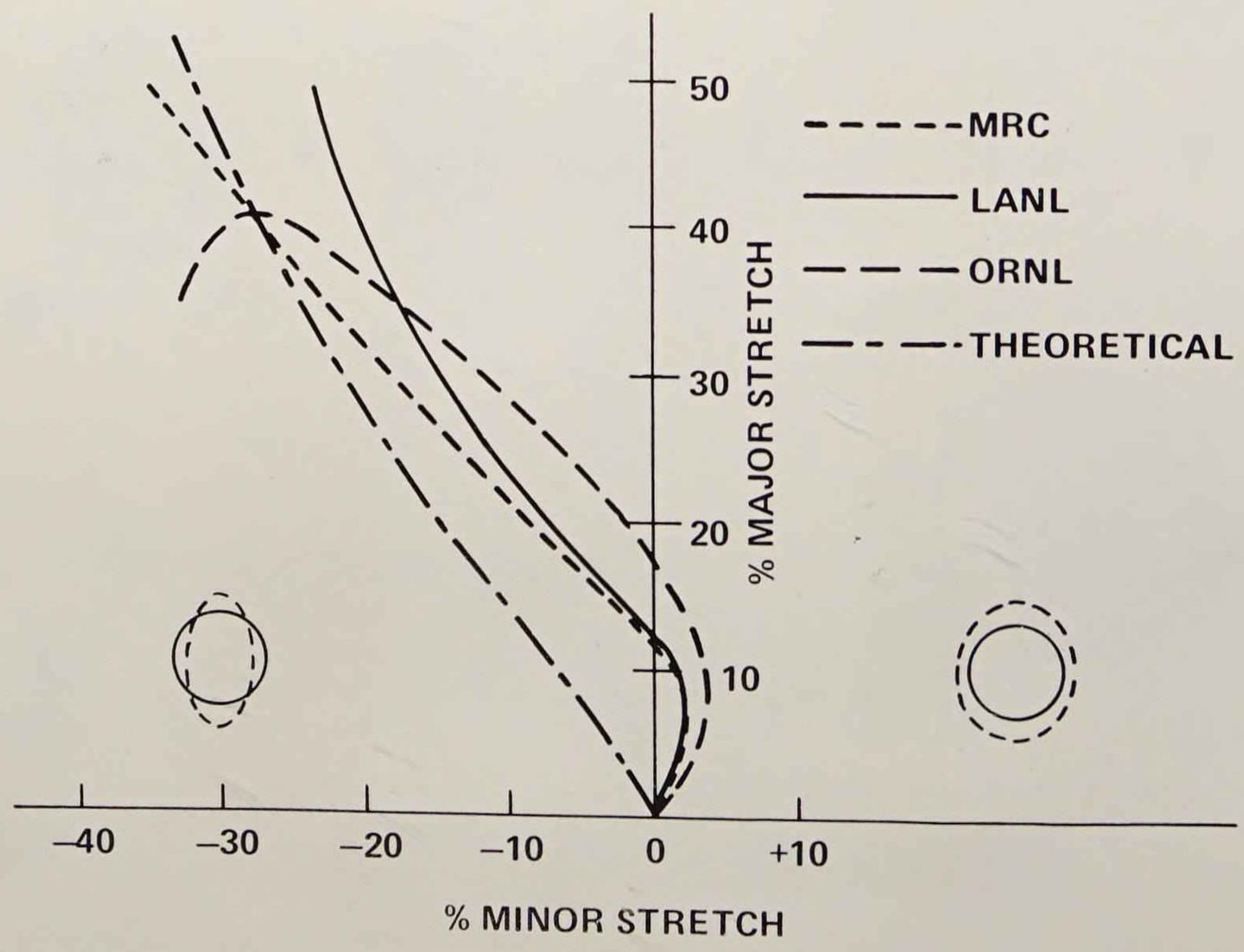


Figure 6 *Employing the Forming Limit Diagram Format, the Measured Strains Involved in GPHS Cup Fabrication at MRC, LANL, and ORNL are compared.*

Table 1 *Characteristics of Cup Fabrication Processes Reviewed as Part of the Iridium Production Technology Program.*

Variable	LANL	MRC	ORNL
Blank Temperature	1000°C	925→650°C	600°C
Tool Temperature	1000°C	250°C	600°C
Number of Draws	1	2	1
Forming Load	~1800 lb	~8000 lb	~10500 lb
Hold-down Force	600 lb	0	3000 lb
Punch Speed	3 in./min	24 in./min	0.5 in./min
Lubricant	Si_3N_4	C[a]	BN
Dye Penetrant[b]	Yes	Yes	Yes

[a] Waster sheet only.
[b] Dye penetrant indications were believed to be the most significant pass-fail criterion; all cup manufacturing processes exhibit this effect to some extent.

were performed among Los Alamos National Laboratory, Mound, and Oak Ridge National Laboratory. The techniques employed by the various participants did not result in reducing the flaking surface grains (Table 1). Forming limit diagram analysis indicated that all methods were similar with respect to strain pattern (Figure 6).

After a final one-hour 1500°C vacuum outgas (designed to remove all traces of volatile oxides which may be present after the process), the metal microstructure has changed from a highly wrought one to yield a material exhibiting an ASTM 6–8 grain size. Although retaining some grain anisotropy due to the warm rolling of the sheet, the as-produced cup grain structure is quite uniform (Figure 7).

Weld Shield

To protect the circumferential gas tungsten arc weld from the plutonium fuel pellet, a weld shield is placed in one GPHS cup. This part is stamped from 0.13-mm iridium foil; the formed piece is rolled over a mandrel, and electron beam butt-welded into a continuous ring.

Decontamination Cover

As an assembly aid, the vent orifice must be protected from air and decontamination solutions during assembly. The decontamination cover provides this protection. This component is formed by blanking discs from 0.13-mm foil and pressure-pad forming to the proper configuration. Because a leak-tight seal is required, a fluorescent dye penetrant inspection is the main quality call-out.

Vent

The vent is a critical component from safety and operational standpoints. The vent permits the helium which results from alpha decay of plutonium-238 to exit the clad, yet retains solid plutonium particulates. The two vent discs are stamped from 0.13-mm foil. A thin layer (72.5 mg) of iridium powder (−325, +400 U.S. standard mesh) is sintered between the two discs. The final part is then less than 0.41-mm thick. The flow rate is 0.075-0.125 cm^3/sec at 7 kPa pressure differential. The component is shown in Figure 8.

Assembly

After piece-part fabrication, electron beam welds are performed to produce the completed Clad Vent Sets shown in Figure 3. Inspections are made for cracks, voids, pores, and penetration; the vent and decontamination cover welds must be leak-tight and fusion continuous. Appearance of the EB welds are shown via

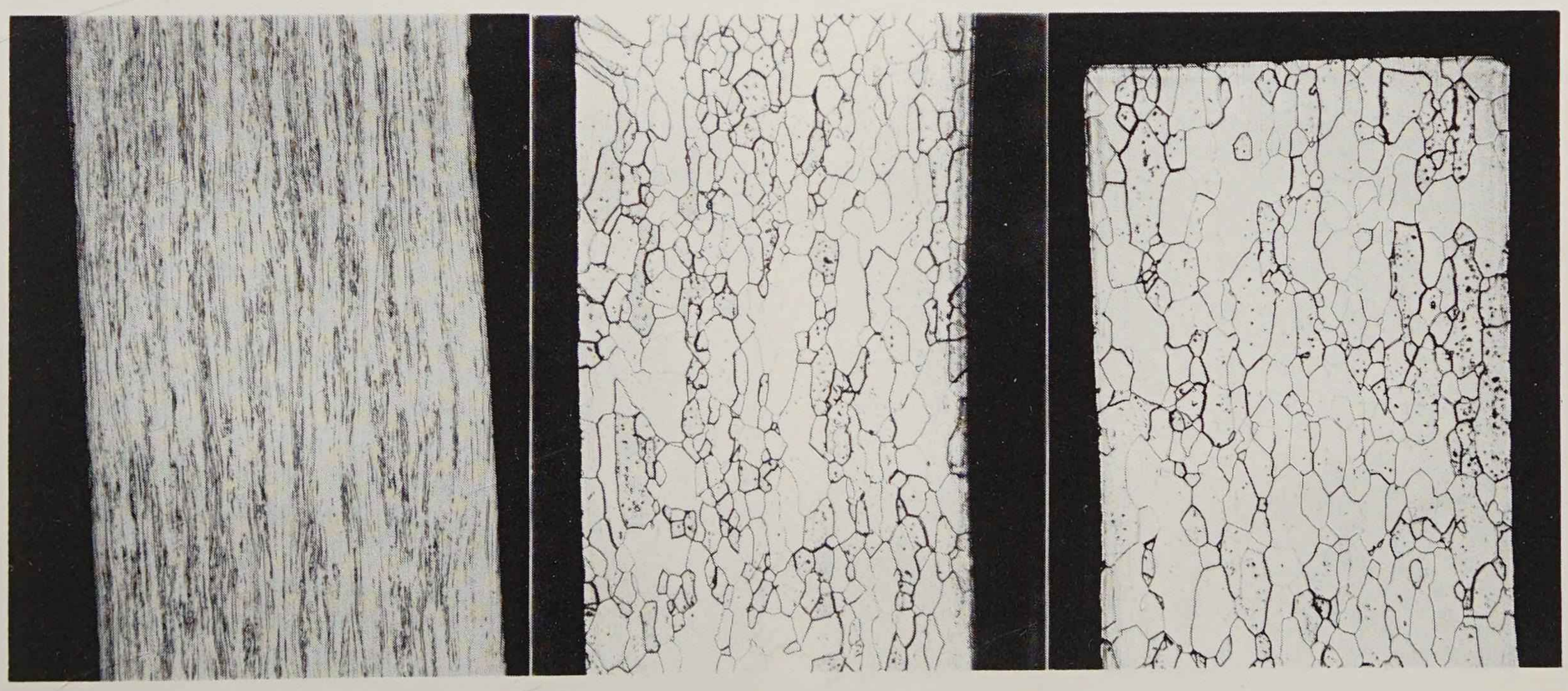
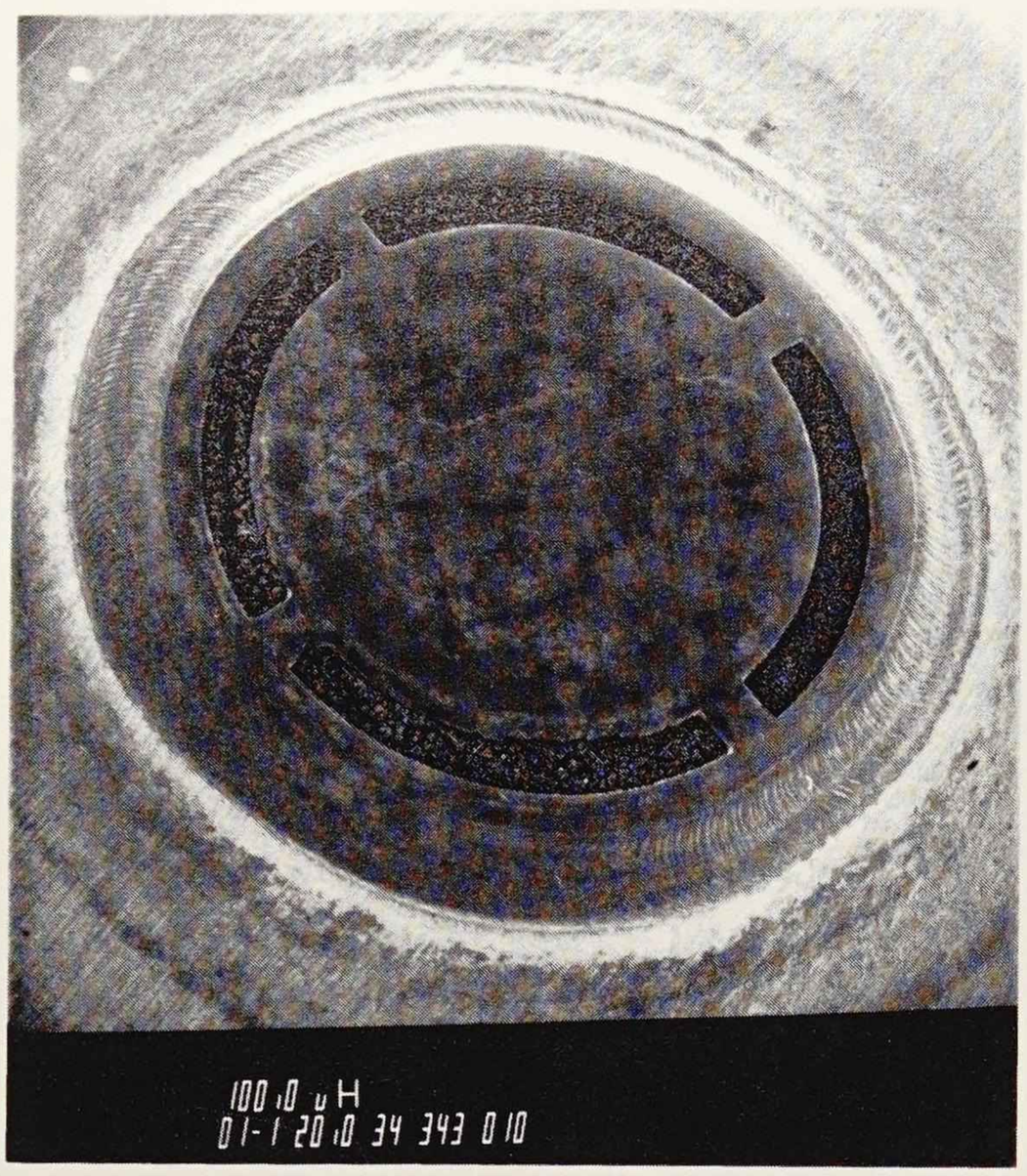


Figure 7 *The Iridium Microstructure is monitored by Performing Metallographic Inspection of the ORNL-produced Blank (left), the MRC-Processed Unworked Center Portion of the Cup (middle), and the MRC-processed Cup Lip (right). Photos are 100X.*



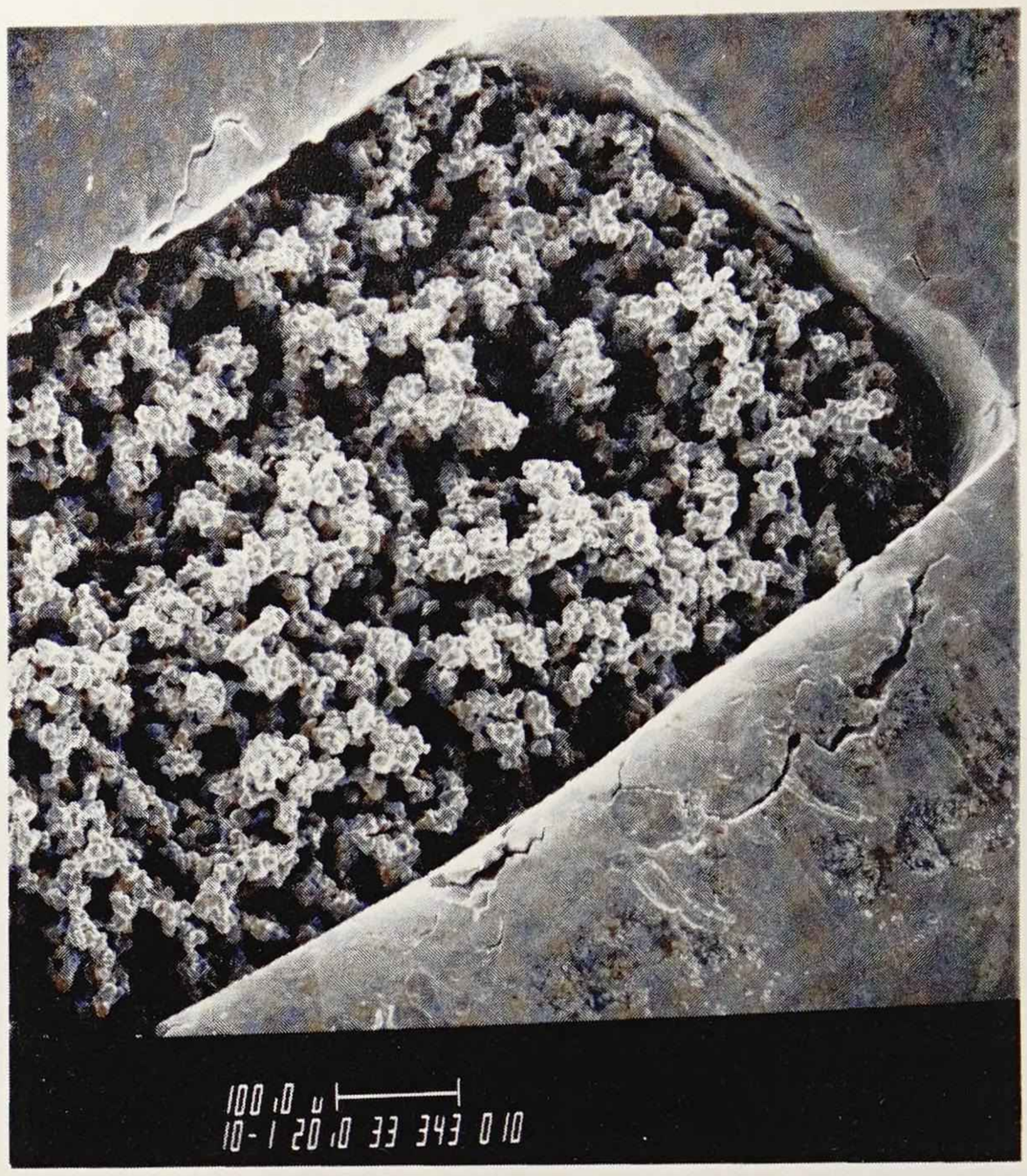
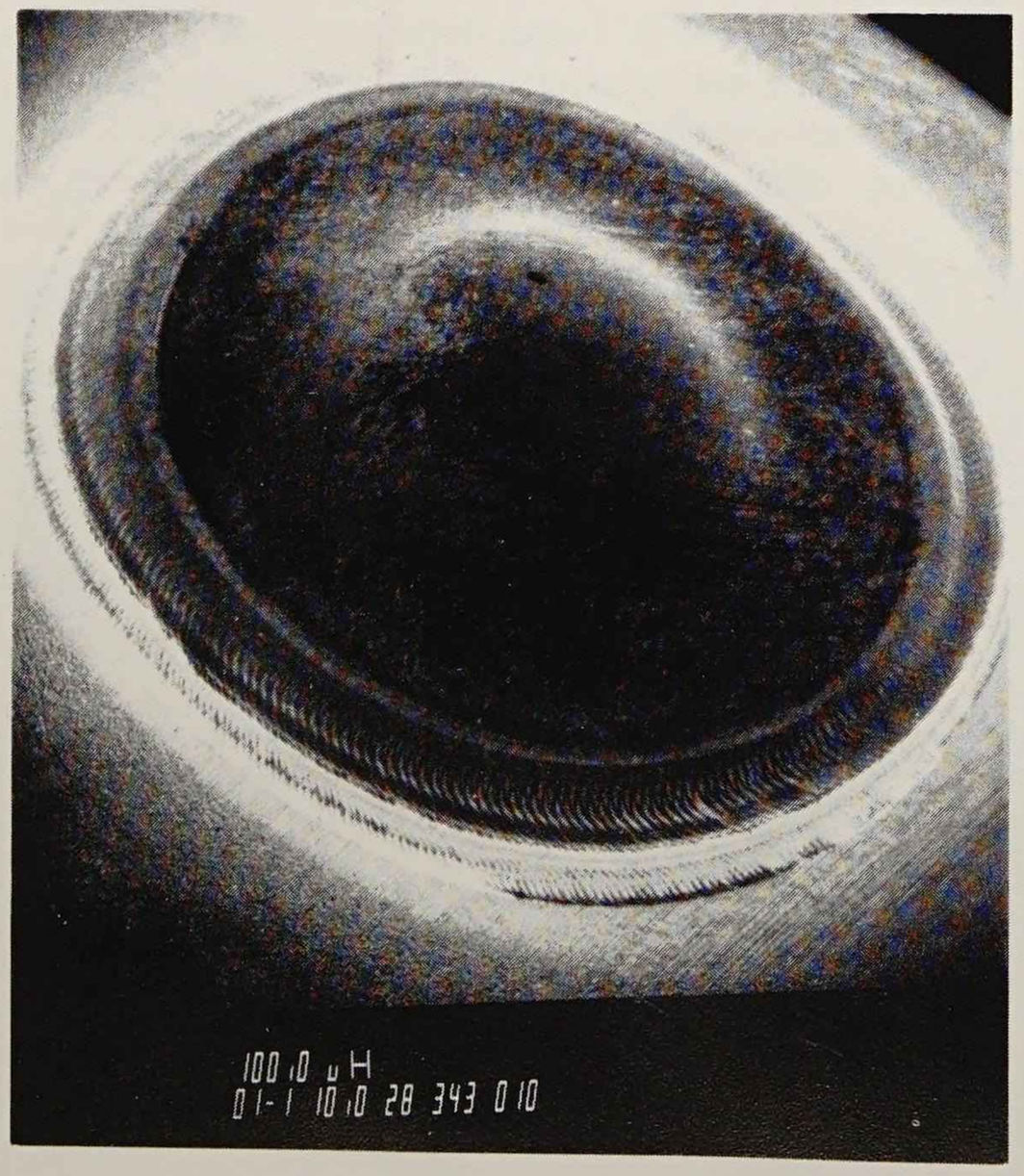


Figure 8 *Scanning Electron Photomicrographs of the Iridium GPHS Frit Vent show the Overall General Appearance, Including the EB Weld (left at 10X) and Detail of the Sintered Iridium Powder in the Frit Area (right at 100X).*



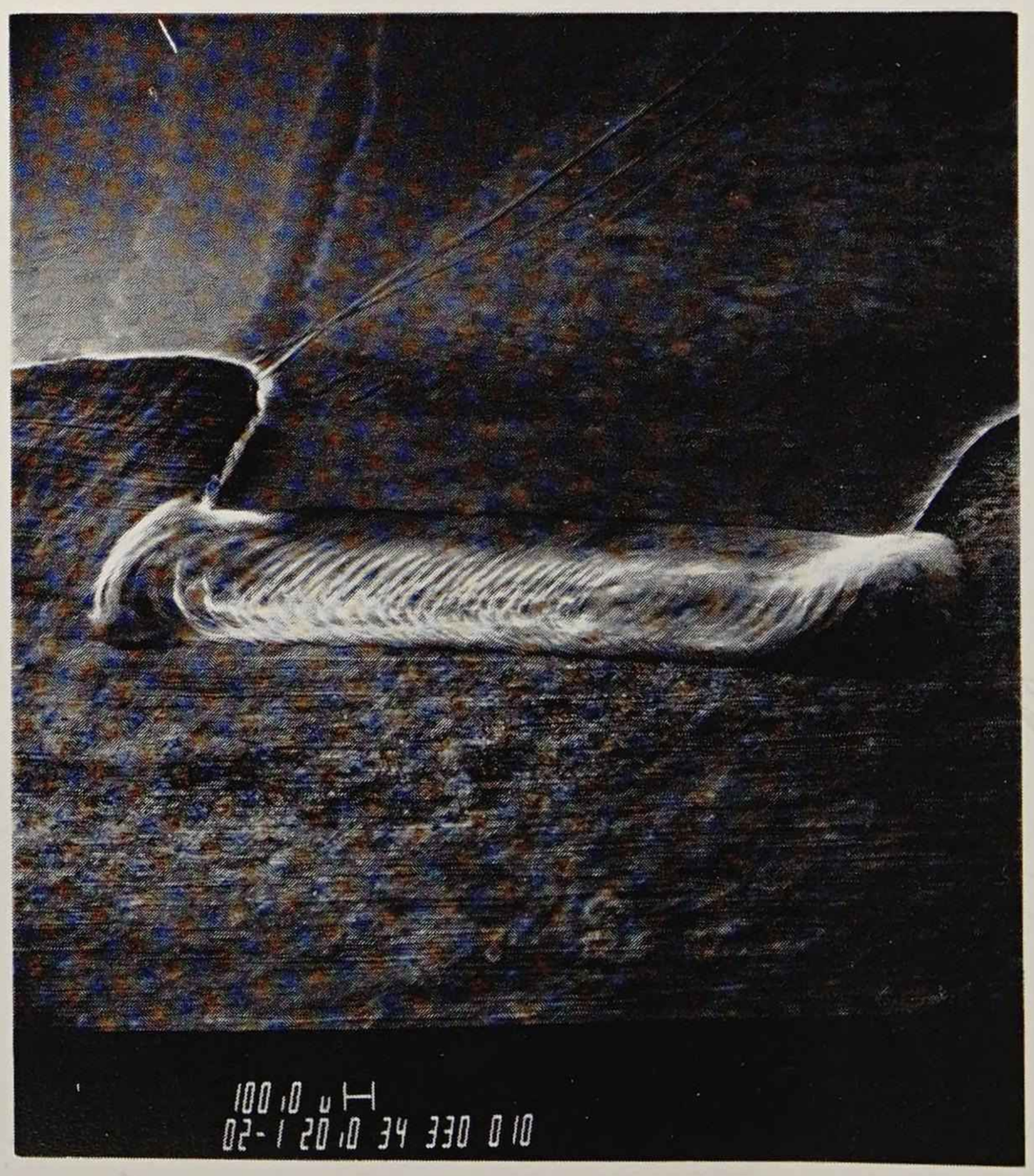


Figure 9 *Examples of GPHS Iridium EB Subassembly Welding are the Decontamination Cover (left at 10X) and the Weld Shield Tab-to-Cup (right at 20X).*

scanning electron microscopy (SEM) in Figure 8 (vent) and Figure 9 (decontamination cover and weld shield tab).

Quality Control

A set of GPHS cups undergoes the following in-process and postprocessing inspections for quality and reliability:

64 dimensional inspections,
2 flow tests,
2 fluorescent dye penetrant checks,
1 helium leak check,
5 visual checks, and
Destructive testing (~1 in 50) for metallography, microhardness, and chemical analyses.

Table 2 summarizes the inspections performed during the process steps necessary to complete one set of GPHS hardware. This close surveillance of parts throughout the process has resulted in a very low reject rate in foil and subassembled parts. The major production problem remaining is related to the inherent difficulty in achieving a uniform material from which to form cups without delaminated or flaked structure.

MRC has produced about 1900 iridium cups since 1980. The 74 percent "flight-quality" yield testifies to the difficulty of manufacturing the component. The 98% usable product resulted in a quite satisfactory process assessment, however.

Piece-part efficiencies were somewhat better: The weld shield yielded 85% prime parts, decontamination cover success was 92% prime, and 91% of the vents produced were of prime quality. Approximately 98% of the subassemblies were acceptable for prime use after the electron beam welding was completed.

Table 2 *Summary of Inspections Performed on a Set of Iridium GPHS Cups throughout and after Processing.*

	Process Steps	Inspection Steps
Cup	20	3
Vent	20	3
Weld Shield	9	2
Decontamination Cover	9	3
Subassembly	12	8
Total	70	19

Summary

Flight-quality iridium components can be fabricated from iridium alloys by modifying standard production processes. A large quantity of metrological and nondestructive evaluation data support the quality of these devices, which, in turn, justify their use in containing plutonium fuel for space system applications.

Acknowledgments

Mound is operated by Monsanto Research Corporation for the U. S. Department of Energy under Contract No. DE-AC04-76DP00053.

References

Liu, C. T. and H. Inouye (1977) *Development and Characterization of an Improved Ir-0.3% W Alloy for Space Radioisotopic Heat Sources*, ORNL-5290, Oak Ridge National Laboratory, Oak Ridge, Tennessee.

Liu, C. T. and S. A. David (1982) *Weld Metal Grain Structure and Mechanical Properties of Iridium Alloy DOP-26*, ORNL-5857, Oak Ridge National Laboratory, Oak Ridge, Tennessee.

Wendeln, D. E. et al. (1972) *Heat Source Capsule Fabrication Technology Program: Final Report January 1971–March 1972*, MLM-1935, Monsanto Research Corporation, Miamisburg, Ohio.

Wyder, W. C. "Iridium Hardware Fabrication for the MHW Heat Source," in *Transactions of the American Nuclear Society 1974 Winter Meeting*, held in Washington, D.C., October 27–31, 1974, pp. 36–37.

Wyder, W. C. (1976) *Warm Hydroforming of Iridium + 0.3 Wt% Tungsten Hemishells*, MLM-2203, Monsanto Research Corporation, Miamisburg, Ohio.

Space Nuclear Power Systems 1984
Edited by M. S. El-Genk and M. D. Hoover
© Orbit Book Company, Malabar, FL, 1985

Chapter 41

Technology Status of Tantalum Alloys for Space Nuclear Power Applications

E. E. Hoffman

Oak Ridge Operations Office
U.S. Department of Energy
Oak Ridge, Tennessee 37831

Tantalum alloys have a variety of properties which make them attractive candidates for application in nuclear power systems required to operate in space at elevated temperatures (1200 to 1600 K) for extended time periods. Most of the technology development on this class of alloys which is pertinent to space system application occurred during the 1960 to 1972 time period under NASA sponsorship. The most extensive data bases resulting from this earlier work were obtained on the alloys T-111 (Ta-8W-2Hf) and ASTAR 811C (Ta-8W-1Re-0.7Hf-0.025C). Emphasis in this paper is directed at the following technical factors: producibility, creep strength, weldability and compatibility. These factors are considered to be the most important elements in the selection of alloys for this application. Review of the available information indicates that alloys of this type are appropriate for application in many systems, particularly those utilizing alkali metals as the working fluid.

Introduction

Many of the reactor/power conversion systems which are currently being evaluated for potential application in space systems are required to operate at very high temperatures in order to meet the electrical power/mass/envelope targets which have been specified. The operating temperatures being considered and the demanding environmental conditions (for example, alkali metal working fluids, ultra-high vacuum) quickly eliminate conventional alloys (iron-, nickel-, and cobalt-base) as viable candidates. For about thirty years, refractory alloys of molybdenum, niobium, tantalum, and tungsten have been considered, tested and evaluated for potential use in the design of high-temperature, compact reactor power systems.

The bulk of the refractory alloy research and development in support of these power system designs has concentrated on alloys of niobium and tantalum. The principal reasons for the focus on these alloys are the relative ease of fabrication of wrought products and the good ductility/toughness characteristics of welded structures of these materials. Alloys of molybdenum and tungsten have many attractive properties for specific applications, such as fuel element cladding, turbine rotors and blades, but present major challenges when considered for complex structural applications because of ductility and weld toughness limitations. This paper only addresses factors important to the selection of tantalum alloys for structural applications in space power systems. The paper by Cox et al. (1985) includes a discussion of the use of tantalum alloys as cladding for specific fuel systems.

Technology Factors Considered

The purpose of this paper is to summarize the technology status of tantalum alloys. The bulk of this data was generated under NASA-Lewis Research Center sponsorship during the 1963–1972 time period as part of the technology support to the NASA-Lewis compact fast reactor concept for which the T-111 alloy was selected as the reference fuel clad and structural alloy (Krasner, Davidson and Diaguila 1971). Because of the very large body of information in the literature on the various tantalum alloys, it will only be possible in this paper to give an overview of this technology. The principal focus of the discussion which follows will be directed at the alloys T-111 (Ta-8W-2Hf) and ASTAR 811C (Ta-8W-1Re-0.7Hf0.025C).

Since most of the concepts currently being considered involve the use of the alkali metals (lithium, sodium, potassium or alloys of sodium and potassium), the emphasis in this review will be on alloys which are compatible with these heat transfer fluids. Niobium- and tantalum-base alloys require small concentrations of stable oxide-forming elements, such as zirconium or hafnium, to prevent gross attack by the alkali metals, particularly lithium. For this reason, the otherwise popular tantalum alloy, 90Ta-10W, was long ago eliminated as a candidate alloy for the space nuclear power systems under consideration and the emphasis put on

alloys such as T-111 and ASTAR 811C which contain small amounts of hafnium.

Only those factors considered to be the most important in the selection of tantalum alloys for complex structural applications will be reviewed in this paper. These factors include producibility, creep strength, weldability, and compatibility. Great reliance will be put on the papers presented at a recent symposium of refractory alloys (U.S. DOE 1984) which attempted to summarize the technology of refractory alloys in general and to identify the remaining technology needs for the specific alloy classes. An earlier conference (NASA 1970) included many informative papers on the status of tantalum alloy technology at that time.

Producibility

During the period 1955 to 1973, a large body of experience was gained in the production of high-quality tantalum wrought products. Table 1 lists a number of tantalum alloys, their composition, and current production status. This information was included in a recent paper by Buckman (1984) which provides an excellent summary of all the important factors in producing tantalum alloys, including melting, primary working, secondary working, heat treatment, and specification requirements. Buckman also describes some of the "lessons learned" during the earlier production of tantalum alloys which should be considered in the upgrading of the specifications used at that time. Of the alloys listed in Table 1, the only alloy indicated as "commercial" which meets the requirement of containing the strong oxide-forming element hafnium is T-111. Even this alloy may be considered commercial in only a limited sense currently and, when ordered to the demanding and necessary requirements of existing specifications, might only be supplied on a best-efforts basis. During the period 1965–1970, approximately 2500 kg of a great variety of high-quality T-111 wrought products, including seamless tubing in sizes ranging from 6 to 116 mm O.D., were commercially produced and utilized on NASA-developed programs. Both the T-111 and ASTAR 811C alloys are very fabricable; the major procurement problem is the limited vendor experience with alloys of this type in recent years.

Table 1 *Composition and Production Status of Tantalum Alloys.*[a]

ALLOY	COMPOSITION (Weight Percent)	STATUS
Ta-2.5W	Ta-2.5W	Commercial
Ta-7.5W	Ta-7.5W	〃
Ta-10W	Ta-10W	〃
KBI Alloy 40	Ta-40Nb	〃
T-111	Ta-8.0W-2.0Hf	〃
T-222	Ta-9.6W-2.4Hf-0.010C	Pilot plant prod.
ASTAR-811C	Ta-8.0W-1.0Re-0.7Hf-0.025C	〃 〃 〃
ASTAR-1211C	Ta-12.0W-1.0Re-0.7Hf-0.025C	〃 〃 〃
ASTAR-1511C	Ta-15.0W-1.0Re-0.7Hf-0.025C	〃 〃 〃

[a] From Buckman 1984.

Procurement specifications were developed by Miketta and Frank (1965) for a number of T-111 and T-222 alloy product forms. A revised T-111 tubing and pipe specification was included in a NASA report (Harrison, Hoffman, and Smith 1975) which reflected "lessons learned" from earlier procurement and component fabrication experience. This latter report also included detailed information on T-111 alloy extrusion parameters.

Production of the alloys T-222, ASTAR 1211C, and ASTAR 1511C has been rather limited. The higher tungsten concentration in these alloys as compared to T-111 and ASTAR 811C results in higher creep strength but at the expense of reduced producibility. Additional information on tantalum alloy producibility is included in a recent paper by Perkins (1982). From the experience base that exists in the U.S., it is apparent that high-quality products can be produced to exacting specifications. However, due to the decreased interest in these materials during the 1973–1983 period, a considerable effort will be necessary to re-establish the required expertise in the commercial arena.

Creep Strength

The melting points of the refractory metals (niobium, 2741 K; molybdenum, 2883 K; tantalum, 3269 K; and tungsten, 3653 K) provide a rough guide of the high-temperature, time-dependent strength properties which can be developed in alloys based on these metals. The considerably higher melting point of tantalum relative to niobium gives the tantalum alloy system a distinct advantage in the development of stronger refractory alloys which must have the good fabrication (weldability, and so on) properties essential to the production of complex components. This apparent advantage must be tempered when considering mass-sensitive applications. For space power systems, the higher density of tantalum alloys vs niobium alloys must be factored into the selection. A review of the creep strength of a large number of refractory metals and alloys was included in a recent paper by Conway (1984).

Long-term (10,000 to 60,000 h) creep strength is of critical importance in the selection of candidate refractory alloys for multi-year space nuclear power system applications. Much of the pre-1963 creep data on tantalum alloys that is reported in the literature is of limited value because of a lack of understanding at that time of the dramatic effect of test-induced contamination on the creep properties of these alloys. Comparative test results reported by Buckman (1966) illustrated the effects of the creep test chamber pressure and the type of pumping system on the creep rate of T-111. These results are summarized in Table 2. A factor of 10 less creep strain was observed in a diffusion-pumped (10^{-5} to 10^{-6} torr) system as compared to that observed in an

Table 2 *Contamination of T-111 Alloy Creep Tested in a Diffusion-Pumped Vacuum System and in an Ion-Pumped System.*[a]

		Diffusion Pumped	Ion Pumped
Pressure (torr)	—Start	4.0×10^{-5}	1.0×10^{-7}
	—Finish	2.8×10^{-6}	4.5×10^{-9}
Temperature (°C)		1371	1371
Stress (psi)		9190	9190
Time (h)		172	172
Strain (percent)		0.3	3.0
Chemical Analysis (ppm)			
Nitrogen	—Before test	10	10
	—After test	10	10
Oxygen	—Before test	15	15
	—After test	290	38
Carbon	—Before test	26	26
	—After test	260	20

[a] From Buckman 1966.

ion-pumped (10^{-7} to 10^{-9} torr) system under otherwise equivalent test conditions. The reduced strain was attributed to the strengthening effect of the oxygen and carbon contamination noted in the diffusion-pumped system. Information on the rate of the contamination of tantalum and a series of tantalum alloys, including T-111 and ASTAR 811C, in low pressure (10^{-6} to 10^{-7} torr) oxygen environments has been reported by Harrison and Hoffman (1968). These studies provide additional support for the requirement of 10^{-8} torr or lower pressure for creep testing of alloys of this type.

In 1963, NASA-Lewis initiated a 10-year creep testing program at TRW-Cleveland which focused primarly on the generation of an extensive data base on the tantalum alloys, T-111 and ASTAR 811C. A major requirement of this high-quality program was that all testing was to be conducted in ultrahigh getter-ion-pumped systems operated in the 10^{-8} to 10^{-10} torr pressure regime to preclude oxygen and carbon contamination of the test specimens. A final report authored by Scheffler and Ebert (1973) of TRW summarized the major results of this program. Table 3 lists some of the highlights of this extensive program. Twelve different heats of T-111 and five heats of ASTAR 811C were utilized in these studies. Figure 1 summarized the T-111 and ASTAR 811C creep data base and illustrates the significant strength advantage of ASTAR 811C at temperatures above 1400 K. This figure also shows the creep strength advantage that coarse-grained ASTAR 811C (annealed at 2255 K) has over fine-grained material (annealed at 1922 K).

A more recent evaluation of the creep behavior of ASTAR 811C has been published by Klopp, Titran, and Sheffler (1980) based on the TRW data. Figure 2, which is taken from this report, compares the 10,000 hour/1 percent strain of Ta-10W, T-222 and ASTAR 811C. The authors suggest that dislocation glide may be the rate-controlling creep mechanism for the higher strength coarse-grained ASTAR 811C. English (1983) recently published what he considers to be a statistically conservative estimate of the temperature/stress required to produce 1% strain in ASTAR 811C in 40,000 h. This data, which is given in Table 4, suggests that this alloy should be useful to approximately 1600 K.

Many of the space reactor studies consider lithium to be an attractive coolant. A designer would like to know the strength behavior of structural alloys in the environ-

Table 3 *Highlights of T-111 and ASTAR 811C Creep Data Base Obtained by TRW Under NASA-Lewis Sponsorship.*[a,b]

	T-111	ASTAR 811C
Number of tests	118	70
Total creep test hours	431,393	250,249
Longest test (h)	38,129	23,692
Number of tests longer than 13,000 h	7	4

[a] From Scheffler and Ebert 1973.
[b] All tests performed in ultrahigh vacua, 10^{-8} to 10^{-10} torr.

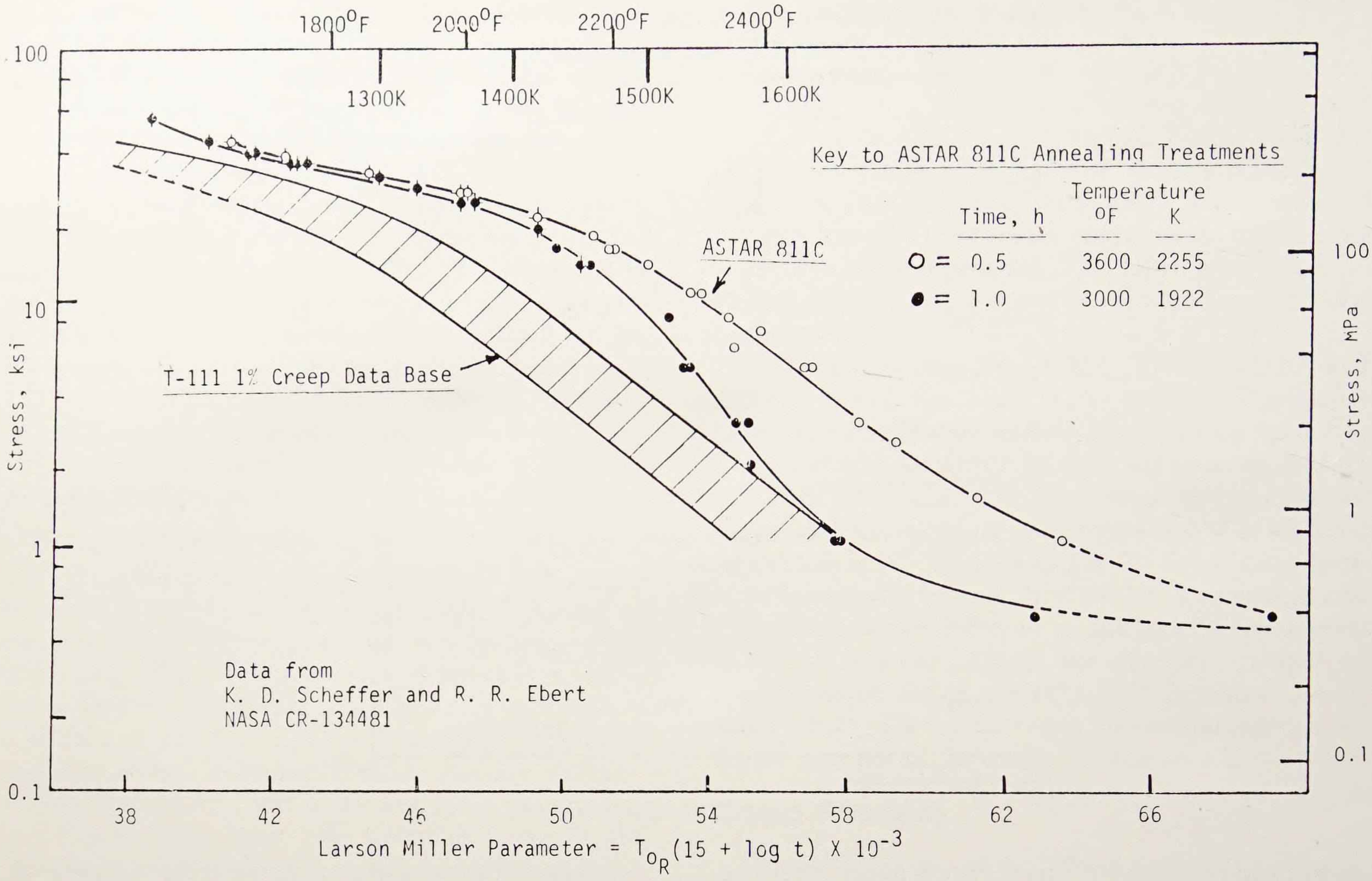


Figure 1 *Temperature / Stress for 1% Creep of Tantalum Alloys T-111 and ASTAR 811C in Two Years.*

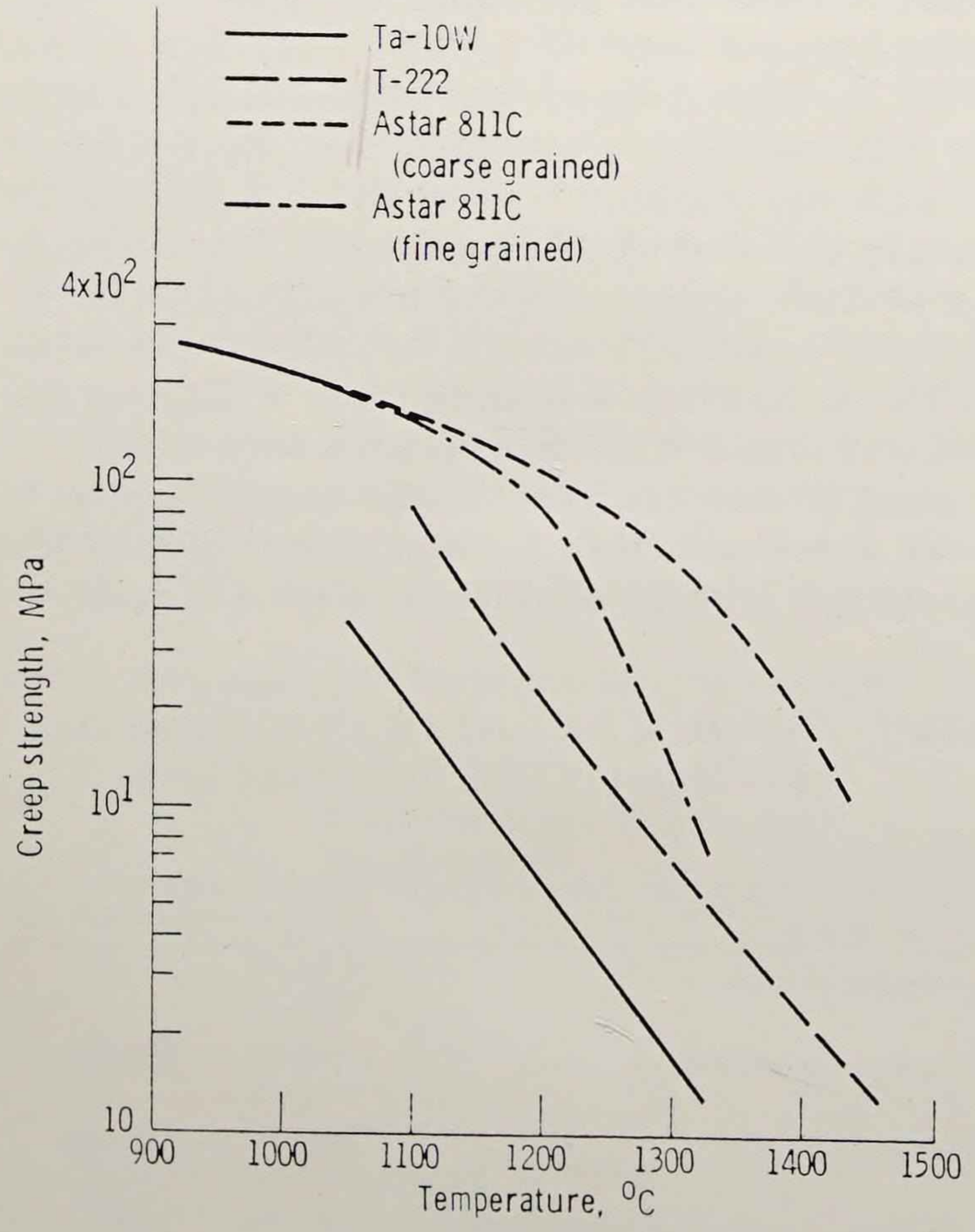


Figure 2 *Creep Strength for 1% Strain in 10,000 Hours for Tantalum Alloys.*

Table 4 *Temperature / Stress Required to Produce 1% Strain in ASTAR 811C in 40,000 Hours.*[a]

Temperature		Stress	
K	°F	MPa	Ksi
1300	1880	155	22
1400	2060	96	14
1500	2240	36	5
1600	2420	7	1

[a] From English 1982.

ment of interest. To the best of the author's knowledge, the data given in Table 5 is the only long-term biaxial stress rupture test data of T-111 in lithium. This Pratt and Whitney report (1965) suggests a slight strength advantage of the T-111 alloy over the W-25Re alloy and a significant advantage over the carbon strengthened Nb-1Zr composition at 1204°C. Other studies at Pratt and Whitney by Cleary (1965) in support of the SNAP-50 program indicated that prior exposure of T-111 specimens to lithium for 1000 h in 1200°C lith-

Table 5 *Biaxial Stress Rupture Tests[a] of Refractory Alloy Tubing.*[b,c]

Alloy	Number of Tests	Maximum Test Duration, h	Estimated 10,000 h/1204°C Rupture Strength, Min., psi
T-111 (Ta-8W-2Hf)	12	2797	6000
W-25Re (at.%)	3	947	4500
PWC-11 (Nb-1Zr-0.1C)	86	5381	1700

[a] Internally pressurized tubes immersed in 1204°C lithium.
[b] Tubing Size: 0.25-inch OD × 0.025-inch wall.
[c] From Pratt and Whitney (1965).

ium had no effect on the 1316°C stress rupture properties of T-111.

The biaxial creep strength of T-111 in a refluxing potassium at 1204°C was determined in two 5000 h tests at General Electric by Brandenberg and Engel (1971) for NASA. These biaxial creep strains and the predicted strains based on uniaxial tests conducted in the vacuum were found to be in good agreement.

Both the long-term creep properties of T-111 and ASTAR 811C and the soundness of the extensive data base on these alloys suggest that these alloys should be strong candidates for space nuclear power applications.

Weldability

One of the major reasons that tantalum alloys were selected by NASA in the mid-1960s for extensive evaluation as advanced structural alloys for space power application was the very good weldability indicated in early studies by Lessman (1966) on seven niobium and three tantalum alloys. The author concluded that the tantalum alloys, Ta-10W, T-111, and T-222 were considered less sensitive to welding than the niobium alloys.

An extensive series of tests reported by Donnelly (1965) was conducted at the Oak Ridge National Laboratory in 1964–65 on 125-mm-thick plates of T-111 and several niobium-base alloys welded by the gas-tungsten arc (GTA) process. High-temperature aging studies of these weldments and subsequent room temperature bend testing revealed excellent ductility of the T-111 alloy and led the investigators to conclude that "this alloy may be one of very few refractory alloys immune to deterioration by aging."

In a recent refractory alloy symposium, an extensive review of the weldability of various refractory alloys, including the tantalum alloys T-111 and ASTAR 811C, was presented by Lessman (1984). The results presented by Lessman, based primarily on a five-year NASA-Lewis-supported program, indicated excellent weldability for the T-111 and ASTAR 811C alloy with very low ductile brittle transition temperatures for weldments of both alloys. These results, which were initially reported by Gold and Lessman (1971), are summarized in Table 6. The authors concluded, "no notch sensitivity has been found in as-welded, post-weld annealed or aged GTA welds in T-111 or ASTAR 811C sheet at temperatures as low as −196°C." As indicated in Table 6, some underbead cracking was detected in multipass T-111

Table 6 *Weldability of T-111 and ASTAR 811C.*[a]

	T-111	ASTAR 811C
Notched tensile tests of as-welded, post-weld annealed[b] and aged[c] specimens	All ductile to −196°C	All ductile to −196°C
Bend tests of as-welded, post-weld annealed and aged specimens	DBTT[d] below −125°C	Highest DBTT 50°C
Multipass welding of plate	Some underbead cracking	No cracking

[a] From Gold and Lessman 1971.
[b] Post-weld anneals: 1 h at 8 temperatures over 1205°C to 1982°C range.
[c] Aging Treatment: 1000 h at 1149°C.
[d] DBTT = Ductile-to-brittle transition temperature.

plate welds. Similar studies on ASTAR 811C showed that this alloy was immune to this problem.

The T-111 alloy was utilized extensively in the fabrication of major test components and systems, and the shop and field welding experience obtained on NASA-Lewis programs during the 1966–1971 time period have been described by Young (1984). Some problems with T-111 weld cracking in heavy section multipass weldments were also described in Young's paper, and it was pointed out that additional development work is needed to eliminate this problem. A paper by Hoffman (1984) at the recent refractory alloy symposium (U.S. DOE 1984) described a number of complex components and systems built of T-111 which were successfully tested at General Electric for NASA-Lewis in the 1965–72 time period.

Compatibility

Because of their unrivaled ability to transfer energy at the elevated temperatures required for compact nuclear reactors for space applications, the alkali metals, lithium, sodium, and potassium, and to a lesser extent cesium, have been extensively evaluated during the past 25 years. In addition to the importance of such factors as producibility, strength, and weldability, it is essential that the selected containment material(s) have excellent long-term compatibility with the working fluids employed in the heat transfer system.

Early experiments with niobium conducted by Hoffman (1959) demonstrated that unalloyed niobium was attacked catastrophically by lithium if the niobium was contaminated with several hundred ppm of oxygen. The solution to this problem in 1960 was to use the niobium alloy, Nb-1Zr. The addition of the strong oxide-forming element zirconium essentially eliminated corrosion of the alloy by lithium provided the oxygen level remained below about 200 ppm, and the alloy was heat treated prior to exposure to lithium.

Subsequent extensive studies by DiStefano (1964), Klueh (1973), Sessions and DeVan (1971), Stecura (1974), Gahn (1974), and Harrison (1970) confirmed and elucidated the "oxygen-disease" mechanism in unalloyed tantalum and the beneficial effects of the presence of the strong oxide-forming element hafnium in tantalum alloys, such as T-111 and T-222, in eliminating oxygen-related attack by lithium. A more detailed account of these studies, as well as all the other compatibility testing of tantalum alloys with alkali metals, is given in a recent survey paper by DeVan, DiStefano, and Hoffman (1984).

No attempt will be made in this paper to cite the dozens of refluxing capsule, thermal convection loop, natural circulation loop, pumped liquid, and pumped boiling loop tests that were conducted in the 1964 to 1974 time period on tantalum alloys in contact with the various alkali metals. Most of the testing utilized lithium and potassium as the heat transfer fluids. Summaries of the most demanding compatibility tests in terms of temperature, test duration, and flow conditions are listed in Tables 7 and 8. Nearly all of the alkali metal compatibility testing of tantalum alloys has been conducted in T-111 alloy containment systems.

Most of the compatibility test results for pumped, high-velocity alkali metal systems have been obtained utilizing lithium as the heat transfer fluid. The only corrosion noted in the lithium tests listed in Table 7 was the pickup or loss of minor concentrations of such elements as hafnium, oxygen, or nitrogen principally from the surface regions of the tantalum alloys. As an example, a thin film of hafnium nitride deposition was noted on the lithium side of the potassium boiler in the high heat flux nucleate-boiling region. In summary, the results of extensive testing of T-111 and limited testing of the other T-111 type alloys listed in Table 7 indicate these materials have excellent compatibility with high-temperature lithium.

Compatibility testing of the tantalum alloys in potassium, sodium, and cesium has been performed primarily under refluxing or boiling test conditions with most of the tests utilizing T-111 as the containment alloy. The most severe tests conducted to date are listed in Table 8. No significant corrosion was noted in any of these experiments with the exception of the 10,000 hour two-loop experiment in which localized attack to a depth of 0.05 mm was noted in the high heat flux, nucleate-boiling region of the potassium boiler. Although the tantalum alloy compatibility data base for potassium, sodium, and cesium is not as extensive as for these alloys in lithium, these alloys have exhibited excellent compatibility with the other alkali metals.

In addition to the compatibility concerns associated with the use of alkali metals as heat transfer fluids, there are also concerns about the compatibility of tantalum alloys with either vacuum environments or inert gases, such as argon or helium containing very low (ppm) concentrations of reactive impurities such as oxygen, nitrogen, or carbon. Under a variety of conditions, these "inert" environments can seriously degrade the properties of tantalum alloys (niobium alloys are similarly affected). An excellent and comprehensive discussion of the problems associated with refractory alloys in "inert" environments is given in a recent paper by DeVan, DiStefano, and Hoffman (1984).

An additional compatibility issue of interest concerning the use of tantalum alloys for space reactor applications is the compatibility of these alloys with the various reactor fuel forms. A review of the compatibility of tantalum, Ta-12W and T-111 with UC, UN, and UO_2 is included in a report by Weaver and Scott (1965). It was concluded that for interface temperatures in excess of 1000°C a barrier material such as tungsten would be required to avoid deleterious interactions between tantalum alloys and the candidate fuel forms.

Table 7 *Summary of Compatibility Testing of Tantalum Alloys in Lithium.*

Containment Material	Specimens	Alkali Metal	Type of Test	Temp., max., °C	Test Duration, h	Remarks
T-111[a]	T-111	Li	Pumped Loop	1370	3000	No significant attack; some minor element transfer
T-111[b]	T-111 ASTAR-811C ASTAR-1211C	Li	Thermal Convection Loop	1370	5000	No significant attack; some mass transfer of nitrogen noted
T-111[c]	T-111 ASTAR-811C ASTAR-811CN	Li	Pumped Loop (fuel element test)	1040	7500	No corrosion; no significant effect on tensile properties
T-111[d]	T-111 T-222 ASTAR-811 ASTAR-811C ASTAR-811CN	Li	Pumped Loop (valve test)	1150	5000	No corrosion; no significant effect on tensile properties
T-111[e]	—	Li	Pumped Loop (Li in primary loop, two-phase K in secondary loop)	1230(Li)	10000	No corrosion.

[a] From DeVan and Long 1975.
[b] From Scheurmann 1974.
[c] From Brandenburg, Hoffman, and Smith 1974.
[d] From Harrison and Holowach 1970.
[e] From Harrison, Hoffman, and Smith 1975.

Table 8 *Summary of Compatibility Test Conditions of Tantalum Alloys in Potassium, Sodium, and Cesium—Essentially No Attack Noted in These Tests.*

Containment Material	Specimens	Alkali Metal	Type of Test	Temp., max., °C	Test Duration, h
T-111[a]	T-111	K	Refluxing Capsule	1200	5000
T-222[b]	—	K	Refluxing Capsule	1315	4000
T-111[a]	T-111	K	Natural Circulation Boiling Loop	1250	3000
T-111[c]	—	K	Pumped Loop (two-phase K in secondary loop, Li in primary loop)	1175	10000
T-111[d]	—	Na	Refluxing Capsule	1315	6271
T-111[e]	T-111	Cs	Refluxing Capsule	1370	300
Ta-10W[e]	Ta-10W	Cs	Refluxing Capsule	1370	300
T-111[f]	—	Cs	Natural Circulation Boiling Loop	1315	246

[a] From DeVan 1966.
[b] From Scheuermann 1974.
[c] From Harrison, Hoffman, and Smith 1975.
[d] From Romano, Fleitman, and Klamut 1967.
[e] From Kleuh 1967.
[f] From Ammon, Begley and Eichenger 1965.

Other Factors

Depending on the specific application of interest, it is obvious that many other factors, in addition to those discussed above, must be considered prior to the selection of an alloy. A number of these additional factors are treated in a report by Moorhead and Stone (1970) on the properties of T-111.

Summary

Some of the most important factors, including producibility, creep strength, weldability, which must be considered in selecting tantalum alloys for use as structural alloys in high-temperature space nuclear power systems, have been reviewed in this paper. The relevant data base that is in place, particularly for the alloys T-111 and ASTAR 811C, leads one to conclude that these compositions should receive serious consideration for future applications. Several minor technology issues, such as microcracking in heavy section T-111 weldments, need further study. The most critical current issue is the re-establishment of the alloy production and processing expertise that existed in 1972 when most of the work on these alloy systems was terminated.

Acknowledgments

The work reviewed in this paper was sponsored by NASA and the U.S. Department of Energy.

References

Ammon, R. L., R. T. Begley, and R. L. Eichinger (1965) "T-111 Cesium Natural Convection Loop," in *AEC-NASA Liquid Metals Information Meeting*, USAEC Report CONF-650411, U.S. Atomic Energy Commission.

Brandenburg, G. P. and L. B. Engel, Jr. (1971) *Determination of Biaxial Creep Strength of T-111 Tantalum Alloy*, NASA-CR-72846, National Aeronautics and Space Administration.

Brandenburg, G. P., E. E. Hoffman, and J. P. Smith (1974) *Pumped Lithium Loop Test to Evaluate Advanced Refractory Metal Alloys and Simulated Nuclear Test Elements*, NASA-CR-134527, National Aeronautics and Space Administration.

Buckman, R. W., Jr. (1966) "Operation of Ultrahigh Vacuum Creep Testing Laboratory," in *Transactions Vacuum Metallurgy Conference*, American Vacuum Society, *pp.* 25–37.

Buckman, R. W., Jr. (1984) *A Review of Tantalum and Niobium Alloy Production*, Report CONF-8308130, NTIS, U.S. Department of Energy.

Cleary, R. E. (1965) "Corrosion Studies of Refractory Metals in Lithium," *AEC-NASA Liquid Metals Information Meeting*, USAEC Report CONF-650411, U.S. Atomic Energy Commission.

Conway, J. B. (1984) "Mechanical and Physical Properties of Refractory Metals and Alloys," in *Proceedings of Symposium on Refractory Alloy Technology for Space Nuclear Power Applications*, Report CONF-8308130, NTIS, U.S. Department of Energy.

Cox, C. M., D. S. Dutt, and R. A. Karnesky (1985) "Fuel Systems for Compact Fast Space Reactors," in *Space Nuclear Power Systems 1984*, M. S. El-Genk and M. D. Hoover eds., Volume 2, Orbit Book Co., Malabar, FL.

DeVan, J. H. (1966) *Compatibility of Structural Materials with Boiling Potassium*, ORNL-TM-1361, Oak Ridge National Laboratory.

DeVan, J. H. and E. L. Long, Jr. (1975) *Evaluation of T-111 Forced-Convection Loop Testing with Lithium at 1370° C*, NASA CR-134745/ORNL-TM-4775, Oak Ridge National Laboratory.

DeVan, J. H., J. R. DiStefano, and E. E. Hoffman (1984) "Compatibility of Refractory Alloy with Space Reactor System Coolants and Working Fluids," in *Proceedings of Symposium on Refractory Alloy Technology for Space Nuclear Power Applications*, Report CONF-8308130, NTIS, U.S. Department of Energy.

DiStefano, J. R. (1964) *Corrosion of Refractory Metals by Lithium*, ORNL-3551, Oak Ridge National Laboratory.

Donnelly, R. G. (1965) "Welding of Refractory Alloys," in *High-Temperature Materials Program Progress Report for Period Ending July 31, 1965*, ORNL-TM-1200, p. 7, and *For Period Ending April 30, 1965*, ORNL-TM-1140, p. 10, Oak Ridge National Laboratory.

English, R. E. (1983) *Power Generation from Nuclear Reactors in Aerospace Applications*, NASA-TM-83342, National Aeronautics and Space Administration.

Gahn, R. F. (1974) *Effects of Low-Pressure Air on Oxygen Contamination and Lithium Corrosion of a Tantalum Alloy, T-111, at 980° and 1260° C*, NASA TN D-7588, National Aeronautics and Space Administration.

Gold, R. E. and G. G. Lessman (1971) *Influence of Restraint and Thermal Exposure on Welds in T-111 and ASTAR 811C*, NASA-CR-72858, National Aeronautics and Space Administration.

Harrison, R. W. and E. E. Hoffman (1968) "Contamination of Tantalum and Tantalum Alloys in Low-Pressure Oxygen Environments," in *Transactions of the International Vacuum Metallurgy Conference*, eds. R. B. Barrow and A. Simkovich, American Vacuum Society.

Harrison, R. W. (1970) "The Effects of Welding Atmosphere Purity on the Lithium Corrosion Resistance of Refractory Alloys," in *Corrosion by Liquid Metals*, eds. J. E. Draley and J. R. Weeks, Plenum Press.

Harrison, R. W. and J. Holowach (1970) *Refractory Metal Values for 1900° F Service in Alkali Metal Systems*, NASA CR-1810, National Aeronautics and Space Administration.

Harrison, R. W., E. E. Hoffman, and J. P. Smith (1975) *T-111 Rankine System Corrosion Test Loop*, NASA-CR-134816, National Aeronautics and Space Administration.

Hoffman, E. E. (1959a) *Corrosion of Materials by Lithium at Elevated Temperature*, ORNL-2670, Oak Ridge National Laboratory.

Hoffman, E. E. (1959b) *The Effects of Oxygen and Nitrogen on the Corrosion Resistances of Columbium to Lithium at Elevated Temperatures*, ORNL-2675, Oak Ridge National Laboratory.

Hoffman, E. E. (1984) "Refractory Alloy Component Accomplishments from 1963 to 1972," in *Proceedings of Symposium on Refractory Alloy Technology for Space Nuclear Power Applications*, Report CONF-8308130, NTIS, U.S. Department of Energy.

Klopp, W. D., R. H. Titran, and K. D. Sheffler (1980) *Long-Time Creep Behavior of the Tantalum Alloy ASTAR 811C*, NASA TP-1691, National Aeronautics and Space Administration.

Klueh, R. L. and D. H. Jansen (1967) *Effects of Liquid and Vapor Cesium on Structural Materials*, ORNL-TM-1813, Oak Ridge National Laboratory.

Klueh, R. L. (1973) *The Effect of Oxygen on the Corrosion of Niobium and Tantalum by Liquid Lithium*, ORNL-TM-4069, Oak Ridge National Laboratory.

Krasner, M. H., H. W. Davison, and A. J. Diaguila (1971) *Conceptual Design of a Compact Fast Reactor for Space Power*, NASA-TM-X-67859, National Aeronautics and Space Administration.

Lessman, G. G. (1966) "The Comparative Weldability of Refractory Metal Alloys," *Welding Journal Research Supplement*.

Lessman, G. G. (1984) "Welding of Refractory Alloys," in *Proceedings of Symposium on Refractory Alloy Technology for Space Nuclear*

Power Applications, Report CONF-8308130, NTIS, U.S. Department of Energy.

Miketta, D. N. and R. G. Frank (1965) *Material Specifications for Advanced Refractory Alloys*, NASA-CR-54761, National Aeronautics and Space Administration.

Moorhead, P. E. and P. L. Stone (1970) *Survey of Properties of T-111 (Tantalum-8Tungsten-2Hafnium)*, NASA TN D-5873, National Aeronautics and Space Administration.

NASA (1970) *Proceedings of Conference on Recent Advances in Refractory Alloys for Space Power Systems*, NASA SP-245, National Aeronautics and Space Administration.

Perkins, R. A. (1982) "Refractory Metals for Nuclear Space Power and Propulsion," in *Proceedings of a Symposium on Advanced Compact Reactor Systems*, National Academy of Sciences.

Pratt and Whitney Aircraft Company (1965) *Fuel and Shield Component Development—SNAP-50*, Report PWAC-484, p. 28, U.S. Atomic Energy Commission.

Romano, A. J., A. H. Fleitman, and C. J. Klamut (1967) "Behavior of Refractory Metals and Alloys in Boiling Sodium and Other Boiling Alkali Metal Coolants," in *Proceedings of the Symposium on Alkali Metal Coolants, Vienna, IAEA*, pp. 67–74.

Scheurmann, C. M. and C. A. Barrett (1966) *Compatibility of Columbium and Tantalum Tubing Alloys with Refluxing Potassium*, NASA TN D-3429, National Aeronautics and Space Administration.

Scheuermann, C. M. (1974) *Mass Transfer in a 1370°C (2500°C) Lithium Thermal-Convection Loop*, NASA-TM X-2986, National Aeronautics and Space Administration.

Sessions, C. E. and J. H. DeVan (1971) *Effects of Oxygen, Heat Treatment, and Test Temperature on the Compatibility of Several Advanced Refractory Alloys with Lithium*, ORNL-4430, Oak Ridge National Laboratory.

Sheffler, K. D. and R. R. Ebert (1973) *Generation of Long Time Creep Data on Refractory Alloys at Elevated Temperatures*, NASA CR-134481, National Aeronautics and Space Administration.

Stecura, S. (1974) *Corrosion of Oxygen-Doped Tantalum by Lithium*, NASA-TMX-2989, National Aeronautics and Space Administration.

U.S. DOE (1984) *Proceedings of Symposium on Refractory Alloy Technology for Space Nuclear Power Applications*, eds. R. H. Cooper, Jr. and E. E. Hoffman, Report CONF-8308130, NTIS. U.S. Department of Energy.

Weaver, S. C. and J. L. Scott (1965) *Comparison of Reactor Fuels for High Temperature Applications*, ORNL-TM-1360, Oak Ridge National Laboratory.

Young, W. R. (1984) "Refractory Alloy Component Fabrication," in *Proceedings of Symposium on Refractory Alloy Technology for Space Nuclear Power Applications*, Report CONF-8308130, NTIS, U.S. Department of Energy.

Space Nuclear Power Systems 1984
Edited by M. S. El-Genk and M. D. Hoover
© Orbit Book Company, Malabar, FL, 1985

Chapter 42

Technology Status of Molybdenum and Tungsten Alloys

W. D. Klopp

Materials Consultant
1542 Mendelssohn Drive
Westlake, OH 44145

The current status and technology for molybdenum and tungsten alloys are reviewed, with emphasis on those properties of interest to the design and fabrication of space nuclear power systems such as SP-100. Although the pace of studies on these materials has been sharply curtailed since 1973, a significant technology base is available, largely from extensive programs conducted during the two decades prior to the mid-1970s. Molybdenum and tungsten alloys are particularly well-suited for space nuclear power system applications because of their superior strength retention at very high temperatures. They also appear to have good resistance to corrosion by liquid alkali metal coolants and good compatibility with candidate fuel materials. Poor low temperature ductility, particularly in impact loading, is a potential limitation to the usefulness of these materials. However, this problem can be alleviated through rhenium alloying (for example, Mo-14 Re) and close control of purity and microstructure. Additional efforts on definition of mechanical properties, in particular low temperature impact ductility and long time creep behavior, are required to qualify molybdenum and tungsten alloys for design into space nuclear power systems.

Introduction

Space nuclear power systems are attractive because of their potentially large electrical power output per unit of mass and relatively compact size. However, the temperature and time requirements are beyond the capabilities of widely-used materials, such as superalloys, and necessitate designs based on the use of refractory metal alloys for applications such as fuel cladding and radiator heat pipes. The basic parameters of the SP-100 system now under study for feasibility, for example, include a power output of 100 kWe, anticipated mission time of seven years, and a total system weight of no more than 3000 kilograms. These basic parameters impose further requirements on the structural materials which relate to long time creep strength, density, low temperature ductility, fabricability and weldability, compatibility with fuel and with liquid alkali metal coolant, and nuclear properties.

Prior to the 1950s, the principal uses of molybdenum and tungsten were as alloying additions, electrical contact materials, and components of incandescent lamp bulbs. However, during the two decades from the mid-1950s to the mid-1970s, a substantial national effort was directed towards development of high temperature alloys based on the refractory metals niobium, tantalum, molybdenum, and tungsten for aerospace and nuclear applications. Included were such areas as basic property studies, development of new alloys, identification of improved consolidation and fabrication techniques, and specialized evaluation for specific advanced applications. This large effort resulted in the creation of a significant refractory metal alloy technology base and associated industrial capability. However, decisions in 1973 to curtail space nuclear power systems work and to employ a ceramic-based insulation system on the Space Shuttle rather than coated refractory metals resulted in a de-emphasis of studies on refractory metal alloys.

The subsequent decreased level of activity has continued until the recent interest in small, compact space nuclear power systems, such as SP-100. This effort is fortunate to be able to draw upon the extensive technology base previously developed.

This paper addresses the status of the technology of molybdenum and tungsten alloys for space nuclear power systems. Tantalum alloys are the subject of another paper at this conference.

Alloys of Interest

Molybdenum and tungsten are both from Group VIa of the Periodic Table and exhibit many similar properties. Their advantages include high melting points and high elastic moduli, which combine to give them exceptional strength to temperatures above the melting points of most conventional materials. A major disadvantage of using molybdenum and tungsten alloys is their ductile-brittle transition at near-ambient temperatures. This tendency towards brittleness necessitates very careful handling during manufacture and during system launch and deployment in space. Properties of molyb-

Table 1 *Selected Properties of Refractory Metals.*

	Molybdenum	Tungsten	Niobium	Tantalum
Melting Point, K	2883	3683	2741	3269
Density, g/cc	10.22	19.3	8.57	16.6
Elastic Modulus, GPa	327	403	98	181
Approximate Recrystallization Temperature, K	1200	1800	1400	1600
Approximate Ductile-Brittle Transition Temperature, K	325	460	140	23
Coefficient of Thermal Expansion near 300 K, 10^6/K	4.9	4.6	7.3	6.5
Thermal Conductivity near 300 K, cal/cm^2/cm/K/sec	.34	.397	.125	.130

denum and tungsten are compared with those of niobium and tantalum in Table 1.

The poor oxidation resistance of molybdenum and tungsten, while not a problem in space use, requires the use of protective or inert environments during heating for fabrication or evaluation as well as during ground systems testing.

Extensive alloying studies have been conducted on molybdenum and tungsten, primarily with the goals of improving high temperature strength and/or low temperature ductility. These alloying studies have shown that finely dispersed second phases, such as reactive metal carbides or thoria particles, are the most effective means for strengthening molybdenum and tungsten at elevated temperatures (Klopp 1975). Solution strengthening, while effective for improving high temperature strength, tends to raise the ductile-brittle transition temperature (DBTT) and to decrease fabricability to a greater extent than does precipitate or dispersion strengthening. An exception to this tendency is rhenium additions, which improve the short-time high temperature strength and decrease the DBTT.

The effects of alloying with rhenium are unique in molybdenum and tungsten. The DBTTs of molybdenum and tungsten can be substantially lowered by alloying with rhenium to produce solution softening at the 5 to 15 percent levels or to produce the rhenium ductilizing effect at the 25 to 50 percent levels (all compositions in weight percent). At rhenium levels about 50 percent in molybdenum or 25 percent in tungsten, sigma phase forms and results in embrittlement.

Numerous alloys of molybdenum and tungsten have been studied and/or developed over the past several decades. Designations, compositions, and available forms of alloys which have been developed to commercial status or which were prominent in research programs are shown in Table 2.

Unalloyed molybdenum and Mo-TZM alloy are available as arc-melted material in a variety of mill

Table 2 *Compositions and Availability of Molybdenum and Tungsten Alloys.*

Alloy Designation	Composition, Wt. Pct.	Current Status	Commercial Consolidation Process[a]	Fabricated Forms Available[b]
Molybdenum	100 Mo	Commercial	AM, PM	FP, R, W, T, M, CS
Mo-14Re	Mo-14Re	Research	—	Not Available
Mo-50Re	Mo-48 to 50 Re	Special Order	PM	FP, R, W, T
Mo-30W	Mo-30W	Commercial	AM	FP, R
Mo-TZM	Mo-.5Ti-.08Zr-.03C	Commercial	AM, PM	FP, R, CS
Mo-Nb-TZM	Mo-1.5Nb-.5Ti-.08Zr-.05C	Research	—	Not Available
Mo-TZC	Mo-1.25Ti-.25Zr-.10C	Special Order	PM	On Request
Mo-MHC	Mo-1.2Hf-.08C	Special Order	PM	On Request
Mo-RHC	Mo-3.8Re-1.1Hf-.06C	Research	—	Not Available
Tungsten	100 W	Commercial	PM	FP, R, W
W-3 or 5Re	W-3 or 5Re	Commercial	PM	FP, R, W
W-25 or 26Re	W-25 or 26Re	Commercial	PM	FP, R, W, T
W-Mo-Re	W-18 Mo-35Re	Special Order	PM	FP, R, W, T
W-.6Nb	W-.6Nb	Research	—	Not Available
W-ThO_2	W-1 to 4ThO_2	Commercial	PM	W
W-RHC	W-4Re-.35Hf-.02C	Research	—	Not Available

[a] AM-arc-melted; PM-powder metallurgy.

[b] FP-flat products; R-rod; W-wire; T-tubing; M-mesh; CS-custom shapes.

forms. Two grades of arc-cast molybdenum are available, a low-carbon grade with 50 ppm carbon maximum, and standard molybdenum with a nominal carbon content of 300 ppm. These grades are both available as foil, sheet, plate, rod, and bar. Powder metallurgy molybdenum is available in the same forms, but the arc-melted (or electron-beam-melted) material would be preferred for nuclear applications because the higher purity would tend to reduce potential problems with liquid metal corrosion resistance and with welding and to reduce undesirable nuclear transmutations.

The Mo-TZM alloy, consolidated by arc-melting or powder metallurgy, is available in a similar variety of mill products, as is arc melted Mo-30W alloy. Powder metallurgy Mo-TZC, Mo-MHC, and Mo-50 Re are available on special order. However, the Mo-14, Mo-Nb-TZM, and Mo-RHC alloys have been produced only as research materials to date and are not currently available on a commercial basis.

Arc-melted tungsten and tungsten alloys are not currently available; all tungsten materials commercially available are produced by powder metallurgy. Forms available include foil, sheet, plate, rod, and wire. The W-26Re and W-Mo-Re alloys are also available as tubing. The W-0.6Nb and W-RHC alloys are not commercially available.

The following sections discuss the suitability of these alloys as structural materials for space nuclear power systems.

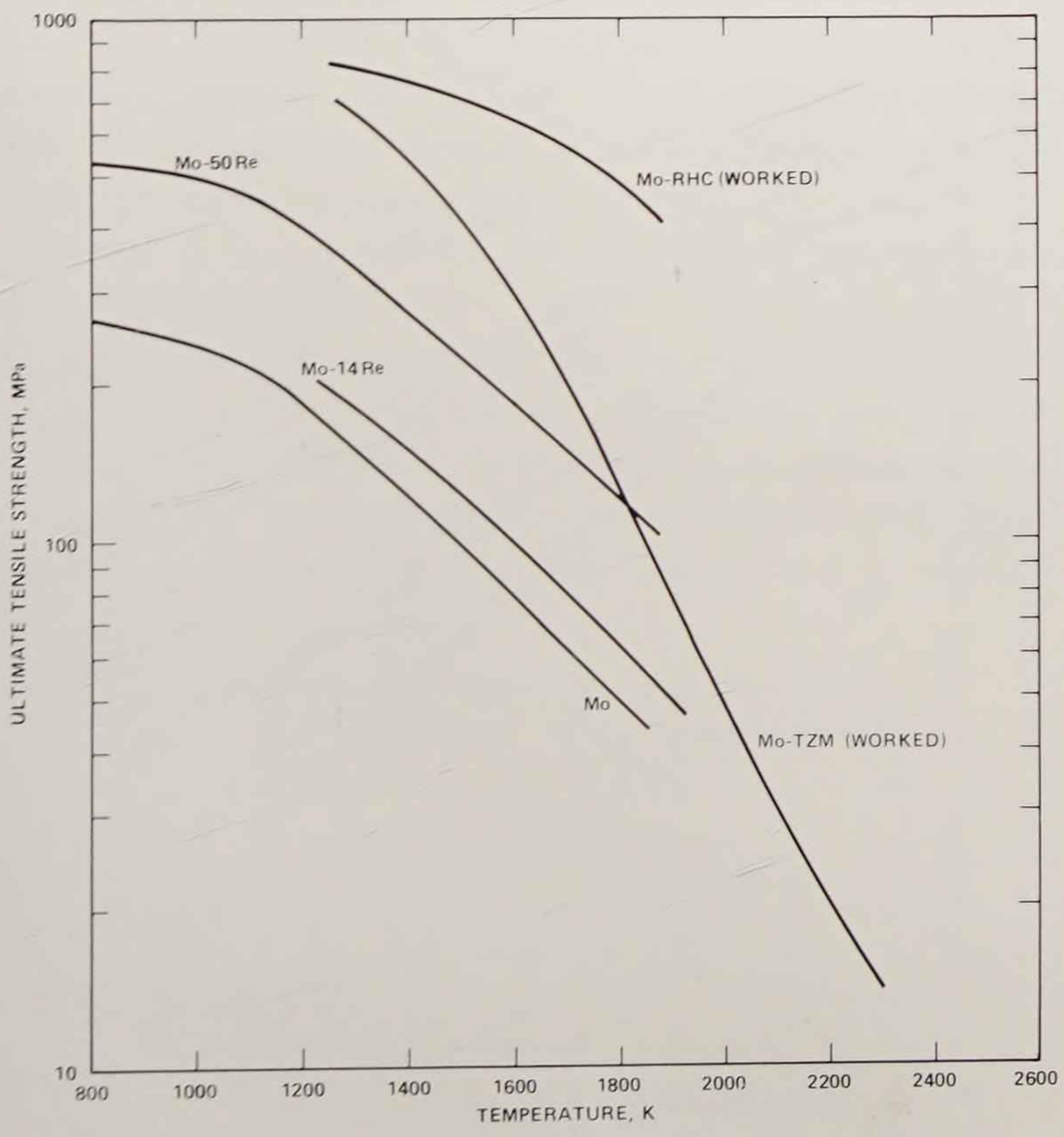


Figure 1 *Ultimate Tensile Strength as a Function of Temperature for Molybdenum and Molybdenum Alloys. Tested in Recrystallized Condition Except Where Noted.*

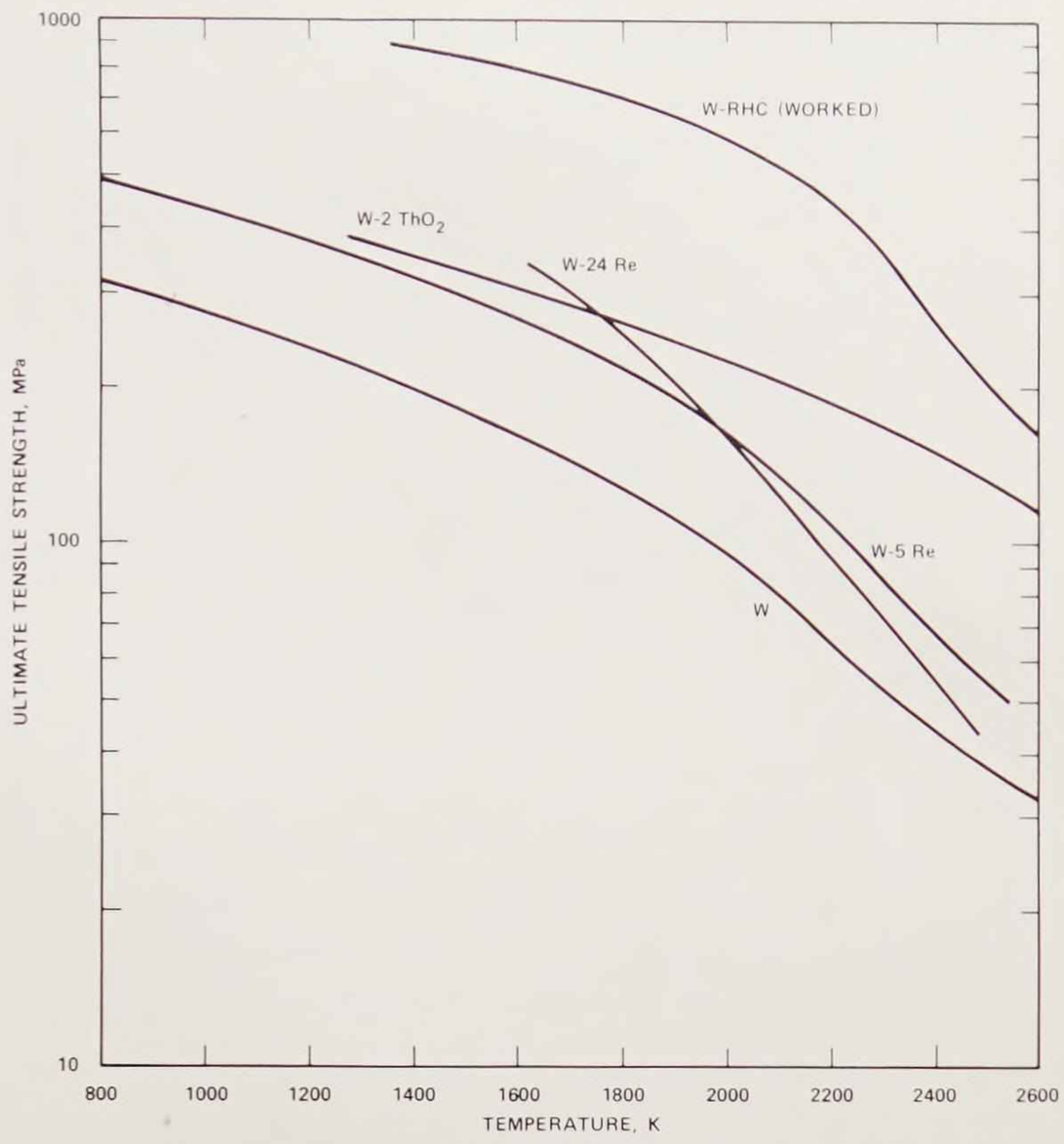


Figure 2 *Ultimate Tensile Strength as a Function of Temperature for Tungsten and Tungsten Alloys. Tested in Recrystallized Condition Except Where Noted.*

Mechanical Properties

High Temperature Tensile Properties

The short-time tensile strengths of molybdenum and tungsten alloys are shown as a function of temperature in Figures 1 and 2 (from Briggs 1961, Hall et al. 1961, King 1969, Klopp and Raffo 1964, Klopp and Witzke 1969 and 1972, Klopp et al. 1966b, Port 1965, Raffo 1969, and Witzke 1975). These data indicate that, for both molybdenum and tungsten, additions of rhenium provide modest strength increases through solid solution strengthening, on the order of 25 to 100 percent. Carbide precipitate-strengthened alloys are considerably stronger, with short-time tensile strength improvements of four-fold to seven-fold at 1500 K. These alloys are the strongest known at elevated temperatures. The W-2ThO_2 alloy also has good high temperature strength, intermediate between those of the solution-strengthened W-Re alloys and of HfC-precipitate-strengthened tungsten. The interesting aspect of W-ThO_2 is its strength retention at very high temperatures, approaching the strength of the carbide-strengthened W-RHC alloy.

High Temperature Creep Properties

Although the high temperature creep properties of molybdenum and tungsten alloys have been studied in numerous programs, all of the available test data are for relatively short times, usually less than several hundred

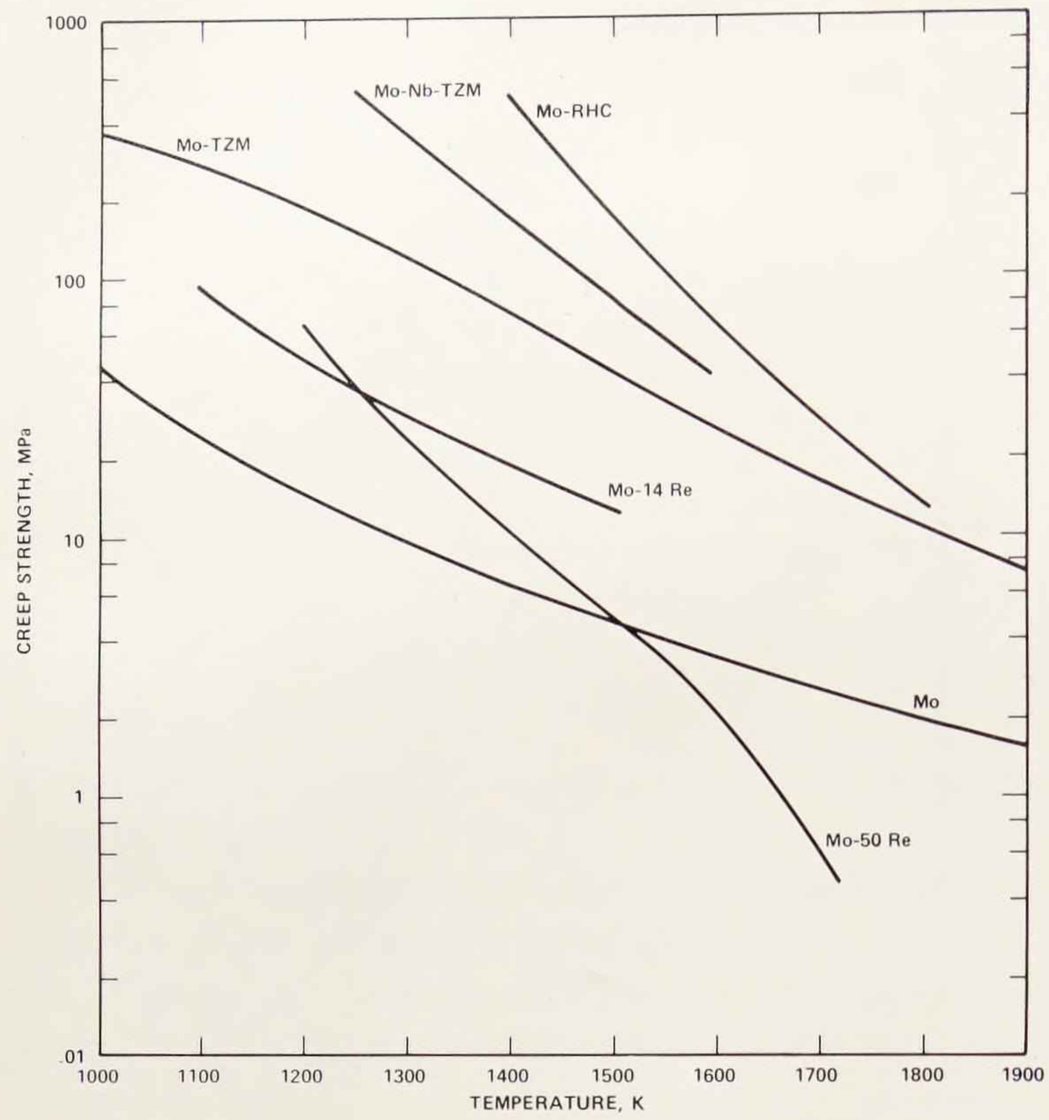


Figure 3 *Extrapolated Stress for 1 Percent Creep Strain in 61,000 Hours as a Function of Temperature for Molybdenum and Molybdenum Alloys.*

hours. This leads to difficulties in accurate estimation of the long time creep data needed to facilitate material selection and system design for a seven-year lifetime since calculated strength properties become increasingly unreliable as they are extrapolated farther and farther outside the time-temperature scopes of the original studies. This situation for molybdenum and tungsten alloys is in contrast to that for niobium and tantalum alloys, for which creep data are available to test times exceeding 10,000 hours.

Calculated creep strengths for 1 percent strain in 61,000 hours (seven years) are shown in Figure 3 for molybdenum alloys and Figure 4 for tungsten alloys. These strengths are extrapolated using the relationship described by Sherby (1962) from short-time data reported by Conway and Flagella (1971), Klopp and Raffo (1964), Klopp and Witzke (1966a, 1969, and 1972), Klopp et al. (1966b), Raffo (1969), Sheffler and Ebert (1973), Stephenson (1969), Vandervoort (1969), and Witzke (1975). In creep, the order of strengthening is similar to that observed in short-time tensile tests. Highest strengths are displayed by the carbide-precipitate-strengthened alloys, with the dilute rhenium-containing alloys having moderate creep strength advantages over the unalloyed metals. In contrast, the Mo-50Re and W-26Re alloys appear weaker in creep than in tensile strength relative to unalloyed molybdenum and tungsten.

The high temperature strength properties of the carbide-strengthened alloys are particularly sensitive to processing conditions and heat treatment. These factors influence the nature and distribution of the strengthening carbides and can cause significant strength differences, for example, among sections of a single ingot processed differently. Considerable effort has been expended, particularly for molybdenum alloys, to identify optimum processing conditions. The strengths of the

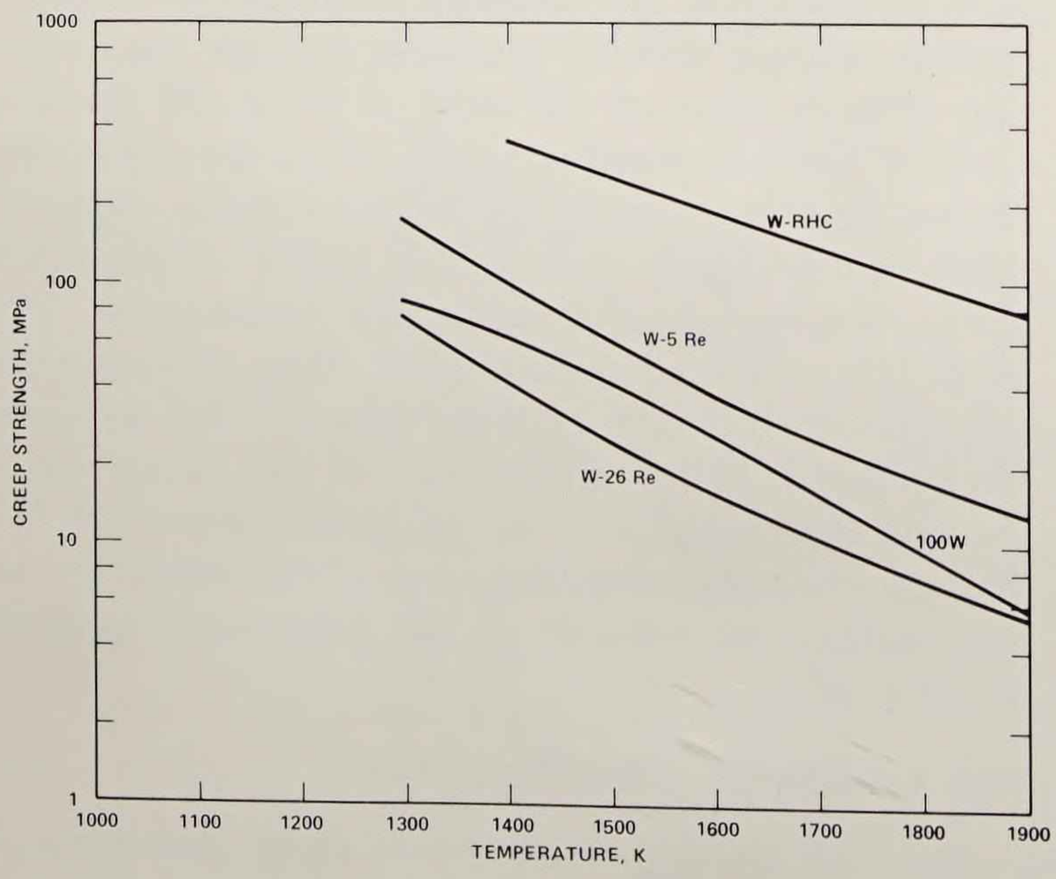


Figure 4 *Extrapolated Stress for 1 Percent Creep Strain in 61,000 Hours as a Function of Temperature for Tungsten and Tungsten Alloys.*

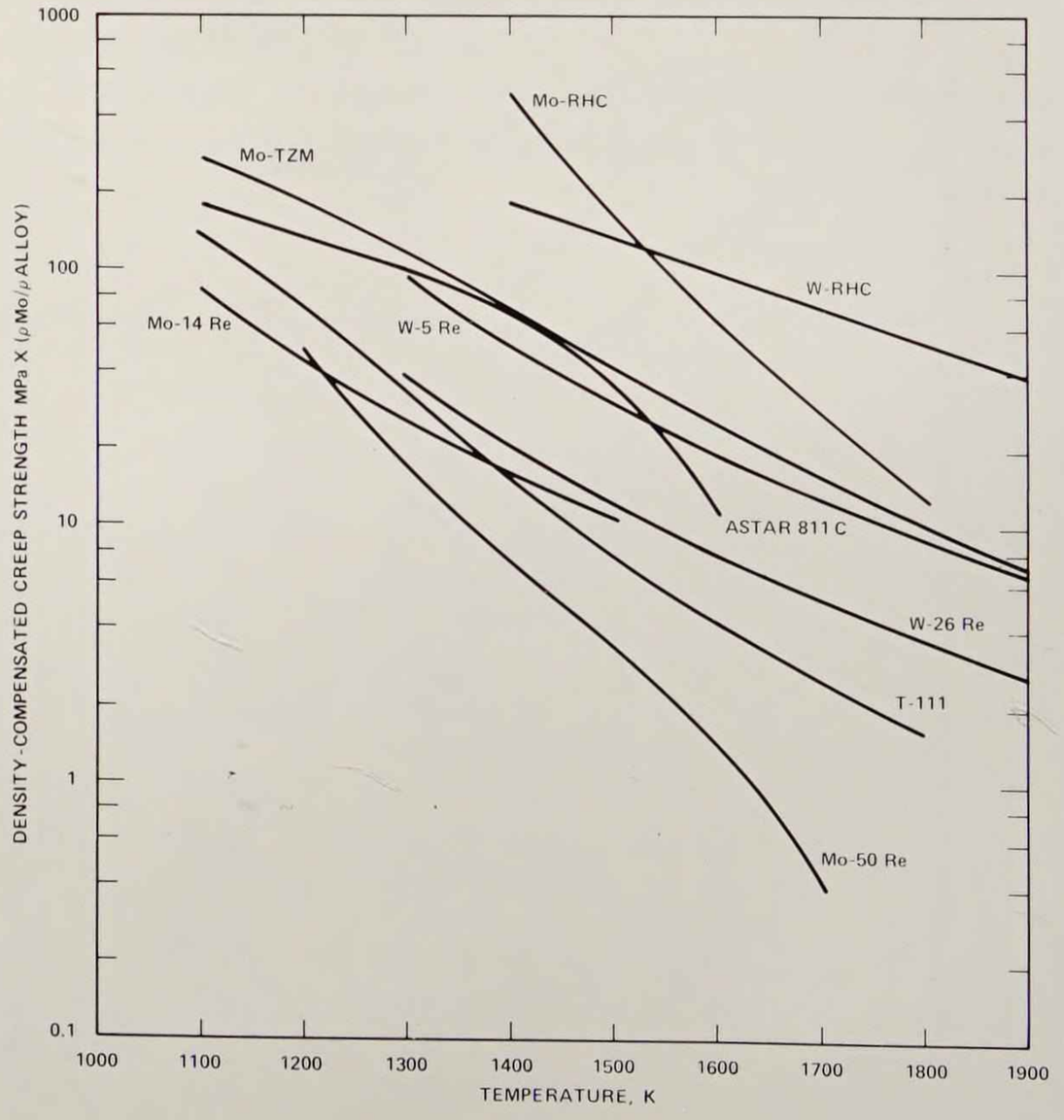


Figure 5 *Density-Compensated Stress for 1 Percent Creep Strain in 61,000 Hours as a Function of Temperature for Selected Alloys, Corrected to Density of Molybdenum.*

carbide-strengthened alloys shown in Figures 1–4 are representative of optimum-processed materials.

The creep strengths of molybdenum and tungsten alloys are compared with tantalum alloys on a density-compensated basis in Figure 5. The strengths of each alloy were multiplied by the ratio of the density of molybdenum to the density of the alloy. At 1400 K, the Mo-50Re alloy is seen to be weakest on this basis, while Mo-14Re and T-111 (Sheffler 1969) have about equal strengths. Astar 811C (Klopp et al. 1980) and Mo-TZM are about three-fold stronger than Mo-14Re and T-111. The Mo-RHC and W-RHC alloys are estimated to be 10-fold stronger than Mo-14Re and T-111.

Although the strength requirements for space nuclear power systems have not yet been defined, the high temperature strengths of molybdenum and tungsten alloys appear adequate.

Low Temperature Ductility

The poor low temperature ductility and fracture toughness of molybdenum and tungsten is a major consideration in assessing their usefulness for space nuclear power system applications. The DBTT is close to or below room temperature for unalloyed molybdenum and ranges from 400 to 460 K for unalloyed tungsten. The DBTTs are affected by alloying and by structural and mechanical factors such as strain rate, grain size, purity, and surface condition, and by environmental factors such as irradiation.

As stated earlier, the most remarkable alloying effects on low temperature ductility are those imparted by rhenium. Two effects have been shown to exist; at low rhenium contents (about 5 to 15 percent), improvement is by the mechanism termed solution softening, while at rhenium contents near the solubility limit, improved ductility is achieved by the mechanism termed the rhenium ductilizing effect. The DBTTs for Mo-Re and W-Re alloys are shown in Figure 6 and 7, respectively (Klopp et al. 1960 and 1966b, and Klopp and Witzke 1972). The solution softening effect is accompanied by a reduction in hardness of the alloy, but no phase change or change in deformation mechanism is evident.

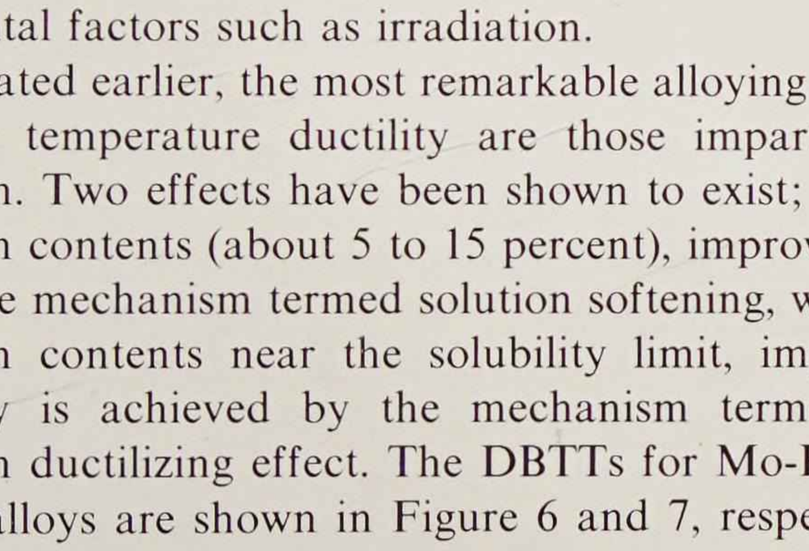


Figure 6 *Ductile-Brittle Transition Temperature as a Function of Rhenium Content for Molybdenum-Rhenium Alloys.*

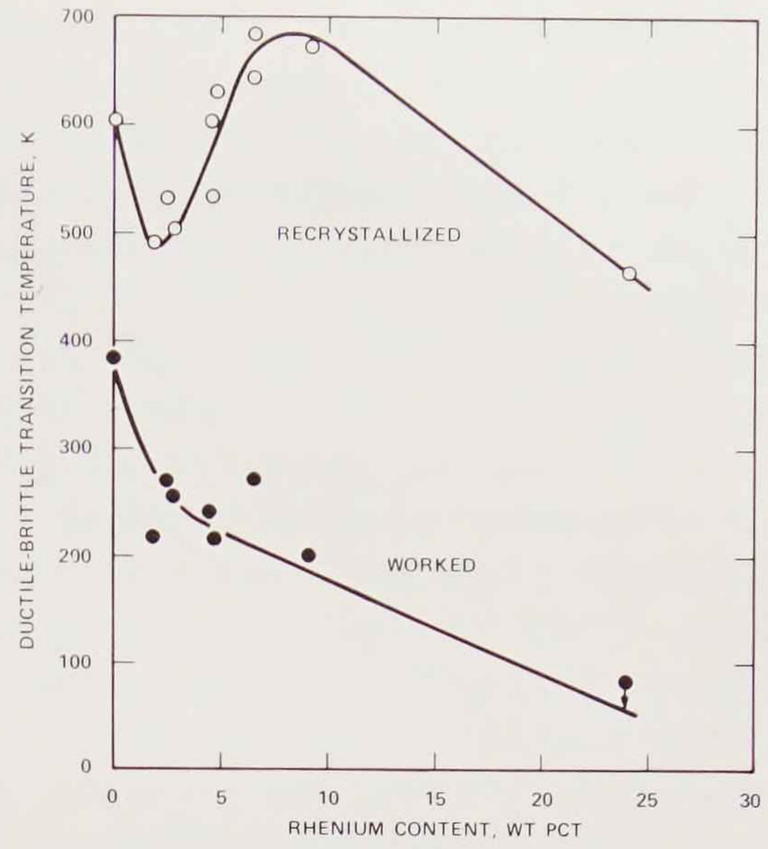


Figure 7 *Ductile-Brittle Transition Temperature as a Function of Rhenium Content for Electron-Beam-Melted Tungsten-Rhenium Alloys.*

In contrast the rhenium ductilizing effect is accompanied by heavy twinning and an increase in the number of slip planes. Hardness decreases attributable to solution softening can be effected in molybdenum by other solutes from Groups VIIa and VIIIa (Stephens and Witzke 1972), but only rhenium has been shown to actually improve ductility. In chromium, ductility improvements through the rhenium ductilizing effect are found in concentrated binary alloys with ruthenium, iron, and cobalt, but no ductilizers other than rhenium have been shown for molybdenum or tungsten.

A partial understanding of the ductility behavior of the Group VIa metals may be derived from the hypotheses advanced by Robins (1959) and by Hahn et al. (1963). Robins has suggested, based on the resonating covalent bond theory, that the highest resonating electron bond stability is achieved when the number of bonding electrons is equal to one-half the effective coordination number. This condition is met with the Group VIa metals, which have 6 bonding electrons and a coordination number of 12. The Group VIa metals are hence electronically stable and have very low lattice solubilities for interstitial elements such as H, O, N, and C. These interstitial elements thus tend to concentrate at lattice defects, where they are electronically more easily accommodated. However, this interstitial concentration at defects reduces the mobility of dislocations and effectively increases the DBTT. Oxygen is the most potent interstitial in this regard.

The presence in the lattice of a large number of defects, such as in a worked structure, reduces the average interstitial concentration at defects, allowing increased plasticity in the lattice. Alloying additions from Group VIIa, such as rhenium, increase the average number of bonding electrons per atom above the stable number of 6 and also reduce the interstitial

solubilities at defects, where the alloying elements tend to segregate because of size differences with the matrix element. The improvement in fabricability and ductility by rhenium thus is likely related to reduction in interstitial solubilities, particularly at defects, effected by the electronic contribution of rhenium.

Available evidence indicates that strain rate also has a significant effect on the low temperature ductility of molybdenum and tungsten, greater, for example, than in niobium or tantalum. As shown in Figure 8 (Atkinson et al. 1961, Seigle and Dickinson 1963, and Wronski et al. 1969), the DBTTs increase significantly with increasing strain rate. For molybdenum, the DBTT is less than 200 K at strain rates of 10^{-4} to 10^{-5} sec^{-1} (typical strain rates for slow bend or tensile testing). However, for impact deformation at strain rates of 10^{2} to 10^{3} sec^{-1}, the DBTT is 500 to 600 K, an increase of 200 to 300 K due to increased strain rate. Similar effects are observed for tungsten. These effects are larger in recrystallized material but are also significant in wrought material. This is an important aspect of molybdenum and tungsten technology because ductility behavior is commonly quoted on the basis of bend or tensile tests conducted at slow deformation rates. However, the critical times during service life are apt to be during handling and during launch. At these times, the loading rates will more likely approximate impact rather than slow loading, with consequent increases in the DBTT. Thus, the important DBTT is that related to impact loading, which for molybdenum and tungsten is always higher than that for bend or tensile loading at slow strain rates.

Structure is also very important to the low temperature ductility of molybdenum and tungsten and their alloys. The DBTT has been shown in several studies to

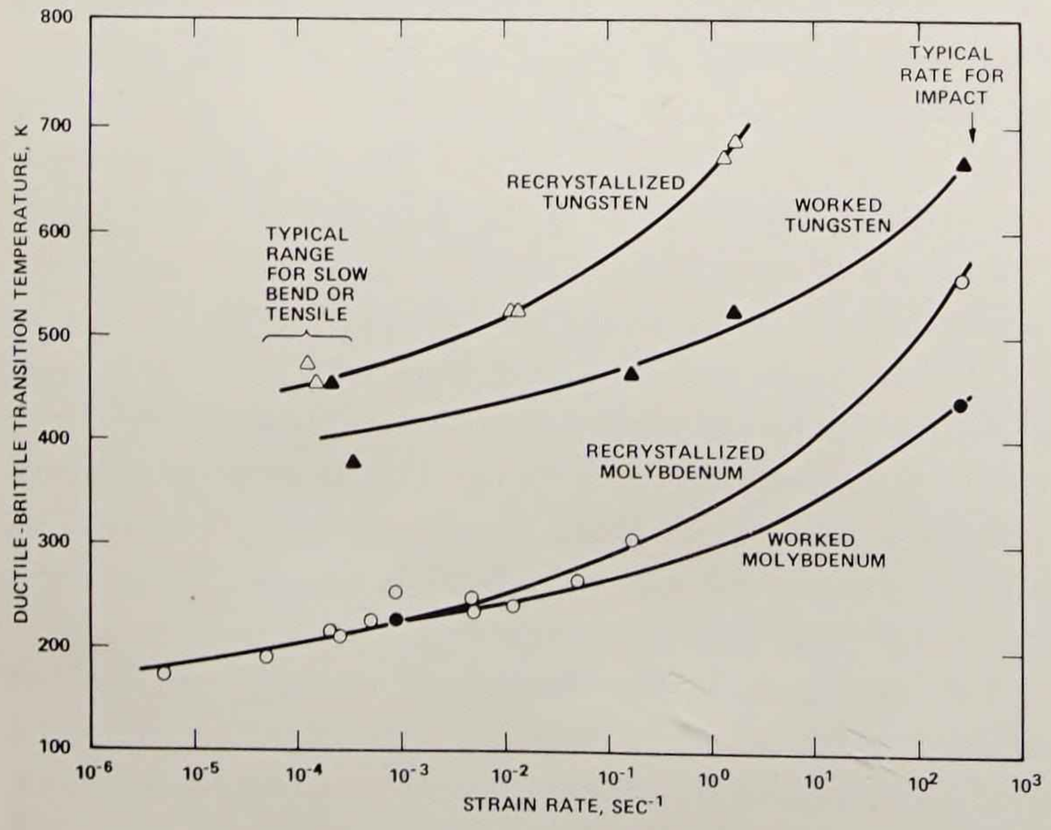


Figure 8 *Ductile-Brittle Transition Temperature as a Function of Strain Rate for Worked and Recrystallized Molybdenum and Tungsten.*

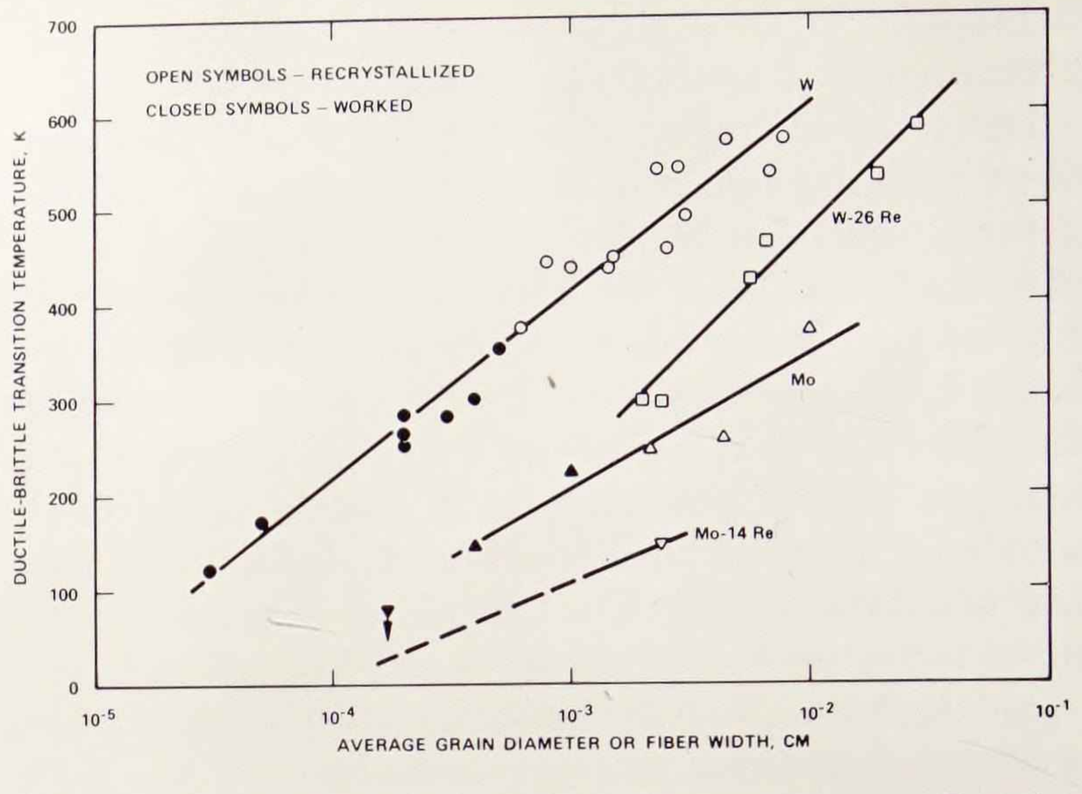


Figure 9 *Ductile-Brittle Transition Temperature as a Function of Average Grain Diameter or Fiber Width for Worked and Recrystallized Molybdenum, Tungsten, and Alloys with Rhenium.*

be greatly influenced by grain size, with finer grained or worked material having substantially better ductility than coarse grained, recrystallized material (Klopp et al. 1966b, Klopp 1968, Klopp and Witzke 1972, and Seigle and Dickinson 1963). The effect of grain size on the DBTT of molybdenum, tungsten, and several of their alloys, is shown in Figure 9. The effect of structure is substantial, as much as 450 K in the case of tungsten.

Purity with respect to interstitials has long been recognized as important to the low temperature ductility of molybdenum and tungsten. Hahn et al. (1963) pointed out that oxygen is the most embrittling of these impurities, nitrogen being intermediate, and carbon the least embrittling to molybdenum, as shown in Figure 10. Semchyshen and Barr (1966) have further shown the effectiveness of carbon as a deoxidizer for arc-melted molybdenum, with beneficial effects on fabricability and ductility. Lowest DBTTs were observed when the residual carbon was low, about 40 ppm.

Recent studies by Kumar and Eyre (1980) demonstrated that oxygen embrittles molybdenum by segregating strongly to the grain boundaries, where it decreases the grain boundary fracture stress and promotes intergranular failure. The tendency for segregation is likely related to the very low solubility for oxygen in molybdenum, determined by Srivastava and Seigle (1974) to range from about 4 ppm at 1700 K to 100 ppm at 2100 K. Carbon decreases the tendency for oxygen segregation and the presence of grain boundary carbides (in limited amounts) may even promote ductility. Thus it is most important for low temperature ductility to maintain low oxygen levels, on the order of a few ppm.

Tungsten and the dilute alloys of molybdenum and tungsten are probably similarly affected by oxygen, although definitive studies have not yet been conducted

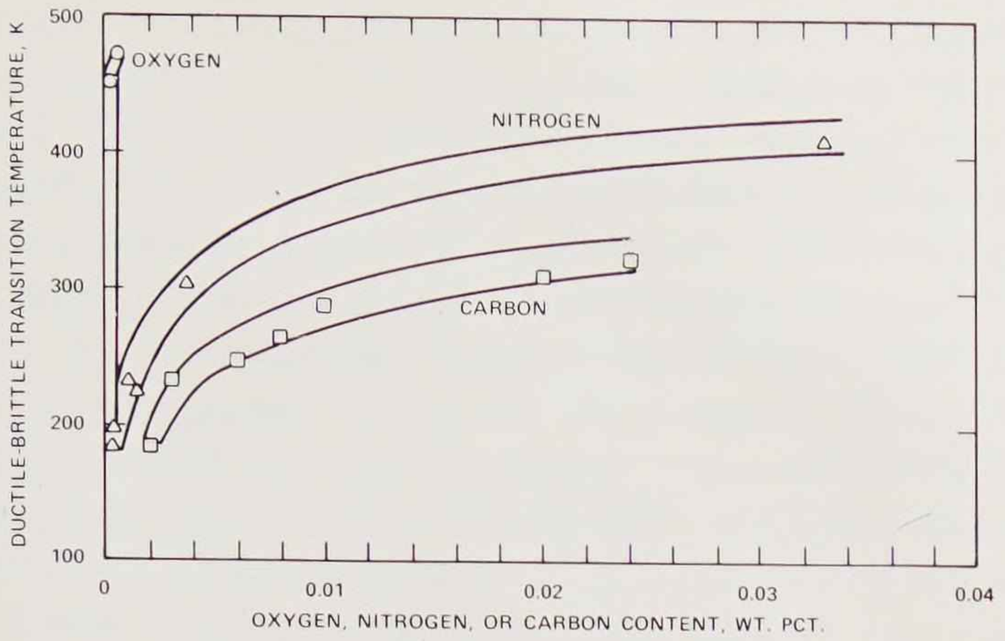


Figure 10 *Ductile-Brittle Transition Temperature as a Function of Oxygen, Nitrogen, or Carbon Content for Molybdenum.*

on these materials. The effects of interstitials in the ductile high-rhenium alloys (Mo-50Re and W-26Re) are unclear.

Low temperature ductility can also be improved in arc-melted and electron-beam-melted tungsten by increasing melting time, as shown by Campbell and Dickinson (1963), Figure 11. These data indicate that the DBTT of tungsten can be reduced by about 50 K by multiple electron-beam remelting. This effect is attributed to a reduction in the levels of metallic impurities such as iron, aluminum, and silicon, since no consistent reduction in interstitial contents was observed with increasing melt time.

Dilute alloying with getter additions has been shown to be quite effective in reducing the DBTTs of molybdenum and tungsten. Semchyshen and Barr (1966) found unnotched Charpy impact DBTTs of 191 and 186 K for worked arc-melted alloys of Mo-0.006Th and Mo-0.003Nd, respectively. In comparison, the best carbon-deoxidized molybdenum had an impact DBTT of 213 K while an impact DBTT of 435 K was reported for unalloyed molybdenum (Seigle and Dickinson 1963). Witzke (1974) observed a lower DBTT for W-0.2Hf than for unalloyed tungsten. Semchyshen and Barr (1966) also observed a low impact DBTT of 144 K for a solution-softened Mo-0.081Cr alloy.

The surface condition and the presence or absence of a contaminated surface layer also affect the DBTTs of molybdenum and tungsten. The removal of 0.02 cm from the surface of Mo-0.5Ti sheet reduced the bend DBTT from 477 to 338 K (Seigle and Dickinson 1963), probably by removal of the contaminated surface layer. Etching or electropolishing of ground tungsten tensile specimens to remove surface scratches reduced the tensile DBTT from 670 to 570–590 K (Stephens 1963). It should be borne in mind that most DBTTs reported for molybdenum, tungsten, and their alloys are determined under the most favorable conditions, in order to enhance reliability and reproducibility of the data. These DBTTs may then be low compared to the actual behavior under less-optimum service conditions.

Representative DBTT values for molybdenum, tungsten, and their alloys are presented in Table 3. Values for the different materials are usually from different studies and may not be directly comparable since they reflect different purities and different processing and testing procedures. However, they do provide some

Table 3 *Ductile-Brittle Transition Temperatures for Molybdenum and Tungsten Alloys.*[a]

		Ductile-Brittle Transition Temperature, K	
		Slow[b]	Impact[c]
Molybdenum	Worked	240	435
	Recrystallized	325	555
Mo-14Re	Worked	< 78	—
	Recrystallized	150	—
Mo-50Re	Worked	115	—
	Recrystallized	< 20	—
Mo-TZM	Worked	200	—
	Recrystallized	255	—
Mo-RHC	Worked	320	—
	Recrystallized	—	—
Tungsten	Worked	400	665
	Recrystallized	460	> 690
W-5Re	Worked	250	—
	Recrystallized	500	—
W-26Re	Worked	170	—
	Recrystallized	300	—
W-RHC	Worked	370	—
	Recrystallized	480	—

[a] Data were selected and averaged from numerous sources. Values listed represent the "best" values for a property which has considerable variability.
[b] Deformed at strain rates of 10^{-4} to 10^{-3} sec^{-1}.
[c] Deformed at strain rate of about 3×10^{2} sec^{-1}.

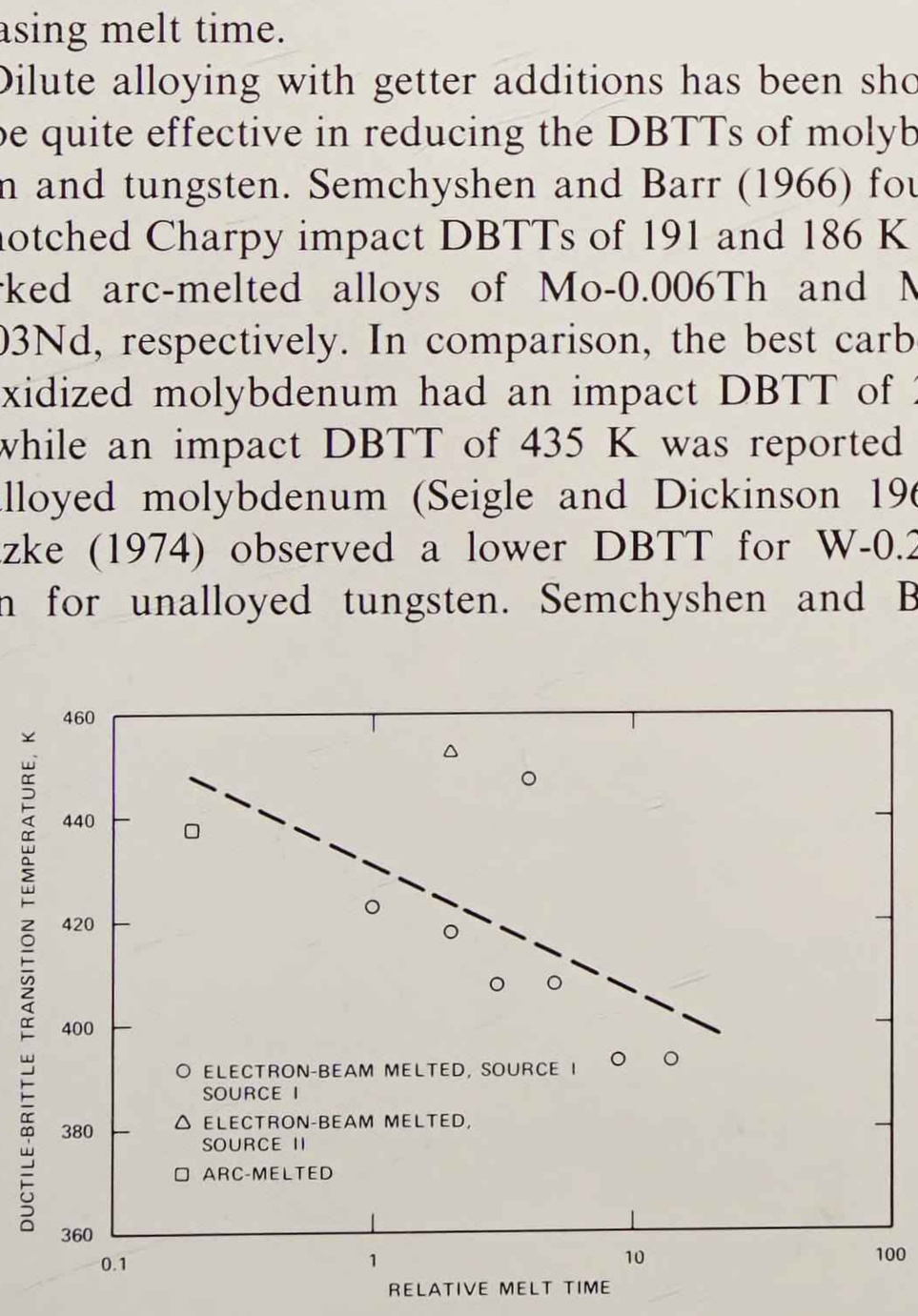


Figure 11 *Ductile-Brittle Transition Temperature as a Function of Relative Melt Time for Tungsten.*

measure of comparison among the alloys of interest. The molybdenum-base alloys have generally lower DBTTs than the tungsten alloys, with lowest values being observed for the Mo-14Re and Mo-50Re alloys. Among the tungsten alloys, lowest DBTTs are again for the W-Re alloys. The high strength HfC-strengthened tungsten alloy has a DBTT approximating that of unalloyed tungsten. Impact DBTTs are 200–250 K higher than those observed in slow straining, but very little impact data are available. Additional data are needed on the impact ductility behaviors of alloys of interest, especially on weldments.

Fabricability and Weldability

Fabrication procedures which have been utilized for molybdenum and tungsten materials consolidated by melting are summarized in Table 4 (Amax Specialty Metals Corp. 1983, Braun et al. 1965, Garfinkle et al. 1968, Klopp and Raffo 1964, Klopp and Witzke 1966a, 1969, and 1972, Klopp et al. 1966b, Merrigan and Lundberg 1983, Raffo 1969, Rhenium Alloys Inc. 1983, and Semchyshen and Barr 1961).

All of the molybdenum and tungsten alloys consolidated by melting are normally extruded hot for primary breakdown of the cast structure. The extrusion temperatures for molybdenum materials have ranged from 1500–1700 K for the unalloyed metal to 2200 K for the high strength Mo-RHC alloy. Secondary fabrication temperatures are several hundred degrees lower. A glass or ceramic extrusion die coating has been employed to prevent excessive die erosion during extrusion. The Mo-50Re alloy is normally consolidated by powder metallurgy, which does not require extrusion. This alloy can be fabricated cold, although warm working at 800 to 1000 K is preferred for complex forming.

Tungsten and tungsten alloys all require hot extrusion from the cast condition. Extrusion temperatures have ranged from 1920–2200 K for unalloyed tungsten to 2480 K for alloys. Temperatures as high as 2810 K have been used for EBM W-26Re, although lower extrusion temperatures would probably suffice. The use of a sintered molybdenum can to encapsulate tungsten alloy billets during extrusion improves fabrication yields.

Qualitative fabricability ratings are shown for the various alloys in Table 4, based on estimated fabrication yields and ease (or difficulty) of producing sound sheet. Unalloyed molybdenum and tungsten and their binary alloys with rhenium, as well as the Mo-TZM alloy, are rated as "good." The HfC-strengthened alloys are less fabricable. The Mo-RHC alloy is rated "fair to good," while the W-4RHC alloy is rated "fair." The latter alloy can be hot rolled to sheet only with difficulty and has been drawn to 0.4 mm wire with yields of only about 20 percent, reflecting its high strength and stiffness.

Weldability is a strong concern for nuclear power

Table 4 *Fabricability and Weldability of Molybdenum and Tungsten Alloys Consolidated by Melting.*

		Extrusion Conditions		Secondary Fabrication		
Material	Melting Process[a]	Temperature, K	Reduction Ratio	Temperature, K	Fabricability Rating	Weldability Rating
Molybdenum	AM, EBM	1500–1700	3 : 1–10 : 1	1090–1450	Good	Fair to Good
Mo-14Re	EBM	1730–1920	6 : 1–8 : 1	1200–1450	Good	Unknown, Probably Good
Mo-50Re	AM	—[b]	—	RT	Very Good	Very Good
Mo-TZM	AM	1600–1800	4 : 1–8 : 1	1150–1310	Good	Fair to Good
Mo-RHC	AM	2200	8 : 1	1420–1640	Fair to Good	Unknown, Probably Fair
Tungsten	AM, EBM	1920–2200	6 : 1–10 : 1	1420–1650	Good	Fair
W-5Re	AM, EBM	2140–2480[c]	8 : 1	1260–1810	Good	Unknown, Probably Fair
W-26Re	EBM	2480–2810[c]	6 : 1	1560–1700	Good	Good
W-RHC	AM	2480[c]	8 : 1	1980–2090	Fair	Unknown, Probably Fair

[a] AM-arc melting; EBM-electron beam melting.
[b] Extrusion requirements not known, small arc-melted button ingots can be fabricated by cold-rolling.
[c] Clad in molybdenum can to facilitate extrusion.

system components. Unfortunately, both molybdenum and tungsten tend to be significantly less ductile in the weld and weld-affected zones than in the non-welded condition. Joining processes which have been studied for molybdenum, tungsten, and their alloys include tungsten inert gas (TIG) welding, electron-beam (EB) welding, laser welding, and brazing. Of these, TIG and EB-welding have received the most attention. Generally speaking, arc-melted materials have better welding characteristics than powder metallurgy materials, since the latter tend to be less pure and to evolve gas during welding, making the weld zone porous and weak. The detrimental effects of interstitial impurities on the strength and ductility of the welded molybdenum and tungsten make environmental control during welding important in order to prevent contamination. This is especially important during TIG welding under an inert atmosphere. The dry box must be evacuated and flushed several times with high purity gas to provide a clean atmosphere. Since electron-beam-welding is conducted in vacuum, there is less opportunity for weld contamination to occur.

Weld zones in molybdenum and tungsten and the alloys are almost invariably weaker and more brittle than unwelded metal. This phenomenon has been termed "weld embrittlement" and has been generally attributed to interstitial impurity segregation to the grain boundaries and to the large grain size in the fusion and heat affected zones.

Details of the weld embrittlement phenomenon have recently been studied by Wadsworth et al. (1983) for Mo-TZM alloy welded by TIG, EB, and laser. This study demonstrated that large grain size in the weld zone rather than impurity segregation is responsible for property degradation. The large grain size causes substantial weakening in the weld zone so that the effective strain rate in this region can be as much as twenty-fold greater than that imposed on the bulk specimen. Since the DBTT of Mo-TZM is raised both by increasing grain size and by increasing strain rate, the overall result is brittle fracture in the weld zone. Increasing the strength of the weld zone, such as by using a higher strength filler metal, should improve the ductility of Mo-TZM. This improved understanding of weld embrittlement should lead to better strength and ductility of weldments in molybdenum and tungsten.

The Mo-50Re alloy is most weldable of the alloys under consideration in this paper. Welds made by TIG or EB are ductile, reflecting the good ductility inherent in the cast alloy. The W-26Re alloy is weldable, but the weldments are not as ductile as the base metal.

Weld studies have not been reported on dilute Mo-Re or W-Re alloys or on HfC-strengthened molybdenum or tungsten. The dilute rhenium alloys should possess weldabilities similar to the unalloyed metals since they are dilute substitutional solid solution alloys. The HfC-strengthened alloys will likely have higher DBTTs in the weld zone, similar to Mo-TZM.

Compatibility with Fuel and Coolant

The principal fuels under consideration for the space nuclear power systems are UO_2, UN, and UC. Thermodynamic data in Table 5 (from Lange's Handbook of Chemistry 1979, and Smithells 1967) indicate that molybdenum, tungsten, and rhenium are stable in contact with the stoichiometric fuels, but the Group IVa elements titanium, zirconium, and hafnium will tend to reduce the fuels. Thus, Mo-TZM and the HfC-strengthened alloys may be incompatible with the fuels, especially over the anticipated seven-year system lifetime.

Observations on corrosion of molybdenum and tungsten in liquid alkali metals are summarized in Table 6. Molybdenum-TZM and Mo-50Re have excellent resistance to lithium in capsule tests for up to 1000 hours at 1920 K (DeMastry and Griesenauer 1967). However, in flowing lithium in a Nb-1Zr loop, Mo-TZM lost carbon and picked up niobium and zirconium, indicating mass transfer by dissolution at the hot end and precipitation at the cold end of the loop (Hoffman and Harrison 1968). Mass transfer can also occur by formation of a stable intermetallic compound; molybdenum has been observed to transfer from capsule walls to rhenium coupons in the interior by formation of a stable Mo_2Re_3 sigma phase on the surface of the rhenium specimen.

Tungsten and W-25Re showed no reaction in molten lithium in 1000-hour capsule tests at 1640 K but surface dissolution and grain boundary attack were evident after similar exposures at 1810 and 1920 K (DeMastry and Griesenauer 1967). Thus, the resistance of tungsten to corrosion by molten lithium may be inferior to that of molybdenum at temperatures of 1810 K and higher but both metals have good resistance up to 1640 K.

The resistance of niobium and tantalum alloys to liquid alloy corrosion is markedly decreased by the presence of oxygen in the niobium or tantalum or in the liquid metal. This is a result of the high stability of liquid alkali metal oxides and their ability to form low-melting complex oxides with oxides of niobium and tantalum. This problem has not been observed with molybdenum and tungsten alloys, possibly due to the low oxygen solubilities in these metals. However, both the structural alloy and the coolant should nevertheless be kept as pure as possible in order to prevent this problem from developing. Materials consolidated by melting rather than by powder metallurgy are preferred for applications requiring liquid metal contact, since the melted materials are generally of higher purity.

Nuclear Considerations

Considerations arising from the nuclear service environment include the neutron cross-sections of the re-

Table 5 *Free Energy Data for Oxides, Nitrides, and Carbides.*

Oxide	$-\Delta F$ at 298 K, Kcal/g at 0	Nitride	$-\Delta F$ at 298 K, Kcal/g at N	Carbide	$-\Delta F$ at 298 K, Kcal/g at C
TiO_2	105.6	TiN	74.0	TiC	43.1
ZrO_2	124.3	ZrN	80.4	ZrC	46.2
HfO_2	122.8	HfN	72	HfC	—
Nb_2O_5	84.4	NbN	49.2	NbC	32.7
Ta_2O_5	91.4	TaN	52.2	TaC	34.6
MoO_3	53.2	Mo_2N	10.3	MoC	− 2.8
WO_3	60.9	—	—	WC	3.4
Re_2O_7	36.4	—	—	—	—
UO_2	128.5	UN	75	UC	41
Li_2O	134.3	Li_3N	36.8	—	—

Table 6 *Liquid Metal Corrosion of Molybdenum and Tungsten.*

Liquid Metal	Alloy	Exposure Conditions: Time, hr	Exposure Conditions: Temperature, K	Type of Test	Results
Lithium	Mo-TZM	1000	1640–1920	Capsule	No attack
		3000	1470	Loop	TZM lost C, picked up Nb and Zr from Nb-1Zr
	Mo-50Re	1000	1640–1920	Capsule	No attack
	W, W-25Re,	1000	1640	Capsule	No attack
	W-.6Nb, W-15Mo	1000	1810, 1920	Capsule	Surface dissolution and grain boundary attack
Sodium	Mo	360	1170	Loop	Small weight gains
		3600	870	Loop	No attack
	W	400	1270	Capsule	No attack
Potassium	Mo-TZM	5000	1370	Loop	No attack

fractory structural materials and radiation-induced damage. The fast neutron absorption cross-sections for the molybdenum and tungsten materials under consideration are given in Table 7 (Kangilaski 1983). From this standpoint, molybdenum has a distinct advantage, since its cross-section, 0.061 barns, is considerably lower than those of tungsten (0.133 barns) or tantalum (0.351 barns). Rhenium, although an important alloying constituent from the ductility standpoint, should be kept low because of its high cross-section, 0.502 barns. The lowest cross-section materials are seen to be molybdenum, Mo-TZM, Mo-RHC, and Mo-14Re. The cross-section of Mo-14Re is approximately one-fourth those of the tantalum T-111 or Astar 811C alloys.

It is well known that irradiation causes subsequent low-temperature hardening in metals. In the case of the bcc refractory metals, this means an increase in the DBTT. Bruch et al. (1955) have shown that the DBTT increases from 243 K for recrystallized unirradiated molybdenum to 343 K after an exposure of 6×10^{20} thermal nvt. Waldron et al. (1965) suggest that hardening in molybdenum results from interactions between interstitial impurities and radiation-induced lattice defects. They further suggest that improved purity with respect to interstitials would decrease the susceptibility to radiation embrittlement. However, this hardening is annealed out at about 1300 K and so would not be expected to occur during service above this temperature.

Radiation-enhanced creep is a potential problem on which little information is available. However, it is not expected to be a limiting factor in reactor design since thermal creep will likely dominate.

Concluding Remarks

Both molybdenum and tungsten alloys have attractive properties for space nuclear power systems. These include high temperature strength properties, good compatibility with candidate fuel materials and liquid metal coolants, and low nuclear cross-sections. The greatest limitation to their use appears to be low temperature brittleness and the possibility of component damage during handling or launch. From this standpoint, the Mo-14Re alloy is especially attractive. Molybdenum and tungsten alloys will require considerably more study, particularly in the area of mechanical properties, to qualify any of the alloys for design into a space nuclear power system. Areas where additional data are

Table 7 *Fast Neutron Cross-Section for Refractory Metals and Alloys.*

Alloy	Cross-Section, barns[a]
Mo	0.061
Mo-14Re	0.093
Mo-50Re	0.205
Mo-TZM	0.060
Mo-RHC	0.074
W	0.133
W-5Re	0.150
W-26Re	0.223
W-RHC	0.149
Nb-1Zr	0.094
Ta-T111	0.345
Ta-Astar 811C	0.337

[a]Weighted for calculated SP-100 neutronic energy spectrum, based on data from Kangilaski (1983).

particularly needed include properties of weldments and creep data for extended times more relevant to mission requirements.

Acknowledgments

The author expresses his appreciation to the University of New Mexico for financial support for travel for presentation of this paper. Thanks are also extended to R. W. Buckman of Westinghouse Advanced Energy Systems, Pittsburgh, PA, for assistance in final figure preparation.

References

Amax Specialty Metals Corp. (1983) *Exploring Molybdenum and Tungsten*, Amax, Refractory Metals Division, Parsippany, NJ.

Atkinson, R. H., G. H. Keith, and R. C. Koo (1961) "Tungsten and Tungsten-Base Alloys," in *Refractory Metals and Alloys*, eds. M. Semchyshen and J. J. Harwood, Interscience Publishers, New York, pp. 319–355.

Braun, H., M. Semchyshen, and R. Q. Barr (1965) "Recent Developments in the Technology of Arc-Cast Molybdenum," in *Plansee Proceedings 1964*, ed. F. Benesovsky, Metallwerk Plansee AG., Reutte/Tyrol, pp. 351–373.

Briggs, J. Z. (1961) "Molybdenum," in *Metals Handbook*, 8th Ed., ed. T. Lyman, Am. Soc. for Metals, Novelty, OH, Vol. 1, pp. 1215–1217.

Bruch, C. A., W. E. McHugh, and R. W. Hockenbury (1955) "Embrittlement of Molybdenum by Neutron Radiation," *Trans. TMS-AIME* 203:281–285.

Campbell, R. W. and C. D. Dickinson (1963) "Effect of Melting Variables on Purity and Properties of Tungsten," in *High Temperature Materials II*, eds. G. M. Ault, W. F. Barclay, and H. P. Munger, Interscience Publishers, New York, pp. 655–668.

Conway, J. B. and P. N. Flagella (1971) *Creep Rupture Data for the Refractory Metals to High Temperatures*, Gordon and Breach Science Publishers, New York.

DeMastry, J. A. and N. M. Griesenauer (1967) "Elevated Temperature Corrosion Studies of Refractory Metal Alloys in Cesium Vapor and Lithium," in *Refractory Metals and Alloys IV*, eds. R. I. Jaffee, G. M. Ault, J. Maltz, and M. Semchyshen, Gordon and Breach Science Publishers, New York, pp. 1169–1187.

Garfinkle, M., W. R. Witzke, and W. D. Klopp (1968) *Superplasticity in Tungsten-Rhenium Alloys*, NASA TN D-4728.

Hahn, G. T., A. Gilbert, and R. I. Jaffee (1963) "The Effects of Solutes on the Ductile-to-Brittle Transition in Refractory Metals," in *Refractory Metals and Alloys II*, eds. M. Semchyshen and I. Perlmutter, Interscience Publishers, New York, pp. 23–63.

Hall, R. W., P. F. Sikora, and G. M. Ault (1961) "Mechanical Properties of Refractory Metals and Alloys Above 2000°F," in *Refractory Metals and Alloys*, eds. M. Semchyshen and J. J. Harwood, Interscience Publishers, New York, pp. 483–504.

Hoffman, E. E. and R. W. Harrison (1968) "The Compatibility of Refractory Metals with Liquid Metals," in *Refractory Metal Alloys*, eds. I. Machlin, R. T. Begley, and E. D. Weisert, Plenum Press, New York, pp. 251–287.

Kangilaski, M. (1983), Personal Communication, General Electric Co., Sunnyvale, CA.

King, G. W. (1969) "Investigation of the Yield Strength of a Dispersion-Hardened W-3.8 vol percent ThO_2 Alloy," *Trans. TMS-AIME* 245:83–89.

Klopp, W. D., F. C. Holden, and R. I. Jaffee (1960) *Further Studies on Rhenium Alloying Effects in Molybdenum, Tungsten, and Chromium*, Contract Number 1512(00), Battelle Memorial Institute, Columbus, OH.

Klopp, W. D. and P. L. Raffo (1964) *Effects of Purity and Structure on Recrystallization, Grain Growth, Ductility, Tensile, and Creep Properties of Arc-Melted Tungsten*, NASA TN D-2503.

Klopp, W. D. and W. R. Witzke (1966a) *Mechanical Properties and Recrystallization Behavior of Electron-Beam-Melted Tungsten Compared with Arc-Melted Tungsten*, NASA TN D-3232.

Klopp, W. D., W. R. Witzke, and P. L. Raffo (1966b) *Mechanical Properties of Dilute Tungsten-Rhenium Alloys*, NASA TN D-3483.

Klopp, W. D. (1968) *Review of Ductilizing of Group VIA Elements by Rhenium and Other Solutes*, NASA TN D-4955.

Klopp, W. D. and W. R. Witzke (1969) *Mechanical Properties of Arc-Melted Tungsten-Rhenium-Hafnium-Carbon Alloys*, NASA TN D-5348.

Klopp, W. D. and W. R. Witzke (1972) *Mechanical Properties of Electron-Beam-Melted Molybdenum and Dilute Molybdenum-Rhenium Alloys*, NASA TM X-2576.

Klopp, W. D. (1975) "A Review of Chromium, Molybdenum, and Tungsten Alloys," *J. Less-Common Metals* 42:261–278.

Klopp, W. D., R. H. Titran, and K. D. Sheffler (1980) *Long-Time Creep Behavior of the Tantalum Alloy Astar 811C*, NASA TP 1691.

Kumar, A. and B. L. Eyre (1980) "Grain Boundary Segregation and Intergranular Fracture in Molybdenum," *Proc. R. Soc. London, Ser. A* 370:431–458.

Lange's Handbook of Chemistry (1979), ed. J. A. Dean, McGraw-Hill, New York, pp. (9-4)–(9-64).

Merrigan, M. A. and L. B. Lundberg (1983) "An Initial Evaluation of Molybdenum-Rhenium Alloy for Reactor Heat Pipes," in *Proceedings, 18th Intersociety Energy Conversion Engineering Conference*, Vol. 4, pp. 1880–1886.

Port, J. H. (1965) "Recent Developments in Rhenium and Rhenium Alloy Technology," in *Plansee Proceedings 1964*, ed. F. Benesovsky, Metallwerk Plansee AG., Reutte/Tyrol, pp. 613–635.

Raffo, P. L. (1969) *Exploratory Study of Mechanical Properties and Heat Treatment of Molybdenum-Hafnium-Carbon Alloys*, NASA TN D-5025.

Rhenium Alloys, Inc. (1983) *Rhenium and Rhenium Alloys*, Rhenium Alloys, Inc., Elyria, OH.

Robins, D. A. (1959) "An Interpretation of Some of the Properties of the Transition Metals and Their Alloys," *J. Less-Common Metals* 1:396–410.

Seigle, L. L. and C. D. Dickinson (1963) "Effect of Mechanical and Structural Variables on the Ductile-Brittle Transition in Refractory Metals," in *Refractory Metals and Alloys II*, eds. M. Semchyshen and I. Perlmutter, Interscience Publishers, New York, pp. 65–116.

Semchyshen, M. and R. Q. Barr (1961) "Extrusion and Mechanical Properties of Some Molybdenum and Tungsten-Base Alloys," in *High Temperature Materials II*, eds. G. M. Ault, W. F. Barclay, and H. P. Munger, Interscience Publishers, New York, pp. 599–626.

Semchyshen, M. and R. Q. Barr (1966) "Research on New Methods for Improving the Ductility of Molybdenum," *J. Less-Common Metals* 11:1–13.

Sheffler, K. D., J. C. Sawyer, and E. A. Steigerwald (1969) "Mechanical Behavior of Tantalum-Base T-111 Alloy," *Trans. ASM* 62:749–758.

Sheffler, K. D., R. R. Ebert (1973) *Generation of Long Time Creep Data on Refractory Alloys at Elevated Temperatures*, NASA CR-134481.

Sherby, O. D. (1962) "Factors Affecting the High Temperature Strength of Polycrystalline Solids," *Acta Met.* 10:135–147.

Smithells, C. J. (1967) *Metals Reference Book*, Interscience Publishers, New York.

Srivastava, S. C. and L. L. Seigle (1974) "Solubility and Thermodynamic Properties of Oxygen in Solid Molybdenum," *Met. Trans.* 5:49–52.

Stephens, J. R. (1963) "Effect of Surface Condition on the Ductility of Tungsten," in *High Temperature Materials II*, eds. G. M. Ault, W. F. Barclay, and H. P. Munger, Interscience Publishers, New York, pp. 125–137.

Stephens, J. R. and W. R. Witzke (1972) "Alloy Hardening and Softening in Binary Molybdenum Alloys as Related to Electron Concentration," *J. Less-Common Metals* 29:371–388.

Stephenson, R. L. (1969) "The Effect of Fabrication Variables on the Creep-Rupture Properties of Molybdenum-Base Alloys," *Trans. TMS-AIME* 245:997–1001.

Vandervoort, R. R. (1969) "On the Possible Influence of Stacking Fault Energy on the Creep of Pure BCC Metals," *Trans. TMS-AIME* 245:2269–2272.

Wadsworth, J., G. R. Morse, and P. M. Chewey (1983) "The Microstructure and Mechanical Properties of a Welded Molybdenum Alloy," *Materials Science and Engineering* 59:257–273.

Waldron, M. B., J. Adam, and B. L. Eyre (1965) "The Behavior of Refractory Metals in Radiation Environments," in *Plansee Proceedings 1964*, ed. F. Benesovsky, Metallwerk Plansee AG., Reutte/Tyrol, pp. 859–879.

Witzke, W. R. (1974) "The Effects of Composition on Mechanical Properties of W-4Re-Hf-C Alloys," *Met. Trans.* 5:499–504.

Witzke, W. R. (1975) *Compositional Effects on Mechanical Properties of Hafnium-Carbide-Strengthened Molybdenum Alloys*, NASA TM X-3239.

Wronski, A. S., A. C. Chilton, and E. M. Capron (1969) "The Ductile-Brittle Transition in Polycrystalline Molybdenum," *Acta Met.* 17:751–755.

Space Nuclear Power Systems 1984
Edited by M. S. El-Genk and M. D. Hoover
© Orbit Book Company, Malabar, FL, 1985

Chapter 43

Thermionic Fuel Element Technology Status

J. W. Holland, M. H. Horner, and L. Yang

GA Technologies, Inc.
P.O. Box 85608
San Diego, California 92138

During the intensive thermionic fuel element (TFE) development program from the mid 1960s to the early 1970s, over a half-million thermionic converter-hours of inpile and out-of-pile testing were accumulated in the United States. When the program was terminated in early 1973, TFEs had operated 12,500 hours ($\sim 1\frac{1}{2}$ years) with projected 3-year lifetimes, and individual laboratory converters operated more than 5 years with stable performance. By the end of 1971, full-scale prototypical TFEs were being routinely manufactured and tested inpile. The high degree of quality yielded reproducible performances within ± 5 percent and no premature or early failures. Primary life-limiting factors had been identifed as: 1) thermionic emitter dimensional increase due to interactions with the fuel and 2) electrical insulator structural damage from fast neutrons. Multiple options for extending TFE lifetimes to 7-years or longer are available and will be investigated in the 1984 and 1985 SP-100 program for resolution of critical technology issues.

Introduction

In a thermionic reactor power system, nuclear energy is converted directly into electricity within multiconverter thermionic fuel elements (TFEs) that comprise the reactor core. In the 108 kWe SP-100 thermionic reactor, the core contains 172 TFEs with each TFE containing 6 thermionic converters connected in series. The TFE and individual converters shown in Figures 1 and 2 are constructed entirely of refractory metals and ceramics.

Development of thermionic converters started with single thermionic devices which were tested out-of-pile with electrical heaters. Some were cylindrical geometry converters constructed of the same materials that would be used in TFE construction. The Mark VI LC-9 is an example. Figure 3 shows the test results of LC-9 which operated at constant performance for over 5 years at an electrode power density of 8 watts/cm^2 and efficiency of 14 percent (Yang and Bruce 1973). The test was still fully operational at program termination in January 1973. We concluded from the results of this test and hundreds of thousands of hours accumulated in similar tests that there are no fundamental mechanisms in out-of-pile converters that would limit lifetimes to less than 7 years.

Over 320,000 hours of inpile converter testing had been accumulated by January 1973 (Fitzpatrick, Yates, and Schwarzer 1973). The majority of these hours were accumulated within TFEs. Figure 4 illustrates the development evolution from single cells to TFEs. As the development progressed, life-limiting mechanisms were systematically identified and solutions found for life-times of 20,000 hours which was the program goal. The data base available in 1973 supported TFE lifetimes of about three years with emitter temperatures of 1800 K. Primary life limiting factors were identified to be 1) thermionic emitter dimensional increases do to fuel-emitter interactions and 2) insulator structural damage from fast neutrons. The result of unrestricted emitter dimensional increases is shorting of the converter electrodes thereby reducing the output voltage to zero. Structural failure of an insulator seal will result in a reduction or loss of the cesium vapor which is necessary for acceptable performance. Structural failure of the sheath insulator can result in increased collector temperature and off-optimum performance.

Fueled-Emitter Technology Status

In the 1960–70 program, TFEs were fueled with either UO_2 or UCZrC. UO_2 was found to be superior in respect to performance stability and compatibility with the tungsten emitter (Holland 1972 and Yang et al. 1972). Therefore, UO_2 was selected for the SP-100 baseline design. Figure 5 shows emitter distortion found in the UO_2 fueled TFE 6F3 as a function of operating time. Straight line extrapolation of the emitter maximum diameter as a function of time shows that the emitters operating at about 1780 K would have contacted the collector after about three years operation. This extrapolation is conservative since experimental data (Zimmermann 1978) show a saturation in fuel swelling for burnups exceeding about one percent. Cor-



Figure 1 *Schematic of In-core Thermionic Fuel Element (TFE).*

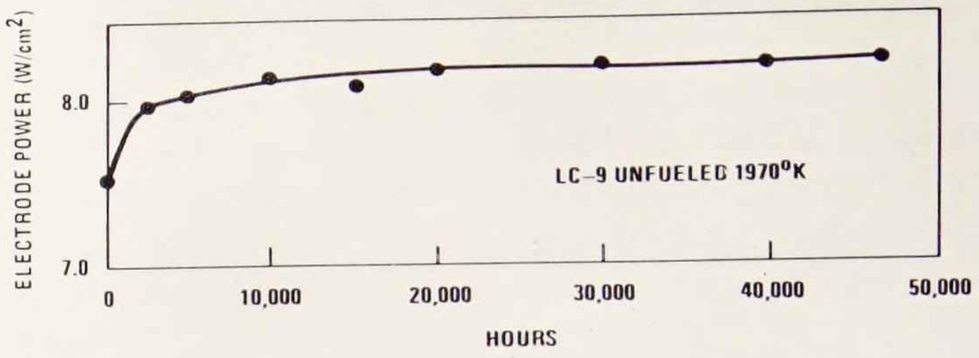
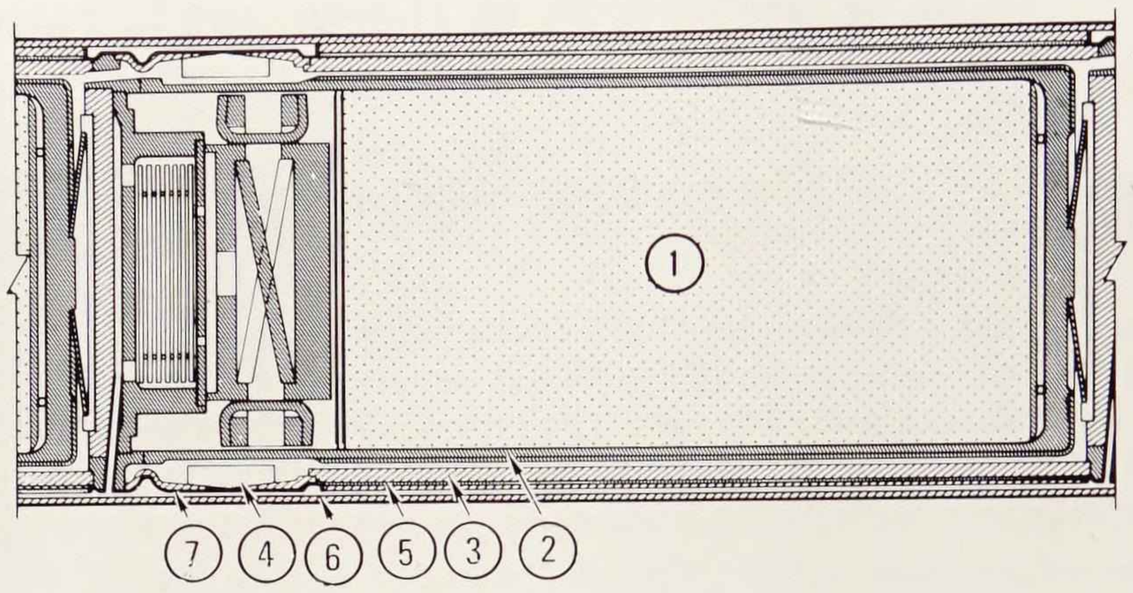


Figure 3 *Performance of Out-of-pile Converter LC-9.*



COMPONENT	PRIMARY FUNCTION	SECONDARY FUNCTION
(1) FUEL (URANIUM OXIDE)	FISSION	(1) CONDUCT HEAT TO EMITTER/RELEASE FISSION GAS
(2) EMITTER (TUNGSTEN)	EMIT ELECTRONS	(2) CONTAIN & RESTRAIN FUEL/CONDUCT HEAT & ELECTRICITY/SEPARATE CESIUM & FISSION GAS
(3) COLLECTOR (NIOBIUM)	COLLECT ELECTRONS	(3) CONDUCT HEAT AND ELECTRICITY/SEPARATE Cs & FISSION GAS
(4) INSULATOR SEAL (ALUMINA/NIOBIUM)	SEPARATE Cs & FISSION GAS	(4) ELECTRICALLY INSULATE EMITTER AND COLLECTOR
(5) SHEATH INSULATOR (ALUMINA/NIOBIUM)	ELECT. INSULATE CONVERTERS	(5) CONDUCT HEAT
(6) SHEATH (NIOBIUM–1% ZIRCONIUM)	ISOLATE CONVERTERS & NaK (PHYSICALLY)	(6) ALIGN EMITTERS & COLLECTORS
(7) INSULATION COATING (ALUMINA)	ISOLATE CONVERTERS FROM SHEATH FOLLOWING Cs ENVELOPE LEAK (ELECTRICALLY)	(7) --

Figure 2 *TFE Component Primary and Secondary Functions.*

relation of the 6F3 data and that of other tests with viscoelastic analyses, in Figure 6, show that SP-100 emitter lifetimes are projected to exceed 7 years. Further inpile testing and improved analysis are planned to confirm this prediction.

The 1.8 mm thick emitters of the baseline design are fabricated in two steps, both using vapor deposition (Yang et al. 1972). The first step is the hydrogen reduction of WF_6 on a hot molybdenum mandrel. The result is a controlled fine grain columnar structure having superior structural qualities for this application. A second step involves vapor depositing a 0.3 mm second layer by the hydrogen reduction of tungsten chloride over the first layer. The deposition is controlled to provide a $\langle 100 \rangle$ preferred crystal orientation surface. This surface typically has a work function of 5.0 electron volts, the high value of which is favorable for thermionic conversion. Fast neutron irradiations of chemically vapor deposited tungsten commensurate with the SP-100 design requirements have not exhibited any significant deleterious changes to the material (Wiffen 1971).

Insulator Technology Status

Lucalox alumina insulators irradiated in the TFE test program of the early 1970s were not subjected to sufficient fast neutron doses to affect their structural integrity. However, in a separate fast neutron irradiation program (Ranken, Frank, and Keilholtz 1972), insulator materials and assemblies were subjected to high enough fast fluences to cause sufficient volumetric swelling that the ceramic bodies were no longer leak tight. This

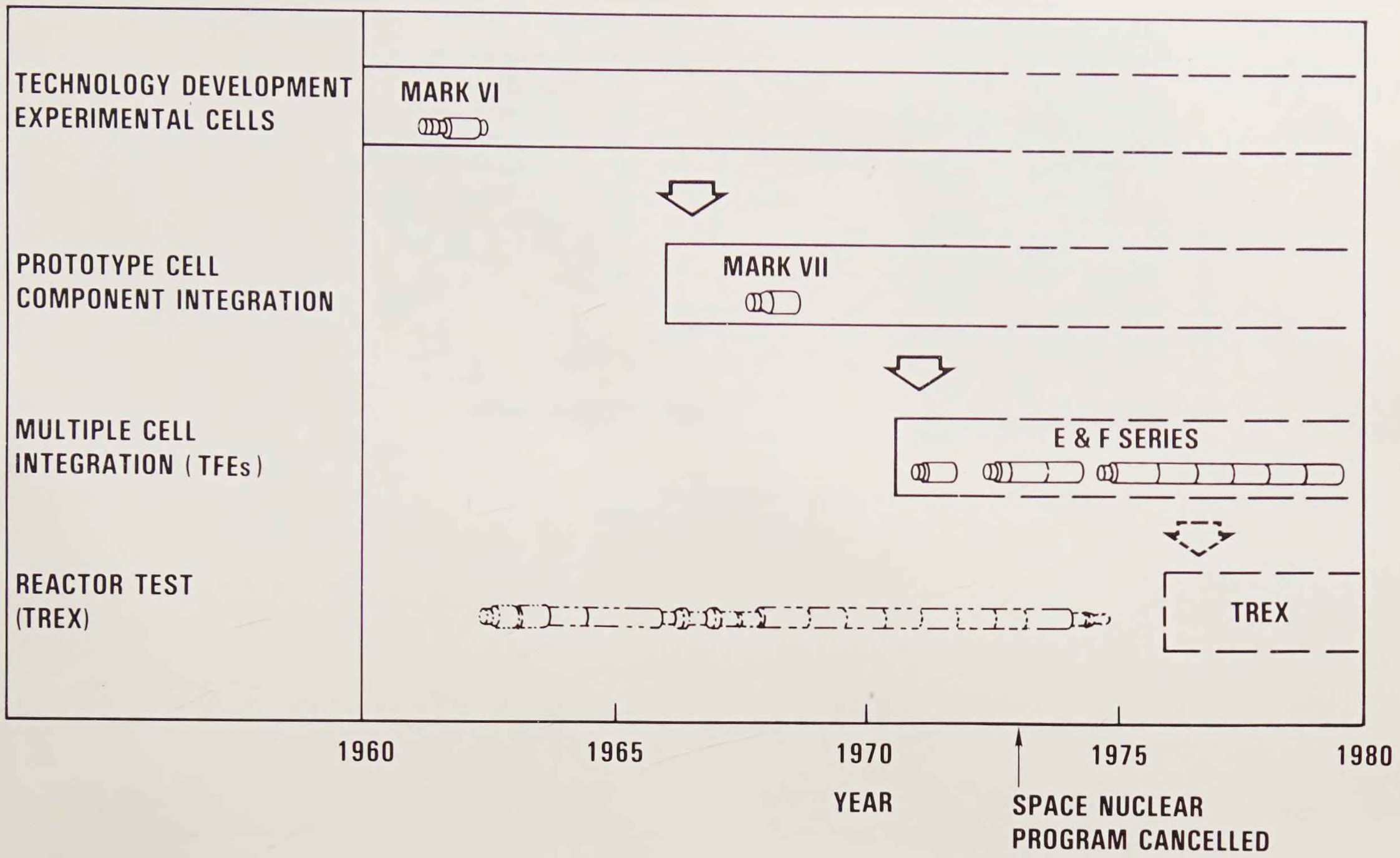


Figure 4 *TFE Development Program Evolution.*

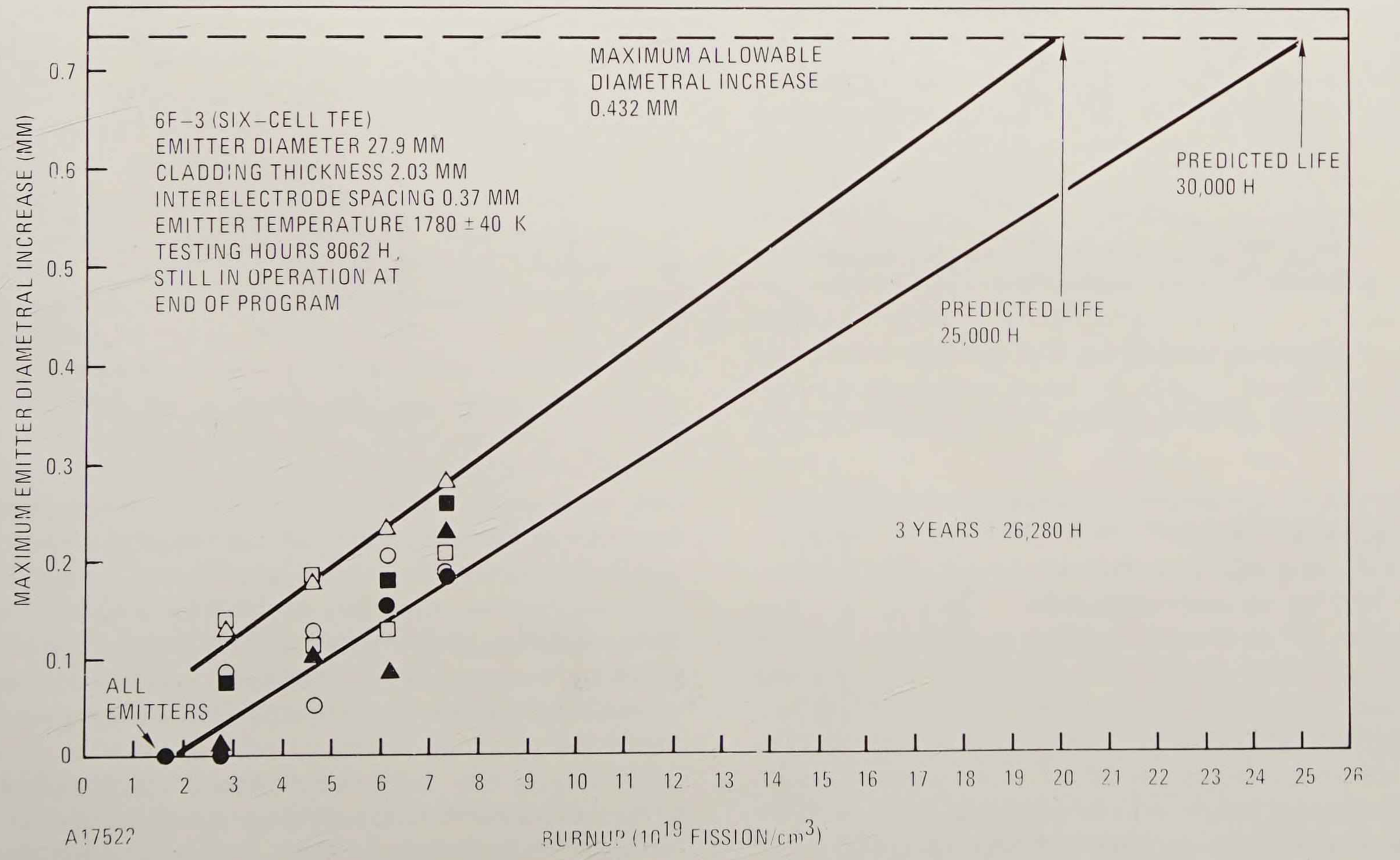


Figure 5 *Forecast of TFE 6F-3 Lifetime.*

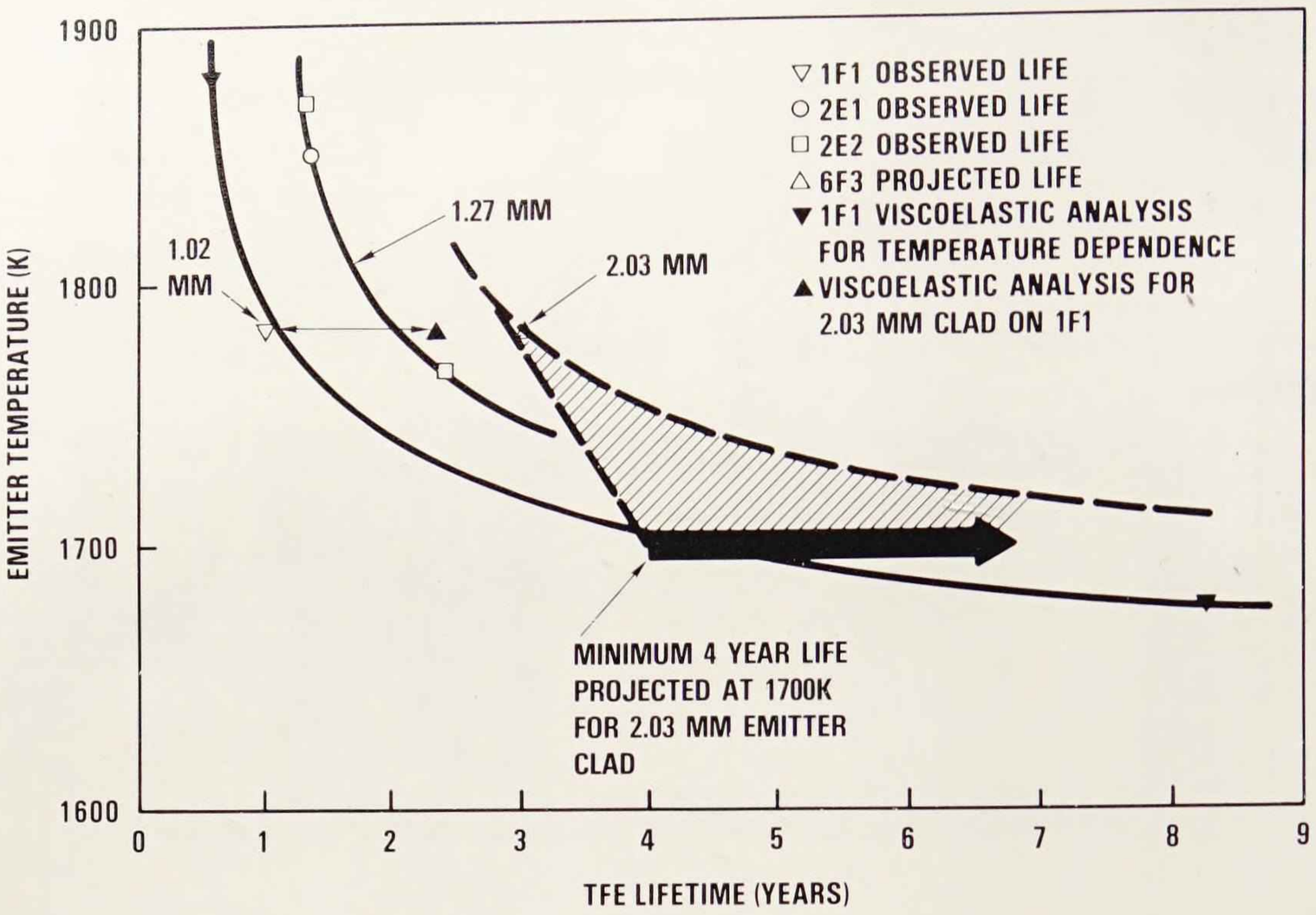


Figure 6 *Fueled Emitter Lifetime Analysis.*

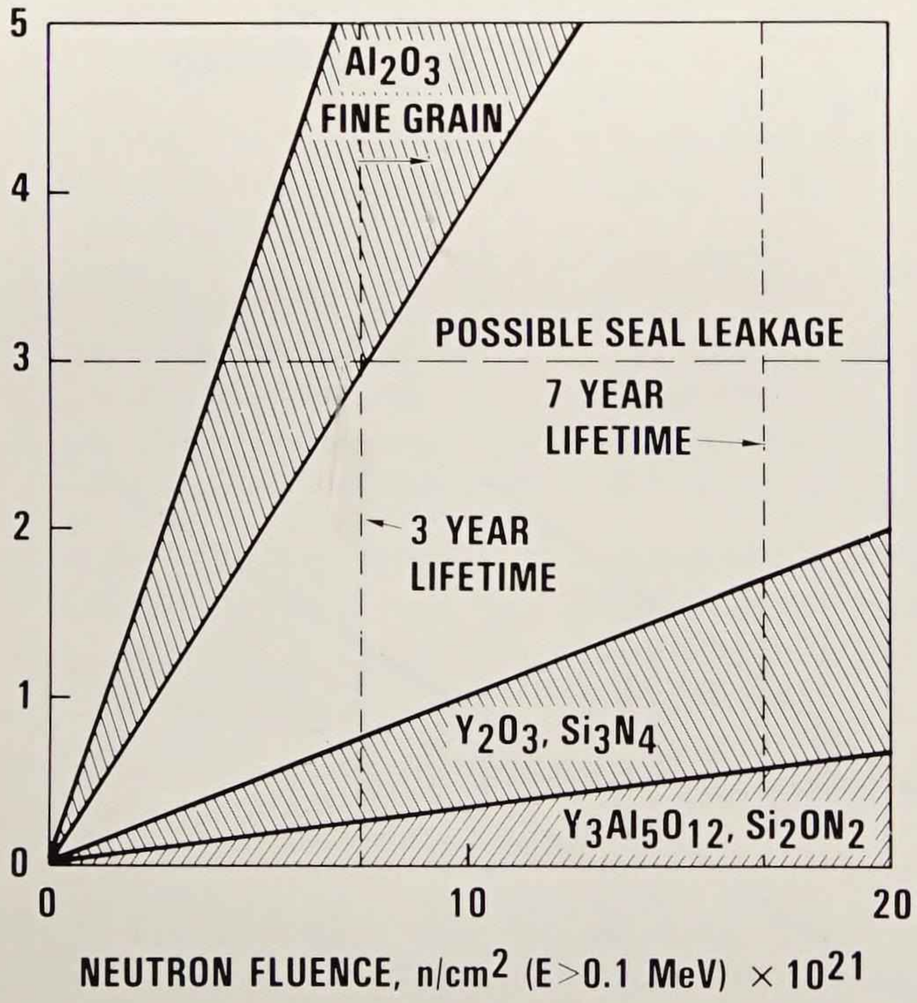


Figure 7 *Insulator Lifetime Improvement Options.*

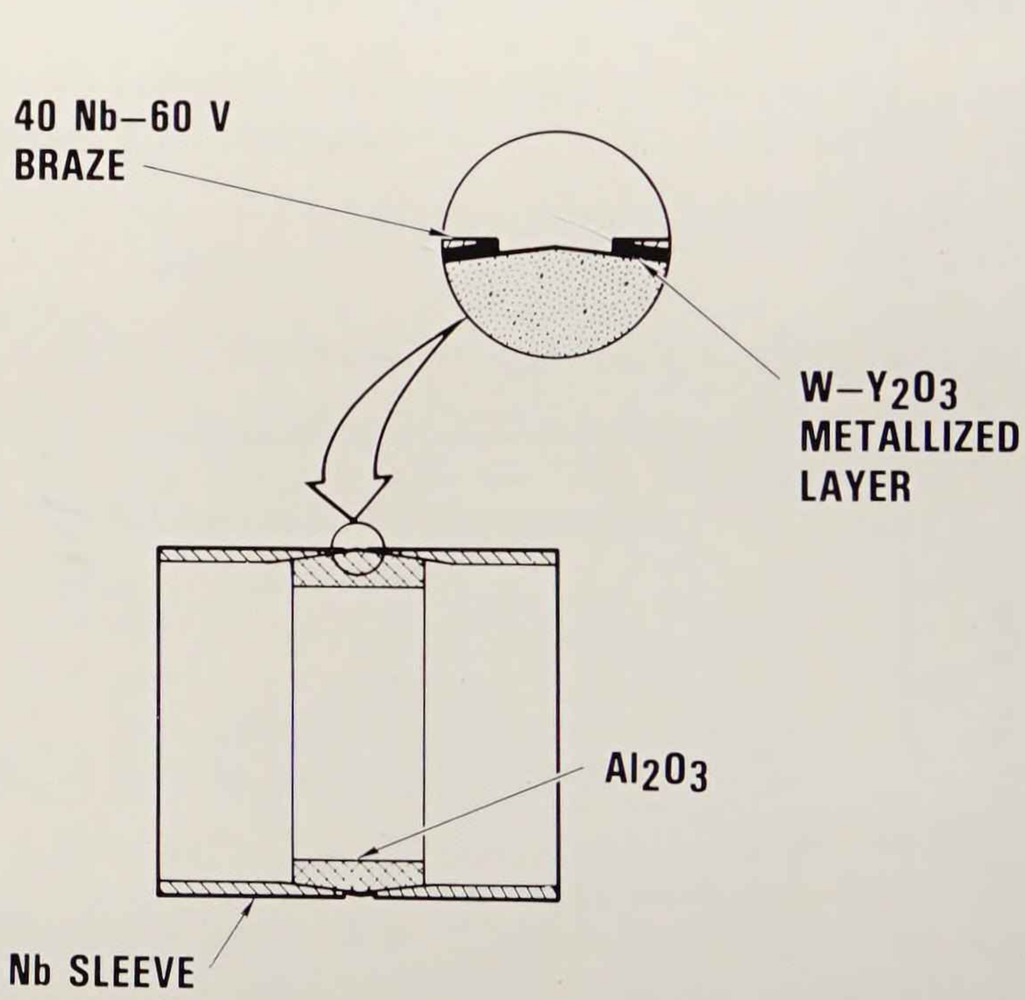


Figure 8 *Interelectrode Insulator Seal.*

occurs when the ceramic has swollen to about 3 volumetric percent. Figure 7 shows the band in which the alumina data fell. Data for very fine grained alumina occupied the right side of the band.

In the SP-100 design the peak fast neutron fluence ($E > 0.1$ MeV) is 17×10^{21} n/cm^2. If fine grained alumina were used, the maximum useful life of the insulator would be about 3 years. Therefore, to meet the SP-100 requirements, insulators with improved radiation resistance will have to be developed. Such development was initiated by Chin and Messick (1972) using Y_2O_3 ceramic. In recent years several alternate candidate insulator materials have been tested to very high fast neutron fluences in the U.S. Department of Energy's Fusion Energy Program. Materials that were demonstrated to have superior dimensional stability are Y_2O_3, $Y_3Al_5O_{12}$, Si_3N_4 and Si_2ON_2 (Clinard 1979 and Clinard and Hurley 1981). The bands within which the volumetric expansion of these materials fall is shown in Figure 7.

The requirement for leak tightness primarily applies to the insulator seal. In the earlier program the insulator seals, shown in Figure 8, where fabricated (Chin and Messick 1972) by brazing tapered niobium cylinders to

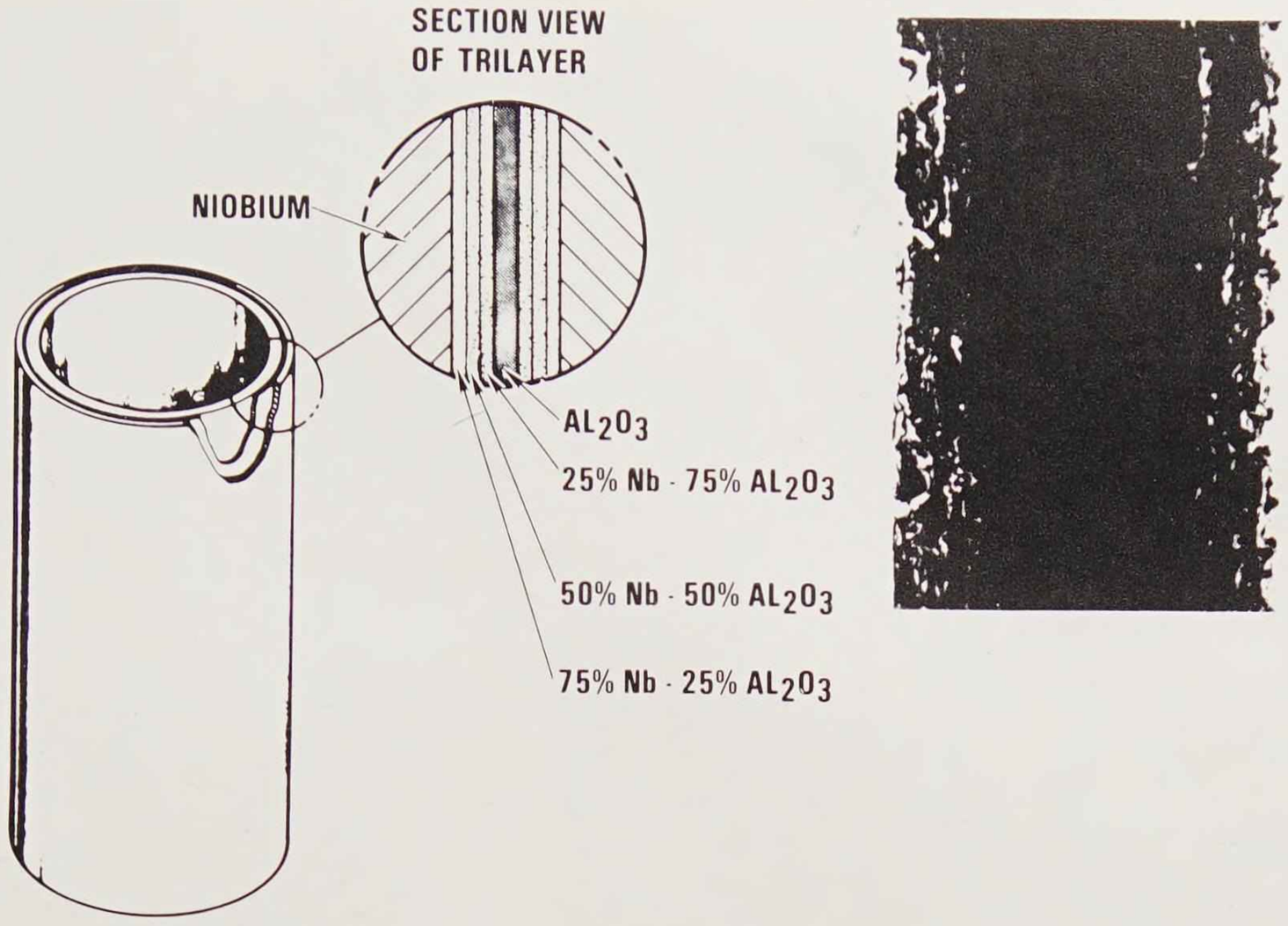


Figure 9 *Graded Trilayers for Thermionic Fuel Element.*

machined and metalized Lucalox ceramic bodies. The ceramic was metalized with tungsten-2 wt. % yttria. Seal brazing was performed in vacuum using vanadium-niobium alloy. The seals were qualified in out-of-pile testing at 1500 K.

The essential requirements for the sheath insulator assemblies are to electrically isolate the thermionic cells from the reactor coolant and to conduct the waste heat from the collector to the sheath which is in contact with liquid metal coolant. The sheath insulator assembly, sometimes called a trilayer, is a layer of ceramic bonded between the two layers of niobium. Niobium has been the material of choice because its thermal expansion coefficient closely matches that of alumina. To assure bond integrity throughout the required thermal cycles, the trilayers were fabricated by plasma spraying a graded cermet over a niobium mandrel starting with 75–25 percent niobium/alumina and then progressing to 50–50, 25–75, 0–100, 25–75, 50–50, 75–25 ratios of niobium to alumina. A niobium sleeve was fit over the cermet and the assembly was gas pressure bonded to form a dense cermet structure. The resulting structure, shown in Figure 9, was used successfully in a number of inpile tests.

Ranken (1972) irradiated trilayers in fast neutron fluences to 6×10^{21} n/cm^2 ($E > 0.1$ Mev) and found separation of the alumina ceramic from the inner niobium collector. The cause was postulated to be due to the fast neutron induced volumetric expansion differences between the niobium and alumina. In the same series of tests, a trilayer made with Y_2O_3 instead of Al_2O_3 did not show separation of the layers. Other candidate insulator materials found to be especially radiation resistant will be investigated in the resumption of trilayer fabrication development.

Cell and TFE Assembly Technology Status

Operations in the manufacturing of the TFEs are discussed in this section. The tungsten emitter is diffusion bonded to a tantalum cylinder by resistance heating the tungsten-tantalum joint (Horner, Grebetz, and Kay 1972). Figure 10 shows the location of the bond. Similar bonds have operated for more than 10,000 hours inpile at prototypical temperature gradients without deterioration.

The remainder of the niobium-niobium and niobium-tantalum joints in the cells and TFEs are electron beam welded. All assembly operations were accomplished in a clean room facility, Figure 11, to which an electron beam welder and a high sensitivity leak detector are functional extensions. Schematics and photographs of cells and TFE in their various stages of assembly are shown in Figure 12. Final processing involved bonding an outer sheath tube of Nb-1 Zr over the six trilayers, the final outgassing, and the loading of cesium into the TFE. The sheath tube bonding was accomplished by

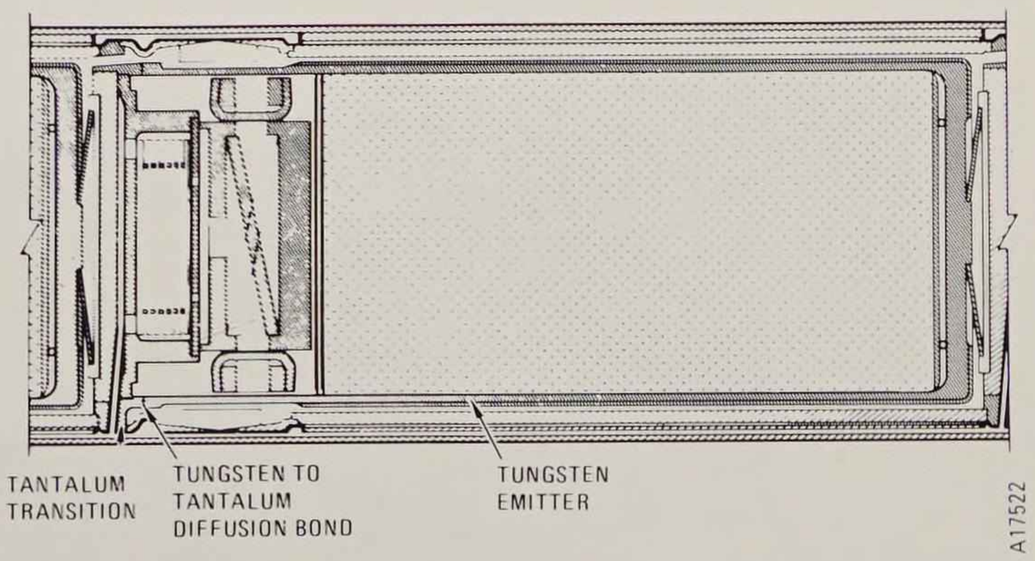


Figure 10 *Location of Tungsten-tantalum Diffusion Bond.*

Figure 11 *TFE Assembly Operations in Clean Room.*

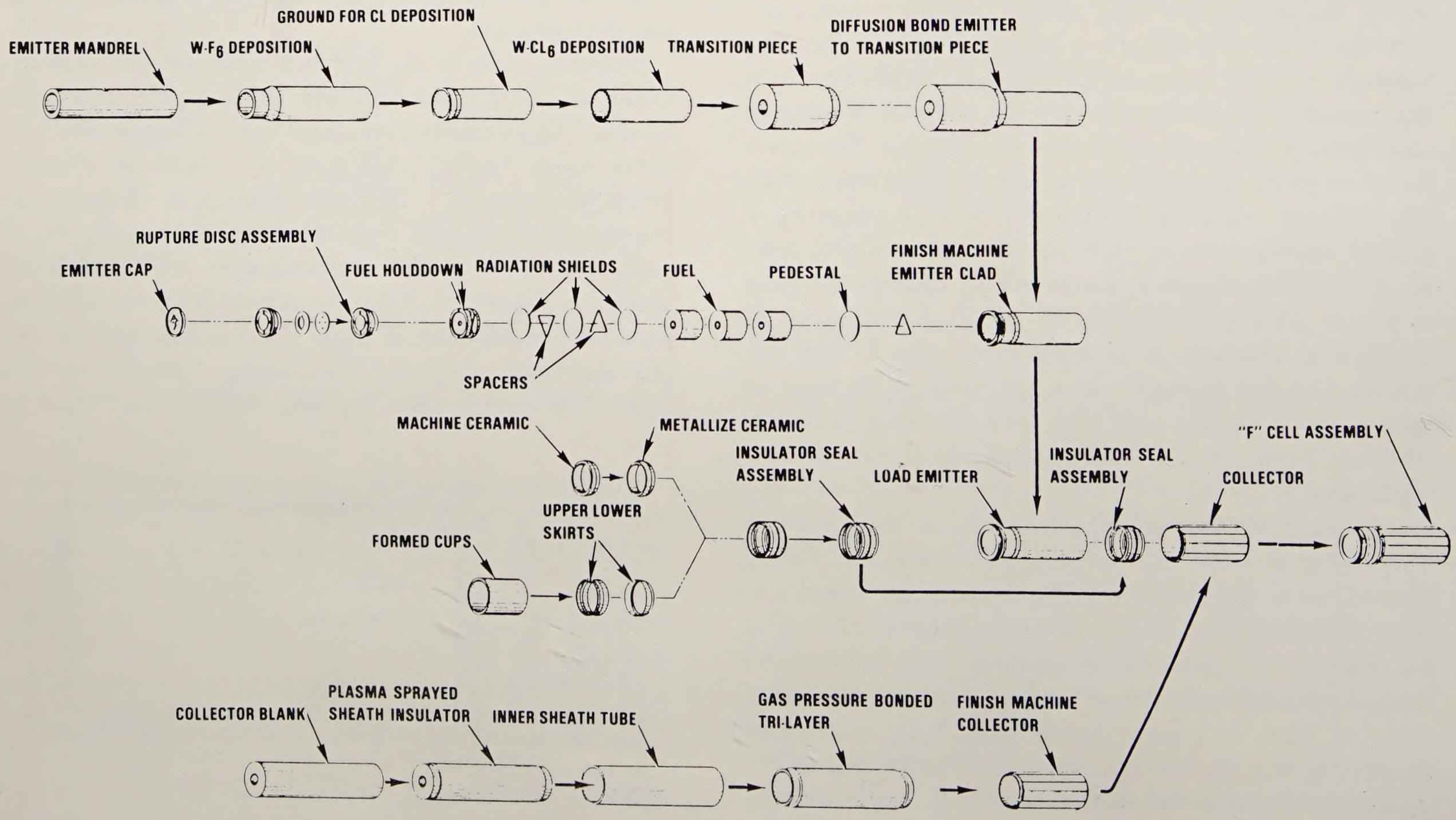


Figure 12A *Converter Fabrication Flow Chart.*

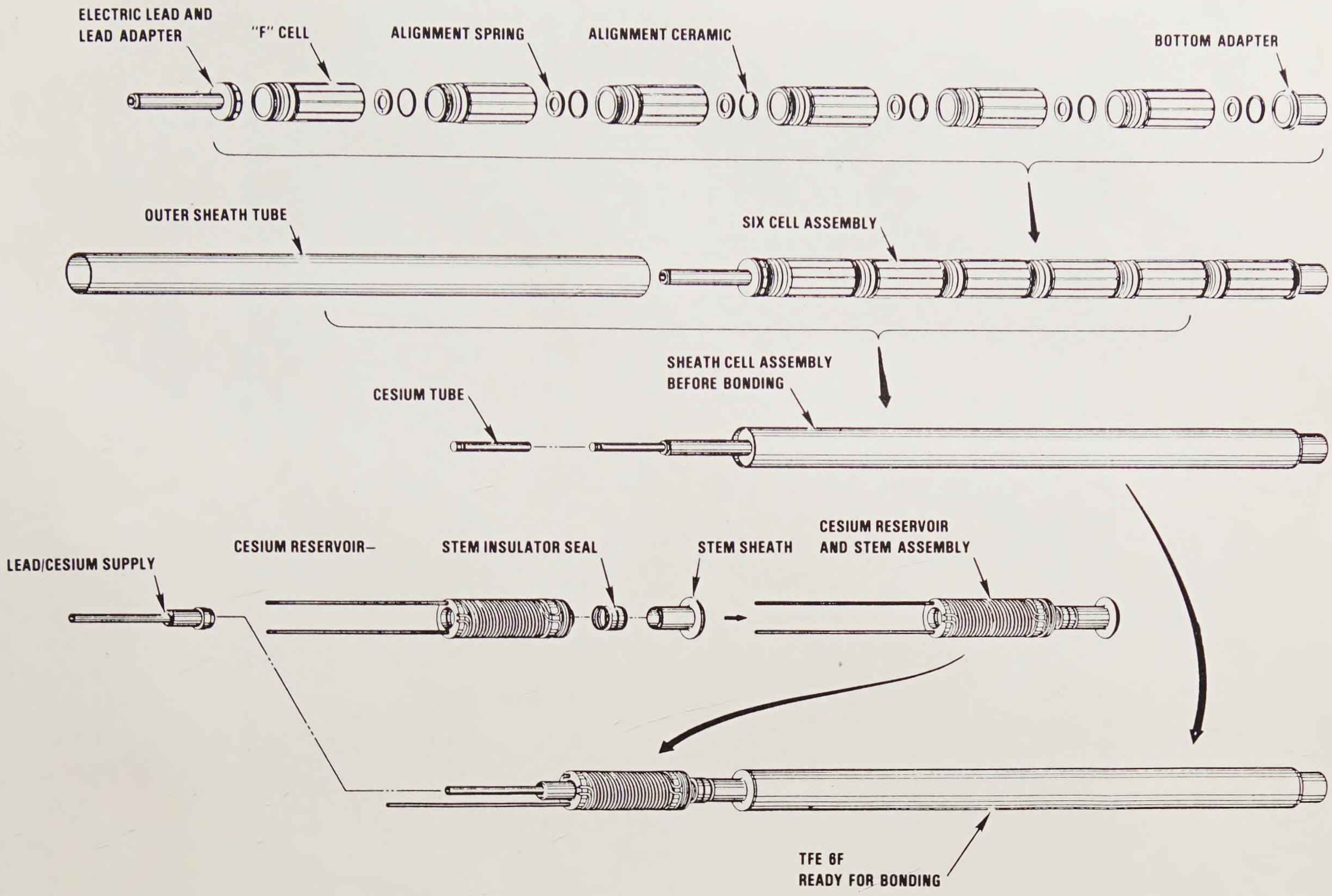


Figure 12B *TFE Assembly Flow Chart.*

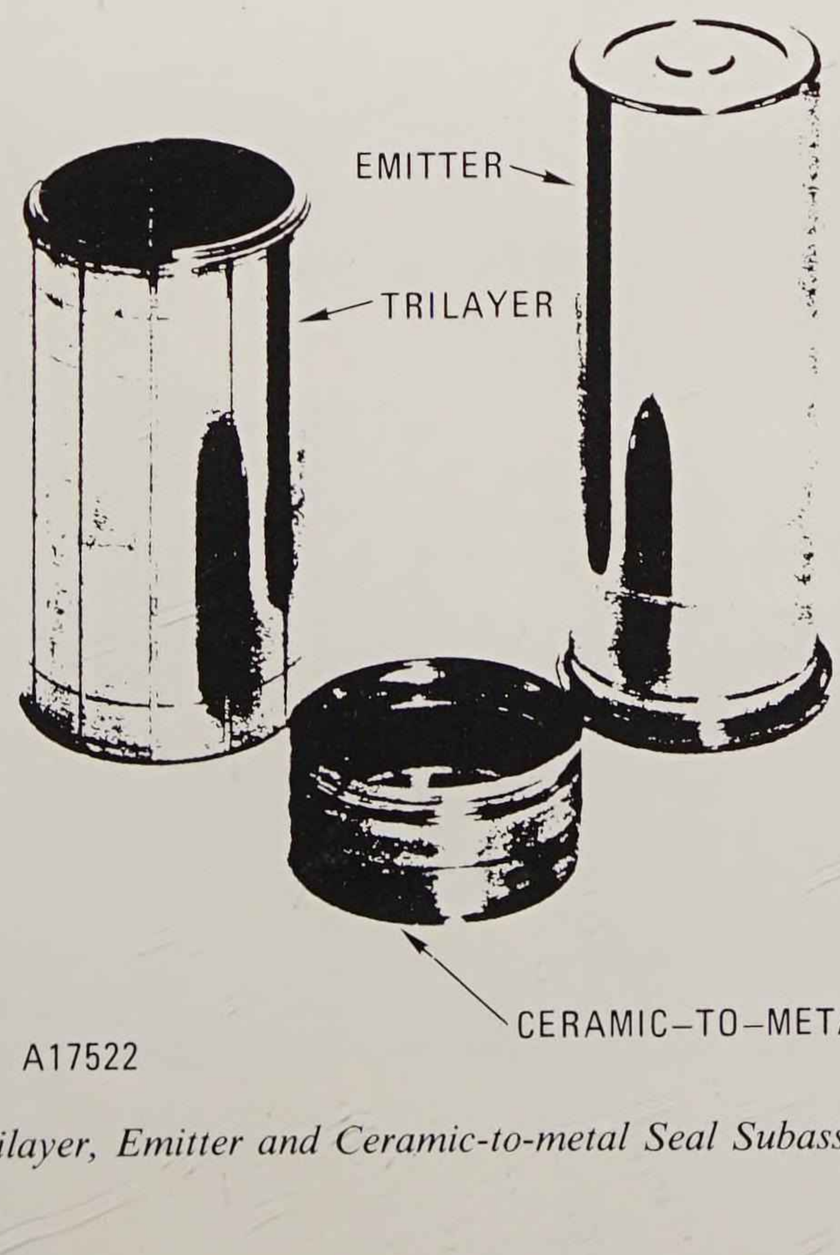


Figure 12C *Trilayer, Emitter and Ceramic-to-metal Seal Subassemblies for F Series Cells.*



Figure 12D *Assembled Converter.*

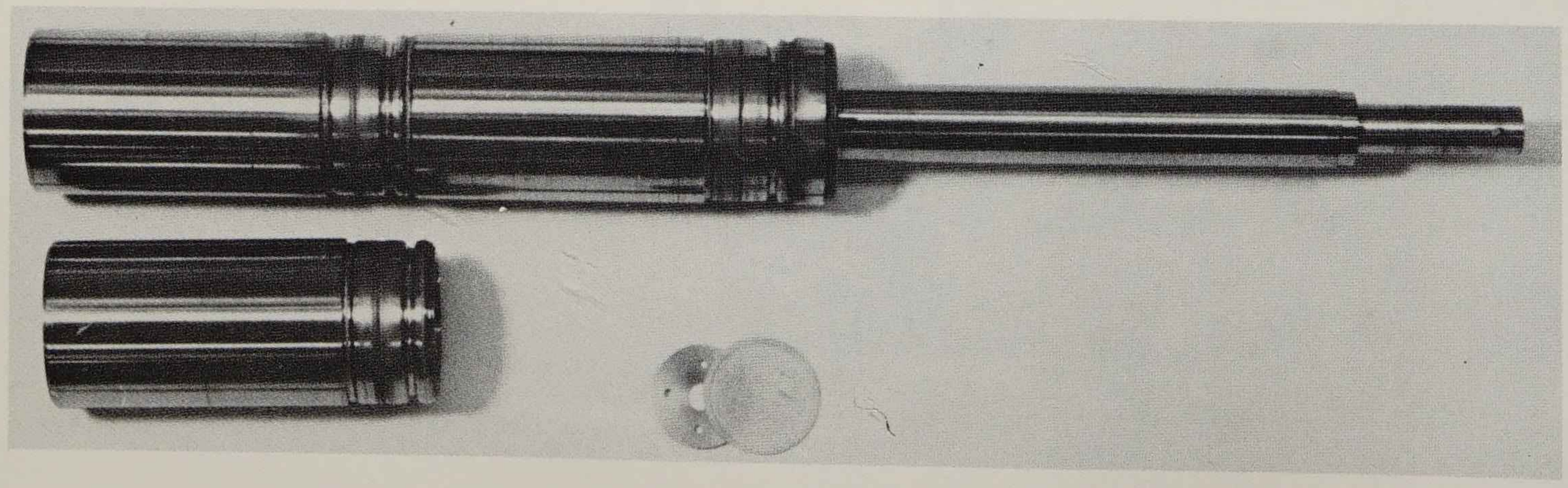


Figure 12E *Partially Assembled TFE Showing Electric Lead Structure.*

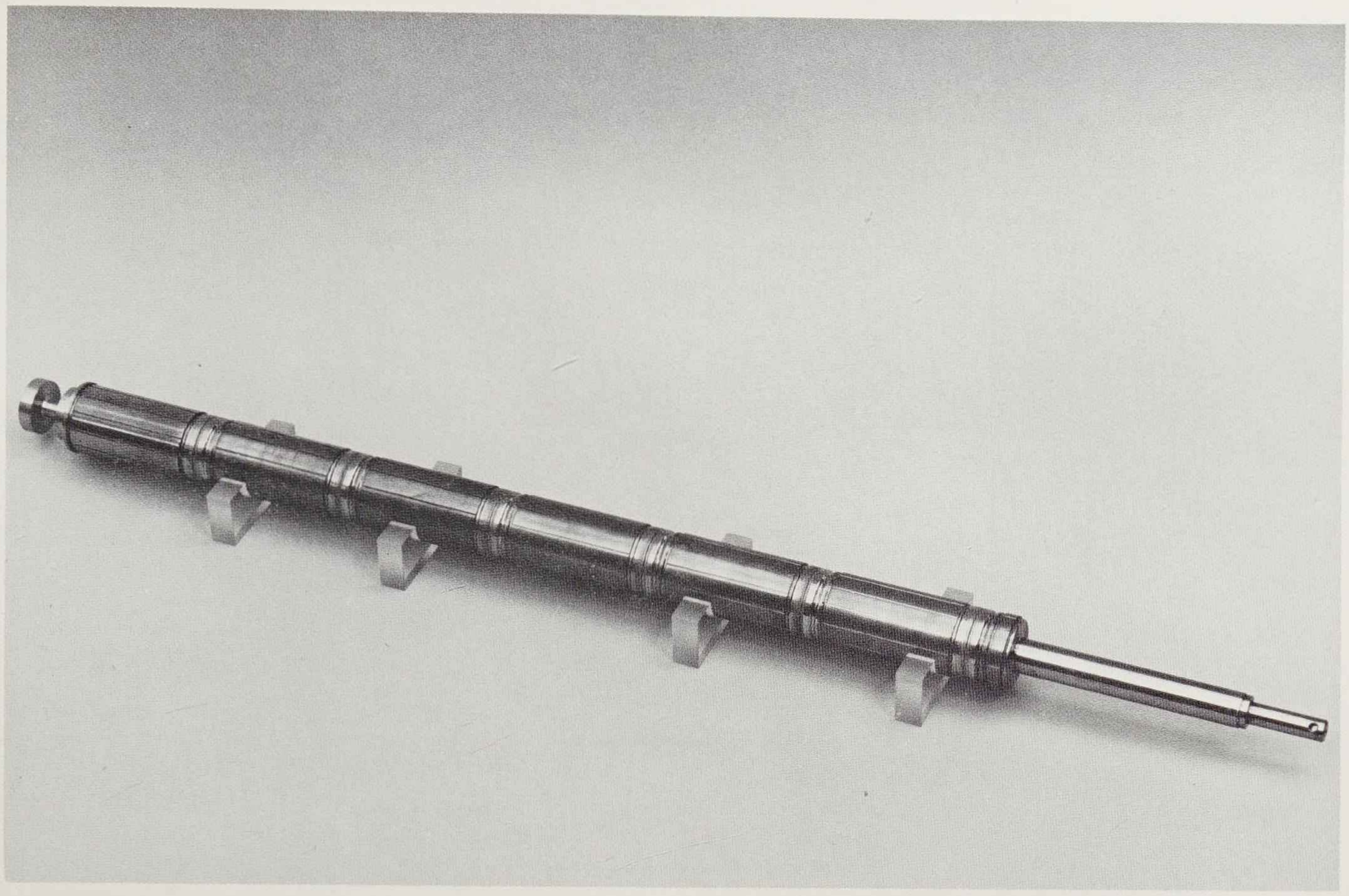


Figure 12F *TFE after Cells, Electric Lead and Alignment Pin Have Been Assembled in Series.*

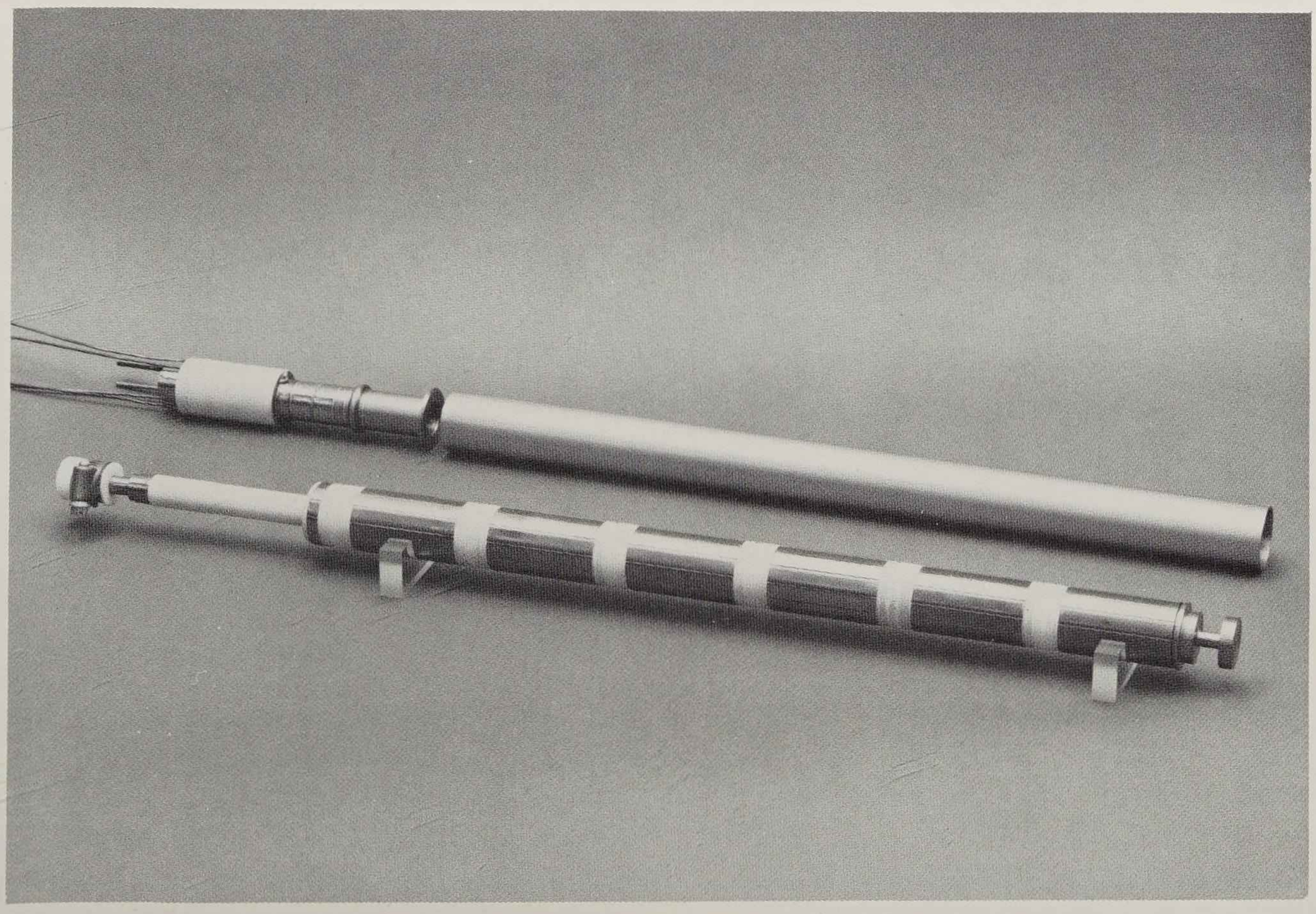


Figure 12G *TFE Subassembly Plasma Sprayed with Al_2O_3 along with Cesium Reservoir and Sheath Tube.*

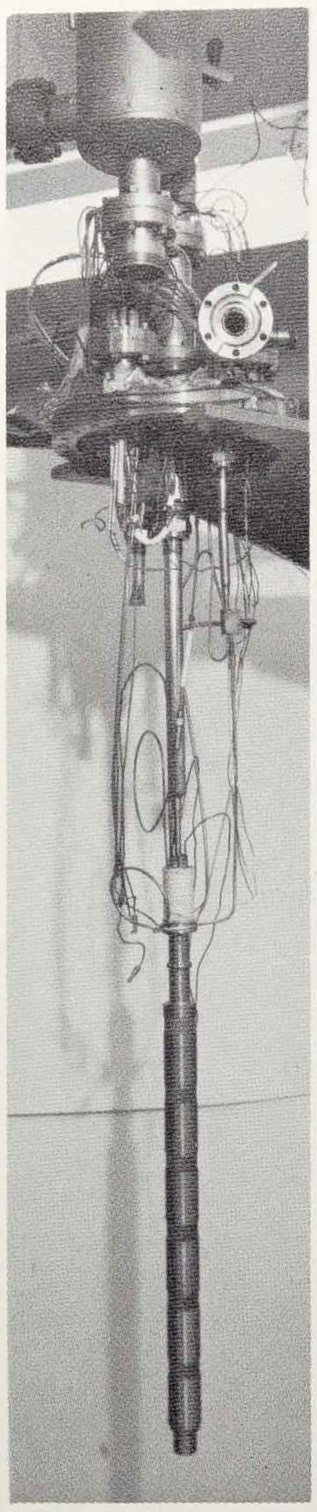


Figure 12H *TFE Ready for Bonding at 1500 K for Four Hours. Tungsten Wire Is Shown Wrapped over the Trilayers.*

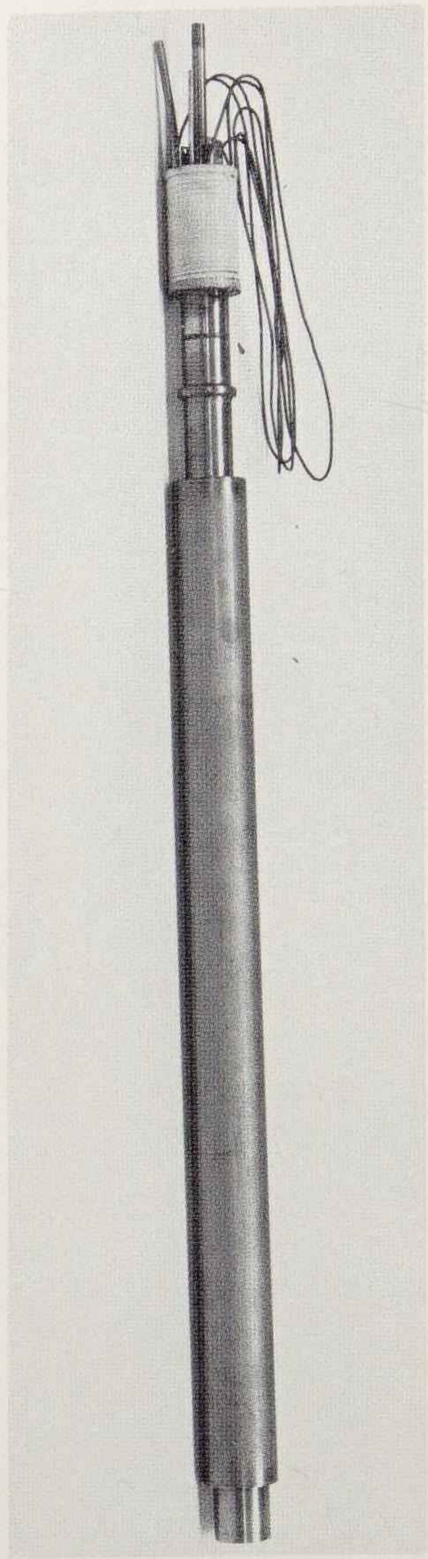


Figure 12I *Completed 6F TFE.*

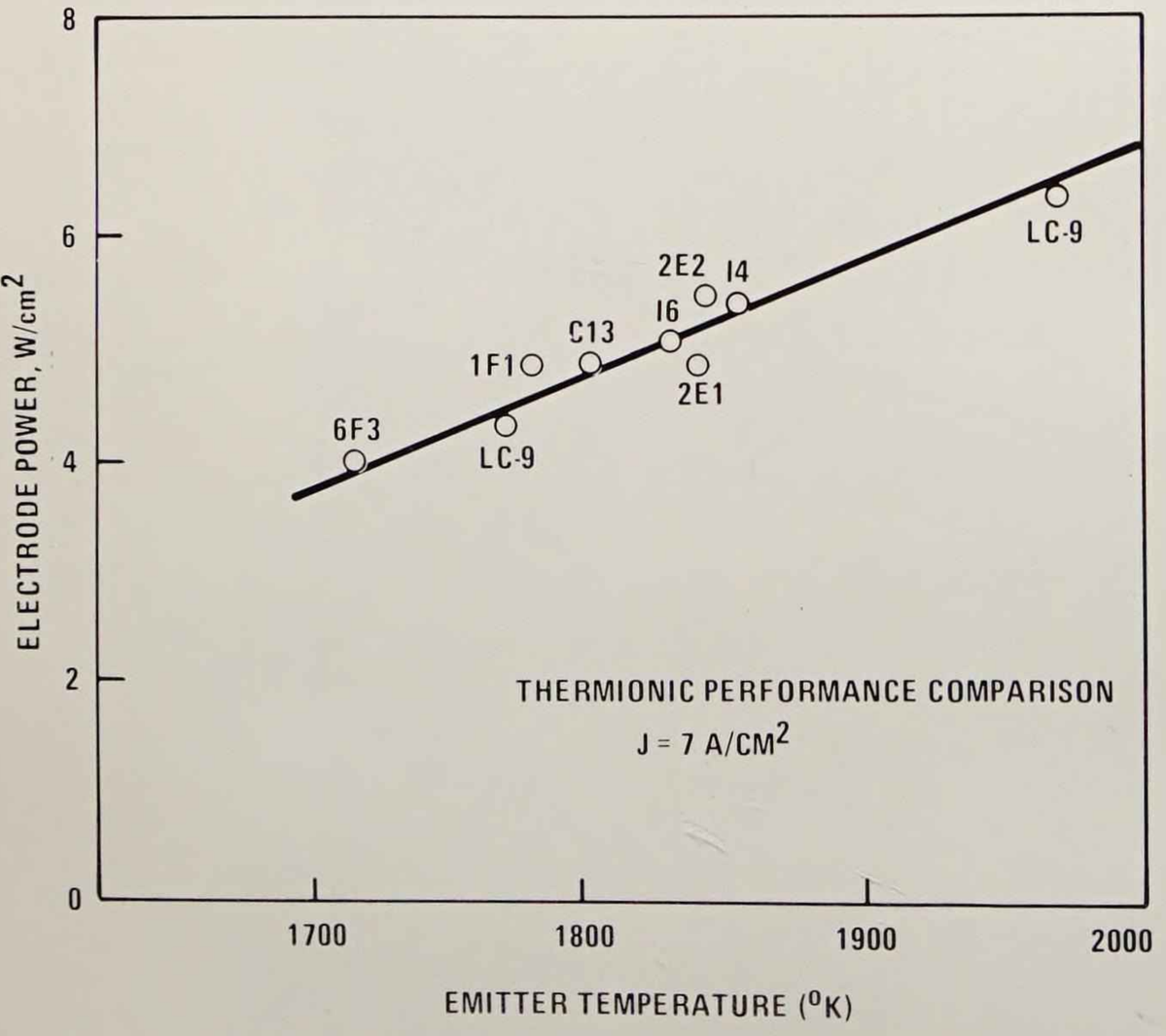


Figure 13 *Performance Comparison of Nonfueled and UO_2-fueled Thermionic Cells and Fuel Elements.*

wrapping the sheath tube with tungsten wire over the trilayer areas and then heating to a 1500 K to cause the sheath tube to be compressively yielded by the differential thermal expansion of tungsten and niobium. A 2–3 micron thick layer of nickel plated onto the inside of the sheath tube before assembly assured an intimate bond. The bond was then inspected ultrasonically.

TFE manufacturing controls instituted in the program yielded performance reproducibility within ±5%, as shown in Figure 13, and no early failures (Holland 1972).

Multiple Options for TFE Lifetime Extension

Alternative development paths are available for resolution of the life limiting phenomena found in the earlier TFE technology program. Figure 14 identifies and classifies these multiple options for extension of TFE lifetime from 3 years to 7 years. To resolve the fueled-emitter dimensional stability issue, design options, performance options and fuel material options are all available. Because emitter distortion has been

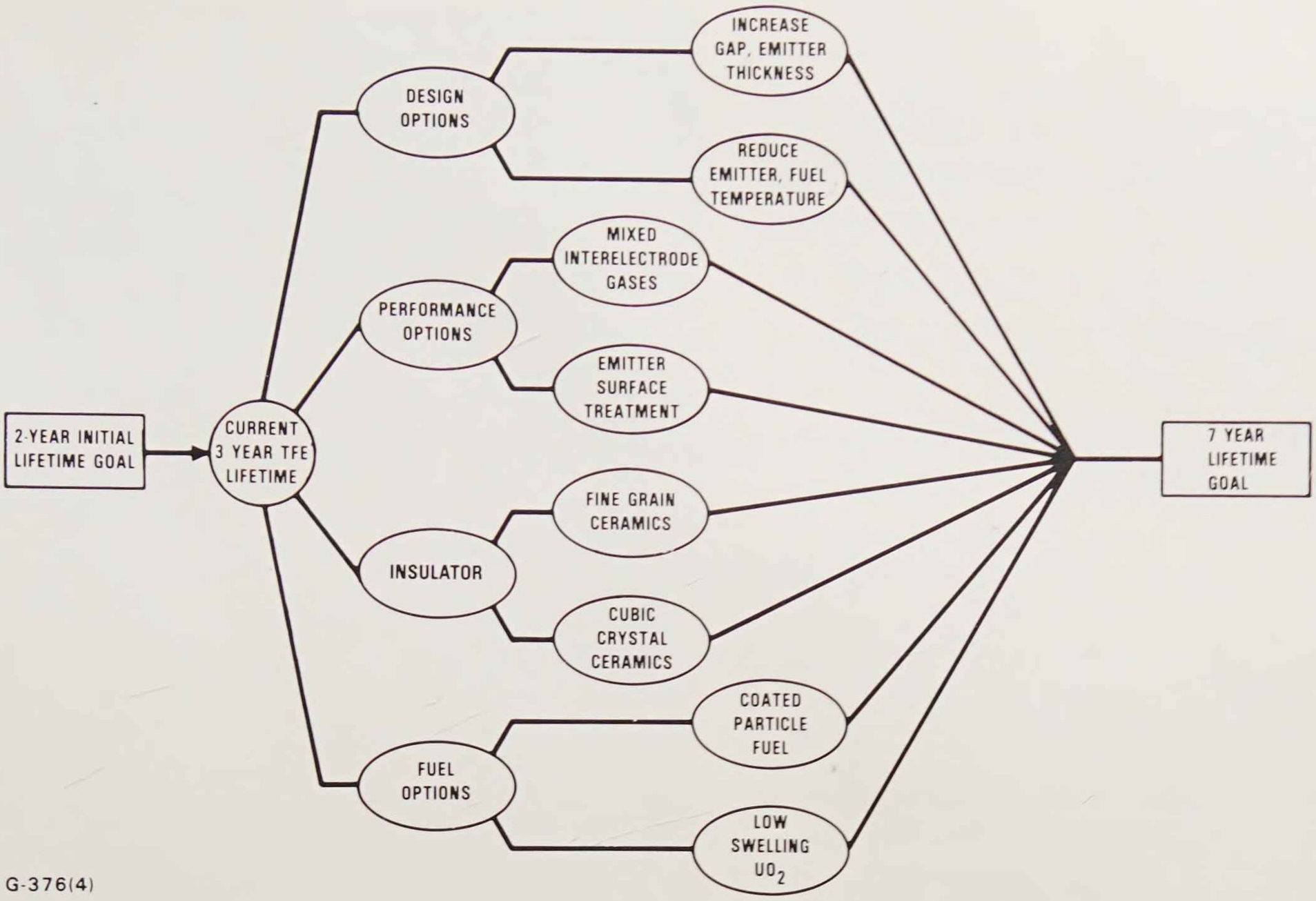


Figure 14 *Multiple Options for Extension of TFE Lifetime.*

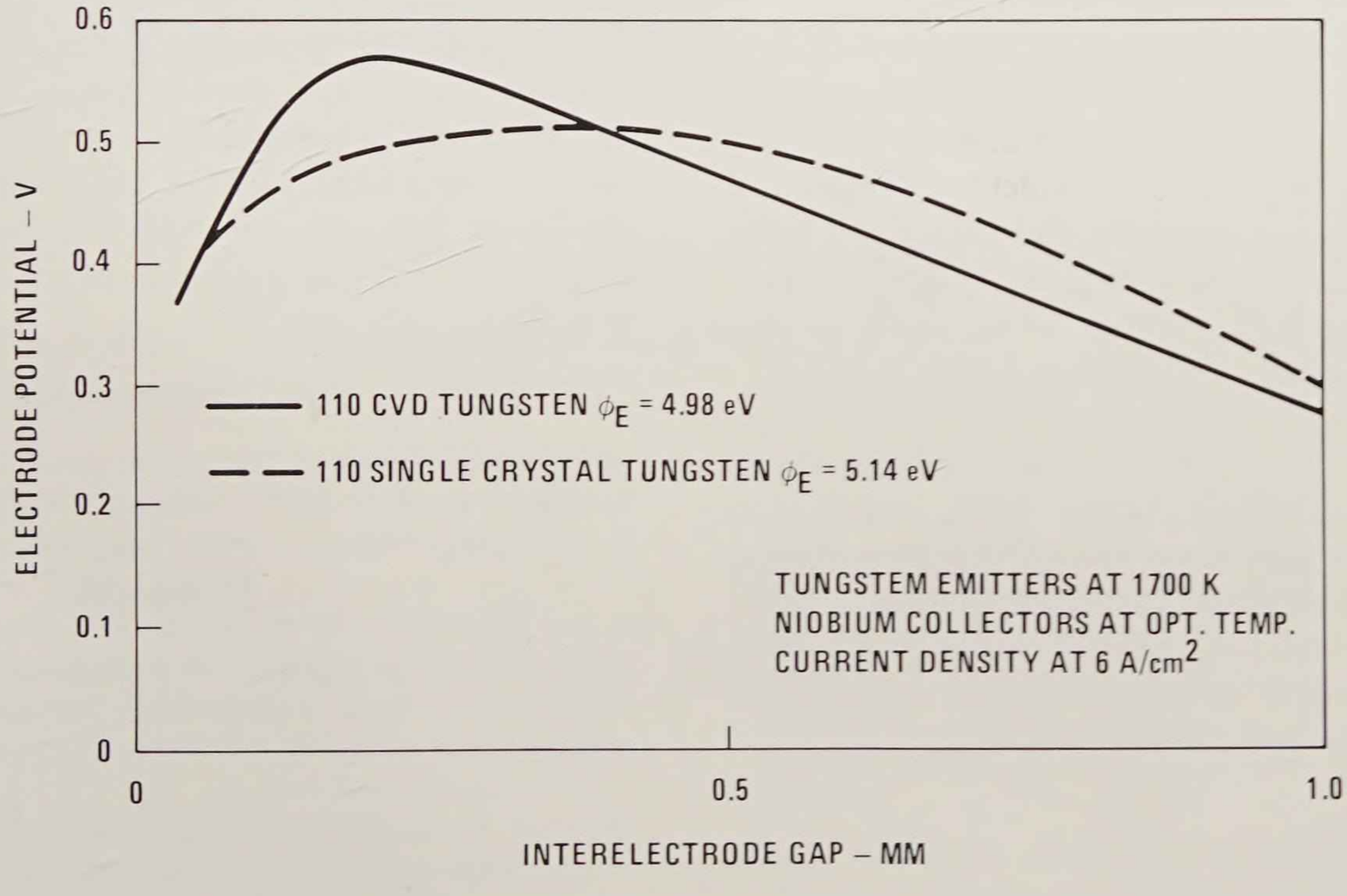


Figure 15 *High Emitter Work Functions Reduce Sensitivity of Performance to Changes in Interelectrode Gap.*

found to be a strong function of emitter temperature, one option is to lower the emitter temperature to 1700 K from the 1800–2000 K values used in the earlier program. Another design option is to increase the emitter thickness. The impact of these options is evident by inspection of Figure 6.

Increasing the interelectrode gap to allow greater emitter dimensional increases provides a third design option related to the performance options. High emitter work functions provide a relative insensitivity of performance to the interelectrode spacing. Figure 15 illustrates this insensitivity in a converter with a nominal ⟨110⟩ single crystal tungsten emitter (Lieb, Donaker, and Rufeh 1969 and Lieb and Rufeh 1970). The higher

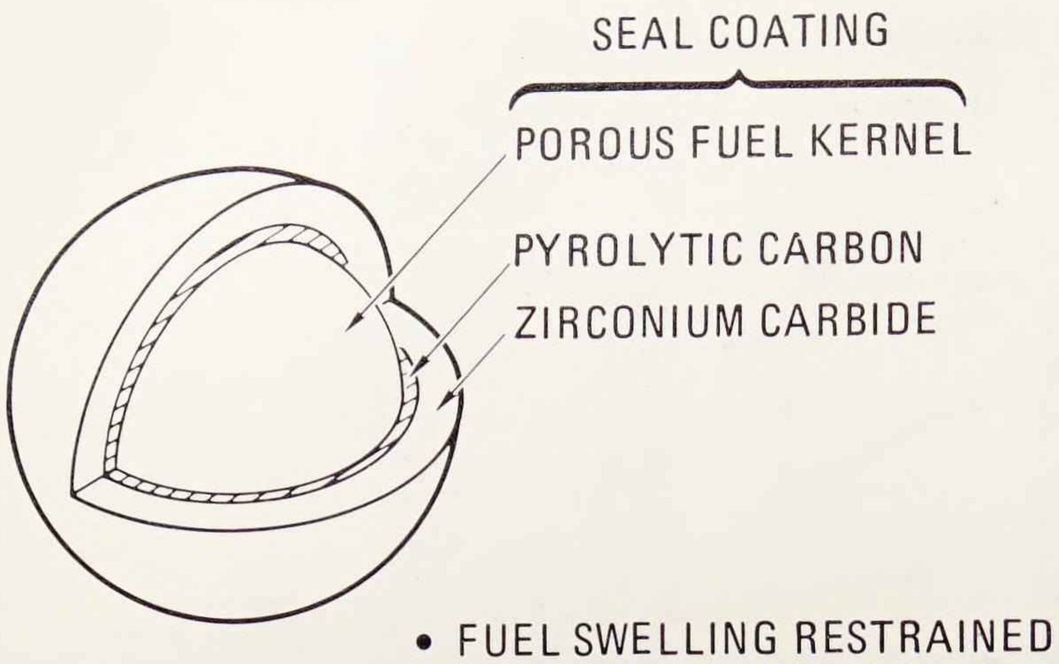


Figure 16 *Emitter Lifetime Improvement Option of Non-swelling Coated Particle Fuel.*

emitter work function reduces the required cesium pressure and the voltage losses and thereby allows larger spacings.

Several fuel material options to the baseline UO_2 fuel are being considered. Application of coated fuel particle technology similar to that developed under the HTGR program offers the potential of complete elimination of fuel clad mechanical interactions and fission gas venting. In this concept the fission gases, Figure 16, are retained within the ZrC coatings which serve as tiny pressure vessels (Gulden and Watson 1982).

To extend insulator lifetimes to seven years or more, irradition resistant insulator materials will be used. As mentioned earlier, Y_2O_3, $Y_3Al_5O_{12}$, Si_3N_4 and Si_2ON_2 have been demonstrated in the US DOE Fusion Energy Program to be dimensionally stable in fast neutron fluences that far exceed the SP-100 requirements. With these ceramics growth to larger systems will not be limited by insulator damage effects.

TFE Testing

A very important addition to the TFE development program in the late 1960s was the establishment of a dedicated thermionic fuel element test reactor (TITR), shown in Figure 17. This TRIGA-type reactor used 70 percent enriched uranium. Erbium was added to the fuel to serve as a burnable poison and to enable core operating lifetimes of 9 megawatt-years. This feature provided for unperturbed TFE operation since the reactor was operated with very little control rod movement for extended durations and without the frequent refuelings normally experienced in fast reactors.

The reactor was designed for simultaneous operation of up to 15 TFEs. Although the fissions in the TFE are produced by thermal neutrons in TITR, the fuel enrichment may be lowered in the TFEs to 5–10 percent and achieve a relatively flat radial power profile and a temperature profile nearly identical to that experienced in a fast reactor, thereby simulating the fuel irradiation conditions of a fast reactor. This is done with the TITR operating at 3 MWt. At this power level the fast neutron fluence (> 0.1 MeV) is the same as the peak fluence to be experienced in the SP-100 fast spectrum thermionic reactor, thereby exposing insulators to the fast fluence to be experienced in the SP-100. Another important capability of the TITR facility is the unrestricted access for instrumentation and the capability for periodic neutron radiography. This latter feature allows for nondestructive measurements of the cell components as the testing progresses. This is particularly important to the determination of emitter deformation rates and the prediction of fueled emitter life.

Conclusion

Our thermionic reactor development program plan calls for a state of TFE technology readiness consistent with seven-year life, by October 1985. With that accomplished, thermionic reactor power systems with their low mass and volume radiators, high performance and multiply redundant energy conversion are the prime candidate not only for fulfilling the SP-100 requirements but also for multimegawatt class space power systems.

Acknowledgments

The work described herein was conducted under the sponsorship of the U.S. AEC, NASA and GA Technologies.

References

Chin, J. and C. W. Messick (1972) "Ceramic-to-Metal Seal Development for Thermionic Fuel Elements," in *Proceedings of the 1972 3rd International Conference of Thermionic Electrical Power Generation*, Vol. 2, pp. 681–692.

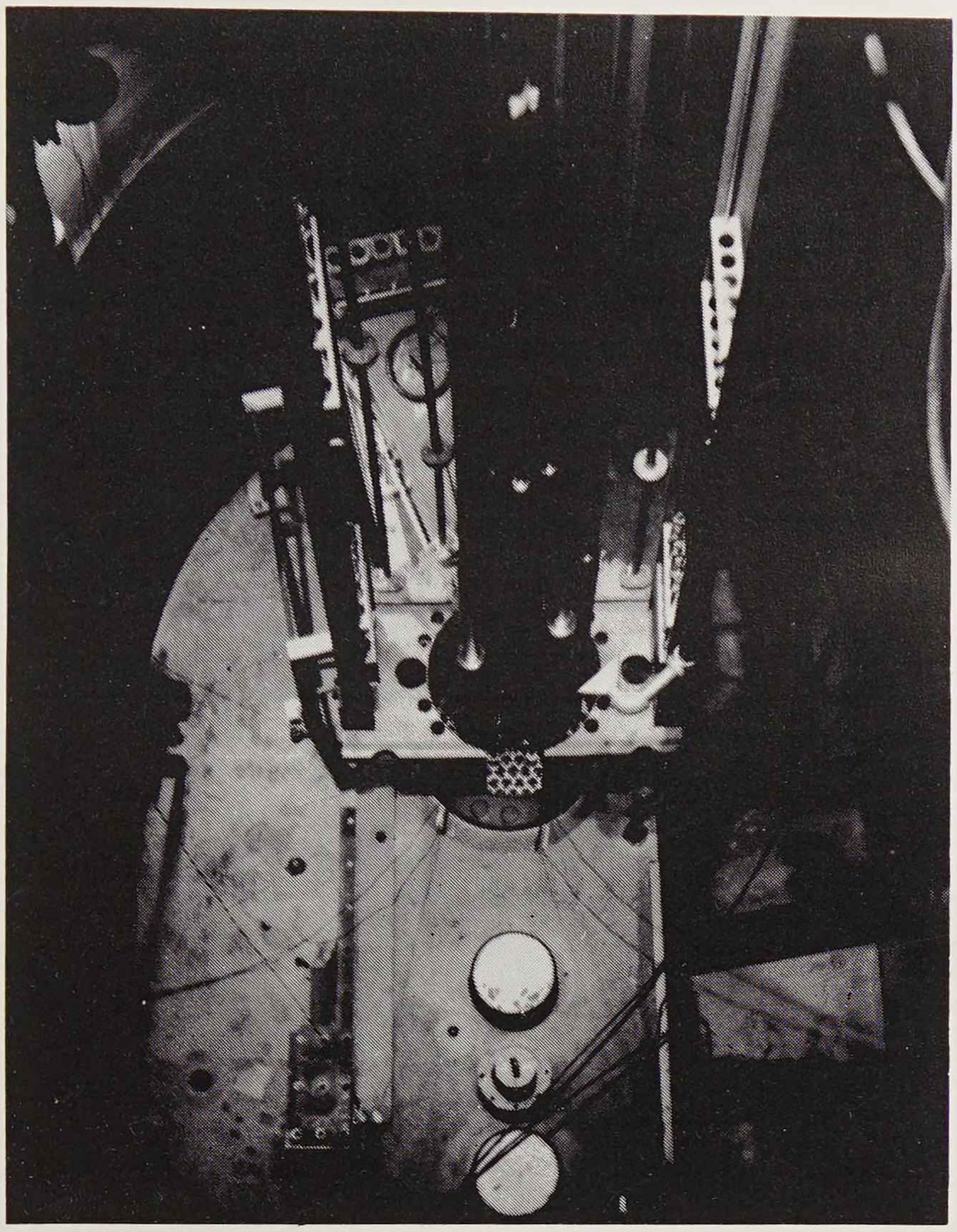
Chin, J. and C. W. Messick (1973) *Development of a Thermionic Reactor Space Power System, Final Summary Report*, USAEC Report Gulf-GA-A12608, pp. 2–26–28, June 30, 1973.

Clinard, F. W., Jr. (1979) "Ceramics for Applications in Fusion System," *J. Nucl. Mat. 85*, and *86*: 393–404.

Clinard, F. W., Jr. and C. F. Hurley (1981) "Ceramic and Organic Insulators for Fusion Applications," *J. Nucl. Mat., 103*, and *104*: 705–716.

Fitzpatrick, G. O., M. K. Yates, and D. Schwarzer (1973) *Development of a Thermionic Reactor Space Power System, Final Summary Report*, USAEC Report Gulf-GA-A12608, pp. 3–33–62, June 30, 1973.

Gulden, T. D. and J. F. Watson (1982) *High-Temperature Fuels for*



- ALLOWS TESTING OF 10–15 TFEs SIMULTANEOUSLY
- SIMULATES TFE REACTOR FAST NEUTRON FLUENCE
- CONTINUOUS INSTRUMENTED ON-LINE, REAL TIME TESTING
- ALLOWS NEUTRON RADIOGRAPHY OF TFEs
- HOT CELL FACILITIES ADJACENT TO TITR
- VERY ECONOMICAL $1M/YR FOR FACILITY

Figure 17 *TRIGA (TITR) Test Facility for Cell and TFE Testing.*

Advanced Nuclear Systems, GA-A16908, GA Technologies, October 1982, pp. 21–29.

Holland, J. W. (1972) "Thermionic Fuel Element Development Status Summary," in *Proceedings of the 1972 3rd International Conference of Thermionic Electrical Power Generation*, Vol. 2, p. 469.

Horner, M. H., J. C. Grebetz, and J. Kay, Jr. (1972) "Multicell Thermionic Fuel Element Fabrication Technology," in *Proceedings of the 1972 3rd International Conference of Thermionic Electrical Power Generation*, Vol. 2, pp. 491–500.

Lieb, D., A. Donaker, and F. Rufeh (1969) "Performance of a Thermionic Converter with a Nominal Single-Crystal ⟨110⟩ Tungsten Emitter and a Niobium Collector," in *Proceedings of the 1969 IEEE Thermionic Conversion Specialists Conference*, Carmel, California, pp. 66–75.

Lieb, D. and F. Rufeh (1970) "Thermionic Performance of CVD Tungsten Emitters and Several Collectors," in *Proceedings of the 1970 IEEE Thermionic Conversion Specialists Conference*, Miami, Florida, pp. 471–479.

Ranken, W. A. (1972) *Quarterly Report on the Space Electric Power R and D Program for the Period Ending October 31, 1972*, LA-5113-PR, pp. 1–28, November 1972.

Ranken, W. A., T. G. Frank, and G. W. Keilholtz (1972) "Effect of Fast Neutron Irradiation on Alumina and Yttria," in *Proceedings of the 1972 3rd International Conference of Thermionic Electrical Power Generation*," Vol. 2, pp. 819–830.

Wiffen, F. W. (1971) "Radiation Damage to Refractory Metals as Related to Thermionic Applications," in *Proceedings of the 1971 IEEE Thermionic Conversion Specialists Conference*, San Diego, California, pp. 156–165.

Yang, L., et al. (1972) "Material Development for Thermionic Fuel-Cladding Systems," in *Proceedings of the 1972 3rd International Conference of Thermionic Electrical Power Generation*," Vol. 2, pp. 873–894.

Yang, L. and R. E. Bruce (1973) *Fabrication and Life Testing of Thermionic Converters*, GA-A12554, pp. 5–8, June 19, 1973.

Zimmermann, H. (1978) "Investigations on Swelling and Fission Gas Behavior in Uranium Dioxide," *J. Nucl. Mat. 75*: 154–161.

Space Nuclear Power Systems 1984
Edited by M. S. El-Genk and M. D. Hoover
© Orbit Book Company, Malabar, FL, 1985

Chapter 44

Static Conversion Systems

R. Ewell and J. Mondt

Jet Propulsion Laboratory / California Institute of Technology
4800 Oak Grove Drive
Pasadena, CA 91109

Historically, all space power systems that have actually flown in space have relied on static energy conversion technology. Thus, static conversion is being considered for space nuclear power systems as well. There are four potential static conversion technologies which should be considered. These include: the alkali metal thermoelectric converter (AMTEC), the thermionic converter, the thermoelectric converter, and the thermophotovoltaic converter (TPV). These four conversion technologies will be described in brief detail along with their current status and development needs. In addition, the systems implications of using each of these conversion technologies with a space nuclear reactor power system will be evaluated and some comparisons made.

Introduction

Static conversion is of primary interest to space nuclear power systems because no dynamic conversion systems have any space experience. Static conversion systems have proven to be highly reliable and capable of long life. The inherent modularity of static converters allows for the development of a single small module that may be used to build up to whatever power level is desired, with whatever redundancy is needed.

The four potential static conversion technologies which should be considered for space nuclear power systems are the alkali metal thermoelectric converter (AMTEC), the thermionic converter, the thermoelectric converter, and the thermophotovoltaic converter (TPV). These four conversion technologies will be described and their current status discussed. In addition, some of the development needs for these technologies will be evaluated. Finally, how these four conversion technologies compare for use in a space nuclear power system will be discussed.

Alkali Metal Thermoelectric Converter

AMTEC is a thermally regenerative electrochemical device based on the unique properties of β''-alumina solid electrolyte. This material has ionic conductivities much larger than its electronic conductivity and can thus act as a permselective barrier in an electrochemical device. As depicted in the schematic of Figure 1, the β''-alumina separates a high temperature liquid sodium reservoir from a low pressure sodium vapor region. Sodium is the preferred working fluid because it results in the highest ionic conductivities and has the most appropriate temperature range. The sodium pressure differential across the β''-alumina gives rise to a concentration gradient with resultant diffusion of sodium ions in the solid toward the low pressure surface. This creates a voltage differential across the β''-alumina, as the ionic sodium conduction occurs. On the low pressure side of the β''-alumina is a porous electrode. Electrical leads make contact with the porous electrode and the liquid sodium reservoir to complete the circuit. When the external circuit is closed, electrons flow through the load, from the liquid sodium reservoir to the porous electrode, to neutralize the sodium ions. The sodium atoms then absorb their heat of vaporization, leave the electrode, move through the vapor space and release their heat of condensation on the condenser surface. The cooled liquid is collected from the condenser and pumped to the high temperature liquid reservoir where it is heated; the cycle is, then, repeated.

Although research on AMTEC has been ongoing for the last twenty years, because it has so far only had a very low level of effort, it is one of the least developed conversion technologies considered for space nuclear power. However, the potential for high efficiency operation has been demonstrated in the laboratory. A self-contained recirculating device had a measured thermal to electric conversion efficiency of 19% for a hot side temperature of 1073 K and a cold side temperature of 473 K, (Hunt, Weber, and Cole 1981).

The major parameters which effect conversion performance are the hot and cold side temperatures and surface emissivities as well as the β''-alumina thickness and electrode performance. As the hot side temperature increases so does the potential electrical power density. However, the maximum operating temperature of an

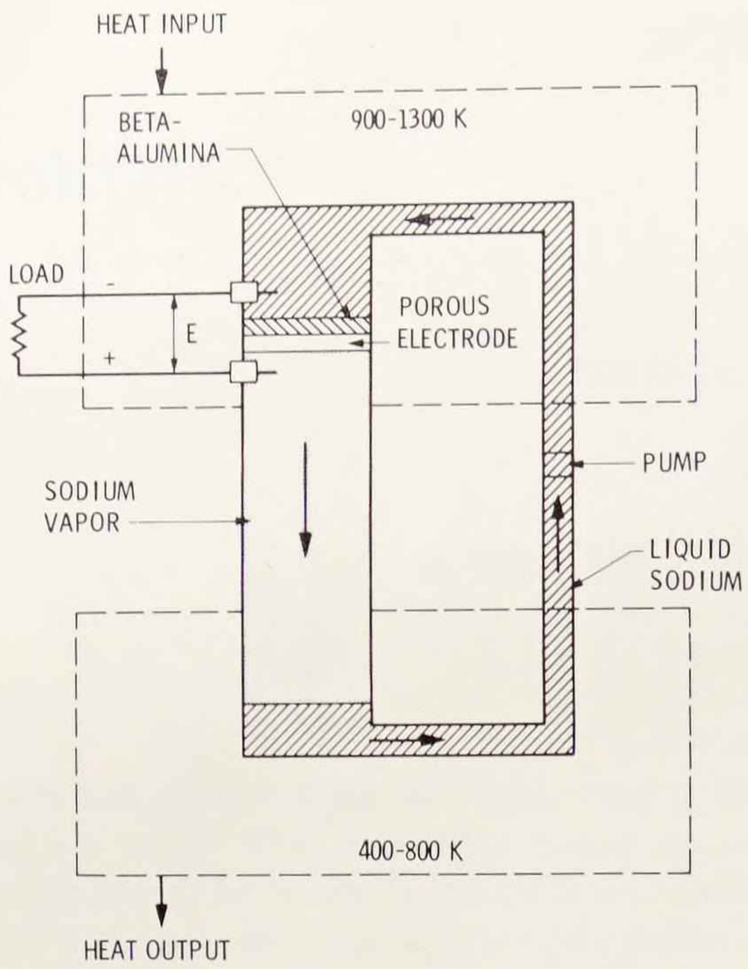


Figure 1 *AMTEC Schematic.*

AMTEC device is limited to about 1350 K because of the strength of the β''-alumina. The β''-alumina needs to be kept thin, to maximize performance, but as temperature increases the strength of the β''-alumina decreases and the sodium pressure increases. Also, as the hot side temperature increases, so do thermal radiation losses from the electrode to the condenser. Thus, the emissivities of the porous electrode and the condenser are very important.

On the condenser side, because liquid sodium is highly reflective, if a thin uniform layer of liquid sodium could be maintained, then the radiation losses could be kept small. However, because of the need to operate in the zero gravity environment of space it will be necessary to utilize capillary forces to collect the sodium. This will require holes or slots in the condenser surface leading to increases in the surface emissivity and thus higher radiation losses. The other alternative is to develop radiation shields; however these must not seriously impede the flow of the sodium vapor. Because the β''-alumina requires a pressure differential across it for operation, as the vapor pressure increases, the performance decreases. Also, since the sodium vapor pressure increases exponentially with temperature, the conversion efficiency is almost independent of condenser temperature up to about 600 K. However, as condenser temperature increases above 700 K, the efficiency decreases quite rapidly. Finally, the performance improves with decreasing β''-alumina thickness because of the decrease in its resistance. The porous electrode performance is also important because it must have low electrical sheet resistance as well as very low resistance to the flow of sodium.

Several key technologies need to be developed before an efficient, long life AMTEC converter will be ready for use in space. The most critical of these is developing an electrode capable of operating at high temperatures and power densities for seven to ten years of continuous operation. Currently, when the device is operated continuously, the porosity of the electrode decreases, by what appears to be a sintering process, resulting in decreased output power. The maximum demonstrated high power lifetime has been less than 1000 hours. Also, a condenser must be designed which will operate in zero gravity to allow recirculation of the liquid sodium. This condenser needs to be highly reflective to minimize parasitic thermal radiation losses, or an effective thermal radiation shield which does not significantly impede the vapor flow must be developed. In addition to the above technologies, a light-weight reliable means of fabricating the device and bonding materials together that will assure hermeticity for the sodium for up to ten years must be developed.

Thermionic Conversion

A thermionic converter is a static device which converts thermal power into electricity through the surface emission of electrons. As shown in Figure 2, it is composed of an emitter or cathode which at one surface receives heat from the reactor and emits electrons from the other, and a collector or anode which collects the electrons and is cooled to a lower temperature than the emitter to limit the back emission of electrons. Electrical leads are then added to utilize the electrical power which is generated.

The rate of electron emission from a hot metal surface is a function of both the metal temperature and the electrostatic energy barrier, work function, at the metal surface that the leaving electrons have to overcome. The kinetic energy of the electrons within the bulk metal increases with increasing temperature allowing a higher fraction of them to escape from the metal surface. The work function measures the energy barrier, or difference, between the minimum internal energy which must be possessed by a leaving electron and the Fermi energy level.

The flow of free electrons from the emitter surface is inhibited by previously emitted electrons which form a cloud of negative charges near the surface. This is called the space charge effect, which acts against the electron flow. To reduce this effect either the interelectrode spacing may be reduced or the gap can be filled with a plasma so that the negative space charge can be neutralized by positive ions. In order to utilize the first method, very small spacing ($\sim$10 μm) is needed, which makes the device impractical to fabricate and its current density will be too low for a space power system. Therefore, most converters rely on the use of an easily ionizable vapor to neutralize the space charge.

Cesium is the most commonly used vapor because it has the lowest ionization potential. In addition, the

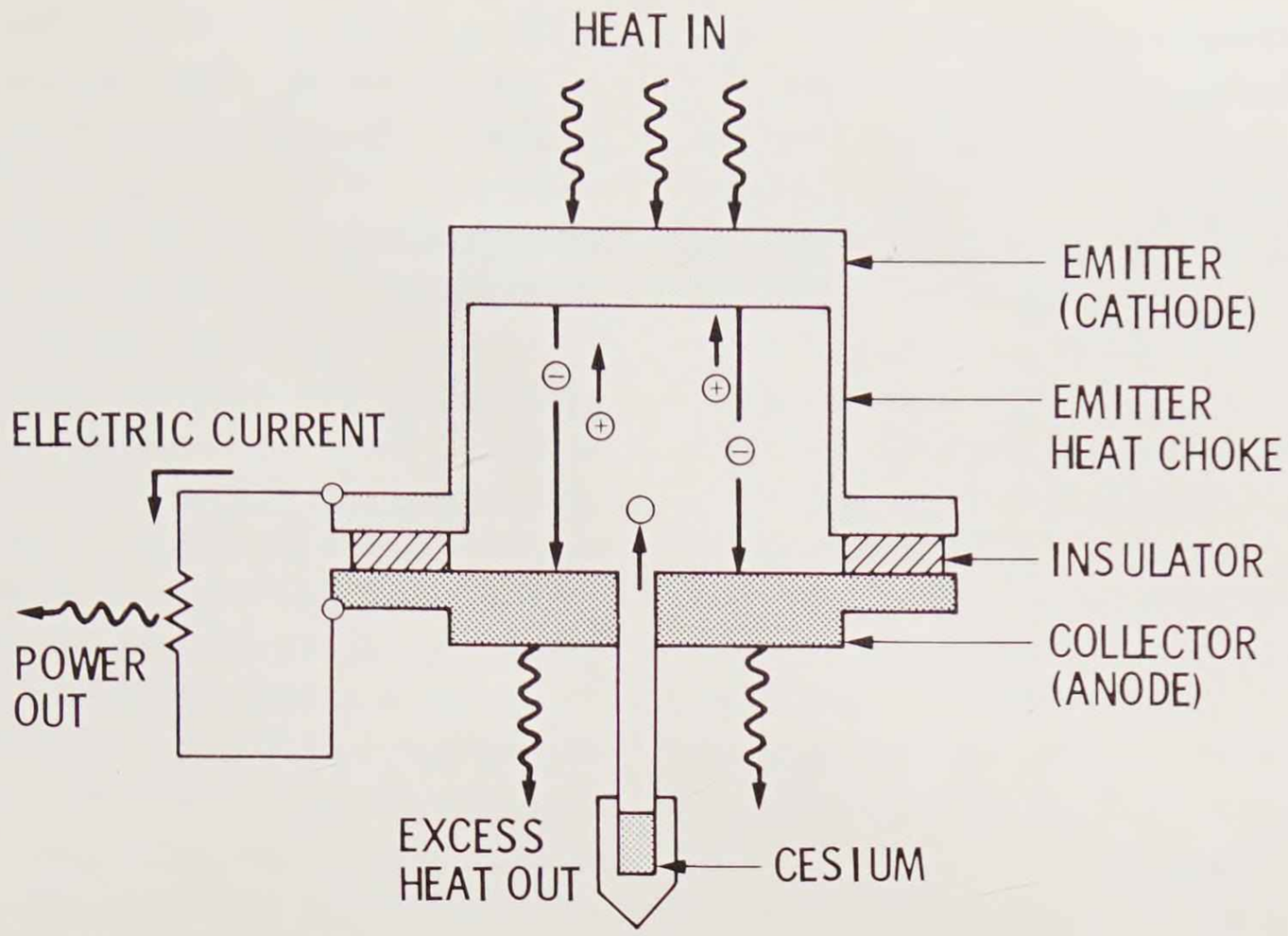


Figure 2 *Thermionic Converter Schematic.*

absorption of cesium atoms has been found to considerably reduce the surface work function of the electrodes down to a level even lower than liquid cesium or any pure metal. Furthermore, atoms evaporating from the emitter surface will primarily be cesium atoms which are continuously being replenished; consequently there is minimal depletion of the emitter material. However, for high power density converters, it is necessary for the cesium vapor pressure to be relatively high, such that the electron mean free path will be small relative to the interelectrode spacing. This results in volume ionization of the cesium as a result of the energetic collisions between the emitted electrons and the cesium atoms. This results in a voltage drop, arc drop, across the interelectrode gap because of the electronic scattering effects induced by the cesium vapor addition. Also, there is a current attenuation because some of the electron current is scattered back into the emitter.

Practical plasma thermionic converters were demonstrated during the late fifties and sixties. The longest converter life test was on a cylindrical converter with an emitter temperature of 1970 K. The converter stably operated in the laboratory with an electrode efficiency of 17% and generated 8 watt/cm^2 for a period of over five years without failure (Britt 1981). However, for space nuclear power, the most appropriate method of using thermionic converters is within the core of the nuclear reactor. In-core thermionic converters were demonstrated during the thermionic reactor space power program of the 1960s. But, all converters which have run inside the reactor core have failed within about a 2-year operating lifetime. The primary failure mechanisms for thermionic converters are electrode distortion which causes a short circuit of the electrodes or envelope leaks which result in cesium loss.

To utilize thermionic converters for space nuclear power, the key technology development is to find a way to increase converter lifetime. This will require a better understanding of fuel swelling and fuel-clad interaction; because for in-core thermionics, the fuel clad is the thermionic emitter. Ideally, the lifetime should be improved with only a minimal impact on performance and mass. Also, it will be necessary to verify the performance of the ceramic electrical insulators which are needed. These must be shown capable of stable, long life operation under the high temperatures, voltage, and nuclear radiation levels that they will be subjected to. These insulators may limit the number of converters which can be connected in series and thus limit the line voltage out of the reactor.

Thermoelectric Conversion

Thermoelectric converters are a solid-state type of direct energy converter. The active materials in a thermoelectric device consist of specially doped semiconductors. A thermoelectric couple has two semiconductor elements; one doped to act as a *p*-type material, and the other doped to function as an *n*-type. Figure 3 portrays a sketch of a unicouple which is the simplest configuration for producing electrical power. In this configuration the hot shoe serves a dual purpose, it receives and concentrates the heat and acts as the hot junction electrode. By removing heat from the cold shoe, a temperature gradient is set up along both the *n* and *p* legs of the couple. This temperature gradient drives the charge carriers in the thermoelectric elements toward the cold end because of the differences in kinetic energy of carriers. Thus, a voltage difference is obtained across the two cold shoes; and if an electrical

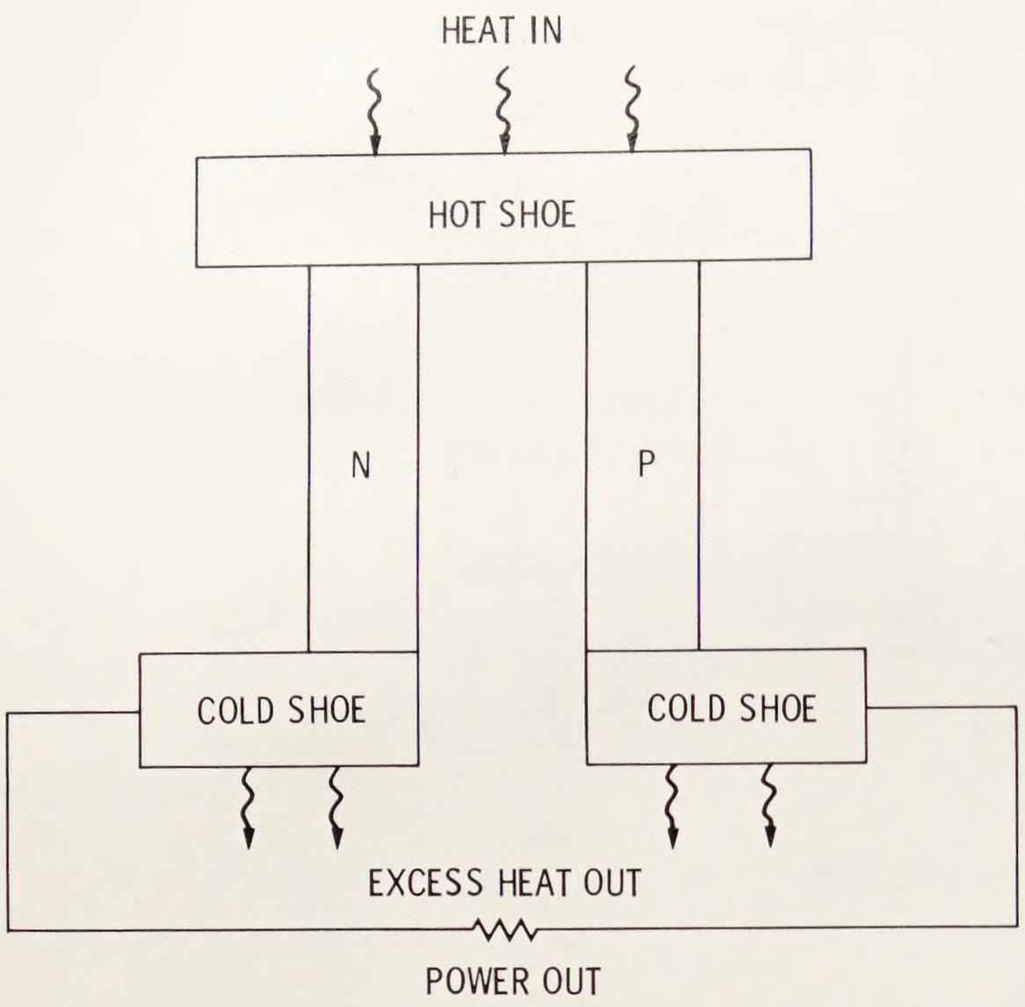


Figure 3 *Thermoelectric Converter Schematic.*

lead connects them together, a current will be driven across a load producing useful work.

Efficient conversion of heat to electricity requires an active thermoelectric material with high values of Seebeck coefficient and electrical conductivity and a low value of thermal conductivity. The temperature difference across the thermocouple, established as a result of heat conduction, sets up voltages across the thermoelectric elements proportional to the Seebeck coefficient, α; thus a high value of Seebeck coefficient is needed. This voltage difference induces a current flow through the thermoelements; therefore to minimize the resistance to the current flow, the electrical conductivity, σ, of the thermoelectric material should be high. Finally, in order to minimize the heat conducted down the thermoelements, the thermal conductivity, k, should be low. These three parameters are combined to form a thermoelectric Figure of Merit, $Z = \alpha^2\sigma/k$, which should be maximized to obtain the highest conversion efficiency.

Thermoelectric conversion has considerable space flight experience through its use in radioisotope thermoelectric generators (RTGs). They were used to provide the electrical power in the recent Voyager flights to the outer planets. Thermoelectric conversion is well characterized and has proven itself to be reliable for continuous operation up to ten years in duration. The thermoelectric conversion efficiency of the silicon-germanium thermocouples used in the Voyager RTGs, which have currently been operating without failure for seven years, was 7%. The limits on thermoelectric conversion efficiency involve the material Figure of Merit and the maximum allowable hot side temperature. Currently, an alloy of silicon and germanium is the best thermoelectric material with flight experience. It has a maximum ten year lifetime operating temperature of 1280 K with an average Figure of Merit of $0.7 \times 10^{-3}K^{-1}$. The hot side temperature is limited by sublimation of the thermoelectric material over its operating lifetime.

The principal area of thermoelectric development is to improve the thermoelectric material Figure of Merit. There are two ongoing development programs trying to accomplish this improvement. The first is trying to improve the performance of standard silicon-germanium through the addition of a ternary, such as gallium-phosphide, to decrease the thermal conductivity. The second approach is to develop an all new refractory thermoelectric material. Currently, two classes of materials are being investigated, the boron compounds and the rare-earth chalcogenides. Both of these are capable of operation at temperatures in excess of 1500 K and have the potential for high figures of merit. The other technology development area will be to construct light weight thermocouples which have an all bonded configuration and are more amenable to mass production.

Thermophotovoltaic Conversion

The TPV converter consists of a photovoltaic cell which faces an incandescent radiator, receives electromagnetic radiation from it, and converts this radiation into electricity. A schematic diagram of such a converter is shown in Figure 4. The efficiency of any photocell is dependent upon the wavelength of the incident light. The conversion of light to electricity occurs through the internal photoelectric effect. An incoming photon is most effective if it has just enough

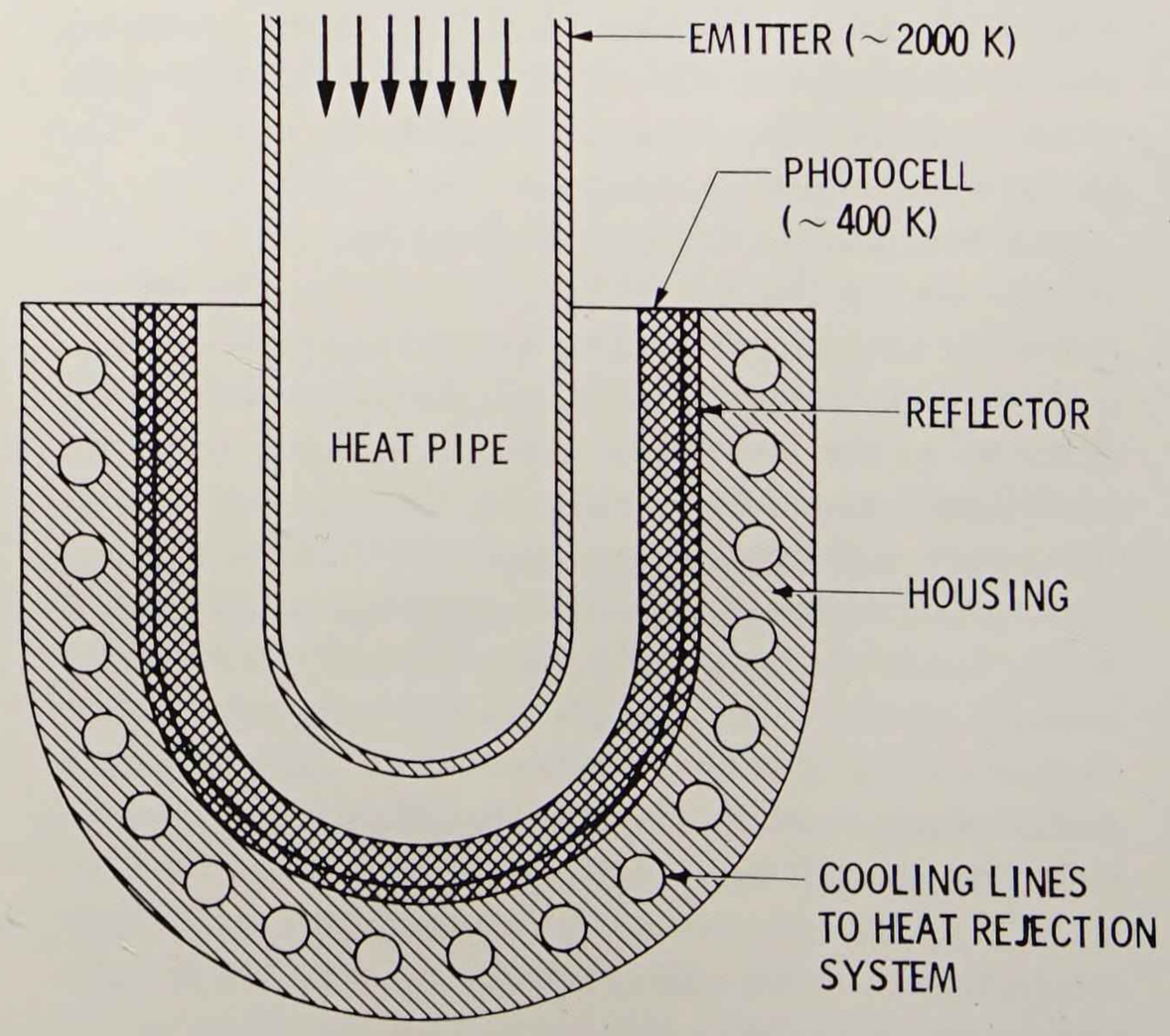


Figure 4 *Thermophotovoltaic Converter Schematic.*

energy to release an electron from its bond in the material crystal lattice. If the light is of longer wavelength, the photons do not have enough energy and it is not used at all. If the wavelength of the light is shorter than required, the photons have more energy than necessary, and only part of the energy is used; consequently the conversion efficiency is reduced.

The concept for thermophotovoltaic conversion is to obtain a better match between the incoming radiation wavelength with the requirements of the photocell. For the case of silicon, the optimum wavelength is about 1 μm. Light from the sun primarily consists of shorter wavelengths. However, light from an incandescant emitter operating near 2000 K shifts the incident spectrum to longer wavelengths. The energy wasted by light with shorter than optimum wavelengths is greatly reduced. However, now more of the light has a wavelength greater than 1 μm and is incapable of exciting the electrons. This energy will not be lost, however, if a reflector is placed at the backside of the photocell to return it to the emitter where it can be reabsorbed and help maintain the high emitter temperature. Furthermore, it may be possible to increase the performance further through the use of spectrally selective coatings. The emitter may be coated with a material that selectively emits in the region of the optimum wavelength. Also, it may be possible to develop coatings, for the front surface of the photocell; these would reflect the incoming light to the emitter except in the region of optimum wavelength.

Thermophotovoltaic conversion was initially pursued during the 1960s, but so far only minimal development has occurred. Some work has proceeded in the development of emitters that emit energy over a narrow frequency range. Also, the concept has been demonstrated in the laboratory. Conversion efficiencies of 30% have been obtained using silicon photocells with emitter temperatures of 2200 K to 2400 K (Swanson 1979). These efficiencies were obtained after modifications had been made to the silicon cells to reduce the parasitic absorptance. Parasitic absorption is any mechanism where the incident light is absorbed in the TPV cell other than by producing electron-hole pairs. It has been reduced by using high purity silicon, and by making improvements in the backside mirror so that less contact absorptance occurs and finally, by developing an all backside contact TPV cell. In addition to the high efficiencies which have been obtained, relatively large power densities of about 5 watts/cm^2 have been obtained. This results from the fact that the incoming radiation density from an enclosed incandescent source is about 1000 times that of the sun. This means that larger back-currents in the cell can be tolerated than for solar cells and thus that a TPV cell can operate at higher temperatures.

In order to make thermophotovoltaics feasible for a nuclear space power system a key development must be finding high temperature materials which have reasonable nuclear radiation hardness. Silicon cells are limited to a maximum operating temperature of about 450 K before reactions with the contacts start to occur. But, it appears that either gallium-arsenide or indium-phosphide cells could be developed which would be capable of higher temperature operation. These materials also have an additional benefit of having a direct band gap and thus allow for the possibility of better TPV cell optimization. However even for these materials, it appears that their operation would be limited to about 500 or 600 K because of back current limitations. Also, there is the question of lifetime in a high nuclear radiation environment which must be better answered for these materials. Finally, there is the question of materials for the heat source and emitter which must operate at quite high temperatures (~2000 K).

Systems Comparison

The requirements for a space power system differ considerably from those for a terrestrial power plant. For a terrestrial power plant cost is of primary importance; thus it is necessary to maximize the conversion efficiency. However, for a space power system, typically, the most important parameter is specific power. It is desirable to obtain the most electric power for the lowest mass. Also, there are often volume and area constraints because the system must be put into space by a launch vehicle which has a limited volume. Since for large space power systems, the radiator must be kept small; high heat rejection temperatures are required. Finally, system lifetime and reliability need to be kept as high as possible.

AMTEC has good potential for use in a space nuclear power system. It is capable of conversion efficiencies of 15 to 20% with radiator temperatures as high as 700 to 800 K. Furthermore, these high efficiencies are obtained with reasonable hot side temperatures of 1300 K or less. AMTEC, like all the other static converters, is modular and thus many devices may be built up in a series/parallel network to increase its reliability. However, an AMTEC converter must be hermetically sealed in order to retain the recirculating sodium throughout its operating lifetime. This, in conjunction with electrode lifetime problems, will require a lot more development work in order to verify the lifetime and reliability of the AMTEC converter.

The thermionic converter is capable of efficient operation with the highest radiator temperature of any of the converters. It does require very high hot side temperatures; but because of its ability to be used inside the reactor core, these may be reliably obtained. However, because the converters are part of the nuclear reactor, it does limit the flexibility in development and limits the use of alternate technologies. Although in-core thermionic converters have been demonstrated,

much additional development is needed to extend their operating lifetime beyond three years.

Although the thermoelectric converter has only moderate efficiencies it has the most flexible operating temperatures. Unlike the other three static converters, its efficiency is an almost constant fraction of Carnot efficiency and depends only on the material Figure of Merit. It is an entirely solid state energy converter which is radiation hard. Thermoelectric converters have the highest proven lifetime and reliability of any of the converter technologies.

The thermophotovoltaic converter, although capable of the highest conversion efficiency of any static conversion device, has the most severe temperature requirements. It needs the highest hot side temperature, but is not capable of operating within the reactor core; in fact it may degrade rapidly in a high radiation environment. Furthermore, it requires the lowest radiator temperature for reasonable performance. The cell temperature needs to be kept below about 600 K to limit back currents to acceptable values. Also, the TPV converter still requires considerable development to prove its lifetime and reliability.

Since, for most space power systems, the hot side temperature will be run as high as is technically feasible, it may be considered fixed; then the radiator temperature can be optimized to obtain the best system performance. For large power systems, the mass of the radiator becomes a significant fraction of the total system; thus it is important to know how the area varies with temperature. Figure 5 shows a comparison of the radiator area requirements for each of the four different converter technologies. The data are presented in the form of the electric power available per unit radiator area as a function of radiator temperature. Each of the conversion technologies was assumed to be a near term improvement over what is currently available. As would be expected, the thermionic converter yields the smallest radiator even with the emitter temperature kept down to 1600 K. The AMTEC and thermoelectric converters have similar radiator requirements. Both are capable of delivering 100 kilowatts of electrical power using a 50 square meter radiator, but the AMTEC does this with a 300 K lower radiator temperature. Finally, the TPV converter requires a radiator nearly five times larger than any of the other converters.

In addition to evaluating radiator size, an attempt was made to compare total system masses as a function of electrical power production, using a simple computer code developed at JPL. It considered that the system had seven components: the nuclear reactor, radiation shield, heat transport, conversion subsystem, primary radiator, power conditioning and control, and the conditioning radiator. Since for a given technology level the hot side temperature was considered fixed, the only parameter optimized was the radiator temperature. The power systems were optimized to obtain the highest electrical power per unit mass.

Figure 6 compares the AMTEC, thermionic, and thermoelectric converters. The TPV converter was not further considered because of the large radiator requirements, as well as the high temperatures which would be needed. It is obvious, from the simple model that was used, that all three conversion technologies are capable of producing 100 kilowatts for 3000 kilograms. Also, although only out-of-core thermionic converters were considered in the mass model, because of a lack of in-core reactor mass data, it is evident that they may be capable of even lower system mass.

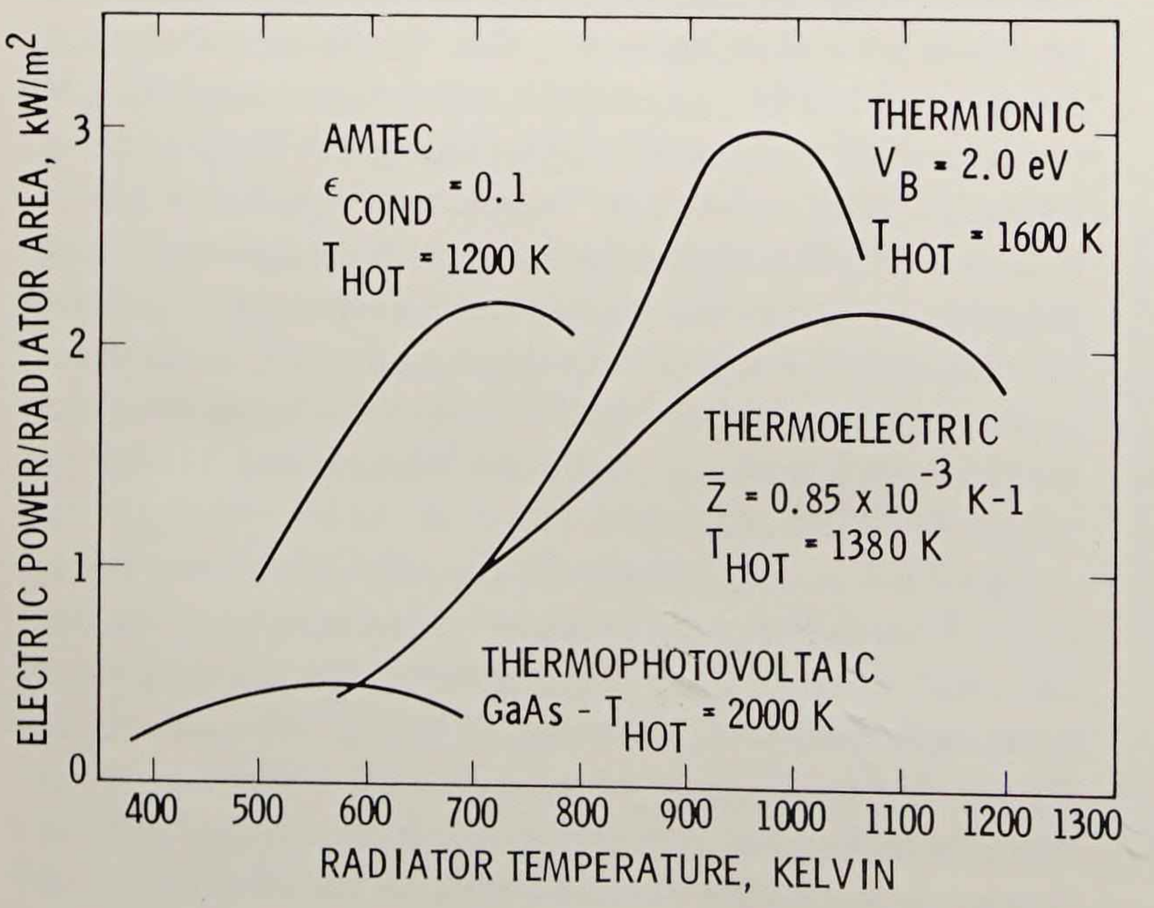


Figure 5 *Radiator Area Comparison.*

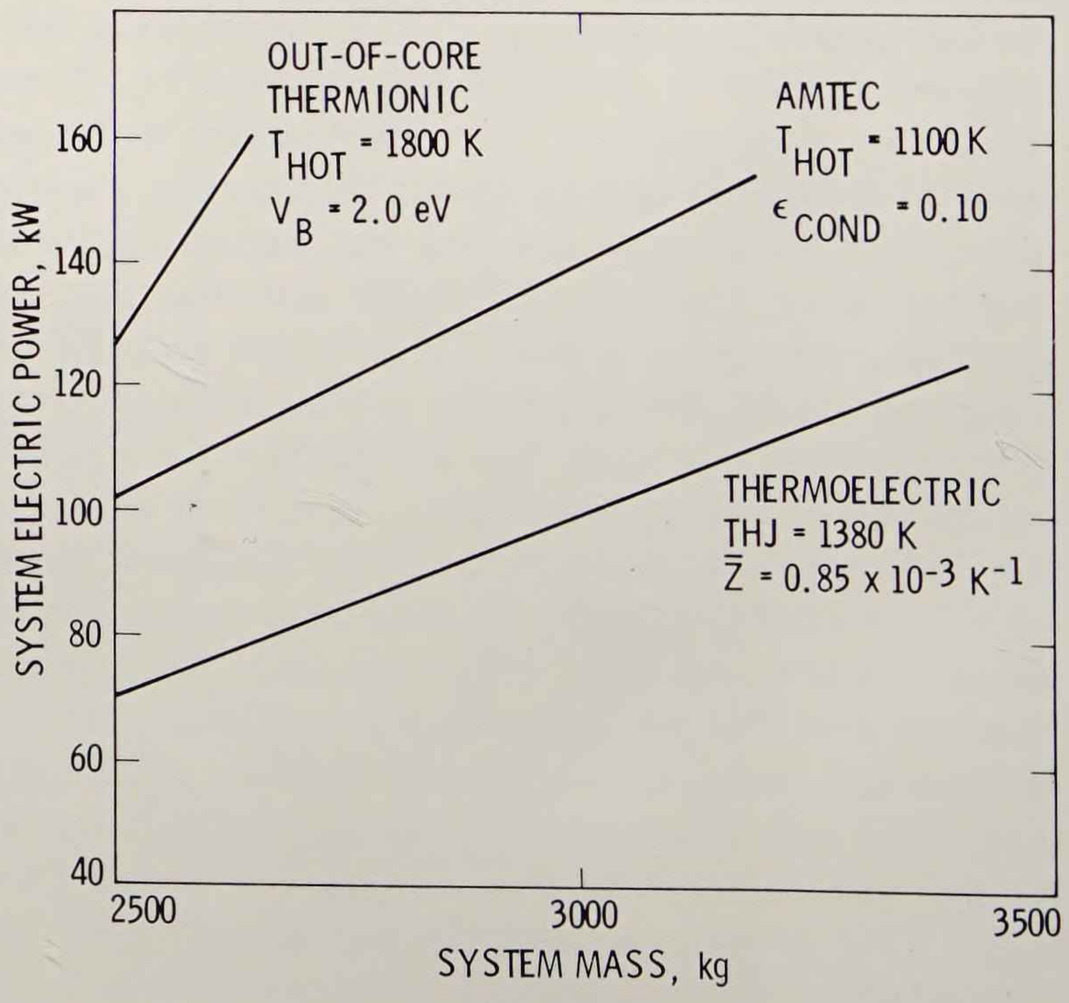


Figure 6 *System Mass Comparison.*

Conclusion

Thermophotovoltaic conversion will result in the least acceptable nuclear space power system because of its need for a very high temperature heat input and its requirement for a large low temperature radiator. The thermionic converter, particularly if it is used inside the nuclear reactor core, will have the smallest radiator and will have the potential to be lightweight. However, considerable development will be required to extend converter lifetime to seven years. The AMTEC converter also shows considerable potential for use in a space nuclear power system. Good performance can be obtained with hot side temperatures in the range of 1100 to 1200 K. However, AMTEC, even more so than the thermionic converter, will require considerable research to assure a reliable converter capable of a long lifetime. Finally, thermoelectric converters not only yield acceptable performance and reasonable radiator sizes for 100 kWe; but are also the only conversion technology which has been proven capable of reliable long life operation.

Acknowledgments

The work described in this paper was carried out by the Jet Propulsion Laboratory, California Institute of Technology, under contract with the National Aeronautics and Space Administration.

References

Britt, E. J. and G. O. Fitzpatrick (1981) *Direct Conversion Nuclear Reactor Space Power Systems*, Report Number AFWAL-TR-82-2073, Vol. I.

Hunt, T. K., N. Weber, and T. Cole (1981) "High Efficiency Thermoelectric Conversion with Beta-Alumina Solid Electrolytes, The Sodium Heat Engine", in *Fast Ionic Transport in Solids*, edited by J. B. Bates and G. C. Farrington, North-Holland Publishing Co., Amsterdam, pages 263–266.

Swanson, R. M. (1979) *Silicon Photovoltaic Cells in TPV Conversion*, Report ER-1272, Research Project 790-2.

Space Nuclear Power Systems 1984
Edited by M. S. El-Genk and M. D. Hoover
© Orbit Book Company, Malabar, FL, 1985

Chapter 45

Alkali Metal Thermoelectric Conversion (AMTEC) for Space Nuclear Power Systems

C. P. Bankston, T. Cole, S. K. Khanna, and A. P. Thakoor

Jet Propulsion Laboratory
California Institute of Technology
Pasadena, CA 91109

The Alkali Metal Thermoelectric Converter (AMTEC) can be a potential direct energy conversion technology for a space nuclear power system. In the laboratory, conversion efficiencies of up to 19% have been demonstrated, and the AMTEC's temperature range of operation makes it compatible with space nuclear power sources. AMTEC performance parameters for a 100 kW electric power system have been calculated at four technological levels. The results project that three AMTEC technological levels can provide a less than 3000 kg system with a radiator area less than 70 m^2. Two of these levels would operate between 1000 K and 1100 K converter temperature and approximately 700 K radiator temperature at 11–12% efficiency. The most advanced level considered would operate between 1180 K and 711 K at 16% efficiency and would weigh 1850 kg with a radiator area of 43 m^2. The status of AMTEC experimental electrode research is also discussed. Molybdenum-titanium alloy electrodes have not shown improvement in lifetime characteristics over state-of-the-art pure Mo electrodes. However, oxygen treatment of a degraded Mo electrode has resulted in restoration of specific power output to 90% of its beginning-of-life specific power; and maintained this level for 60 hours. Evidence is also presented that the dominant sodium transport mechanism in the porous electrode is not vapor flow, but possibly surface diffusion. The experimental progress reported, especially the potential shown for oxidized molybdenum electrodes, and the projected performance of a 100 kW space nuclear power system warrant continued AMTEC research and development.

Introduction

The Alkali Metal Thermoelectric Converter (AMTEC) is a thermally regenerative electrochemical device for high efficiency, direct thermal to electrical energy conversion (Weber 1974 and Cole 1983). Its operation derives from the unique sodium ion conducting properties of beta″-alumina solid electrolyte (BASE) (Kummer 1972). Experimental results have shown that the AMTEC possesses conversion efficiencies much higher than other direct thermoelectric devices. An efficiency of 19% (Hunt et al. 1981) and a power density of 1 W/cm^2 (Hunt et al. 1978) have been demonstrated in laboratory devices, while calculations indicate that a 25–30% conversion efficiency may be achieved with an optimized design (Hunt et al. 1978). Further, the AMTEC has no moving mechanical parts and its hot side temperature (900–1300 K) makes it compatible with either the General Purpose Heat Source (GPHS) (Shock 1980) or the projected SP-100 nuclear space power reactor (Buden et al. 1983). For these reasons, the AMTEC has been studied at the Jet Propulsion Laboratory for several space power applications.

The operating cycle of the AMTEC is illustrated in Figure 1. A closed vessel is divided into a high-temperature/pressure region in contact with a heat source and a low-temperature/pressure region in contact with a heat sink. These regions are separated by a barrier of BASE which has an ionic conductivity much larger than its electronic conductivity. The high-temperature/pressure region contains liquid sodium at T_2, and the low-pressure region contains mostly sodium vapor and a small amount of liquid sodium at T_1. Electrical leads make contact with a (positive) porous electrode which covers the low pressure surface of the BASE and with the high temperature liquid sodium (negative electrode). When the circuit is closed, sodium ions are conducted through the BASE due to the difference in vapor pressures (or chemical activity) across the BASE, while electrons flow to the porous electrode surface through the load producing electrical work. The unique feature of the AMTEC cycle is that sodium vapor is expanded nearly isothermally through the BASE causing the sodium atoms to separate into sodium ions and electrons. The AMTEC thus converts the work of isothermal expansion of sodium vapor directly to electric power. A return line and an electromagnetic pump circulate the sodium working fluid through the AMTEC. More details on the AMTEC cycle may be found in Weber (1974), Cole (1983) and Hunt et al. (1978).

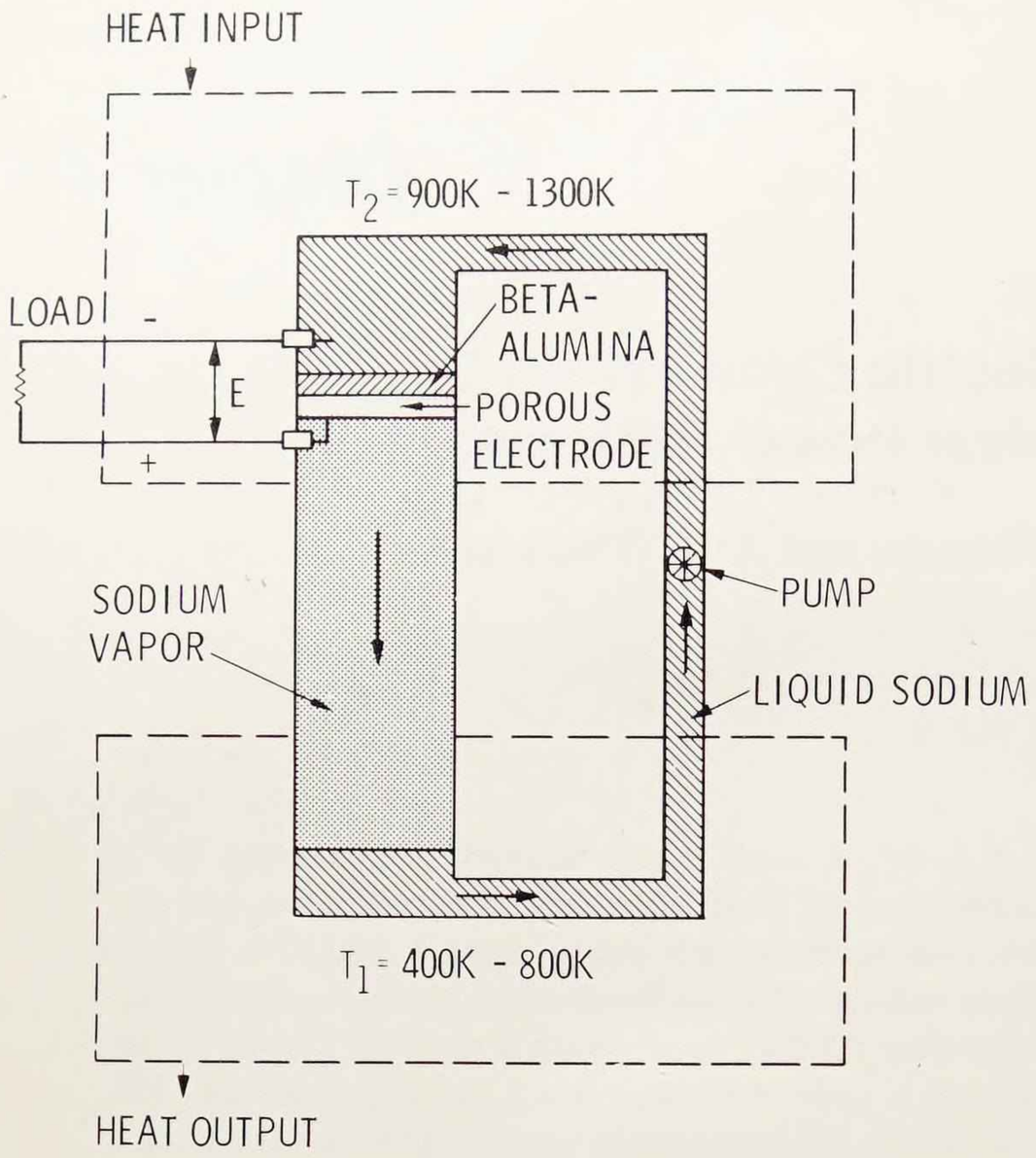


Figure 1 *AMTEC Device Schematic.*

Work on the AMTEC concept has to date been focused on the development of a long life, high power porous electrode. State-of-the-art electrodes are now composed of either magnetron sputter deposited molybdenum 1–3 μm thick or a bi-conductor cermet composed of a mixture of molybdenum and BASE powders. In the thin film molybdenum electrode, power densities are initially high (near theoretical), but the power output decays by a factor of 3–5 in the first 1000 hours of operation. Power output usually remains stable thereafter. For the cermet electrode power densities are very low initially, but can be stable for up to approximately 10,000 hours (Hunt 1983). Present research is directed toward maintaining the initial high output of molybdenum thin film electrodes and improving the initial power density of the bi-conductor cermet electrode.

Applications and design studies of the AMTEC have been quite limited. Subramanian and Hunt (1982 and 1983) have studied solar energy conversion to electricity using the AMTEC at the focus of a tracking parabolic dish. They found the weight and cost of an (~20 kW) AMTEC system to be significantly less than those for heat engines or other generators being considered for terrestrial solar-to-electric conversion. Predicted efficiencies are near 30% in the AMTEC converter-receiver system and near 40% when a bottoming cycle was added. This may also have implications for spacecraft utilization. However, using the AMTEC for space power generally requires a radioisotope or reactor heat source. In this regard, two studies have been conducted. Bankston et al. (1983) have projected the performance of a small power system (900 W) similar to the design of the state-of-the-art radioisotope thermoelectric generator (RTG) (Cockfield et al. 1980). This concept used the AMTEC as a replacement for the Si–Ge thermocouples and the results showed a potential improvement in performance by a factor of 3 to 5 in specific power. That study also briefly considered a larger, reactor-powered AMTEC system with similar projections of high specific power. Ewell (1983) extended these projections for AMTEC to a one megawatt electric system for comparison with other conventional and advanced conversion systems. He found that the AMTEC is very competitive with other concepts (thermoelectrics, thermionics, Brayton, Rankine and Stirling), while requiring the lowest hot side temperature of the conversion devices considered.

The results reported in this paper are divided into two parts. First, attention is directed toward system objectives established by the SP-100 project to develop a 100 kW space nuclear electric power system. AMTEC performance parameters for such a system have been calculated based on previously used design strategies (Bankston et al. 1983). The major operating characteristics of a 100 kW electric AMTEC system have been determined and are reported for various technological levels assuming a heat pipe cooled nuclear reactor heat source (Buden et al. 1983). Second, recent experimental findings are presented and the status of the technology is discussed. The accumulated data indicate significant potential for AMTEC in space utilization.

100 kW Electric Nuclear Power System

The present study has taken a more detailed look at specific AMTEC technological levels that meet SP-100 power and mass requirements. Converter and radiator masses are taken from the earlier study by Bankston et al. (1983) which looked at only one technological level and a much larger power output. Since power output and parasitic thermal losses both scale with the area of the BASE, the size and mass of an AMTEC system can be readily scaled according to power requirements. The overall geometry of the AMTEC system concept is shown in Figure 2. The UO_2 fueled reactor (Buden et al. 1983) is cooled by 120 lithium heat pipes which deliver their energy to AMTEC converters. The AMTEC cells are mounted on the molybdenum hot shoe cone radiatively coupled to the heat pipes emerging from the reactor core and shield. Details of the fabrication and connection of individual cells are given by Bankston et al. (1983). The inner surface of the surrounding radiator also acts as the sodium condenser.

Operating parameters and system performance are based on AMTEC voltage vs. current characteristics (Cole 1983):

$$V = a - b\ln(I + \delta) - Ihr_0, \qquad (1)$$

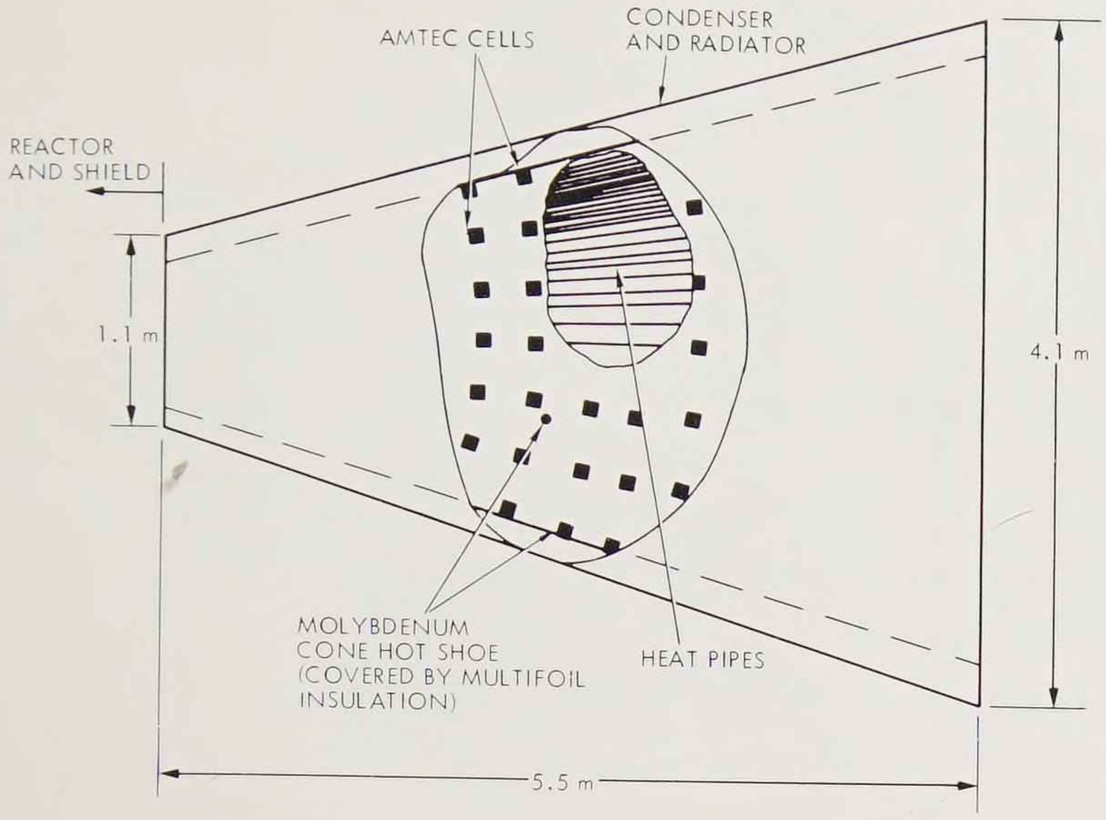


Figure 2 *AMTEC Reactor Power System Concept.*

where a, b, and δ depend on temperatures T_1 and T_2, and r_0 is the resistivity of the BASE which is also dependent on T_2. I is current density in A/cm^2 and h is BASE thickness in cm. The relationships for a, b, δ and r_0 are given by Bankston et al. (1983). Efficiency is given by:

$$\eta = IV/\left[IV + I(L + C\Delta T)/F + Q_{\text{loss}}\right], \qquad (2)$$

where L is the latent heat of vaporization for sodium, C is the specific heat of liquid sodium, and F is the Faraday. Q_{loss} is the sum of parasitic conductive and radiative heat losses.

Equations (1) and (2) were used to calculate voltage, power and efficiency vs. current curves to determine optimum operating points for specific temperatures and parameters representing various AMTEC technological levels. Figure 3 contains plots for the four levels considered. For these calculations the resistivity of the BASE was adjusted to include porous electrode sheet resistance and contact resistance, and thermoelectric voltage drop across the BASE giving an effective $r_0 = 2\Omega - \text{cm}$. Also, the voltage was further reduced because of the porous electrode sodium flow polarization (back pressure). These are consistent with the assumed porous electrode technological level and experimental results.

For the AMTEC SP-100 system, reactor and shield masses for the appropriate power levels were taken from Ewell (1982). Heat pipes mass was calculated using 0.035 kg/kW/m. The power conditioning equipment and radiator were assumed to operate at 95% efficiency with a total mass of 22 kg. The combined AMTEC cell and radiator mass was taken to be 16.67 kg/m^2 of radiator area (Bankston et al. 1983). In the previous study, an active heat pipe radiator was proposed. For the present design, a passive radiator would be sufficient.

Electrical and thermal loss estimates are reflected in system performance calculations including sodium line shunting, lead resistances, structural support conduction losses (5%–10%) and radiation losses from the hot shoe and AMTEC cells to the condenser. Insofar as radiation losses are concerned, the emissivity of the AMTEC cells was taken to be 0.8 and the emissivity of the multifoil covering and insulating the area of the hot shoe not covered by AMTEC cells was assumed to be 0.12. Note that for these designs, less than 50% of the hot shoe area is covered by AMTEC cells. The condenser emissivity has been varied to determine its effects on system performance. If the condenser is covered with a smooth film of liquid sodium, it would be highly reflective ($\simeq 98\%$). However, if a wick or some other non-smooth surface is needed to collect and transport the sodium, then reflectivity may be reduced.

The results of 100 kW_e system calculations are given in Table 1. In Table 2 major subsystem masses are listed and in Figure 4 we have shown how system mass varies with power level. The total mass for each level includes a 5% margin for miscellaneous contingencies. We assume in all projections that the electrode lifetime problem (to be discussed further in the experimental section) will be solved and that a high power, long life electrode will be available. Also, AMTEC cells and electrical connections would be connected in a series and parallel network compatible with power conditioning equipment and for redundancy (Bankston et al. 1983).

The near term system (#1) assumes no improvement in beginning-of-life electrode performance and a commercially available BASE thickness of 0.065 cm. The authors believe that the condenser emissivity of 0.08 is achievable in the near term, including a liquid sodium collection design for the condenser surface. For the near term, the total system mass exceeds somewhat the SP-100 design targets.

Improved designs *A* and *B* (nos. 2 and 3) assume improvements in porous electrode performance and condenser emissivity. In both cases, the mass is less than 3000 kg. Design #3 (improved *B*) represents the lowest temperatures possible for the reactor and converter while maintaining a radiator in the 60–70 m^2 range at 700 K. Employing the design considered here, the Advanced level (#4) represents the most optimistic performance expected for the AMTEC in the long term. Its performance easily meets SP-100 type requirements although the physical design has not been optimized. We strongly believe that other design options should be fully explored to ensure that the AMTEC's unique characteristics will be most advantageously employed. For example, because only a small area of the hot shoe cone is covered by AMTEC cells, the properties of the multi-foil strongly affect parasitic radiation losses. Conductive coupling in a liquid sodium loop is one alternative design which should be considered. To date, system projections have had to be limited to designs previously developed for other thermoelectric devices.

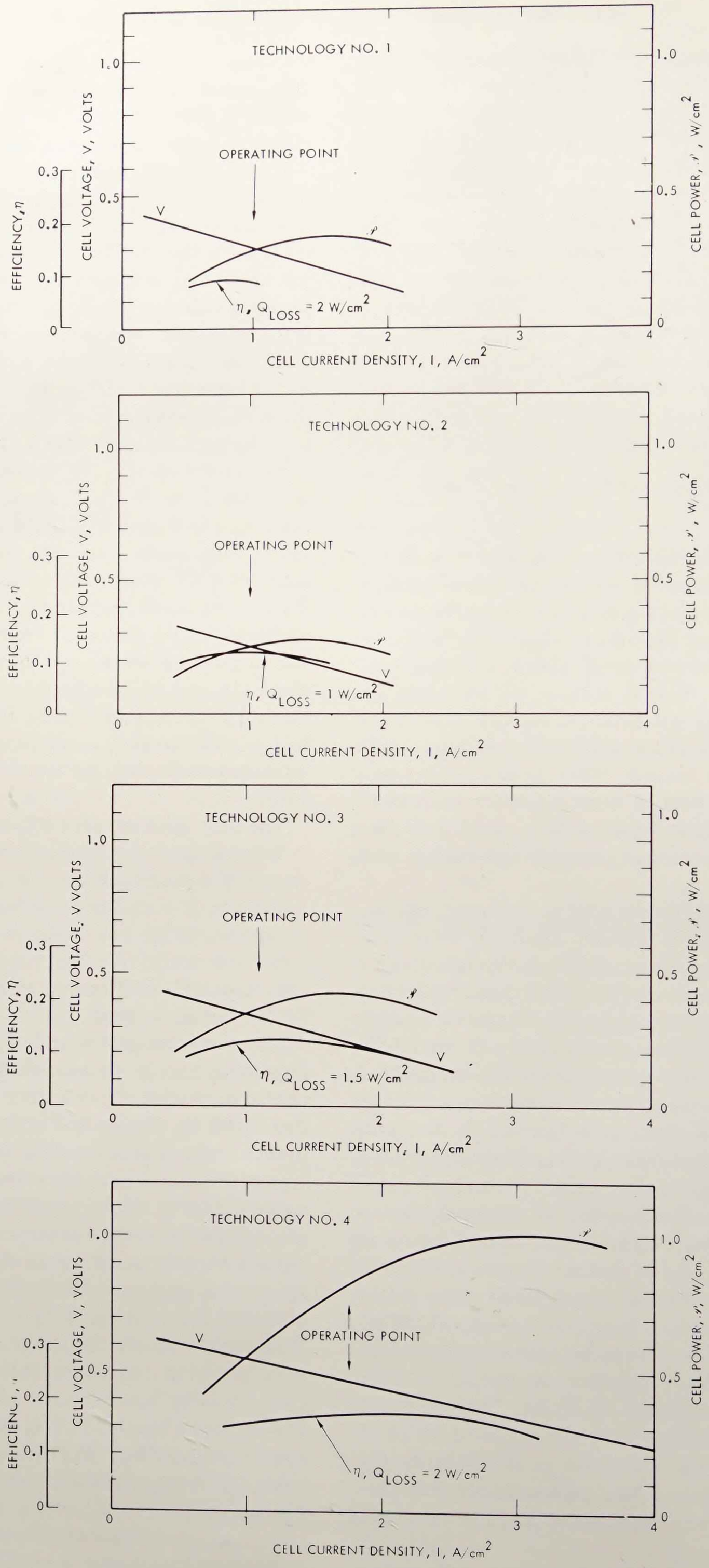


Figure 3 *Voltage, Power and Efficiency vs. Current Density Design Curves.*

Table 1 *AMTEC Heat Pipe Reactor Systems: 100 kWe.*

	Reactor Temp (K)	Converter Temp T_2 (K)	Radiator Temp T_1 (K)	Reactor Power (kW_t)	System Efficiency	Total Mass (kg)	Radiator Area m^2	Cell Current Density (A/cm^2)	Cell Power Density (W/cm^2)	Condenser Emissivity	Base Thickness (cm)	PE[a]
1. Near Term	1200	1080	711	1190	8.5%	3050	96	1.0	0.3	.08	.065	.90
2. Improved A	1100	1000	700	900	11%	2445	70	1.0	0.25	.05	.065	.95
3. Improved B	1200	1080	711	825	12%	2218	60	1.1	0.36	.05	.065	.95
4. Advanced	1300	1180	711	615	16%	1770	43	1.75	0.82	.035	.05	.98

[a] Fraction of ideal porous electrode performance. State-of-the-art, beginning-of-life electrodes are 0.90.

Table 2 *Masses (kg) of Major Subsystems for AMTEC 100 kW Electric Power System*

	Total	Reactor	Shield	Converters and Radiator	Power Conditioning	Heat Pipes
1. Near Term	3050	355	730	1600	22	196
2. Improved A	2445	330	660	1167	22	148
3. Improved B	2218	320	635	1000	22	136
4. Advanced	1770	285	560	717	22	101

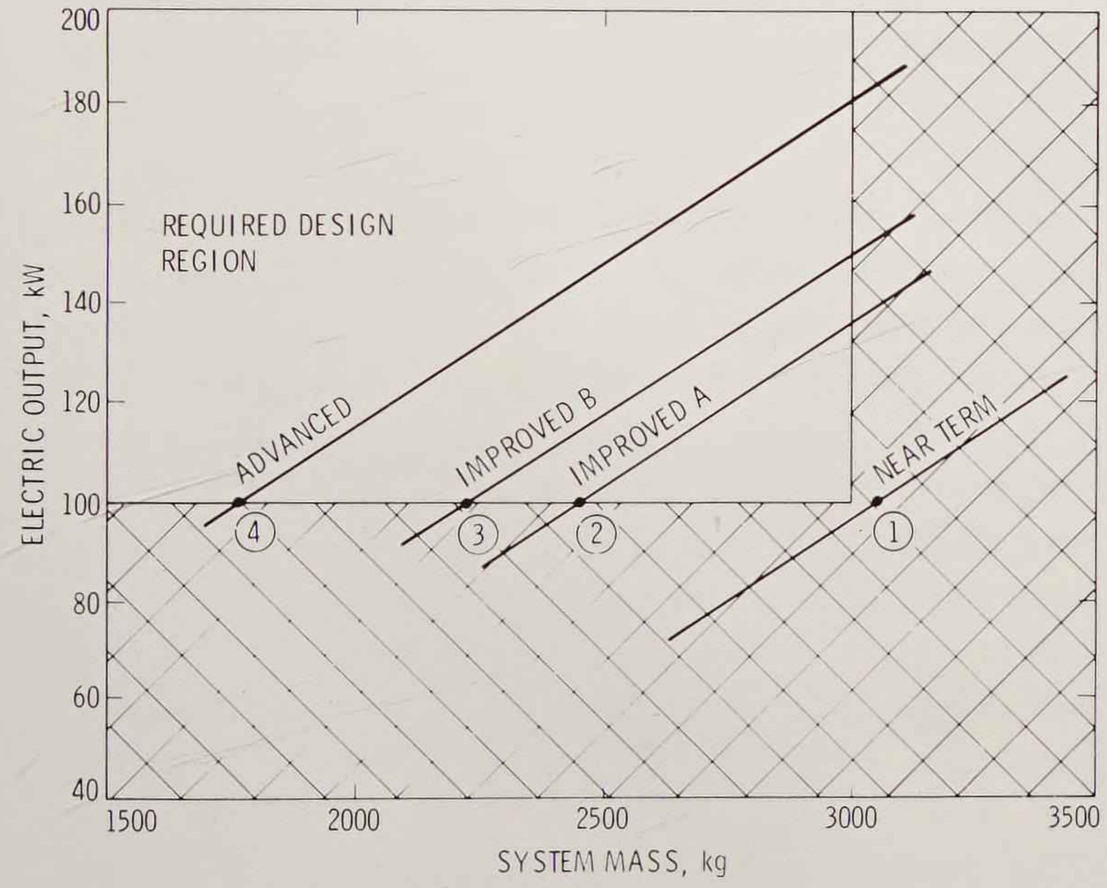


Figure 4 *AMTEC System Electric Output vs. Mass for Different Technological Levels.*

Finally, the development of advanced, deployable light weight radiator concepts (Elliott 1984 and Mattick et al. 1981) could extend the applicable temperature range for AMTEC. For example, an AMTEC system could be operated between $T_2 = 900$ K and $T_1 = 500$ K, and a system efficiency of 10–20% appears feasible (Hunt 1978). In this temperature range state-of-the-art reactor technology could be utilized, thus greatly reducing reactor development costs for any space nuclear power system.

Experimental Status

As mentioned earlier, AMTEC research has emphasized the development of long life, high power electrodes. In addition, recirculating devices have been built that have demonstrated high efficiency (19%) (Hunt et al 1981) and more recently long lifetime potential (10,000 hrs) (Hunt 1983). These milestones have been achieved in separate devices using thin film molybdenum and cermet electrodes respectively. At JPL, experimental work has been directed toward the thin film electrode with the objective of extending the observed high initial power densities to the 10,000–100,000 hour range.

Electrode research studies have been conducted utilizing JPL's AMTEC experimental test cell (ETC). The ETC (described in detail by Bankston et al. 1983) consists of a stainless steel vacuum chamber in which a cylindrical BASE tube 1.5 cm in diameter and up to 30 cm long is suspended. The BASE tube is closed at one end, filled with sodium and a heater well inserted to provide thermal input. Heat is supplied by using an electric resistance heater inserted into the heater well. Test electrodes are deposited on the outer (vacuum) side of the tube and electrical leads are run from these via vacuum feed-throughs to measurement apparatus. The heater well serves as the negative electrode. The deposited porous electrodes are typically cylindrical stripes 1–10mm wide on the BASE tube. After evaporating from the porous electrode the sodium condenses on the inner walls of the ETC.

All metallic, thin film electrodes are deposited at JPL using DC magnetron sputtering equipment. Co-sputtering of up to three different elements allows alloy electrodes to be accurately formulated and deposited. For molybdenum and Mo alloys, electrodes 1.5–2 μm thick have been found to give the best performance. An increase in thickness from 2 μm to 6 μm (factor of 3), decreased the power output by approximately the same factor of 3 for a Mo electrode. Thicknesses less than 1 μm result in increasingly larger sheet resistances and also the thickness becomes of the same order of magnitude as the surface roughness of the BASE. Wall thicknesses of the BASE tubes tested range from 1.2–1.7 mm.

Mo Alloy Electrodes

Molybdenum and two molybdenum alloy electrodes have been deposited on BASE tubes and the current versus voltage characteristics measured (Cole et al. 1983). The titanium alloys were selected due to their anticipated lower sintering rate than pure molybdenum, since sintering and pore closure has been proposed as a mechanism for the observed electrode decay. The results are presented in Figures 5 and 6 for 2.4 cm^2 electrodes, 1.5–2 μm thick using 0.5 mm Mo wire current leads. At the beginning of tests, maximum specific powers from the electrodes (Figure 5) were 0.85, 0.70 and 0.62 W/cm^2 for Mo, 1% and 3% Ti respectively when operating at 1173 K. After initial data were taken, the electrodes were kept at 1073 K for 53 hr. and at 1173 K for 113 hr. with voltage-current measurements made at intervals to measure the rate of change of electrochemical parameters. Figure 6 shows that all three exhibited power loss with time by a factor of 2–3 at approximately the same rate.

A duplicate set of Mo and Mo-Ti alloy electrodes was deposited on polished single crystal sapphire substrates for microscopic examination before and after

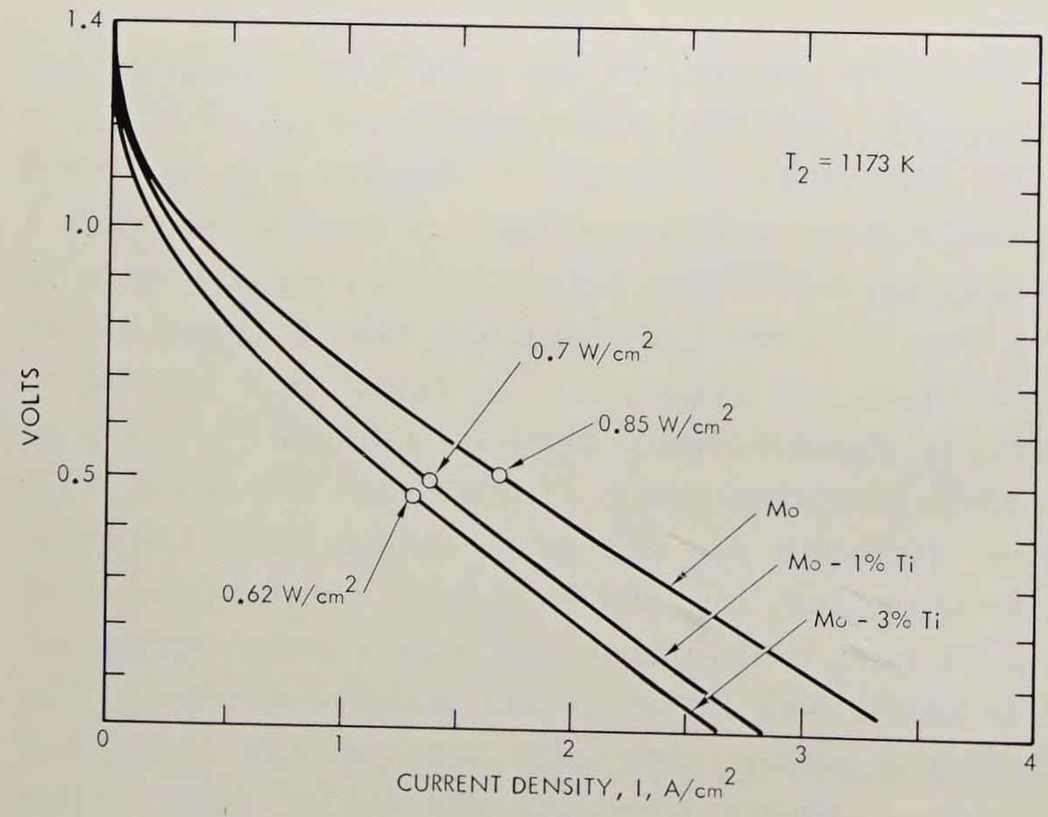


Figure 5 *Voltage vs. Current Characteristics for Mo and Mo-Alloy Electrodes.*

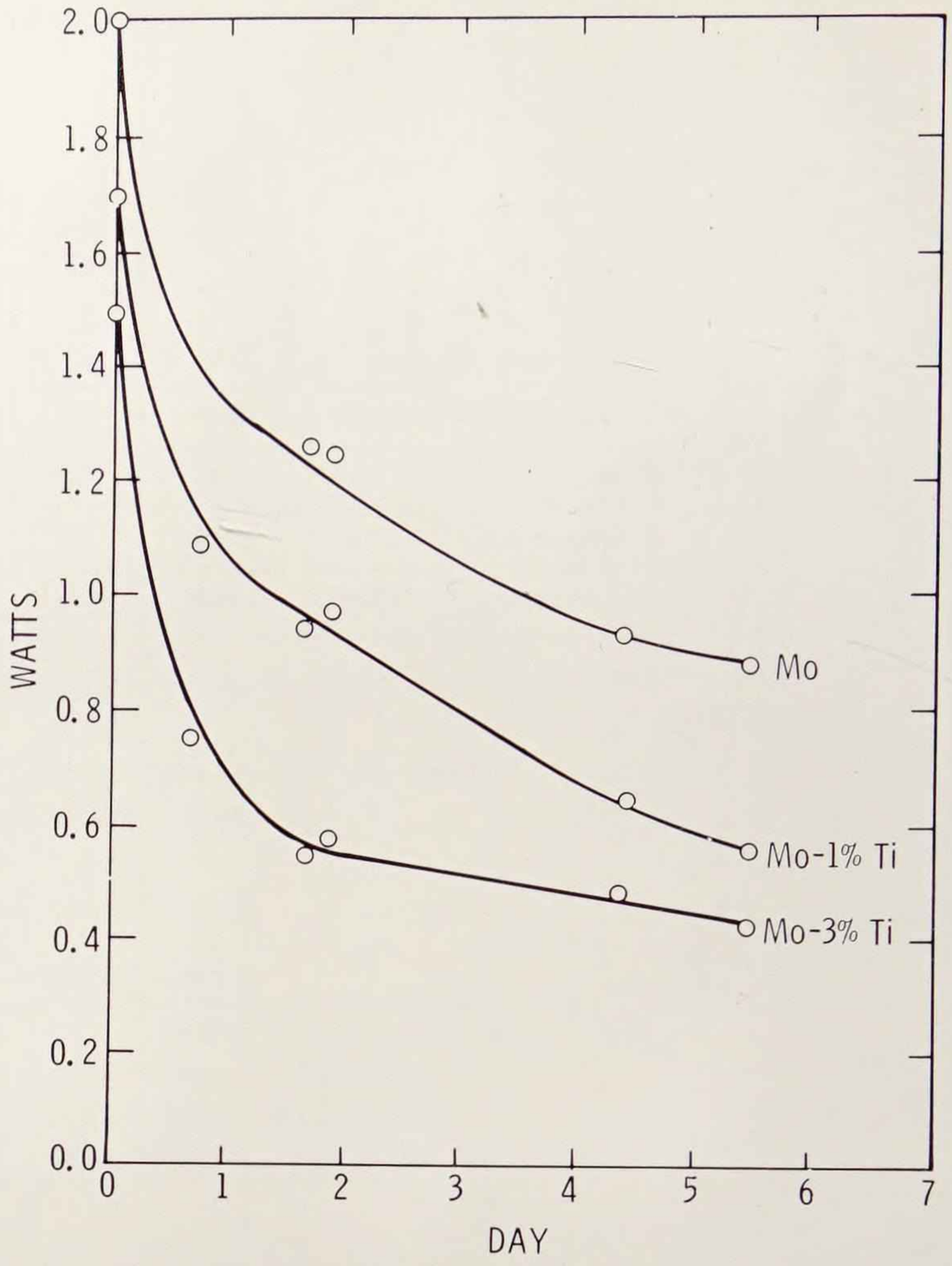
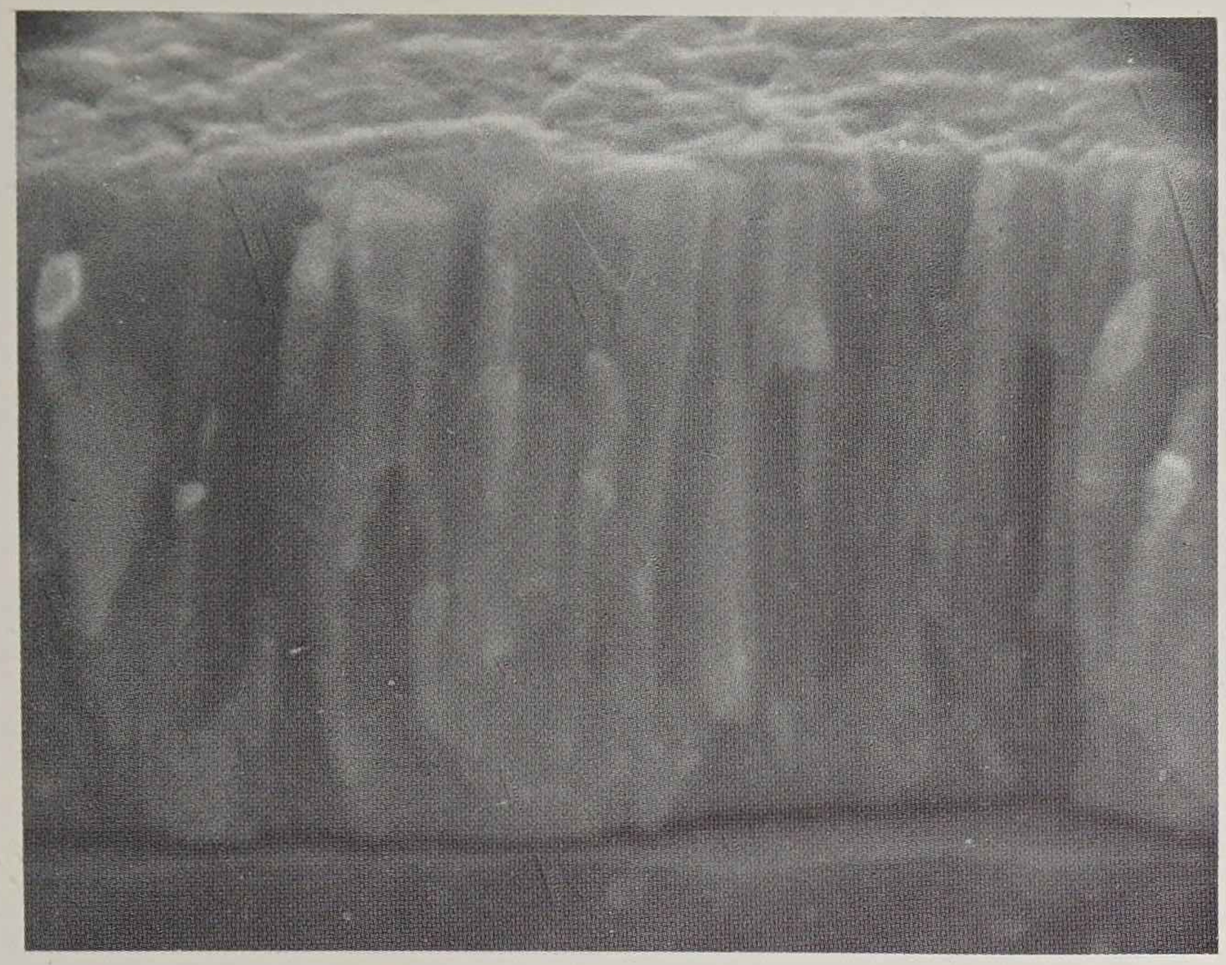


Figure 6 *Power vs. Time for Different Porous Electrode Materials at T_2 = 1173 K.*

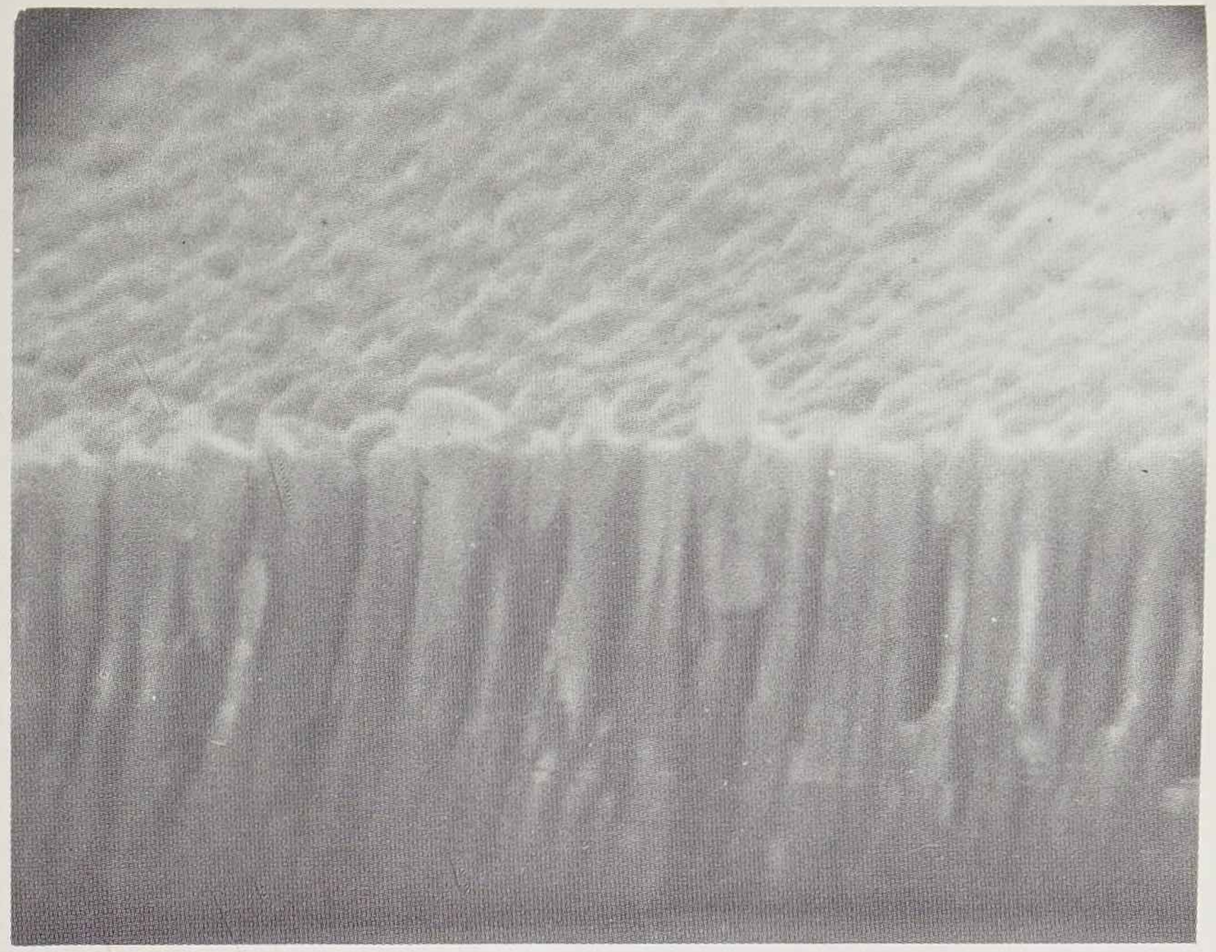
high temperature cycling. All three electrodes show a fine columnar grain structure under SEM examination with the columns normal to the plane of the electrode as shown in Figure 7 (upper photos). Vacuum annealing at 1273 K caused marked changes in the granular morphology (Figure 7, lower photos). These changes were characterized by a breakup of the columns into short polygonal grains and general coarsening of the structure particularly near the substrate-electrode interface (Figure 7). Thus, sintering did occur in all three electrodes, which is consistent with the degradation data. However as discussed later, the reason for the initial higher power density for pure Mo is not clear and other electrochemical mechanisms are probably involved.

Porous Electrode Flow Characteristics

Transient electrochemical measurements have also been made on several test electrodes. These measurements consisted of establishing a steady state current in an electrode and then interrupting this steady state with a fast transistor switch. The rationale for this measurement is that immediately after the switch opens all of the ohmic voltage drops in the cell which are due to the flow of current vanish and the difference between the voltage at this instant and at open circuit is due to sodium flow polarization.

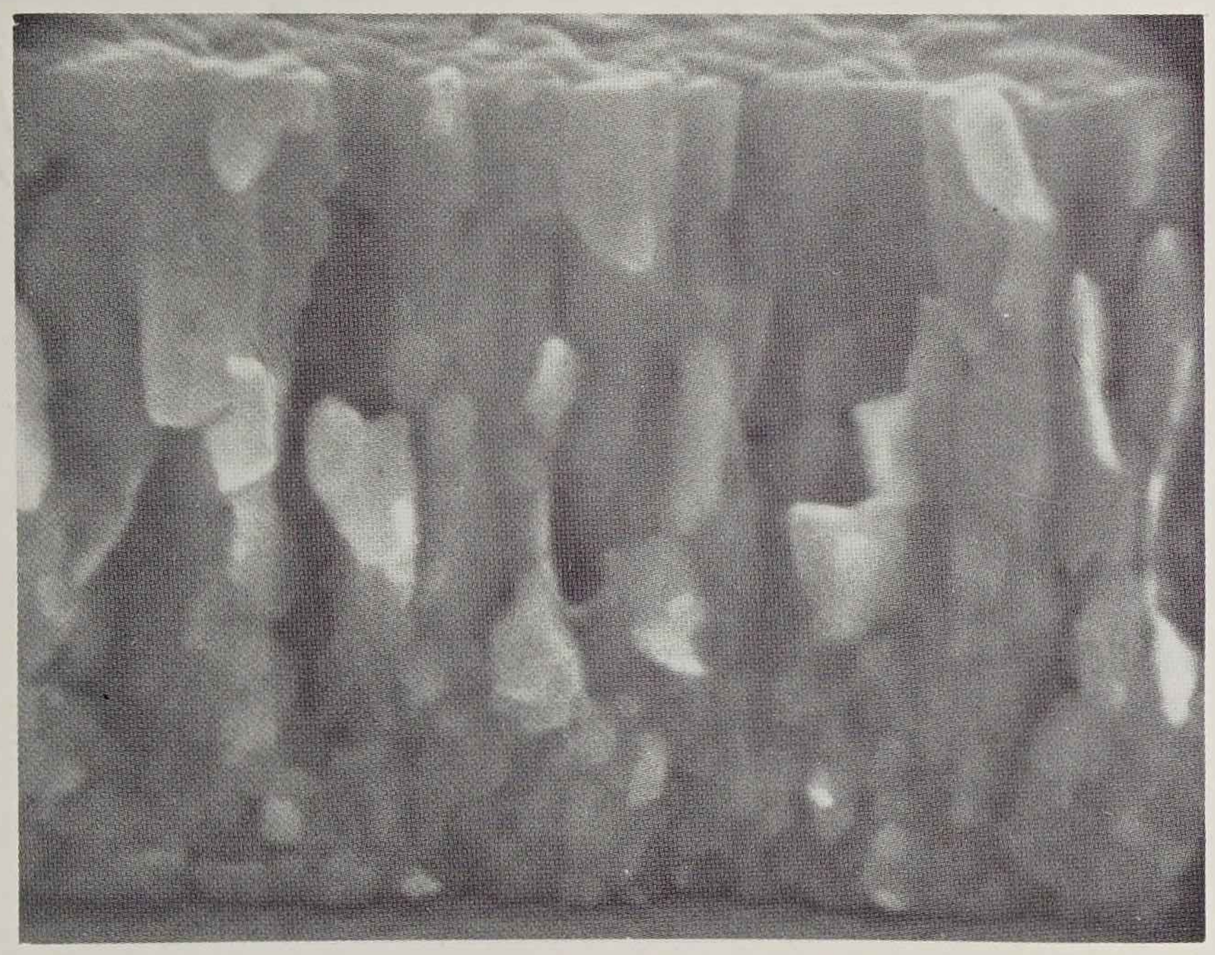


PURE Mo - AS DEPOSITED

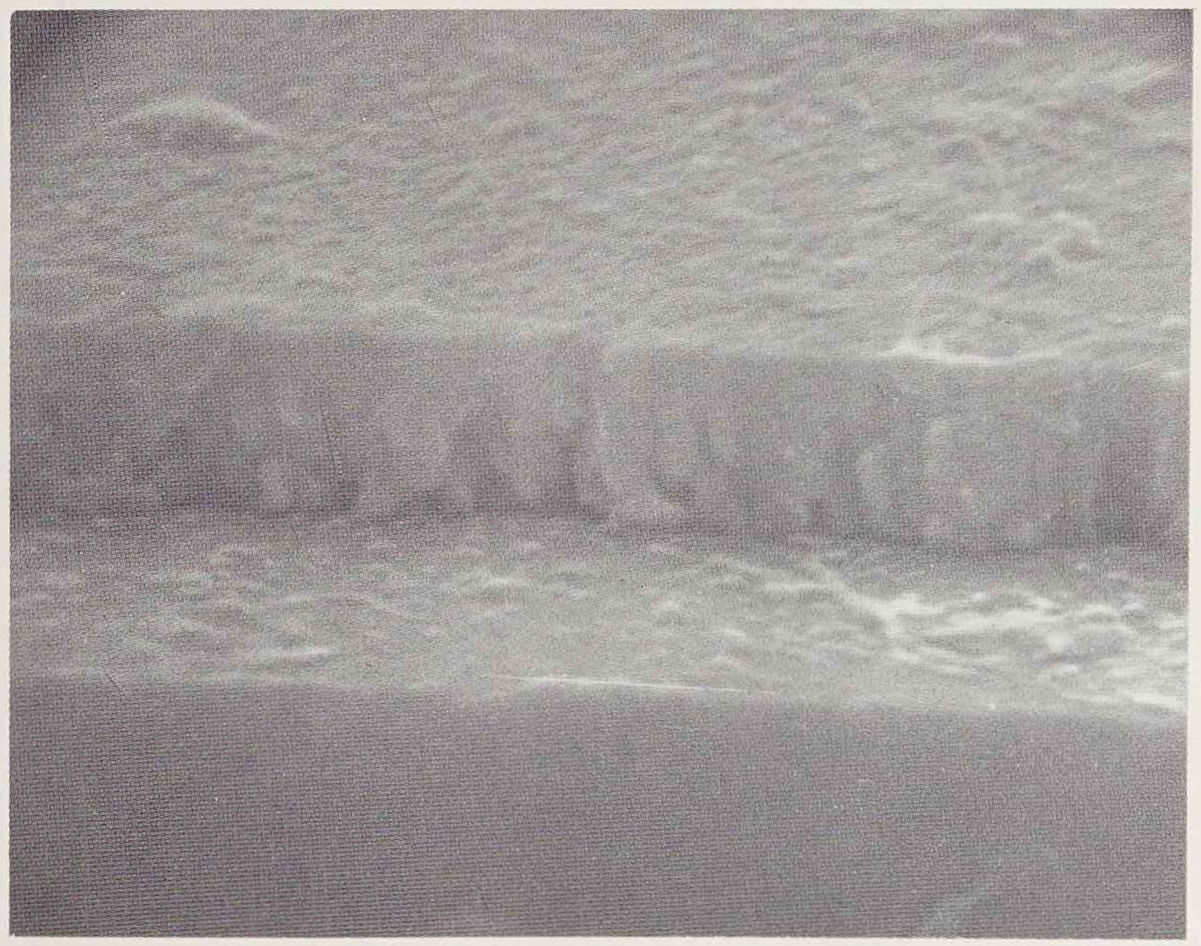


Mo - 1% Ti ALLOY (NOMINAL)
AS DEPOSITED

1 μm



PURE Mo - ANNEALED AT
1000°C FOR 8 hr



Mo - 1% Ti ALLOY (NOMINAL)
ANNEALED AT 1000°C FOR 8 hr

Figure 7 *SEM of Porous Metal Electrode Films Sputter Deposited on Sapphire Substrate.*

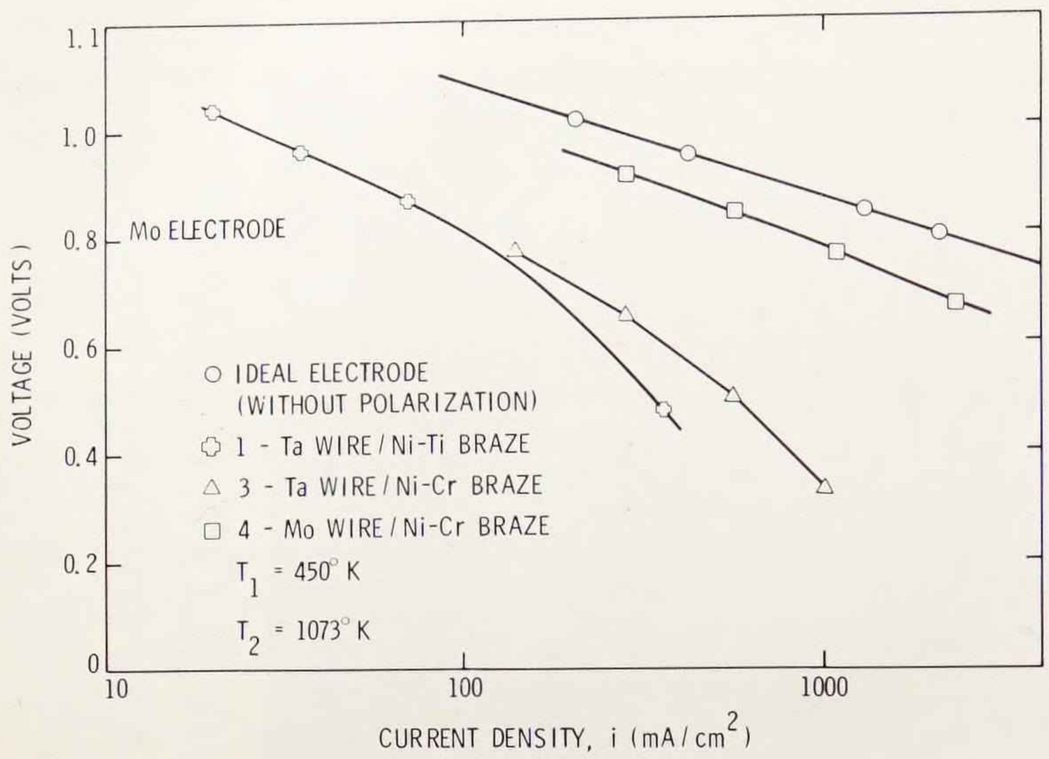


Figure 8 *Tafel Plots: Comparison of Experimental Electrode Performance with Ideal Electrode.*

Figure 8 presents results from the transient measurements for several Mo electrodes using different current buss wires and attachment techniques. Here we have plotted voltage versus current with all ohmic losses experimentally subtracted and compared with the theoretical maximum. This gives an indication of electrode performance in relation to an "ideal", zero flow impedance electrode. We see that the Mo electrode with Mo current lead attached by a nickel-chromium braze is very near the optimum. The data continue to show that the highest power densities are achieved with sputter deposited Mo electrodes and Mo current collection wires.

The measured transient voltage difference described above can also be related quantitatively to the flow polarization or back pressure across the electrodes. It can be shown that the measured difference is equal to:

$$\Delta V = \frac{RT_2}{F} \ln\left(\frac{P + \Delta P}{P}\right), \tag{3}$$

where ΔV is in volts, R is the gas constant, T_2 is the converter temperature, F is the Faraday, P is the sodium vapor pressure at the electrode outer surface and ΔP is the pressure difference (rise) across the electrode. $P + \Delta P$ is then the effective pressure at the electrode/BASE interface. P is given by the relation (Cole 1983):

$$P = (2\pi MRT_2)^{1/2}\left(\frac{I}{F}\right), \tag{4}$$

where M is molecular weight and I is current density (A/cm^2).

Using equations (3) and (4), we then calculate ΔP once ΔV is measured. For the 1.5–2 μm Mo electrodes, ΔV ranged from 0.23 V at beginning-of-life to 0.38 V after more than 100 hr at 1073 K or greater. For $\Delta V = 0.23$ V, $T_2 = 1073$ K and $I = 1.0$ A/cm^2, the calculated $\Delta P = 40$ Pa at the beginning of electrode life.

For comparison, an estimate of the pressure drop was also calculated assuming molecular (Knudsen) flow (Kennard 1938) through pores of a size determined from the scanning electron microscope photographs of the duplicate sample electrodes in the following manner. The electrode was assumed to be made of densely packed (touching) cylindrical grain columns 0.1 μm diameter in a square array. The remaining open area was divided into an equal number of pores and an effective cylindrical diameter of 0.05 μm determined. Using this pore diameter and an electrode thickness of 1.5 μm, the Knudsen number is approximately 10,000. Thus the molecular (Knudsen) flow relationship can be used to calculate ΔP (Kennard 1938):

$$\Delta P = (3/4)\, Q\left(\frac{RT}{2\pi}\right)^{1/2} \frac{l}{a^3}\,\frac{1}{N}, \tag{5}$$

where Q is the mass flow rate of sodium per cm^2, l is pore length (electrode thickness), a is pore radius and N is the number of pores per cm^2 (10^{10}).

Equation (5) yields a ΔP of approximately 400 Pa needed to sustain a Knudsen flow rate equivalent to 1.0 A/cm^2 at 1073 K. This assumes a cylindrical, straight pore geometry. If the vapor path were more complex, a greater ΔP would result. A larger number of smaller diameter pores having the same total pore area would also produce a larger ΔP. This is important because SEM photographs can only give an upper bound for pore radius (a).

The calculations show that if vapor flow is the dominant transport mechanism, the sodium pressure drop through the electrode should be a factor of 10 (or greater) larger than experimentally observed at the beginning of life. The approach to the electrode degradation problem must address the question "Why are the Mo electrodes so highly efficient when first deposited?" Another mechanism such as surface diffusion must play a dominant role. The possible explanation now being studied is that the observed behavior is due to the formation of a sodium-molybdenum bronze (Na_xMoO_3, $x = 0$ to 1) on the surface of the electrode pores. These materials possess both electronic and ionic conductivity. Sodium may form a partial monolayer in the bronze phase along the pore surfaces and transport may be enhanced due to the excellent conductance properties of the bronze.

Oxidized Mo Electrodes

Initial experiments employing oxygen treatment of a deposited electrode support the hypothesis that the enhanced conductance (bronze) surface layer forms on the pore surfaces. Exposure of a degraded Mo electrode to O_2 at a pressure of 130 Pa at 973 K for a period of 10 minutes followed by passage of sodium through the electrode restored the specific power output to ~90% of its beginning-of-life specific power (Figure 9). Furthermore the specific power continued at this level for 60

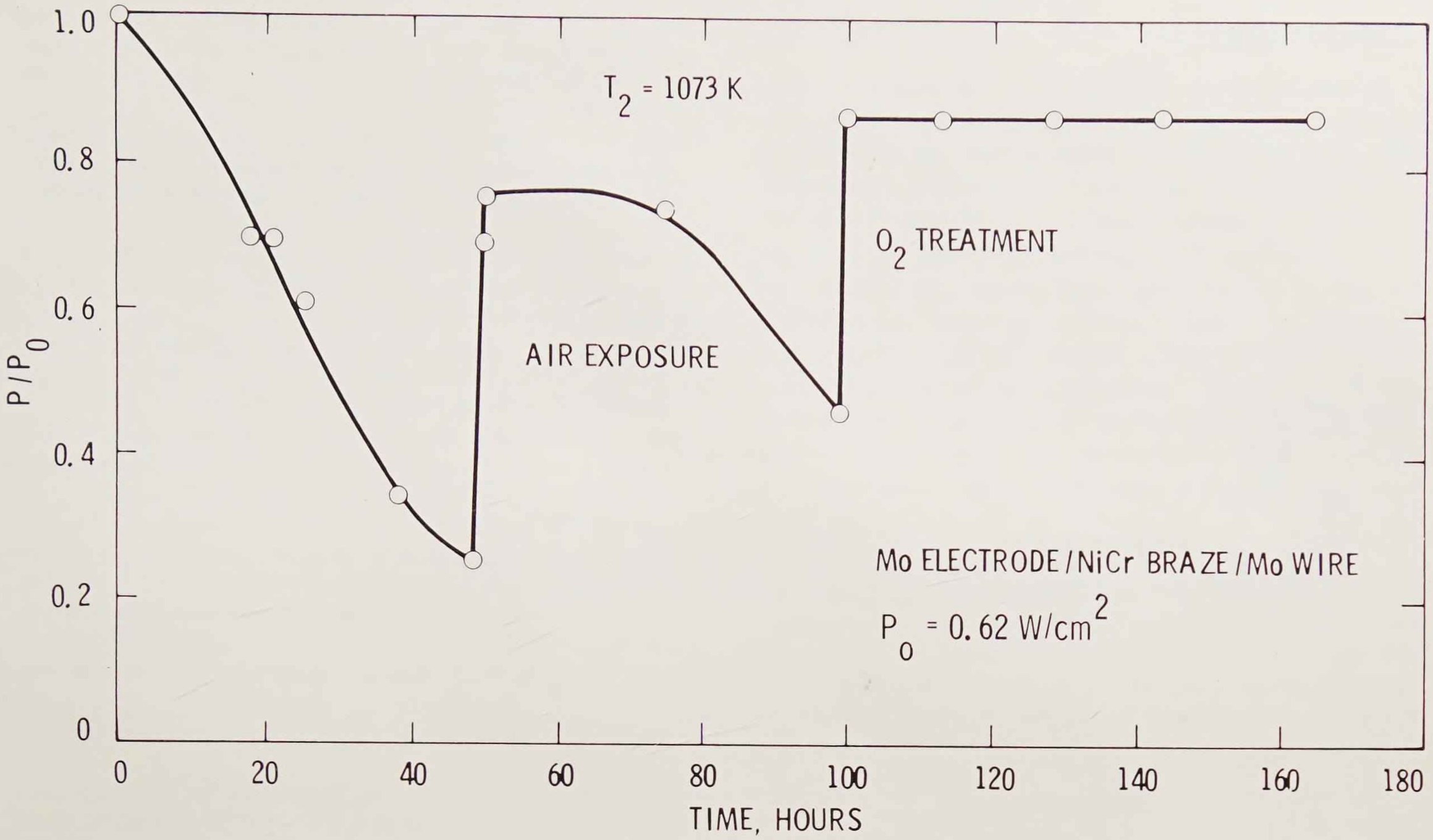


Figure 9 *Power vs. Time for Mo Electrode Treated with Oxygen.*

hours at 1073 K with no detectable degradation in performance at which time sodium was depleted from the reservoir. This treatment was suggested after it was observed that some restoration in specific power occurred after exposure of the electrode to ambient air at room temperature. Presumably, a bronze may be formed in the oxidation process. The experimental results illustrated in Figure 9 indicate a stable level that is the longest high power period reported to date for a thin film, metallic electrode. Degradation of the untreated electrodes may be due to progressive chemical reduction of the pore surface layer by sodium flow thereby reducing the ionic/electronic conductivity. In fact, measured polarization voltages (ΔV) for degraded electrodes are in the range expected for Knudsen flow (approximately 0.4 V or greater). Also, electrode degradation is strongly temperature dependent (Cole 1981). Since physical changes in the electrodes do occur, a combination of chemical and physical effects are likely. Experiments to identify these mechanisms are continuing.

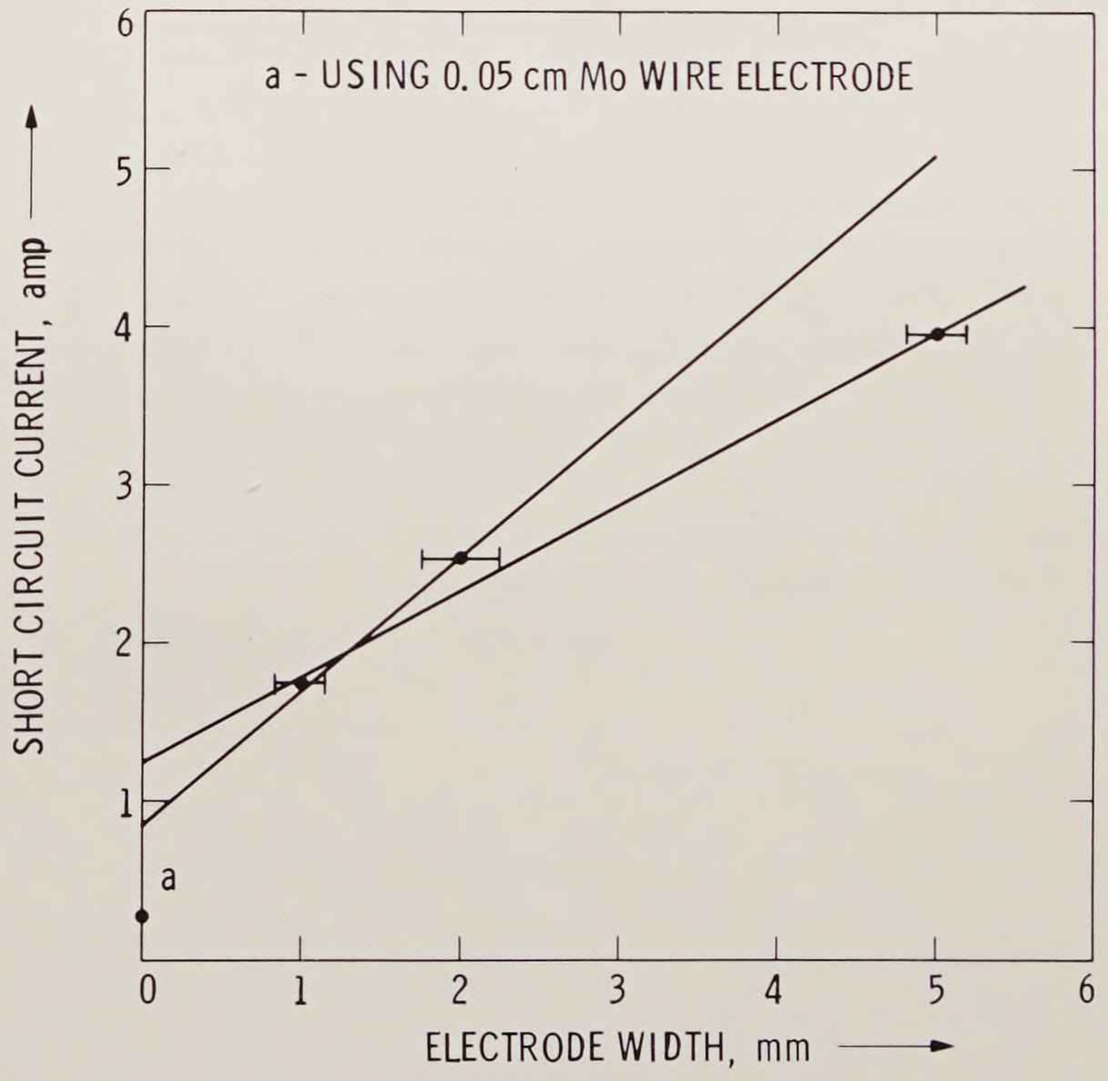


Figure 10 *Short Circuit Current vs. Porous Electrode Width Data Illustrating Electron Spreading.*

Grid Electrodes

Preliminary studies using a series of cylindrical Mo electrodes of decreasing width seem to indicate that electrons can spread from the edge of an electrode for distances as large as a few tenths of a millimeter. We infer this phenomenon from the plot of short circuit current versus electrode width in Figure 10 for sputter deposited Mo electrodes 1.5–2 μm thick. It may be possible to use this characteristic to design a microgrid electrode with a thick collector grid but a very large percentage open area. In this electrode, flow polarization would be small and not strongly affected by the chemical and physical processes which otherwise degrade porous electrode performance.

Conclusions

Research on the AMTEC has continued to show significant progress. Current emphasis is on long life electrode development where several promising electrode systems are under study. Of particular note is the potential for lifetime stability at high power indicated for the oxidized Mo electrode. Because no technical barriers have yet been encountered, the design and assembly of a high efficiency, practical power system appears feasible once a durable high power electrode is developed. In view of the projected payoff illustrated in Figure 4 for space nuclear power system performance, continued AMTEC research and development is warranted for long term space power requirements.

Acknowledgments

The research described in this paper was carried out by the Jet Propulsion Laboratory, California Institute of Technology, and was sponsored jointly by the National Aeronautics and Space Administration and the Air Force Office of Scientific Research. The authors would like to thank Mr. D. C. Schneider for his assistance in the conduct of testing at JPL.

References

Bankston, C. P., T. Cole, R. Jones, and R. Ewell (1983) "Experimental and Systems Studies of the Alkali Metal Thermoelectric Converter for Aerospace Power," *J. Energy* 7(5):442.

Buden, D. and J. A. Angelo (1983) "Space Reactors—Past, Present, and Future," in *Proceedings of the 18th Intersociety Energy Conversion Engineering Conference*, Vol. 1, AIChE, New York, p. 61.

Cockfield, R. D., R. F. Hartman, and C. E. Kelly (1980) "RTG Power Sources for the International Solar Polar Mission," in *Proceedings of the 15th Intersociety Energy Conversion Engineering Conference*, Vol. 2, AIAA, New York, p. 1043.

Cole, T. (1981) "High Efficiency Thermoelectric Conversion with Solid Electrolytes—Theoretical Analysis," in *Proceedings of Workshop on Thermally Regenerative Electrochemical Systems*, DOE/SERI Report, SERI CP-234-1577, p. 109.

Cole, T. (1983) "Thermoelectric Energy Conversion with Solid Electrolytes," *Science*, *221*(4614):915.

Cole, T., C. P. Bankston, S. K. Khanna, and A. Thakoor (1983) "Studies of Alkali Metal Thermoelectric Converter (AMTEC) Electrodes," in *Electrochemical Society Fall Meeting, Extended Abstracts*, Vol. 83-2, p. 615, October 9–14, 1983.

Elliott, D. G. (1985) "External-Flow Radiators for Reduced Space Powerplant Temperatures," in *Space Nuclear Power Systems 1984*, M. S. El-Genk and M. D. Hoover eds., Orbit Book Co., Malabar, FL.

Ewell, R. (1982) "Nuclear Thermoelectric Space Power," in *Fourth International Conference on Thermoelectric Energy Conversion*, Arlington, TX, March 10–12, 1982.

Ewell, R. (1983) "Energy Conversion for Megawatt Space Power Systems," in *Proceedings of the 18th Intersociety Energy Conversion Engineering Conference*, AIChE, New York, p. 87.

Hunt, T. K., N. Weber, and T. Cole (1978) "Research on the Sodium Heat Engine," in *Proceedings of the 13th Intersociety Energy Conversion Engineering Conference*, SAE, Warrendale, PA, p. 2011.

Hunt, T. K., N. Weber, and T. Cole (1981) "High Efficiency Thermoelectric Conversion with Beta″–Alumina Solid Electrolytes, The Sodium Heat Engine," in *Fast Ionic Transport in Solids*, edited by J. B. Bates and G. C. Farrington, North-Holland Publishing Co., Amsterdam, p. 263.

Hunt, T. K. (1983) Ford Scientific Research Staff, private communication.

Kennard, E. H. (1938) *Kinetic Theory of Gases*, McGraw-Hill, New York, p. 304.

Kummer, J. T. (1972) "β-Alumina Electrolytes," in *Progress in Solid State Chemistry*, Vol. 1, edited by J. O. McCaldin, Pergamon Press, New York, p. 141.

Mattick, A. T. and A. Hertzberg (1981) "Liquid Droplet Radiators for Heat Rejection in Space," *J. Energy*, *5*:6.

Shock, A. (1980) "Design Evolution and Verification of the General Purpose Heat Source," in *Proceedings of the 15th Intersociety Energy Conversion Engineering Conference*, Vol. 2, AIAA, New York, p. 1032.

Subramanian, K. and T. K. Hunt (1982) "Solar Residential Total Energy System Using the Sodium Heat Engine—A Concept Study," in *Proceedings of the 17th Intersociety Energy Conversion Engineering Conference*," IEEE, New York, p. 1474.

Subramanian, K. and T. K. Hunt (1983) "Solar Thermal/Electric Power Conversion Using the Sodium Engine," in *Proc. ASME Solar Energy Conference*, April 1983.

Weber, N. (1974) "A Thermoelectric Device Based on Beta-Alumina," *Energy Conversion 1*(4):1.

Part 7

THERMAL MANAGEMENT

Space Nuclear Power Systems 1984
Edited by M. S. El-Genk and M. D. Hoover
© Orbit Book Company, Malabar, FL, 1985

Chapter 46

Overview of Thermal Management Issues for Advanced Military Space Nuclear Reactor Power Systems

Tom Mahefkey

U.S. Air Force Wright Aeronautical Laboratories
Wright Patterson Air Force Base, Ohio 45433

This paper summarizes the functional and system imposed design constraints and developmental issues related to military space nuclear power thermal management. The envisioned requirements related to power level, power form and profile, operating duration, and life encompass a wide variety of conceptual future military spacecraft missions. "Baseload", near-constant power output, and "burstload", high peak to average power profile requirements introduce a wide spectrum of potential space reactor configuration needs with a corresponding range of steady state and transient, periodic thermal management technological needs. Spacecraft system operational conditions and design constraints (allowable power/payload mass and volume fractions, survivability and endurability, autonomy, integrability, and orbital operations considerations) impose additional thermal management technological needs. Candidate thermal management technologies are described in terms of their attributes and state of development.

Introduction

This paper presents a summary of the functional and system imposed design constraints and developmental issues related to military space nuclear power system thermal management. The envisioned functional requirements related to power level, power form, power profile, operating duration, and life encompass a wide variety of conceptual future military spacecraft missions (Klein 1983). These "baseload", near-constant power output, and "burstload", high peak to average power profile requirements introduce a wide spectrum of potential space reactor configuration needs with a corresponding range of thermal management technological needs (National Research Council 1983). Further, spacecraft system operational conditions and design constraints (allowable power/payload mass and volume fractions, survivability and endurability, autonomy, integrability, and orbital operations considerations) impose additional thermal management technological needs.

Space Nuclear Reactor Thermal Management Defined

The scope of spacecraft nuclear thermal management generally encompasses thermal design issues related to the core, converter, converter waste heat radiator, and reactor auxiliary components (shield, power processing, control mechanisms).

In addition to these power generation related design considerations, additional thermal design considerations are introduced by operating environmental considerations, such as natural and core radiation effects, as well as space vacuum, external corpuscular and radiation threats.

Finally, total thermal integration of the host spacecraft, its payload subsystems, as well as its functional subsystems such as payload waste heat radiator, attitude control, and structure, form an important and strongly coupled subset of the nuclear powered spacecraft thermal management problem.

Thermal Management Design Requirements

The conceptual military mission classes of interest give rise both to the open cycle (ROVER, NERVA) and to the closed cycle (SNAP-50) power system concepts, as well as to the hybrid configurations for pulsed power, dual propulsion/power applications, and multimodal (standby, alert, burst modes) operating conditions. Thermal management issues must address both steady state and transient heat transfer as well as those thermal control operating conditions related to the integrated nuclear powered spacecraft. These thermal issues are specifically related to orbital startup (and, perhaps, shutdown and restart), payload power demand load following, compensation for converter, power and payload electronic degradation and/or failures, and heat rejection/transport segment degradation and contamination.

Orbital operation sequences, such as radiator and separation boom deployment, orbital transfer (for example, LEO to GEO, low earth orbit to geosynchronous earth orbit) and evasive maneuvers, and launch and

flight safety considerations (boost, rendezvous, resupply, and reentry mission phases) also introduce system level, thermal design considerations.

Unique requirements for military applications include external threat survivability, structural and thermomechanical dynamic maneuvering loads, effluence thrust and contamination cancellation, as well as reconstitution considerations.

Thermal Management Technological Issues

For the open cycle applications, the need for an integrated payload waste heat management offsets the unintegrated three-to-one specific reactant consumption advantage of open-cycle nuclear (as compared with chemically fueled) systems. Post-burst, isotope decay heat removal requirements also offset the specific weight advantages of the open cycle reactors, although a variety of novel decay heat utilization schemes have been proposed (Myrabo et al. 1983). The Brayton cycle conversion for either open cycle nuclear or combustion driven power generation is favored over MHD due to enthalpy extraction (hence, lower reactant inventory) advantages. Long term reactant (H_2) storage and boiloff loss minimization will be required, introducing needs for active cryo refrigeration and increased on-board baseload power. Consequently, reactant resupply may be necessary for these open cycle missions. For rapid start-up, pre-power generation reactant coolant flow mass penalties and transient thermal shock mechanical loads unique to the reactor heat source must be considered.

For closed cycle applications, thermal management configuration alternatives for candidate thermoelectric, thermionic, and dynamic conversion schemes generally employ heat pipe radiators. For static energy conversion, the ratio of radiator mass to converter mass is relatively constant with increasing power, while this mass fraction increases dramatically for dynamic conversion schemes. At power levels in excess of 10 MWe, conceptual studies generally show that the power system radiator is the heaviest single system component. This trend gives rise to the need for an interest in novel, power cycle heat rejection techniques such as external flow radiators including the droplet, capillary film, or dust particle concepts for ultra-high power, baseload system applications.

Therefore, for the first generation reactors, heat pipe radiators having highly effective C/C composite material fin materials and a projected performance in the range of 5–10 kg/m^2 will serve as the basic power cycle heat rejection subsystem. This selection is probable for the same reason their use is currently favored for nonnuclear spacecraft applications; namely, reliability, minimum armor mass penalty, and threat rejection attributes. Although advanced external flow radiators offer the potential for 10-fold radiator mass reduction, their use may be intrinsically limited to spacecraft where contamination is not a major design consideration.

Heat pipe core-to-converter heat transport can provide minimum baseload power system specific weight (kg/kW) in the 10–1000 kW range (Buden et al. 1979). Cores cooled by heat pipe introduce novel compatibility issues concerning uncertain fuel swelling-thermal interface conductance stability even at modest (1500 K) core temperatures. Liquid metal cooled, in-pile thermionic systems operating at a performance maximizing 1800–1900 K core-converter interface temperature regime, offer extremely important scaleability and performance attributes for military baseload systems of up to several megawatts output. However, they require further resolution of fuel swelling issues and emitter distortion mechanisms in this temperature regime. The intrinsic survivability of the thermionic system's 1000 K radiator is noteworthy.

Brayton cycle conversion for baseload power requirements in excess of several megawatts is attractive from a specific mass standpoint; however, its lower temperature (500–600 K), heat rejection-cycle efficiency dependency may preclude its use for these military applications requiring compactness, maneuverability, and survivability. The Brayton cycle, coupled with an external flow radiator concept, offers much potential for megawatt class applications if the internal (O_2 embrittlement of refractories) and external (free surface radiator) contamination problems can be remedied.

Although the development of thermoelectric configuration options is imminent, their performance and growth potential, based on a practical limit of unity for the ZT product, are uninspiring. This limit necessitates deployable heat rejection radiators for Space Transportation System (STS) launched spacecraft with power outputs in excess of 100–300 kWe. Degradation properties of advanced high temperature thermoelectrics materials currently under development have not yet been characterized; most likely, their performance will not significantly exceed the current beginning of life (BOL) nominal efficiency of 7 percent already demonstrated by Si–Ge couples. However, thermoelectrics could be applied to low temperature, heat rejection heat pumps.

Presently, the most difficult thermal management problem lies not with heat transport and rejection in the reactor system, but with the low temperature (~300 K) heat transfer and heat rejection regime associated with the power processing, the payload component waste heat management, and the transient pulse heat rejection. The size and scale, transport distance limitations, and required heat flux loads represent thermal management limits which require major enabling breakthroughs in technology.

Some of the high powered spacecraft related thermal management integration problem solutions lie in developing high temperature (>400 K) power electronics; others, however, will be minimized by developing high temperature, high specific performance (>50 w/kg), volumetrically compact space nuclear reactor power system technological candidates. Such power system capabilities could require less than the traditional 30 percent spacecraft payload mass allocation, thereby providing additional payload capability.

Conclusion

It is concluded that thermal management design issues related to the nuclear reactor and energy conversion system, as well as the power processing and payload components represent significant technological development challenges. Solutions of design problems is mandatory to assure nuclear power system functional and performance objectives are attained.

Acknowledgments

This work was performed at the U.S. Air Force Wright Aeronautical Laboratories.

References

Buden, David et al. (1979) *Selection of Power Plant Elements for Future Reactor Space Electric Power Systems*, Los Alamos Scientific Laboratory Report LA-7858, September 1979.

Klein, Gail A. (1983) *Proceedings of the Multimegawatt Space Power System Needs and Capabilities Workshop*, March 1–3, 1983, NASA Jet Propulsion Laboratory Report D-665, 3 July 1983.

Myrabo, L. N., J. R. Powell and T. E. Botts (1983) "Concepts for Space Nuclear Multi-Mode Reactors," in *Proceedings of 18th Intersociety Energy Conversion Conference*, Vol. 1, page 69–75, AICHE.

National Research Council (1983) *Proceedings of the Symposium on Advanced Compact Reactor Systems*, November 15–17, 1982, National Research Council Committee on Advanced Nuclear Systems, National Academy Press, Washington, D.C.

Space Nuclear Power Systems 1984
Edited by M. S. El-Genk and M. D. Hoover
© Orbit Book Company, Malabar, FL, 1985

Chapter 47

Liquid Metal Heat Transfer Issues

H. W. Hoffman and G. L. Yoder

Oak Ridge National Laboratory
P. O. Box Y
Oak Ridge, Tennessee 37831

An alkali liquid metal cooled nuclear reactor coupled with an alkali metal Rankine cycle provides a practicable option for space systems/missions requiring power in the multi-megawatt range. Thermal issues relative to the use of alkali liquid metals for this purpose are identified as these result from the nature of the alkali metal fluid itself, from uncertainties in the available heat transfer correlations, and from design and performance requirements for system components operating in the earth orbital microgravity environment. It is noted that, while these issues require further attention to achieve optimum system performance, none are of such magnitude as to invalidate this particular space power concept.

Introduction

An alkali metal cooled nuclear reactor coupled with an alkali metal Rankine cycle provides an option for achieving desired multimegawatt (electric) power levels for space systems (Jones, MacPherson and Nichols 1985). Proposals have generally linked a potassium boiling/condensing thermodynamic cycle for power conversion with either (1) a single-phase liquid (lithium) cooled nuclear energy supply through an intermediate heat exchanger or (2) a boiling potassium cooled reactor through an efficient liquid-vapor separator. Both concepts were studied intensively in the 1950–1965 period, with the conclusion by the Oak Ridge National Laboratory based on extensive analysis and experimentation that the latter (or direct cycle) offered high reliability in a system that was simple and of low specific weight (Fraas 1967). Among the factors examined in detail during this period were the thermal characteristics of the alkali liquid metals (thermophysical and thermodynamic propeties; heat, mass, and momentum transfer).

In the sections following, this paper describes some of the thermal issues affecting design and performance of the liquid metal system deriving from the physical and chemical nature of alkali liquid metals, discusses existing uncertainties in current heat transfer correlations, and considers the consequence of the microgravity environment on system thermal hydraulics. It should be noted at this point that, while the issues raised regarding the use of alkali metals in power generation and conversion systems are relevant to the development of these systems, none are of such magnitude as to negate the concept. There is need, in some instances, to refine understanding of thermal-hydraulic transport phenomena identified in the earlier work and, in a different aspect, to verify and improve correlations needed for system design and optimization.

Alkali Liquid Metal Coolant Characteristics

The alkali liquid metals attracted early attention as coolants for nuclear reactors because of their excellent heat transfer characteristics. In addition, the capability of operation at high liquid temperatures with low system pressures occasions improved thermal efficiencies while reducing cost/weight penalties associated with use of lower boiling temperature fluids. Pertinent properties for several of the alkali metals of interest in space power application are compared in Table 1. Note particularly the wide liquid range, which enables flexibility in cooling design and adds an element of safety (through the high boiling temperature).

Being elemental materials, further significant advantage accrues to the alkali liquid metals through their thermal decomposition resistance. However, the alkali

Table 1 *Alkali Liquid Metal Thermal Parameters*

Fluid	Melting temperature (°C)	Atmospheric boiling temperature (°C)	Thermal conductivity (at saturation) (W/m · C)
Li	179	1317	45.8
Na	98	883	52.1
NaK-56*	19	826	19.4
K	64	760	31.3
Cs	28	669	18.5

*56 weight % Na.

metals are, as a class, very reactive chemically, combining energetically with many other materials. Of particular consequence are their flammability in the presence of oxygen and water (liquid or vapor) and less violent reactions giving rise to surface contamination affecting thermal performance. This behavior dictates care in ground handling for space power systems. Isotope activation can be a disadvantage to the extent that shield weights are affected; however, separation to remove the offending isotope will generally minimize this problem. The discussion in the following paragraphs deals with uncertainties that can be ascribed to the chemical reactivity of the alkali metals.

Oxide Effects

A dominant early observation in the study of alkali metal heat transfer was the highly erratic nature of the results. While much was known by the chemist working principally *in vitro*, the engineer was much less experienced and encountered numerous problems. Thus, the pioneering study by Untermeyer (1949) was victimized by the dissolution of the iron heat transfer test section by the flowing liquid metal, giving data that, when correlated in standard form, varied with time. Another major problem was the presence of oxide and nitride contaminants associated with poorly understood handling procedures and apparatus design. Results of some exploratory tests (Borishanskii, Zablatskaya, and Ivashchenko 1961) are shown in Figure 1, where a plot of the reciprocal of the Nusselt modulus ($N_{Nu} = hD/k$) against the Peclet modulus ($N_{Pe} = DGc_p/k$), with D = tube diameter, G = mass flux, h = heat transfer coefficient, c_p = fluid specific heat, and k = fluid thermal conductivity, clearly shows the effect of oxide contamination (measured in ppm of O_2) on the heat transfer. A second illustration of the sensitivity of heat transfer to

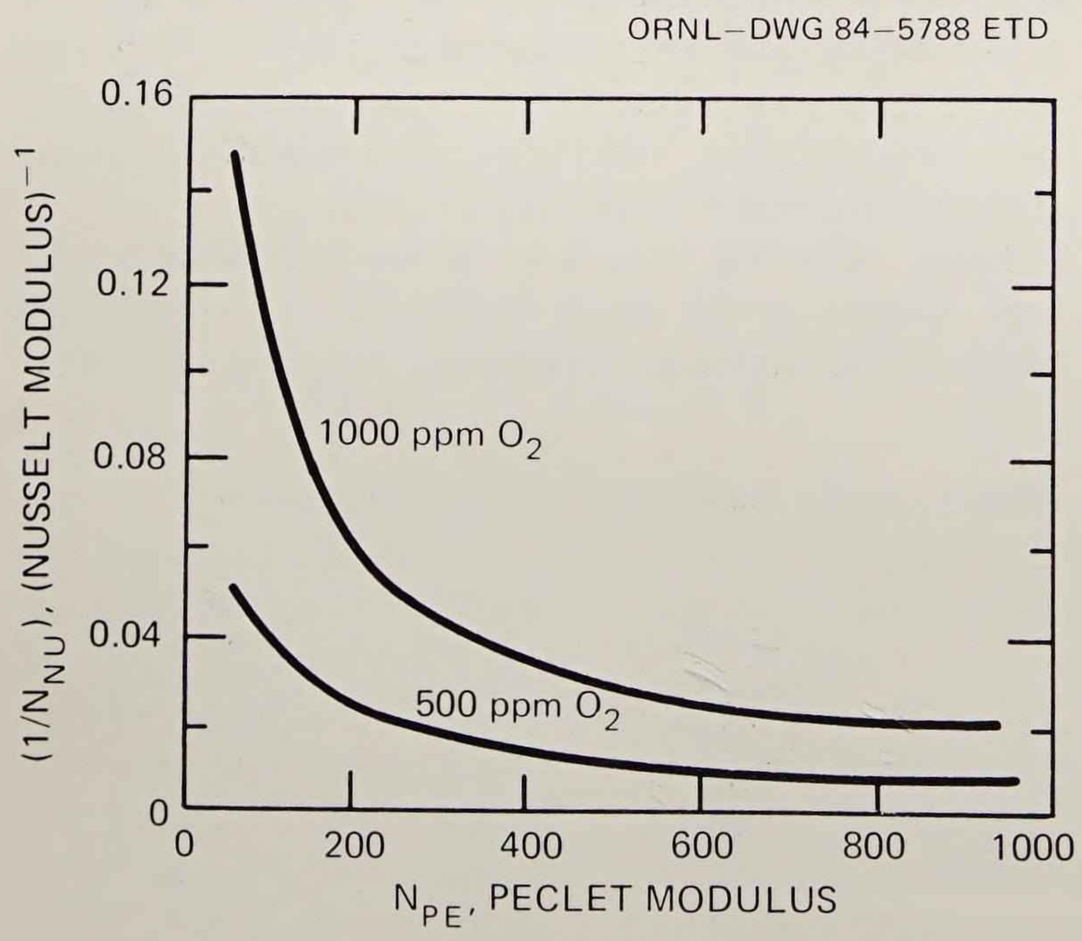


Figure 1 *Effect of Oxygen Impurity on Heat Transfer with Sodium.*

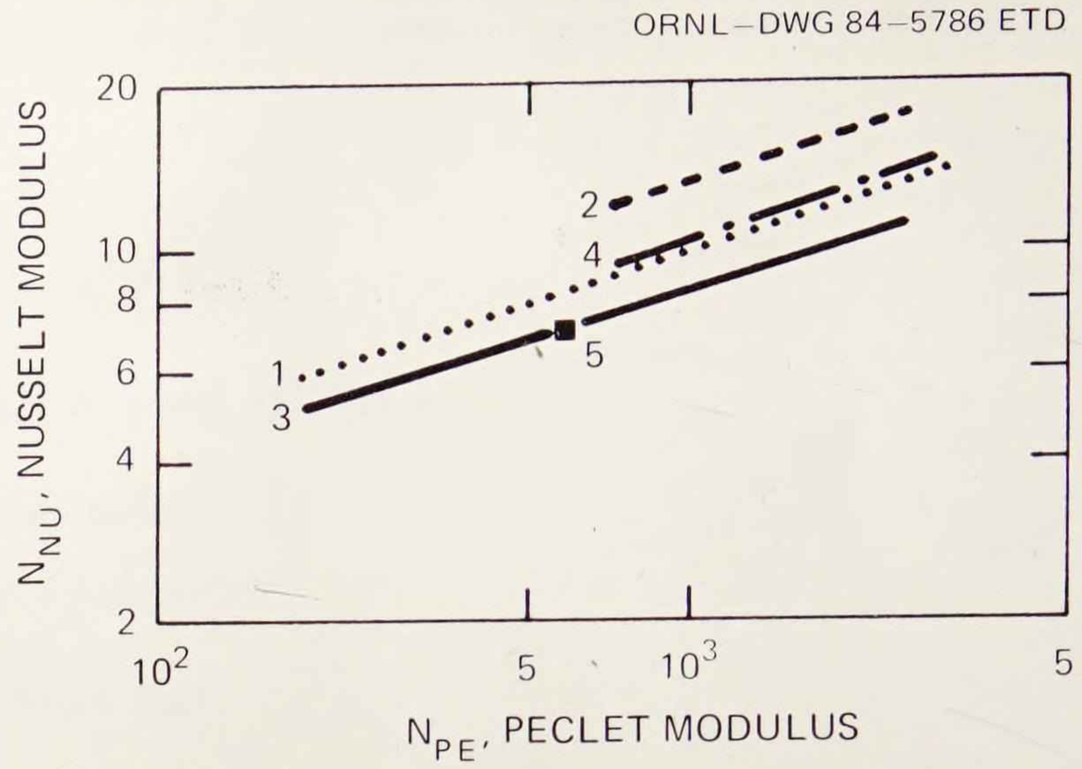


Figure 2 *Effect of Oxide/Nitride Contamination on Lithium Heat Transfer—1) initial charge of lithium; 2) introduction of fresh purified charge; 3) after dump of second charge to sump and recharge; 4) in situ repurification; and 5) single point after 2nd dump to sump and recharge.*

surface contamination is shown in Figure 2, where data obtained at ORNL in a small lithium forced-convection loop are compared. The sequence of events pictured was as follows:

1. Curve 1—results with initial charge of lithium to system
2. Curve 2—results after dump of initial charge and introduction of fresh purified charge
3. Curve 3—results after dump of second charge to sump, mixing with sump contents, and subsequent recharge into system
4. Curve 4—results after some *in situ* repurification
5. Curve 5 (single data point)—results after 2nd dump to sump, mixing with sump fluid, and recharge into system.

While termination of the program funding for this latter study prevented quantification of the results, the data do show that relatively minor amounts of surface contamination by lithium oxides (and possibly nitrides) can cause substantial changes in the heat transfer (a factor of perhaps 2 in Nusselt modulus). Means for obtaining and maintaining system coolant purity need demonstration.

Surface Wetting

In a correlary aspect, the high chemical activity of the alkali metals promotes surface wetting (through reaction to eliminate surface metallic oxides, adsorbed gases, and residual oils/greases). For single-phase heat transfer, this is of some consequence in that data with mercury on wetted surfaces (Friedland 1961) indicate that heat transfer is not affected by entrained inert gases; while with the surface unwetted, the inert gas blanketing the surface reduces heat transfer by as much as 30%.

Table 2 *Wall Superheat Estimates for Boiling of Alkali Liquid Metals*

Fluid	Superheat for boiling initiation (°C)	
	Normal surface	Polished surface
Water	17	50
Sodium	144	433
Potassium	69	208
Rubidium	56	167
Cesium	39	117

Of much greater significance is the effect of surface wetting on two-phase heat transfer. An instructive analysis by Krakoviak (1963) showed that the superheat (wall to saturated fluid temperature difference, ΔT_{sat}) required to initiate boiling on a surface was inversely proportional to the radius of the available nucleating cavities. Due to the "cleaning" capability of the alkali liquid metals, as noted above, the population of operable cavities is skewed to the small sizes.

As a first approximation, the wall superheat requirement for boiling of the alkali metals can be determined through comparison with data for water, thus circumventing the need to know r_c, the critical cavity radius. Using as a base $\Delta T_{sat} = 17°C$ for water boiling on a commercial metallic surface (a normal cavity distribution) and $\Delta T_{sat} = 50°C$ for boiling on a polished and degreased glass surface (nucleating sites skewed to small sizes), estimated superheats for alkali metal boiling are as given in Table 2.

Experimental studies (Hoffman and Krakoviak 1964) with potassium boiling at high surface heat flux in a vertical stainless steel tube showed the high amplitude surface temperature oscillations predicted by analysis. Extended analysis and further experimentation on surfaces containing artificial cavities (Edwards and Hoffman 1965) provided quantitative confirmation. Data obtained by these latter investigators for potassium in forced convection boiling on a smooth surface are shown in Figure 3 (solid symbols); note that superheats of the order of 280°C were sustained. By comparison with the curves developed from theory, the effective cavity size on the smooth surface is suggested to be of the order of 2.5×10^{-5}cm radius.

Since the radial temperature profile for liquid metals in forced flow is relatively flat, the energy stored in the flow is high; and vaporization on nucleation is very rapid. The pressure pulse associated with this cyclic superheating-vaporization behavior is intense, and extended operation in this mode could lead to substantial mechanical damage to the system.

Means for effecting nucleation at lower wall superheats have been tested and shown to be successful; for example, ORNL investigators have studied the nucleation characteristics of reentrant cavities artificially formed in the boiling surface and of rings around the heater rod that leave a thin annular gap for vapor generation. Superheats measured with reentrant cavities of 5.5×10^{-3}cm and 7.5×10^{-3}cm radius—shown by the lower data set (open symbols) in Figure 3—are substantially reduced (to about 7°C) from those on the as-received smooth surface. Comparison with prediction is quite reasonable. This result needs demonstration under the microgravity conditions of earth orbit.

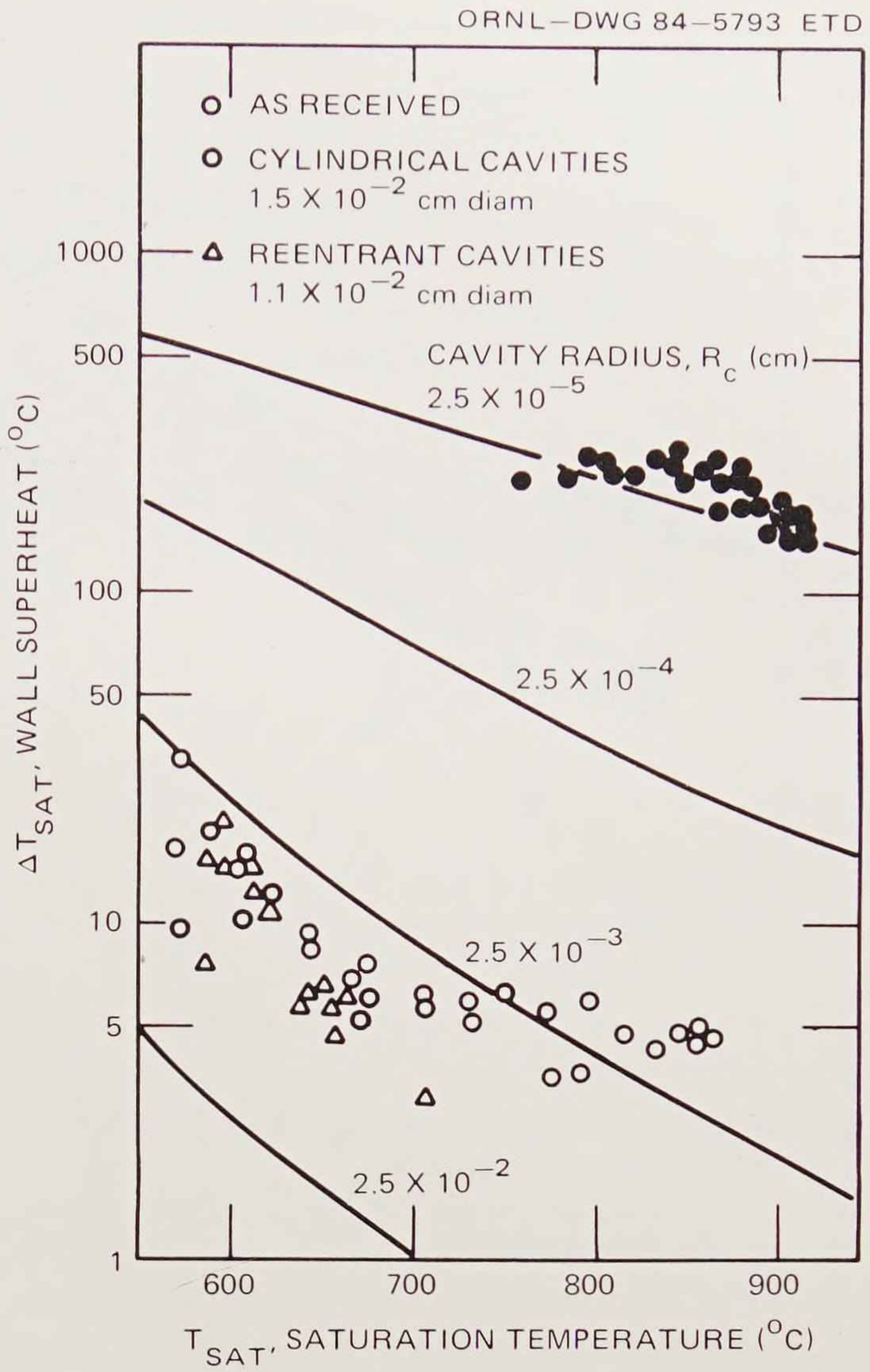


Figure 3 *Potassium Forced-Convection Boiling on a Surface with Reentrant Cavities.*

Liquid Metal Heat Transfer

Liquid metal heat transfer is described in Figure 4 in terms of the dependence of the Nusselt modulus on the Peclet modulus (Reynolds–Prandtl product); the limiting cases of constant wall heat flux and constant wall temperature heat transfer in circular tube geometry as derived from theory (Martinelli 1947 and Lyon 1951) are given. Compared with theory are three data sets typical of those obtained in experimental studies on heat transfer with alkali metals in forced convection flow through circular tubes (cross hatched regions). A generally accepted empirical correlation is also shown (Lubarsky and Kaufman 1956). While some of the

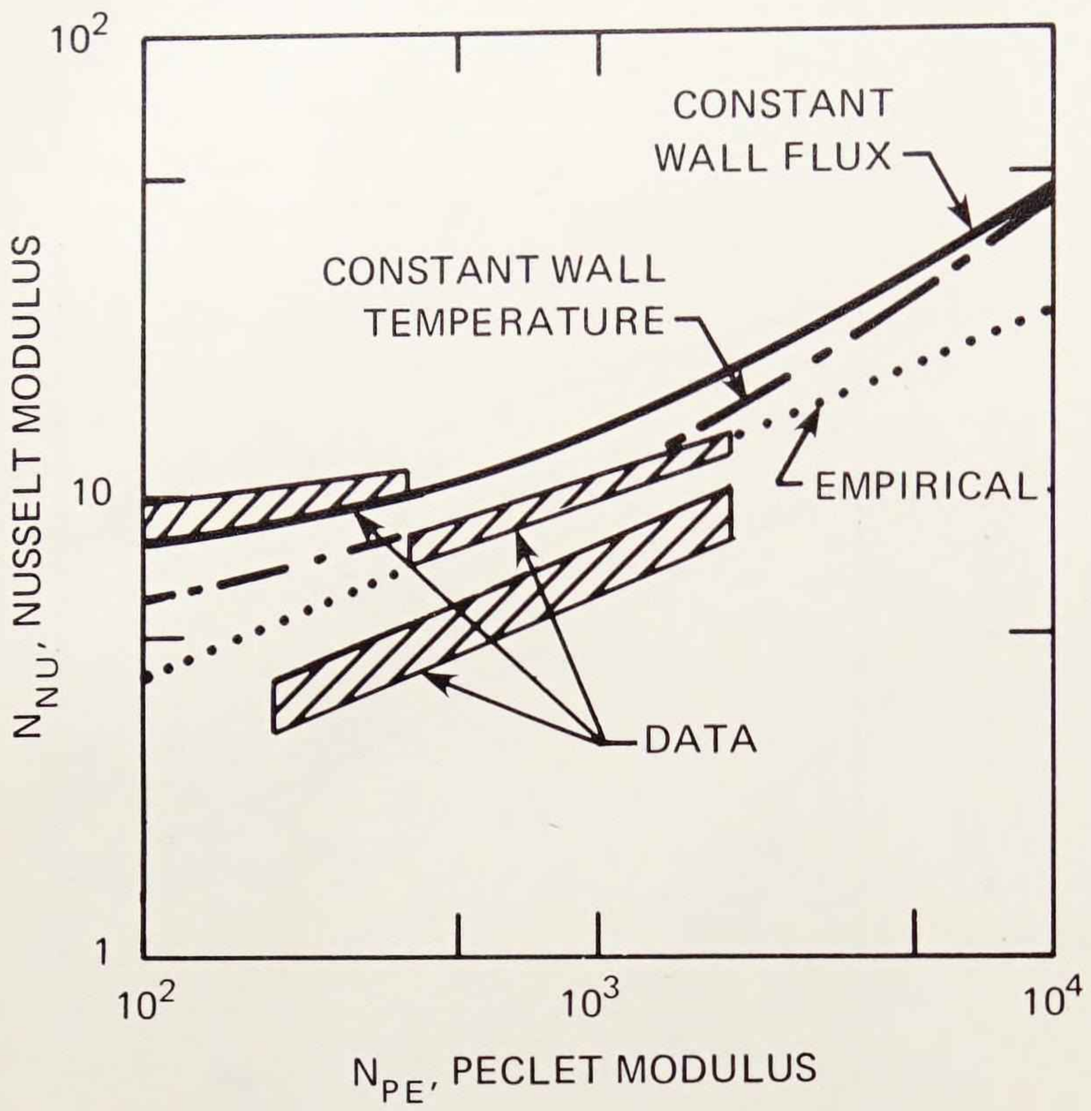


Figure 4 *Comparison of Liquid Metal Heat Transfer Theory and Experiment.*

observed discrepancy between data and theory can be ascribed to the anomolous characteristics of alkali liquid metals discussed in the previous section, Figure 4 illustrates the uncertainty that exists in the description of liquid metal heat transfer as it impacts optimizing the thermal design of space nuclear heat exchange systems where weight/volume considerations are paramount. These uncertainties extend into the realm of rod bundle heat transfer, where only limited experimental confirmation of theory exists.

The energy conservation equation for liquid metal heat transfer simplifies to the form:

$$N_{\mathrm{Nu}} = A + B\left(\frac{\epsilon_H}{\epsilon_M} N_{\mathrm{Pe}}\right)^C, \qquad (1)$$

where the eddy diffusivity ratio, ϵ_H/ϵ_M (thermal /momentum), is generally assumed to be unity and the constants A, B, and C have been developed both theoretically and extracted from experimental data for several important geometries (Table 3). This correlation results from substantive simplifiction of the general energy equation; thus, it has been assumed in obtaining Equation 1 that:

1. flow is incompressible and plug-type,
2. properties are not temperature dependent,
3. there are no volumetric heat sources,
4. turbulent thermal diffusion is represented by the molecular law,
5. axial thermal diffusion is neglected, and
6. the geometry is symmetrical.

Table 3 *Constants for Use in Equation 1*

Geometry	Boundary condition	A	B	C
Tubes	Constant wall flux	7.0	0.025	0.8
	Constant wall temperatures	5.0	0.025	0.8
	Empirical		0.625	0.4
Parallel plates	Constant wall flux	5.8	0.020	0.8
Rod bundle	Parallel flow	A[a]	0.0155	0.86
	Empirical		B[b]	0.45

[a] $A = 6.66 + 3.126\ (\mathrm{P/D}) + 1.184\ (\mathrm{P/D})^2$ for rod pitch (P) to diameter (D) ratios > 1.35.
[b] $B = 0.58\ (D_e/D)^{0.55}$, where D_e = bundle equivalent diameter.

A semi-quantitative examination of several of these assumptions provides an indication of the state of uncertainty associated with the use of the theoretically derived heat transfer correlations:

Axial Diffusion

For $N_{\mathrm{Pe}} \sim 10$, the error in N_{Nu} is estimated to be about 5%; for $N_{\mathrm{Pe}} > 100$, this error reduces to about 1%.

Eddy Diffusivity Ratio

From experimental measurements, the eddy diffusivity ratio in Equation 1 can be described by:

$$\frac{\epsilon_H}{\epsilon_M} = 0.0046\left(\frac{N_{\mathrm{Pe}}}{N_{\mathrm{Pr}}}\right)^{0.46}, \qquad (2)$$

where N_{Pr}, the Prandtl modulus $= c_p\mu/k$ with μ being the fluid viscosity. Evaluation for several values of the Peclet modulus indicates ϵ_H/ϵ_m to vary from 0.32 at $N_{\mathrm{Pe}} = 50$ to 1.26 at $N_{\mathrm{Pe}} = 1000$.

Plug Flow

The ratio of the Nusselt modulus for fully developed flow to that for plug flow (K^+) is shown in Table 4. The plug flow assumption thus introduces an error of 6% (conservative) at low N_{Pe} to 66% (optimistic) at high N_{Pe} for flow in a circular tube.

Table 4 *Ratio of Fully Developed to Plug Flow Nusselt Modulus*

	K^+	
Geometry	$N_{\mathrm{Pe}} = 1000$	$N_{\mathrm{Pe}} = 50$
Parallel plates	1.80	1.04
Circular tube	1.66	0.94

System Thermal Hydraulics

In addition to the limits imposed by alkali liquid metal thermal behavior, chemical activity, and theory uncertainties, each component required in a Rankine

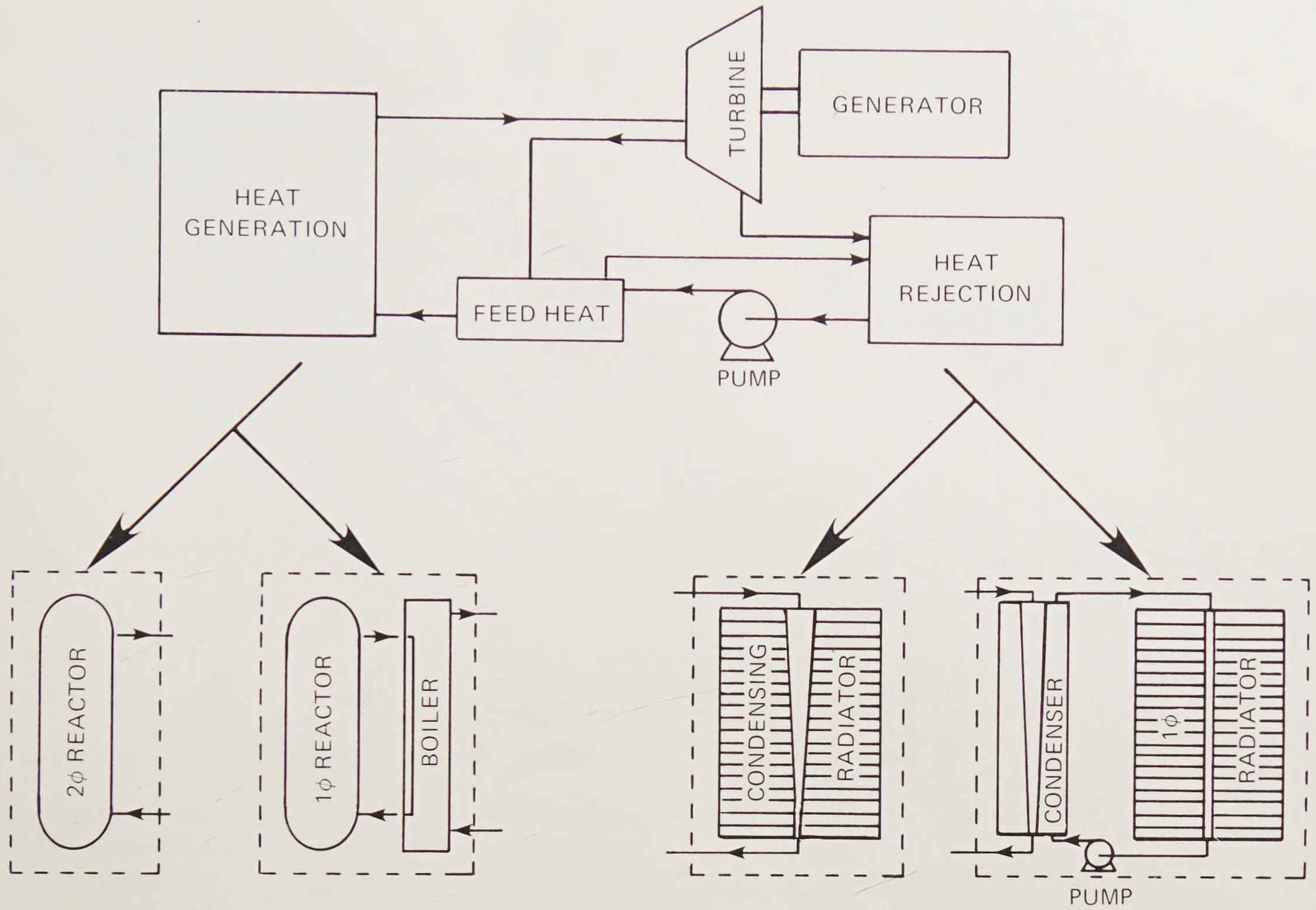


Figure 5 *Schematic of Liquid Metal Cooled Reactor / Liquid Metal Rankine Cycle Options.*

cycle system has other limitations indirectly related to the working fluid. These limitations must also be addressed before components can be designed and system operating limits established.

Several liquid metal Rankine cycle options are available which trade off thermal and hydraulic stability problems against system complexity and reliability; four are shown in Figure 5. The most simple mechanically incorporates a liquid metal boiling reactor and a direct condensing radiator (single loop system); the most complex, uses a liquid cooled reactor with a separate boiler and a tapered tube condenser with separate liquid cooled radiator circuit (3 loop system). It has been estimated that a 20% increase in mechanical reliability and a 30 to 40% decrease in system weight could be realized by utilizing a single loop rather than a three loop system (Fraas and Michael 1966).

Problems associated with liquid metal Rankine cycle systems generally parallel those encountered in other two phase flow applications; principally, control of the liquid-vapor interface. However, in the microgravity environment of the space application, these problems can be more acute. The paragraphs following identify these concerns for the principal system components.

Radiator/Condenser

The largest component (by weight or volume) in the rankine cycle power system is the radiator or condenser/radiator. Since liquid metal cycles operate at low pressure with high sink temperatures, radiators for this system will be smaller and lighter than for systems using other thermodynamic fluids. Several radiator types have been suggested: (1) direct where the working fluid condenses within the radiating surfaces, and (2) indirect where the condensing working fluid transfers its thermal load to a separate radiator circuit. The indirect radiator can be either pumped single-phase liquid loops or heat pipe arrays.

The simplest of these concepts, the direct condensing radiator (Figure 6), utilizes reflectors at the rear surface of tapered condenser tubes to increase the effective radiative area and to act as meteoroid bumpers, thus reducing needed armor load on the tube surface. Radiating surface temperatures very close to the liquid metal saturation temperature are possible, since temperature drops associated with condensation at the inside surface and conduction through the tube wall are both small. As noted, the attendant higher radiating surface temperature results in reduced radiator surface area and, hence, weight. Control of the two-phase condensing liquid may be a problem, since the condenser exit must be 100% liquid in order to prevent pump cavitation. The suggested tapered tube geometry (Miller 1962) generates proper liquid film flow through a combination of surface tension and vapor velocity drag effects, mitigating microgravity effects. Limited analysis of ta-

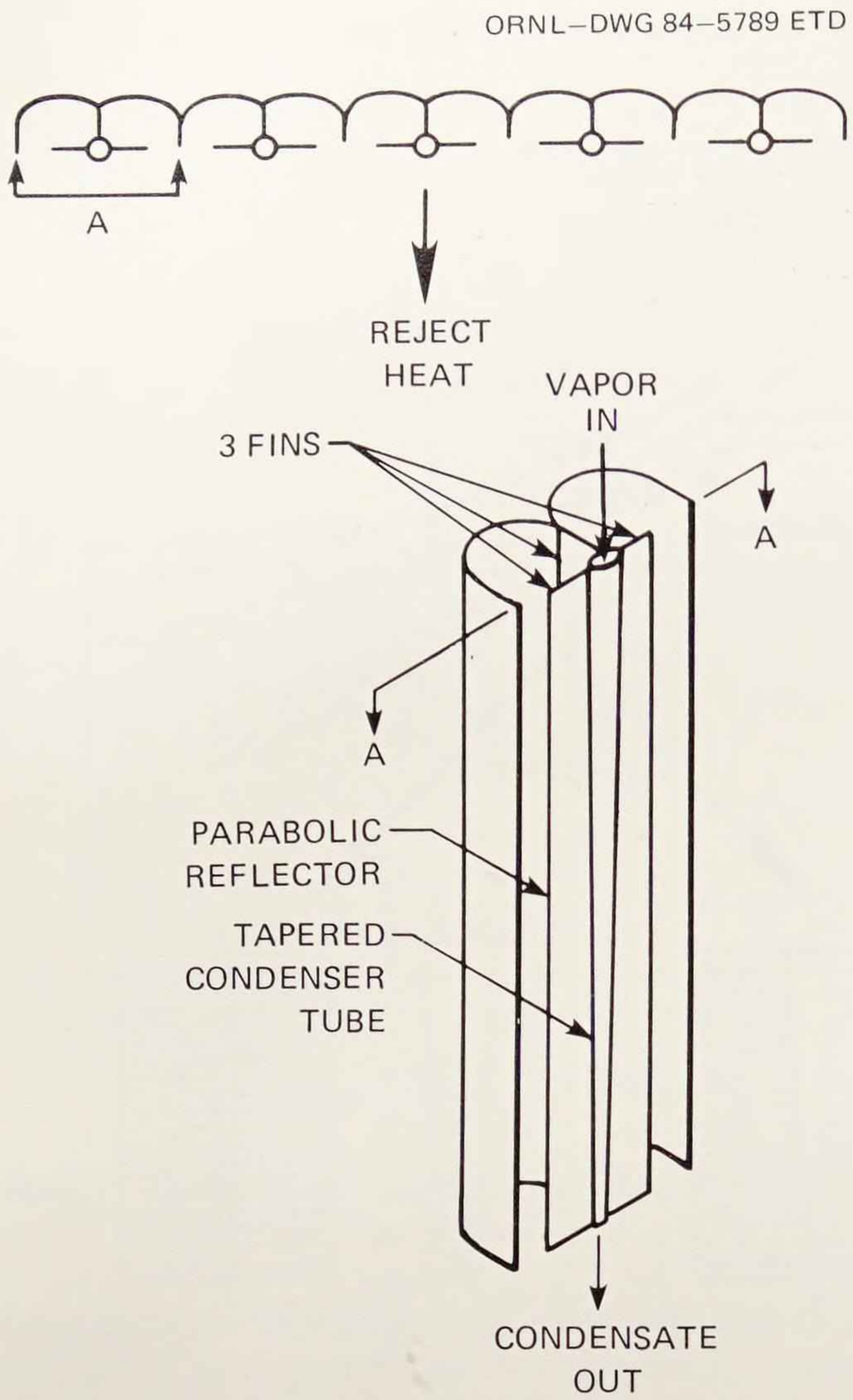


Figure 6 *Schematic of a Direct Condensing Radiator Concept.*

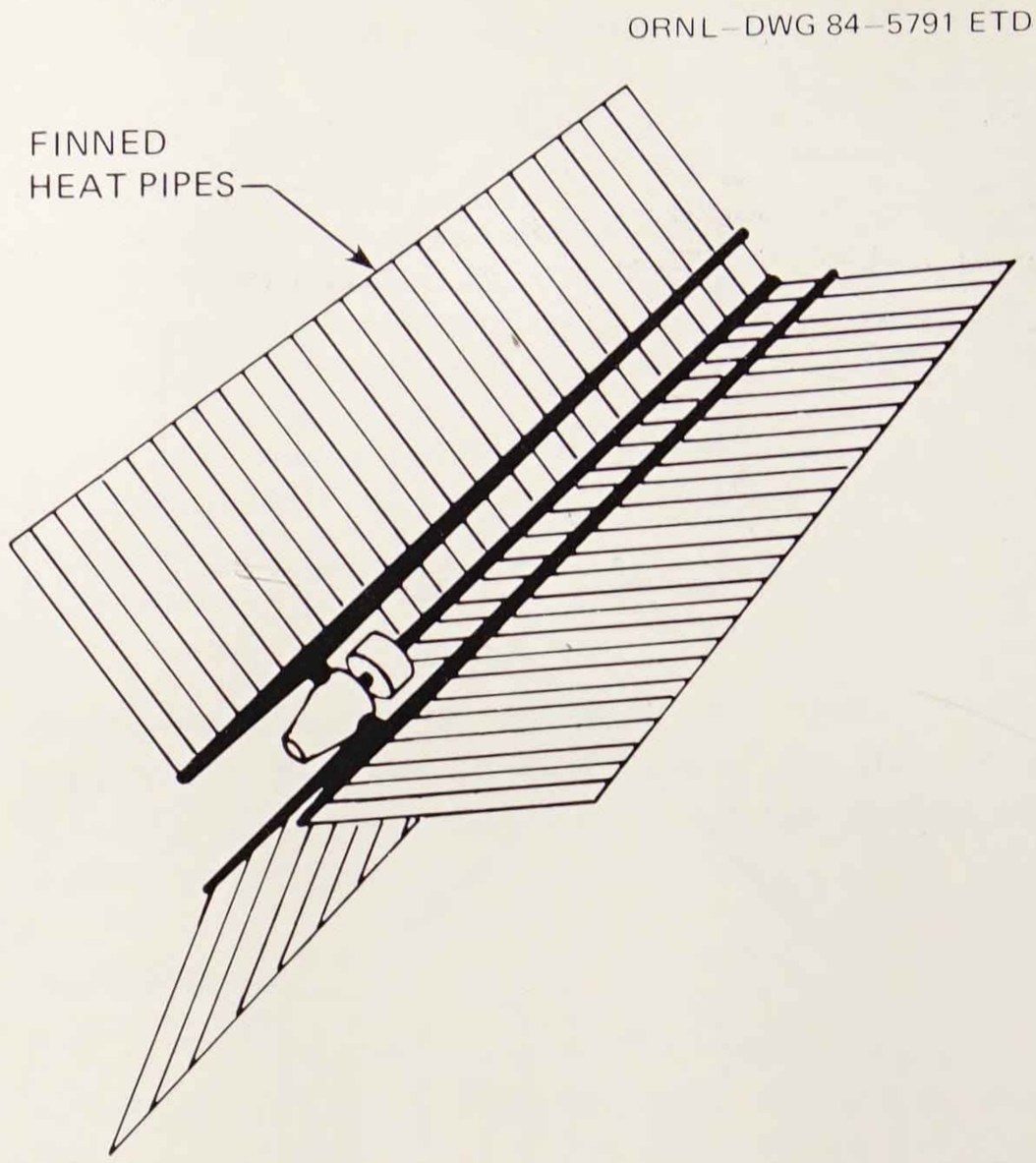


Figure 7 *Schematic of a Heat Pipe Radiator Concept.*

pered tube condensers (Korsmeyer 1963) showed encouraging results. However, in this radiator concept, vulnerability exists for loss of the full working fluid inventory through meteor impact.

A variant on this concept (see Figure 5) interposes an intermediate heat exchanger between the cycle fluid and the radiator. The power conversion cycle working fluid condenses in tapered tubes and transfers heat to a single-phase liquid pumped loop. Some radiator circuit redundancy can be accommodated, thus avoiding catastrophic effects due to meteoroid impact. The introduction of the intermediate heat exchanger (the condenser) does result in some loss in cycle efficiency by lowering the radiating surface temperature.

A second type of indirect heat sink offers maximum protection against meteoroid impact risks by transferring the condensing heat load to the radiating surface through an array of liquid metal heat pipes (Figure 7). The alkali metal vapor (for example, potassium) in the Rankine power conversion cycle condensing on the inboard end of a bank of heat pipes vaporizes the heat pipe fluid (for example, cesium), thus transporting the reject heat to the radiator surface. The large number of individual heat pipes assures that loss of some through meteoroid penetration will have little impact on overall system performance. Two-phase liquid control in this configuration may be more difficult than in the previous two concepts due to intrusion of the evaporator end of the heat pipes into the two-phase flow in the condenser channels.

A novel radiator concept has been recently proposed (Mattick and Hertzberg 1982) which uses direct radiation from hot liquid droplets for heat rejection. The droplets are sprayed as a thin sheet directly into space and re-collected an appropriate distance downstream. Since the droplets can be small (and hence, provide very large total surface area radiating to the space environment) and since the temperature drop associated with a containment surface is eliminated, significant weight savings over conventional radiators is possible. Although generally associated with other thermodynamic cycles, the concept can be applied to the Rankine cycle. Thus, in Figure 8, a portion of the working fluid flow extracted upstream of the primary circulating pump would be processed through a "liquid droplet radiator." The collected cooled droplets would be used in a contained spray chamber to condense the turbine exit vapor. Substantial mechanical development of the concept is needed. Flash vaporization of the liquid droplets on exposure to the vacuum environment of space may be a significant problem through loss of thermodynamic working fluid inventory; other concerns include condensation on cold external surfaces of the power system and/or condensed cloud formation around the spacecraft. Control of droplet trajectory may also be difficult, particularly under maneuvering conditions such as accelerations/decelerations associated with orbital repositioning or reorientation of system axis.

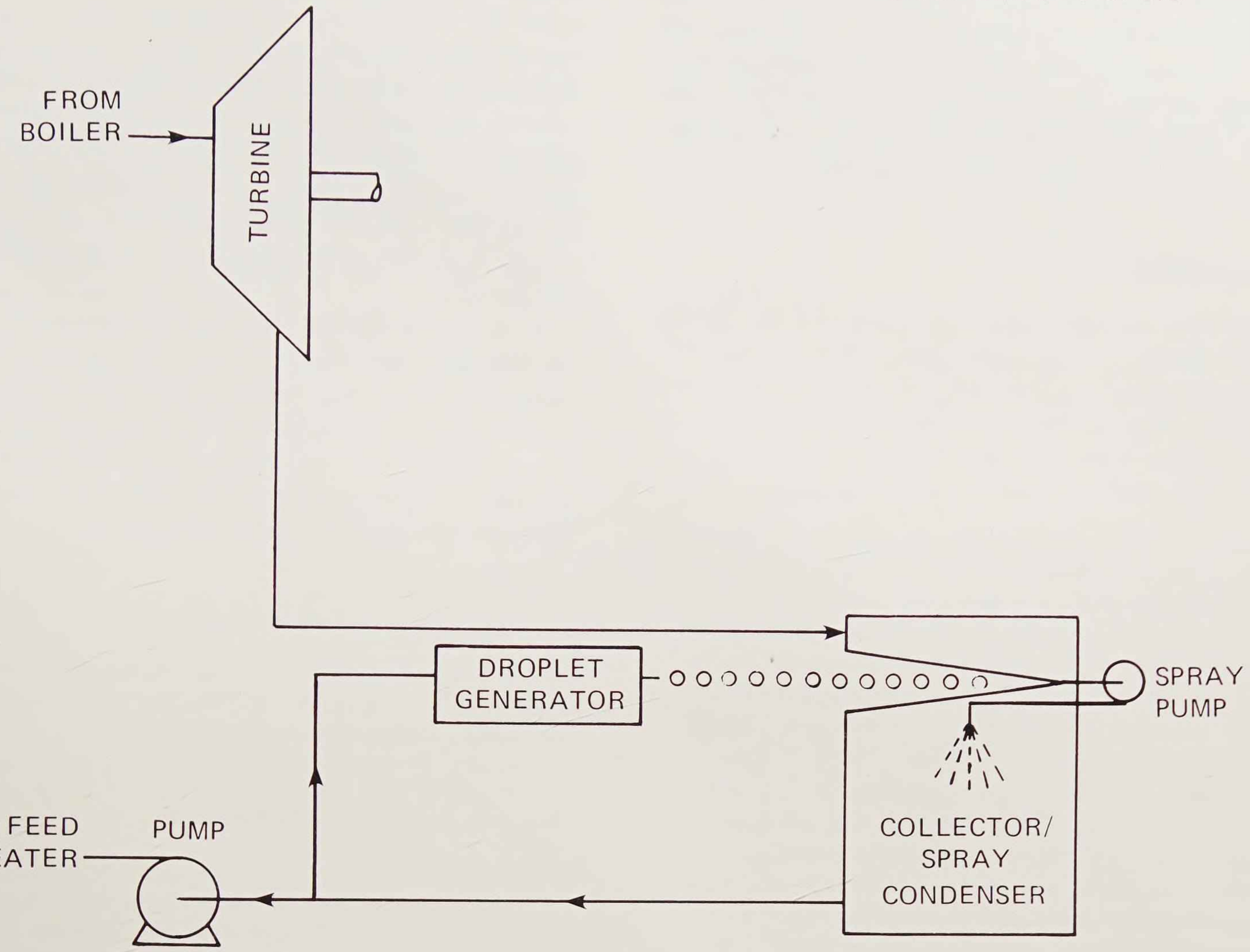


Figure 8 *Schematic of a Liquid Droplet Radiator Concept.*

Boiler

Two conventional boiler concepts have been proposed for space power applications, both of which depend on good liquid control for operational success. The first design uses liquid-vapor separation devices at the boiler exit to extract the liquid from a relatively low quality, two-phase flow and returns the liquid to the boiler inlet; the second is a once-through boiler that evaporates the liquid to high qualitity in a single pass. For each configuration, nucleate boiling occurs at the heated surface (fuel rods or boiler tubes), and removal of the vapor from the surface and transport of the vapor to the boiler exit in the presence of low-gravity forces must be a concern. Incomplete knowledge in respect to alkali metal boiling inserts a degree of uncertainty into standard operating characteristics of the alkali metal power generation and conversion systems and, to an even greater extent, into any off-normal operation.

For the low-quality boiler, the principal issue rests on the performance of the liquid vapor separator in the microgravity field to assure the necessary high-quality flow at the turbine inlet. This can be accomplished by inducing a swirl flow that moves the liquid to the separator surface from which it can be extracted by flow dividers or through porous plugs. Research must address the swirl generation (strength and maintenance) necessary to achieve the required levels of liquid separation and the effects of both thermal and acceleration transients on system performance. In the thermal aspect, though data exist on the critical heat flux with boiling alkali metals and on the superheat required for bubble nucleation, refinement of this information is needed to maximize system efficiency while assuring against heat transfer surface melting or other physical damage.

In the high-quality boiler, boiling is accomplished inside tubes heated by single-phase liquid cooling the nuclear core. To achieve complete evaporation within a reasonable boiler length, all liquid must remain on the heated surface. Again, swirl flow inducers are used to suppress the normal flow regime transitions in forced convection boiling and to return any entrained liquid to the tube inside surface. Porous surface coatings using surface tension to retain the liquid are a suggested alternative.

A third boiler possibility is a flash evaporator. In this design, liquid heated to a high temperature would be flashed through nozzles to a pressure below the saturation pressure associated with that temperature. The

effectiveness of this process would depend on liquid-vapor heat transfer characteristics and the degree of thermal non-equilibrium introduced into the flow. Nozzle design would be critical in respect to this latter problem and to the avoidance of nozzle erosion. Further systems analysis is needed to establish the viability of this concept.

Conclusions

Alkali liquid metals have been proposed as nuclear reactor coolants and thermodynamic cycle working fluids in space power applications because of their desirable thermophysical properties and good heat transfer characteristics. However, their high chemical reactivity can occasion degraded thermal performance:

1. Oxides/nitrides formed within the liquid flow due to in-leakage of these gaseous contaminants during ground handling or testing can deposit on cooler surfaces, decreasing the effective Nusselt modulus by as much as 100%, and therefore increasing the required heat exchanger size. Quantifying these effects will decrease the required heat exchanger design factors and reduce system mass.
2. Solubility of containment materials in the alkali metal coolant can lead to loss in high-temperature mechanical performance due to selective removal of alloy constituents and to flow blockage due to mass transfer (deposition) of the dissolved material into lower temperature (lower solubility) zones. Consequences (containment damage and/or performance derating to avoid the excessive surface temperatures) can be mitigated by using refractory alloys for which experience indicates reduced mass transfer.
3. Good wetting of metallic heat transfer surfaces by the alkali metals results in skewing of boiling cavity size distributions to the very small sizes, effecting high superheats to achieve bubble nucleation (Δt_{sat} = 100–500°C) and, in consequence, the possibility of equipment damage due to significant temperature and pressure oscillations. Surface designs which decrease the required superheat are necessary before safe operation of the systems can be assured.

In addition to these phenomenological issues embedded directly in the nature of alkali liquid metals, factors associated with liquid-vapor separation and transport (particularly in the low-gravity environment of earth orbit) and with uncertainties in heat transfer correlations (particularly in rod bundles) can affect the design and performance of the Rankine power conversion cycle. Discrepencies between existing heat transfer theory and measured data are presently as large as 50%; while other parameters such as eddy diffusivities, which are not completely quantified, seem to affect heat transfer to a somewhat lesser extent. Experimental characterization of the heat transfer will be necessary before detailed system design can proceed.

While problems with liquid metals in Rankine cycle systems/components will generally parallel those encountered with other two-phase fluids in similar equipment, the low-gravity condition will exacerbate liquid-vapor interface control. The effect of the micro-gravity environment on thermal mixing within the reactor core, transient thermal and hydraulic response of the sytem, and surface blanketing by inert gas are relatively unknown. Ingenious earth-based experiments and ultimately zero gravity experiments will be required to resolve these issues in order to obtain optimum system performance.

All of the problems identified are amenable to solution through improvement in the understanding of the thermal mechanisms operant, refinement of correlations for heat transfer in realistic rod bundle geometries, and demonstration that the effects of the microgravity environment on system thermal, hydraulic, and mechanical behavior can be mitigated by proposed concepts.

Acknowledgments

Oak Ridge National Laboratory is operated for the U.S. Department of Energy by Martin Marietta Energy Systems, Inc., under contract DE-AC05-84OR21400.

References

Borishanskii, V. M., N. I. Ivashchenko and T. V. Zablotskaya (1961) "The Calculational Heat Transfer in Tubes for the Tubulent Flow of Liquids with Small Prandtl Numbers", *Atomnayz Energiya*, **II**, pp. 426–430.

Cooke, J. W. (1964) "Thermophysical Property Measurements of Alkali Metals," in *Proceedings of 1963 High-Temperature Liquid-Metal Heat Transfer Technology Meeting*, Oak Ridge National Laboratory Report, Report ORNL-3605, pp. 334–350.

Edwards, J. A. and H. W. Hoffman (1965) "Superheat with Boiling Alkali Metals," in *Proceedings of Conference on Application of High-Temperature Instrumentation to Liquid Metal Experiments*, Argonne National Laboratory Report ANL-7100.

English, R. E., R. L. Cummings, R. L. Davies, T. P. Moffitt, and U. H. von Glahn (1966) "Potassium Rankine Systems Technology" in *Space Power Systems Advanced Technology Conference*, NASA Report SP-131, pp. 201–238.

Fraas, A. P. and J. W. Michel (1966) *Comparison of 1-, 2-, and 3-Loop Systems for Nuclear Turbine-Generator Space Power Plants of 300 kW to 5 MW of Electrical Output*, Oak Ridge National Laboratory Report ORNL-TM-1366.

Fraas, A. P. (1967) *Summary of the MPRE Design and Development Program*, Oak Ridge National Laboratory Report ORNL-4048.

Friedland, A. J., O. E. Dwyer, M. W. Maresca and C. F. Bonilla (1961) "Heat Transfer to Mercury in Parallel Flow through Bundles of Circular Rods," in *International Developments in Heat Transfer, Proceedings of the 1961–62 International Heat Transfer Conference*, pp. 526–534.

Hoffman, H. W. and A. I. Krakoviak (1964) "Forced-Convection Saturation Boiling of Potassium at Near Atmospheric Pressure," in *Proceedings of 1962 High-Temperature Liquid-Metal Heat Transfer Technology Meeting*, Brookhaven National Laboratory Report BNL-756, p. 182.

Jones Jr., J. E., R. E. MacPherson, and J. P. Nichols (1985) "Multi-megawatt Space Nuclear Power Concept," in *Space Nuclear Power Systems 1984*, M. S. El-Genk and M. D. Hoover eds., Orbit Book Co., Malabar, FL.

Krakoviak, A. I. (1963) *Notes on the Liquid-Metal Boiling Phenomenon*, Oak Ridge National Laboratory Report ORNL/TM-618.

Korsmeyer, R. B. (1963) *Condensing Flow in Finned, Tapered Tubes*, Oak Ridge National Laboratory Report ORNL/TM-534.

Lubarsky, B. and S. J. Kaufman (1956) *Review of Experimental Investigations of Liquid-Metal Heat Transfer*, NACA Report 1270.

Lyon, R. N. (1951) "Liquid-Metal Heat Transfer Coefficients," *CEP*, **47**: 75–79.

Martinelli, R. C. (1947) "Heat Transfer to Molten Metals," *Trans. ASME* **69**: 947–959.

Miller, A. J. (1962) *Space Power Program Semiannual Progress Report for Period Ending December 31, 1961*, USAEC Report ORNL-3270, Oak Ridge National Laboratory, pp. 54–55.

Mattick, A. T. and A. Hertzberg (1982) "Liquid Droplet Radiator—An Ultralight Weight Heat Rejection System for Efficient Energy Conversion in Space," *Acta Astronautica*, **9**(3): 165–172.

Untermeyer, S. (1949) *Heat Transfer Experiments with Bismuth Alloys*, Argonne National Laboratory Report.

Space Nuclear Power Systems 1984
Edited by M. S. El-Genk and M. D. Hoover
© Orbit Book Company, Malabar, FL, 1985

Chapter 48

Heat Pipe Technology Issues

M. A. Merrigan

P. O. Box 1663
Los Alamos National Laboratory
Los Alamos, NM 87545

Recent heat pipe development work at Los Alamos National Laboratory has involved performance testing of typical space reactor heat pipe designs to power levels in excess of 19 kW/cm^2 axially and 300 W/cm^2 radially at temperatures in the 1400 to 1500 K range. Operation at conditions in the 10 kW/cm^2 range has been sustained for periods of up to 1000 hours without evidence of performance degradation. The effective length for heat transport in these heat pipes was from 1.0 to 1.5 M. Materials used were molybdenum alloys with lithium employed as the heat pipe operating fluid. Shorter, somewhat lower power density, molybdenum heat pipes have been life tested at Los Alamos for periods of greater than 25,000 hours at 1700 K with lithium and 20,000 hours at 1500 K with sodium. These life test demonstrations and the attendant performance limit investigations provide an experimental basis for heat pipe application in space reactor design and represent the current state-of-the-art of high temperature heat pipe technology.

Introduction

Heat pipes are a self-starting, self-regulating, high efficiency means of transferring heat under high vacuum and zero gravity conditions. They are a logical choice for incorporation into space nuclear power system designs. Many current design concepts employ heat pipes both for high temperature heat transport from the reactor to the power converters and in system primary heat rejection.

Additional uses for heat pipes at or near reactor temperatures may be found in applications such as electromagnetic pump cooling, radiation shield cooling, control drum and motor cooling, and in start-up and shut-down thermal conditioning of liquid metal pumped heat transfer loops. As detail designs are developed heat pipes will also be used in the control of power conditioning equipment, in control electronics cooling, and in low temperature waste heat radiators for these systems.

Figure 1 illustrates these potential applications schematically. Current attention is focused on the two direct heat transport applications shown; primary heat transport from the reactor to the power conversion system and reject heat transport from the power conversion system to a surface radiating to deep space. These applications have received the most attention in recent experimental investigations and are the primary interest in current discussions of heat pipe technology.

In these applications the most interesting characteristics of heat pipes are their passive operation and their ability to function over an extreme range of temperature, starting from below the melting temperature of the working fluid, without the need for thermal preconditioning. The passive operation can provide for automatic handling of reactor decay heat as well as for restart after extended periods of nonoperation without the need for stored power for pumps or controls. The fact that heat pipes operate with minimal temperature differences is of importance in radiation coupled systems and in radiant heat rejection systems. Added to these operational advantages is the fact that heat pipe heat transfer systems are, by their nature, highly redundant systems offering multiple, independent heat transfer paths.

Primary Heat Transport Heat Pipes

The operating requirements imposed on heat pipes used as primary heat transport devices in space nuclear

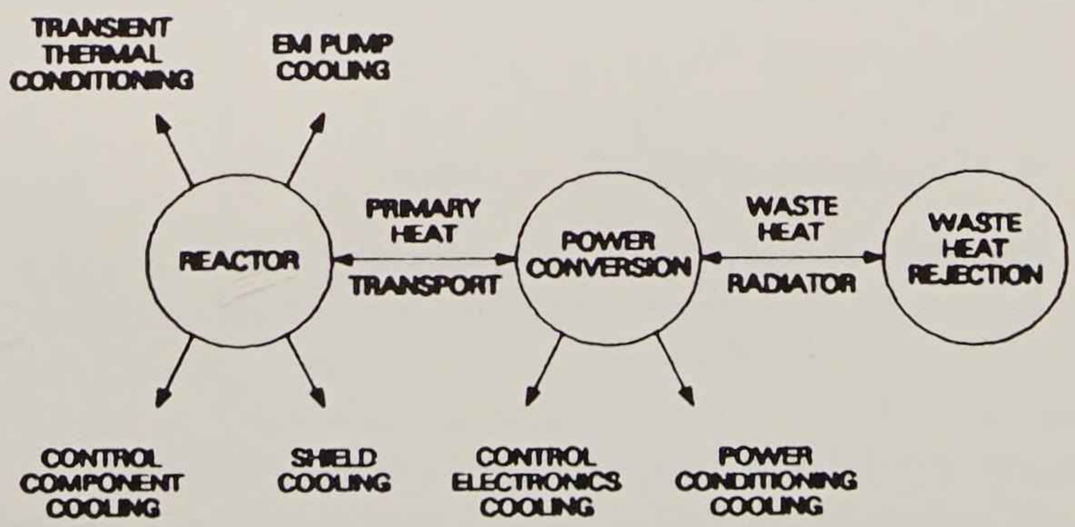


Figure 1 *Heat Pipe Applications in Space Power Systems.*

power systems are

- Cold start from ~200 K,
- Stable operation during shutdown,
- Restart after shutdown,
- 7–10 yr operating life, and
- Fractional power operation.

Perhaps the most difficult of these requirements to satisfy within the present state-of-the-art will be operation of radiantly coupled heat pipes at a fraction of their design power for extended periods, and the demonstration of stable operation of heat pipes under a wide range of transient conditions. Demonstration of other operational requirements such as low temperature cold start with radiation coupling and extended operation at high temperature without loss of performance, will require further work but should not involve severe development problems.

Critical high temperature, high power applications for primary heat transport will be near the current state of the art of heat pipe technology in terms of power density, operating temperature, and lifetime. Use of heat pipes as the primary nuclear reactor core heat transfer mechanism, coupling directly to the power conversion system, will entail operation of the heat pipes at the reactor core temperature and at high power density. With space nuclear power systems constrained to high operating temperatures by low conversion efficiencies and the need for radiant heat rejection, reactor temperatures will be in the 1000 K to 1700 K range. For the reactor core heat pipes this implies the use of alkaline metal working fluids and refractory alloy structures. Performance characteristics necessary for the reactor core cooling applications will involve radial power densities in the 100 W/cm^2 range and axial power densities of $> 10\ kW/cm^2$ over heat transport distances of 3 to 5 m (Koenig and Ranken 1982). These power levels are necessitated by system weight constraints, which lead to compact reactor designs, and by the need to maintain subcriticality during water immersion in the interests of safety, which requires minimizing heat pipe volume within the reactor core.

Typical values of performance requirements for these primary heat transport applications are

- Temperature: 1000 K to 1700 K,
- Axial power density: 10 to 15 kW/cm^2,
- Radial power density: 50 to 150 W/cm^2,
- Transport distance: 3 to 5 m, and
- Temperature difference: < 10 K.

In applications where the heat pipes are coupled directly into the reactor core there may be an additional requirement for the heat pipes to bend around the radiation shield, incorporating two or more bends of nearly 90° in their length.

In reviewing the status of heat pipe technology in the light of these requirements the heat pipe design may be considered in terms of the physical elements involved, specifically the enclosure, the capillary structure, and the working fluid. Consideration must also be given to the problems involved in assembling these elements into the desired configuration. The resulting heat pipe designs may be characterized in terms of the steady state performance limits implied by the working fluid and operating temperature, and by the transient characteristics.

Enclosure Materials

Over the temperature range of interest for primary heat transport the enclosure material used for the heat pipes will be a refractory material with the usable range for various alloys determined from creep strength considerations. Other criteria of concern in material selection will be the ductile-brittle-transition temperature, chemical compatibility with the heat pipe working fluid and external coolants and, for cases where in-core use is entailed, thermochemical and mechanical compatibility with the fuel in the accompanying radiation environment.

Another factor affecting the choice of alloys will be fabricability, particularly if secondary operations such as bending are entailed in the heat pipe manufacture. In general, heat pipe use will probably not be the criteria of concern in alloy selection for space power systems so long as the heat pipe working fluid does not have excessive vapor pressure at the operating temperature of the system.

Working Fluids

Candidate working fluids in the temperature range of interest for primary heat transport will be the alkaline metals and their alloys. Vapor pressure curves for potassium, sodium, and lithium are given in Figure 2. Design values of operating pressures in heat pipe applications will usually be 0.1 Bar or greater in order to minimize

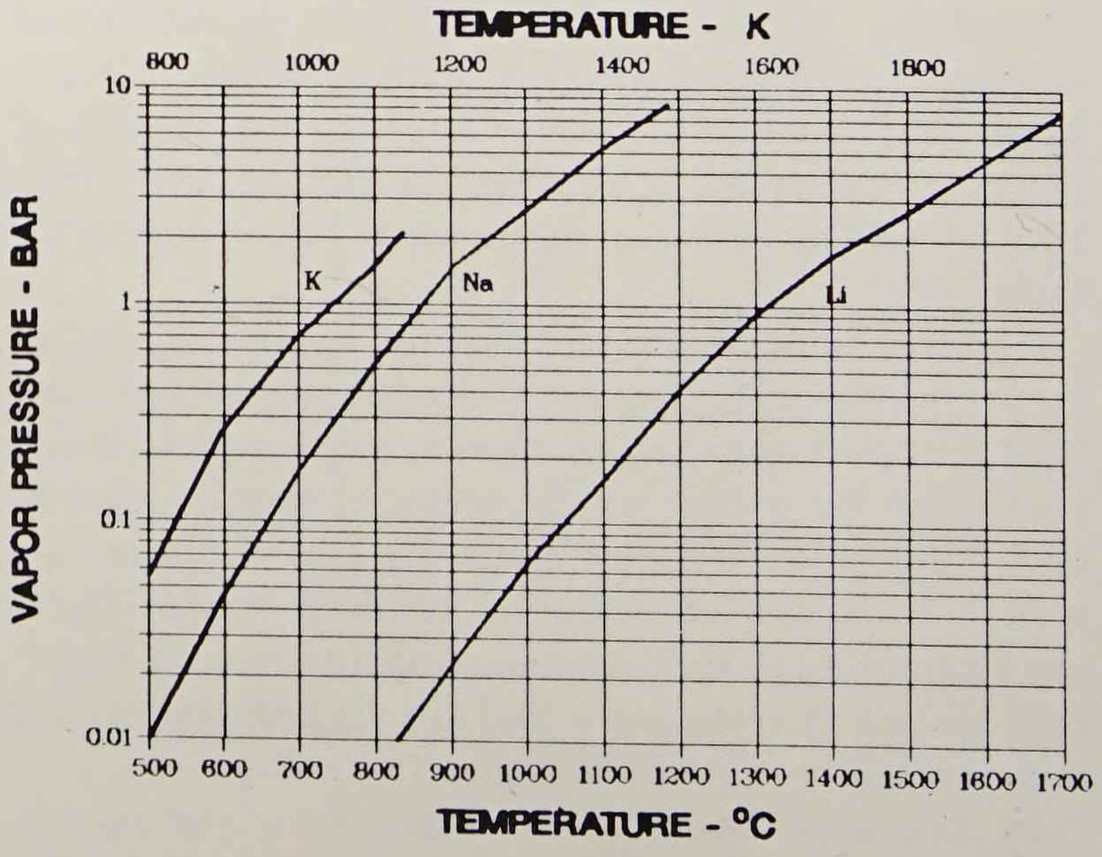


Figure 2 *Liquid Metal Vapor Pressure.*

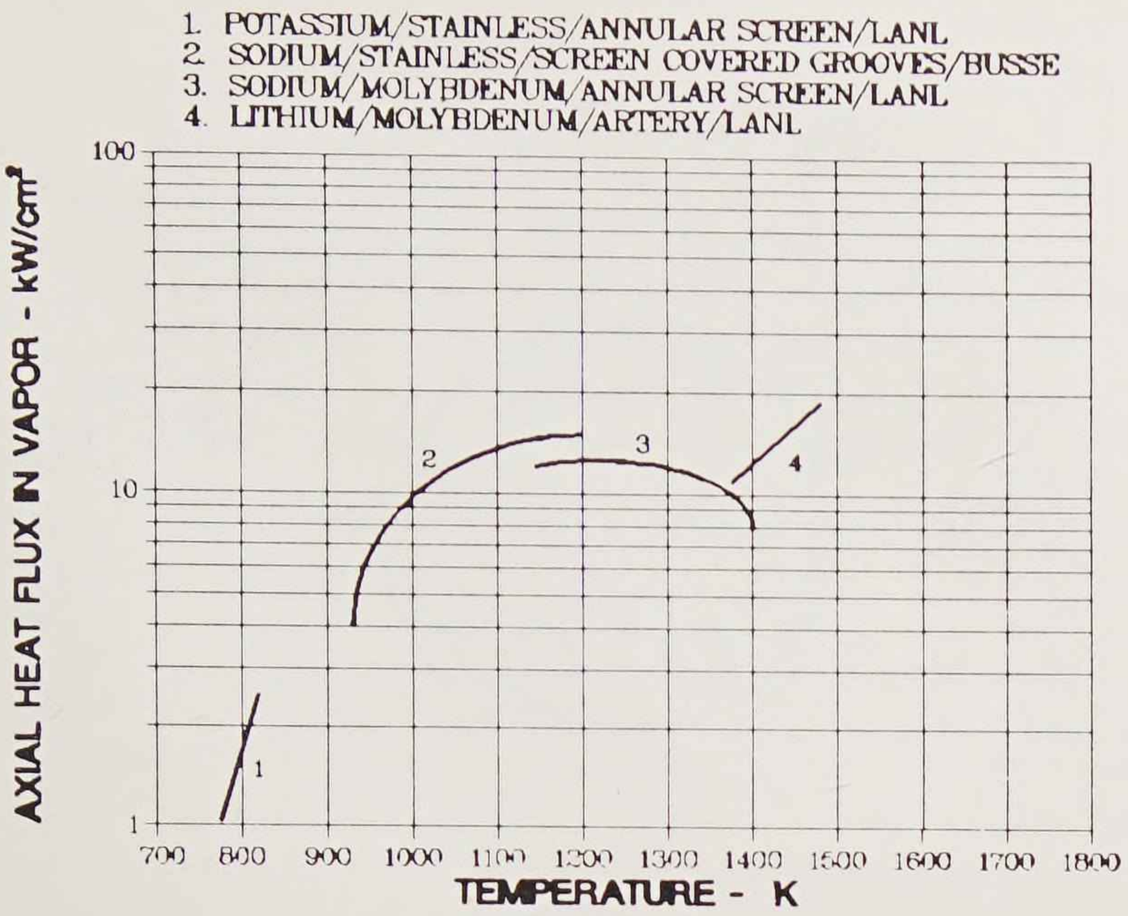


Figure 3 *Demonstrated Values of Axial Heat Flux.*

effects of residual gases or radiation product gases on performance. Upper pressure limits will be determined by the creep strength characteristics of the heat pipe enclosure material.

The usable temperature range of the working fluids will be determined by the heat pipe heat transport capacity as well as the vapor pressure. Maximum demonstrated values of axial heat flux density for alkaline metal heat pipes are summarized in Figure 3. Values in the range of interest for primary heat transport (> 10 kW/cm^2) have been achieved in sodium and lithium heat pipes over the range of 1000 K to 1500 K (Vinz and Busse 1973 and Merrigan et al. 1982). Demonstrated values for radial power density are in excess of 300 W/cm^2 over the entire range from 800 K to 1500 K and therefore not a severe design constraint for current heat pipe cooled reactor designs (Keddy and Martinez 1982).

Wick Materials

These experimentally confirmed radial and axial power density values were achieved in heat pipes designed for extreme performance. Duplication of these values will require the use of some form of arterial heat pipe design with a fine pore wick structure having good permeability. For the typical primary heat transport performance requirements wick structure requirements will be

- Pore diameter: 30–50 μm,
- Permeability: 6×10^{-12} m^2 artery
  6×10^{-14} m^2 annular, and
- Bendable during fabrication.

Values of wick permeability required will depend on the wick configuration used. For the classic artery configuration shown in cross section in Figure 4a the flow path length through the wick structure from the artery to the furthest point of the liquid-vapor interface will be equal to half the distance between adjacent arteries while for the configurations shown in 4b, c and d the corresponding flow path length will be approximately equal to the wick thickness. The required wick permeability for equivalent performance from these different configurations will therefore differ by approximately two orders of magnitude assuming isotropic properties (Merrigan et al. 1982).

A variety of methods of producing wick structures with the desired characteristics are available. The 50 μm pore size requirement will require multiple layer of screen material of approximately 400 mesh if conventional screen wick fabrication techniques are used. If coarser mesh wire screen is used it must be treated to reduce the pore size. Methods that have been used for pore size reduction of refractory screen wick include chemical vapor deposition (CVD) coating of the wires as shown in Figure 5 and mechanical compaction of layers of screen. Either of these methods is capable of reducing the pore size of 150-200 mesh screen wicks to the required 30-50 μm range.

Difficulties in producing practical wick structures are related to the reduction in permeability seen in compacted screen wicks and the difficulties in scaling CVD process to the lengths required. Given an adequate development program the CVD scaling problem may be overcome through the use of zone deposition processes that would allow fabrication of indefinite lengths of

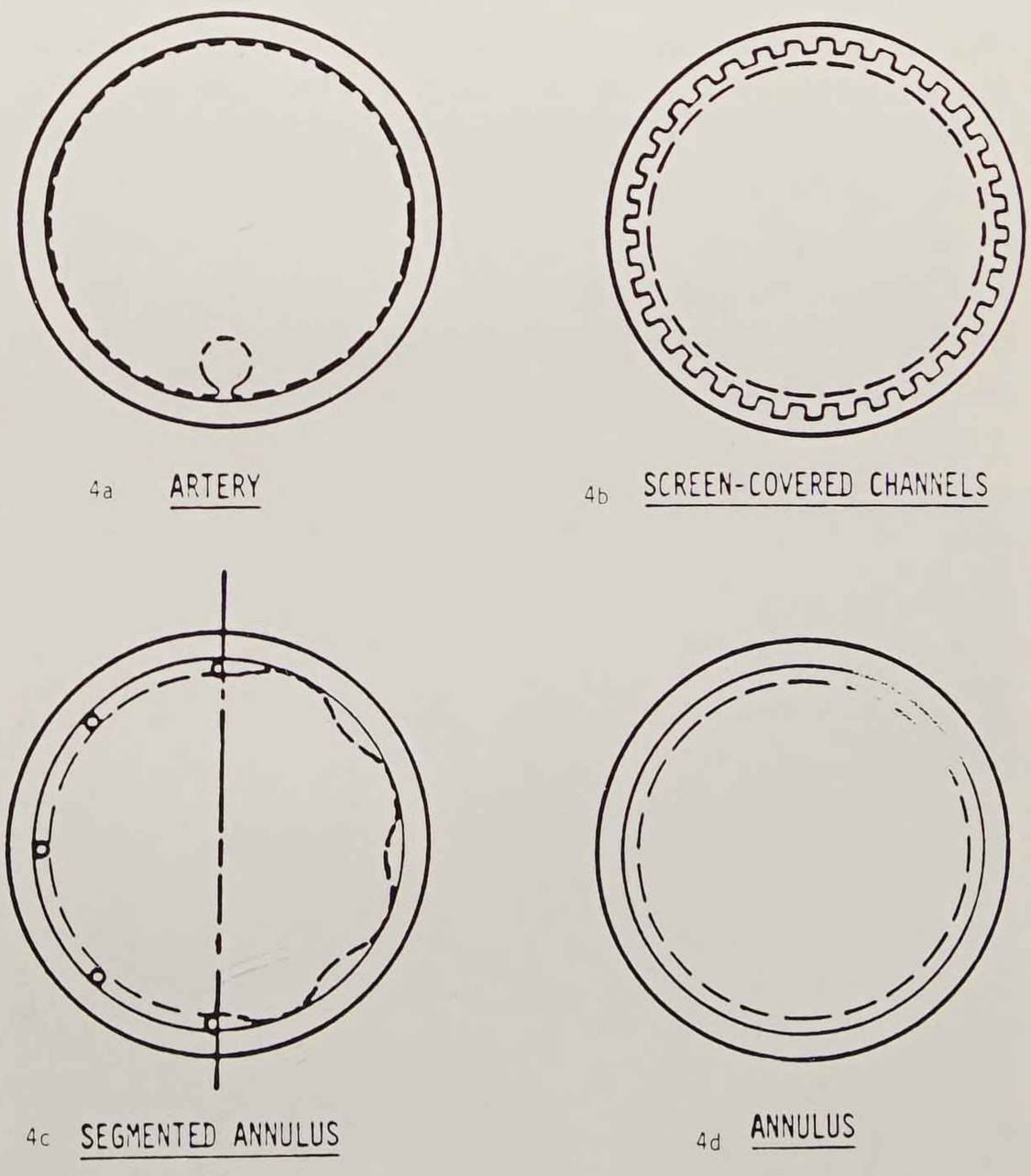


Figure 4 *Heat-Pipe Wick Structures.*

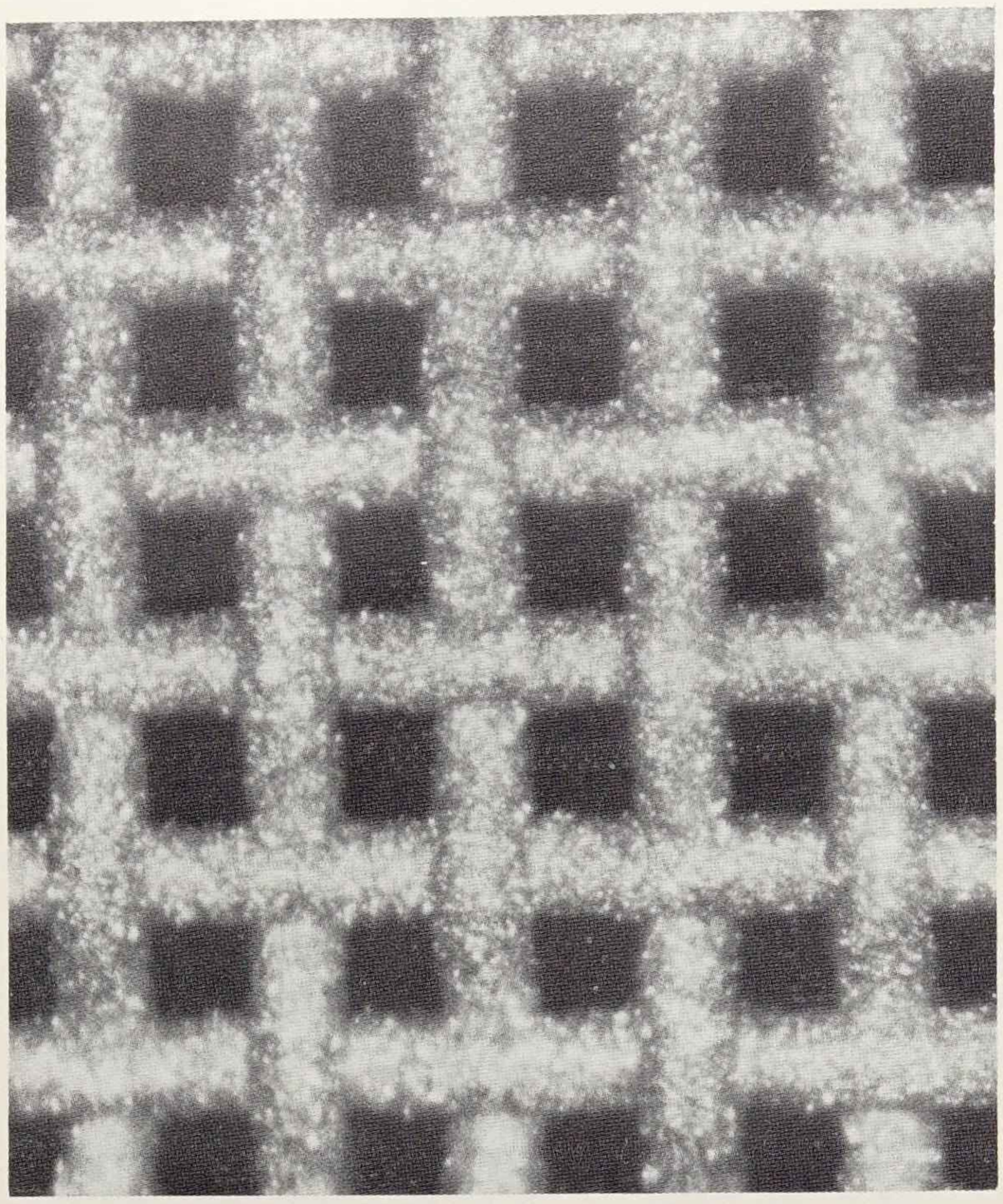


Figure 5 *CVD Coated Screen Wick.*

wick structure; however the reduced permeability of compacted screen wicks is inherent and will limit their use to annular or channel wick heat pipe designs.

Alternatives to screen wicks exist in powder metal or microsphere compacts, either of which may be used to form wick structures with integral artery passages as illustrated in Figure 6. As with CVD structures the primary impediment to their use in long heat pipes lies in the fabrication facility requirements, particularly the need for large, high temperature, high pressure furnaces for hot isostatic pressing. These facility requirements have led to the development and use of 400 mesh molybdenum-rhenium alloy screen wick materials for

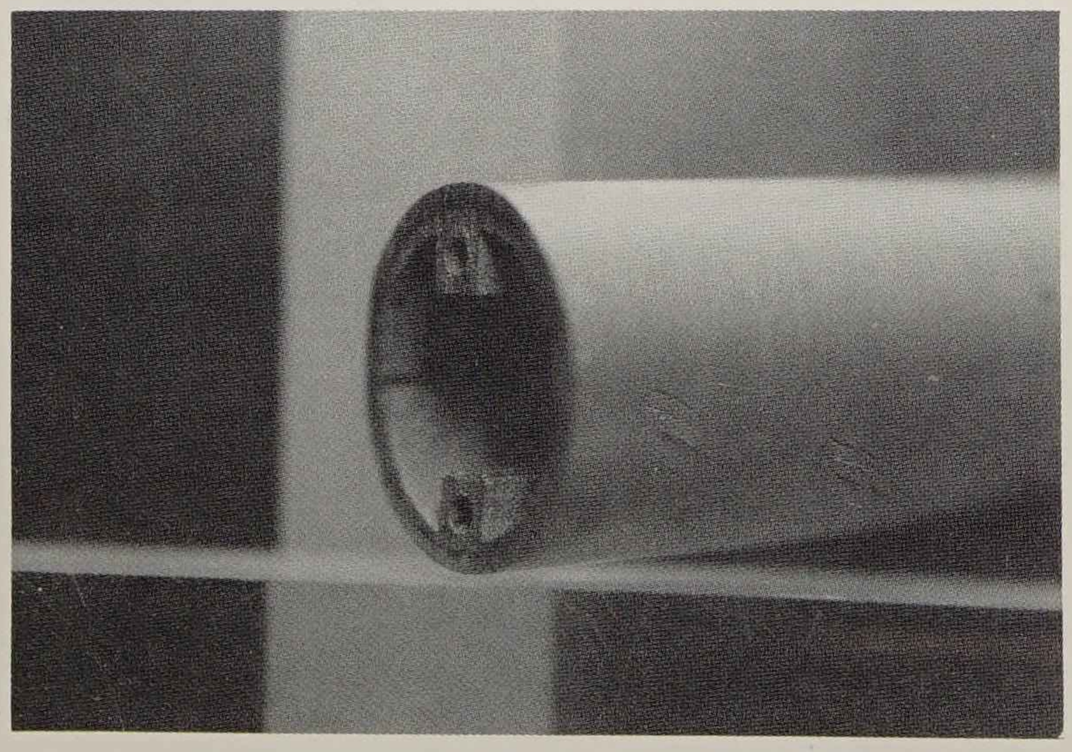


Figure 6 *Niobium Porous Metal Artery Wick inside 15.9-mm-o.d. Molybdenum Tube.*

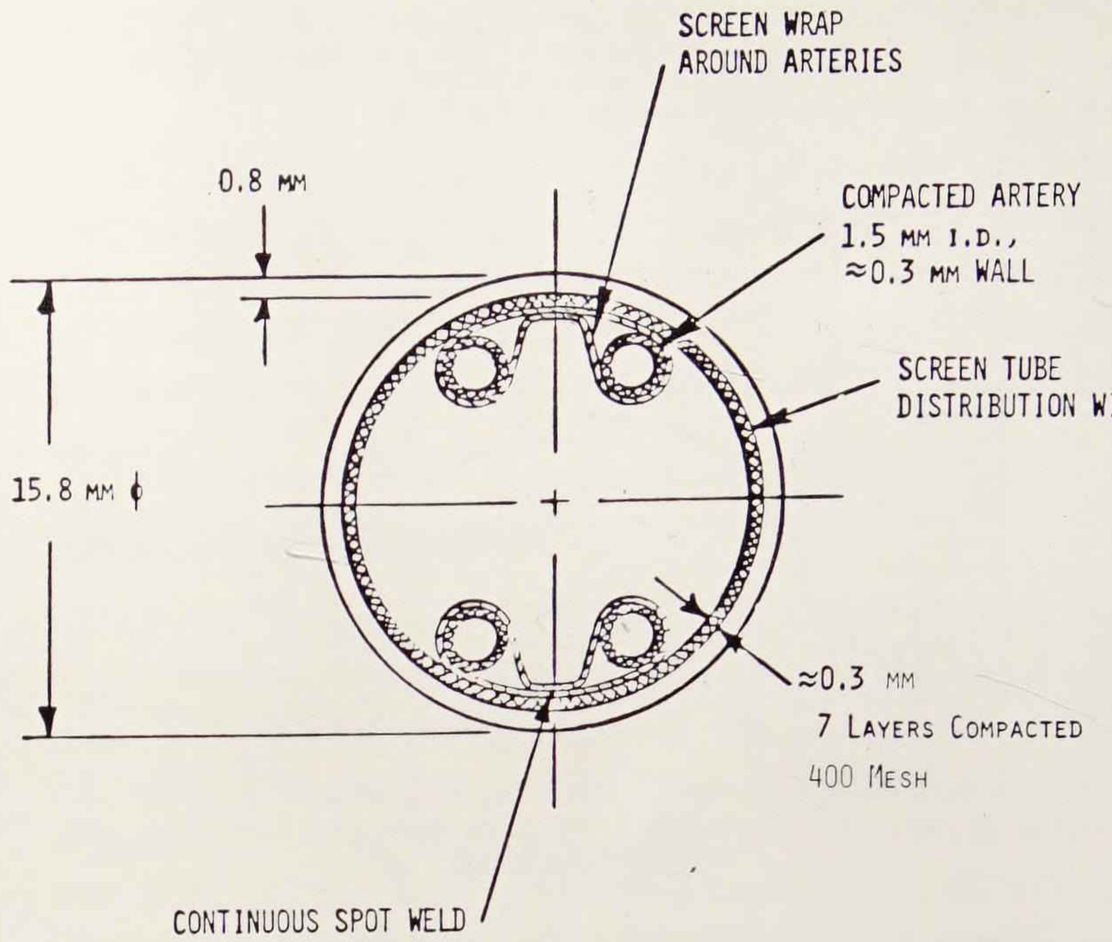


Figure 7 *Screen Wrap-Compacted Artery Heat Pipe Configuration.*

the high temperature, high power heat pipe development work conducted at Los Alamos National Laboratory for the SP-100 program (Ranken 1982).

A cross section of one of these screen artery and distribution wick structures is shown in Figure 7. A 2-m long, 1.58-cm diameter, molybdenum-lithium heat pipe of this construction has been tested to 22.6 kW throughput on the program. Peak power axial density achieved in test was greater than 19 kW/cm^2 without dryout (Merrigan et al. 1983).

Waste Heat Radiator Heat Pipes

The second direct heat transport application of heat pipe technology to space nuclear power systems is in the area of primary power radiators. Performance requirements for radiator heat pipes under typical system operating conditions are

- Temperature: 8700 to 1000 K,
- Axial power density: 0.5 to 1.0 kW/cm^2,
- Radial power density: 2 to 20 W/cm^2,
- Transport distance: 4 to 8 m, and
- Temperature difference: < 20 K.

The operating temperature range will be approximately 500 K below that considered for the primary heat transport heat pipes with radial and axial power densities of 10% to 20% of those for the high temperature applications. Thermal transport performance limits of radiator heat pipes will not generally control their application, except in designs employing extreme lengths or complex geometry. Primary concerns in technology development for radiator heat pipes involve the reduction of weight per unit area of radiating surface while maintaining end-of-life heat transfer capability. In addition the normal heat pipe material concerns of

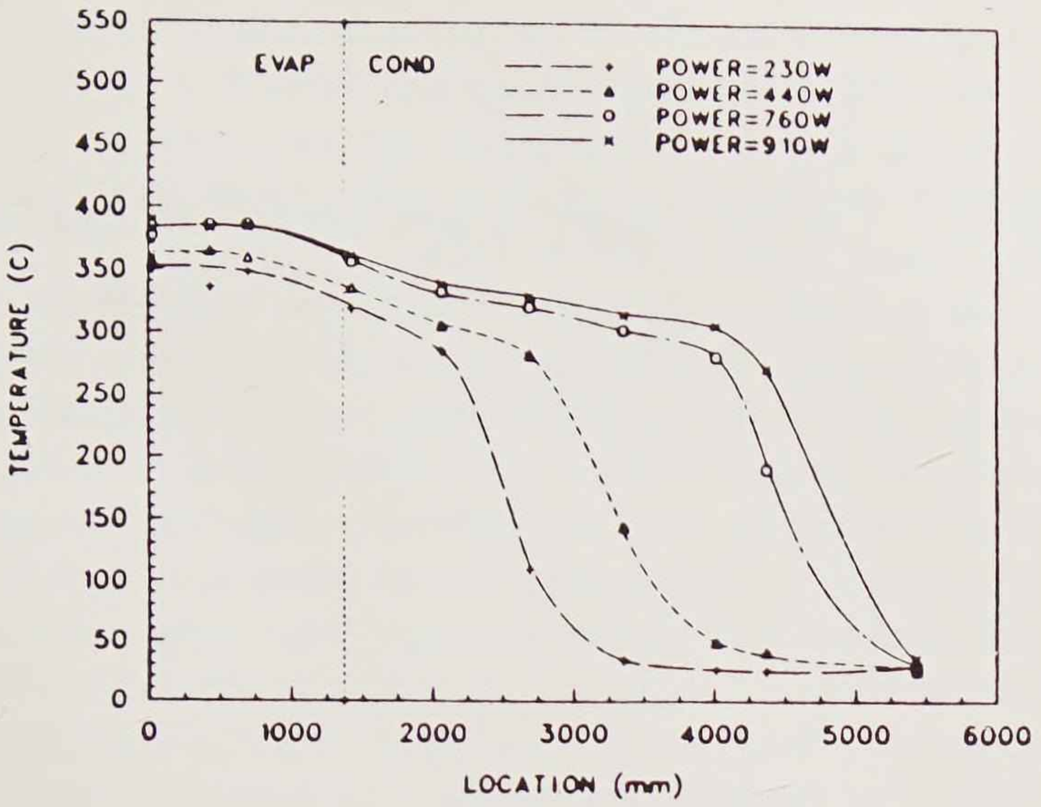


Figure 8 *Axial Temperature Profiles of RAD-3 during Start-Up.*

strength at temperature and working fluid compatibility apply.

A high emissivity for the radiating surfaces is necessary, either intrinsic to the heat pipe material or as a stable coating. Loss of radiating surface over the life of the system will occur primarily as a result of meteoroid penetration of the heat pipes. The rate of loss may be calculated from meteoroid velocity-density models if the behavior of the materials used is known to be ductile under hypervelocity impact (Lundberg et al. 1982). Cracking of heat pipe walls in brittle failure will increase the damage incurred over a given period of time and make prediction of loss rate difficult. These heat pipe material criteria favor the use of titanium-potassium systems to about 800 K, stainless steel or superalloy-sodium from 800 K to ~900 K and niobium alloy-sodium in the 900 K to 1100 K range.

Some operational concerns for radiator heat pipes involve start-up of the system from below the freezing temperature of the heat pipe working fluid, operation with radiation coupling at a fraction of design power, and for deployable radiator configurations, the need to bend the heat pipe before or during operation. Capabilities in each of these areas have been demonstrated in heat pipe development programs at Los Alamos. Figure 8 (Girrens 1982) shows temperature profiles along a 5.5-m, titanium-potassium heat pipe at successive inter-

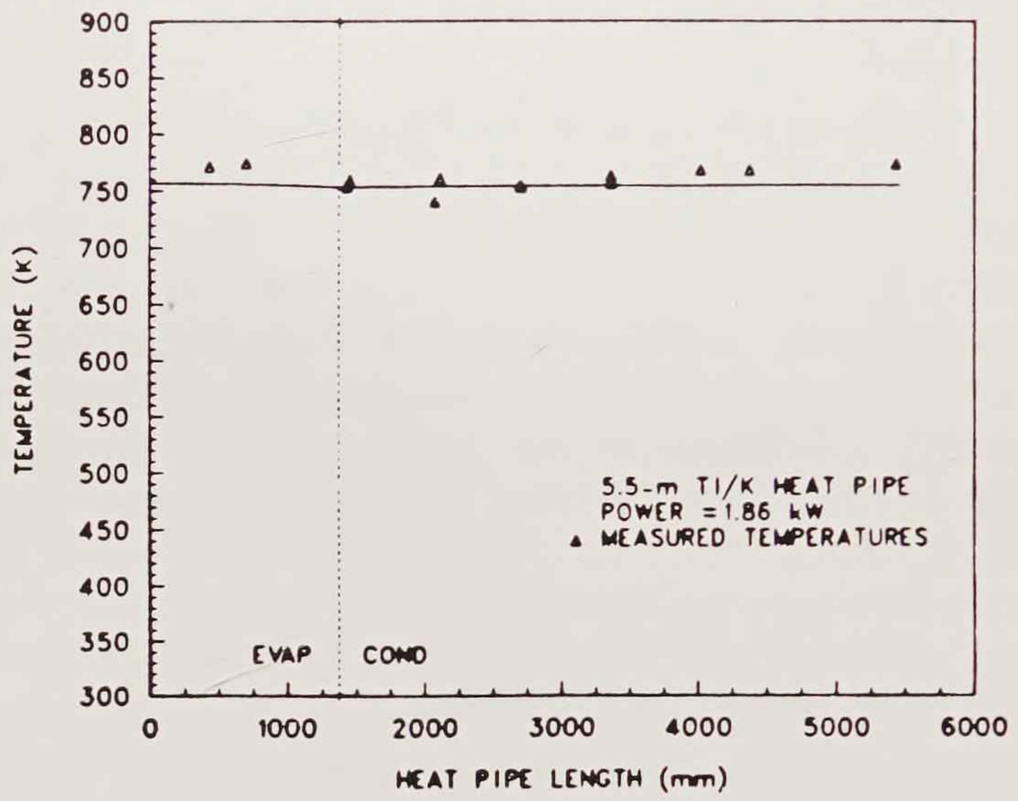


Figure 9 *Comparison of Analytical and Measured Temperature Profile at Maximum Operating Power.*

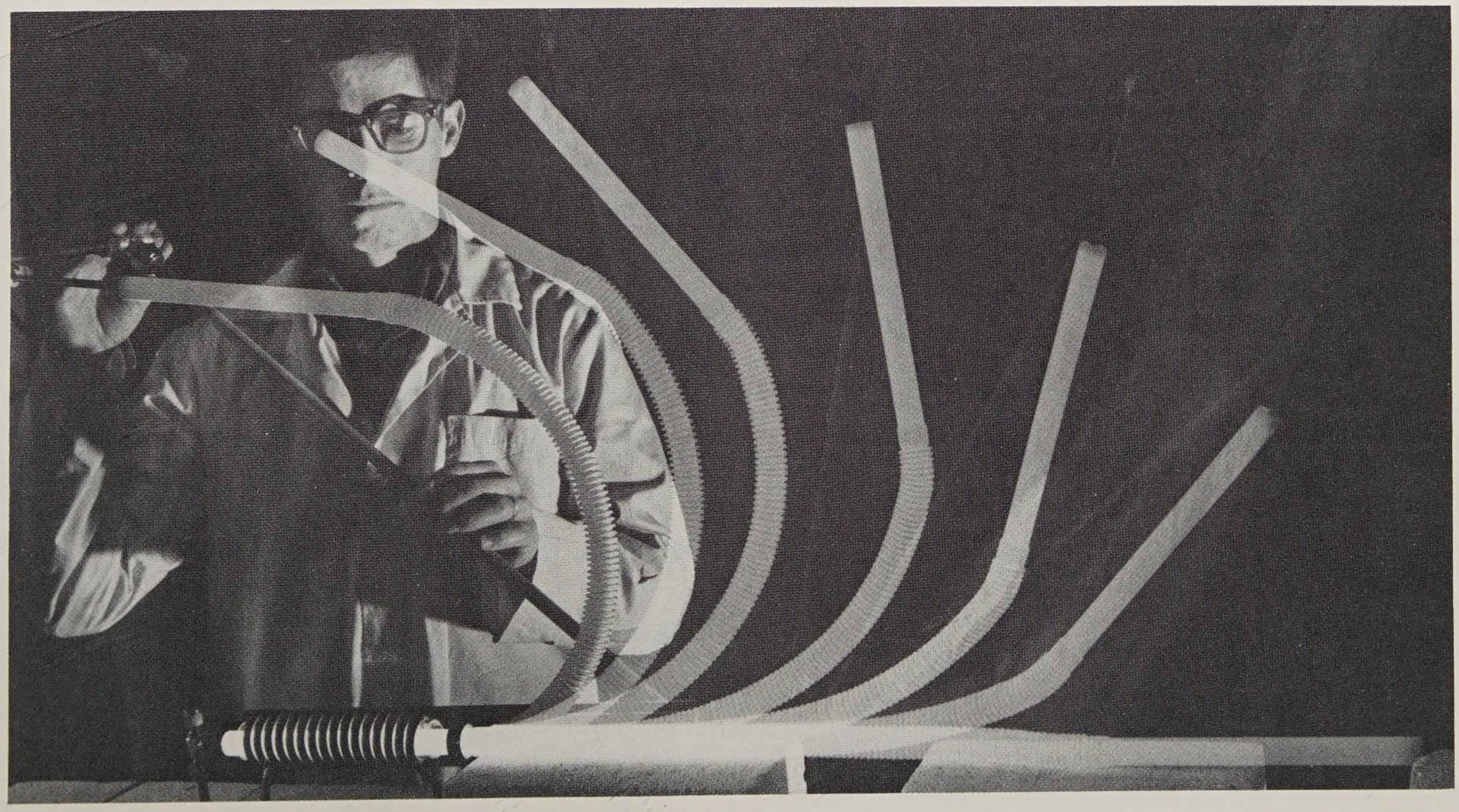


Figure 10 *Flexible Heat Pipe.*

vals of one hour during a deliberately slow start-up transient. It may be observed that the condenser end of the heat pipe was held below the freezing temperature of the potassium working fluid for more than 4 hours without depletion of the working fluid supply in the evaporator region of the heat pipe. This is possible with alkaline metal working fluids because the extremely low value of vapor pressure at the triple point limits mass transfer to the frozen region of the condenser.

The temperature profile of the same heat pipe operating under conditions of 1.86 kW and 760 K is given in Figure 9. This steady-state temperature profile serves to illustrate the isothermal nature of heat pipe heat transfer, even over working lengths of 5.5 m. This characteristic is of particular advantage in radiation coupled systems.

Operation of a radiator heat pipe during bending is demonstrated in the multiple exposures of Figure 10. This sodium-stainless steel, flexible heat pipe has been repeatedly bent through a 180° arc while operating at approximately 900 K as well as when the sodium working fluid was frozen. When operating in the straight, deployed configuration the performance of this heat pipe is comparable to that of a conventional, rigid design.

Lifetime Demonstration

In both primary heat transport and waste heat radiator applications for space nuclear power systems reliable operation of the heat pipes over multi-year periods is required. Internal thermochemical changes in high temperature heat pipes can affect their performance through alteration of fluid properties such as surface tension, through plugging or erosion of wick structures and through local accumulation of gas or liquid reaction products. Boiling limits may be altered by changes in wetting characteristics of the fluid or nucleation site changes. Demonstration of the required lifetimes at realistic values of temperature and mass flow is essential to the choice of heat pipes for system design concepts. A summary of relevant high temperature heat pipe life test data is given in Table 1.

Table 1 *Summary of High Temperature Heat Pipe Life Tests.*

Fluid	Material	T(K)	Hrs	Failure
Lithium	Mo	1700	25,400	Evap. penetration
Lithium	TZM	1775	10,500	
			10,400	Weld failures
			9,800	
Lithium	W-26 Re	1875	10,000	Test terminated
Lithium	Nb-1Zr	1776	9,000	Test terminated
Sodium	Mo	1600	19,304	Continuing
Sodium	TZM	1500	19,304	Continuing
Sodium	Mo	1600	23,742	Continuing
Sodium	304 Stainless Steel	1073	12,760	Test terminated
Sodium	Inconel 617	973	> 15,000	Pin holes, evaporator
Sodium	Nb-1Zr	1120	16,000	
Potassium	Ti	900	5,000	Test terminated
Potassium	347 Stainless Steel	780	6,500	Test terminated

This summary, while not exhaustive, includes most available test data involving exposure of over 5000 hours for the material combinations and temperature ranges of interest. What is not shown in this or similar life test data summaries is that the directed heat flux for the majority of these tests was low. Most test capsules are radiation loaded without high emissivity surface treatment so that total power input is a few kilowatts and the directed power throughput to the condenser less than half of the input. Mass flow rate dependent corrosion mechanisms may not be disclosed by this type of testing.

Recently Los Alamos has initiated a life test of a 2-m, radiation loaded, molybdenum-lithium heat pipe operated at 1500 K with a measured power throughput of 14 kW. This test has been operated for more than 1000 hours with a single interruption and without apparent deterioration of heat pipe performance. Continuation and extension of this type of testing is necessary to provide a reliability basis for space nuclear power system applications. Understanding of the life controlling phenomena is essential. It will enable the development of accelerated test methods that will permit the accumulation of an adequate data base for reliability predictions in a reasonable length of time. It will also enable control of the life-limiting thermochemical degradation mechanisms. This understanding should come from the development of analytic models for equilibrium chemistry and reaction kinetics within the heat pipes. These models will have to be verified by tests involving close control of heat pipe internal chemistry.

A first step to these goals has been taken with the development of equilibrium thermochemical models for the molybdenum-sodium heat pipes tested at Los Alamos. These models have been successful in predicting vapor phase mass transport of molybdenum in sodium heat pipes under dryout conditions. Within the present state of knowledge, the observations pertaining to the factors affecting the lifetime of high temperature alkaline metal, heat pipes are quite general:

1. In chemical models and in practice, mass transport is primarily a function of containment levels in the tube and screen material and in the working fluid rather than being caused by basic solubility phenomena.
2. Maintaining a region of the heat pipe at temperature without a liquid phase present, as in evaporator dryout, leads to more severe corrosion than would otherwise be encountered.
3. Failures often occur at welds or areas where materials are not homogeneous.

Quantification of these observations, as to allowable levels of containments, will require further research.

Transient Behavior of Heat Pipes

An area of concern for heat pipe applications in space reactor systems is the behavior of the devices under transient load conditions, both during startup and shut down of the system and through operational variation of thermal loads. In laboratory testing of high power, radiation coupled heat pipes it has been observed that dryout during shutdown is possible if conditions are not properly controlled. An example is illustrated in Figure 11 based on data taken during test of a 2-m molybdenum-lithium, annular wick heat pipe at Los Alamos. This heat pipe, which had been treated to obtain a surface emissivity of approximately 0.65, had been operated for an extended period with 14 kW throughput at 1500 K. During shutdown of the test for equipment maintenance the power coupled into the evaporator region of the heat pipe by RF induction was reduced in approximately 800 W increments. At a temperature of 1300 K and an input power level of about 7.2 kW, the heat pipe developed a hot spot in the evaporator region, triggering complete test shutdown.

Subsequent examination of the heat pipe showed that lithium had been transferred from the evaporator region of the annulus to the condenser, apparently due to the continued high rate of radiation heat transfer from the condenser after the internal transfer of heat by the lithium vapor had become limited by sonic vapor velocity conditions at the evaporator exit. This test shut down was to some extent an artifact of the test method, caused by the constant power characteristics of RF induction heating, however if the evaporator reservoir of lithium were limited and the thermal capacitance of the structure surrounding the evaporator were high, a similar dry-out situation could occur in a space power application.

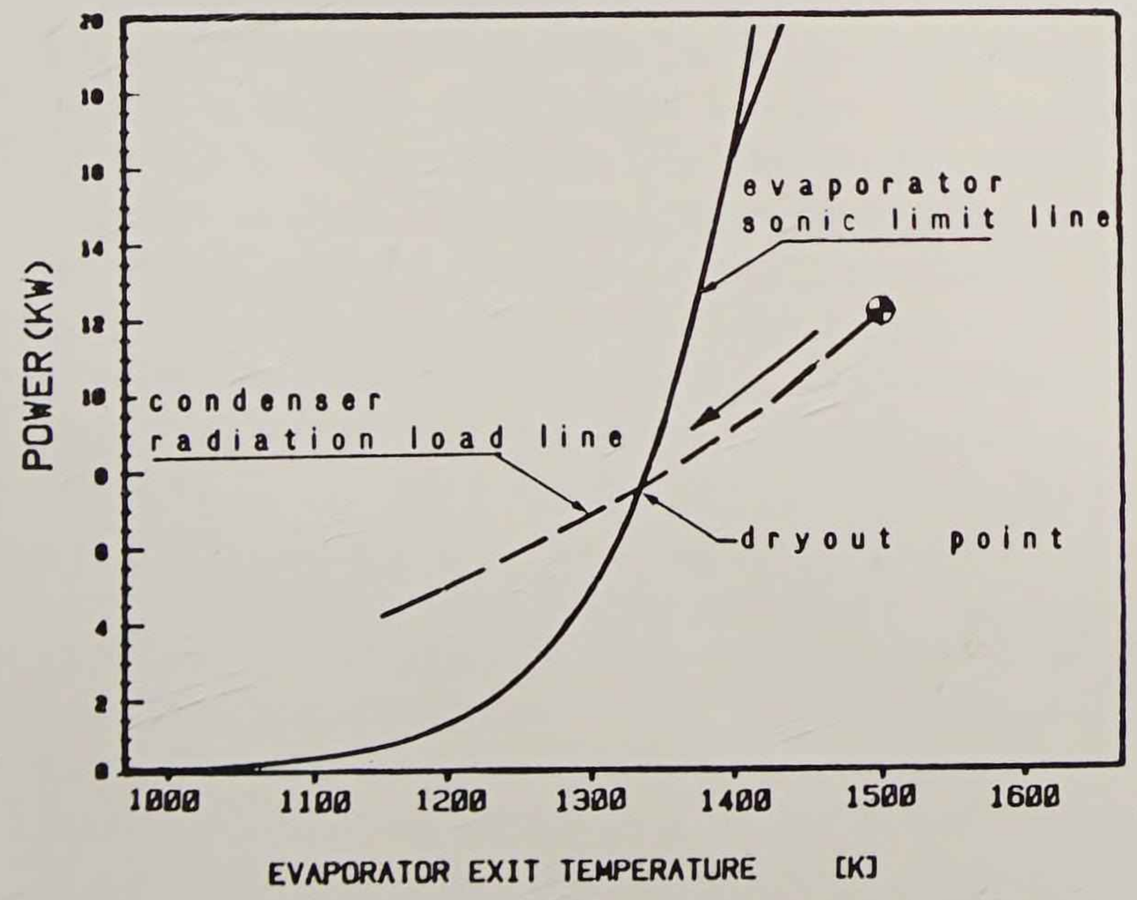


Figure 11 *Transient Performance of 2-m Heat Pipe.*

In heat pipes employing homogeneous wicks an inert, non-condensible gas might be used to alleviate start-up and shut-down problems, however control of such a gas in an artery heat pipe to ensure continuous artery fill is difficult. The determination of stable operating limits for heat pipes under the transient conditions to be expected in space nuclear power applications will be essential to their successful integration into such systems. Both analytic modeling and experimental verification under realistic conditions will be required.

Summary

Recent heat pipe development work at Los Alamos National Laboratory has involved performance testing of typical space reactor heat pipe designs to power levels in excess of 19 kW/cm^2 axially and 300 W/cm^2 radially at temperatures in the 1400 to 1500 K range. Operation at conditions in the 10 kW/cm^2 range has been sustained for periods of up to 1000 hours without evidence of performance degradation. The effective length for heat transport in these heat pipes was from 1.0 to 1.5 m. Materials used were molybdenum alloys with lithium employed as the heat pipe operating fluid. Shorter, somewhat lower power, molybdenum heat pipes have been life tested at Los Alamos for periods of greater than 25,000 hours at 1700 K with lithium and 20,000 hours at 1500 K with sodium. These life test demonstrations and the attendant performance limit investigations provide an experimental basis for heat pipe application in space reactor design.

Demonstrated performance for long heat pipes operating under space radiator conditions includes the transport of 2.6 kW and 920 K in a radiation loaded 4.4-m, sodium/stainless steel heat pipe developed by Thermacore Corporation for the Nuclear Electric Propulsion Program and the transport of 2.4 kW at 773 K in a radiation loaded, potassium/titanium heat pipe developed by Los Alamos National Laboratory. Flexible heat pipes intended for use in deployable space radiators have also been demonstrated at Los Alamos, with continuous operation achieved during bending of the pipe through 180°.

Technology development needs for space nuclear power heat pipe applications involve determination of the performance capabilities of specific heat pipe designs as a function of operating temperature, power density and local environmental conditions as well as the determination of the transient behavior of the devices during start-up, shut-down, and load variation. Finally an important concern in the application of heat pipes in a space nuclear power system is the lifetime to be expected and the type of performance degradation to be expected over the operating life. Prediction of operating lifetime of heat pipes will require the develop-

ment of mass transport/corrosion chemistry models and their verification in controlled life tests.

Acknowledgments

Work performed at Los Alamos National Laboratory under U.S. Department of Energy Contract Number W-7405-ENG-36.

References

Girrens, Steven P. (1982) *Design and Development of a Titanium Heat Pipe Space Radiator*, LA-9251-MS, Los Alamos National Laboratory, Los Alamos, NM, March 1982.

Keddy, E. S. and H. E. Martinez (1982) "Development of High Temperature Liquid Metal Heat Pipes for Isothermal Irradiation Assemblies," in *Proc. 17th Intersociety Energy Conversion Engineering Conference*, August 1982, Los Angeles, California.

Koenig, D. R. and W. A. Ranken (1982) "Design Options for the SP-100 Thermoelectric Nuclear Space Power Plant," in *Proc. 17th Intersociety Energy Conversion Engineering Conference*, August 1982, Los Angeles, California.

Lundberg, L. B., S. J. Bless, S. P. Girrens, and J. E. Green (1982) *Hypervelocity Impact Studies on Titanium, Titanium Alloys, and Beryllium*, LA-9417, Los Alamos National Laboratory, Los Alamos, NM, August 1982.

Merrigan, M., C. Prenger, H. E. Martinez, and J. Runyan (1982) "Artery Heat Pipes for Space Power Systems," in *Proc. 17th Intersociety Energy Conversion Engineering Conference*, August 1982, Los Angeles, California.

Merrigan, M. A., J. E. Runyan, H. E. Martinez, and E. S. Keddy (1983) "Development and Test of a Space Reactor Core Heat Pipe," in *Proc. AIAA 18th Thermophysics Conference*, June 1983, Montreal, Canada.

Merrigan, M. A., E. H. Martinez, E. S. Keddy, J. Runyan, and J. E. Kemme (1983) "Performance Demonstration of a High Power Space Heat Pipe Design," in *Proc. 18th Intersociety Energy Conversion Engineering Conference*, August 1983.

Ranken, W. A. (1982) *Space Reactors, January–March 1981*, LA-9198-PR, Los Alamos National Laboratory, Los Alamos, NM, January 1982.

Vinz, P. and C. A. Busse (1973) "Axial Heat Transfer Limits of Heat Pipes Between 25 W/cm^2 and 15.5 kW/cm^2," in *Proc. International Heat Pipe Conference*, 1973.

Space Nuclear Power Systems 1984
Edited by M. S. El-Genk and M. D. Hoover
© Orbit Book Company, Malabar, FL, 1985

Chapter 49

Liquid Droplet Radiator Technology Issues

A. T. Mattick and A. Hertzberg

University of Washington, FL-10
Seattle, WA 98195

The operation of the liquid droplet radiator (LDR) is analyzed to establish design constraints for the LDR components and to predict the performance of an integrated LDR system. The design constraints largely result from mass loss considerations: fluid choice is governed by evaporation loss; droplet generation techniques must be capable of precise aiming of $> 10^5$ droplet streams; and collection losses must be less than 1 droplet in 10^7. Concepts for droplet generation and collection components are discussed and incorporated into a mass model for an LDR system. This model predicts that LDR's using lithium, Dow 705 silicone fluid, or NaK may be several times lighter than heat pipe radiators.

Introduction

The generation of high powers in space presents problems of thermal management that have only recently been seriously addressed. In particular, the practicality of high continuous power hinges on the development of radiators which can reject large heat loads, yet which do not completely overwhelm the power source and conversion system in mass and transport volume. The most technically advanced radiators for space applications are those using solid surfaces (tube and fin, or heat pipe designs, for example), but the necessity of using relatively thick walls (for good conduction and micrometeoroid protection) usually results in quite large radiator masses, and compromises power system performance.

The liquid droplet radiator (LDR) is one of a number of new concepts developed over the past few years for achieving much lower specific masses than are possible with conventional solid surface radiators (SSR). The LDR utilizes direct radiation of waste heat by recirculating free streams of heated liquid droplets, eliminating the conducting and protective surfaces of the SSR. By using submillimeter droplets, the area to mass ratio of an LDR droplet cloud may be one or two orders of magnitude larger than that of the radiating surfaces of SSR's, and the small volume of the LDR radiating liquid allows compact stowage before deployment.

Initial studies of the LDR concept carried out at the University of Washington were reported by Mattick and Hertzberg (1981 and 1982). These studies established the basic heat transfer characteristics of a radiating droplet sheet, demonstrated that the droplets could be produced and collected in space with components that were, in principle, relatively simple, and identified several space applications in which the LDR could be of significant benefit. This paper presents a more detailed investigation of the operation of the LDR, and focuses on the design requirements for the LDR fluid-handling components and the technology issues that must be solved to meet these requirements.

The design constraints that result from the use of a sheet of droplets to reject waste heat are first discussed. LDR performance is evaluated for several low vapor pressure liquids, and models of droplet generation and collection devices with the potential of meeting the design constraints are described. Next, results of a parameter study of an LDR system incorporating these component models are presented. It is shown that an LDR system including a generator, collector, support structure, pump, and manifolds, as well as the droplet sheet, can be $\simeq 5$ times lighter than the lightest solid surface radiators. Finally, the key technological issues facing the development of practical LDR systems are discussed. Although these issues are difficult, they do not appear to require any fundamental breakthroughs.

LDR Design Considerations

The operation of the LDR is illustrated in Figure 1. Heat rejected from a power cycle is transferred to the LDR fluid, which is then formed into a sheet of liquid droplets aimed toward a collector. The droplets radiate energy in transit, and the cooled liquid is then collected, repressurized, and recirculated back to the power cycle. The use of two parallel, oppositely directed droplet sheets eliminates the need for a long return pipe (vulnerable to micrometeoroids), although a larger pump work would be required to generate the droplet streams.

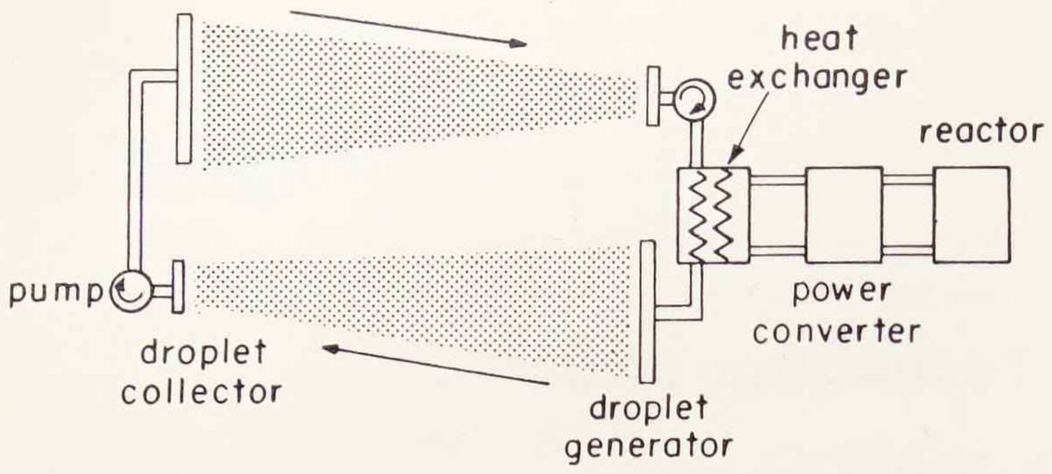


Figure 1 *Schematic of a Double-pass Liquid Droplet Radiator for Use in a Space Nuclear Power System.*

The primary design constraint for the LDR is that fluid loss via misaiming, splashing, and evaporation, be kept to a minimum. For a solid surface radiator the puncture of coolant manifolds by micrometeroids is the most serious potential cause of fluid loss and is the mass-limiting factor of such radiators. For the LDR, fluid loss due to micrometeoroids passing through the droplet sheet is negligible (Mattick and Hertzberg 1982). Evaporation is the single most important mass loss mechanism for the LDR since it determines which fluids are usable; the properties of these fluids in turn influence the design of LDR components and the performance limits of an LDR system.

Fluid Choice vs LDR Power/Mass

As shown by Mattick and Hertzberg (1981), the vapor pressure of the liquid should be $< 10^{-7}$ Torr at the peak droplet temperature if the evaporation loss over durations of years is to be kept less than the mass of droplets in the droplet sheet. To be practical, the liquid must have a considerably lower vapor pressure at its freezing point (or high viscosity) to provide a useful energy/mass, $c\Delta T$, for heat rejection. Our survey of a large number of fluids has yielded only a few that satisfy the vapor pressure criteria, and which are readily available and stable. The properties of the most promising candidate liquids are listed in Table 1. In addition to the six liquids shown in the table, many organic fluids have been found which exhibit suitably low vapor pressures, but are insufficiently well characterized to be considered as candidate LDR fluids at this time. Also, gallium and indium, although suitable from a vapor pressure standpoint, are probably too rare to be practical.

LDR performance is governed chiefly by the density and emissivity of the liquid. A useful figure of merit for comparing the performance of radiators is the quantity $F = \text{emissivity}/(\text{mass}/\text{area})$, since at a given temperature, $\text{power}/\text{mass} = F\sigma T^4$. The highest performance solid surface radiators (heat pipes) have a mass/area $\tilde{\rho} \simeq 5\text{kg}/\text{m}^2$ and an emissivity $\epsilon \simeq 0.85$, resulting in $F_{ssr} \simeq 0.17\ \text{m}^2/\text{kg}$. An isolated droplet has $F_d = 6\epsilon_0/\rho D$ ($\epsilon_0 =$ material emissivity, $\rho =$ density, $D =$ droplet diameter). For 100 μm diameter droplets, F ranges from $\simeq 0.85\ \text{m}^2/\text{kg}$ for tin to $\simeq 36\ \text{m}^2/\text{kg}$ for Dow 705 silicone fluid. The use of sub-millimeter droplets in place of solid surfaces thus has the potential for very high performance.

A more accurate assessment of LDR performance must take into account the view factors of droplets in a droplet sheet; the sheet figure of merit F will be smaller than the isolated droplet figure of merit F_d due to scattering and absorption of radiation by droplets in the sheet. Although an LDR could be designed to use a sparse droplet sheet with widely separated droplets (view factors $\simeq 1$), the projected area of the sheet would be much larger than the projected area of a solid

Table 1 *Properties of Candidate Radiator Fluids.*

Liquid	Lower Temperature Limit $T_{min}(K)$	Upper Temperature Limit $T_{max}(K)$[e]	Density $\rho(\frac{g}{cm^3})$	Emissivity ϵ_0[f]	Viscosity $\mu(cp)$	Specific Heat $c(\frac{J}{g \cdot K})$
Na-K-Cs[a]	195	280	1.5	.05 – .2	1.4 – 4	—
Na-K[b]	261	320	.87	.05 – .2	.7 – 1.2	.96
Dow 705[c]	270	320	1.1	.5 – .7[g]	50 – 10^3[h]	1.67
Sn-Pb-Bi[d]	370	580	9.5	.05 – .2	—	—
Li[d]	460	540	.5	.05 – .2	.6	4.2
Sn[d]	505	1100	6.8	.05 – .2	1 – 2	.26

[a] Tepper (1980)
[b] Jackson (1955)
[c] Dow 705 silicone fluid
[d] Smithells (1955)
[e] Temperature at which yearly evaporation loss $\simeq$ sheet mass. Vapor pressures from Nesmeyanov (1963) for metals, Raoult's law for alloys.
[f] Liquid metal emissivities are estimates.
[g] Dow 705 emissivity measured in authors' laboratory.
[h] Dow viscosity data provided by T. Mroz, NASA Lewis Res. Ctr.

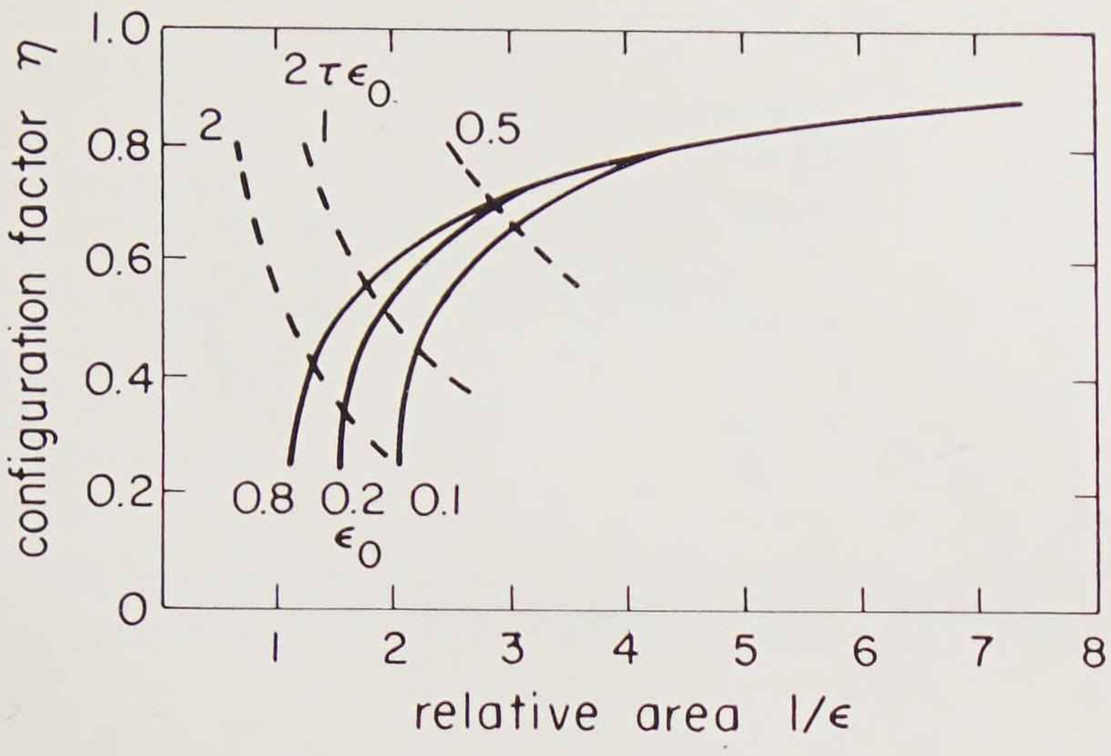


Figure 2 *Droplet Sheet Configuration Factor vs Relative Area of Droplet Sheet for Liquid Emissivities $\epsilon_0 = 0.1$, 0.2, and 0.8. Configuration Factor Is (Sheet Power/Mass)/(Droplet Power/Mass). Relative Area of Unity Corresponds to a Black, Solid Surface Radiator.*

surface radiator. This would likely result in unacceptably large masses for the droplet generation and collection components. For a dense droplet sheet the reduction in radiation effectiveness due to finite droplet view factors may be characterized by a configuration factor $\eta \equiv F/F_d$. This factor has been computed by numerically solving the equation of radiation transfer within the sheet to determine the hemispherical sheet emissivity ϵ, and by using the relation $F = \epsilon/\tilde{\rho}$, where $\tilde{\rho}$ is the mass/(radiating area of the sheet). (Radiating area is twice the projected area.) The sheet emissivity ϵ depends on the liquid emissivity ϵ_0, and the optical depth of the sheet $\tau = n\pi D^2 S/4$, where n = number density of droplets and S = thickness of the sheet. The mass/area $\tilde{\rho} = \tau D\rho/3$. Figure 2 shows configuration factor η vs relative sheet area $1/\epsilon$ for liquid emissivities ϵ_0 of 0.1, 0.2, and 0.8, and illustrates the tradeoff between low mass (high η) and minimum area (highest ϵ). A reasonable compromise is to choose $\tau \simeq 1/2\epsilon_0$ which yields $\eta \simeq 0.5$, $\epsilon \simeq 0.5$, and $F \simeq 0.5 F_d$.

Taking the configuration factor into account Figure 3 shows a performance comparison between an advanced SSR and droplet sheets using 100 μm diameter droplets of various liquids. Considering that an LDR system will likely be > 2 times heavier than the droplet sheet alone, it is evident that LDR's using Sn and Sn-Pb-Bi will only offer an improvement over heat pipes if droplets much smaller than 100 μm are used, while LDR's using Li, NaK, and Dow 705 and droplet diameters $\gtrsim 100$ μm may be considerably lighter than heat pipe radiators.

Droplet Sheet Parameters and Scaling

In order to determine the operational constraints on the droplet generation and collection components of the LDR, an initial estimate of the physical parameters of a droplet sheet for a given heat rejection application must be obtained. We consider a triangular sheet of length L (in the direction of droplet travel), width W at droplet insertion (converging to a very small waist at the collector), and thickness S. This convergent geometry minimizes the collector's aperture and mass. The aspect ratio is defined by $\alpha = W/L$.

For this geometry, the sheet emissivity will increase in the direction of droplet travel (z-direction) since the droplet number density and optical depth increase. For varying optical depth, the power/mass is given by $\bar{\eta} F_d \sigma T_e^4$, where $\bar{\eta}$ is the average configuration factor over the sheet, and $T_e \simeq \sqrt{T_0 T_1}$ is the effective radiating

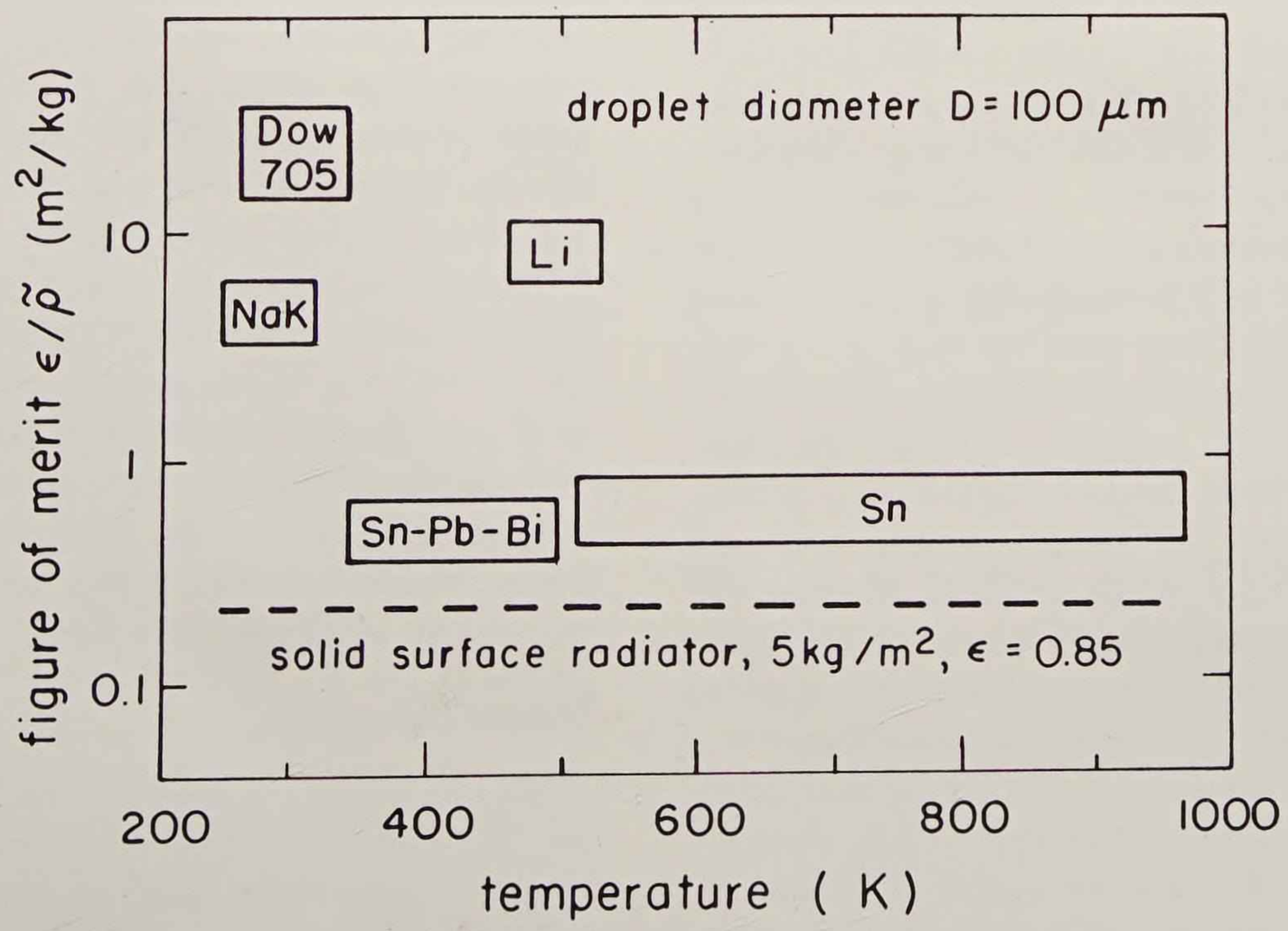


Figure 3 *Droplet Sheet Figure of Merit for Candidate Radiator Liquids vs Radiation Temperature.*

Table 2 *Droplet Sheet Parameters ($P = 100\ kW$, $\alpha = .4$, $D = 100\ \mu m$)*

Liquid	Effective Radiating Temperature T_e(K)	Sheet Length $L(m)$	Sheet Thickness S(cm)	Number of Droplet Streams N_s	Mass of the Sheet m_s(kg)
Dow 705	300	30	1.6	4×10^5	12
Lithium	490	12	4	4×10^5	2.4
Tin	800	5	6	2.5×10^5	9

temperature for a droplet insertion temperature T_0 and collection temperature T_1. We have found that for a triangular sheet, it is reasonably accurate to use $\bar{\eta} \simeq \eta_m$, where η_m is the configuration factor at the midpoint of the sheet ($z = L/2$). This approximation is equivalent to modeling the triangular sheet by a rectangular sheet (constant ϵ) of length L, width $W/2$. Thus, for a given aspect ratio α and power P, the length $L = (P/\alpha\epsilon\sigma T_e^4)^{1/2}$.

The sheet thickness $S = 4\tau\lambda_x\lambda_y\lambda_z/\pi D^2$, where λ_x and λ_y are the lateral droplet spacings at the midpoint and λ_z is the droplet spacing in the direction of travel. The spacing λ_z is typically in the range $3D$–$8D$ for droplet generation methods thus far considered, and for the present estimates, we assume $\lambda_z = 5D$. We also choose $\lambda_y = 5D$, $\lambda_x = 5D$ at the midpoint of the sheet to avoid excessive agglomeration of droplets over most of the sheet length. With these assumptions, $S = 500D\tau/\pi$. As shown above, a reasonable mass-area compromise results from the choice $\tau \simeq 1/2\epsilon_0$ yielding $\epsilon \simeq 0.5$, so that while the sheet area is fairly insensitive to ϵ_0 and D, the thickness S scales as D/ϵ_0. The number of droplet streams $N_s = WS/(2\lambda_x\lambda_y) = \alpha LS/50D^2$, and N_s scales as $\sqrt{P}/\epsilon_0 T_e^2 D$.

Based on the above model, the sheet parameters L, S, N_s, and the sheet mass m_s are given in the Table 2 for a 100 kWt radiator using 100 μm droplets of either Dow 705, Li, or Tin, and with aspect ratio $\alpha = 0.4$. The sheet length decreases markedly with increasing droplet temperature, as expected, while the thickness variations (1.6–6.0 cm) reflect the variation of emissivities among the liquids. By coincidence the number of droplet streams ($N_s = 2 - 4 \times 10^5$) is nearly the same for these liquids.

The use of small droplets yields a high figure of merit in comparison with solid surface radiators, but also limits the peak power that can be radiated by a droplet sheet. This results from the higher cooling rates and shorter transit times t for small droplets. Because the droplet speed v is limited as discussed below, the sheet length $L = vt$ and power are also limited. For a given liquid having emissivity ϵ_0 and temperature limits T_0, T_1, and for droplet diameter D, average optical depth for the sheet of τ, the radiation time $t = c\Delta T/F_d\eta\sigma T_e^4$.

For viscous liquids the droplet speed is limited by pumping power considerations. Consider, for example, a power cycle with cycle efficiency η_c, using a droplet radiator with efficiency η_p of converting work to droplet kinetic energy. The overall efficiency of cycle + radiator is

$$\eta_0 = \eta_c - (1 - \eta_c)/(\eta_p/h - 1),$$

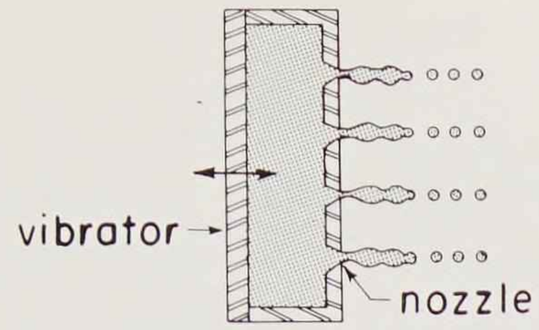
where h is the ratio of droplet kinetic energy to radiated thermal energy, $h = v^2/2c\Delta T$. For $\eta_c = 0.2, \eta_p = 0.8$, a ratio $h = 0.03$ will reduce the overall efficiency by $\simeq 15\%$. Thus we require $h < 0.03$ or $v < \sqrt{0.06c\Delta T}$. Although this applies for all fluids, for non-viscous fluids another velocity constraint may be even more restrictive. For production of uniform, accurately aimed droplets, the jet flow at the generator must be non-turbulent; that is, $\mathrm{Re} < 2000$, where $\mathrm{Re} \simeq v\rho D/\mu$, so that $v < 2000\mu/\rho D$. This condition applies for $D > D^* = 2000\ \mu/\rho\sqrt{0.06c\Delta T}$; $D^*(\mathrm{Dow\ 705}) = 1100\ \mu\mathrm{m}$, $D^*(\mathrm{Li}) = 20\ \mu\mathrm{m}$, $D^*(\mathrm{Sn}) = 10\ \mu\mathrm{m}$. The maximum power $P = \alpha(vt)^2\epsilon\sigma T_e^4$ may be estimated using these constraints: $P(\mathrm{Dow\ 705}) \simeq 50\ MW$, $P(\mathrm{Li}) \simeq 12\ MW$, and $P(\mathrm{Sn}) \simeq 8\ MW$.

LDR Component Design and System Performance

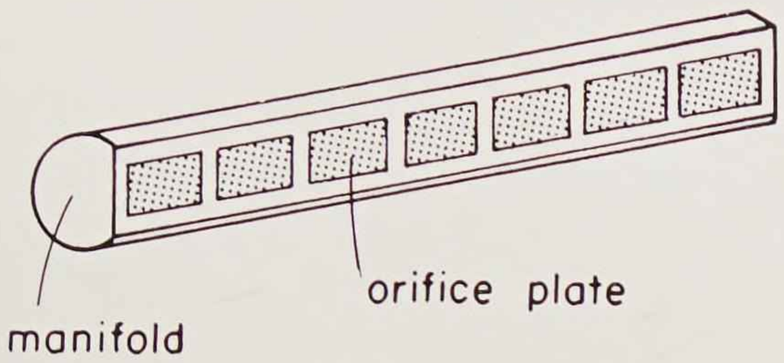
Having examined some aspects of LDR design that result from the use of a droplet sheet to radiate waste heat, we now turn to the components for generation and collection of droplets. A primary requirement for these components is that they function with a minimum of mass loss due to factors such as misaiming or splashing. Since transit times will typically be in the range 1–10 seconds, a fractional mass loss of $< 10^{-7} - 10^{-8}$ must be maintained for LDRs with operational lifetimes > 1 year. Thus, splashing losses at the collector may not amount to more than one drop per $10^7 - 10^8$ drops collected. Because the number of droplet streams ranges between $5 \times 10^5 - 5 \times 10^6$ for powers of 100 $kW - 10\ MW$, *no* stream can be lost due to misaiming without an intolerable mass loss.

Droplet Generation

Among various means that have been considered for the generation of droplets, the scheme illustrated in Figure 4 appears the most promising for LDR applications. The droplets are formed by the break-up of jets (via surface tension instability) issuing from orifices in a



(a)



(b)

Figure 4 *Schematic of an Orifice-array Droplet Generation System Showing (a) the Principle of Generation Using an Orifice Plate and (b) an Overview of the Droplet Generator.*

pressurized manifold. An oscillating pressure may be applied to the liquid to aid in producing droplets of uniform size and spacing. The LDR droplet generator might consist of a number of orifice plates mounted on a long tubular manifold.

Orifice arrays have proven capable of producing accurately directed ($\sim$1 mrad) streams of droplets $\lesssim 50\mu$m in diameter in the ink jet printing industry (Kuhn and Meyers 1979) and even better aiming accuracies have been achieved with 10–100 μm droplets in fusion target research (Hendricks, Robinson, and Calliger 1976). The aiming accuracy reflects the precision and reproducibility of fabricating small orifices. Orifice shape irregularities of a few percent, tiny burrs upstream of the orifice, or partial clogging can lead to abrupt, unpredictable changes of stream trajectories. The principal issue facing the development of this technique for the LDR is the ability to scale orifice fabrication techniques to arrays of $> 10^5$ orifices which will strictly maintain directional accuracy over durations of years. Ink jet printing applications, for example, use arrays of 10–100 orifices and stream direction can be controlled by electrostatic deflection, a technique that would be impractical for LDR applications.

The jet stability appears to be best with cylindrical orifices with rounded edges and $L/D \lesssim 1$, or with tapered cylindrical orifices with the taper inward in the direction of flow. These profiles yield discharge coefficients C_D ranging from $\simeq 0.7$ at low Reynolds numbers to $\simeq 0.85$ at Re $\simeq 2000$ (Levanoni 1977). (The jet (and droplet) speed $v = C_D\sqrt{2P/\rho}$, where P is the manifold pressure.) Above Re = 2000, turbulence degrades the uniformity of the droplet stream. The jet contracts to a diameter D_j smaller than the orifice diameter by a factor that ranges from 0.62 for small L/D orifices and high Reynolds numbers, to 1.0 for larger L/D and low Reynolds number.

The dynamics of droplet formation was first analyzed by Rayliegh (1879) who demonstrated that surface tension forces amplify sinusoidal perturbations on a cylindrical jet until the jet finally pinches off into discreet droplets. The amplification rate for inviscid fluids rises from zero at wavelengths λ_z shorter than the jet circumference πD_j to a maximum at $\lambda_z = 4.51 D_j$, and then decreases for longer wavelengths. Mass conservation requires a droplet diameter $D = (3D_j^2\lambda_z/2)^{1/3}$, so that from an initial inviscid jet with a flat spectrum of microscopic perturbations ("noise") should emerge droplets of diameter $D = 1.89D_j$, spacing $\lambda_z = 2.38D$. Viscosity broadens the amplification vs wavelength curve, and droplet spacings up to $8D$ can be produced by acoustically driving the fluid at the appropriate frequency.

The aiming tolerances of orifice generators could be eased by the use of ferrofluid LDR liquids and magnetic focusing of the droplet trajectories. A study of this scheme is currently in progress at Brookhaven National Laboratories (Botts and Powell 1984); in this study the deflection of small ferrofluid droplets has been demonstrated. In addition, such magnetic effects might be useful for splash inhibition at the droplet collector.

To obtain a first order estimate of the mass of a center-fed spray bar generator illustrated in Figure 4, we impose the condition that the fractional pressure drop from the center to the ends be less than 0.1 in order that the droplet speed be uniform to $\simeq 5$ percent across the droplet sheet. The pressure decrease along the tube (turbulent flow) is given by Prandtl and Tietjens (1957) as:

$$\frac{dp}{dx} = 0.133\rho\bar{u}^2/2R_t^{1/4}r,$$

where $R_t = \rho\bar{u}r/\mu$, $\bar{u}$ is the average speed, and r is the tube radius at distance x from the center. The mass flow along each arm of the tube decreases linearly with distance x as fluid is lost through the orifices:

$$\dot{m} = \tfrac{1}{2}\dot{m}_0(1 - 2x/W) = \pi r^2\bar{u}\rho,$$

where $\dot{m}_0 = \frac{2}{3}\tau_0 v D\rho W$ is the LDR mass flow rate, for droplet speed $v = C_D\sqrt{2P/\rho}$, optical depth τ_0 at the generator, and droplet diameter D. The masses of fluid in the generator and sheet are, respectively:

$$m_g = 2\pi\rho\int_0^{W/2} r^2\,dx$$

$$m_s = \frac{2}{3}WL\tau_0\rho D.$$

From these equations we obtain:

$$m_g/m_s = 0.17G\left[\left(\frac{P}{\Delta P}\right)^8 (C_D\tau_0)^{-5}\left(\frac{W}{D}\right)^3 R_0^{-2}\right]^{1/19}\frac{W}{L},$$

where G is a factor that depends on the taper of the tube ($G = 1$ for a straight tube; $G = 0.85$ for a taper from radius r_0 at center to 0.5 r_0 at the ends) and R_0 is the Reynolds number of the orifice flow. Taking $G = 1$, a fractional pressure loss of 0.1 ($P/\Delta P = 10$), expressing W in meters, and D in units of 100 μm, we obtain:

$$m_g/m_s \simeq 0.85\alpha\left[\frac{W(\mathrm{m})}{D(100\ \mu\mathrm{m})}\right]^{.16}\left[C_D\tau_0\right]^{-.26}\left[\frac{2000}{R_0}\right]^{.1}.$$

For $\alpha = 0.4$ the mass of liquid in the generator will be about 1/3 the mass of the droplet sheet for a wide range of applications, given the small sensitivity of m_g/m_s to all parameters except aspect ratio α. The tube diameter (straight tube) is found to be

$$D_{\mathrm{tube}}(\mathrm{cm}) \simeq 4\left[W(\mathrm{m})\right]^{.6}\left[D(100\ \mu\mathrm{m})\right]^{.4},$$

and is fortuitously comparable to the sheet thickness. The contribution of the tube shell to the generator mass will be small.

Droplet Collection

The droplet collector is the LDR component with the least developed technology base because it must perform a function for which there has been little prior need. It must be able to efficiently capture the incoming droplet stream with very small mass loss due to splashing or leakage, and to form the droplets into a continuous, pressurized liquid for transfer back to the power cycle. In the absence of gravity, the collector must employ some mechanism to create a body force on the fluid to repressurize it. Several mechanisms have thus far been considered: electrostatic, magnetic, or electromagnetic forces, inertial forces (of the droplet stream itself, or using an ejector), centrifugal forces, and surface tension. Although it has not been established which of these approaches is most practical, the two concepts illustrated in Figure 5 have received the most attention.

The centrifugal collector concept developed at the University of Washington and Mathematical Sciences Northwest, Inc., shown in Figure 5a, is simply a rotating drum in which the droplets strike and adhere to a conical target surface and migrate to the drum periphery by centrifugal acceleration. The drum is slightly tapered so that the liquid flows to a trough at the rear and is collected by fixed scoops. The vanes shown in the figure are to maintain a uniform distribution of fluid around the drum.

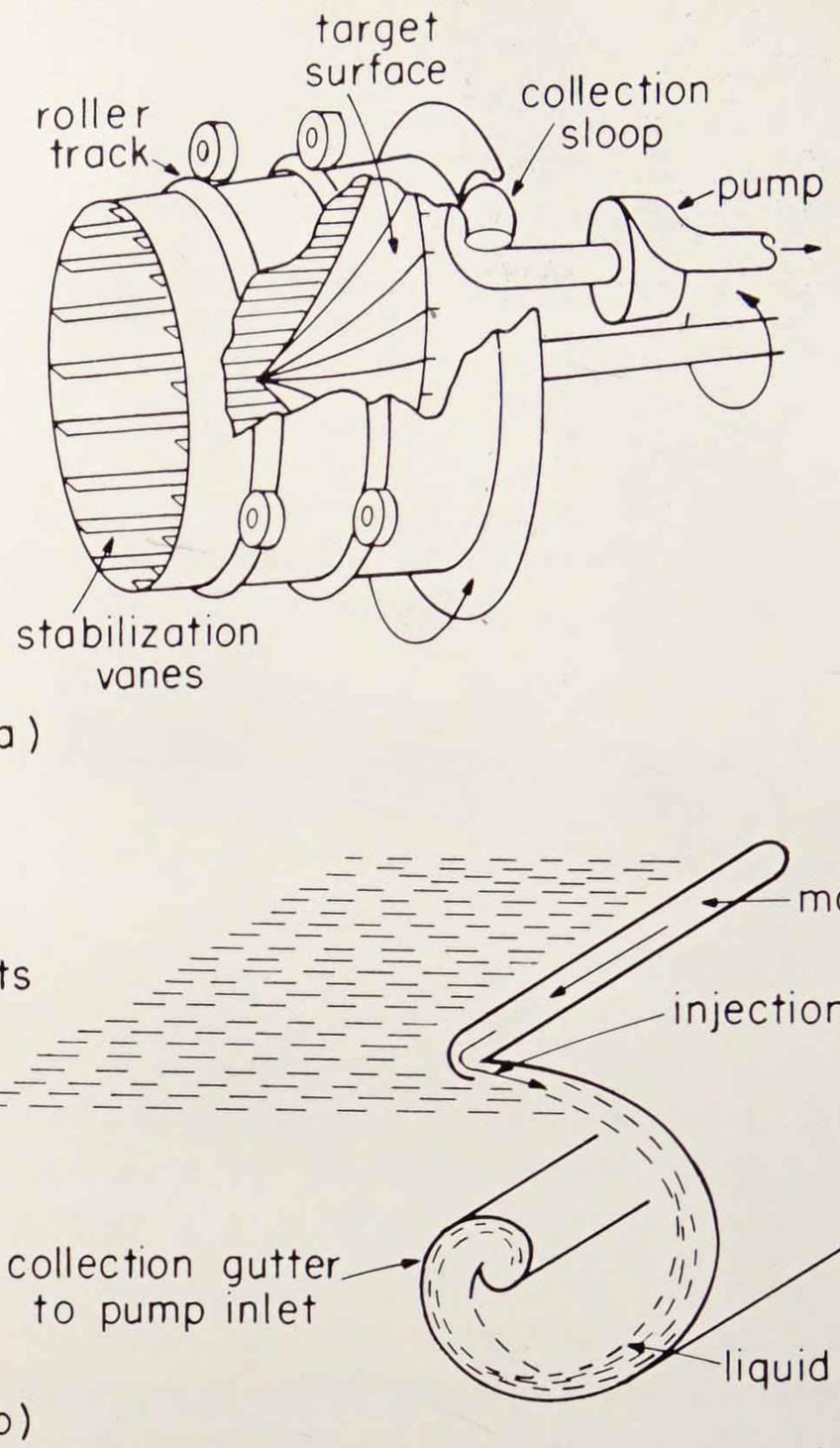


Figure 5 *Droplet Collection Concepts for a Liquid Droplet Radiator Using (a) a Rotating Shroud Collector (UW-MSNW) and (b) a Film-Injection Collector (Grumman Aerospace).*

The film injection collector of Figure 5b has been proposed by Grumman Aerospace. This collector relies on momentum of both the droplets and injected fluid to generate body forces for liquid transfer to the collection gutter. The combination of a high incidence angle of droplets on the liquid film and the reduced impact velocity of droplets due to the film motion could serve to inhibit splashing.

Clearly, a significant effort is required to demonstrate whether either collection concept will be effective in space. Realization of either scheme will require a better understanding of fluid transport under the combined action of surface tension, centrifugal and inertial forces in zero gravity. Principal issues include the degree of splash inhibition attainable from proper target surface selection and geometry (rotating collector) or film motion (film-injection collector) as well as wetting and fluid migration to the collector exterior.

LDR System Model

Based on the design considerations discussed above, a computer model of the LDR system has been drawn

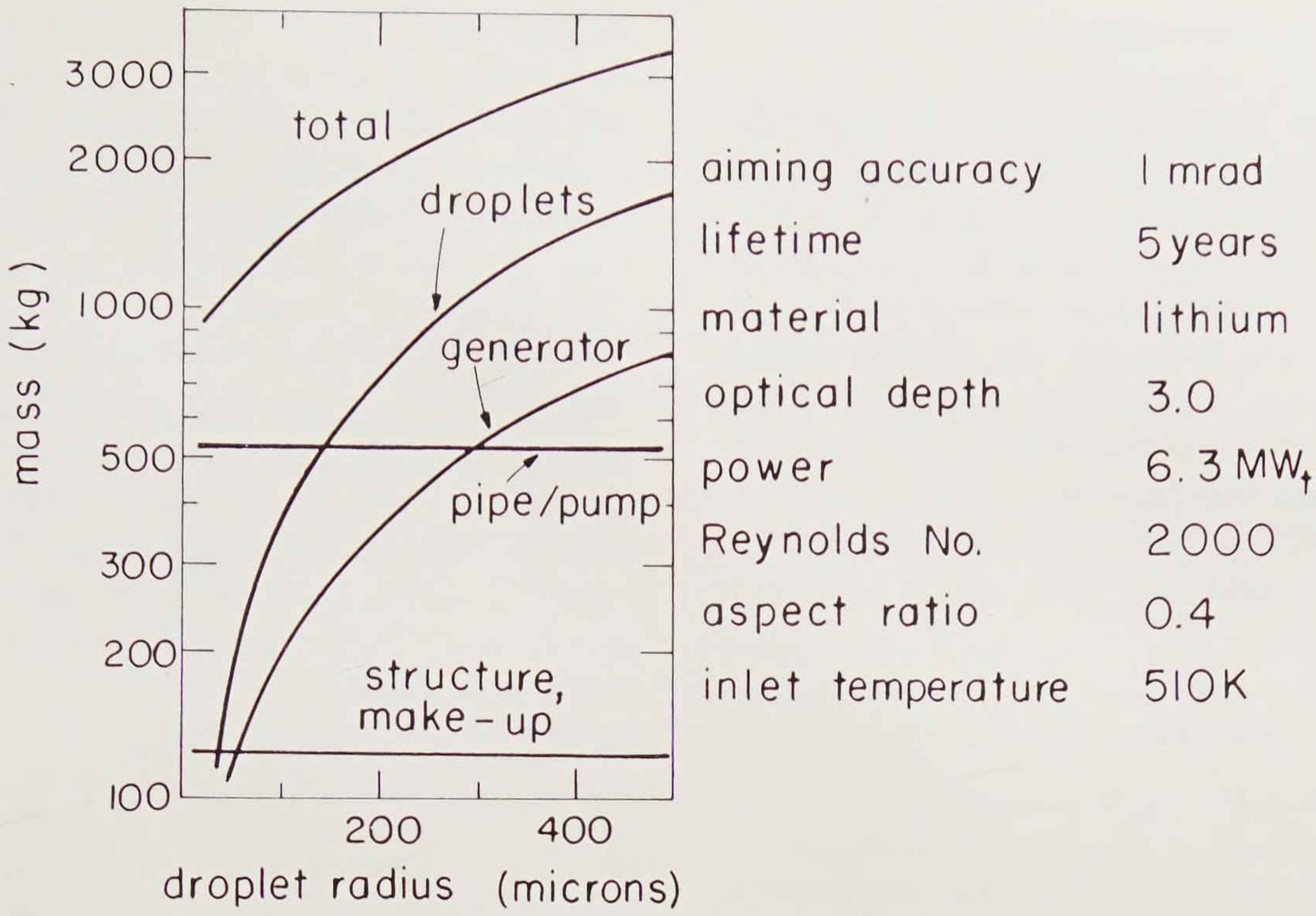


Figure 6 *Radiator and Component Masses vs Droplet Radius for a 6.3 MW Liquid Droplet Radiator Using Liquid Lithium.*

up for computing system mass and performance for a specified heat rejection requirement. This model assumes a triangular sheet geometry with spray bar generator and rotating collector, and includes a support structure, pump, and (for single-pass LDRs) a fluid return pipe. The operating characteristics and masses of the latter three components are based on standard engineering design and existing hardware, while mass and fluid dynamic models for the droplet sheet and generator have been given above. The collector mass is approximated by a cylinder with an aperture $\simeq 4$ times the droplet spread due to misaiming, an $L/D \simeq 1$, and a wall thickness sufficient to protect against micrometeoroid puncture. A simple hydraulic model is used to calculate the collector rotation rate and drive power needed for the LDR's mass flow rate. Input parameters for the program include fluid properties, radiated power, droplet diameter, aiming accuracy, peak droplet temperature, radiated power, droplet diameter, aiming accuracy, peak droplet temperature, sheet aspect ratio and optical depth, and radiator lifetime. The program computes the components' sizes and masses, flow rate, pressures, and evaporative mass loss. Despite uncertainties regarding the performance of the largely conceptual generator and collector components, it is felt that this model provides a reasonable approximation to what might be achievable with a practical LDR. (A detailed description of the model is given by Mattick and Taussig (1984)).

The variation with droplet radius of component mass and total radiator mass for a single-pass 6.3 *MW*t lithium radiator is shown in Figure 6. As expected the performance is best for smaller droplets. At radii below $\simeq 120$ μm the return pipe and pump dominate the radiator mass. For the 510 K insertion temperature, the make-up mass is a small fraction of the total mass. The 1 mrad aiming accuracy leads to a collector mass less than 5 percent of the total mass. This indicates that considerably poorer aiming accuracies could be tolerated before the collector mass becomes dominant.

The variation in power/mass for LDRs using various fluids is shown in Figure 7 as a function of peak droplet

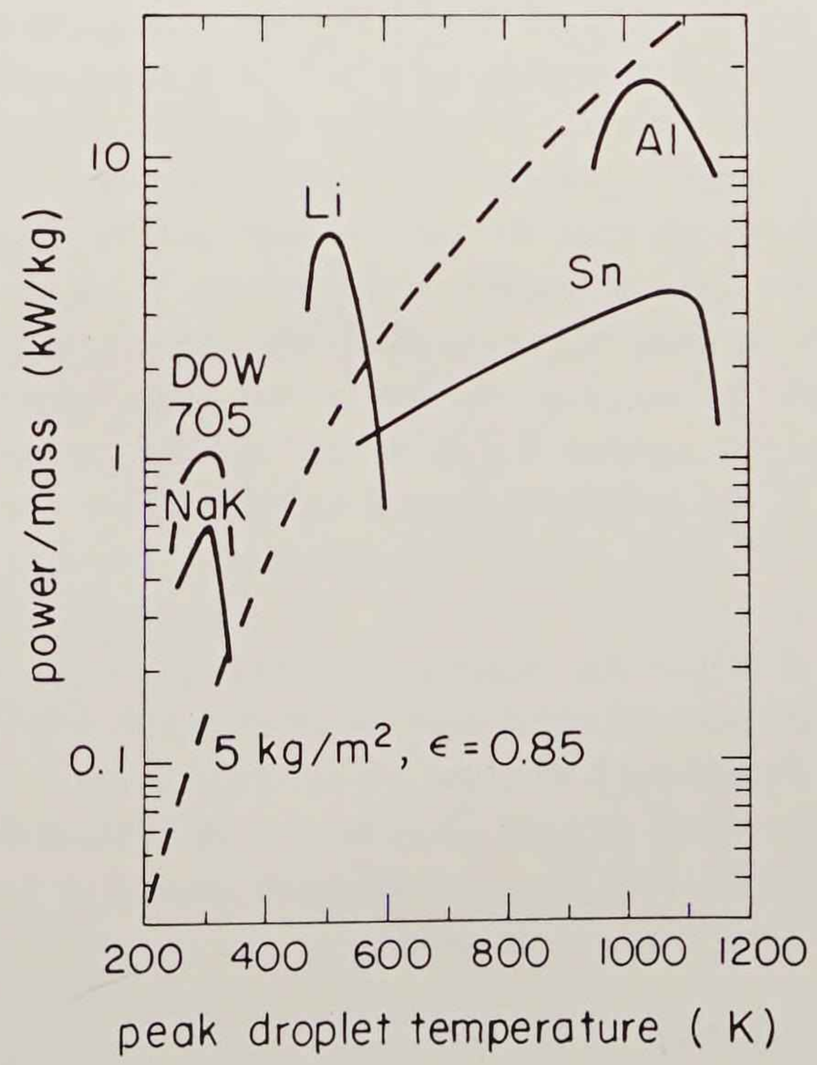


Figure 7 *Power per Mass of Liquid Droplet Radiator vs Peak Droplet Temperature. The Dashed Curve Corresponds to an Advanced Heat Pipe Radiator.*

temperature and is compared with the power/mass of a heat pipe radiator with mass/area = 5 kg/m^2, emissivity $\epsilon = 0.85$. The Dow 705 curve assumes a double pass radiator, and all other curves assume a single pass model with a return pipe. LDR systems using Dow 705, Li, or NaK can be 5–10 times lighter than heat pipes. Although tin and aluminum LDR systems are somewhat heavier than heat pipes for the system model chosen, by using a two pass configuration (no return pipe) and droplets < 50 μm in diameter, both Sn and Al LDRs would weigh less than heat pipes. Moreover, for LDR and heat pipe systems of comparable weight, the LDR has the advantage of compact stowage and simple deployment.

Key Technology Issues

We have demonstrated that in principle, at least, a liquid droplet radiator system can be much lighter than the most advanced solid surface radiators. It is fully appreciated, however, that a sound technology base for the LDR does not yet exist, and that many fundamental science and engineering issues must be resolved before the LDR becomes a practical power system component. In this section we will outline the key technology issues that must be addressed at this stage of LDR development.

Droplet Generation

Although the use of orifice arrays for droplet generation is an established technique in ink jet printing, the application of this technique for LDR generators will require significant technological advancement because of the very large number of LDR droplet streams and the necessity of maintaining absolute aiming accuracy over periods of years. Besides the question of fabricating $> 10^5$ orifices which are precisely aligned, it must be demonstrated that the orifices will not be degraded due to erosion or material deposition in long term operation. It does not seem likely that stream misdirection could be rectified in space. An issue which has arisen in the current LDR orifice testing program is wetting of the orifice substrate exterior. This not only can lead to fluid loss at the generator, but can also degrade the aiming of streams. The directional characteristics of liquid jets during transient operation (start-up and shut-down) must also be established. Finally, it must be determined whether an acoustic drive is necessary to produce a droplet sheet having suitable radiative characteristics, and if so, an efficient means of providing this drive must be devised.

Droplet Collection

The various techniques for droplet collection that have thus far been proposed have little basis in practice. Fundamental studies of liquid transport in zero gravity must be carried out to determine which scheme has greatest merit. While some aspects of collector operation can be tested in a gravity field, zero-gravity tests will be required to verify most analytical predictions of a collector's performance. Splashing and wetting phenomena are central issues for effective collector operation.

LDR Liquids

LDR component design and performance are strongly influenced by the properties of the LDR liquid chosen for a given application. Only a few liquids have thus far been identified as attractive candidates. The radiative, thermodynamic, and fluid properties of these liquids need to be better characterized to accurately assess their usefulness for LDR applications. The stability of silicone fluids in the space environment must be determined, and the corrosiveness of the liquids, particularly the liquid metals, to nozzle substrate materials must be established. It would be useful to search for or develop additional low vapor pressure liquids for the LDR in order to enlarge the range of missions in which the LDR could be used. The possibility of enhancing the emissivity or reducing the vapor pressure of LDR liquids by using additives or coatings should also be investigated.

In addition to these key issues which are fundamental to the development of practical LDR designs, there are a number of other areas that must be investigated which relate to the integration of the LDR with space power systems. These include the radiator-power cycle interface, LDR attitude control and the operation of the LDR during maneuvers, charging characteristics of the droplet sheet in the space plasma, and contamination of the spacecraft by the LDR fluid as well as fluid contamination by spacecraft effluent.

Summary and Conclusions

Constraints on LDR performance and LDR component design were established by analyzing the radiative properties of a droplet sheet as a function of sheet parameters and liquid properties. The power/mass of the droplet sheet was shown to depend strongly on the liquid properties, and among the low vapor pressure fluids considered here, lithium, Dow 705 silicone fluid, and NaK were found to give a decided performance advantage of the LDR over conventional radiator designs. (Tin and tin eutectic alloys would also be advantageous if the use of droplets < 50 μm in diameter proves feasible.) LDRs with heat loads > 100 kWt will require $> 5 \times 10^5$ droplet streams and no stream can be lost due to misaiming without incurring an intolerable mass loss. At the collector, the loss due to splashing must be < 1 droplet in 10^7. Some design concepts for droplet generation and collection subject to these mass loss constraints were presented and were incorporated into a system model for the LDR. By varying the input

parameters—droplet size, speed, temperatures, optical depth, for example—design points were found for which LDR systems using Li, NaK, and Dow 705 were $\simeq 5$ times lighter than heat pipe radiators at a given thermal load and heat rejection temperature. Finally, the key issues of LDR technology were reviewed.

A vigorous program of fundamental and engineering studies, aimed at resolving these issues and developing practical LDR components, is currently being carried out under NASA and Air Force sponsorship. Although the problems are certainly challenging, there is at present no reason to believe that their solutions will require fundamental technology breakthroughs. The LDR does invoke the use of fluid control processes that have little precedent in space systems, but their realization appears to depend on a straightforward, if laborious, extension of current technology and design practice. The availability of a lightweight and easily transportable radiator would considerably ease the design constraints on the energy source (nuclear reactor, for example) and conversion components of a space power system, and this fact strongly argues that the level of R&D effort devoted to the LDR and other lightweight radiator concepts be comparable to that devoted to conversion and energy source technology.

Acknowledgments

This work was supported by NASA grant NAG 1-327 and AFRPL contract F04611-81-K-0040.

References

Botts, T. E. and J. R. Powell (1984) "Magnetic Focusing of Liquid Droplet Sheets for Rejection of Heat in Space," presented at the *First Symposium on Space Nuclear Power Systems*, Albuquerque, N.M., Jan. 11–13, 1984.

Hendricks, C. D., K. S. Robinson, and R. J. Calliger (1976) "Examination of Fluid Droplet Collisions," UCRL Preprint 78493.

Jackson, C. B. (1955) *Liquid Metals Handbook, Sodium (NaK) Supplement*, Atomic Energy Commission.

Kuhn, L. and R. A. Meyers (1979) "Ink Jet Printing," *Scient. Am.* 240 (April):162–178.

Levanoni, M. (1977) "Study of Fluid Flow through Scaled-up Ink Jet Nozzles," *IBM Jl. Res. Dev.* 21:56–68.

Mattick, A. T. and A. Hertzberg (1981) "Liquid Droplet Radiators for Heat Rejection in Space," *J. Energy* 5:387–393.

Mattick, A. T. and A. Hertzberg (1982) "The Liquid Droplet Radiator—An Ultralightweight Heat Rejection System for Efficient Energy Conversion in Space," *Acta Astron.* 9:165–172.

Mattick, A. T. and R. T. Taussig (1984) "New Thermal Management and Heat Rejection Systems for Space Applications," Final Report, Air Force Rocket Propulsion Laboratory Contract F04611-81-K-0040.

Nesmeyanov, An. N. (1963) *Vapor Pressure of the Elements*, Academic Press, New York.

Prandtl, L. and O. G. Tietjens (1957) *Applied Hydro- and Aeromechanics*, Dover, New York, p. 42.

Rayleigh, L. (1879) "On the Instability of Jets," *Proc. Lond. Math. Soc.* 10:4–13.

Smithells, C. J. (1955) *Metals Reference Handbook*, Butterworths, London, Vol. 2, pp. 575–618.

Tepper, F., J. King, and J. Greer (1967) "Multicomponent Alkali-Metal Alloys," in *The Alkali Metals*, The Chemical Society, London, pp. 23–31.

Space Nuclear Power Systems 1984
Edited by M. S. El-Genk and M. D. Hoover
© Orbit Book Company, Malabar, FL, 1985

Chapter 50

Magnetic Droplet Radiator Collectors

T. E. Botts, J. R. Powell, and F. L. Horn

Department of Nuclear Energy
Brookhaven National Laboratory
Building 820M
Upton, New York 11973

Radiating heat via a droplet sheet offers a light weight, easily deployable means of rejecting energy from a spacecraft. Uncertainties in the trajectory of the droplets and splashing in the droplet collector can lead to unacceptable coolant mass losses. A study conducted at Brookhaven National Laboratory has investigated using ferrofluids with magnetic collectors to reduce these potential losses. Streams of ferrofluid droplets have been produced through 100 and 150 μm orifices. These droplets have been accelerated in excess of five "*g*'s" using permanent magnets and have been observed to behave stably and remain intact. Preliminary testing with thirty-seven parallel streams indicates that, except for collector splashing, multiple streams behave, from a fluid's viewpoint, like single streams. Single drops impacting under conditions known to produce satellite drops following impact were observed for varying magnetic conditions. At roughly one kilogauss, all incoming material would be captured under weightless conditions. Rebounding material tends to flow along lines of magnetic flux. Trade studies indicate that a range of conditions exists over which magnetic collections offer a weight advantage over a heat pipe radiator or droplet radiator with a large collector.

Introduction

As spacecrafts become larger, more complex, and more powerful, thermal management becomes an increasingly important issue. Heat must be rejected from a range of devices including refrigerators used to maintain cryogens in the liquid state as well as to cool charged particle accelerators, high powered radar, and large IR detector arrays. The energy rejected from power cycles may well represent one of the most stressing thermal management problems currently confronting designers of future spacecraft.

Radiation to the colder parts of the sky is the only means available for rejecting energy from a spacecraft without exhausting mass to space. However, the low temperatures that are most desirable from a thermodynamic viewpoint require very large amounts of radiating area for rejecting energy. In the case of a power cycle, the peak temperature is quite often fixed by materials' limitations; and, in addition, an increase in the reject temperature can adversely impact cycle efficiency. For these and other reasons, historically the radiator has either been a massive part of a space power system or else the power system has operated with a fairly small temperature differential, thus making all of the other components rather unwieldy.

One means of overcoming this dilemma has been to attempt to design an ultra-light weight, space radiator. Dust (Hedgepeth 1978), moving belt (Schuerch and Robbins 1964), finned tube (Mackay 1963), heat pipe (Werner and Carlson 1977), and droplet (Mattick and Hertzberg 1980) concepts have all been pursued at some point. Although all the concepts have shown some

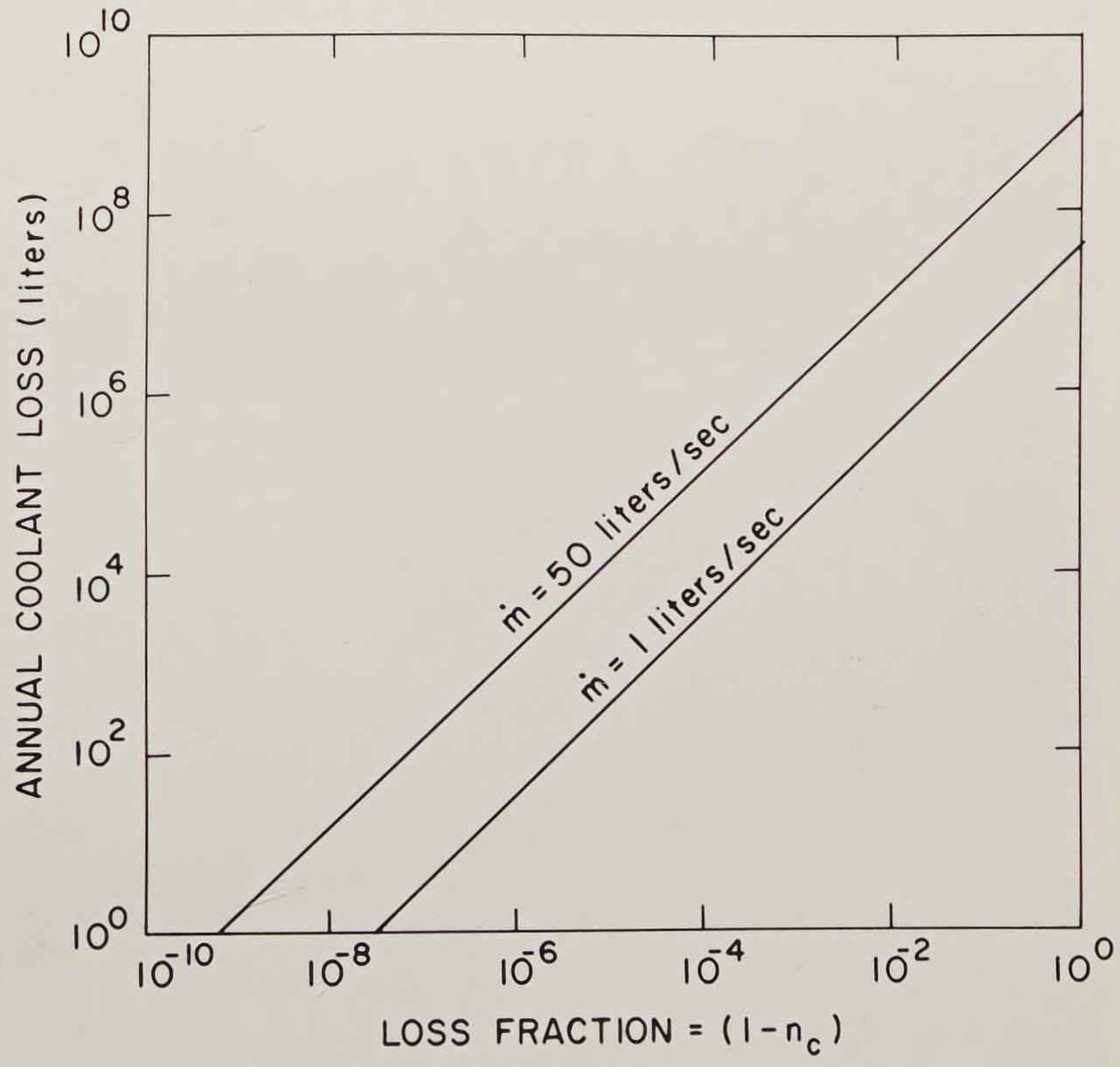


Figure 1 *Annual Coolant Loss Rate as a Function of Loss Fraction for Droplet Radiator Collector.*

indication that they could be engineered into workable system, each concept presents some difficulties.

Droplet collection, for example, may be a difficult task because of the very high efficiency demanded of the collector unit. Figure 1 shows the annual mass loss of coolant as a function of collection efficiency, n_c, for a ten megawatt liquid droplet radiator (LDR). Losses significantly less than the ppm level are clearly required. Low losses are required to minimize spacecraft contamination as well as to minimize the makeup weight penalty.

Losses of radiating fluid can result from a wide range of events or conditions such as:

1. Directional dispersions which occur at the generator;
2. Velocity dispersions which occur at the generator;
3. Droplet charging, and the resultant dispersion due to Coulombic repulsion;
4. Evaporation of droplet material;
5. Spacecraft accelerations;
6. Incident pulsed radiation which imparts a force to the particles;
7. Splashing in the collector; and
8. Collisions between droplets.

Evaporation also limits the peak droplet temperature. Spacecraft accelerations of an unplanned sort and pulsed illumination of the droplet sheet by hostile forces would be intermittent and may need to be lived with. Other directional and velocity dispersion sources will, on a continuous or semicontinuous basis, cause some

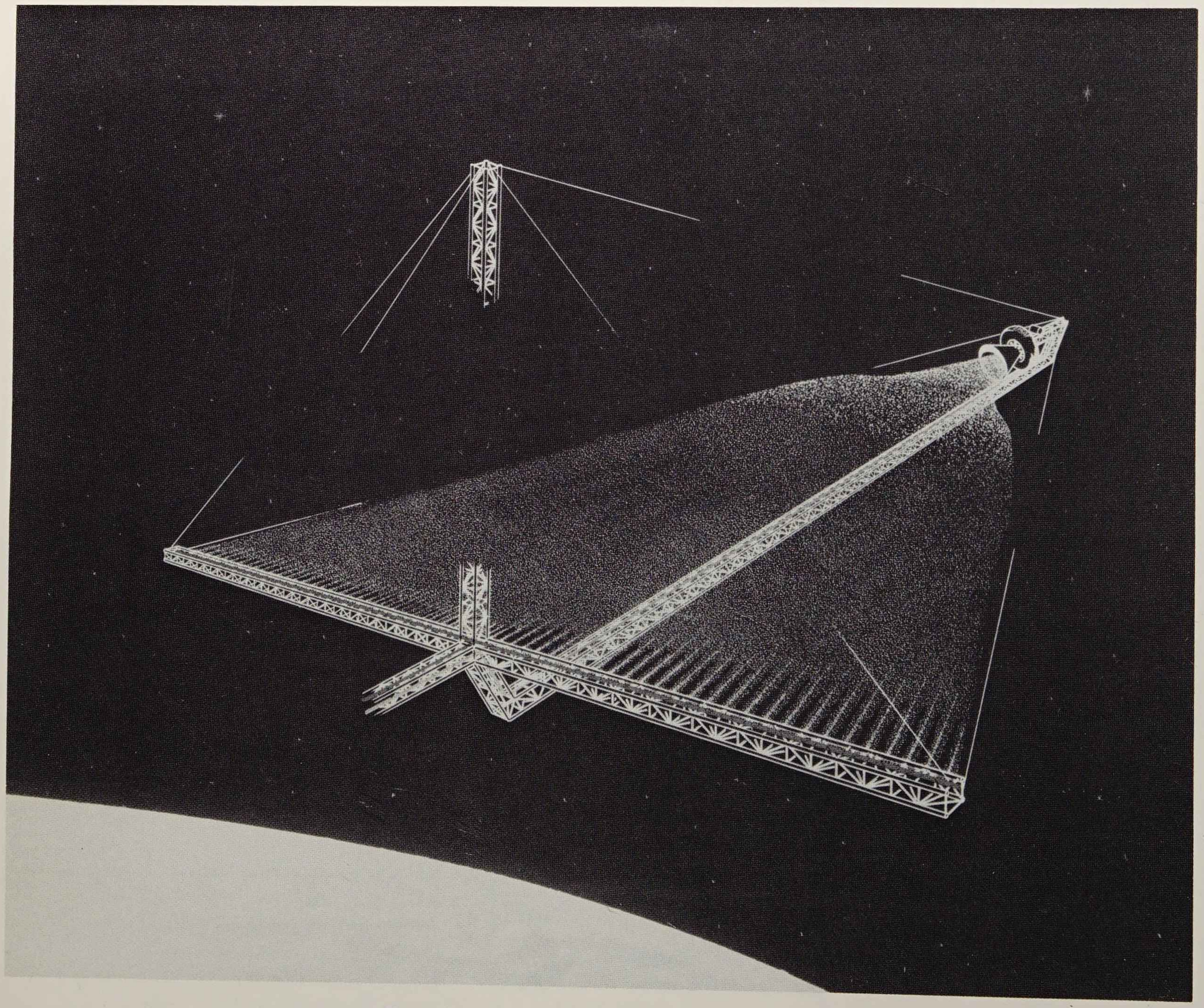


Figure 2 *Magnetic Droplet Radiator in Operation.*

droplet trajectories to fall outside the collector. Two means of overcoming this problem exist. First, a larger collector can be built. Larger collectors, however, have greater weight, greater radar cross section, and other unattractive characteristics. In addition a larger collector could not guarantee that splashing would not still pose a potential loss mechanism.

A second solution involves applying a body force, either electric or magnetic, to the particles to steer them into the collector. Due to spacecraft charging, charge exchange in the collector, and other considerations such as internal forces within the sheet inducing repulsion, magnetic forces were thought to be a more fruitful area for pursuit rather than electric forces.

Figure 2 illustrates a magnetically focused droplet radiator. The radiator working fluid is either a ferrofluid, marketed by Ferrofluidics Corporation of Nashua, New Hampshire, or else a slurry of small ferromagnetic particles. In this case, a superconducting solenoid provides the magnetic field which accelerates and focuses the droplet sheet.

Ferrofluid Droplet Streams

Single and multiple streams of ferrofluid were created using 100 and 150 μm aluminum or sapphire orifices. A piezoelectric transducer was used to form individual droplets. This stream size provided easily observable droplets, although smaller orifice sizes can be made.

Vacuum in the free-fall zone is obtained with a rotary pump. Pressure is measured both with a dial gauge and a thermocouple gauge. Base pressures between one and five Torr are used. It has been observed that at higher working pressures, drag forces become significant at fairly low velocities and may perturb the generator. Both the ferrofluid and Dow–Corning 702 silicone vacuum oil (DC-702) contain significant amounts of absorbed gas. By pumping on these fluids for three or four days, most of the absorbed gas can be removed. Additional gas is absorbed by using a cover gas or air to drive the generator; during a run, however, this amount is small when it is compared with what is present in the "as delivered" condition of either gas.

A cobalt-samarium permanent magnet is used to create a magnetic field in the vacuum vessel. The magnet measures $0.025 \times 0.025 \times 0.010$ m and is magnetized parallel to the short-side. Figure 3 shows the magnetic field strength of this magnet along an axis in parallel with its magnetization. In order to facilitate clean up, the magnet is housed in a plastic box which limits the distance between the chamber and the magnet to 0.032 m. To verify jet and droplet stream stability in the presence of such a field, the magnet is placed on a linear motion feed-through which allows the magnet to approach the stream, approximately thirty centimeters below the generator. The magnet can also be placed in the catch tray behind the plexiglas wedge used to

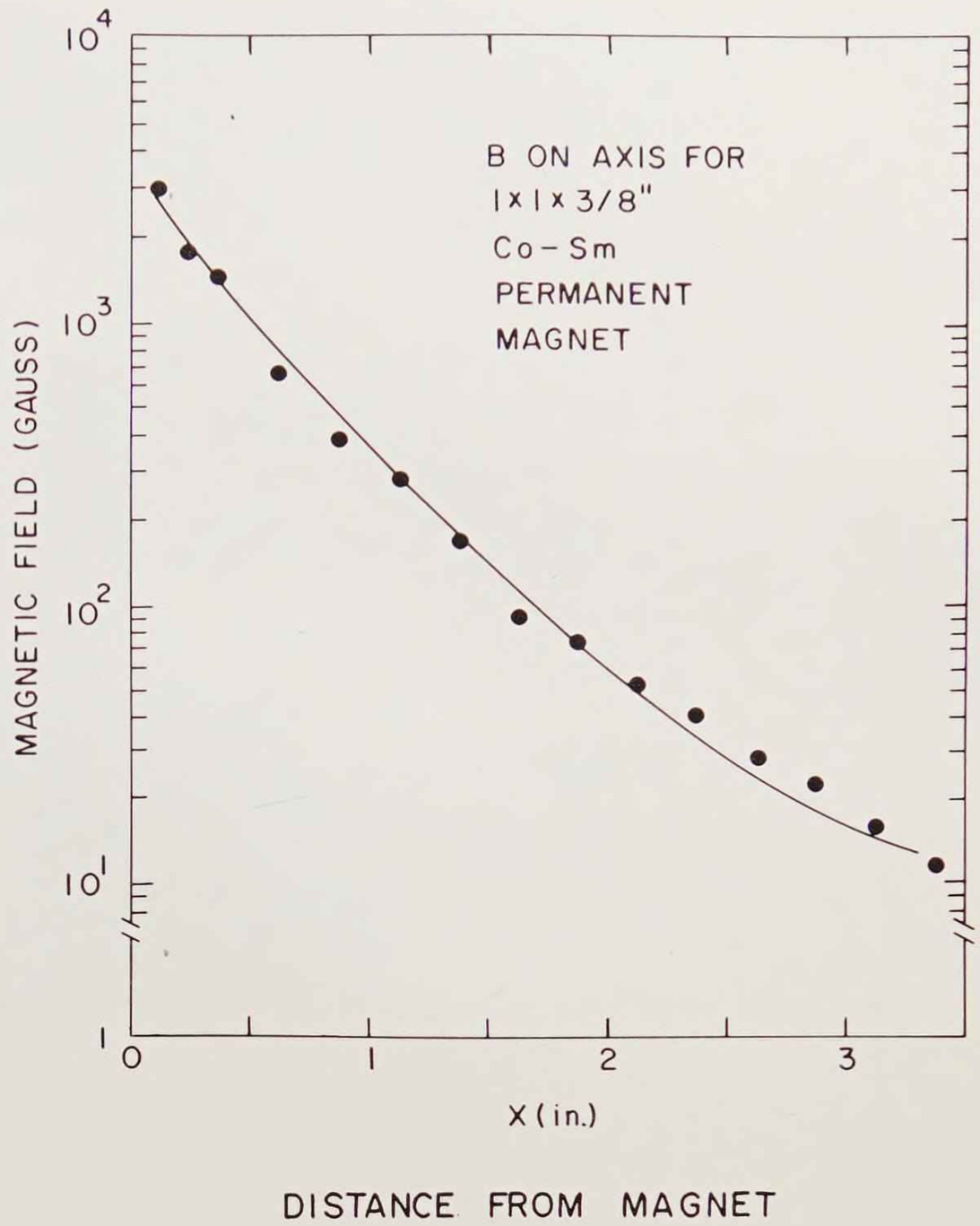


Figure 3 *Magnetic Field Strength of Co-Sm Permanent Magnet.*

study the droplets' impact. For this application, it cannot be moved during any specific run.

Ferrofluid droplet streams were observed in the presence of various magnetic fields, which are shown in Figures 4 and 5. In all cases, the droplet stream remains stable as well as the droplets at accelerations as high as five to ten "g's." These accelerations may seem high, but accelerations near the collector surface of this level may well occur.

Multiple Jet Studies

Multiple droplet streams have been observed as well. Figure 6 shows silicone oil jets from thirty-seven 100 μm orifices, 0.0010 m apart, in a hexigonal array. The jets are being driven at four kilohertz. The apparent wiggling of the streams is caused by the entire generator plate responding to the oscillating pressure. An actual generator would be made of thicker stock with counterbored feeds to the orifices. Most importantly, over the distances investigated, a generator plate with a relatively large number of orifices can operate stably.

The multiple jets of ferrofluid, mixed with DC-702 and outgassed, are shown in Figure 7. These jets are generally stable. Within the constraints of the magnetic fields which can be produced with a small bar magnet, they do not appear to become unstable when bent. However, because of the higher jet velocity, they are

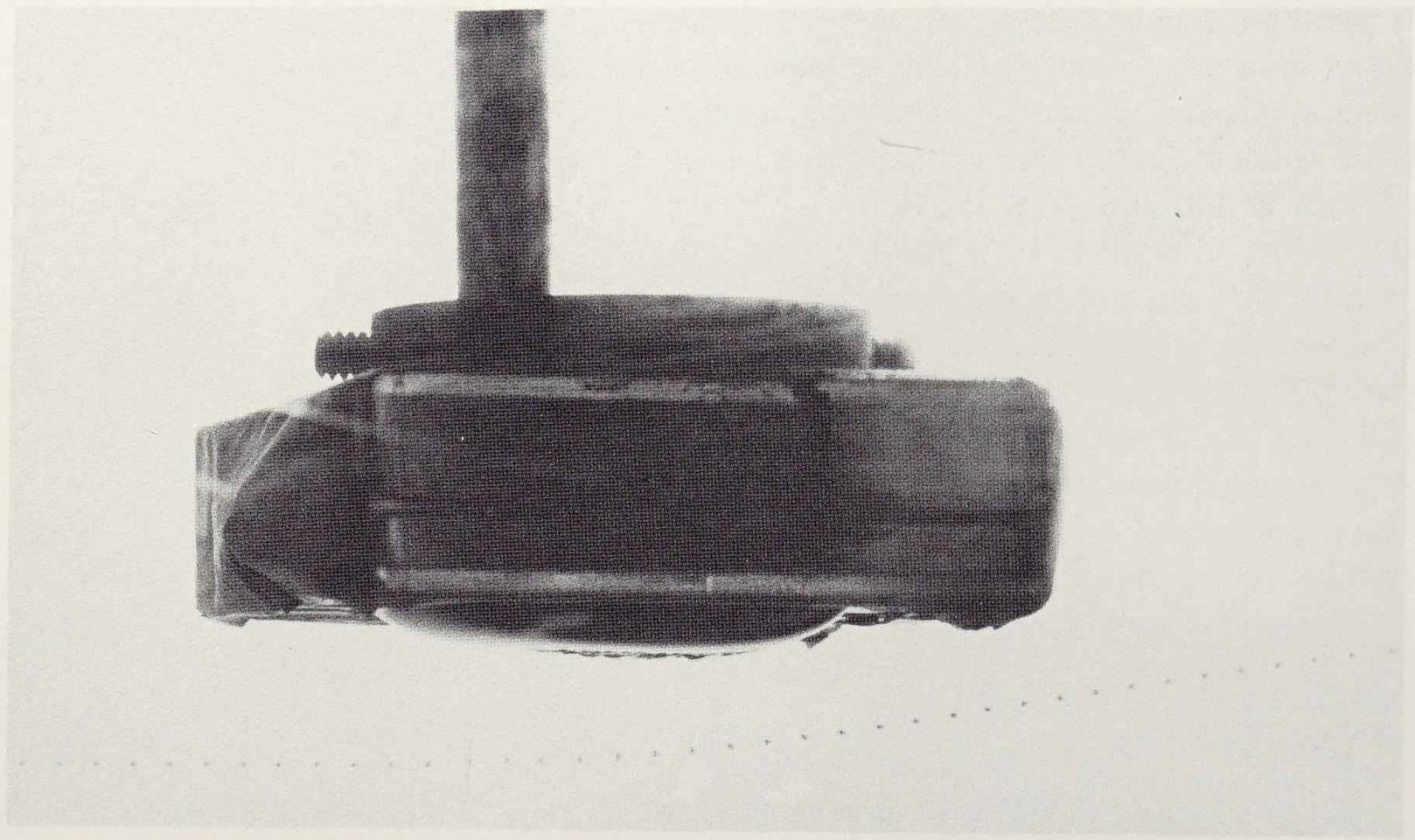


Figure 4 *Ferrofluid Droplets and Magnet. Peak Field is 1.5 kG.*

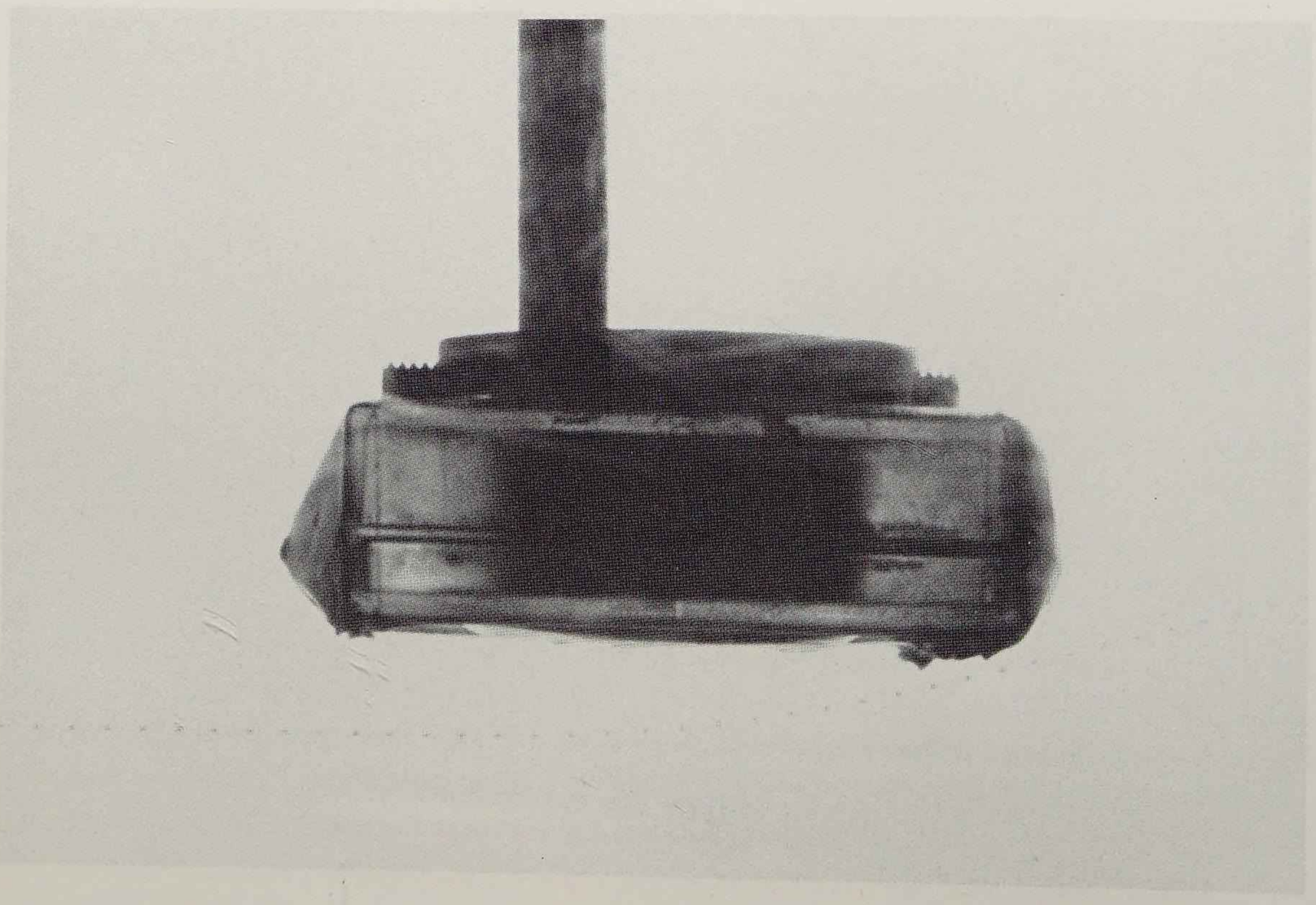


Figure 5 *Ferrofluid Droplets and Magnet. Peak Field is 2.0 kG.*

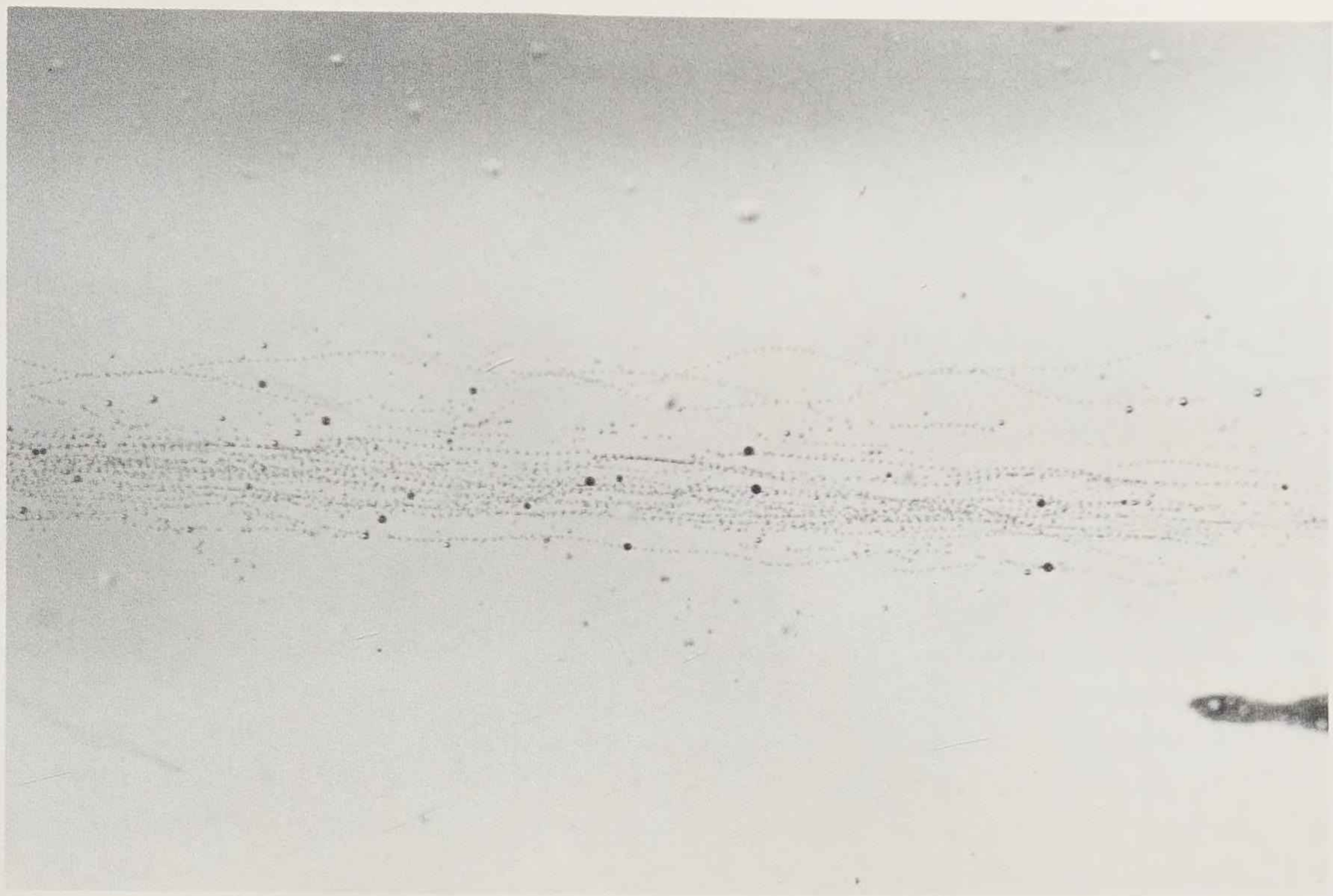


Figure 6 *Multiple DC-702 Streams, 4 kHz.*

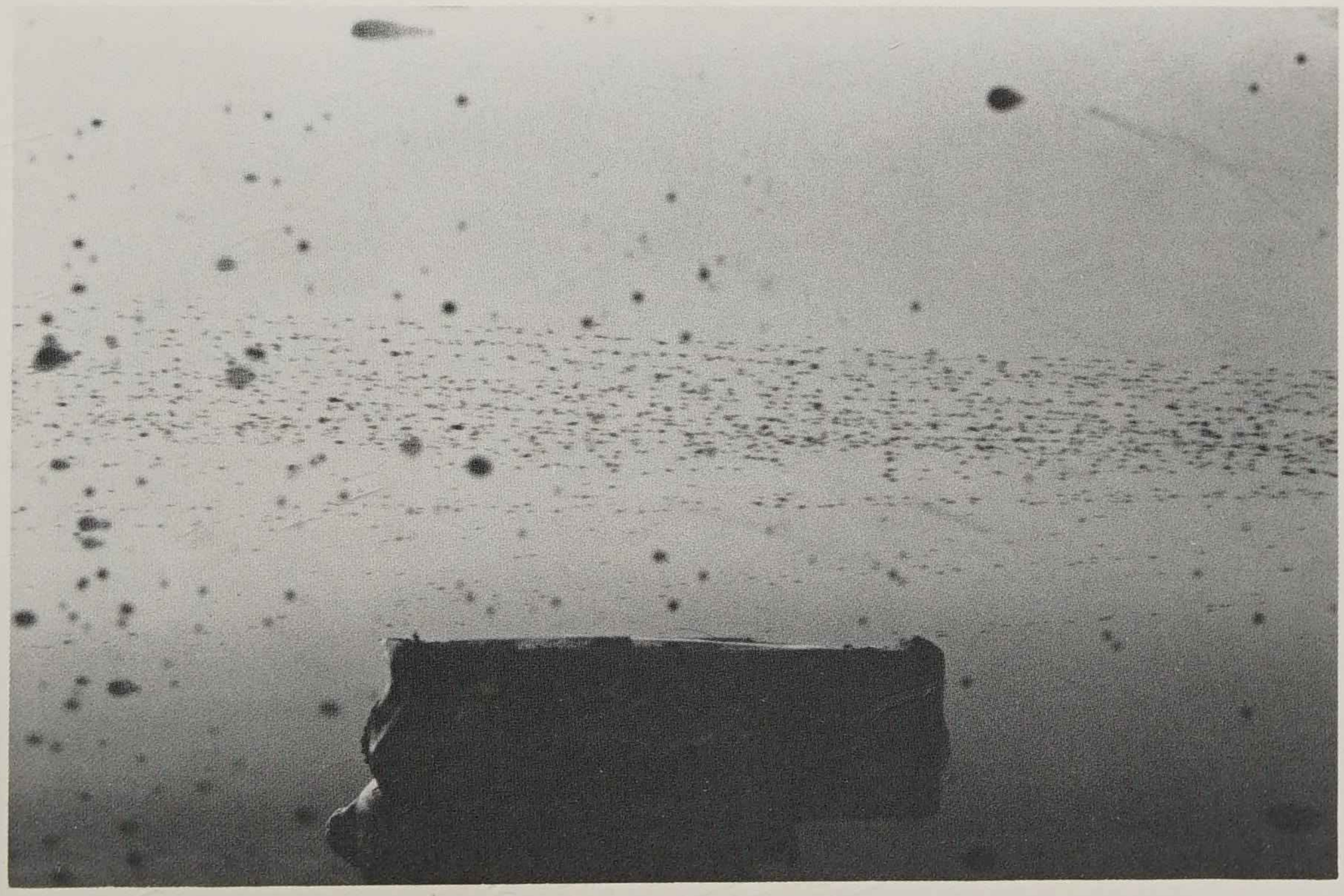


Figure 7 *Multiple Ferrofluid Streams and Magnet.*

not as clearly photographed. Since larger droplets are formed from fluid which wets the generator plate, generator plate wetting may be a serious issue in an LDR's design.

Ferrofluid Splashing

Single drops impacting on wetted surfaces have been observed photographically in order to begin assessing the influence of magnetic fields on splashing. An incoming droplet can be described by its angle of incidence to the collector, its Weber number (the perpendicular Weber number (1 to 20) will probably be the significant parameter), its collector surface type, and the droplet's material state. A liquid drop is used in all cases. Its normal impact velocity may vary between 0.5 and 5 meters per second, its particle diameter may vary between 500 and 200 μm, its density may vary between 50 and 200 kg/m^3; and its surface tension may vary between 2.0×10^{-2} (oil) and 4.0×10^{-2} (metal) N/m. Thus, a Weber number between 0.025 and 500 might describe a droplet entering a collector. Furthermore, droplets impacting upon the collector surface will interact with other splashes.

Splashing can cause the formation of small satellite drops. In the first set of observations, a drop having a Weber number near unity was impacted upon a glass slide wetted with a thin layer, $\sim$10 μm, of silicone oil. Each drop impacted the slide with its velocity normal to the slide.

Magnetic induction at the impact surface was varied between 50 and 3000 gauss. The magnetic field was produced by using a cobalt-samarium permanent magnet. Interestingly, all drops fell roughly twenty-five centimeters before impacting the slide. Because of the presence of the magnetic field, the impact velocity for the kilogauss environment was quite a bit higher than the free-fall velocity.

A value of 51 gauss for the magnetic induction at the slide surface allows the ferrofluid to flow across field lines and to behave like such a fluid in a field-free environment. Figure 8 shows most of the drop's mass rebounding away from the slide as a continuous element. Several small satellite droplets ($r < 50$ μm) may be seen around the primary event. In this case, the magnetic forces are insufficient to recover the ejected fluid in a zero gravity environment.

As can be seen in Figure 9, at the higher field



Figure 8 *Ferrofluid Impacting on Slide Surface at 51 Gauss.*

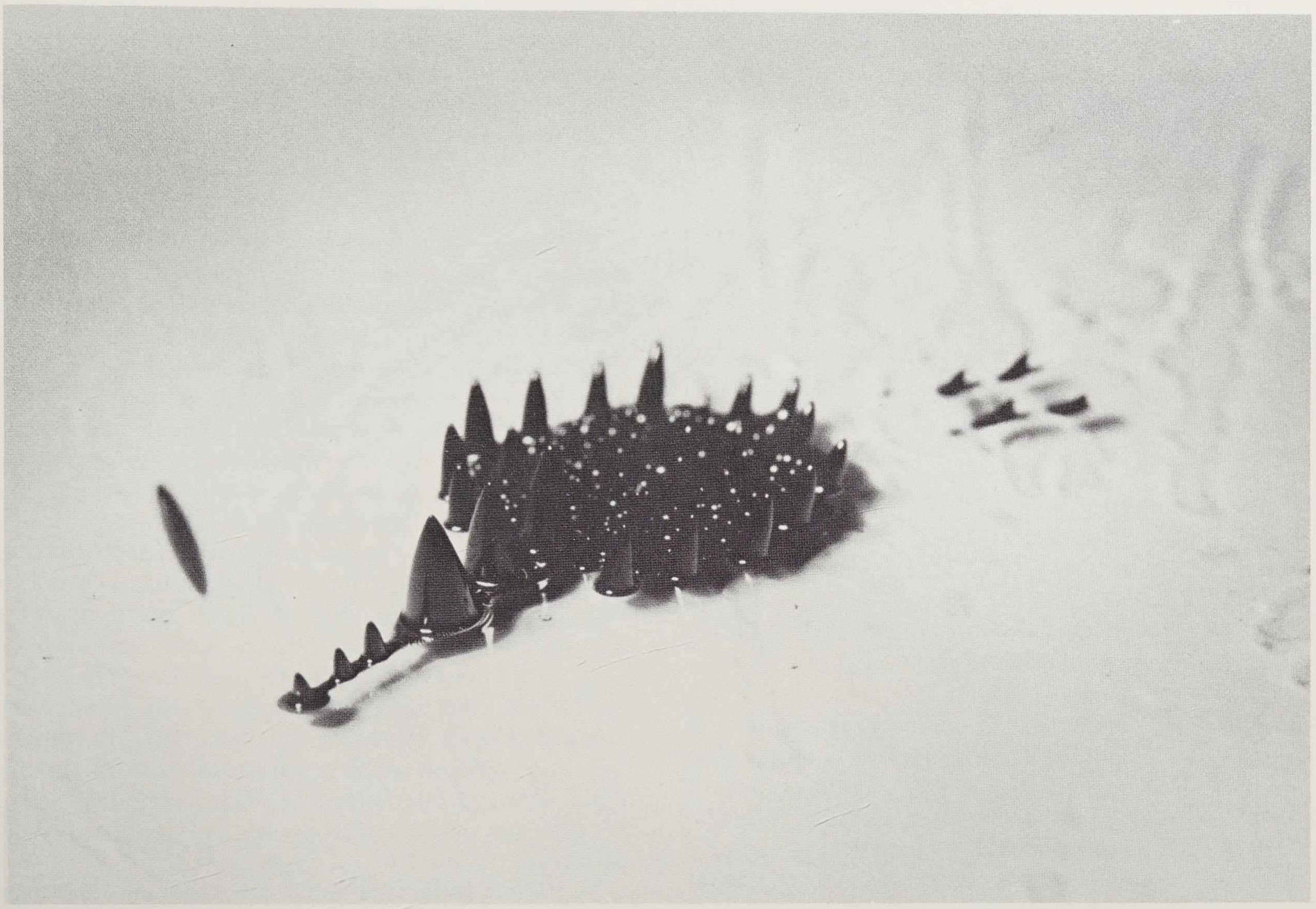


Figure 9 *Ferrofluid Impacting on Slide Surface at 1.44 kG.*

strength of 1.44 kilogauss the rebounding column of fluid is halted fairly soon after its formation. It then tumbles back down onto the collector surface where no satellite droplets were observed, thus indicating recovery in a zero gravity environment.

Radiator Scaling

In order to assess how magnetic collection affects the weight of a liquid drop radiator system, trade studies were undertaken. These studies examined three options: a larger collector for a non-magnetic LDR, a LDR with magnetic focusing, and a conventional heat-pipe radiator. For magnetic LDRs, the acceleration of the droplets toward the collector is on the order 1 to 10 m/s^2 for droplets at the extreme edge of the sheet, assuming a maximum distance from the center of the collector of 1.5 times their "miss" distance. Some form of splash suppression may be necessary for non-magnetic LDRs, which probably would have an associated weight penalty. However, this possibility was not included in the study.

Two different working fluids and temperatures were chosen for investigation. Specific power values for a non-magnetic LDR were obtained from the University of Washington (Hertzberg and Mattick 1983) and Mathematical Sciences Northwest (Taussig 1983). These radiators were considered to be the base-line design. No magnets were used in them and it was assumed that a magnetic LDR behaves identically to a conventional LDR, except for the addition of the magnets. On Figures 10 and 11, the variation in base-line specific power was the result of a larger collector. This design, however, does not assure that all splashes were collected.

Figure 10 shows the variation of a NaK LDR specific power with droplet sheet divergence angle for different magnet technologies and required accelerations. Superconducting magnets, and lower accelerations have a smaller weight penalty. As the divergence angle increases, the distance over which the droplets must be accelerated to assure successful collection also increases. In order to do this, the peak field must concomitantly increase, with the weight of the electromagnet.

As a means of comparison, a conventional heat-pipe radiator is also shown on this plot. For the lower bound

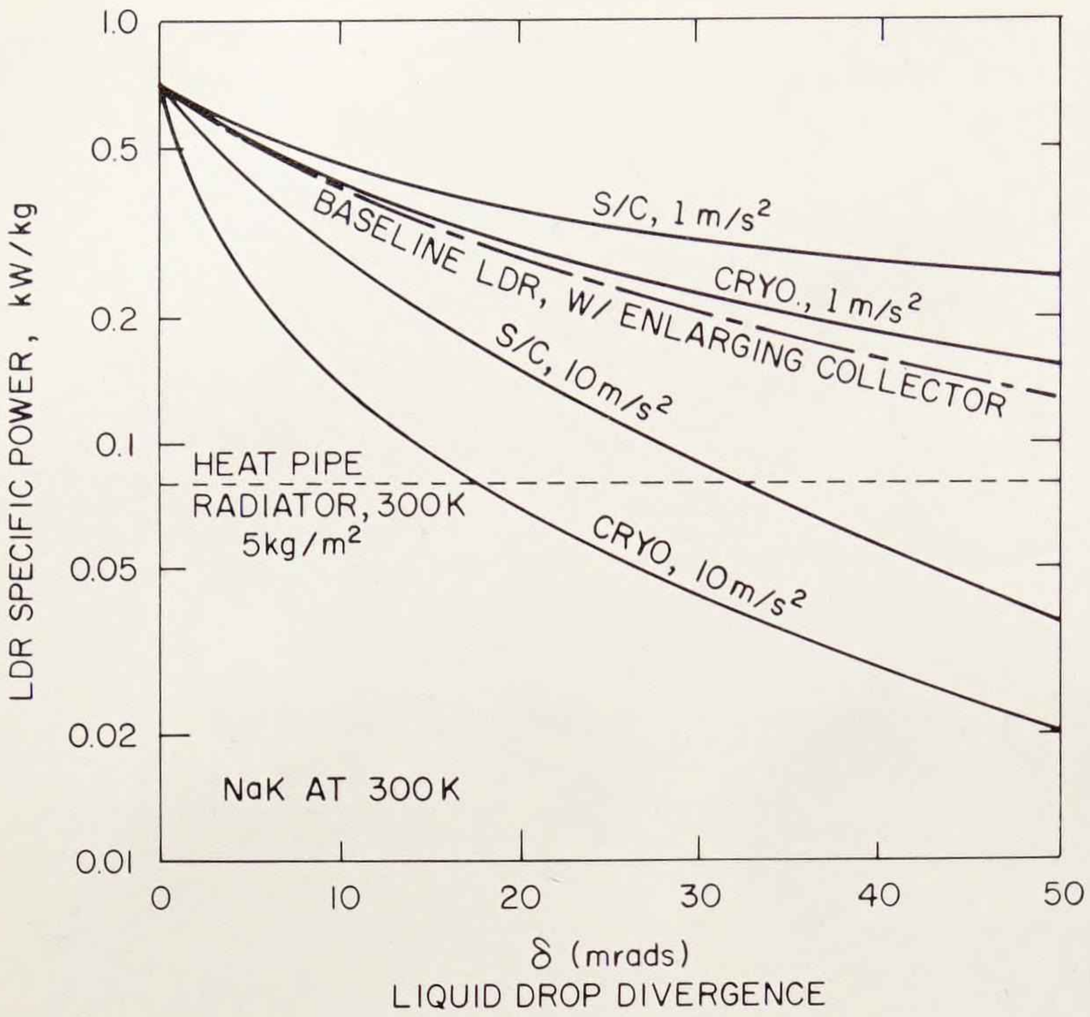


Figure 10 *Specific Power of a NaK-Based Magnetic LDR as a Function of Divergence Angle.*

of one meter per second per second accelerations out beyond fifty milliradians divergence, the droplet radiator shows a clear performance advantage regardless of magnet technology. At the higher acceleration limit, the LDR has a performance advantage out to eighteen mrad with a cryogenic aluminum magnet and thirty-three mrad with a superconducting magnet.

A higher temperature radiator, based on liquid lithium, was considered as well. Cryogenically-cooled magnets offer a performance advantage over heat-pipes

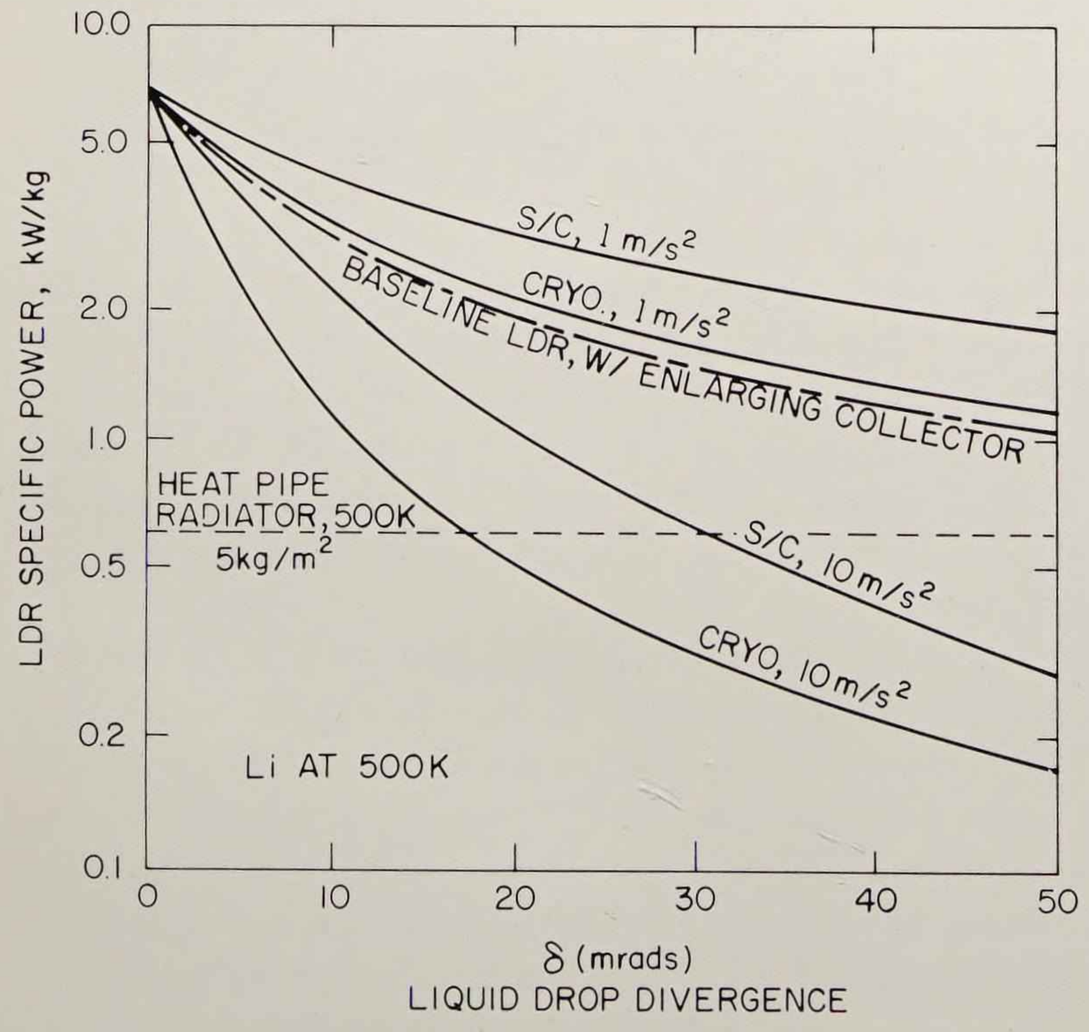


Figure 11 *Specific Power of a Li-Based Magnetic LDR as a Function of Divergence Angle.*

below eighteen mrad, while a superconducting magnet increases the angle to over thirty mrad. At the lower acceleration level, a clear performance advantage still exists well beyond fifty mrad. This advantage of LDRs is shown in Figure 11.

Summary

The use of magnetic fluids in a liquid droplet radiator holds promise for collecting a divergent droplet sheet with a minimum weight penalty as well as eliminating fluid losses due to collector splashing. Superconducting magnets appear to have a significant performance advantage over cryogenically-cooled normal electromagnets, if the increased complexity can be accommodated. Both technologies offer a significant performance advantage to fairly large divergences over heat pipe or finned tube-type technologies.

It has been demonstrated that existing ferrofluids can be used to form droplet jets by using orifices as small as 100 μm; and smaller orifices should work as well. Commercial sapphire and drilled aluminum orifices both were shown to perform well over the range of 100 to 150 μm diameter. Additionally, it was shown that although electric discharge machined (EDM) orifices were too rough to perform adequately, a multiple orificed plate of drilled aluminum did perform adequately. Parallel jets of both silicone oil and ferrofluid were produced.

Ferrofluid droplet streams, both single and multiple, were shown to be stable under the influence of an applied magnetic field. For the size droplets considered, it was observed that they maintained their integrity at accelerations of several "*g*'s" and that neighboring streams did not perturb each other.

Drops of ferrofluid were impacted on a wetted glass surface at conditions that produced splashing and satellite drop formation without a magnetic field-applied to the surface. Drops were photographed for a range of applied magnetic field strengths. As the field strength increased so did the ferrofluid's resistance to cross field lines, consequently suppressing radial motion during impact. Some elasticity remained because the fluid rebounded up along lines of flux. However, at fields approaching one kilogauss and at gradients of nearly one kilogauss per centimeter, all the observed rebounding material was captured.

Acknowledgment

This work was performed under the auspices of the Rocket Propulsion Laboratory, Edwards AFB, CA 93523.

References

Hedgepeth, J. M. (1978) Ultralight structures for space power, in *Radiation Energy Conversion in Space*, *Progress in Astronautics and Aeronautics*, Vol. 61.

Mackay, D. B. (1963) *Design of Space Power Plants*, Prentice Hall, Englewood Cliffs, NJ.

Mattick, A. T. and A. Hertzberg (1980) "Liquid droplet radiators for heat rejection in space," Presented at the *15th Intersociety Energy Conversion Engineering Conference*, Seattle, WA.

Mattick, A. T. and A. Hertzberg (1983) Personal Communication, University of Washington, Seattle, WA.

Schuerch, H. and W. Robbins (1964) *Rotary deployable solar space power supply*, Report CR-122, NASA, Washington, D.C.

Taussig, R. G. (1983) Personal Communication, Mathematical Sciences Northwest, Bellevue, WA.

Werner, R. W. and G. A. Carlson (1977) *Solar power satellite system definition study*, Boeing Aerospace Corp., Report D-180-22876-2, Vol. 2, Seattle, WA.

Space Nuclear Power Systems 1984
Edited by M. S. El-Genk and M. D. Hoover
© Orbit Book Company, Malabar, FL, 1985

Chapter 51

Rotary Radiators for Reduced Space Powerplant Temperatures

David G. Elliott

Jet Propulsion Laboratory
California Institute of Technology
4800 Oak Grove Drive
Pasadena, California 91109

If new radiator concepts can achieve radiator weights below 3 kg/m^2, nuclear space powerplants can operate at temperatures below 900 K and use stainless steel construction. Tube-and-fin or heat-pipe radiators weigh at least 5 kg/m^2 because the tube walls must be thick enough to prevent or limit meteoroid punctures. However, radiators that require no meteoroid protection can be built using low-vapor-pressure liquids that can be exposed directly to space. One possible design for such a radiator is the "rotary radiator" that uses centrifugal force to move the liquid across a thin radiating disk and uses surface tension to retain the liquid despite meteoroid punctures.

Introduction

Can nuclear space powerplants operate at conventional temperatures with conventional materials and achieve low weight? No, if present radiator designs are used. Yes, if innovative radiator concepts can achieve radiator weights in the 1–3 kg/m^2 range. Radiator designs that could achieve such weights have been proposed by Weatherston and Smith (1960), Schuerch and Robbins (1964), Hedgepeth (1978), Mattick and Hertzberg (1981), Mattick and Taussig (1983), and Prenger and Sullivan (1983).

The purpose of this paper is to present an example of a practical concept for a radiator weighing less than 3 kg/m^2 and to show that such a radiator could make it possible to build lightweight nuclear space powerplants at reactor temperatures below 900 K, permitting stainless-steel construction.

Effect of Radiator Weight on Powerplant Temperature Requirements

The weights of 100 kWe Brayton and Rankine powerplants were calculated using the assumptions of Table 1. Figure 1 presents the weights as a function of reactor outlet temperature for three different values of radiator weight per unit area: 1, 3, and 10 kg/m^2. The highest radiator weight represents conventional tube-and-fin designs, and the lower weights represent advanced radiator concepts. Each point on the curves in Figure 1 gives the minimum powerplant mass found by varying the radiator temperature at fixed reactor temperature.

Figure 1 shows that as the reactor temperature is reduced the powerplant mass increases. The increase is due to two effects: (a) increased radiator area and (b) increased conversion system weight as efficiency moves to lower values because of increased radiator/reactor temperature ratio. The reactor temperatures required for a powerplant mass of 3000 kg at radiator weights of 1, 3, and 10 kg/m^2 are 650 K, 800 K, and 1060 K for Rankine cycles and 750 K, 930 K, and 1200 K for Brayton cycles.

The radiator areas required for the powerplants are shown in Figure 2. The radiator areas for Brayton and Rankine cycles are nearly equal at high reactor temperatures, but the area for Brayton cycles rises to twice that of Rankine cycles at low reactor temperatures.

Nothing would better assure successful development of a longlife space powerplant than restricting the temperatures to a level permitting stainless steel construction of the reactor and conversion system. The temperature capability of 316 stainless steel (ASME 1983) is presented in Figure 3. At 1 percent creep in 10 years the allowable stress ranges from 150 MPa (20,000 psi) at 800 K to 7 MPa (1000 psi) at 1100 K. A practical stress level is about 70 MPa (10,000 psi) and this can be achieved at 900 K. A reactor outlet temperature of 900 K can be considered to be the level that permits stainless steel construction.

Figure 2 shows that, at 900 K reactor temperature, the required radiator area for a 100 kWe powerplant is 250 m^2 for Rankine cycles and 400 m^2 for Brayton cycles; flat circular radiators would have diameters of 13 m and 16 m, respectively.

Figure 4 shows the effect of radiator temperature on radiator area and powerplant mass. For Rankine cycles the powerplant mass is insensitive to radiator temperature, but the radiator area increases by a factor of 5 as

Table 1 *Powerplant Assumptions*

Brayton Cycle

Three stages, with two reheats and two intercooling steps.
50°C temperature drop between reactor outlet and turbine inlet.
50°C temperature drop between compressor inlet and radiator outlet and between recuperator outlet and radiator inlet.
0.92 turbine efficiency, 0.85 compressor efficiency, and 0.95 recuperator effectiveness.
Compressor pressure ratio 1.05 times turbine pressure ratio.
Specific heat ratio 1.66.
Electric output 0.85 of shaft power.
Radiator heat rejection 0.7 of black body.

Rankine Cycle

50°C temperature drop between reactor outlet and turbine inlet.
50°C drop between condensing temperature and radiator temperature.
Cycle efficiency (shaft/thermal) 0.6 of Carnot based on turbine inlet temperature and condensing temperature.
Electric output 0.85 of shaft power.
Radiator heat rejection 0.7 of black body.

Powerplant Mass, Both Cycles, at 100 kWe

Reactor and shield	1100 kg
Heat exchangers plus turbomachinery	1 kg per kW of reactor power
Electrical equipment	250 kg
Radiator	Required area times mass per unit area
Structure	10 percent

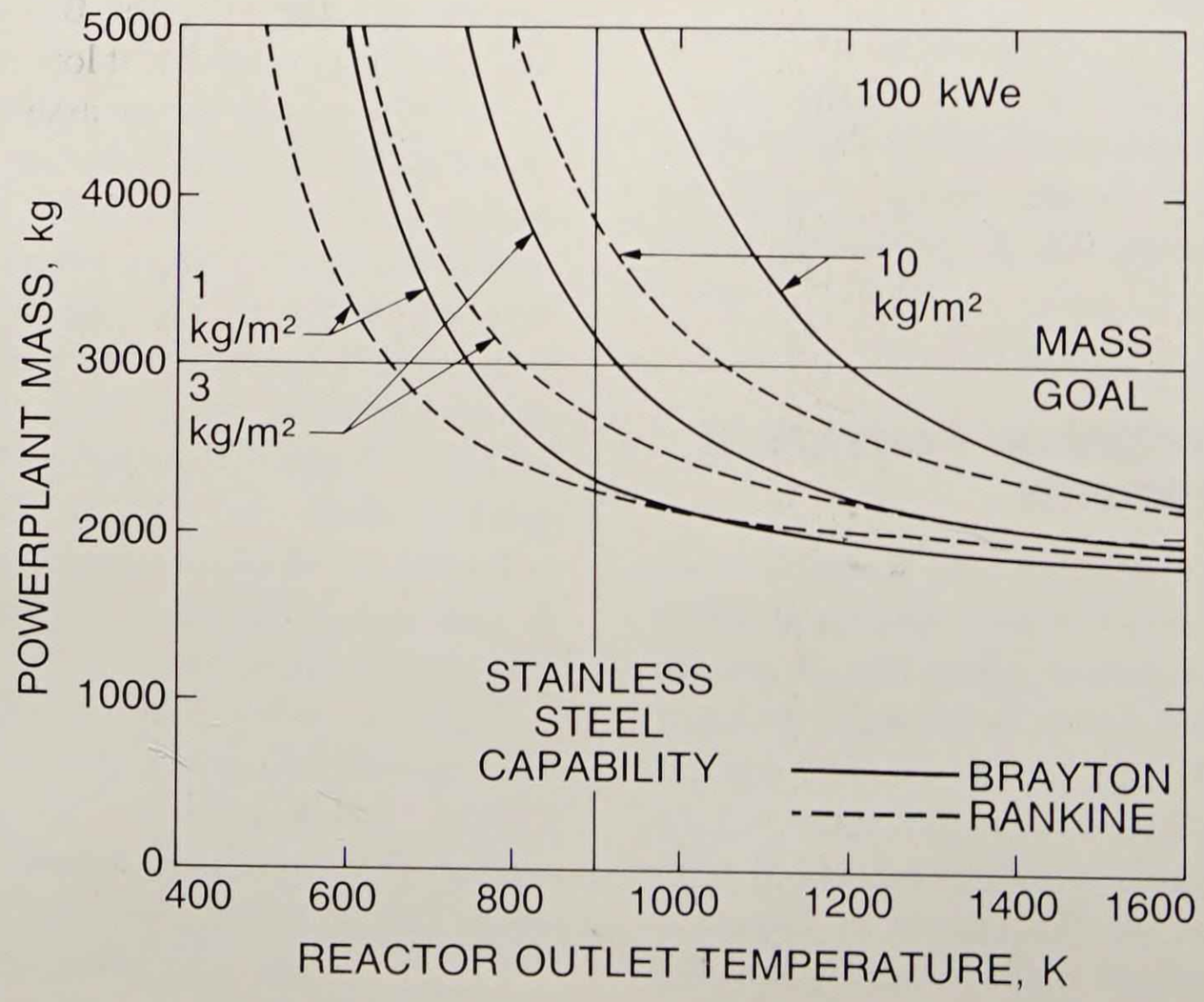


Figure 1 *Effect of Radiator Mass per Unit Area on Required Reactor Temperature. Radiator Mass Less than 3 kg/m² Permits Stainless Steel Construction of the Reactor and Conversion System.*

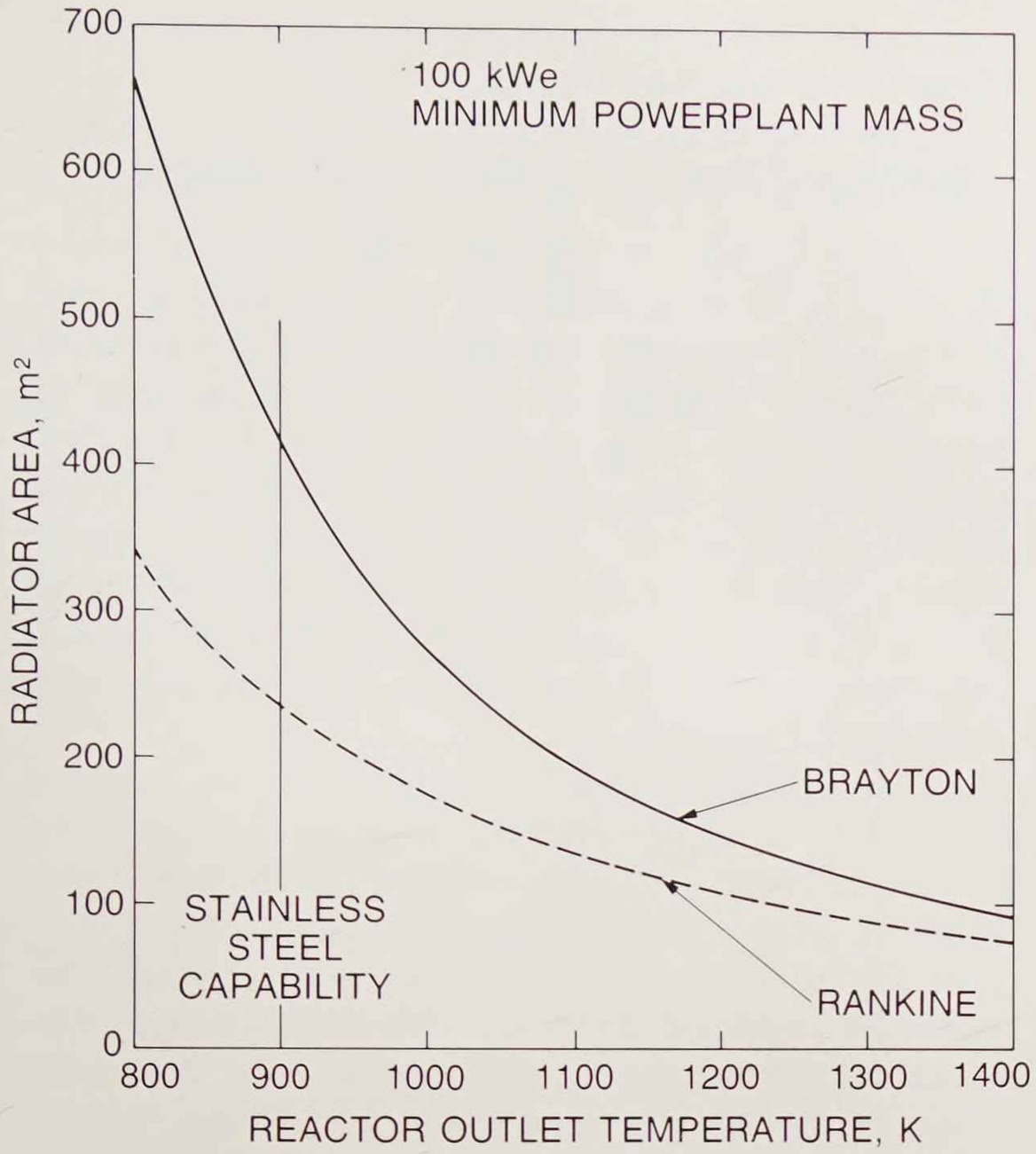


Figure 2 *Radiator Areas for Minimum Powerplant Mass.*

the radiator temperature is decreased from 600 K to 300 K; radiator temperatures of 450-600 K give the best combination of weight and area. The Brayton cycle has lower optimum radiator temperatures, ranging from 300 K, where area starts to rise rapidly, to 500 K, where the weight starts to rise rapidly. At these low temperatures, the heat received from the earth and sun requires additional radiator area. From Ellis and Rankin (1983) the effective sink temperature for a radiator with one side

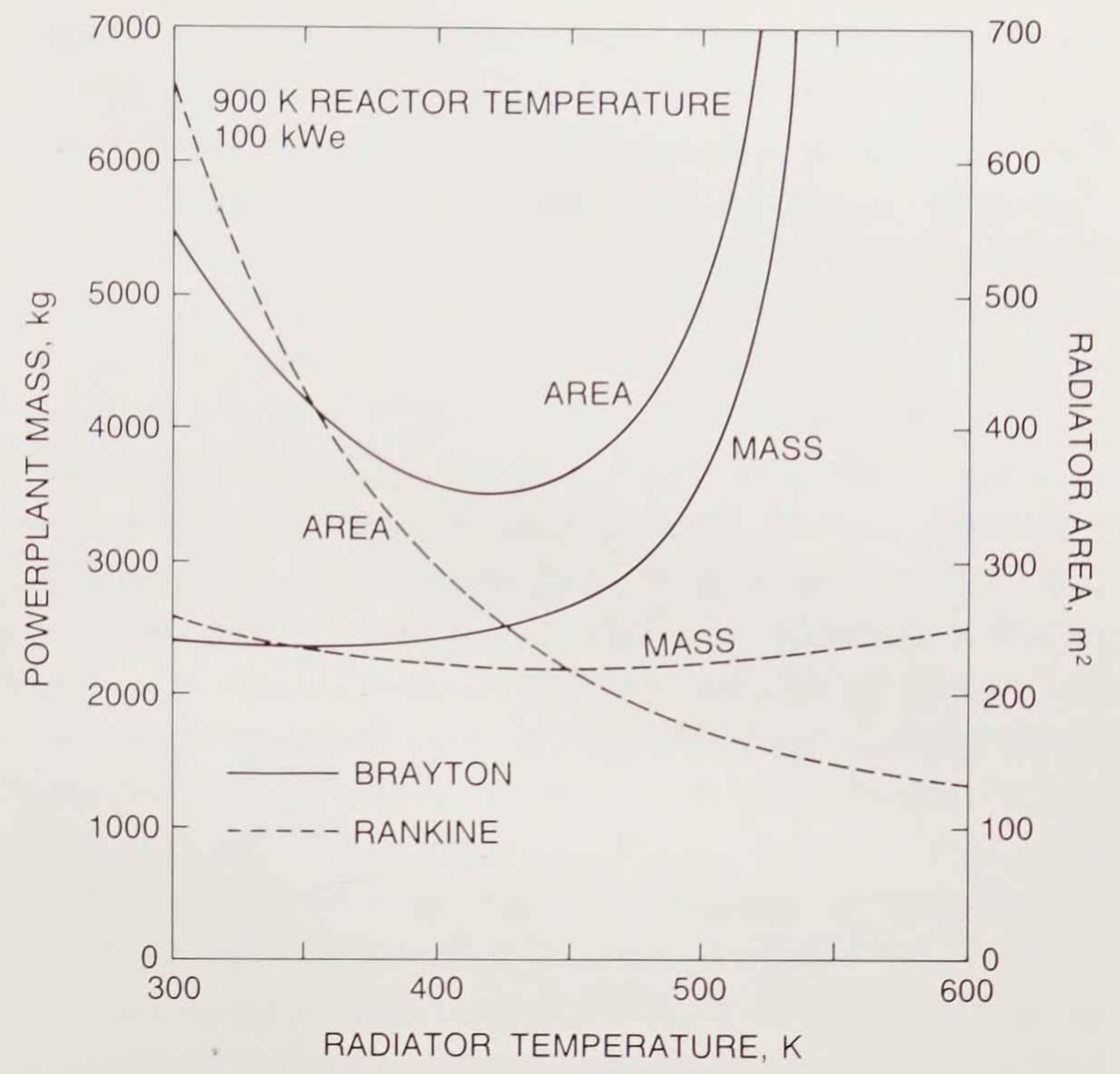


Figure 4 *Effect of Radiator Temperature on Radiator Area and Powerplant Mass at 900 K Reactor Temperature.*

facing the Earth, but no sun exposure, is 220 K; with one side also facing the sun, the effective sink temperature is 270 K. The area of a 350 K radiator must be increased by 20 percent for earth exposure and by another 30 percent for sun exposure.

Radiator Weight Limitations Due to Meteoroid Protection

With single-loop radiators the tube walls must be thick enough for a high probability of zero punctures. Figure 5 shows the weight of aluminum or stainless steel

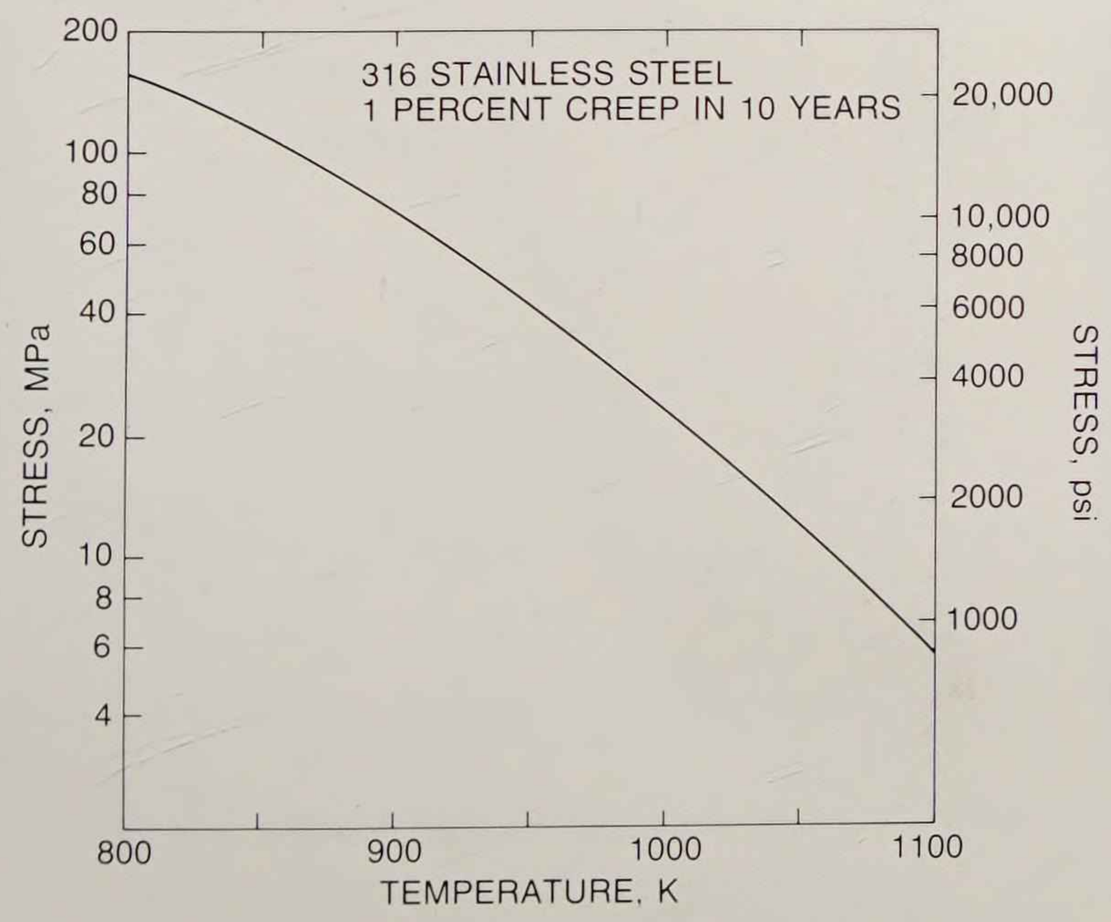


Figure 3 *Creep Strength of Stainless Steel.*

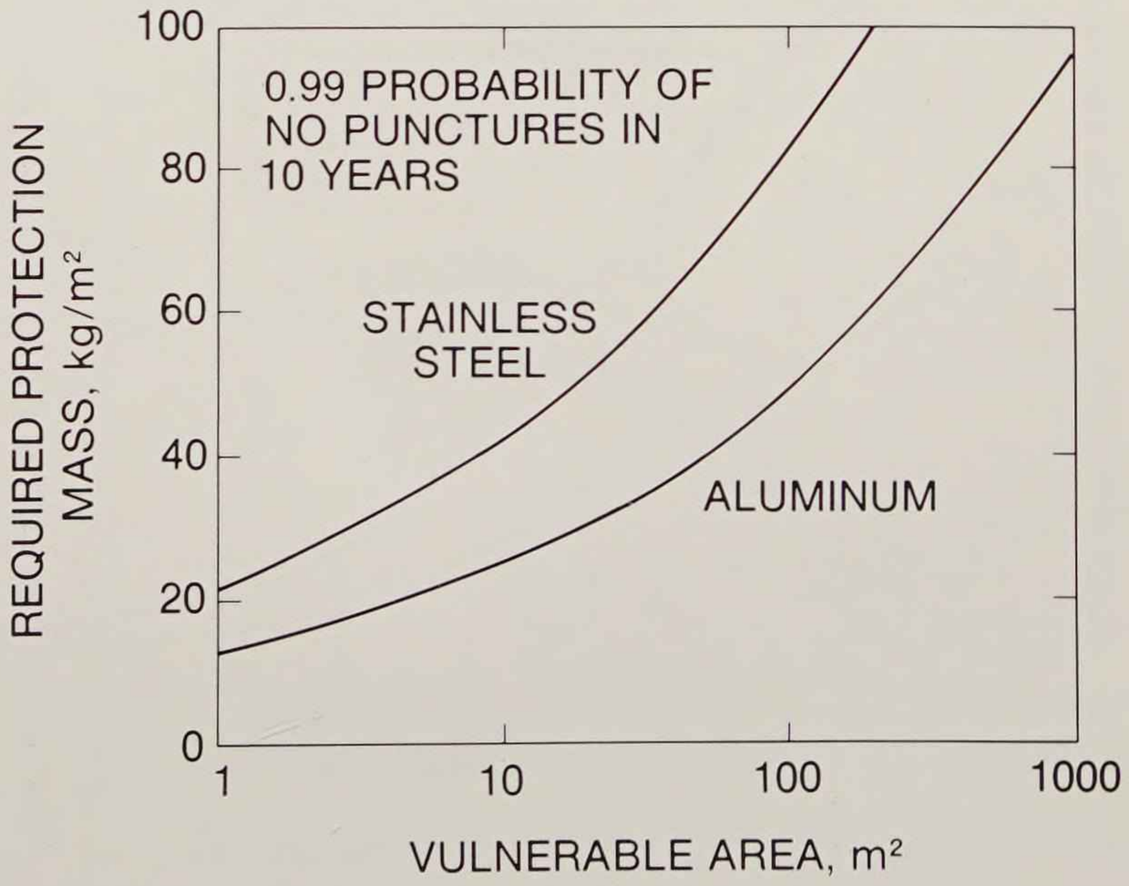


Figure 5 *Metal Sheet Mass per Unit Area Required for Prevention of Meteoroid Punctures.*

sheet needed to prevent meteoroid punctures, as a function of the area to be protected. The calculations use the equations and data of Cour-Polais (1969) and Frost (1970) for orbits of 1000 to 6000 km altitude. As the vulnerable area increases, the metal thickness required for a given probability of no penetration in a given time (here, 0.99 probability in 10 years) increases due to an increase in the probable upper limit of the meteoroid size encountered. For aluminum, the required protection thickness ranges from 5 mm (13 kg/m^2 sheet mass) at 1 m^2 vulnerable area to 35 mm (95 kg/m^2) at 1000 m^2. The thickness required for stainless steel is less, but the weight is higher.

Because of the thick tube walls required for preventing meteoroid punctures, radiator designers minimize tube area and maximize fin area. For example, a 100 m^2 radiator might have only 10 m^2 of tubes, required 20 kg/m^2 of tube armor according to Figure 5; thus, the actual meteoroid protection material weighs only 2 kg/m^2 based on total radiator area. However, the heavy fins are an indirect cost of meteoroid protection, and the total weight attributable to meteoroid protection is typically 5 to 10 kg/m^2.

Thinner tube walls are possible with segmented radiators, such as heat pipe radiators, where loss of some of the segments is allowed. Figure 6 shows the required meteoroid protection mass, per m^2 of vulnerable area, when 10 percent of the radiator segments can be lost. The protection mass can be cut in half, compared with a single-loop radiator, by using about thirty segments. The protection mass can be reduced to below 5 kg/m^2 by using several hundred segments.

Further weight reductions might be possible with composite materials that are lighter or more penetration-resistant than aluminum.

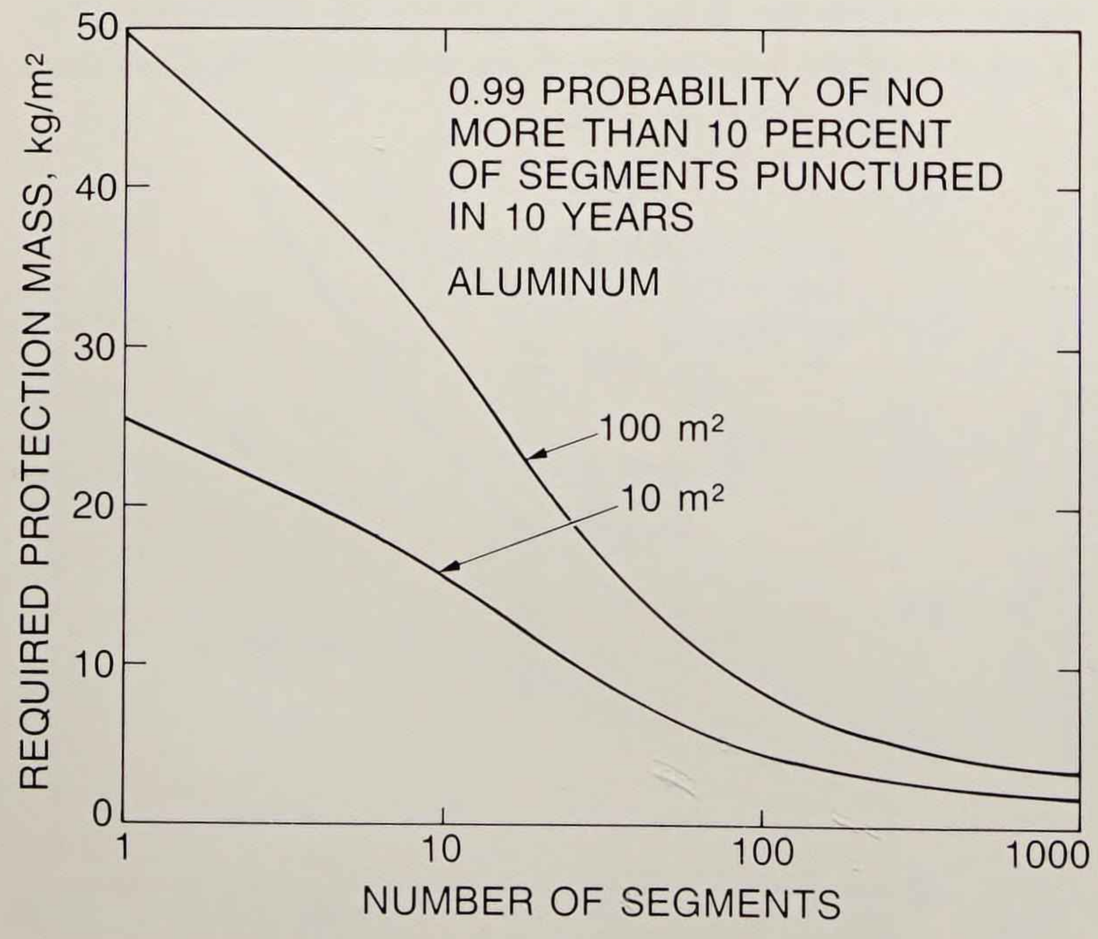


Figure 6 *Meteoroid Protection Mass Required for Segmented Aluminum Radiators, Showing the Reduction in Protection Mass Possible if a Large Number of Segments Are Used and 10 Percent of the Segments Can Be Punctured.*

Meteoroid-Immune Radiator Concepts

To achieve radiator weights in the 1-3 kg/m^2 range, the tube walls must be so thin that the tubes or other fluid-carrying passages will be punctured thousands of times. Figure 7 shows the problem. The number of meteoroid holes per m^2 punctured in 100 m^2 of aluminum sheet in 10 years is plotted against aluminum sheet weight. At 0.25 kg/m^2 sheet weight, which might permit 1 kg/m^2 overall radiator weight, there will be 500 holes per m^2. Segmentation at a scale small enough to allow a significant portion of the radiator to escape puncture would be impractical.

Most of the holes in a 0.25 kg/m^2 sheet are between 0.5 and 1.0 mm in diameter; however, holes of 6–10 mm diameter are possible at the 0.01 probability level. Figure 8 shows the diameter of the maximum (0.01 probability) puncture as a function of sheet mass. The maximum hole size increases with sheet thickness because a given meteoroid tears a larger hole in a thick sheet. The maximum hole sizes are 5 to 10 mm in very thin sheets but over 100 mm in thick sheets. The curves end at the thickest sheet that has 0.01 probability of receiving a single puncture.

Two classes of radiator concepts have been proposed that can operate despite meteoroid penetration. Heat can be radiated from a thin metal belt periodically reheated by passage through a heat exchanger—the "belt radiator" concept (Weatherston and Smith 1960 and Schuerch and Robbins 1964). Or a heat-transfer medium can be used that has acceptable evaporation loss when exposed to space—the particle radiator (Hedgepeth 1978), the liquid droplet radiator (Mattick

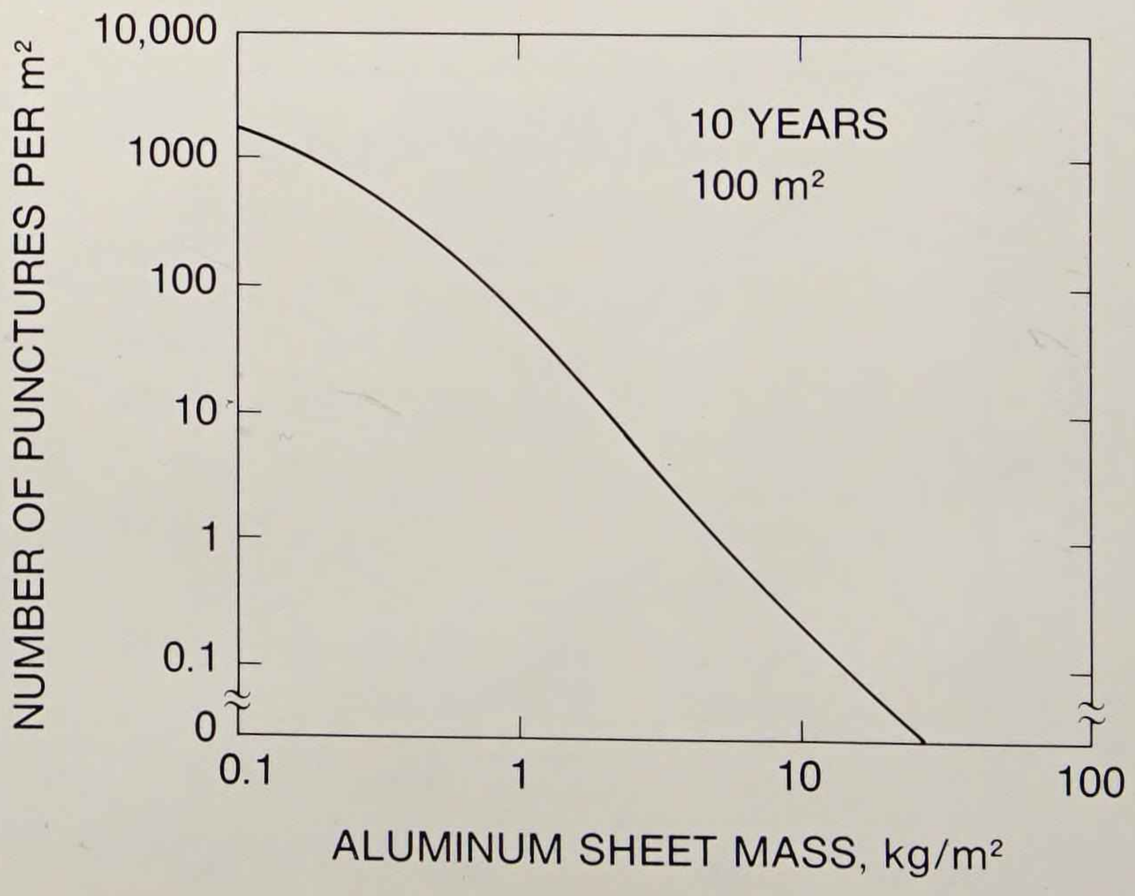


Figure 7 *Number of Meteoroid Punctures in 100 m^2 of Aluminum Sheet in 10 Years, as a Function of Sheet Mass per Unit Area.*

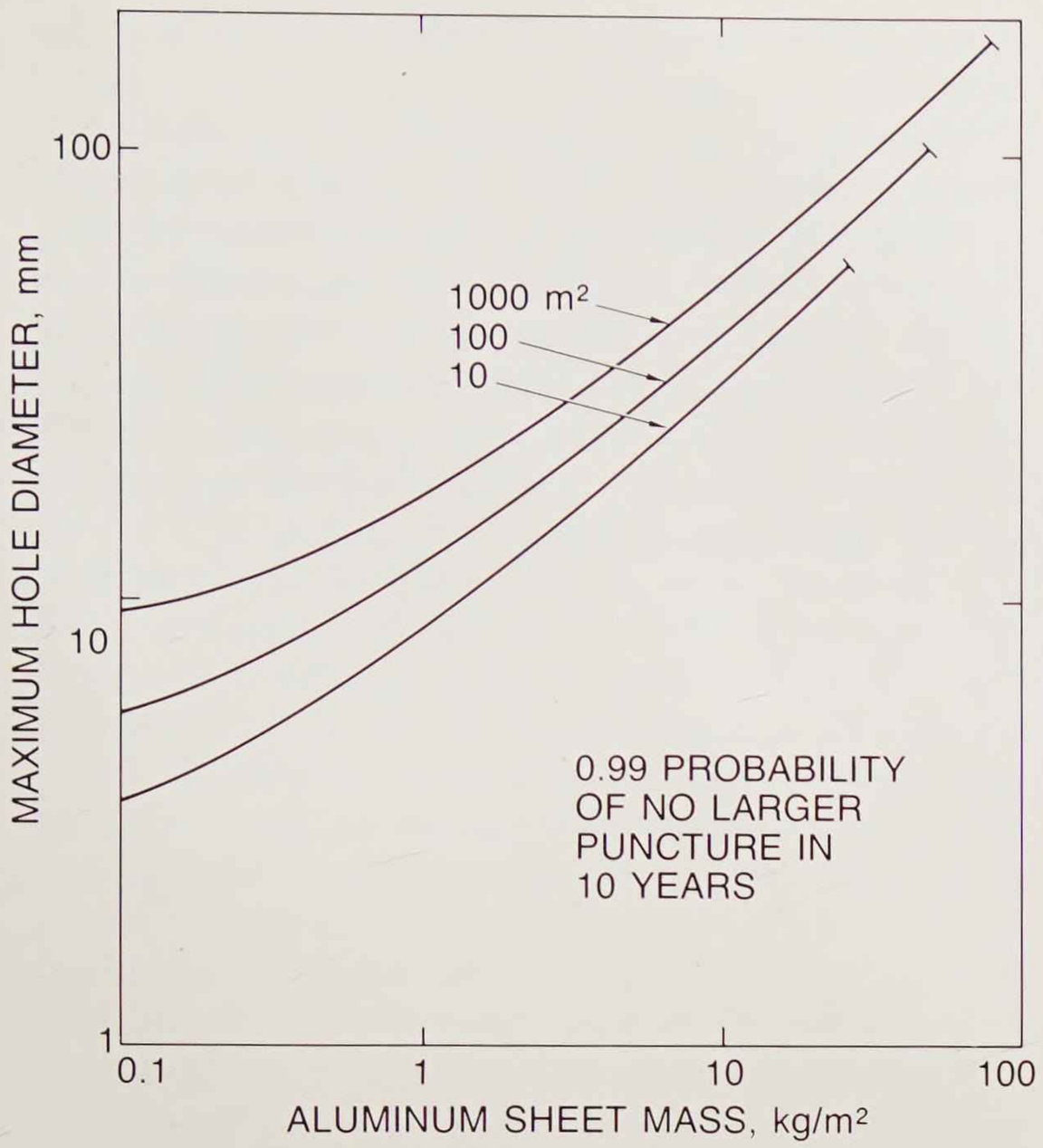


Figure 8 *Maximum Meteoroid Puncture Size in Aluminum Sheet in 10 Years.*

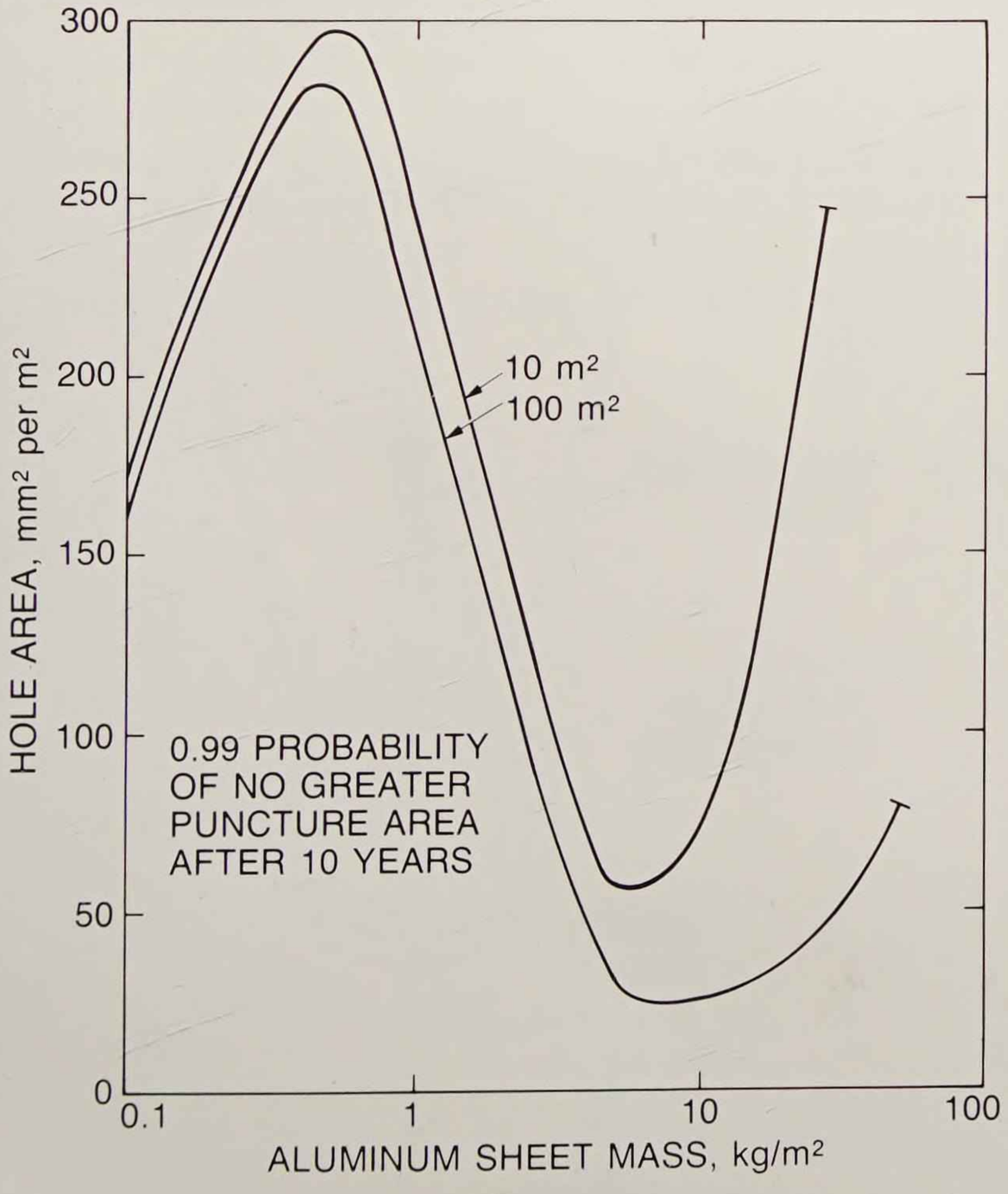


Figure 9 *Meteoroid Puncture Area Accumulated in Aluminum Sheet in 10 Years.*

and Hertzberg 1981 and Mattick and Taussig 1983) and film-flow radiators (Prenger and Sullivan 1983).

In liquid droplet radiators the radiating surface is liquid. In film-flow radiators the radiating surface is a thin solid sheet, and the area of fluid exposed to space vacuum is the hole area produced by the meteoroid punctures. Figure 9 shows the hole area per m^2 punctured in various thicknesses of aluminum sheet over a 10 year span. As the sheet thickness and mass increases, the number of holes decreases but the hole size goes up, and the hole area goes through a maximum and then a minimum. The last area on the right of the curves is from the single hole in the thickest sheet penetrated. The maximum hole area occurs at 0.15 mm sheet thickness (0.4 kg/m^2 sheet mass) and is 300 mm^2 per m^2 of sheet area (0.03 percent).

Figure 10 shows the evaporation loss of two liquids suitable for liquid droplet or film-flow radiators—silicone diffusion pump oil (DC 705) at 300–400 K and lithium just above its melting point of 455 K. Using vapor pressure data from Dow-Corning (1979) and Nesmeyanov (1963), evaporation loss curves are plotted both for exposure of the entire liquid surface to space and for exposure through only the meteoroid hole area. An acceptable evaporation loss, consistent with a 1 kg/m^2 radiator weight, might be 0.1 kg/m^2 in 10 years. Figure 10 shows that this loss can be achieved with silicone oil at 300 K with full-area exposure and at 360 K with exposure through the meteoroid punctures only. The same loss can be achieved with lithium at 500 K with full-area exposure and at 630 K with exposure through the punctures.

At the optimum radiator temperatures of powerplants operating at 900 K reactor temperature (Figure 4), it can be seen that lithium would be a suitable radiator fluid for Rankine cycles, and silicone oil would be suitable for Brayton cycles.

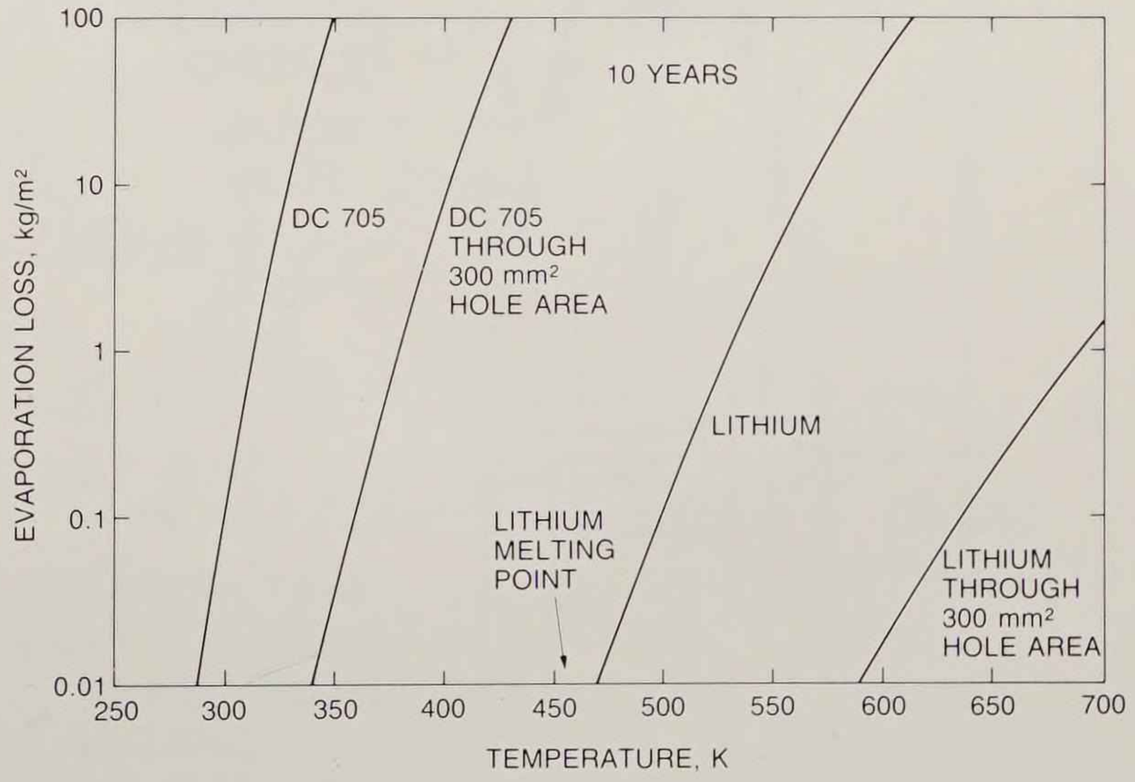


Figure 10 *Evaporation Loss of Liquid Films in 10 Years, per Unit of Film Area, with Both Full-Area Exposure to Space and Exposure only Through Meteoroid Punctures.*

A problem that must be dealt with in radiators with fluid evaporation is possible contamination of the spacecraft by condensing vapor.

Rotary Radiator

A film-flow radiator that rotates to drive a liquid film across a thin disk was suggested by D. R. Koenig of Los Alamos National Laboratory and described as the "rotating balloon" radiator by Prenger and Sullivan (1983). Rotation provides a force to move a heat-transfer liquid across a radiating sheet without imposing any force normal to the sheet to cause leaks when the sheet is punctured. The liquid can be retained on the sheet by surface tension.

Figure 11 is a sketch of a rotary radiator designed for a 100 kWe Brayton cycle operating at 900 K reactor temperature. The radiator uses silicone oil (DC 705) as the working fluid. The radiator consists of an aluminum shell 17 m in diameter formed by two parallel, slightly conical aluminum disks 0.1 mm thick spaced 0.6 m apart at the center. The disks have a high-emissivity coating on the outside. The disks are fastened at their circumference to a circumferential aluminum channel 35 mm deep and 8 mm thick. The radiator rotates around a stationary liquid injection assembly, with a labyrinth seal on one disk. Liquid-injection nozzles are mounted at a 2 m radius inside the shell. A stationary scoop for recovering the liquid from the circumferential channel is mounted on an arm extending from the liquid injection assembly.

In operation, the radiator rotates at 1 rad/s (10 rpm). Liquid at 390 K and 1.9 kg/s flows onto the disks at 2 m radius. The liquid forms a 0.14 mm film on each disk and flows outward at 0.3 m/s relative velocity, driven by centrifugal force. Because of the slight cone angle the liquid has a component of acceleration normal to the disks of 0.1 m/s^2 which assures positive contact.

The liquid takes 30 s to reach the circumference. At the circumference the films have thinned to 0.08 mm and slowed to 0.2 m/s relative velocity. The liquid flow path relative to the disks is mainly radial; the liquid slips back only 10 deg relative to the disks. The normal acceleration component increases to 0.4 m/s^2. The liquid cools to 310 K due to radiation of 250 kW of heat from the disks (assuming a sink temperature of 220 K, corresponding to orientation edge-on to the Sun, but with one side facing the Earth).

When the liquid reaches the circumference of the disks it flows into the circumferential collector channel and forms a liquid layer. The liquid is removed as it encounters the stationary scoop. The 8.5 m/s liquid velocity entering the scoop provides the pressure to maintain flow through the discharge line and back to the conversion-system heat exchanger.

The power required to rotate the radiator is only about 160 W. Half of that power goes into fluid friction and half into exit kinetic energy.

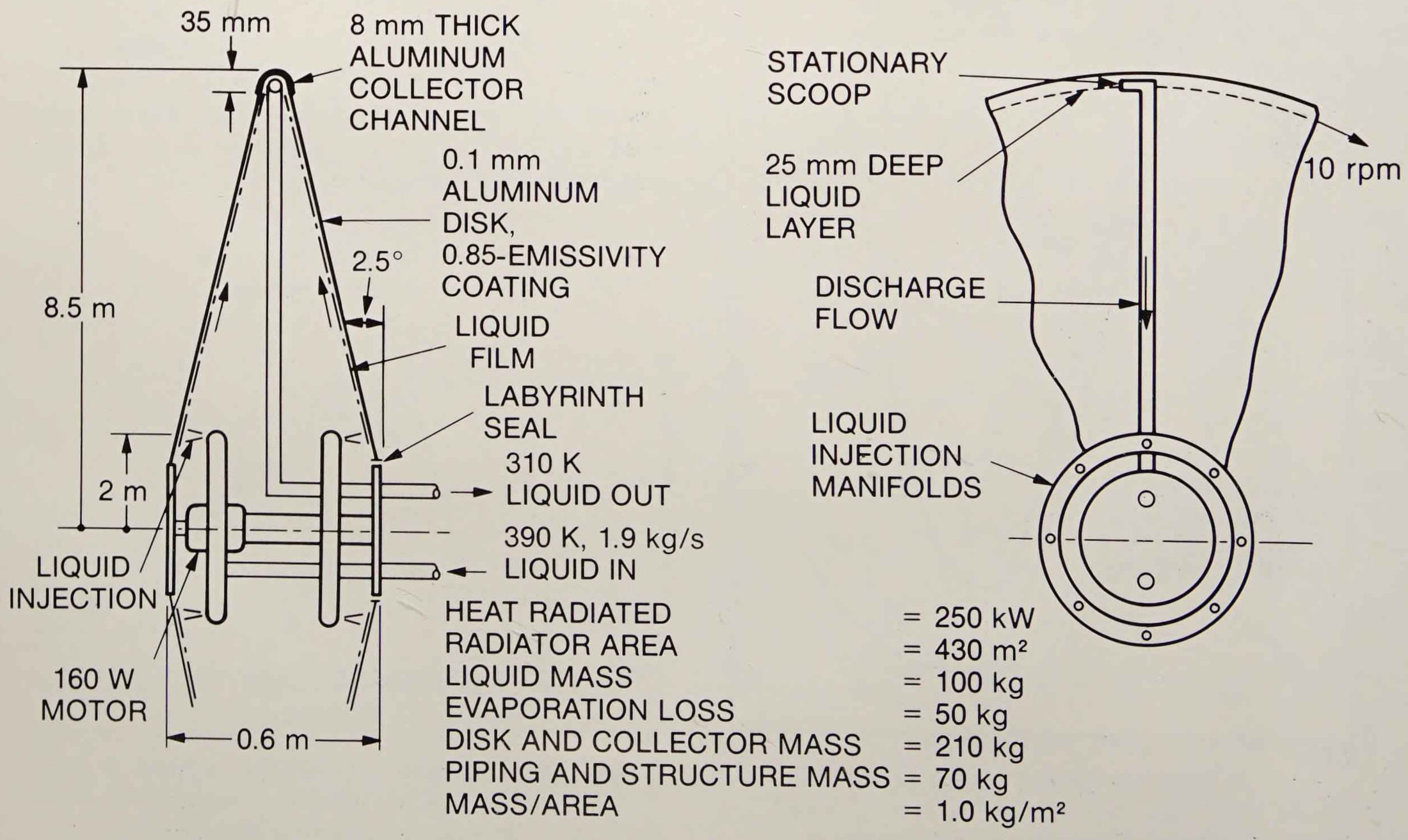


Figure 11 *Rotating Disk Radiator for 900 K Brayton Cycle.*

The 8 mm wall thickness of the cricumferential collector channel provides 0.99 probability of no punctures of the channel. The disks, however, will each be punctured about 100,000 times by the end of 10 years. Surface tension provides containment of the liquid at the puncture holes. The maximum puncture diameter, at 0.99 probability, is 10 mm. Surface tension prevents the liquid from escaping from a hole of that size if the outside of the disk is nonwetting. At the 0.4 m/s^2 maximum normal component of acceleration, surface tension will support a column of silicone oil 30 mm deep whereas the film is less than 1 mm thick. In addition, an external collector channel can be added to catch any escaping drops, which will travel only in the plane of rotation.

The evaporation loss of DC 705, integrating over the temperature distribution, would be 25 kg. An equal amount might be lost through the labyrinth seal, giving a total evaporation loss of 50 kg.

The liquid film weighs 60 kg, and the amount of liquid in the collector and piping is about 40 kg. The total liquid inventory required (including evaporation makeup) is 150 kg. The disks weigh 120 kg and the collector channel weighs 90 kg. The total mass of the disk, collector, and liquid is 360 kg. This weight is less than 1 kg per m^2 of radiating area, showing that radiator weights in the 1 to 2 kg/m^2 range may be possible with rotary radiators.

Conclusion

New radiator concepts such as the rotary radiator may make it possible to build radiators without meteoroid protection. Radiator weights of 1-2 kg/m^2 may be possible. Such weights would permit larger-area, lower-temperature radiators that would make it possible to build lightweight space nuclear powerplants at reactor temperatures below 900 K, permitting stainless-steel construction.

Acknowledgments

The research described in this paper was carried out by the Jet Propulsion Laboratory, California Institute of Technology, under contract with the National Aeronautics and Space Administration.

References

ASME (1983) "1983 Code Cases, Nuclear Components," *ASME Boiler and Pressure Vessel Code*, ASME, New York.

Cour-Palais, B. G. (1969) *Meteoroid Environment Model-1969 (Near Earth to Lunar Surface)*, NASA SP-8013, NASA, Washington, DC.

Dow Corning (1979) *Silicone Diffusion Pump Fluids*, Form No. 22-724-79, Dow Corning Corporation, Midland, MI.

Ellis, W. E. and J. G. Rankin (1983) "Heat Buses Will Operate Like a Public Utility," *Astronautics and Aeronautics*, March 1983, pp. 56–61.

Frost, V. C. (1970) *Meteoroid Damage Assessment*, NASA SP-8042, May 1970, NASA, Washington, DC.

Hedgepeth, J. M. (1978) "Ultralightweight Structures for Space Power," in *Radiation Energy Conversion in Space, Progress in Astronautics and Aeronautics*, ed. M. Summerfield, AIAA, New York, Vol. 61, pp. 127–135.

Mattick, A. T. and A. Hertzberg (1981) "Liquid Droplet Radiators for Heat Rejection in Space," *J. Energy* 5:387–393.

Mattick, A. T. and R. T. Taussig (1983) *New Thermal Management and Heat Rejection Systems for Space Applications*, Annual Report, University of Washington/Math Sciences Northwest, Seattle, WA.

Nesmeyanov, A. N. (1963) *Vapor Pressure of the Chemical Elements*, Elsevier Publishing Company, New York.

Prenger, F. C. and J. A. Sullivan (1983) "Conceptual Designs for 100-MW Space Radiators," in *Symposium On Advanced Compact Reactors*, National Academy Press, Washington, DC, pp. 383–404.

Schuerch, H. and W. Robbins (1964) *Rotary, Deployable Space Solar Power Supply*, NASA CR-122, NASA, Washington, DC.

Weatherston, R. C. and W. E. Smith (1960) "A Method for Heat Rejection from Space Powerplants," *ARS J.* 30:268–269.

Space Nuclear Power Systems 1984
Edited by M. S. El-Genk and M. D. Hoover
© Orbit Book Company, Malabar, FL, 1985

Chapter 52

Thermal Analysis of Radiation Shields for Space Reactors Using Analytical and Finite Element Methods

William J. Barattino
Air Force Institute of Technology
University of New Mexico
Albuquerque, New Mexico 87131

Mohamed S. El-Genk
Department of Chemical and Nuclear Engineering
University of New Mexico
Albuquerque, NM 87131

A finite element program (FEM) that uses a Newton–Raphson iteration and simplex elements has been developed to determine the temperature distribution in a multi-layered radiation shield with internal heating, temperature dependent thermal conductivities, and radiative boundary conditions. The temperature distribution in a 1-D slab shield using the FEM differed by less than 1 percent from the exact analytic solution for both adiabatic and isothermal front surface conditions. The temperature distribution in a 2-D shield with radiating surfaces at the top and back surface was also evaluated using the FEM.

Introduction

In the 1960s and early 70s, much work was done on the development and optimization of radiation shield for both manned and unmanned space missions (Barattino, El-Genk, and Voss 1985). In general, tungsten and lithium hydride have emerged as the best materials for attenuating gamma radiation and fast neutrons, respectively. However, a number of unresolved issues remained regarding the thermal performance of the shield, which becomes more important at today's higher power requirements (in excess of 100 kWe). Some of these issues are the need to maintain the lithium hydride between 600 and 680 K during steady-state operation, which may require active cooling of the shield; and the need to minimize induced thermal stresses, which can cause excessive cracking of the shield (Welch 1967).

The minimum temperature of 600 K was recommended to minimize radiolytically induced hydrogen dissociation from the Li metal, and the accompanying swelling of the shield. Above 600 K, the volume expansion of the LiH remains below 6 percent for a wide range of fast neutron fluences (10^{16} to 10^{20} nvt). Since the density of LiH after being cast into stainless steel matrix remains below 94 percent of theoretical density, this volume expansion does not cause structural deformation to the shield. The upper operating temperature of LiH was limited to 680 K to reduce the effect of losing the dissociated hydrogen from the shield through the punctures caused by meteoroid impact. For typical shield outer casing thicknesses (0.15 to 0.25 cm), the dose rate at the dose plane will not change due to hydrogen loss if the LiH remains below 680 K (Welch 1967).

At the higher power levels of today's space reactor designs (100 kWe to multi-MWe), the need for thermal analysis of the shield is even greater than during the SNAP program. Figure 1 is a preliminary design of the shield that was suggested for the Los Alamos heat pipe reactor (Ranken 1982, JPL 1982, and El-Genk et al. 1985). With the irregular geometry, multi-layered materials, radiative boundary conditions, temperature dependent thermal properties, and possibly internal cooling, an analytic solution is not feasible. Therefore, a numerical solution method must be adapted for the radiation shield.

In considering the complex shield geometry which leads to irregular meshes, a finite element method has marked advantages over finite difference methods in terms of better geometric approximation, less computer storage, and faster convergence times for solutions (Bathe 1982 and Huebner and Thornton 1982).

Approach

As a part of an ongoing research program at the University of New Mexico, a thermal and stress analysis computer code is under development to study the thermal performance of the radiation shield for space nuclear reactors. A finite element program is being developed using 3-node (simplex) elements and a Newton–Raphson iteration scheme to handle the irregular geometry of the shadow shield, and the non-linear governing equations due to temperature dependent properties and the radiative cooling at the outer surface of the shield.

The uniqueness of this package lies in the development of an analysis tool in a single package, specifically designed to perform the coupled neutronics-

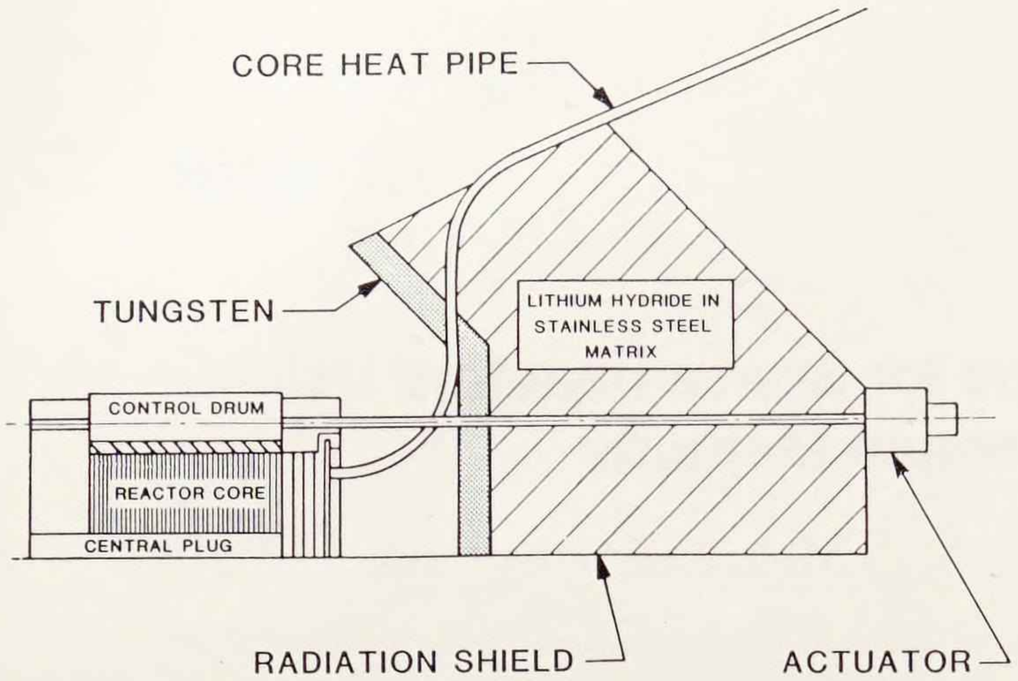


Figure 1 *Preliminary SP-100 Reactor Shield Design.*

temperature-stress/strain problem of a nuclear reactor. The coupling of the temperature effect on the energy deposition as determined by the neutronics model is a feedback effect that will be incorporated into this package.

As with any numerical tool, the numerical results must be validated in some manner. This paper presents a comparison between two exact analytical solutions for 1-D, W-LiH shield and the finite element method regarding the temperature distribution in the shield. Results of the 1-D test cases are compared against those of the finite element program.

With the excellent results obtained for the 1-D problems, the FEM is used to calculate the temperature distribution in a 2-D, W-LiH shield. The 2-D shield is radiatively cooled at the top and sides. Berger build-up factors are included in the internal heating rates to account for the effects of secondary gammas. For both the 1-D and 2-D test cases, the effects of an adiabatic and isothermal front surface condition of the shield are compared.

Because the final geometry of the shield for space nuclear reactor systems has not yet been determined, a certain degree of flexibility will be considered in defining the shield geometry to be analyzed. Figure 2 is a generalized shield design with selected angles and lengths identified. The angles θ, α, ϕ, and lengths L_1, L_2, L_3 and L_4 will be determined by the radiation transport design. By changing these known parameters, a variety of shield geometries can be represented. Figure 2 includes several possible considerations. The ability to define a geometric shape for the shield based on known angles and lengths will be incorporated in the generation of the calculation mesh in the shield.

In this paper, the appropriate theory for solving a non-linear temperature problem using Newton–Raphson iteration is reviewed, and the resulting system of equations are adapted to a finite element solution using simplex elements. Application of the theory is demonstrated with the 1-D and 2-D problems discussed above.

Finite Element Theory

Before discretization of the shield into finite elements, the governing equation and boundary conditions must be represented by a functional which represents a Pois-

NOMENCLATURE

English

a: Thickness of W in 1-D slab (cm)
b: Thickness of 1-D slab (cm)
$[B_r]$: Shape function derivatives
$B(\mu, x)$: Gamma buildup factor as function of μ and x
b_1, b_2, b_3: Simplex shape function derivatives with respect to x coordinate
c_1, c_2, c_3: Simplex shape function derivatives with respect to y coordinate
F_{i-j}: View factor of back surface i to surface j
$[K_R]$: Thermal radiation matrix
$[K_T]$: Thermal stiffness matrix
$\kappa(T)$: Linearized radiant heat transfer coefficient $= \epsilon\sigma(T^{s2} + T_\infty^2)(T^s + T_\infty)$
K(T): Thermal conductivity as a function of temperature (W/cm-k)
l: Surface length between two boundary nodes
LiH: Lithium hydride
$[N]$: Shape functions of simplex element
Q_{IHG}: Internal heat generation vector
Q_{SHF}: Surface heat flux vector
Q_{R}: Surface radiation vector
q''': Internal heat generation (W/cm^3)
q'': External heat flux (W/cm^2)
q_L: Internal heating at W—LiH interface (W/cm^3)
q_0: Internal heating core—W interface (W/cm^3)
S: Surface area (cm^2)
$T(x)$: Temperature
$T^{(e)}$: Finite element temperature (K)
ΔT: Residual temperature (K)
V: Volume (cm^3)
W: Tungsten

Greek

μ: Gamma attenuation coefficient (cm^{-1})
Σ_R: Neutron removal cross section (cm^{-1})
Δ: Area of triangle (cm^2)
ϵ: Emissivity of radiating surface
σ: Stefan–Boltzman constant (W/cm^2-K^4)

Subscripts

a, ∞: Ambient
b: Back surface of 1-D slab
γ: Gamma
i: ith iteration
int: W-LiH interfaces
L: Lithium hydride
N: Neutron
W: Tungsten
W_0: Core-tungsten interface
1, 2, 3: Local node number of the element

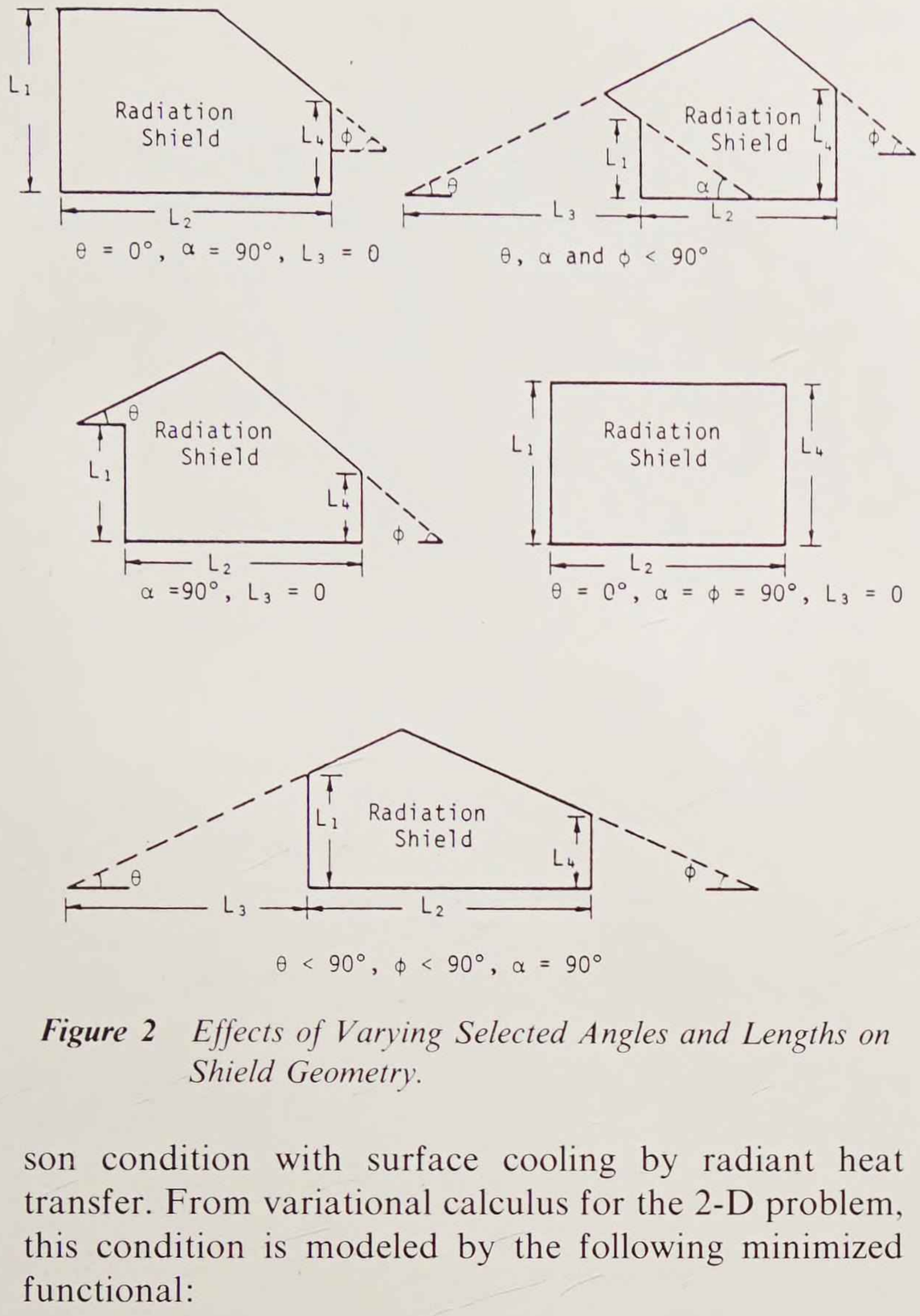


Figure 2 *Effects of Varying Selected Angles and Lengths on Shield Geometry.*

son condition with surface cooling by radiant heat transfer. From variational calculus for the 2-D problem, this condition is modeled by the following minimized functional:

$$\int_V \delta T'[k]T'\,dV = \int_V \delta T q'''\,dV + \int_s \delta T^s q^s\,dS + \int_s \delta T \kappa(T)(T_\infty - T^s)\,dS, \quad (1)$$

where

$$\delta T' = \frac{\partial}{\partial T_i}\left[\frac{\partial T^{(e)}}{\partial x}\right], \qquad \frac{\partial}{\partial T_i}\left[\frac{\partial T^{(e)}}{\partial y}\right], \quad (1a)$$

$$[k] = \begin{bmatrix} k_x & 0 \\ 0 & k_y \end{bmatrix}, \quad (1b)$$

$$T' = \begin{bmatrix} \frac{\partial T}{\partial x} & \frac{\partial T}{\partial y} \end{bmatrix} = \begin{bmatrix} \frac{\partial N}{\partial x} & \frac{\partial N}{\partial y} \end{bmatrix}\{T_i\} = [B_T]\{T_i\}, \quad (1c)$$

$$\delta T = \frac{\partial T^{(e)}}{\partial T_i} = [N]. \quad (1d)$$

Using a Newton–Raphson iteration for heat flow equilibrium, the iteration scheme for determining the temperature is

$$\{T_i\} = \{T_{i-1}\} + \{\Delta T_i\} \quad (2)$$

with ΔT_i being the temperature increment.

Substituting Equation (2) into (1) yields the following system of algebraic equations:

$$[K_T + K_R]\{\Delta T_i\} = \{Q_{\text{IHG}}\} + \{Q_{SHF}\} + \{Q_R\} - \{Q_{k_{i-1}}\} \quad (3)$$

where

$[K_T]$ = thermal stiffness matrix

$$= \int_v [B_T]^t [k_i][B_T]\,dV, \quad (3a)$$

$[K_R]$ = thermal radiation matrix

$$= \int_s \kappa_{i-1}[N^s]^t[N^s]\,dS, \quad (3b)$$

$\{Q_{\text{IHG}}\}$ = internal heat generation vector

$$= \int_v \{q'''\}[N]\,dV, \quad (3c)$$

$\{Q_{\text{SHF}}\}$ = surface heat flux vector

$$= \int_s \{q''\}[N]\,dS, \quad (3d)$$

$\{Q_R\}$ = surface radiation vector

$$= \int_s \kappa_{i-1}[N^s]^t[N^s](\{T_\infty\} - \{T_{s_{i-1}}\})\,dS, \quad (3e)$$

$\{Q_{k_{i-1}}\}$ = thermal energy vector

$$= \int_v [B_T]^t[k_{i-1}][B_T]\{T_{i-1}\}\,dV. \quad (3f)$$

The system of equations resulting from Equation (3) must now be solved for $\{\Delta T_i\}$, which is the only unknown in the system of equations. Once $\{\Delta T_i\}$ is known, the nodal temperatures, $\{T_i\}$, are determined from Equation (2).

The advantage of this approach becomes apparent when one observes that the only unknown in the set of equations is $\{\Delta T_i\}$. Thus, a direct elimination solution is possible. The surface integrals will only be evaluated for those elements on the boundary of the shield.

This procedure also allows for the temperature dependence of the thermal conductivities for each element based on the previously calculated temperature. The

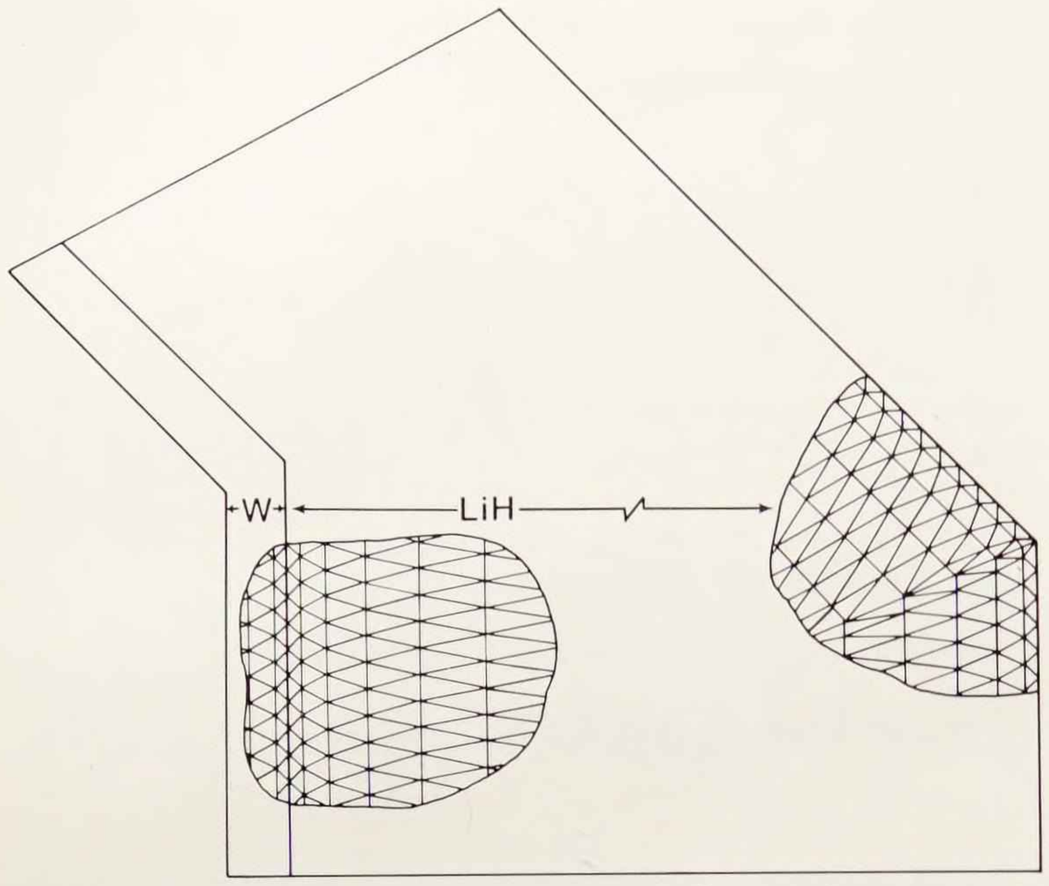


Figure 3 *Discretized Reactor Shield using Simplex Elements.*

iterations continue until some prescribed convergence limit is reached for both temperatures and energy balances.

Method of Solution

The simplest of the finite elements used to discretize a solid continuum is the 3-node (simplex) triangle. Figure 3 illustrates how the simplex element can be used to generate a mesh. The spacing of the mesh can be reduced at interfaces and surfaces.

The advantage of the triangular shape is that it can easily adapt to the sharp geometric features of the most complex of shield designs. The 3-node element also allows for a closed form solution of the integrals of Equations 3a through 3f, thus avoiding the need for local mapping of each element into the $n-\xi$ plane, re-mapping into global coordinates through use of the Jacobian matrix, and integrating with a Gauss-quadrature or some similar technique.

The disadvantage of the 3-node triangle is the linear variation in value of the field variable (temperature in this problem) which results in a constant first derivative throughout the element. Thus, in areas of the shield with steep temperature gradients (such as radiative boundaries), a large number of elements are required to properly capture this gradient.

Considering only heat conduction through the shield, heat radiation at the surface, and using the closed form solutions (formulas for determining the closed form solution of any simplex elements can be found in any basic text on finite elements) for the simplex elements over an area (corresponding to the interior of the 2-D shield) and a line integral (corresponding to surfaces), the following set of equations for each element result from equation (3):

$$\frac{1}{4\Delta}\begin{bmatrix} b_1 & c_1 \\ b_2 & c_2 \\ b_3 & c_3 \end{bmatrix}\begin{bmatrix} k_x & 0 \\ 0 & k_y \end{bmatrix}\begin{bmatrix} b_1 & b_2 & b_3 \\ c_1 & c_2 & c_3 \end{bmatrix}\begin{Bmatrix} \Delta T_i^1 \\ \Delta T_i^2 \\ \Delta T_i^3 \end{Bmatrix}$$

$$+\frac{\kappa_{i-1}(T)l}{6}\begin{bmatrix} 2 & 1 \\ 1 & 2 \end{bmatrix}\begin{Bmatrix} \Delta T_i^s \\ \Delta T_i^s \end{Bmatrix}$$

$$=\frac{\Delta}{12}\begin{bmatrix} 2 & 1 & 1 \\ 1 & 2 & 1 \\ 1 & 1 & 2 \end{bmatrix}\begin{Bmatrix} q_1''' \\ q_2''' \\ q_3''' \end{Bmatrix}$$

$$+\frac{\kappa_{i-1}(T)l}{6}\begin{bmatrix} 2 & 1 \\ 1 & 2 \end{bmatrix}\begin{Bmatrix} T_\infty - T_{i-1}^s \\ T_\infty - T_{i-1}^s \end{Bmatrix}$$

$$-\frac{1}{4\Delta}\begin{bmatrix} b_1 & c_1 \\ b_2 & c_2 \\ b_3 & c_3 \end{bmatrix}\begin{bmatrix} k_x & 0 \\ 0 & k_y \end{bmatrix}$$

$$\times\begin{bmatrix} b_1 & b_2 & b_3 \\ c_1 & c_2 & c_3 \end{bmatrix}\begin{Bmatrix} T_{i-1}^1 \\ T_{i-1}^2 \\ T_{i-1}^3 \end{Bmatrix} \tag{4}$$

where

$$b_1 = y_2 - y_3 \tag{4a}$$

$$b_2 = y_3 - y_1 \tag{4b}$$

$$b_3 = y_1 - y_2 \tag{4c}$$

$$c_1 = x_3 - x_2 \tag{4d}$$

$$c_2 = x_1 - x_3 \tag{4e}$$

$$c_3 = x_2 - x_1 \tag{4f}$$

The variables b_1, b_2, b_3 and c_1, c_2, c_3 result from the evaluation of $\partial N_i/\partial x$ and $\partial N_i/\partial y$ from Equation (3). Because the x and y coordinates of the nodes for a given mesh remain constant, one can readily see that the heat flow within an element will remain constant. The system of equations developed in Equation (4) for each element is assembled for all elements of the mesh and the unknown temperature increment $\{\Delta T_i\}$ is solved for each node point. The final temperatures are then determined from Equation (2). Figures 4 and 5 present schematics of the 1-D and 2-D shield geometries which are analyzed in the next section.

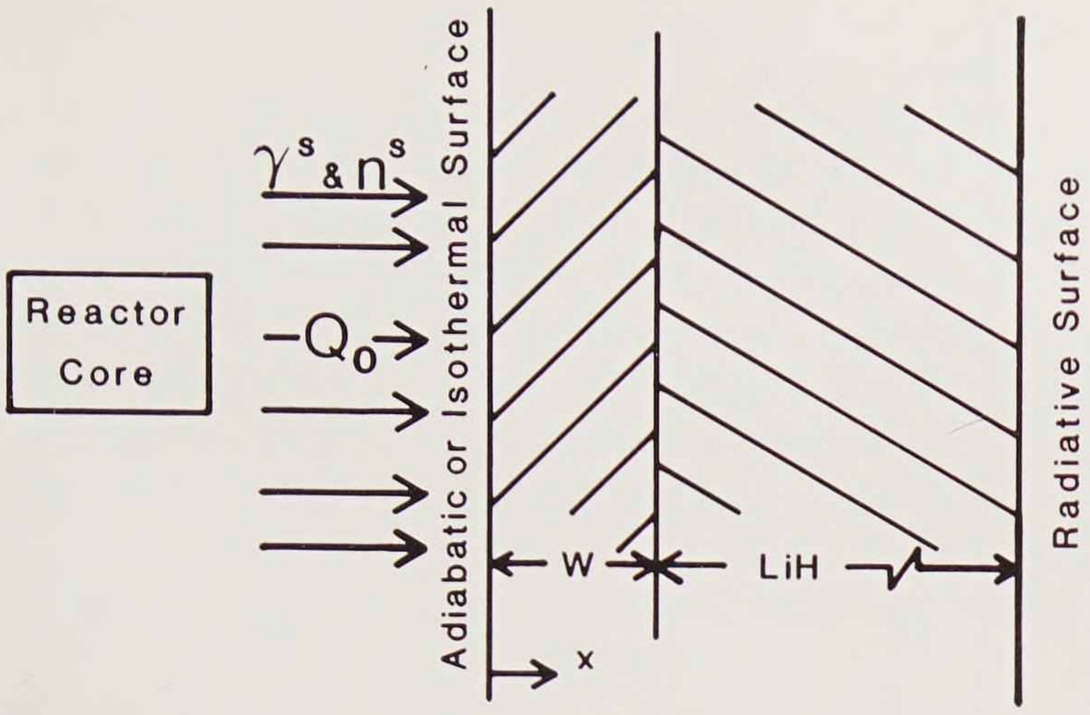


Figure 4 *Shield Configuration for 1-D Temperature Analysis.*

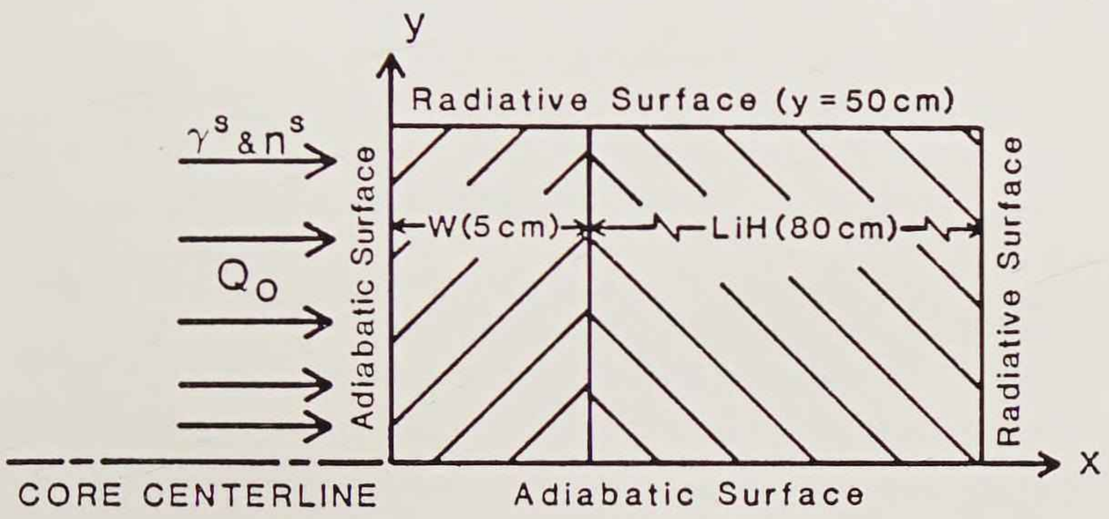


Figure 5 *Shield Configuration for 2-D Analysis (Adiabatic Front).*

Comparison of Analytical and Finite Element Results

To test the accuracy of the Newton–Raphson method with simplex elements, the 1-D temperature distribution in a W-LiH shield (see Figure 4) was determined using both analytical and finite element methods. The two-layered shield is internally heated by gamma radiation and neutrons, cooled by thermal radiation to space, and is either insulated or kept at constant temperature at its front surface. Heating rates at the front surface of the shield are assumed constant along the entire core-shield interface.

The governing equation for the temperature distribution in each region is a Poisson equation with constant thermal conductivities. The internal heating rates in the shield are determined by each region's respective neutron removal and gamma absorption cross sections. The exact analytical solutions for this problem are contained in Appendix 1.

Figure 6 shows the 1-D results for both the adiabatic and isothermal front surface conditions. The excellent agreement between the analytical and FEM solutions is readily apparent. The maximum difference between the two solutions was less than 0.1 percent.

The isothermal front surface represents an actively cooled surface condition. For this problem, it was assumed that the shield's front surface was designed to be maintained at 600 K. This design temperature is based on the need for maintaining the LiH temperature between a range of 600 to 680 K (and realizing that the maximum temperature will occur within the shield because of internal heat generation).

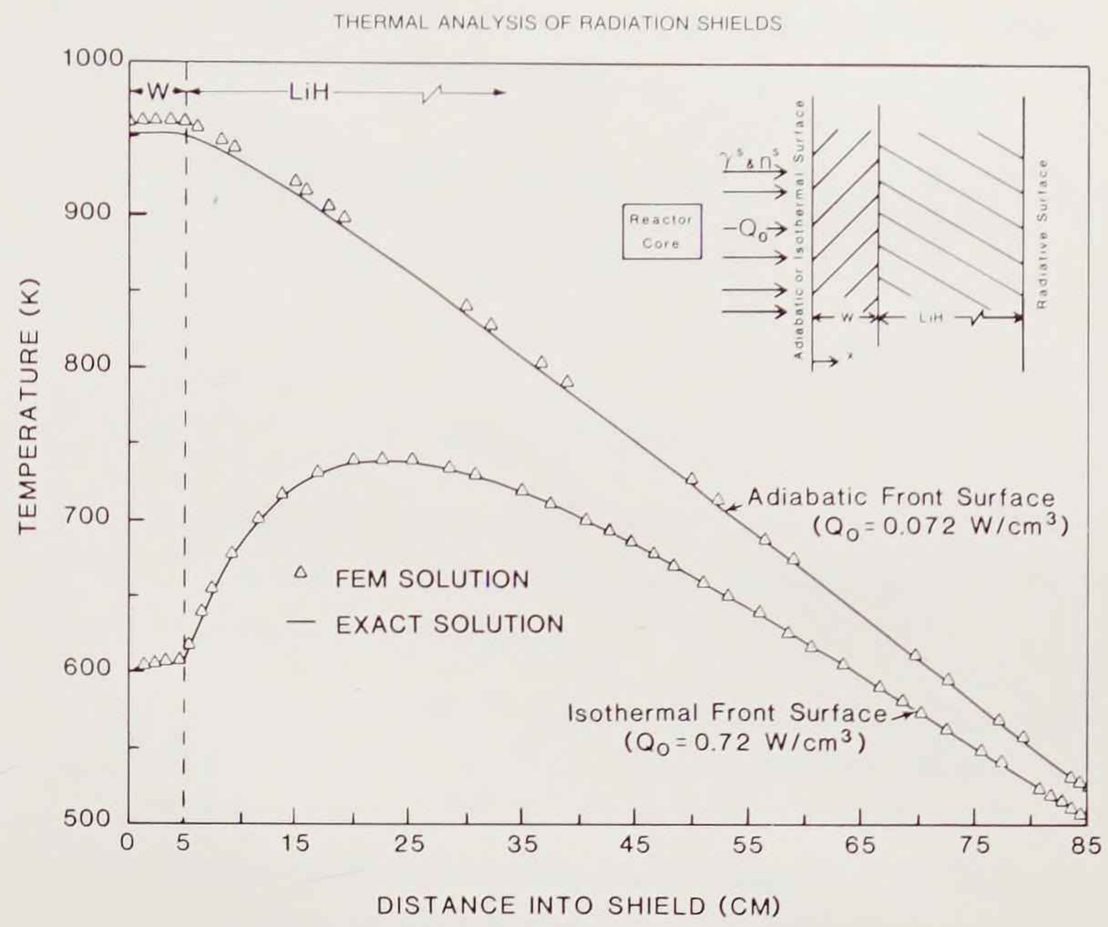


Figure 6 *Comparison of Analytic and Finite Element Methods for Temperature Distribution in a 1-D, W-LiH Slab Shield.*

The effect of an adiabatic front on the LiH temperature is readily observed from Figure 6. The maximum LiH temperature for the adiabatic front is 960 K for an initial heating rate of 0.072 W/cm^3, and 738 K for the (600 K) isothermal front with an order of magnitude higher initial heating rate of 0.72 W/cm^3. While the difference between the two front surface conditions is less pronounced for the multi-dimensional problem, it does illustrate that careful engineering consideration must be given to the front surface shield design based on the core power level.

The FEM program was run as a 1-D model by setting the heat flux equal to zero at $y = 0.0$ and $y = 1.0$, and reading shield centerline temperatures at $y = 0.5$ (for all x). For a 156 node mesh, the CPU time required was 3 minutes, 17 seconds for 26 iterations. However, from Figure 7, one observes that the radiating surface temperature (and, hence, all temperatures throughout the shield) had converged to within 0.1 K of its final value after only 10 iterations. (This result was repeated for a variety of test cases.)

The CPU time required for the analytical solution was only 0.5 seconds for this problem. Needless to say, a numerical method is generally not an optimum solution technique for a 1-D problem. However, these results are essential to gain confidence in the use of simplex elements to solve non-linear temperature problems in a multi-dimensional shield geometry. The tem-

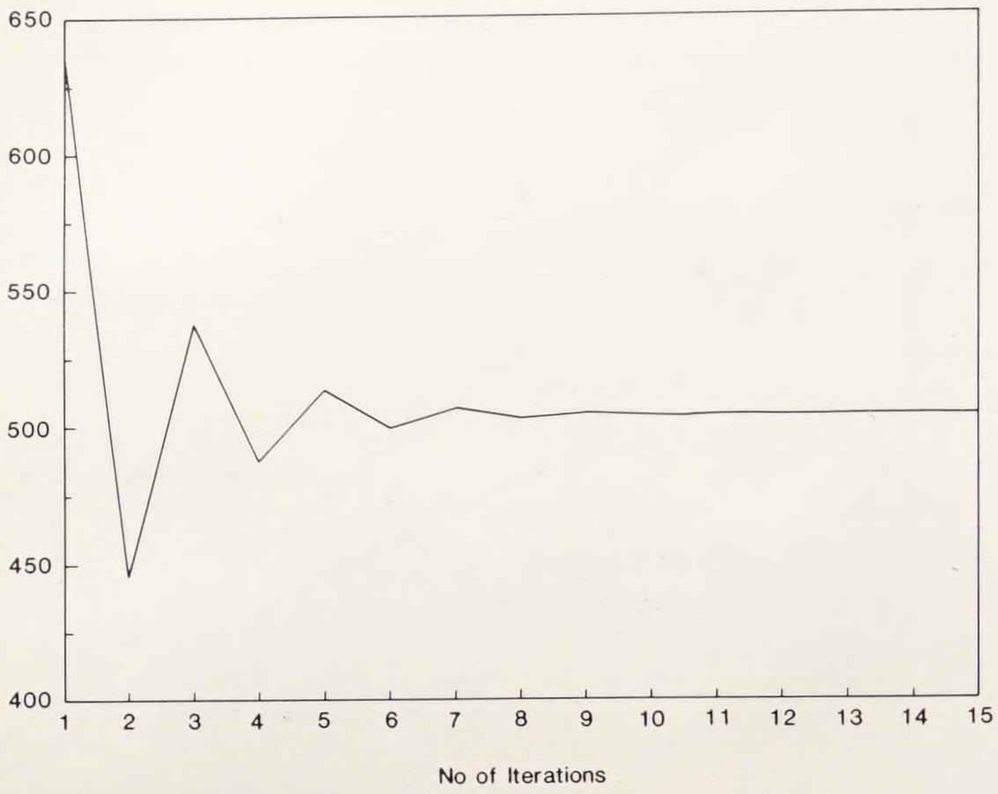


Figure 7 *Change in Radiative Surface Temperature vs. Iteration for a 1-D, W-LiH Slab.*

perature predictions using the FEM in a 2-D, LiH shield geometry are presented and discussed in the following section.

2-D Temperature Calculations

The heat generation was included in the same manner as in the 1-D problem with the exception that Berger buildup factors for W and LiH were included to account for the effects of secondary gamma production. Figures 8 and 9 show the temperature contours within the shield for both the adiabatic and isothermal front surface conditions.

While these preliminary results are not intended to serve as the basis for design decisions, they do provide some insights into the thermal anlaysis of the shield. The 2-D model provides an additional heat rejection surface. This additional surface results in lower temperatures at higher initial heating rates (corresponding to a higher operating power level for the core) when comparing the 1-D adiabatic with the 2-D adiabatic front surface.

Even for the isothermal front surface condition, the likelihood of a passively cooled shield maintaining LiH temperature within the range of 600 to 680 K appears remote. The steepness of the temperature gradient in the LiH portion of the shield indicates the need for close coupling between the neutronics and temperature analysis of the shield. For example, the effects of varying the isotopic content of Li-6 and Li-7 may dramatically change the temperature distribution (and ultimately, thermal stresses/strains) within the shield.

The shield of Figures 8 and 9 (85×50 cm) was discretized using a mesh of 253 nodes. Since an exact temperature solution is not available for even this simple geometry, but non-linear problem, a check on the accuracy of the FEM solution is made by comparing

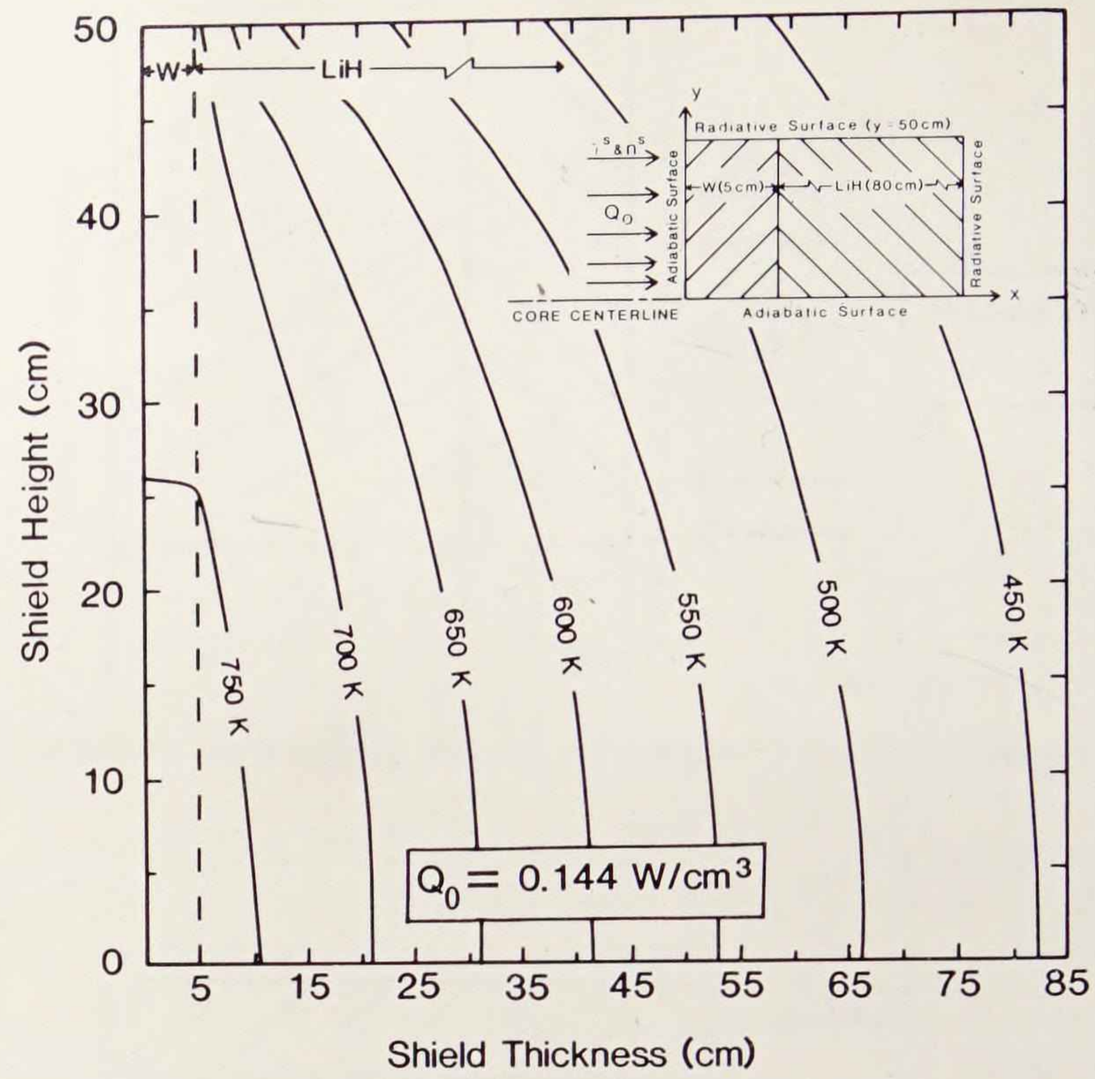


Figure 8 *Temperature Contours for a 2-D, W-LiH Slab Shield with Adiabatic Front Surface.*

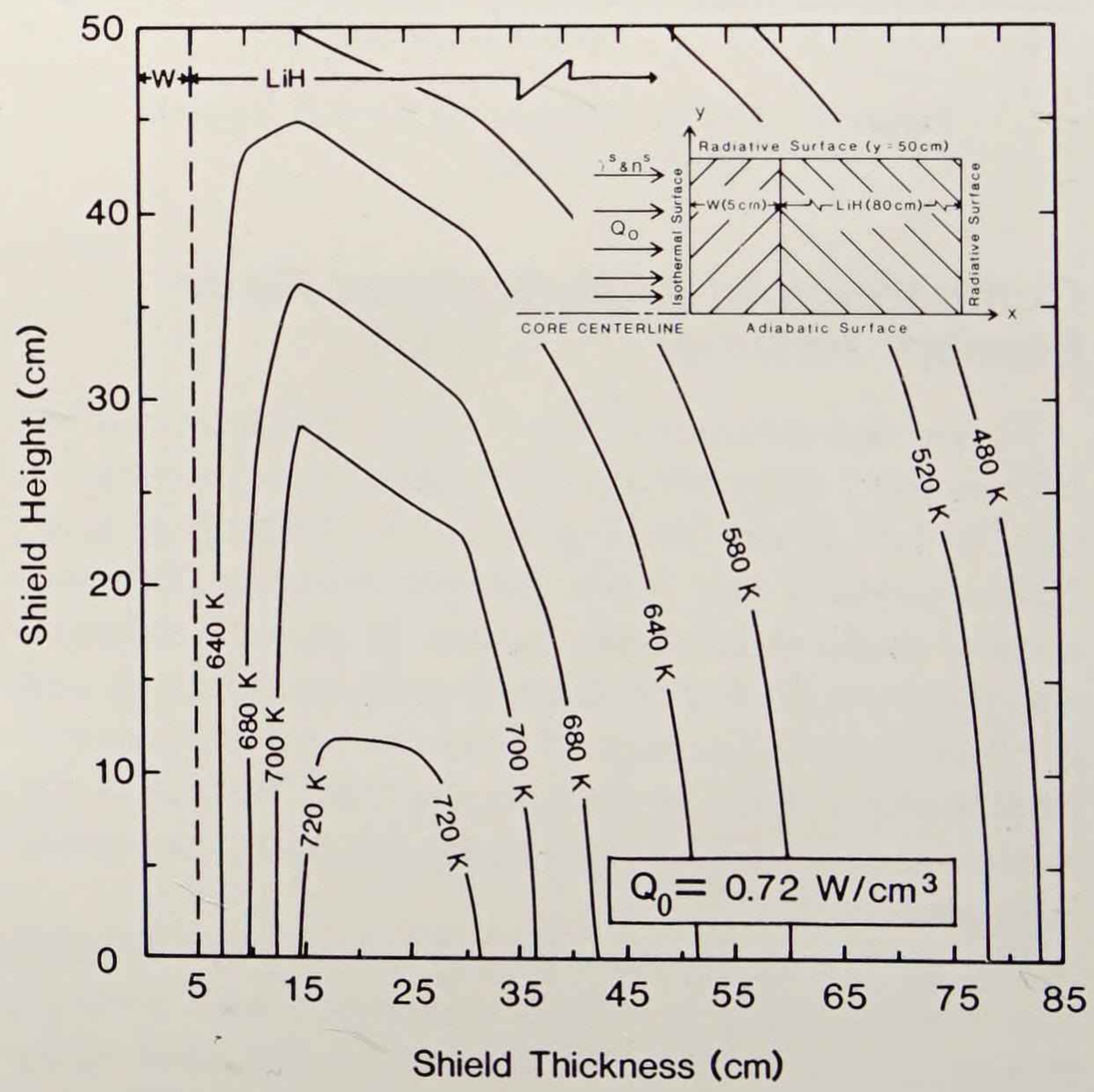


Figure 9 *Temperature Contours for a 2-D, W-LiH Slab Shield with Isothermal Front Surface.*

the energy deposited in the shield with the total heat leaving all surfaces as determined by the final temperature distribution. For this coarse mesh, the energy balance differed by only 2 percent. Thus, the simplex element proves to be quite effective for the 2-D, non-linear temperature problem as well.

Summary and Conclusions

A finite element computer code is being developed to perform thermal and stress analysis calculations of radiation shields for space nuclear reactors. The finite element program uses 3-node (simplex) elements and a Newton–Raphson iteration scheme to handle the irregular shape of the shield as well as the non-linear governing equations due to temperature properties and the radiative cooling at the outer surfaces of the shield.

The temperature distribution in a 1-D, W-LiH shield is calculated using both the exact, analytical solution and the finite element technique. The difference between the two methods was less than 0.1 percent. 2-D temperature calculations in a W-LiH shield are performed using FEM. Results indicated that additional cooling of the shield at its top surface causes the temperature in the shield to be much lower than that predicted by the 1-D calculation for the same operating conditions. Therefore, realistic temperature/stress analysis should consider actual shield geometry and boundary conditions.

The excellent agreement between closed form solutions and the finite element method using a Newton–Raphson iteration for the 1-D, W-LiH shield shows that the 3-node (simplex) element can accurately determine the temperature distribution of irregularly shaped space reactor radiation shields for which exact, analytical solutions are not attainable. The 2-D (and 3-D axisymmetric) thermal analysis can now be accurately completed, with the output used to determine thermal stresses/strains in the shield. Future work at the University of New Mexico will include completion of the coupled neutronics-temperature-stress/strain model and demonstration of its use for an actual space reactor shield design.

Acknowledgments

This research was conducted at the University of New Mexico under the Sponsorship of the Air Force Institute of Technology, Wright-Patterson Air Force Base, Ohio.

References

Barattino, W. J., M. S. El-Genk, and S. S. Voss (1985), "Review of Previous Shield Analysis for Space Reactors," in *Space Nuclear Power Systems 1984*, M. S. El-Genk and M. D. Hoover eds., Vol. 2, Orbit Book Co., Malabar, FL.

Bathe, Klaus-Jurgen (1982) *Finite Element Procedures in Engineering Analysis*, Prentice-Hall, Inc., New Jersey.

El-Genk, M. S., D. M. Woodall, V. F. Dean, and D. Louie (1985), "Review of the Design Status of the SP-100 Nuclear Power System" in *Space Nuclear Power Systems 1984*, M. S. El-Genk and M. D. Hoover eds., Vol. 1, Orbit Book Co., Malabar, FL.

Huebner, K. H. and E. A. Thornton (1982) *The Finite Element Method for Engineers*, John Wiley and Sons, New York.

JPL (1982) *SP-100 Conceptual Design Description*, Jet Propulsion Laboratory, Pasadena, CA, June 1982.

Ranken, W. A. (1982) *SP-100 Project Semi-Annual Technical Progress Review*, Los Alamos National Laboratory, Los Alamos, NM, October 1982.

Welch, F. H. (1977) *Lithium Hydride Technology: III. Properties of Lithium for SNAP Shielding Applications*. NAA-SR-9400, Vol. III. Atomics Internationals May 1977.

Appendix A

Derivation of Analytical Solution for 1-D, W-LiH Slab Shield with Radiative Back Surface and Either Adiabatic or Isothermal Front Surface

The accuracy of the finite element method to determine the temperature distribution of the shield was validated by comparing the numerical results with 1-D closed form analytical solution. Figure 4 is a schematic of the problem setup used for the comparison.

The governing equations and boundary conditions for this problem during steady-state operation are as follows:

Tungsten Region $[0 \leqslant x \leqslant a]$:

$$\nabla \cdot \left[k_w(T) \nabla T_w(x) \right] + B_w(\mu_w, x) q_{0_\gamma} e^{-\mu_w x} + q_{0n} e^{-\Sigma_{R_W} x} = 0 \quad \text{(A-1)}$$

with:

$$T(x = 0) = T_0 \text{ (constant front surface temp)} \quad \text{(A-2a)}$$

or

$$-k_w \frac{dT_w(x = 0)}{dx} = 0 \text{ (adiabatic front surface)} \quad \text{(A-2b)}$$

and

$$T(x = a) = T_{\text{int}} \quad \text{(A-3)}$$

Lithium Hydride Region $[a \leqslant x \leqslant b]$:

$$\nabla \cdot \left[k_L(T) \nabla T_L(x) \right] + B_L(\mu_L, x) q_{L_\gamma} e^{-\mu_L (x-a)} + q_{L_n} e^{-\Sigma_{R_L}(x-a)} = 0 \quad \text{(A-4)}$$

with:

$$T(x = a) = T_{\text{int}} \quad \text{(A-5)}$$

$$T(x = b) = T_F \quad \text{(A-6)}$$

$(B_L q_{L\gamma})$ and q_{L_n} at $x = a$ are determined through the use of the following relations:

$$B_L(\mu_L, a) q_{L_\gamma} = B_w(\mu_w, a) e^{-\mu_w a}, \tag{A-7}$$

$$q_{L_n}(a) = q_{0_n} e^{-\Sigma_R w^a}. \tag{A-8}$$

It is assumed that heating in the shield will occur as a result of gamma and neutron interactions in the shield. The gamma heating results from the heat generated due to photoelectric absorption, compton scattering, and pair production. The gamma buildup factor is an empirical value which accounts for the heating effects of secondary radiations. The value of the buildup factor is based on the gamma energy, attenuation coefficient, and shield geometry. For a multi-layered shield, when the thickness of the outermost layer of the shield (for example, LiH) exceeds 2–3 mean free paths, the buildup factor of the outermost layer is generally used for shield design (but based on the total number of mean free paths along the line of sight through all the materials). Because the buildup factor was assumed to be constant within a particular material region, it is mathematically equivalent to consider the initial gamma heating rate to be the product of $(B_w \cdot q_{0w})$ and neglect mention of buildup. For this reason buildup was not discussed in the main text for the 1-D problem. It is used in this Appendix for the purpose of completeness.

Analytical Solution

Assuming constant thermal conductivities and buildup factors throughout the tungsten and lithium hydride, the analytical solutions for each region during steady-state operation are obtained as follows:

Tungsten Region $(0 \leqslant x \leqslant a)$:

Adiabatic Front Surface:

$$T_w(x) = T_{\text{int}} + B_w \frac{q_{0_\gamma}}{k_w \mu_w^2}\left[e^{-\mu_w a} - e^{-\mu_w x} + \mu_w(a - x)\right]$$

$$+ \frac{q_{0_n}}{k_w \Sigma_R^2}\left[e^{-\Sigma_R a} - e^{-\Sigma_R x} + \Sigma_R(a - x)\right]. \tag{A-9}$$

Constant Temperature Front Surface:

$$T_w(x) = T_0 + B_w \frac{q_{0_\gamma}}{k_w \mu_w^2}(1 - e^{-\mu_w x}) + \frac{q_{0_n}}{k_w \Sigma_{r_w}^2}(1 - e^{-\Sigma_{R_w} x})$$

$$+ \frac{x}{a}\left[(T_{\text{int}} - T_0) + B_w \frac{q_0 \gamma}{k_w \mu_w^2}(e^{-\mu_w a} - 1)\right.$$

$$\left. + \frac{q_{0_n}}{k_w \Sigma_{R_w}^2}(e^{-\Sigma_{R_w} a} - 1)\right]. \tag{A-10}$$

Lithium Hydride Region $(a \leqslant x \leqslant b)$:

Adiabatic Front Surface:

$$T_L(x) = \left[\frac{x - a}{b - a}\right] T_b - \left[\frac{x - b}{b - a}\right] T_{\text{int}}$$

$$+ \frac{B_L q_{L_\gamma}}{k_L \mu_L^2}\left[e^{-\mu_L(b-a)}\left[\frac{x - a}{b - a}\right]\right.$$

$$\left. - \left[\frac{x - b}{b - a}\right] - e^{-\mu_L(x-a)}\right]$$

$$+ \frac{q_{L_n}}{k_L \Sigma_{R_L}^2}\left[e^{\Sigma_{R_L}(b-a)}\left[\frac{x - a}{b - a}\right]\right.$$

$$\left. - \left[\frac{x - b}{b - a}\right] - e^{-\Sigma_L(x-a)}\right]. \tag{A-11}$$

Constant Temperature Front Surface:

$$T_L(x) = T_b + \frac{B_L q_{L_\gamma}}{k_L \mu_L^2}\left[e^{-\mu_L(b-a)} - e^{-\mu_L(x-a)}\right]$$

$$+ \frac{q_{L_n}}{k_L \Sigma_{R_L}^2}\left[e^{-\Sigma_{R_L}(b-a)} - e^{-\Sigma_{R_L}(x-a)}\right]$$

$$+ \left[\frac{x - b}{b - a}\right]\left[(T_b - T_{\text{int}}) + \frac{q_{L_\gamma}}{k_L \mu_L^2}(e^{-\mu_L(b-a)} - 1)\right.$$

$$\left. + \frac{q_{L_n}}{k_L \Sigma_{R_L}^2}(e^{-\Sigma_{R_L}(b-a)} - 1)\right]. \tag{A-12}$$

Determination of T_{int} and T_b

To determine the W-LiH interface temperature, T_{int}, and the back surface temperature, T_b, energy balances at each surface are used. For T_{int}, the following balance is made:

$$-k_w \frac{dT_w}{dx} = -k_L \frac{dT_L}{dx} \qquad (\text{at } x = a) \tag{A-13}$$

The following expressions for the interface temperature are obtained:

Adiabatic Front Surface:

$$T_{\text{int}} = T_b + \frac{B_L q_{L_\gamma}}{k_L \mu_L^2}\left[e^{-\mu_L(b-a)} + \left[(b - a)\mu_L - 1\right]\right]$$

$$+ \frac{q_{L_n}}{k_L \Sigma_{R_L}^2}\left[e^{-\Sigma_{R_L}(b-a)} + (b - a)\Sigma_{R_L} - 1\right]$$

$$+ B_W \frac{q_{0_\gamma}}{\mu_w} \frac{(b - a)}{k_L}\left[1 - e^{\mu_W a}\right]$$

$$+ \frac{q_{0_n}}{\Sigma_{R_W}} \frac{(b - a)}{k_L}\left[1 - e^{-\Sigma_{RW} a}\right]. \tag{A-14}$$

Constant Temperature Front Surface:

$$\left[\frac{k_w}{a}+\frac{k_L}{b-a}\right]T_{\text{int}}$$

$$=\left[\frac{k_w}{a}\right]T_0+\left[\frac{k_L}{b-a}\right]T_b$$

$$+\frac{B_L q_{L_\gamma}}{\mu_L^2}\left[\mu_L+\frac{1}{b-a}\left(e^{-\mu_L(b-a)}-1\right)\right]$$

$$+\frac{q_{L_N}}{\Sigma_{R_L}^2}\left[\Sigma_{R_L}+\frac{1}{b-a}\left(e^{-\Sigma_L(b-a)}-1\right)\right]$$

$$+\frac{B_W q_{0_\gamma}}{\mu_w^2}\left[\frac{1}{a}\left(1-e^{\mu_W a}\right)-\mu_W e^{-\mu_W a}\right]$$

$$+\frac{q_{0_n}}{\Sigma_{R_W}^2}\left[\frac{1}{a}\left(1-e^{-\Sigma_{R_W} a}\right)-\Sigma_{R_W} e^{-\Sigma_{R_W} a}\right] \quad \text{(A-15)}$$

To determine the back surface temperature, T_b, the following energy balance is made at $x = b$:

$$-k_L\frac{dT_L}{dx}=\epsilon\sigma F_{ij}\left(T_b^4-T_a^4\right) \quad \text{(A-16)}$$

When the view factor at the back surface is taken as unity, the following expressions for T_b are obtained:

Adiabatic Front Surface:

$$T_b=\left[T_a^4+\frac{B_W q_{0_\gamma}}{\mu_W\epsilon\sigma}\left(1-e^{-\mu_W a}\right)+\frac{q_{0_n}}{\Sigma_W\epsilon\sigma}\left(1-e^{\Sigma_W a}\right)\right.$$

$$+\frac{B_L q_{L_\gamma}}{\mu_L\epsilon\sigma}\left(1-e^{-\mu_L(b-a)}\right)$$

$$\left.+\frac{q_{L_n}}{\Sigma_L\epsilon\sigma}\left(1-e^{-\Sigma_{R_L}(b-a)}\right)\right]^{0.25} \quad \text{(A-17)}$$

Constant Temperature Front Surface:

$$\epsilon\sigma\left(T_b^4-T_a^4\right)$$

$$=-\left[\frac{B_L q_{L_\gamma}}{\mu_L}e^{-\mu_L(b-a)}+\frac{q_{L_n}}{\Sigma_{R_L}}e^{-\Sigma_{R_L}(b-a)}\right.$$

$$+\frac{1}{(b-a)}\left[k_W\left(T_b-T_{\text{int}}\right)\right.$$

$$+\frac{q_{L_\gamma}}{\mu_L^2}\left(e^{-\mu_L(b-a)}-1\right)$$

$$\left.\left.+\frac{q_{L_n}}{\Sigma_{R_L}^2}\left(e^{-\Sigma_{R_L}(b-a)}-1\right)\right]\right]. \quad \text{(A-18)}$$

Baseline Case Data

The following conditions were used as the baseline case for the sample problem:

Nuclear Input Data

$\mu_W = 0.667\ \text{cm}^{-1}$
$\mu_L = 0.0444\ \text{cm}^{-1}$
$\Sigma_{R_W} = 0.2120\ \text{cm}^{-1}$
$\Sigma_{R_L} = 0.1178\ \text{cm}^{-1}$

Thermal Input Data

$k_w = 1.3\ \text{W/cm-k}$
$k_L = 0.05193\ \text{W/cm-k}$
$q_{0_\gamma} = 0.036\ \text{W/cm}^3$
$q_{0_n} = 0.36\ \text{W/cm}^3$
$B_W = 10.0$
$B_L = 10.0$
$\epsilon = 0.8$
$T_A = 310\ \text{K}$

Geometric Data

$a = 5.0\ \text{cm}$
$b = 85.0\ \text{cm}$

Space Nuclear Power Systems 1984
Edited by M. S. El-Genk and M. D. Hoover
© Orbit Book Company, Malabar, FL, 1985

Chapter 53

Thermal Management of High Power Space Based Systems

Han Hwangbo and W. S. McEver

MRJ, Inc.
10400 Eaton Place
Fairfax, VA 22030

Conventional techniques of using a portion of the spacecraft skin for radiation of waste heat will be inadequate for high powered payloads (50 to 100 kWe) due to the lack of sufficient area. A Shuttle type system using a pumped single phase fluid loop could be scaled up to higher power but this type of system would require excessive pump power and weight. A pumped two-phase heat transfer loop has a much lower pumping requirement due to the higher latent heat of vaporization of the fluid in comparison to the sensible heat it can absorb through a temperature change. Concepts for an evaporator and a condenser for a pumped two-phase system are described. The condenser uses capillary grooves and a separate pumped condensate return line to achieve high heat transfer coefficients and stable operation due to the separation of the vapor and liquid flows. The cold plate evaporator uses wicks to contain the liquid and transport it to the heated surface. It can also function as a condenser for warming components. Control concepts for the cold plate are discussed. Concepts for deployment or erection of large space radiators are also considered.

Introduction

Future spacecraft payloads with very high electrical power requirements (10~100 kWe) will impose stringent demands on the thermal subsystem design. Since most of the electrical energy consumed in the spacecraft will ultimately be converted to low temperature thermal energy, efficient means must be provided for absorbing, transporting, and disposing this waste heat. The size and mass of the thermal control system will be quite large even in comparison with the primary power source. For example, Ranken (1981) describes a space nuclear reactor/thermoelectric system (SPAR) with a radiator area of 64 m^2 for 100 kWe output. If all the electrical energy were rejected to space as thermal energy at 293 K, the required radiator area would be 300 m^2 (for an emittance of 0.8). The large difference in area is due to the T^4 dependence of the Stephan–Boltzmann law. The SPAR radiator operates at 775 K while the low temperature radiator is at 293 K. Clearly there is a very strong incentive to make the heat transfer processes as efficient as possible in order to minimize the temperature difference between heat source and radiator. A radiator operating at 273 K would have to be 33 percent larger than one at 293 K, for example. In this paper we discuss present space thermal management techniques and the reasons that they are inadequate for high powered spacecraft. Advanced concepts such as active two-phase heat transfer loops are discussed along with work done at MRJ on the design of cold plate (two-phase boilers) and condensers suitable for operation in 0-g with two-phase thermal systems. Concepts for deployment or erection of large low temperature radiators are also considered.

Conventional Spacecraft Thermal Management

Present-day unmanned spacecraft rely on solar arrays for their electrical power and thus have very modest thermal requirements in terms of heat rejection. Typically, heat producing units are located on the outside skin of the spacecraft which is usually an aluminum honeycomb for structural stiffness. The outside face of the radiator is covered with a high emittance (ϵ) low solar absorptance (α) material which is typically a second surface mirror (SSM) composed of a silver mirror covered with a SiO_2 film. The mirror gives the low absorptance while the SiO_2 film gives a high emittance. Typical values are $\alpha/\epsilon = 0.08/0.8$ at the beginning of life and 0.20/0.8 at end of life. The low solar absorptance properties of the mirror are quite important since the radiator may be exposed to full or partial sun during a portion of the orbit and the solar flux of 1350 W/m^2 is much larger than the 334 W/m^2 emitted by a surface at 293 K with $\epsilon = 0.8$.

The thermal design engineer must consider both the worst case hot and cold conditions for the radiator sizing. Worst case hot conditions are with maximum expected solar input, maximum power dissipation, and end of life solar absorptance. Cold conditions occur with no solar input (eclipse condition) and minimum

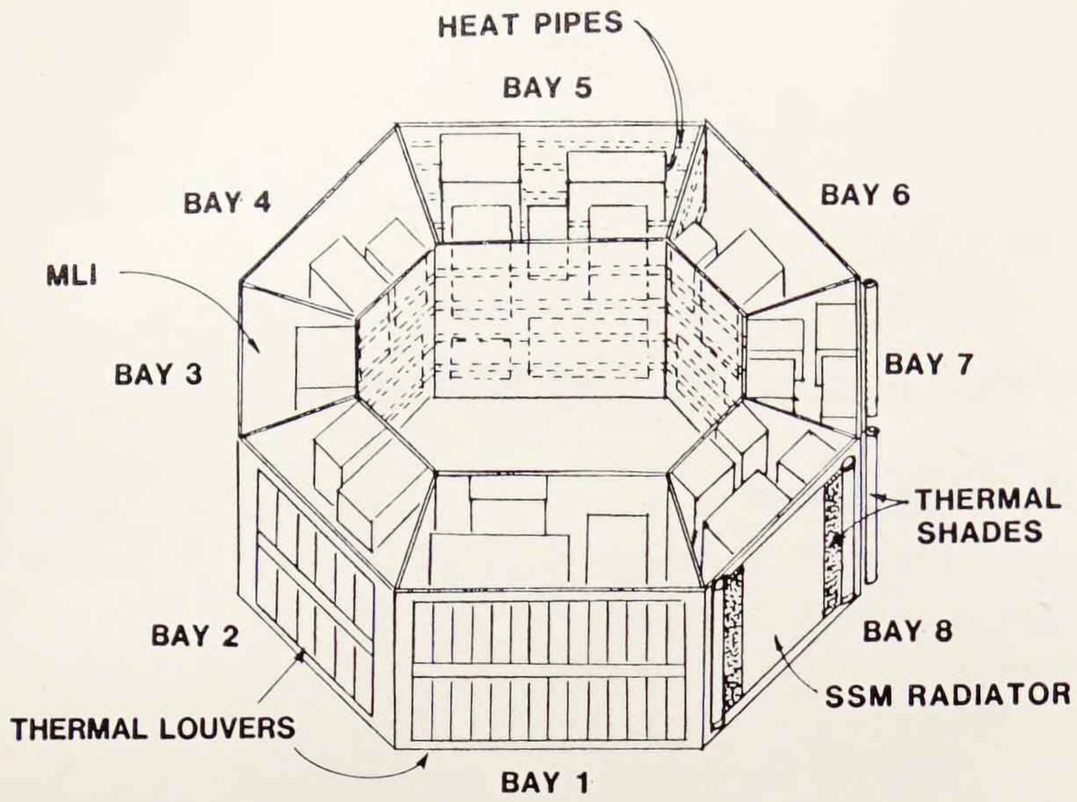


Figure 1 *Illustration of Present-day Thermal Control Techniques for Un-manned Spacecraft.*

unit power dissipation. Electric heaters can be used to maintain temperatures of payloads during the cold condition. The sizing of these heaters and their energy use impacts on the battery storage requirements. Generally there is more than enough spacecraft skin area to serve as radiator. Unused portions of the skin are covered with multi-layer insulation (MLI). Interior components can generally be cooled by allowing them to radiate to a radiator panel or the heat can be transported from the interior to a radiator by using heat pipes.

Temperature control is obtained by use of electrical heaters, thermostatically controlled louvers, adjustable shades or variable conductance heat pipes (VCHP). VCHP's use a controlled quantity of non-condensible gas in the condenser section of the heat pipe to control the thermal conductance between the heat source and space radiator. Louvers control the conductance between the space sink and the radiator. Hwangbo (1983) has recently described the use of a motorized thermal shade (MTS) to control temperature through adjustment of the radiator area exposed to the space sink. When compared to louver temperature control the MTS provides better utilization of radiator area because of lower net solar absorption and less blockage of the radiator area. When compared to VCHP temperature control, the MTS was found to have lower total overall costs including development, fabrication, and qualification.

The thermal control concepts discussed above are depicted schematically in Figure 1. A moderately complex spacecraft with only a kW or two of electrical power to dissipate might utilize several of these techniques. However, for a payload with higher power dissipation, these techniques will have very limited application for a variety of reasons; the principal one being a lack of sufficient area on the external surface of the spacecraft. A 4.2 m diameter by 10 m cylinder has a total surface area of only 160 m^2 which is far smaller than the minimum of 300 m^2 required (not allowing for solar heating) to dissipate a 100 kW thermal load at 293 K. A second reason is the cost and complexity of the thermal control system which would have to be developed for each heat producing part of the payload. The high-powered interior components would have to be cooled by heat pipes, specially developed for each piece of equipment. Heat pipes of unusual design would be difficult to test and space qualify on Earth due to the adverse effects of gravity on their operation. The thermal system would be the "tail that wags the dog".

Pumped Fluid-Loop Spacecraft Thermal Management

Clearly a high powered spacecraft must be cooled (and heated) by the more conventional systems that we use for the thermal control of the high power system on Earth. The Space Shuttle is the leading example of this approach. A simplified schematic of the Shuttle thermal control system is shown in Figure 2. A similar system is also used in the NASA/ESA Spacelab. The Shuttle System is composed of three main heat transfer loops. The first loop is the Shuttle air distribution system. Cabin air is circulated and picks up latent and sensible heat from the occupants and equiment and is cooled and de-humidified by chilled water. The chilled water loop delivers the absorbed heat to the third loop which is a Freon 21 loop transporting the heat to the space radiators which are exposed when the Shuttle cargo bay doors are opened. Heat rejection when the doors are closed during ascent and re-entry is through the use of water evaporative coolers or "water boilers". Water is used inside the cabin fluid loop because of its safety while Freon 21 is used in the outside radiator loop because of its low freezing point and low toxicity to the ground personnel who service the system.

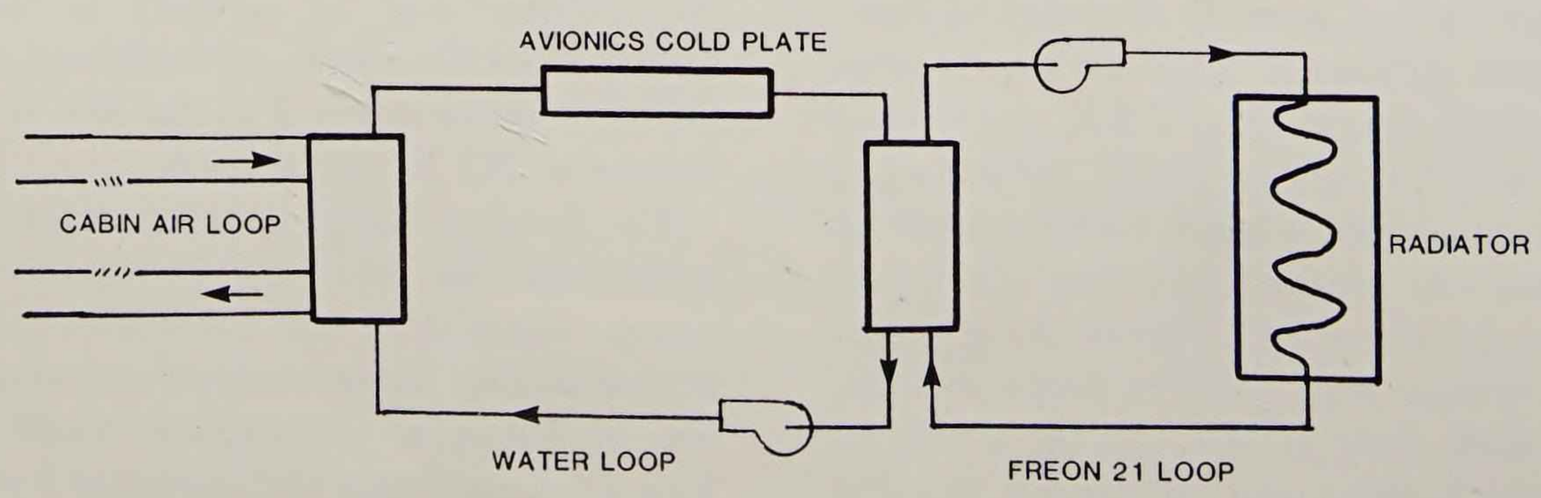


Figure 2 *Shuttle-type Pumped Single-phase Fluid Thermal Transport System.*

The Shuttle thermal control system is an example of a system using sensible heat transfer, that is, the exchange of heat is accompanied by the increases or decreases in the temperature of the fluids. The system is also series connected. This means that downstream component temperatures are affected by the heat inputs of upstream components. A parallel flow system was not adopted because of the weight penalties and system complexity from the additional piping, valves, and controls that would be required.

It is certainly possible that a Shuttle-type thermal system could be scaled up to the 100 kW level. However, the pumping power requirements associated with such a system have been estimated by Ellis and Rankin (1983) to be as high as 3 kW. The large temperature changes in the Shuttle System (28°C or 50°F) are also detrimental to good radiator efficiency due to the T^4 radiation law. One good feature of this system is its thermal performance is essentially independent of gravitational effects. This greatly simplifies the testing and qualification of the system components.

Future Thermal Control Systems

The thermal system concept that has received the most study for use in future complex very high-powered space systems is that of the thermal utility. A thermal utility is simply a system for transporting heat from dispersed sources to a central radiator. The thermal utility differs from a Shuttle type system in that a parallel flow arrangement would be employed to eliminate the temperature changes with load that is inherent with a series flow system. In this respect the thermal utility is similar to the recirculating chilled water systems that provide equipment cooling and air conditioning in buildings on earth. However, the premium for light weight and efficiency is much higher for the space based thermal utility. With single phase thermal transport systems, efficiency can be improved by increasing the fluid flow rate which minimizes temperature differences both through the higher thermal capacitance rate of the fluid and through higher heat transfer coefficients. Higher flow rates lead to increased system weight from larger pipes and fluid inventory and to larger pumps and valves.

The disadvantages of a single phase heat transport system can be overcome by use of a pumped two-phase system (Ollendorf, Fowle, and Almgren 1981 and Ellis and Rankin 1983). A two-phase system used the latent heat of vaporization of the fluid rather than its heat capacity. For example, Freon 21 has a specific heat capacity of 1.0 kJ/kg-°C and a latent heat of 242 kJ/kg. To compare the thermal transport properties of single-phase and two-phase fluids, one must factor in the temperature rise of the single-phase fluid. The Shuttle system has a temperature rise of 28°C which gives the single-phase Freon 21 system an effective thermal capacity of 28 kJ/kg. This is less than 12% of the latent heat capacity of Freon 21. Thus, a system which vaporizes the thermal transport fluid has a much smaller mass flow rate requirement than a single phase system. Additional benefits are the higher heat transfer coefficients associated with vaporization and condensation and the fact that the heat transfer occurs at constant temperature. With ammonia as the working fluid pump power requirements should only be a few hundred watts for a two-phase system designed to carry 100 kW.

The use of a pumped two-phase thermal transport system in 0-g requires development of two components: the evaporator (or cold plate heat exchanger) and the condenser. Recently at MRJ, Hwangbo and McEver (1983) studied the feasibility of a novel condenser concept that utilizes surface tension forces and suction draining of condensate to achieve very high heat transfer coefficients. A schematic of the MRJ condenser concept is shown in Figure 3. Vapor condenses on the

Figure 3 *Schematic of MRJ Condenser Concept Using Pumped Condensate Recovery.*

crests of capillary grooves and is pulled off into the trough of the groove through the action of surface tension forces. The condensed liquid is sucked out of the groove and into a separate condensate tube by a pump. The primary resistance to heat transfer is the film of condensate. A Nusselt-type analysis of the dynamics of condensate flow under surface tension forces showed that with the proper shape of the condensing surface, heat transfer coefficients an order of magnitude higher than those obtainable with conventional smooth surface condensers should be possible. Furthermore, the study showed that uniform heat transfer coefficients could be obtained down the length of the condenser and that liquid subcooling could be achieved.

Very little is known about combined liquid and vapor flow in 0-g. For condensation inside a tube it is assumed that the flow will be annular with the vapor on the inside and the liquid flowing along the wall of the tube or pipe. As the liquid film becomes thick, the vapor-liquid shear forces cause waves to form. These waves eventually bridge over giving rise to what is called slug flow. The pressure drops associated with these types of flows are subject to considerable uncertainty. In the MRJ condenser, the liquid and vapor flow are separate which will lead to a more uniform and stable operation.

One possible area of application of the MRJ condenser is at the interface between the two-phase thermal utility and a space radiator. The space radiator would be constructed of high capacity heat pipes (Alario, Brown, and Kosson 1983). A schematic of the system is shown in Figure 4. Sub-cooled liquid is pumped to the cold plate evaporators where it is vaporized and piped to the condenser. For temperature control under part load operation, a valve allows some of the vapor to bypass the condenser and combine with sub-cooled liquid from the condenser.

The cold plate evaporator is another very important part of the pumped two-phase system. Ideally, the liquid flow to the cold plate should be regulated to assure a high quality flow at the outlet (quality is the ratio of vapor mass flow to total flow). A high quality flow in the vapor return line (~0.9) will minimize total system flow and provide a more stable system than if there were a large percentage of liquid flow in the vapor line. To provide a high quality flow at the outlet of the cold plate, the plate design should prevent the vapor from entraining the liquid through frictional shear forces.

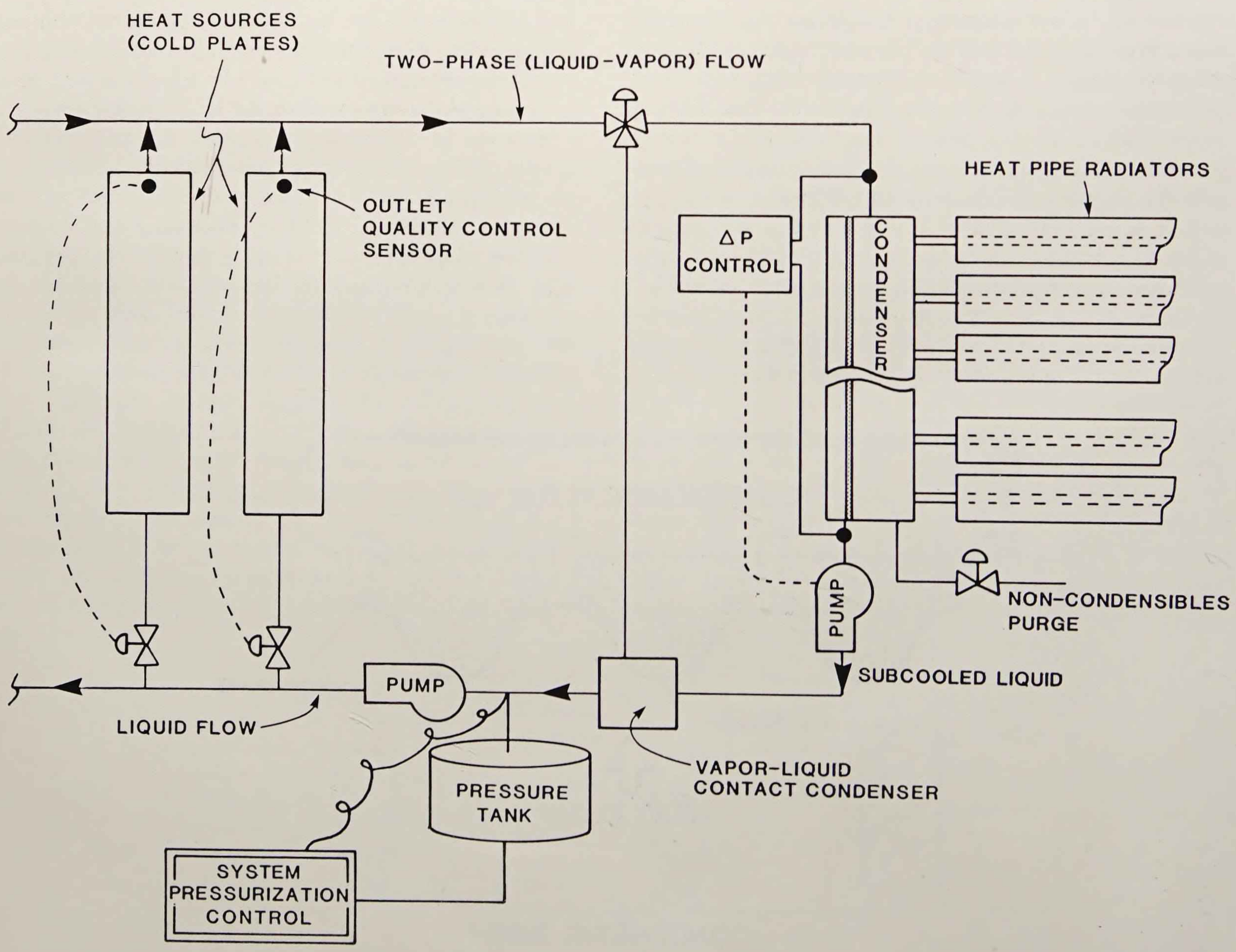


Figure 4 *System Schematic for Two-phase Space Cooling Application Using MRJ Condenser Concept.*

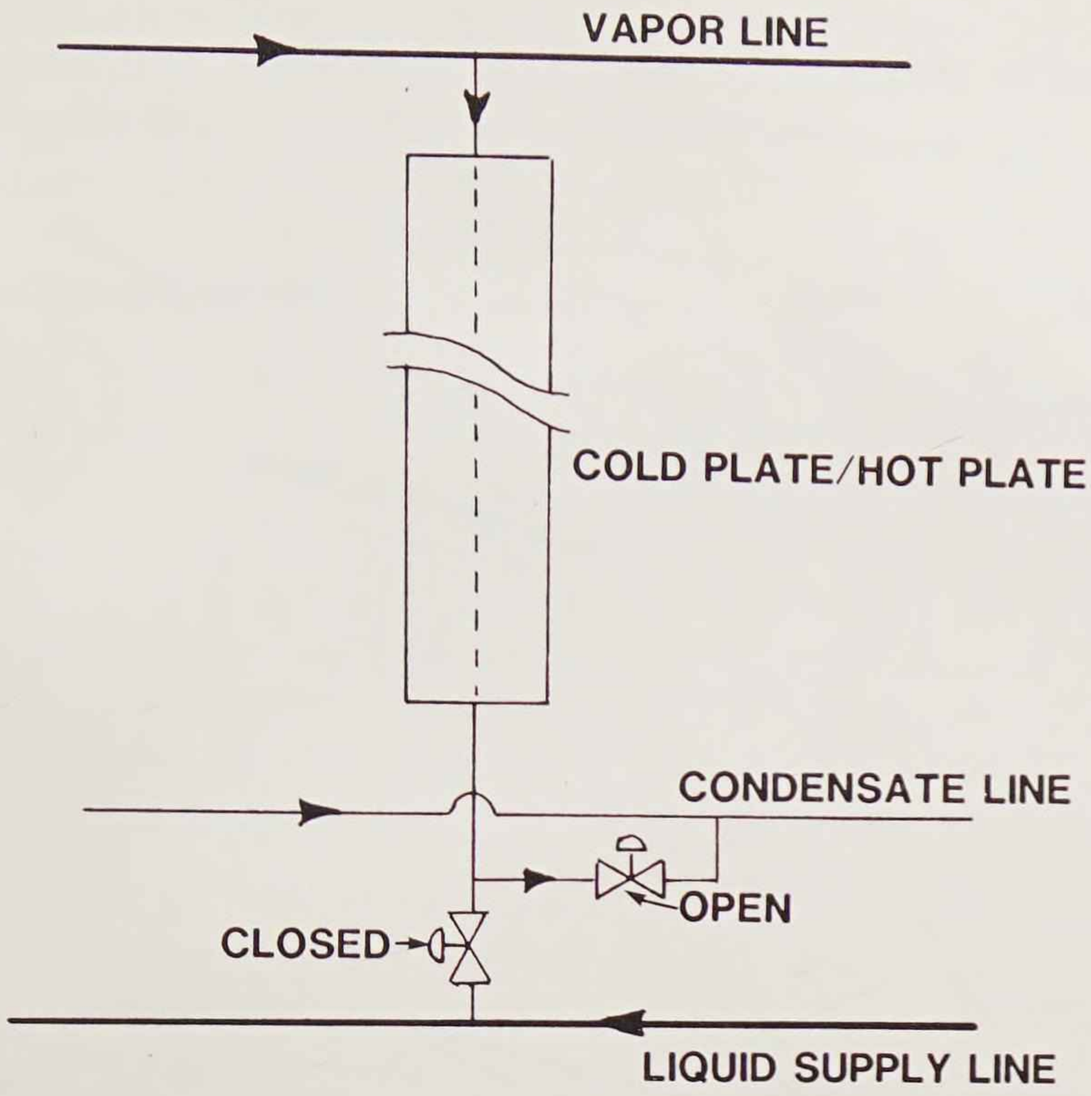


Figure 5 *Schematic of a Two-Phase Heat Exchanger Operating as a Condenser (Hot Plate Mode).*

Means should also be provided for complete liquid coverage of the heated areas.

Another desirable feature of the cold plate is for it to act as a condenser if the temperature of the heat source falls below that of the two-phase loop. In this way waste heat could be shared between components and the use of electrical heaters will be minimized. In this mode the cold plate would be acting as a hot plate. A schematic of the hot plate mode of operation is shown in Figure 5. A separate condensate return line is required. Control and movement of the liquid from the liquid lines to and from the evaporating and condensing region will be accomplished through the action of capillary or surface tension forces.

One concept of a cold plate/hot plate (CPHP) that is presently being studied at MRJ is shown in Figure 6. The arrows show the direction of flow of the liquid and vapor while in the cold plate mode. The device has the basic form of a conventional cold plate with the addition of a hollow interior which is lined with a wick structure. Liquid enters the interior through tubes and is distributed to the wick via small holes in the tube. In our figure heat flow is only from one side and the wick on the opposite side of the CPHP is used to store excess liquid. Vapor flows from the interior to external piping through a manifold. The manifold is shown with a comb type screen to intercept large liquid droplets and return them to the wick.

As discussed above, control of the CPHP is necessary. Two types of control strategies are under investigation. One concept is for the cold plate to be fed liquid as needed with the wick structure serving as a liquid reservoir. A graded porosity wick structure will assure that liquid is always maintained in contact with the heated surface. Depletion of the liquid can be sensed in several ways. One method is simply by an increase in the temperature of the hot plate. Another is through the use of fluid sensing devices such as miniature heated themistors or capacitance sensors.

The second control strategy being studied is real time control of the fluid flow rate by use of a quality control sensor. One approach to quality measurement is to measure the pressure drop of the two-phase flow through a calibrated orifice and compare this with the pressure drop expected for a given quality and total mass flow rate. The total mass flow rate could be

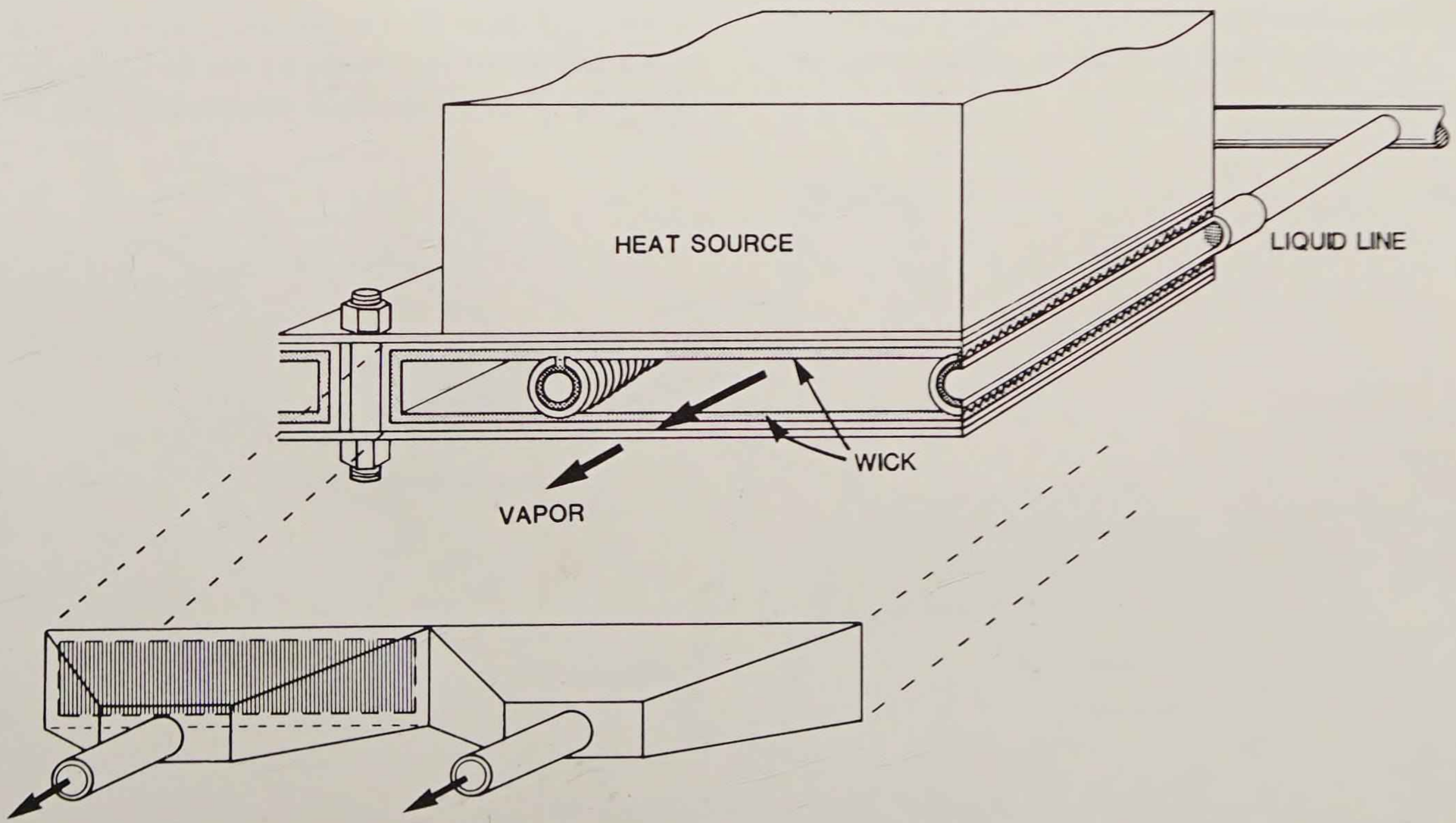


Figure 6 *Combined Evaporator (Cold Plate) and Condenser (Hot Plate) Concept.*

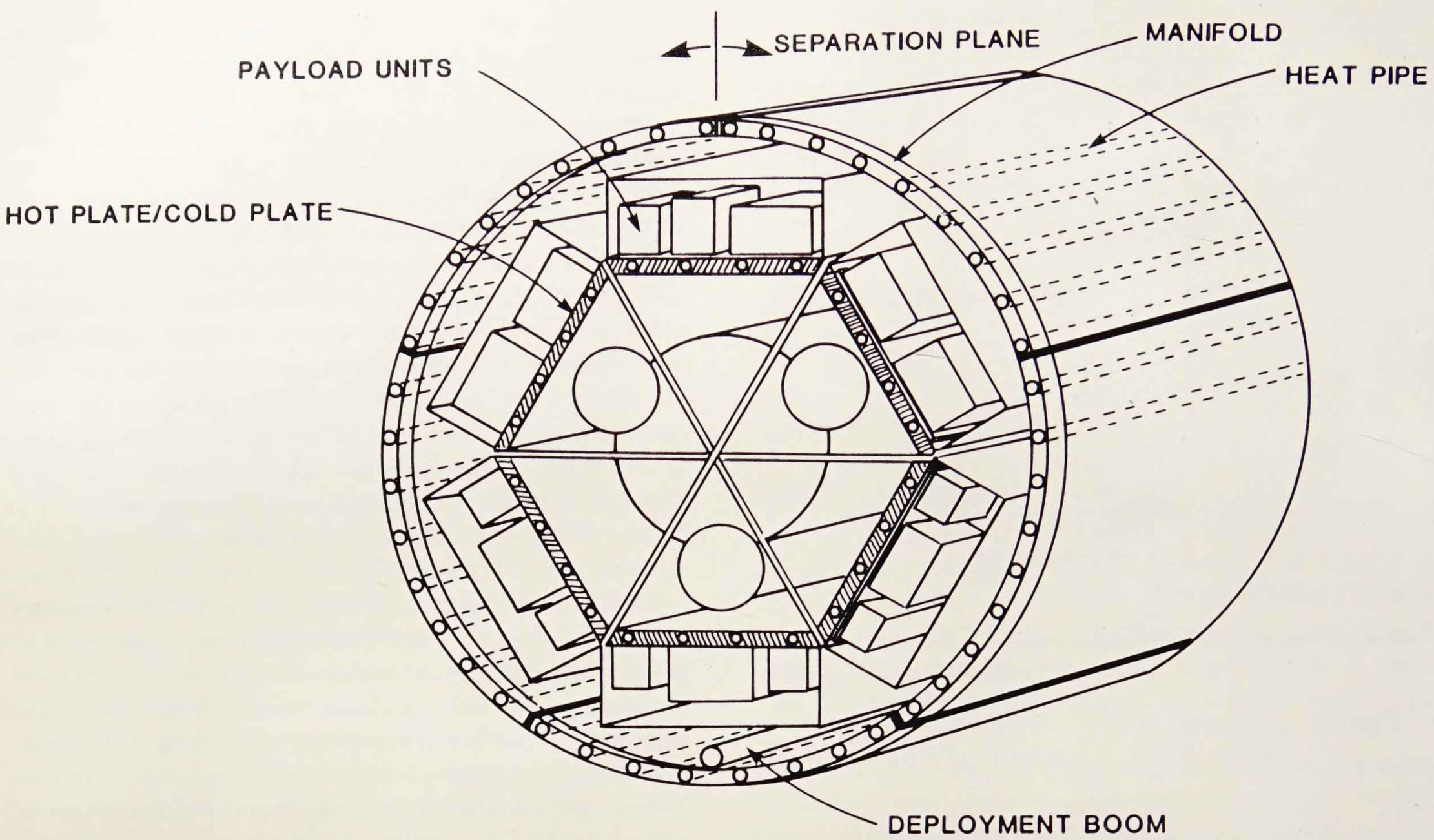


Figure 7 *Spacecraft Cross-Section Showing Deployable Heat Pipe Radiator in Stowed Position.*

obtained from a pressure drop measurement in the liquid line.

Radiator Concepts

Because of their very large size, space radiators must be either erected or deployed. A space constructable radiator as described by Ellis and Rankin (1983) will use long (15 m) heat pipe radiators dry mounted to an interface heat exchanger. The high pressures necessary for good contact conductance are provided by thermal expansion bolts which will also allow replacement of defective heat pipes.

Large radiators can be deployed much like solar arrays. The Shuttle radiator is one example. As with solar arrays, the un-deployed radiator will be in segments surrounding the spacecraft. In the concept shown in Figure 7, payload heat sources such as electronics modules are mounted to a cold plate forming the exterior of the spacecraft and covered with multi-layer insulation. This provides easier maintenance and adjustments during the pre-launch testing and qualification phases as well as in orbit. A deployed radiator system is shown in Figure 8. Liquid and vapor transport lines would run down the center of the booms to a condensing radiator interface heat exchanger. The radiator is

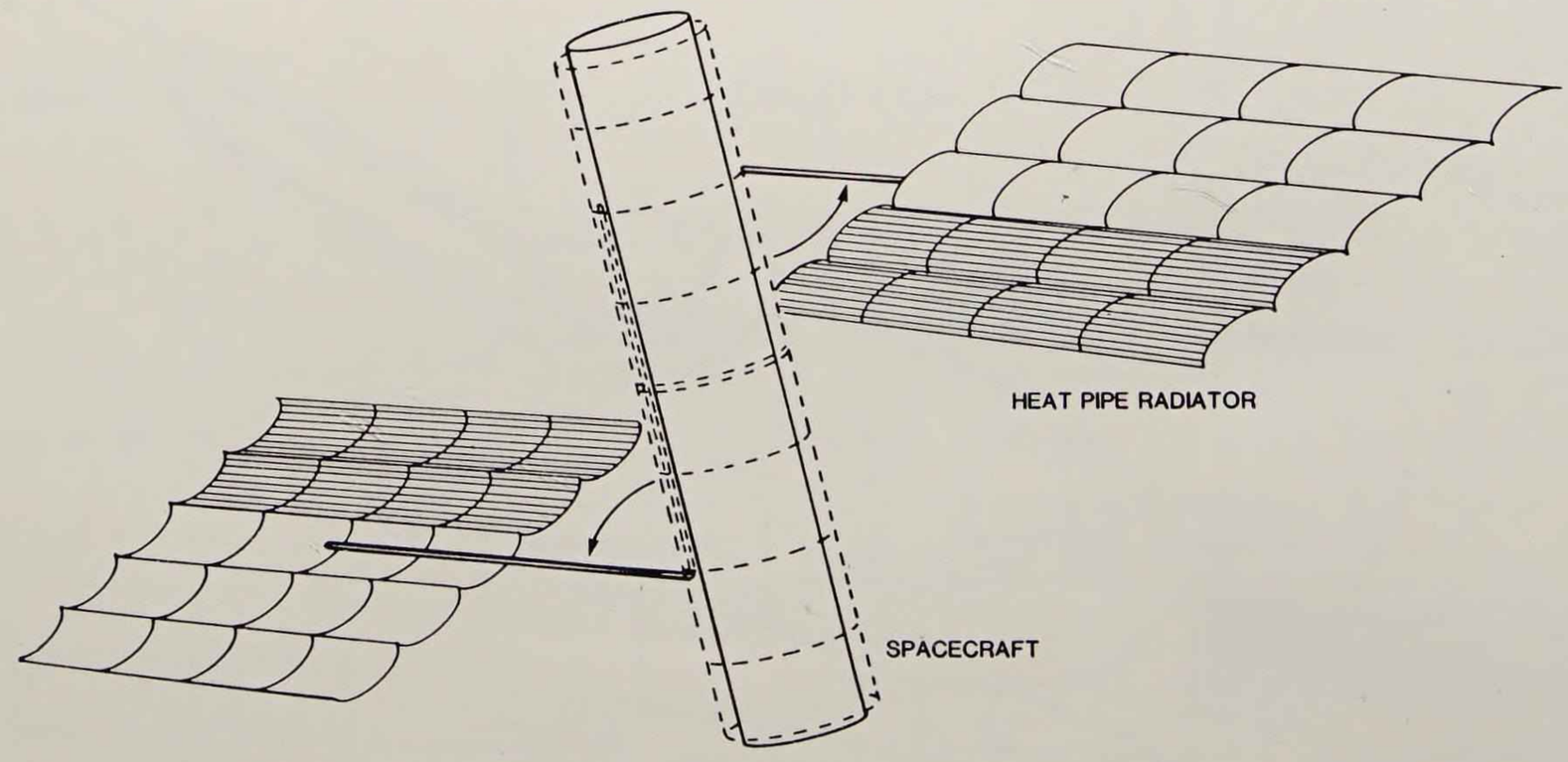


Figure 8 *Radiator in Deployed Position.*

composed of multiple heat pipe/fins bonded to the condenser. Note that deployment of the radiator gets it out of the way of the spacecraft and allows both sides of the radiator to be used.

Conclusions

The use of spacecraft skin for heat rejection radiator surfaces is not feasible for very high powered payloads because of area requirements. Thermal design simplicity as well as system efficiency favors a centralized thermal utility with a fluid transport loop carrying heat from dispersed heat sources to a common radiator. A two-phase pumped loop has a number of advantages over a single phase system such as is used on the Space Shuttle. Among these are

- lower pump power,
- small pipe sizes,
- higher heat transfer coefficients, and
- isothermal operation.

Two-phase systems are gravity sensitive, requiring special designs for the evaporator (cold plate) and condenser sections to assure stable and efficient operation. A condenser design under development is expected to be useful as the interface heat exchanger between the two-phase loop and a heat pipe radiator. The condenser utilizes surface tension forces and a separate pumped condensate line to provide high heat transfer coefficients and stable operation due to separation of the vapor and liquid flows.

A cold plate evaporator which also uses the surface tension forces for liquid control has been proposed. The cold plate can be reversed to serve as a condenser to supply heat to a cold component. A high quality flow (high percentage of vapor flow) is preferable to minimize total system flow rate and eliminate flow and pressure drop instabilities associated with two-phase flow.

Acknowledgments

The work reported in this paper was partially supported by the National Science Foundation and the National Aeronautics and Space Administration.

References

Alario, J., R. Brown, and R. Kosson (1983) "Monogroove Heat Pipe Development for the Space Constructible Radiator System," AIAA Paper 83-1431.

Ellis, W. E. and J. G. Rankin (1983) "Heat Buses will Operate Like a Public Utility," *Astronautics and Aeronautics 21*:56–61.

Hwangbo, H. (1983) "Motorized Thermal Control Shade," in *Proceedings of the International Symposium on Environmental and Thermal Control Systems for Space Vehicles*, held in Toulouse, France, October 4–7, 1983, pp. 345–349.

Hwangbo, H. and W. S. McEver (1983) "Surface Tension Effects in a Space Radiator Condenser with Capillary Liquid Drainage," AIAA Paper 83-1525.

Ollendorf, S., A. Fowle, and D. Almgren (1981) "Thermal Management of Instruments on Space Platforms Using a High Capacity Two-Phase Heat Transport System," in *Advances in Heat Pipe Technology*, ed. by D. A. Reay, Pergammon Press, Oxford, pp. 525–530.

Ranken, W. A. (1981) "Heat Pipe Development in the SPAR Space Power System," in *Advances in Heat Pipe Technology*, ed. by D. A. Reay, Pergammon Press, Oxford, pp. 561–574.

Space Nuclear Power Systems 1984
Edited by M. S. El-Genk and M. D. Hoover
© Orbit Book Company, Malabar, FL, 1985

Chapter 54

Multi-Megawatt Space Power Thermal Management System Requirements

Robert T. Taussig

Mathematical Sciences Northwest, Inc.
2755 Northup Way
Bellevue, Washington 98004

Multi-megawatt space power systems will require a novel approach to manage the enormous amounts of waste heat generated. Mission constraints such as average and peak power requirements, power sytem duty cycle, on-board end use power requirements, and mission lifetime, orbit parameters, maneuver and attitude control accelerations, speed of deployment, and other related requirements are used to define the amounts, the temperatures, and the temporal duration of waste heat production. These quantities are then applied to the design and optimization of the thermal management system based on a thermal bus. Applications include 100 kW to 1 MW space platforms and burst mode missions requiring up to several hundred MW of electric power.

Introduction

The key features distinguishing multi-megawatt space power thermal management systems from existing technology are the sheer size of such systems, the need to deal with waste heat from a multitude of different on-board power sources, the requirement of maintaining maneuverability in such systems, and the desire to make the thermal management equipment invulnerable to external attack. Existing systems scarcely generate more than 25 kW of on-board power, and these systems expend most of that power for thermal control of living quarters and communication equipment (Barthelemy et al. 1979). The planetary explorers have utilized radioisotope generators which produce most of their waste heat in the thermoelectric cells since they are only 7 to 10 percent efficient (Stapfer et al. 1980).

Similarly, satellites employing photovoltaic cells also generate most of their waste heat in the solar cell arrays, whose surfaces double as radiators for the waste heat. Consequently, efficient high power sources present a new challenge in which the power conditioning equipment and multitude of on-board end uses of power also will generate sizeable fractions of the total waste heat. Some of the newer high power missions may also "export" a large fraction of the power as electromagnetic energy or energetic particles, so that the waste heat rejection may no longer be nearly equal to the amount of power produced on the spacecraft.

Multiple waste heat sources, each with its own duty cycle and control temperature, present a particularly interesting class of thermal design problems. These can be optimized to yield a minimum thermal control system weight which is subject to system redundancy and lifetime requirements. With an increase in power output, the thermal management equipment mass becomes more prominent and, as a result, the potential benefits of optimization are correspondingly larger.

Approach

The concept of a thermal bus offers one of the most attractive ways to unite several waste heat sources and to raise their average radiator temperature (Ellis and Rankin 1983 and Rankin and Marshall 1983). Techniques for optimizing the basic design of a thermal bus system are developed below for those cases where each waste heat source is approximated by different temperatures but the same duty cycle. When infrequent bursts of power are required, the thermal bus concept is modified to include intermediate thermal storage to spread the burst power waste heat rejection over a longer period of time.

The principal components of thermal management systems are identified first. Then the key variables affecting component masses are described so that an appropriate optimization procedure can be developed. This procedure is applied to several model problems and then extended to more realistic thermal management systems.

High power missions currently in the conceptual and planning stages have been examined in order to extract realistic constraints applicable to our analysis. These missions include a multi-source space platform as well as a burst power, directed energy device. The results of applying the thermal bus concept to these two cases

suggest key technological problems which must be overcome in order to make this approach practical.

High Power Systems Requirements

The need for high power missions is driven by the knowledge that future mission capabilities will be enhanced enormously by increased power. Communications to wide ground areas are limited by the power per unit area which a space transmitter can deliver for situations where the ground receiver has a very limited amplification capacity (Kinnucan 1980 and Bekey and Naugle 1980). Similarly, industrial thermal processing in space will require continuous high power for melting and refining materials (NASA 1977a). Propulsion and directed energy devices push these requirements still higher (Mahefkey 1980). At the upper limit, a lunar station would require very high power to support life and processes for an entire community. The power ranges, peak-to-average power requirements, mission lifetimes, and mission designations allow us to classify generic mission requirements into the following three categories:

1. 25 kW to 100 kW; peak-to-average power of 1; ten year lifetime (for example, space radar, space platforms)
2. 100 kW to 1 MW; peak-to-average power of 1; three year lifetime (for example, electric propulsion, space processing)
3. 1 to 100 MW peak power; peak-to-average power of 10 to 1000; five year lifetime (for example, directed energy devices, EM launchers)

These generic requirements do not represent any single mission, but they do help to focus our attention on particular problems facing the thermal system designer. For example, Class 1 missions stress the need for high reliability and long lifetimes; Class 2 missions require relatively high, sustained levels of power where propulsion for orbit raising is one of the key uses; and Class 3 introduces the need for very high burst powers with a lower, but continuous, need for station keeping power. Each of these classes leads to a different thermal management system design approach.

Thermal Management Systems for High Power

The concept of a thermal bus is illustrated schematically in Figure 1, which shows various types of waste heat sources linked by a circulatory system. The main elements of this system include the pipes and pumps of the circulation system, heat exchangers to the waste heat sources, thermal storage from pulsed waste heat sources, refrigerators for cryostorage and for the thermal control of living quarters, radiator(s), and the sensor/control system (indicated by the dashed lines in Figure 1). The particular form of the thermal bus shown in Figure 1 is a series configuration of the waste heat

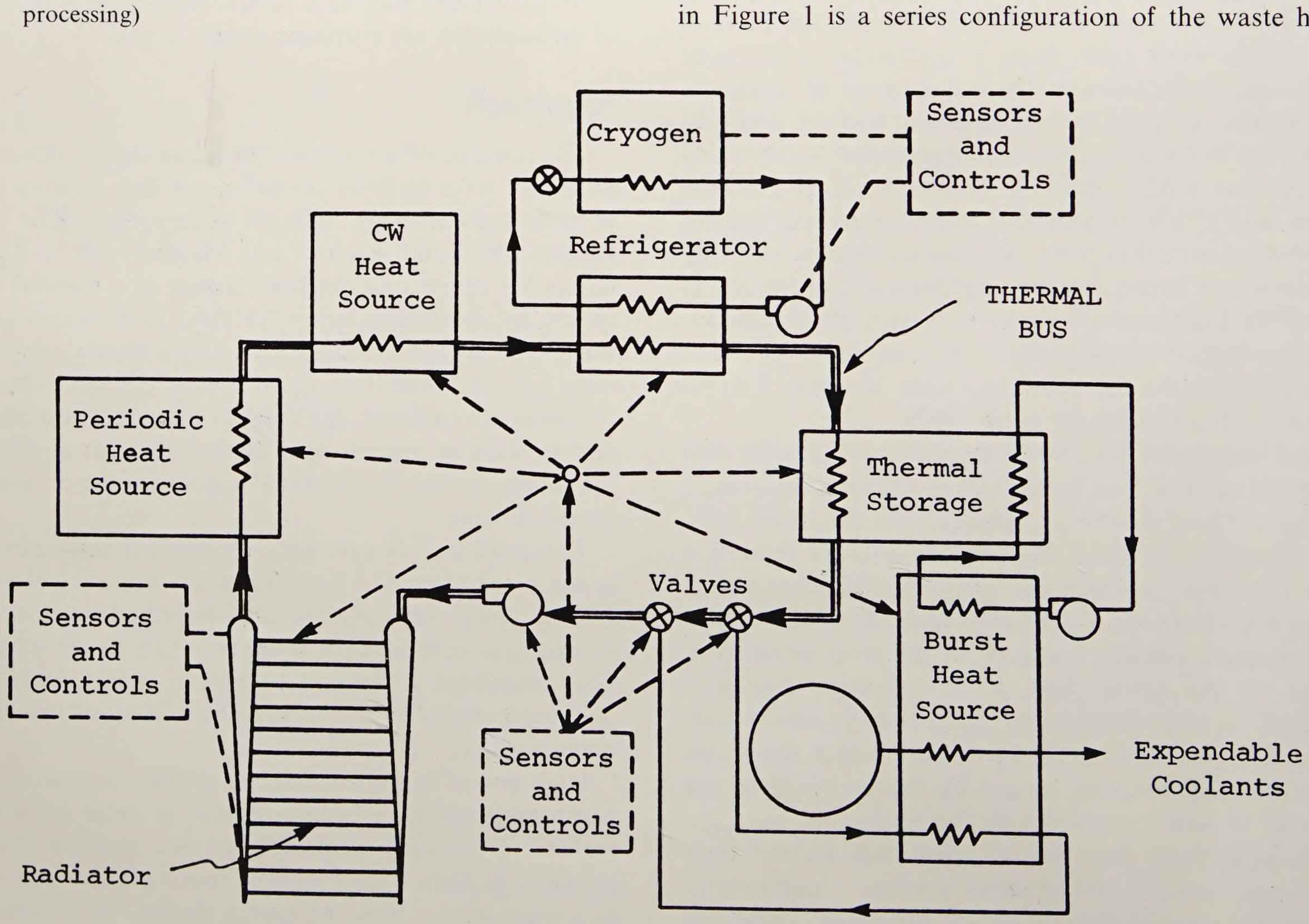
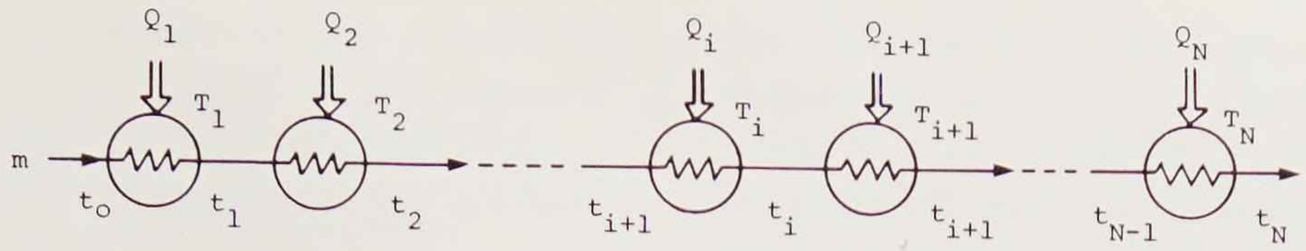
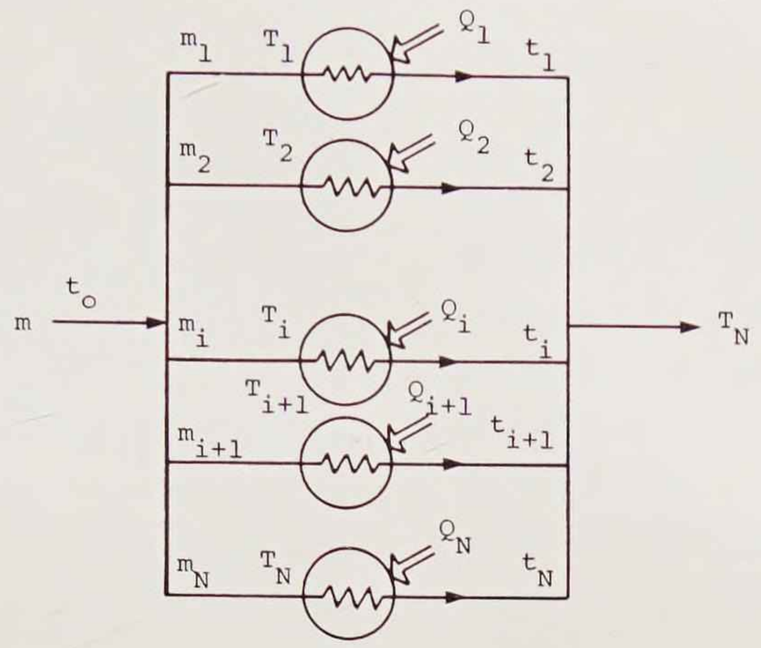


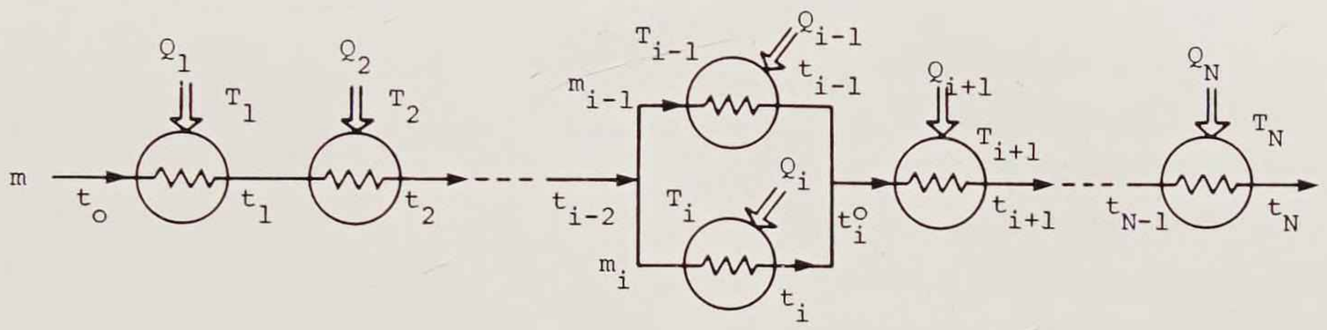
Figure 1 *Schematic of a Multi-Source Thermal Management System.*



a) Series Thermal Bus



b) Parallel Thermal Bus



c) Combined Parallel/Series Thermal Bus

Figure 2 *Model Thermal Bus Configurations (m = mass flow rate, t_i = flow temperature, T_i = waste heat source temperature, Q_i = waste heat transferred).*

sources. It also is possible to have a parallel bus, as shown in Figure 2, where different types of thermal buses are compared. Mixed networks with coupled parallel and series subsections are possible, too. Each of these configurations has its own merits, depending on the amount and temperature of the waste heat rejected by each source. Redundancy can be introduced into this approach by creating two or more thermal buses which coexist, each capable of removing the entire heat load but operating normally at a fraction of the full load.

System Optimization Procedure

The chief system masses are the pumps, pipes, heat exchangers, and the radiator, with the radiator mass predominating. Since the radiator mass varies as T_{rad}^{-4}, we would like to arrive at a system which provides as high a radiator temperature as possible. This strategy assumes that the waste heat source temperatures are already fixed and that the optimization consists of choosing the best order in which the waste heat sources reject their heat into the thermal bus. This must be done without requiring excessively large heat exchanger heat transfer areas, A_{HX}, long pipe runs, or large pumps. An initial optimization is described below which minimizes the allowable mass flow rate in order to maximize the radiator temperature.

Allowable mass flow rates for each heat exchanger are determined by the amount of heat, Q_i, rejected at the waste heat source temperature, T_i, to the thermal bus. In order to transfer heat into the thermal bus, the outlet flow temperature (as well as the inlet flow temperature) must be less than the waste heat source temperature. That is,

$$t_i = t_{i-1} + \frac{Q_i}{m_s c_p} < T_i \qquad [1]$$

using the notation illustrated in Figure 2. This condition can be rewritten as a constraint on the thermal bus mass flow m_s:

$$m_s \equiv \frac{Q_i}{c_p(t_i - t_{i-1})} \geqslant m_i \qquad [2]$$

The lower bound m_i is defined as

$$m_i = \frac{Q_i}{c_p(T_i - T_{i-1})} \qquad [2a]$$

which is expressed entirely in terms of known quanti-

ties; namely, the waste heat source properties. The actual temperatures, t_i, do not have to be determined in order for this optimization to proceed.

Therefore, in a series network like that of Figure 2a, the minimum mass flow required must satisfy the general constraint,

$$m_s \geqslant \max(m_i), \qquad \text{for} \quad i = 1 \text{ to } N \qquad [3]$$

in order to guarantee heat transfer into the bus from each waste heat source. This expression assumes that the heat sources are ordered by increasing temperatures so that $\Delta T_i = T_i - T_{i-1}$ is always positive. This expression may overestimate the minimum mass flow needed since actual inlet temperatures t_{i-1} can be much less than T_{i-1} for that heat exchanger which determines the maximum value in Equation [3]. It is necessary to refine these estimates in an actual design. However, the result shown in Equation [3] has the advantage of allowing an immediate estimate of the minimum mass flow needed to minimize radiator mass without having to solve the details of the thermal transfer problem first.

Suppose now that we change the order in which the thermal bus accesses the heat sources by removing heat source j and inserting it between sources $i-1$ and i. This will allow us to determine the circumstances under which reordering the waste heat temperatures (and sources) will lead to a lower mass flow than that given by Equation [3]. In this example, heat source j is now surrounded on each side by lower temperature sources $i-1$ and i. The mass flow constraints must be altered so that

$$m_s' > \frac{Q_i}{c_p(T_j - T_{i-1})} \qquad \text{so that} \quad t_j < T_j \qquad [4]$$

$$m_s' > \frac{Q_j}{c_p(T_i - T_{i-1})} \qquad \text{so that} \quad t_j < T_i \qquad [5]$$

$$m_s' > \frac{Q_i}{c_p(T_i - T_{i-1})} \qquad \text{so that} \quad t_i < T_i \qquad [6]$$

The minimum mass flow corresponding to Equation [3] above may be decreased if

$$\frac{Q_j}{c_p(T_j - T_{j-1})} > \frac{Q_j}{c_p(T_i - T_{i-1})} \qquad [7]$$

where the left hand side represents the corresponding mass flow constraint defined for the original, monotonically increasing temperature series. Combining Equations [3] and [7], we see that the global mass flow constraint may be less restrictive (that is, $m_s' \leqslant m_s$) if

$$T_j - T_{j-1} < T_i - T_{i-1} \qquad [8]$$

Consequently, the temperature series may be optimized further for a minimum mass flow by reordering the heat sources so that the temperatures satisfy conditions of Equation [8].

The temperature of the liquid delivered by the thermal bus to the radiator is

$$t_N = t_{N-1} + \frac{Q_N}{c_p m_s} = \sum_{i=1}^{N} \left(\frac{Q_i}{c_p m_s} \right) + t_0 \qquad [9]$$

once the global mass flow constraint has been met. The form of this expression is independent of the series order, since the mass flow constraint guarantees sufficient heat extraction from each source. Equation [9] shows that t_N will be maximized by making m_s as small as possible. The series reordering relations derived above provide a procedure for minimizing m_s.

Parallel configurations (Figure 2b) can be treated in the same way. In this case, the mass flow through each individual path of the thermal bus circuit must satisfy

$$m_i \geqslant \frac{Q_i}{c_p(T_i - t_0)} \qquad [10]$$

and, consequently, the total mass flow m_p must be

$$m_p \geqslant \sum_{i=1}^{N} \frac{Q_i}{c_p(T_i - t_0)} \qquad [11]$$

Similarly, the temperature of the fluid delivered by the bus to the radiator is given by

$$t_N = \sum_{i=1}^{N} \left(\frac{Q_i}{c_p m_p} \right) + t_0 \qquad [12]$$

which has exactly the same form as the temperature expression for the series circuit, except for the fact that the mass flow must satisfy a different constraint.

To find out whether the parallel or series circuit offers the lowest mass radiator, we can compare their respective radiator temperatures as follows:

$$\frac{(t_N - t_0)_s}{(t_N - t_0)_p} = \frac{m_p}{m_s} \qquad [13]$$

The ratio on the right hand side will depend on the detailed values of Q_i and T_i. However, it is possible to use a model problem to illustrate some simple circumstances when one choice or the other is preferred. To do this, assume that the heat sources and their temperatures can be written as

$$Q_i = (i)^{\alpha} \cdot Q \qquad \text{where} \quad Q = \text{constant and } \alpha \text{ may be positive or negative,} \qquad [14]$$

$$T_i = T_{i-1} + \Delta T \quad \text{and} \quad \Delta T = \text{constant.}$$

Then the mass flows for the parallel and series circuits

can be rewritten as

$$m_p = \sum_{i=1}^{N} \frac{(i)^{\alpha} Q}{c_p i \Delta T} = \frac{Q}{c_p \Delta T} \sum_{i=1}^{N} (i)^{\alpha - 1} \qquad [15]$$

$$m_s = \max\left(\frac{(i)^{\alpha} Q}{c_p \Delta T} \right) \qquad \text{for} \quad i = 1 \text{ to } N \qquad [16]$$

From these two expressions, one can see that $m_p \gtrless m_s$ as $\alpha \lessgtr 1$. For this model problem, we conclude that the parallel circuit leads to a higher radiator temperature when $\alpha > 1$. The inequality $\alpha > 1$ is true when the amount of waste heat to be rejected from successive sources in the circuit increases faster than their temperatures in this circuit.

Parallel flow sections in a series network also may reduce the radiator mass (Figure 2c). Local constraints on the mass flow through the parallel sections can be expressed as

$$m_{i-1} \geqslant \frac{Q_{i-1}}{c_p(T_{i-1} - T_{i-2})} \qquad [17]$$

$$m_i \geqslant \frac{Q_i}{c_p(T_i - T_{i-2})} \quad \text{and}$$

$$m \equiv m_{i-1} + m_i \geqslant \frac{Q_{i-1}}{c_p(T_{i-1} - T_{i-2})} + \frac{Q_i}{c_p(T_i - T_{i-2})}$$

which automatically satisfies the series mass flow constraint for Q_{i-1}. If $T_{i-1}, T_i < T_{i+1}$ then the mixed flow leaving the parallel section will satisfy the constraint

$$t_i^0 = \beta t_{i-1} + (1 - \beta) t_i < T_{i+1} \qquad [18]$$

$$\text{where} \quad \beta = \frac{m_{i-1}}{m}$$

without any further constraints on mass flow. Assuming that $T_{i-1} < T_i$ without any loss in generality, then the minimum flow requirement for a series network may be reduced further when

$$\frac{Q_{i-1}}{c_p(T_{i-1} - T_{i-2})} + \frac{Q_i}{c_p(T_i - T_{i-2})} < \frac{Q_i}{c_p(T_i - T_{i-1})} \qquad [19]$$

or

$$\frac{Q_{i-1}}{c_p(T_{i-1} - T_{i-2})} \left[\frac{T_i - T_{i-2}}{T_{i-1} - T_{i-2}} \right] < \frac{Q_i}{c_p(T_i - T_{i-1})} \qquad [20]$$

where the factor in square brackets on the left is greater than 1. This is the local analog to the inquality $\alpha > 1$ described above, which determines when a parallel circuit is more desirable than a series circuit.

The procedures described above allow the designer to choose between parallel and series circuit configurations for the thermal bus as a way to minimize the total mass flow through the circuit and to deliver the highest waste heat temperature to the radiator. A more comprehensive optimization must combine this design process with estimates of the heat exchanger, pump, and piping masses (including the fluid inventory).

Burst Power Thermal Management Systems

Burst power imposes very special requirements on the thermal management of waste heat, since a radiator sized to reject the full rate of waste heat production would be large and heavy. It is much more attractive to store some fraction of the burst waste heat as it is produced and to reject it continuously, over a longer period of time at a lower rate. Similarly, if the power system were sized to produce all of the burst power just when it was needed, it also would have to be very large and its instantaneous waste heat production rate would impose the same problems for the radiator. Consequently, electric energy also can be stored on a cw basis so that it can be released over a much shorter period when the burst power is required. The combination of electric and thermal energy storage provides a total reduction in thermal management system mass for certain ranges of burst power duty cycle (fraction of time the burst power is on), certain pulse power time durations, and magnitudes of pulse power. To determine when such advantages exist, one must include the mass scaling for individual components in such calculations.

Figure 3 shows a schematic diagram for a burst power system. Power and heat transfer are indicated by arrows. Double lines indicate transfer at all times, single solid lines indicate transfer between burst power pulses (for $\tau - \tau_L$), and dashed lines indicate transfers occurring only during the pulse (for τ_L).

During burst power operation, power is supplied both from the power conversion system, which always operates at a steady level, and from the electrical energy storage unit (for example, batteries or homopolar generators). This relationship is expressed by

$$P_B = P_e + \eta_r P_S \qquad [21]$$

where η_r is the energy recovery efficiency from storage. Waste heat is generated by energy recovery and by the end use (for example, laser) of the burst power:

$$Q_L = P_B - P_L = \left(\frac{1}{\eta_L} - 1 \right) P_L \qquad [22]$$

$$Q_r = P_S - \eta_r P_S = (1 - \eta_r) P_S \qquad [23]$$

Part of that waste heat, Q', is stored as thermal energy (assumed to be 100 percent efficient input and output), and the remainder, Q_1, is transferred to the radiator as

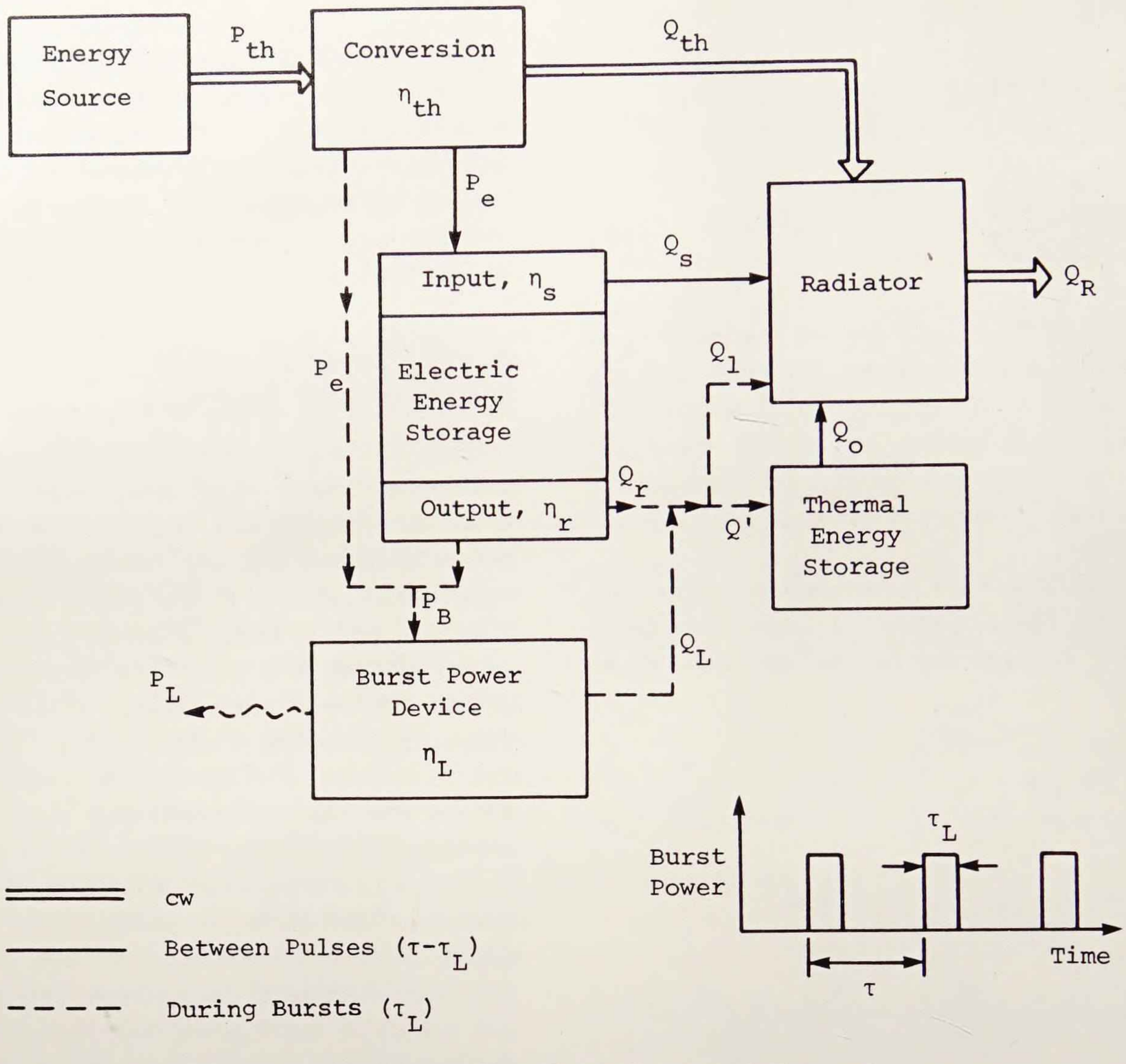


Figure 3 *Schematic of a Burst Power System with Energy Storage.*

it is being generated: $Q' + Q_1 = Q_r + Q_L$. The thermal energy storage unit is sized so that the radiator rejects waste heat at a constant rate, $Q_R = Q_{th} + Q_S + Q_0 = Q_{th} + Q_1$.

Between laser pulses (that is, for times $\tau - \tau_L$), all of the power conversion output is transferred to electrical storage with a storage efficiency η_S and at a rate of $\eta_S P_e$. The electric energy storage unit is sized to deliver all of its stored energy at the rate P_S during time τ_L:

$$P_S \tau_L = \eta_S P_e (\tau - \tau_L) \qquad [24]$$

The storage process creates waste heat at a rate

$$Q_S = P_e - \eta_S P_e = (1 - \eta_S) P_e \qquad [25]$$

Equations [21] through [25] allow us to express the power and heat transfers in this system as dimensionless ratios to the burst output power, P_L. It is useful to describe the system's behavior in terms of $\beta = P_B / P_e$, which is the peak-to-average power ratio (Figure 3); β is one of the key mission parameters described in Section 3. The duty cycle, $\delta = \tau_L / \tau$, is another key mission parameter which is related to β through the equation

$$\beta = 1 + \eta_0 \frac{(1 - \delta)}{\delta} \qquad [26]$$

This equation simply states that the cw power supply in this system must be sufficient to overcome the "round-trip" losses represented by the combined storage efficiency, $\eta_0 = \eta_r \eta_s$, in order to supply the burst power.

We have applied this thermal management system to a burst power application with the following component mass models:

Nuclear reactor/shield

(Buden 1982) $W_N = 12.65(P_{th})^{-1/2}$ kg/kW(th)

Power conversion

(Young and Ketch 1977) $W_c = 0.22$ kg/kW(e)

Electric energy storage

(NASA 1981) $W_e = 30.33$ kg/(kW · hr)

Burst power end user

$$W_L = 5.45 + 1.15 \times 10^4 (P_L^{-1}) \text{ kg/kW}(L)$$

(Taussig, Klosterman and Willenberg 1981)

Thermal energy storage

(NASA 1981) $W_t = 7.87$ kg/(kW · hr)

Radiator

$$W_R = 5.19 \times 10^{10} [T_R^{-4}(\text{K})] \text{ kg/kW(th)}$$

(Meier, Ginens and Dickenson 1980) [27]

The expression for the total mass of the system is

$$M_{tot} = W_N P_{th} + W_C P_e + W_e P_S \tau_L + W_L P_L + W_t Q' \tau_L + W_R Q_R \qquad [28]$$

Dividing this expression by P_L and substituting from Equations [21]–[27] gives an expression for the total mass which is entirely in terms of the component efficiencies, the peak-to-average power ratio, the radiator temperature, the burst power, and the burst period. Figure 4 summarizes calculations for a particular choice of component efficiencies. The results in Figure 4 indicate the energy storage begins to pay off in substantial weight reductions when the burst period is shorter than 100 seconds. These benefits reach diminishing returns when the burst time is much shorter than 10 seconds.

These effects also depend on the absolute burst power level. For example, for values of 10 MW or less, the total mass per unit burst output power increases, indicating that the total mass is nearly constant; but, for powers greater than 10 MW, the power per unit mass ratio is nearly constant, indicating a total mission mass which increases linearly with power output. At small power output ($\leqslant$ 10 MW), this effect is primarily due to the burst power end use mass model, which has an irreducible mass component associated with aiming and transmitting devices. For burst powers greater than 10 MW, the advantages of energy storage can reduce the total system mass by nearly a factor of two, if the peak-to-average power is 5 or larger.

Clearly, a more detailed model should be used to fully optimize a burst power system. Even the simple case studied here needs to be investigated further to determine the impact of different radiator temperatures and component efficiencies on the results shown in Figure 4. This mass-mission model also provides a very direct way to investigate the impact of alternative and advanced technologies. For example, each of the weight coefficients can be varied according to the power conversion system, energy storage units, radiator concepts, and burst power devices being considered. Similarly, the efficiencies can each be varied depending on the technologies and their operating conditions.

The thermal bus approach also will work with the burst power missions if one uses it to collect and reject those portions of the waste heat which are being generated within the system on a cw or frequent periodic basis. Hence, the optimization procedure discussed in the preceding section can be applied here once the power level, burst time, and peak-to-average power ratio have been selected. An iteration is required to obtain the most desirable radiator temperature since the

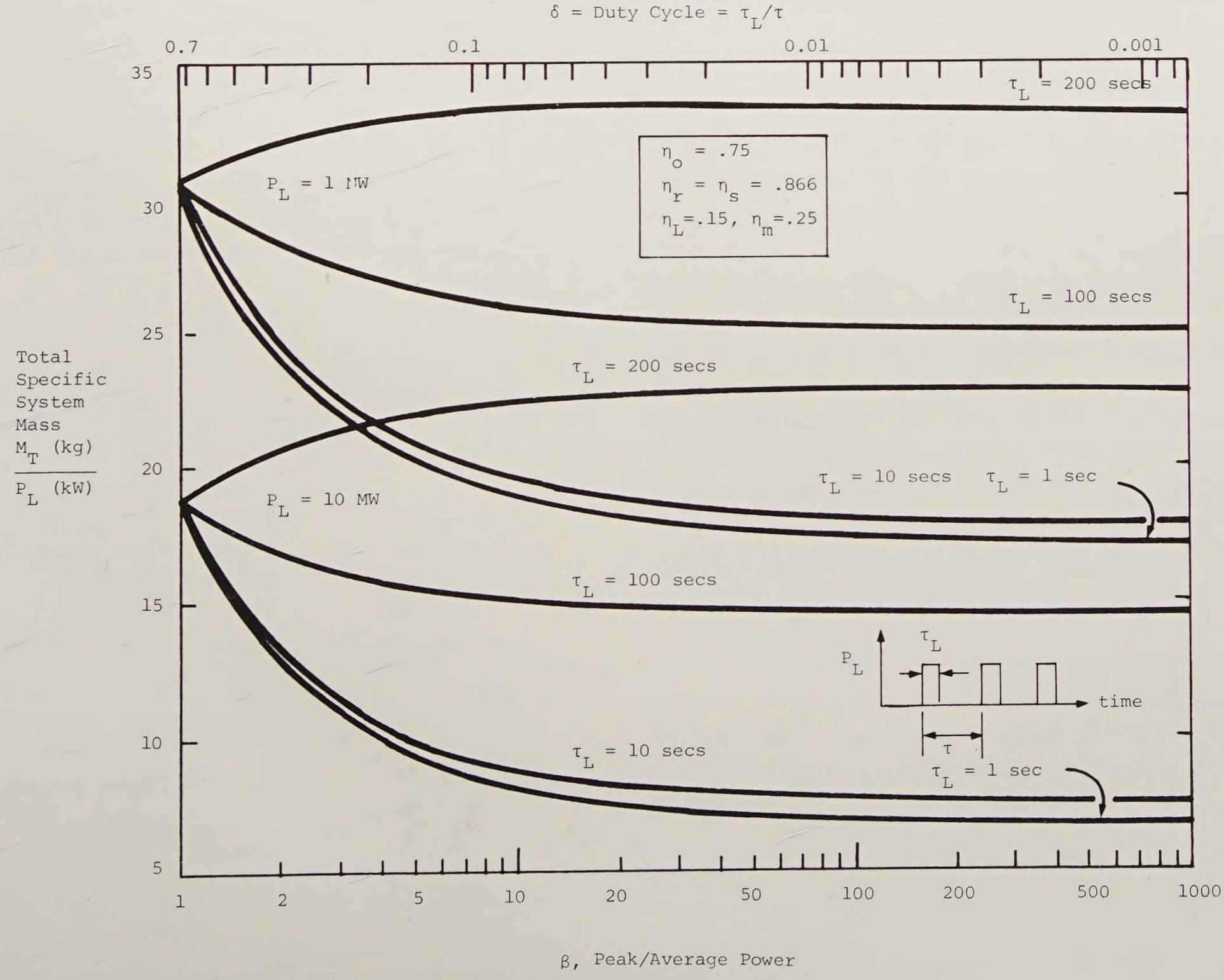


Figure 4 *System Mass Benefits of Electrical and Thermal Energy Storage for Burst Power Devices (P_L = Output Power).*

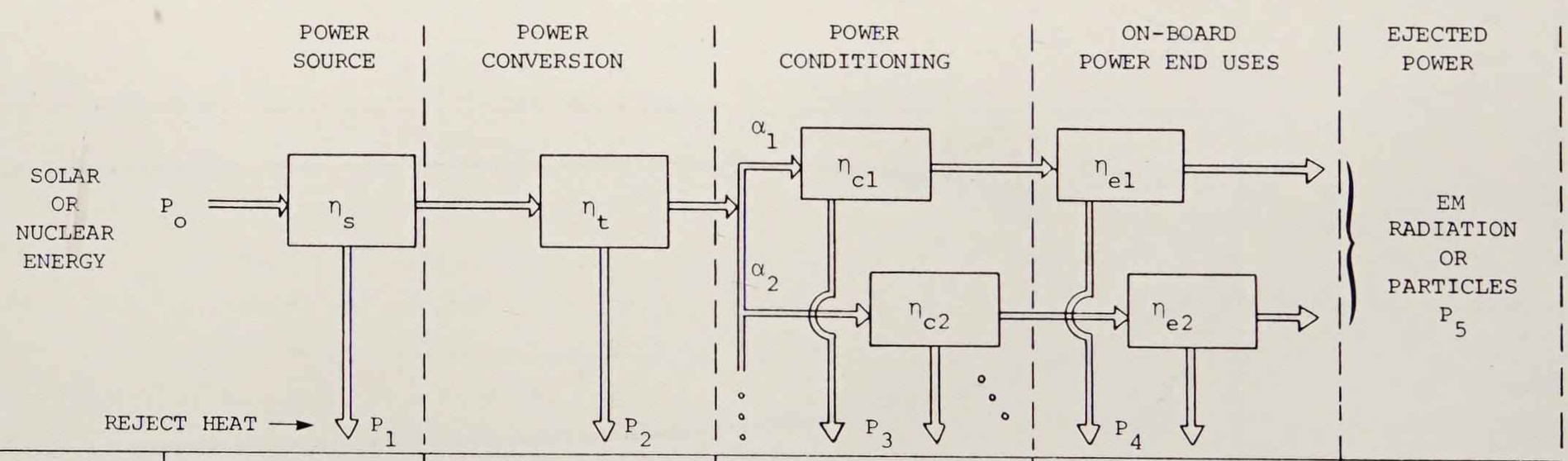
thermal bus subsystem and the total mission mass both involve this parameter.

Thermal Management Technology for High Power Systems

As the preceding discussion pointed out, the management of waste heat from high power multi-source systems depends greatly on the temperatures, duty cycles, and amounts of waste heat generated by each source. The waste heat characteristics depend on the efficiency and on the power input and output of each source.

Figure 5 illustrates two examples of high power systems designs with many sources of waste heat. The first example assumes that an advanced gallium arsenide photovoltaic array powers the mission, in this case a space-based radar. The power source losses are associated with residual reflection and absorption in coatings applied to the solar cell surfaces to increase their emissivity and reduce reflection of sunlight. These losses are estimated to be about 3 percent (or less) for an array perpendicular to the sun's rays (NASA 1976). The solar cells convert incident radiation with an efficiency of approximately 18 percent when operated at temperatures less than approximately 300 to 320 K, the temperature range at which the array must operate if it acts as its own waste heat radiator (NASA 1976). The power must be converted up to a higher voltage to drive the klystrons which supply power to the radar antenna. The klystrons themselves have a combined efficiency of approximately 75 percent under the best of circumstances, ignoring other losses in power conditioning (NASA 1977b). We assume that the antenna efficiency is about 85 percent for this particular case (NASA 1977b). The waste heat as a fraction of the total input power P_0 is indicated algebraically in the top row of Figure 5, and actual numbers corresponding to this particular example are shown in the third row. Since a planar solar array was used, which acted as its own radiator in this case, only the klystron and antenna losses need to be considered. The antenna also is a distributed surface which may be capable of radiating its own waste heat; a detailed calculation of its effective surface area is needed in order to make this determination for a given antenna temperature. Thus, only the power conditioning and klystron components need a thermal collection loop and radiator.

Example 2 in Figure 5 exhibits a contrasting situation where there are no large natural surface areas over which the waste heat is created. Thus, this case requires a more complete thermal management system to collect and reject the waste heat. The interesting aspect of



Power Fraction $\frac{P_i}{P_o}$, i = 1 to 5	$(1 - \eta_s)$	$\eta_s(1 - \eta_t)$	$\alpha_1\eta_s\eta_t(1 - \eta_{c1})$	$\alpha_1\eta_s\eta_t\eta_{c1}(1 - \eta_{e1})$	$\alpha_1\eta_s\eta_t\eta_{c1}\eta_{e1}$
Space Radar (Photovoltaics)					
η	97% (Anti-reflection Coating)	18% (GaAs, Flat Array)	75% (Klystrons)	85% (Antenna)	-
$\frac{P_i}{P_o}$	3%	79.5%	4.4% ($\alpha_1 = 1$)	2.0%	11.1%
Space Platform (Nuclear Reactor)					
η	95% (Insulated Reactor Shell)	25% (Brayton)	75% (Klystrons)	99% (Magnet Refrigeration)	-
$\frac{P_i}{P_o}$	5%	71.3%	5.9% ($\alpha_1 = 1$)	0.2%	17.6%

Figure 5 *Two Examples of Waste Heat Distribution from Multi-Source, High Power Space Systems.*

Example 2, which corresponds to a nuclear powered space station (for instance, a manned laser power station for supplying remote propulsion power to space tugs) is that the power produced on-board is largely exported. In addition, the proportion of waste heat generated at the klystron stage has increased compared to the previous example. This means that the thermal bus system can capitalize on the higher fraction of high temperature waste heat from the klystrons to help boost the radiator temperature. In the next section, we shall apply the thermal bus optimization procedure to this case.

Space Platform Application

The example of the space platform power system described in Figure 5 has been analyzed according to the thermal management procedures in Section 6. The thermal bus concept has been applied in a series, parallel, and a mixed parallel/series combination. The temperatures and waste heat loads are summarized in Table 1. Lower limits to the bus mass flow, using the (m)max formulae from Equations [3] and [11], respetively, for the series and parallel cases, are also shown in Table 1. Rearranging the series configuration by inserting the highest temperature heat source between the lower two temperature sources has also been examined. The temperatures do satisfy the condition $T_4 - T_3 = 50$ K $\leqslant T_2 - T_1 = 200$ K, a necessary condition for this approach in order for it to reduce the system mass. However, we have not affected the maximum mass flow requirement in this way since the mass flow through the Brayton cycle waste heat exchanger is unchanged. Thus, rearranging the series configuration does not appear to be effective in this particular case.

A parallel/series combination has been tried where the lowest two heat sources are in parallel and the other two are in series. This rearrangement will be advantageous if the condition represented by Equation [20] is met for sources 1 and 2. Substituting the appropriate values from Table 1 shows that this inequality is correct; in this case, the maximum mass flow requirement is reduced to 49.5 kg/s.

The preceding analysis suggests design guidelines for optimum thermal bus design. After such estimates are made, it is still necessary to confirm them with actual calculations and to refine the optimum by including other considerations such as the other power system and spacecraft component masses. A more careful consideration of the series configuration shows that the actual mass flow through the thermal bus can be a little lower than the minimum calculated by these estimates. The reason for this is that the output temperature from the first heat source (that is, at 300 K) will be substantially lower than the heat source temperature if the mass flow prescribed by this bounding procedure is used. Thus, the entry temperature to the second heat source, which sets the mass flow requirements, will be lower than 300 K, implying that a revised bound using this lower temperature should be used. With a lower inlet temperature, a lower mass flow bound is allowed. In fact, the bound reduces to approximately 47.2 kg/s, even lower than the combined parallel/series configuration. This result emphasizes the need to refine the procedure after the initial estimates are made.

Table 1 *Thermal Bus Mass Flow and Fluid Outlet Temperature Estimates for a High Power Space Platform (see Example 2, Figure 5).*

(a) Waste Heat Source Characteristics

	T_i (K)	Q_i (MW)*	Source
$i = 1$	300	0.10	Refrigeration
2	500$^+$	13.46	Brayton Cycle
3	750	3.37	Klystrons
4	800	1.42	Reactor Shell

*For $P_5 = 10$ MW

$^+$ Minimum Cycle Temperature

(b) Thermal Bus Estimates*

	m (kg/s)	t_4 (K)	m Constraint Eqn. #
Series	53.8	543	3
Parallel	56.6	529	11
Series/Parallel	49.5	566	20

*Assume $C_p = 1.25$ kJ/(kg K)

Summary

The concept of a thermal bus was applied to high power systems as a thermal management technique to minimize spacecraft mass subject to various mission parameters such as peak/average power, duty cycle, waste heat source temperatures, and amounts of waste heat produced. This scheme was supplemented with electrical and thermal energy storage for burst power applications in order to minimize the total system mass. Temperature and mass flow constraints for parallel, series, and mixed flow thermal bus configurations were derived and applied to a 10 MW space platform to determine the conditions for maximum radiator temperature. The burst power application was examined for a range of powers from 1 to 100 MW, pulse times from 1 second to 100 seconds, and duty cycles ranging from 1 to 0.001. Significant mass benefits (for example, 50 percent decrease in mass) appear possible for this application. While this result depends on the choice of mission parameters, the examples illustrate the benefits of the thermal management approach developed in this paper.

Acknowledgments

This paper is based on material also presented at the AIAA 22nd Aerospace Sciences Meeting, Reno, NV, January 9–12, 1984.

References

Barthelemy, R. R., J. W. Stearns, R. J. Koester, and E. Stofer (1979) "Aerospace Power Systems—A Building Surge," *Aeronautics and Astronautics* 17:64–72.

Bekey, J. and J. E. Naugle (1980) "Just Over the Horizon," *Astronautics and Aeronautics*, 18:64–76.

Buden, D. (1982) "Overview of Space Reactors," in *Proceedings of the AFOSR Special Conference on Prime Power for High Energy Space Systems*, Volume 1, Norfolk, Virginia, February 1982, p. IV-1-10.

Ellis, W. E. and J. G. Rankin (1983) "Space Station Thermal Requirements," *Astronautics and Aeronautics* 21:56–61.

Kinnucan, P. (1983) "Pentagon Studies Space-Based Radar," *High Technology*, June 1983, pp. 33–35.

Mahefkey, T. (1980) "Future Space Power—The DOD Perspective," Volume 1, 15th IECEC Conference, Seattle, Washington, August 1980, pp. 89–94.

Meier, K. L., S. P. Ginens, and J. M. Dickenson (1980) "Titanium Heat Pipes for Space Power Systems," 15th IECEC, Seattle, Washington, August 1980, pp. 762–766.

NASA (1976) *System Definition Space-Based Power Conversion Systems*, Final Report, Study Contract NAS8-31628, The Boeing Aerospace Company, November 1976.

NASA (1977a) *Space Settlements: A Design Study*, eds. R. D. Johnson and C. Holbrow, NASA Report No. NASA-SP-413.

NASA (1977b) "Microwave Power Transmission Systems," *Solar Power Satellite System Definition Study*, Report No. D180-22876-4, Volume IV, Part II, prepared by the Boeing Aerospace Company for NASA-Johnson Space Center, December 1977, pp. 77–79.

NASA (1981) *Overview Study of Space Power Technologies for the Advanced Energetics Program*, ed. R. Taussig, NASA Report No. CR-16569, October 1981, prepared by MSNW, pp. 2–176 to 2-189.

Rankin, J. R. and P. F. Marshall (1983) "Thermal Management System Technology Development for Space Station Applications," 13th Intersociety Conference on Environmental Systems, SAE Paper No. 831097, July 1983.

Stapfer, G. et al. (1980) "Advanced Thermoelectric Material Development at JPL," Paper 809317, 15th IECEC, Seattle, Washington, August 1980.

Taussig, R. T., E. L. Klosterman, and H. J. Willenberg (1981) *Space Laser Power Transmission*, NASA Report No. 1183-1, July 1981, prepared by MSNW.

Young, W. E. and G. W. Kelch (1977) *Closed Cycle Gas Dynamic Laser Design Investigation*, NASA Report No. CR-13510, January 1977, prepared by Pratt & Whitney.

Space Nuclear Power Systems 1984
Edited by M. S. El-Genk and M. D. Hoover
© Orbit Book Company, Malabar, FL, 1985

Chapter 55

Radiator Concepts for High Power Systems in Space

Jason R. Feig

Air Force Rocket Propulsion Laboratory
DYSS, Stop 24
Edwards AFB CA 93523

The demand for new enabling concepts to carry out the task of heat rejection in space at high powers is growing. The history of some ideas dates back to the early 1960's, while others are recent additions. Several concepts are described in varying detail depending upon their level of technology development and the amount of available information. It is clear that a goal to significantly reduce the overall weight of space power systems can be achieved through the use of new radiators. Other advantages in these concepts include, survivability, compact storage (deployability) and lower temperatures that will result in better overall power system efficiencies.

Introduction

Many of the numerous space missions being considered by the U.S. Air Force and NASA have in common the need for electrical power. Furthermore, the magnitude of that power is far greater than for any previously considered array of mission scenarios. Producing this power, unfortunately, also generates large amounts of waste heat. Current conventional radiator technology provides the user with only these designs that require employing several Space Shuttle flights to simply put the structure into orbit. The magnitude of the problem can be seen in Figure 1. Efficiencies here were assumed to be 18 percent and rejection temperatures 1000 Kelvin. In addition to the requirements on technology and hardware development, the mission requirements and system integration issues play a leading role in not only radiator design, but concept feasibility. At present, the Air Force and NASA are considering a wide range of potential applications requiring high power including: Space Based Radar, Nuclear/Electric Orbit Transfer Vehicles, Space Base Weapon Systems and Space Station. Power requirements for these applications could range from one hundred kilowatts to over one hundred megawatts.

Current plans for the development of a space nuclear reactor estimate the need for many millions of dollars to conduct research. The drive towards high reactor temperatures will require new materials and thermal management technology in and around the reactor hardware. Figure 2 illustrates how an impovement in radiator specific mass could affect reactor outlet temperatures. Projections for some advanced concepts, discussed later in this paper, lie near the 1 kg/m^2 curve. The mass goal of 3000 kg indicated in the figure is desirable under the DOE/NASA/DARPA SP-100 program. Indeed, an advanced lightweight radiator coupled with a high temperature reactor could produce very efficient power systems.

Several of the novel heat rejection concepts being studied today dispel from previous design philosophy the need to contain the working fluid inside an array of tubes or within heat pipes. Instead, the heated fluid is exposed directly to the space environment where it cools due to radiation processes, but no conduction or convection is involved. The removal of these containment devices on the heat transfer fluid can result in an order of magnitude reduction in the weight of the radiating surface.

Heat Pipes

Many of the advanced, near term, heat rejection concepts are directed at Space Station technology. It has been determined that a shuttle-type tube radiator would be adequate for the station, but it would be massive and mechanically complex. In fact, a 100 kW radiator of this type would consist of 19000 feet of tubing. Redundancy adds to the problem but is necessitated by the threat of single point failure caused by micrometeoroid damage. A heat pipe radiator is promising because of its modularity and because it may be space constructable. Large volume and heavy weights are the biggest complaint against heat pipes, and efforts to reduce both are being conducted. However, it is felt by many that a new approach to radiating waste heat is necessary now; the remainder of this report discusses several suggested approaches.

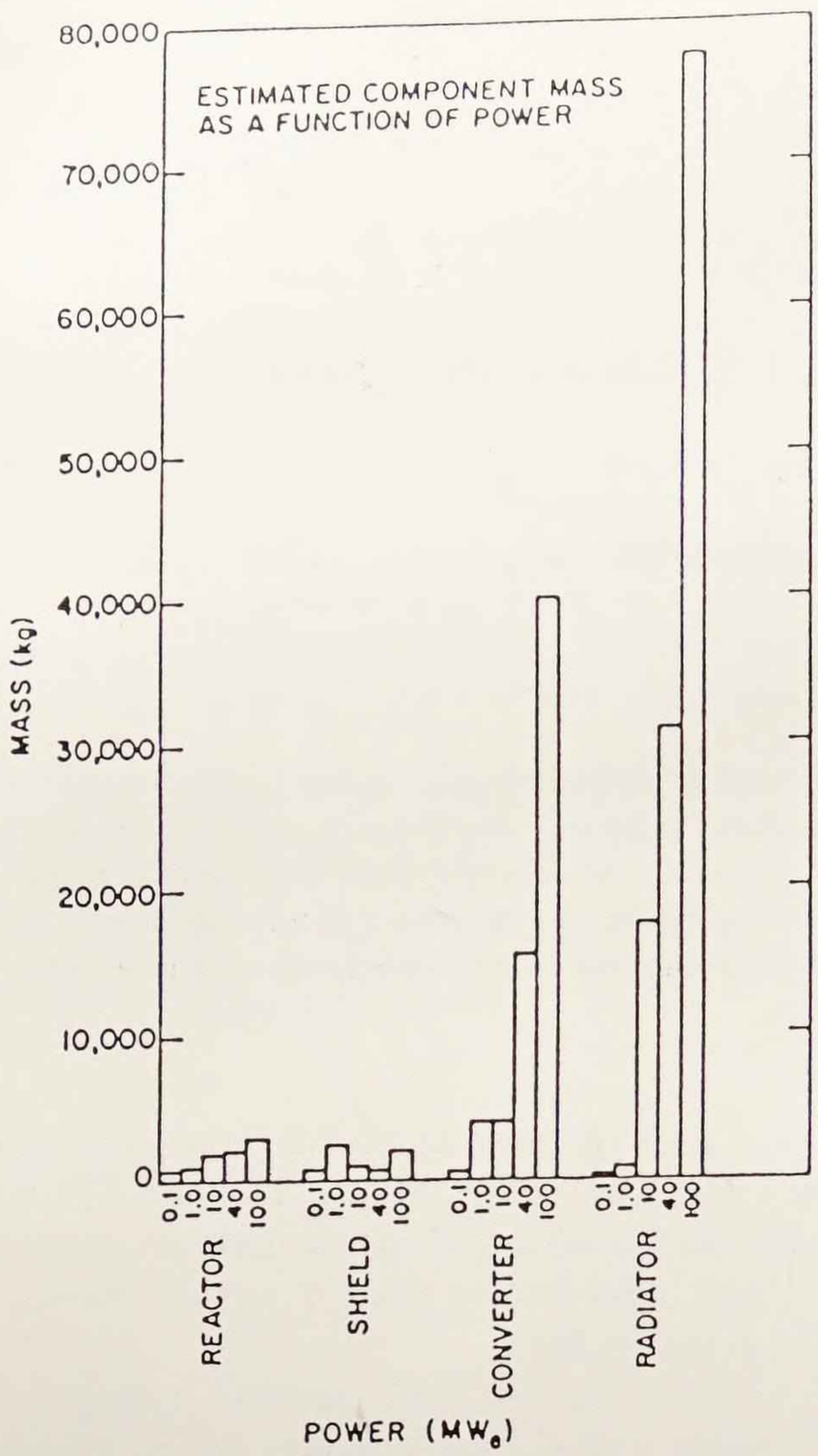


Figure 1 *Nuclear Power System Weight Distribution as a function of Power Rating (from Buden and Angelo 1982).*

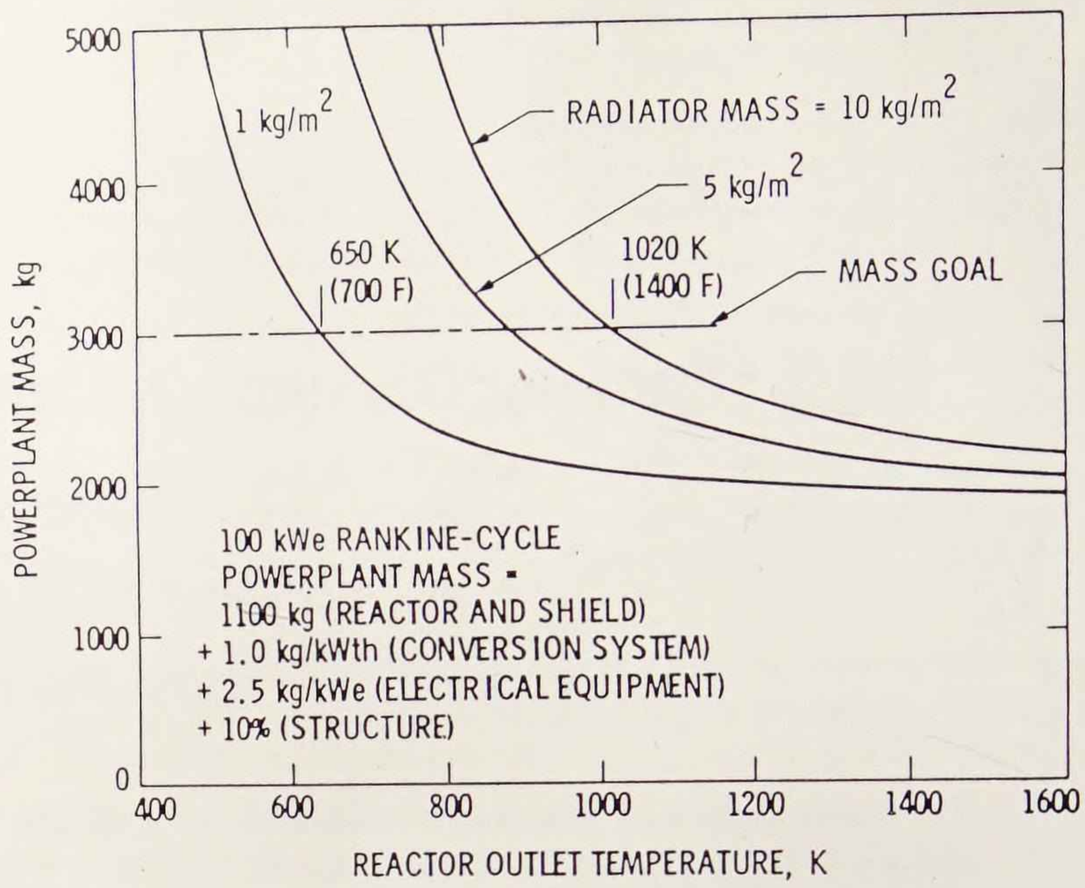


Figure 2 *Impact of Radiators on Reactor Temperatures (Courtesy of Jet Propulsion Laboratory).*

Liquid Droplet Radiator

The Liquid Droplet Radiator (LDR) is currently being studied jointly by the Air Force and NASA. As illustrated in Figure 3 the working fluid is pumped through a heat exchanger to the liquid droplet generator, a pressurized chamber with numerous micron-sized orifices. Liquid jets are formed as the fluid emerges from the orifices. With induced vibration, the jets break up into a stream of droplets with uniform and predictable size and spacing. The drops maximize the surface area to volume ratio. Through selective orientation of the orifice arrays, a droplet stream with a controlled trajectory travels to a liquid droplet collector. Radiant heat transfer occurs during the transit between the generator and the collector. The collector captures the streams, consolidates them, and delivers a continuous fluid to the pump inlet. The pump pressurizes the cooled fluid to system pressure and returns it to the heat exchanger for repeat of the cycle. The size and mass of droplet stream are a function of waste heat load, droplet size, operating temperature, and optical and thermal properties of the working fluid.

Through the replacement of solid surfaces with liquid droplets, an order of magnitude reduction in the weight of the radiating area may be achievable. Other advantages include invulnerability of the droplet sheet to micrometeoroid damage, and the ability to store a po-

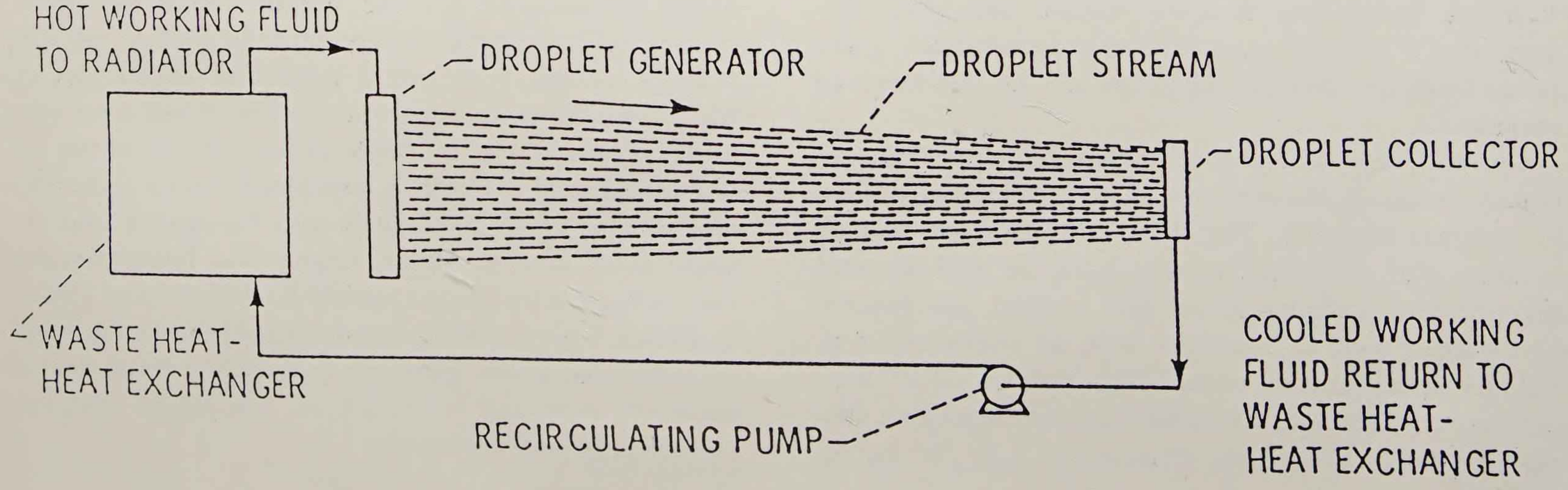
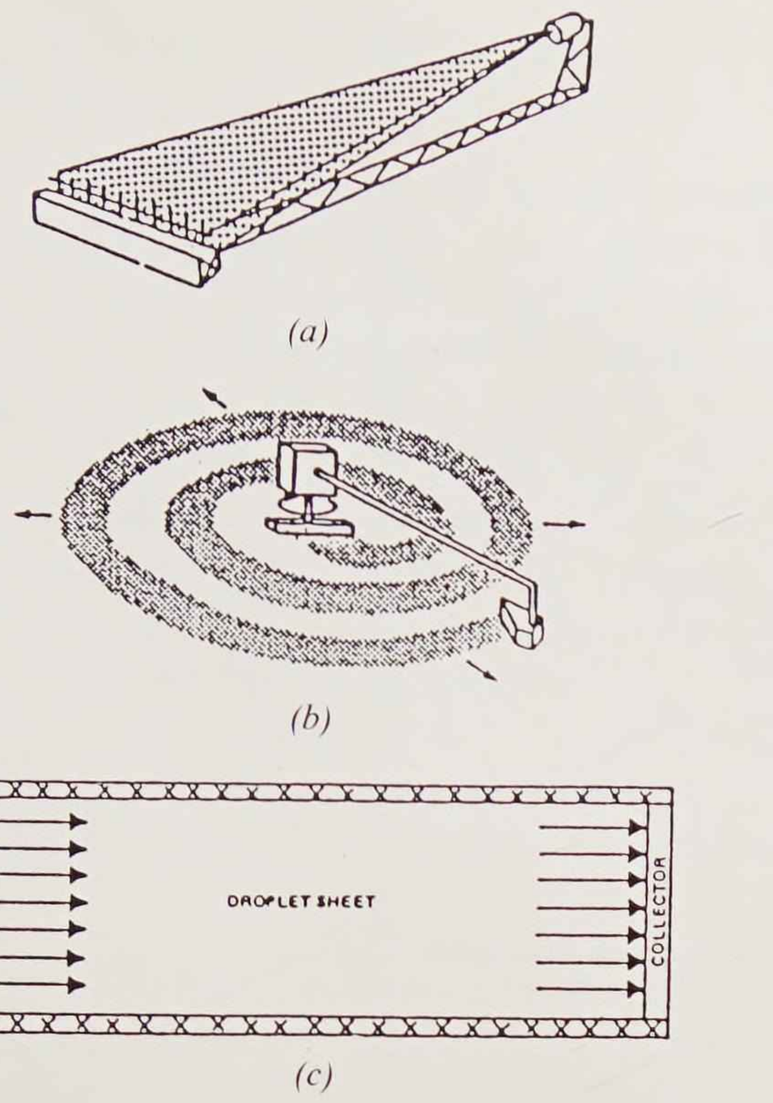


Figure 3 *Liquid Droplet Radiator Concept.*



(a)

(b)

(c)

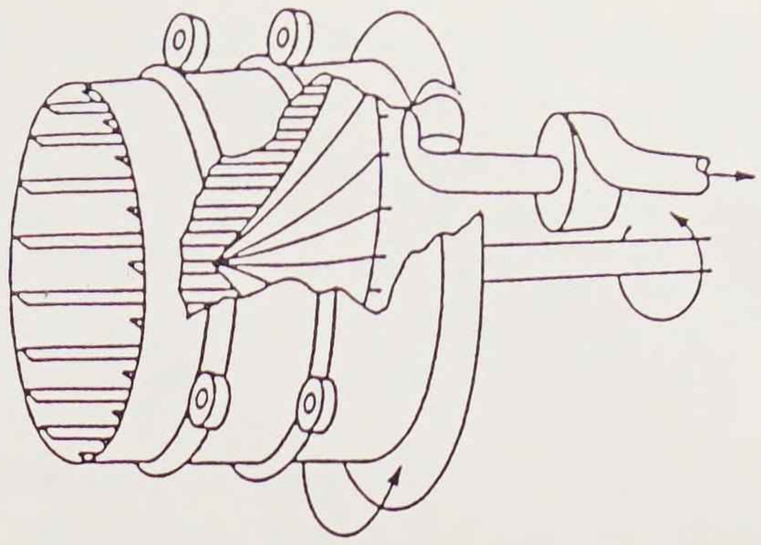
Figure 4 *Possible Liquid Droplet Radiator Configurations.*

tentially large radiating area inside a smaller container. The LDR is currently receiving widespread attention. A large data base exists on the technology of generating uniform, accurately directed streams of droplets in the 100 micron size range. The best known application is the ink-jet printer.

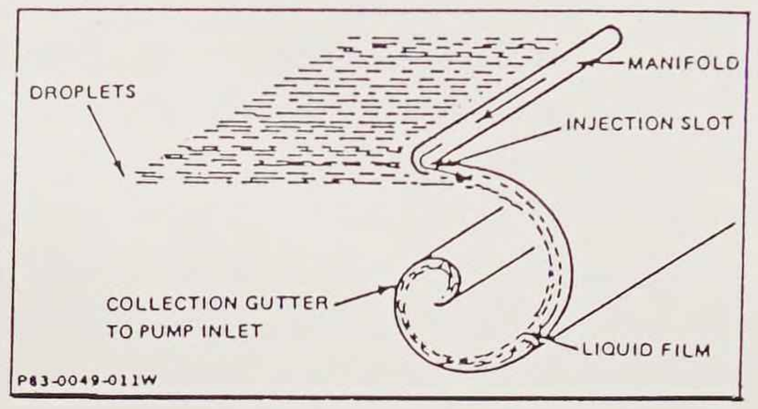
Figure 3 is intended to be generic in nature and does not necessarily represent any preferred configuration. In fact, each of the configurations shown in Figure 4 could become a desirable option, depending on the particular mission.

The collection of the droplets in space is a technology area lacking a substantial data base. Because of this, many conceptual designs have been generated and many of these are discussed by Prenger and Sullivan (1982). Two concept types currently under funded study are shown in Figure 5. The first concept uses induced rotational forces to drive the incoming fluid to the outer edge where it is collected and fed into a pump or possibly another droplet generator. This type of collector assumes a focused incoming sheet of droplets. The second concept creates a moving surface by injecting fluid along the inner collector wall as shown. This collector configuration may be independent of length and may allow for a non-focused droplet sheet.

Another potentially applicable collection scheme being pursued employs a phenomena known as dielectrophoresis. As seen in Figure 6, a field gradient is created between an outer and inner collector surface which causes the droplets to migrate towards the center. This approach could be useful not only in its own right as a collector, but as a back up effect on another type of device. This approach is under study by the McDonnell Douglas Co.



(a)



(b)

Figure 5 *Liquid Droplet Radiator Collection Schemes (from (a) Mattick and Taussig 1982 and (b) Courtesy of Grumman Aerospace).*

As part of the current research, some systems work was conducted to determine operating characteristics of the LDR and compare it to conventional and heat pipe radiators. Analysis has included computer modeling. The power conversion system consists of the heat source heat exchanger, recuperator, and the radiator heat exchanger plus rotating equipment, ducting, and liquid coolants in the heat source and radiator heat exchangers. Figure 7 shows the payoff in system mass when an LDR is used over an advanced heat pipe radiator. These results suggest that a three to four-fold decrease in mass is possible.

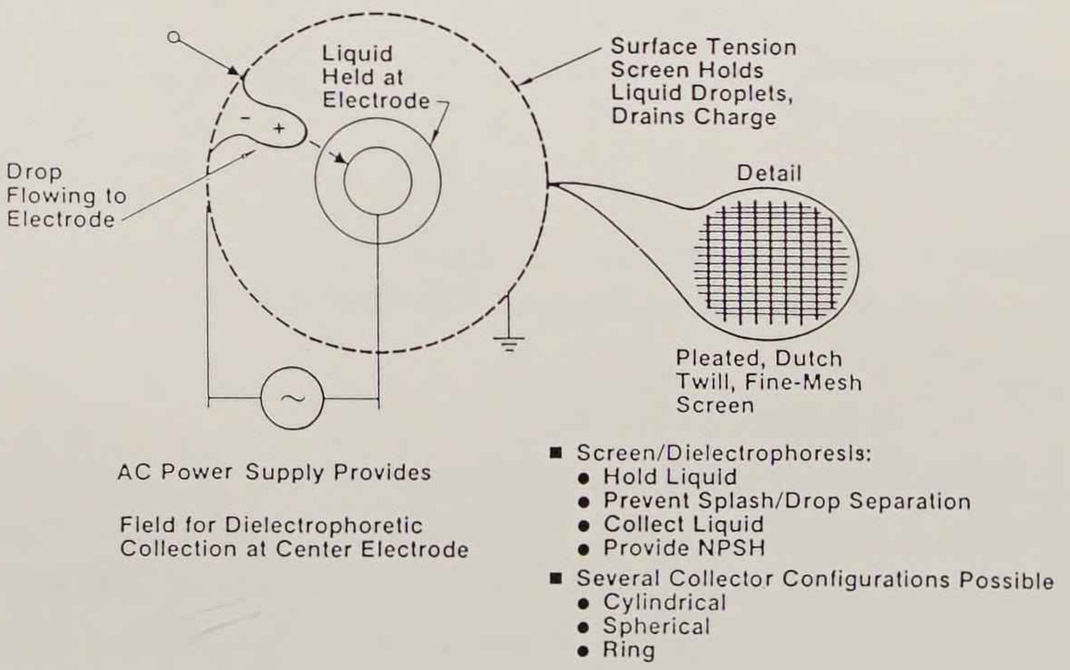


Figure 6 *Operation of Electrophoretical Dielectrophoretic LDR Collector (Courtesy of McDonnell Douglas Astronautics Co.).*

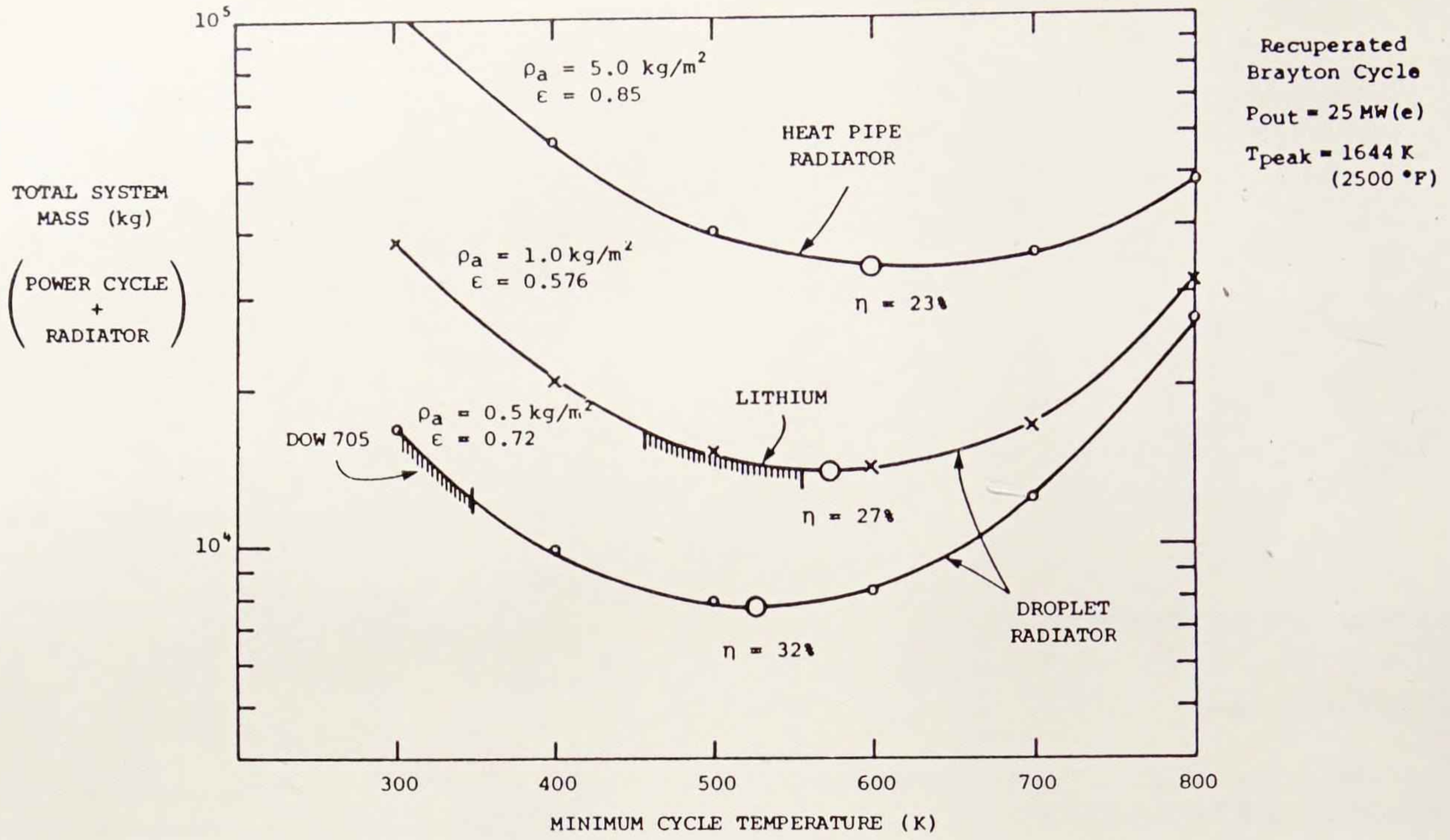


Figure 7 *Brayton Cycle Performance for an LDR and a Heat Pipe Radiator.*

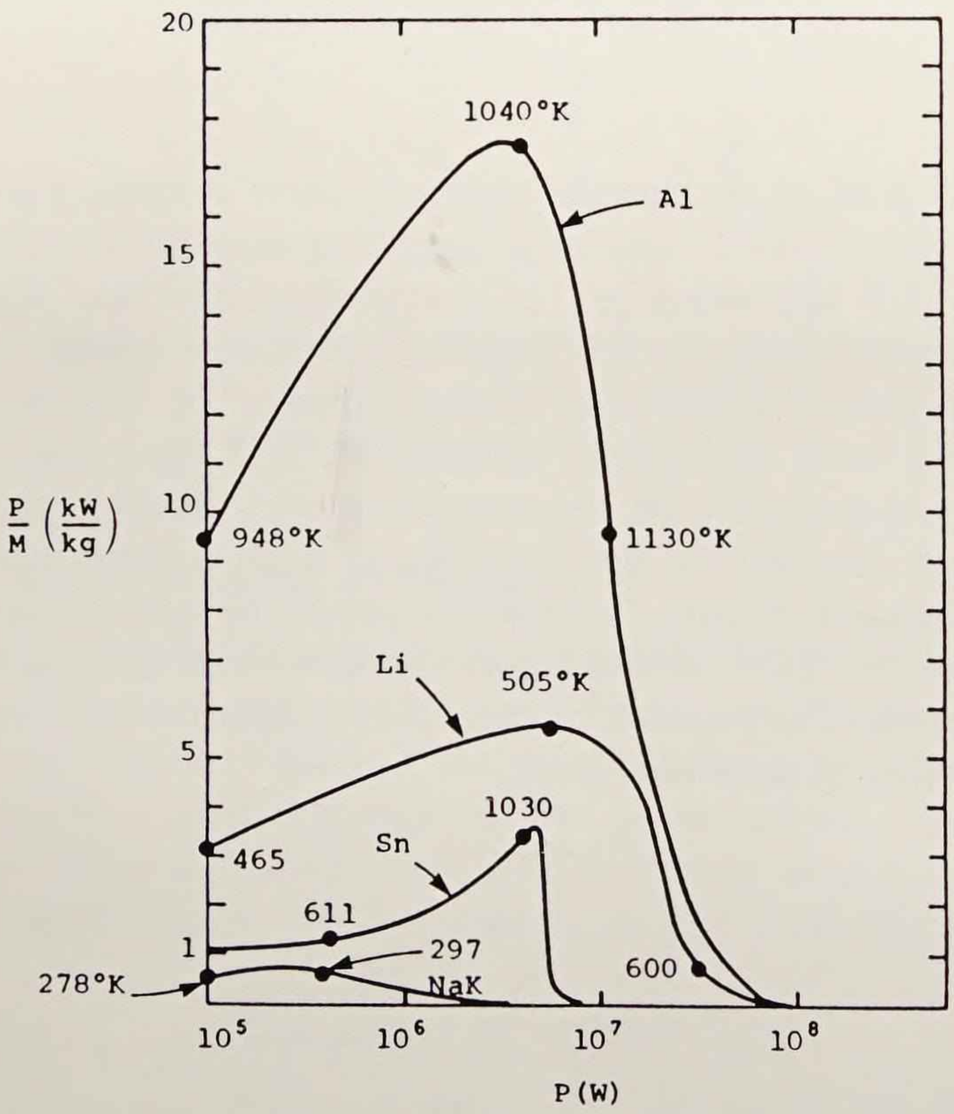


Figure 8 *LDR Performance vs. Power Radiated (Courtesy of Mathematical Sciences Northwest).*

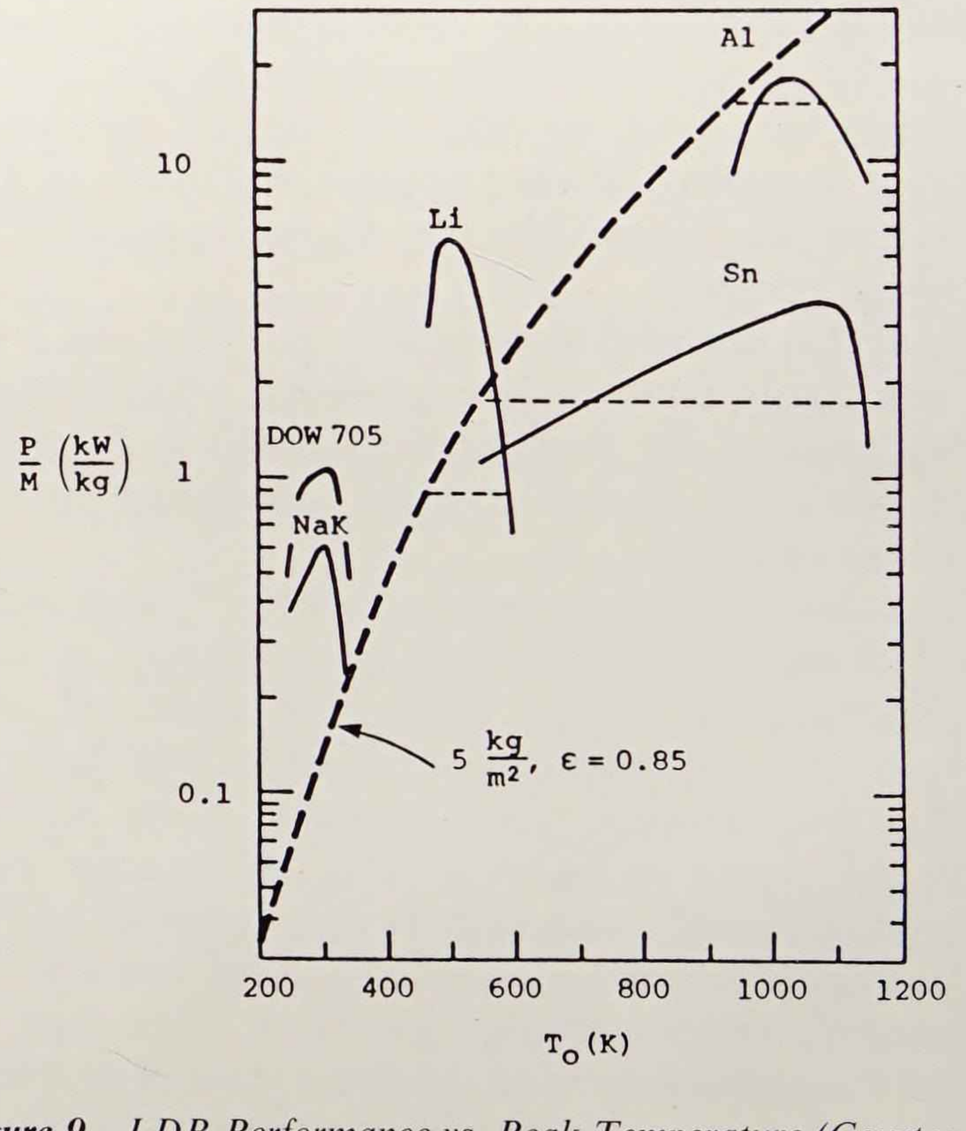


Figure 9 *LDR Performance vs. Peak Temperature (Courtesy of Mathematical Sciences Northwest).*

LDR Performance vs Radiated Power is shown in Figure 8 for Aluminum, Tin, Lithium, and NaK. The first three peak near 5 MW and NaK at about 200 kW. Higher powers may be obtained using multiple radiators. Figure 9 shows Performance vs Peak Temperature, with heat pipe power/mass shown as the dashed line for comparison assuming 5 kg/m^2. Lithium and Dow 705 oil systems are approximately five times lighter than heat pipes, whereas aluminum and tin LDR's are not very attractive in this comparison. However, it must be noted that there are many criteria that must be examined, such as overall system efficiency, to determine what type of LDR is best suited for a particular mission, and therefore a more comprehensive comparison is warranted.

Magnetic Options for the Liquid Droplet Radiator

Exposure of a fluid directly to space immediately draws criticism, and justifiably so, from those particularly concerned with spacecraft contamination issues. Fluid lost by evaporation or inefficiencies in radiator fluid management may unfortunately end up on important sensors or degrade thermal coatings. It is also known that contaminants in the area of a sensor can distort incoming light and cause misinterpretation of the data. Because of this, approaches to aid in controlling exposed fluid are being investigated.

An experimental program has been carried out by the Brookhaven National Laboratory to investigate the possibility of using ferromagnetic fluids, also called ferrofluids, and magnets to aid in managing the radiator liquid. It was demonstrated that ferrofluids can be formed into droplet sheets and remain stable. It must be noted that ferrofluids used in this study may not be suitable for LDR use; however, the application and potential for similar fluids exists. Two configurations for the LDR were considered and are shown in Figure 10.

Several types of magnets are available for possible use in this application. If a low strength field is desired then permanent magnets, normal electromagnets or superconducting magnets may be used. Only superconducting magnets appear useful above 0.7 Tesla because normal electromagnets become very heavy and require higher power inputs. Permanent magnets cannot achieve more than 0.5 Tesla. However, it is still unclear exactly what field strengths will be required.

The Brookhaven experimental studies included the generation of single and multiple droplet streams, and ferrofluid splashing studies. A small cobalt-semarium magnet was used in all cases. Splashing single drops of ferrofluid under various field strengths has shown that fields on the order of a kilogauss will contain both incoming and splashed fluid. Also, splashed fluid will flow only along magnetic flux lines. It was concluded from these initial experiments that the use of magnetic principles deserves further study. Longer run times with a continuous working fluid loop, and a longer free fall region would greatly aid observations, particularly multiple splash events.

Using magnets in space may, in addition to helping solve many problems, create others. One complicating

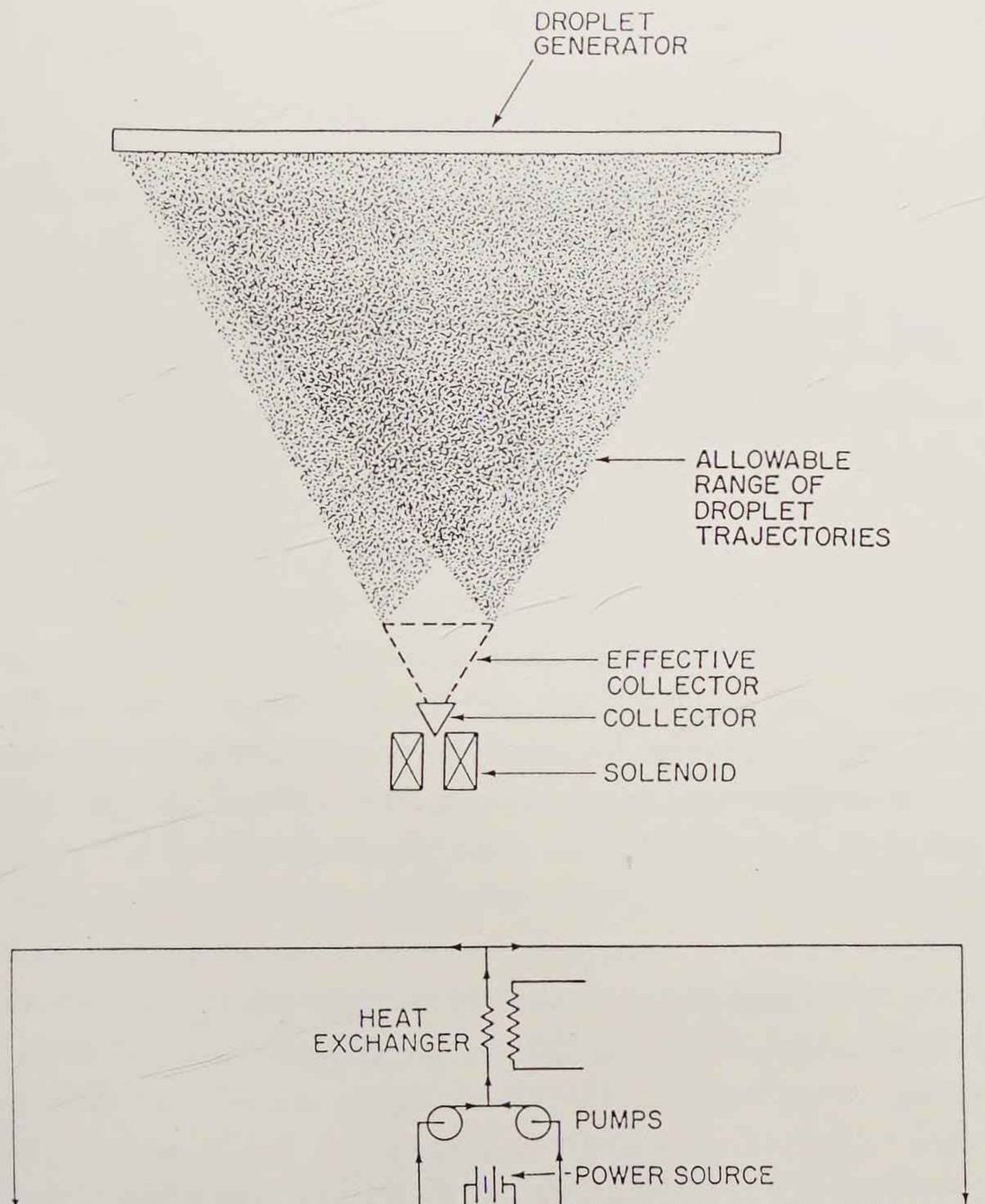


Figure 10 *Configurations for the LDR Using Magnets (from Botts et al. 1983).*

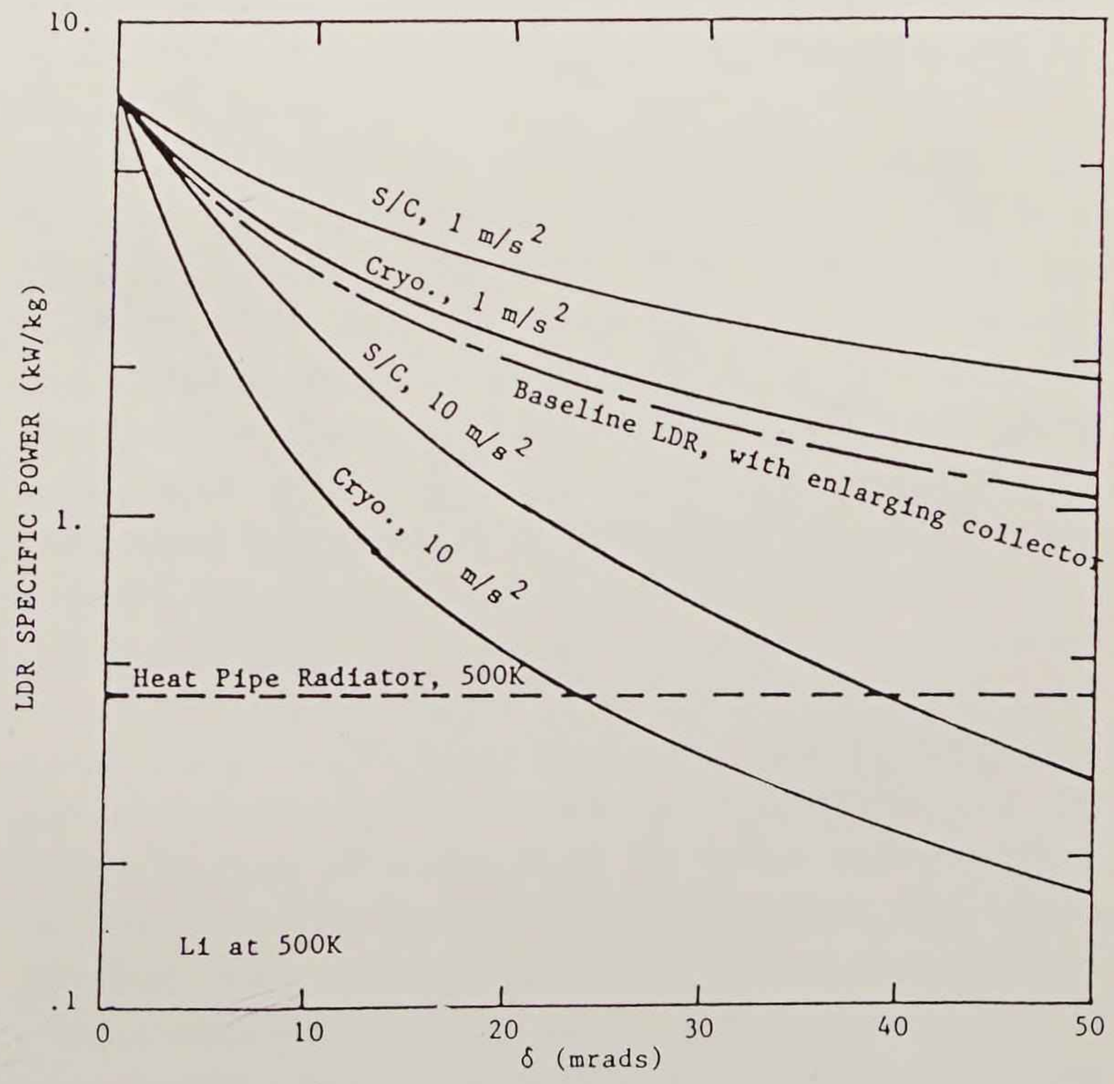


Figure 11 *Specific Power of a Magnetic LDR as a fuction of Divergence Angle (from Botts et al. 1983).*

factor is the additional complexity involved in this approach, an admittedly difficult problem to quantify. Analysis therefore was aimed at assessing the impact on specific power. A representative graph constructed during this analysis is shown in Figure 11. It shows the penalty involved in using both superconducting and normal electromagnets based on the divergence angle acceptable for the radiator sheet. The zero divergence angle axis represents a non-magnetic radiator. Similar analyses were conducted for other possible LDR fluids, with similar results.

Belt Radiator

Weatherston and Smith (1960) are credited with the first suggestion to use a moving belt radiator in space. The belt surface provides the radiating area, and the heat is supplied to the belt by heated rollers or by passing the belt through a chamber of fluid. Their preliminary calculations indicated that the radiator system specific mass could be reduced to 2.5 kg/m^2. Recent analytical and experimental studies by the Astro Research Co. have shown that a significant improvement in the concept can be achieved by using low vapor pressure substances to increase the heat transfer rate between the belt and the drum. Using modern materials such as Kapton or beryllium, specific masses less that 1 kg/m^2 may be obtainable.

Figure 12 illustrates how two moving belt radiators might be mounted perpendicular to a solar array system in order to reject waste heat. This particular orientation is desirable because it avoids solar heating of the radiators. However, the location in close proximity to the solar arrays may not be desirable because of the tendency to raise solar array cell temperatures.

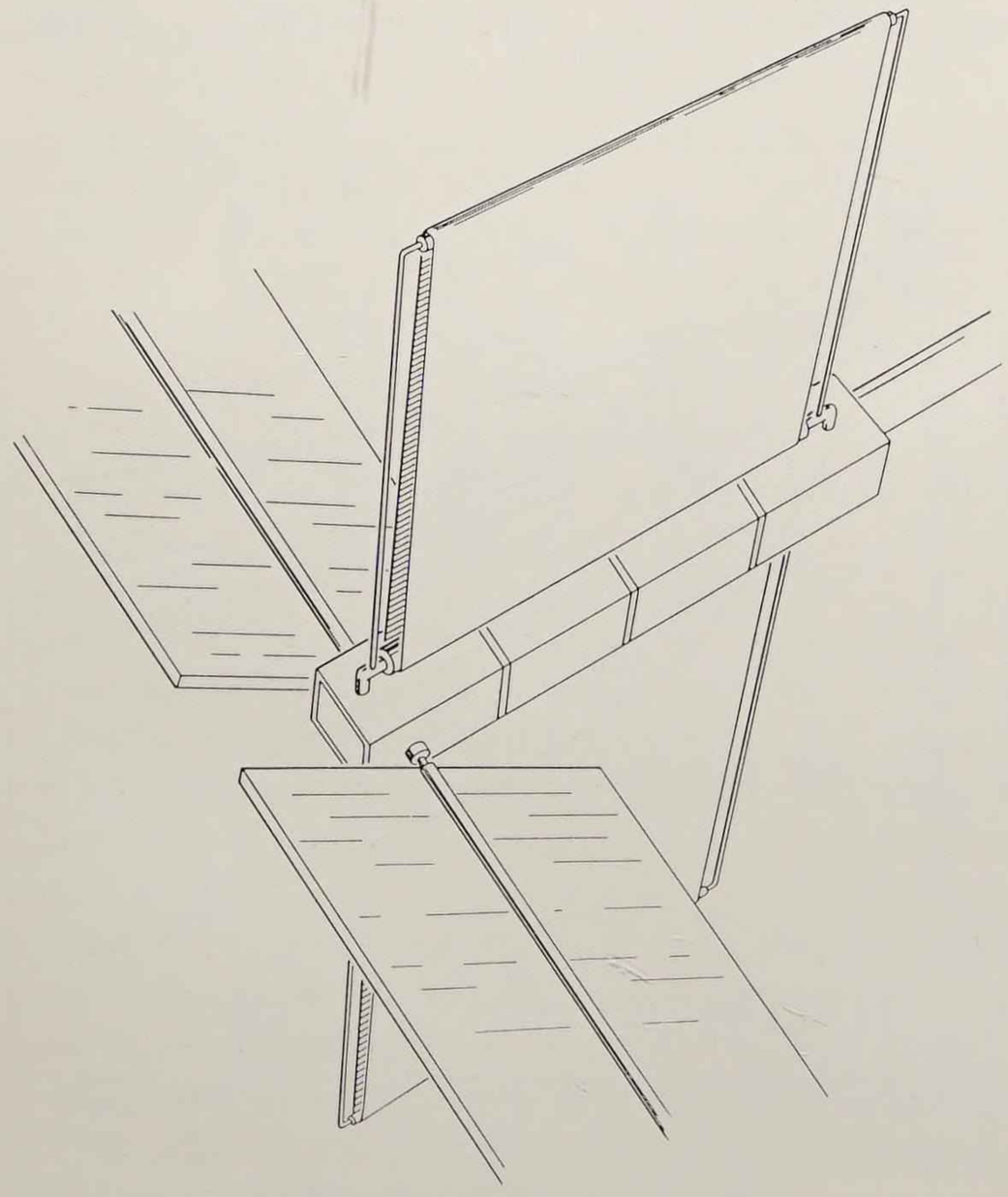


Figure 12 *Two Moving Belt Radiators Mounted Perpendicular to Spacecraft Solar Arrays (from Knapp 1984).*

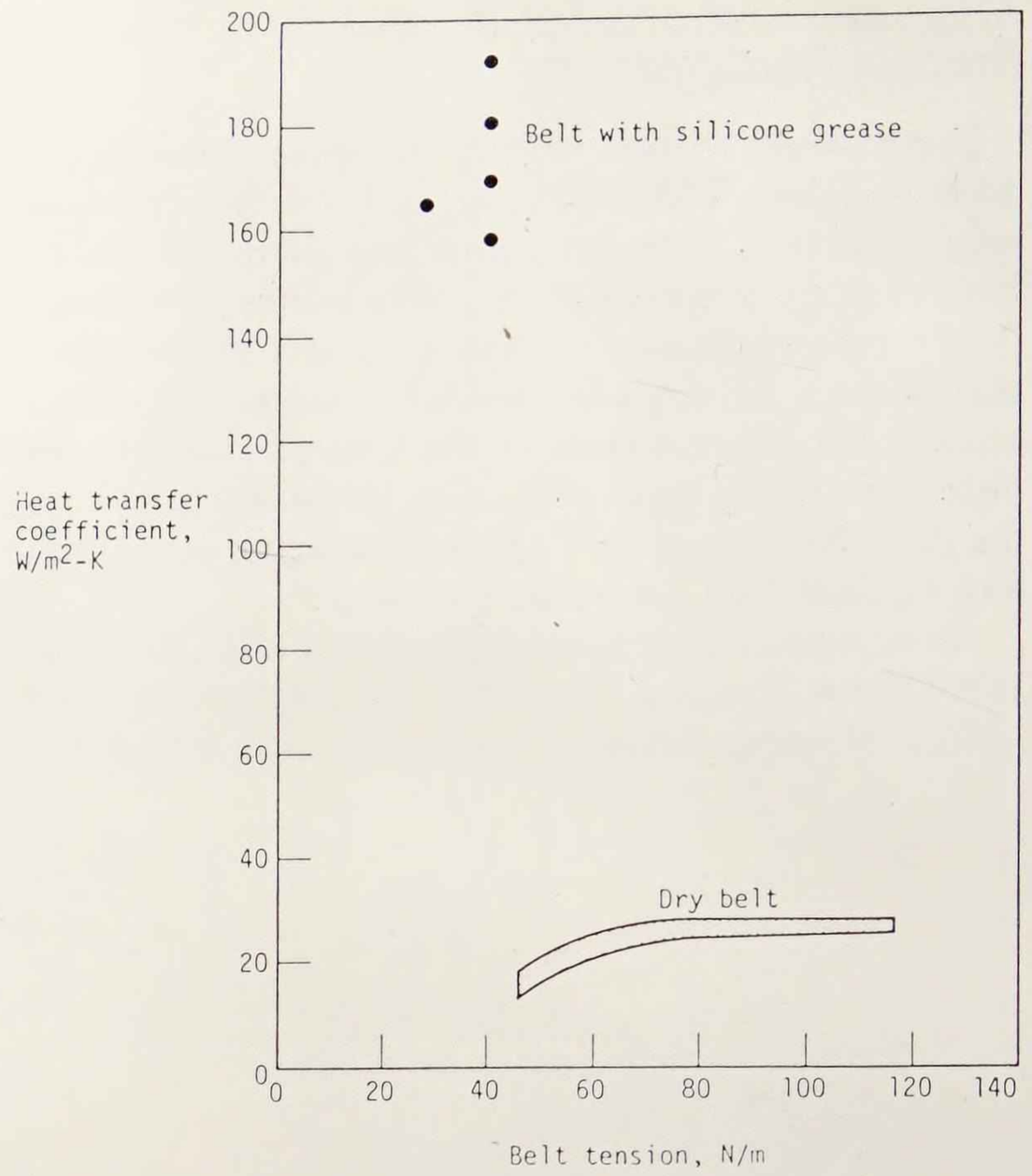


Figure 13 *Experimental Results for a Belt Radiator showing the Influence of Low Vapor Pressure Grease on Heat Transfer to a Moving Belt Radiator (from Knapp 1984).*

Tests that were conducted to determine the first order effect of adding a coating between the drum and belt were not designed to make measurements of high absolute accuracy or to reproduce the cold conditions of the space environment. However, some significant results were achieved as shown in Figure 13. Tests with a dry belt and drum resulted in heat transfer coefficients that were below 30 W/m^2-K and increased with belt tension up to a value of around 70 N/m. Tests with a silicone "grease" coating increased the heat transfer coefficient to a range between 158 and 192 W/m^2-K at belt tensions lower than those used with the dry belt.

These results have direct application to the parametric numerical analysis conducted assuming a Kapton belt moving over a drum. The overall heat transfer coefficient includes the coefficient between the hot fluid and the drum, and the drum with the belt. The influence of the overall coefficient on the total specific mass is shown in Figure 14 for a nominal fluid temperature of 300 K and a belt velocity of 1 m/sec. The experimental results helped confirm that a value of 100

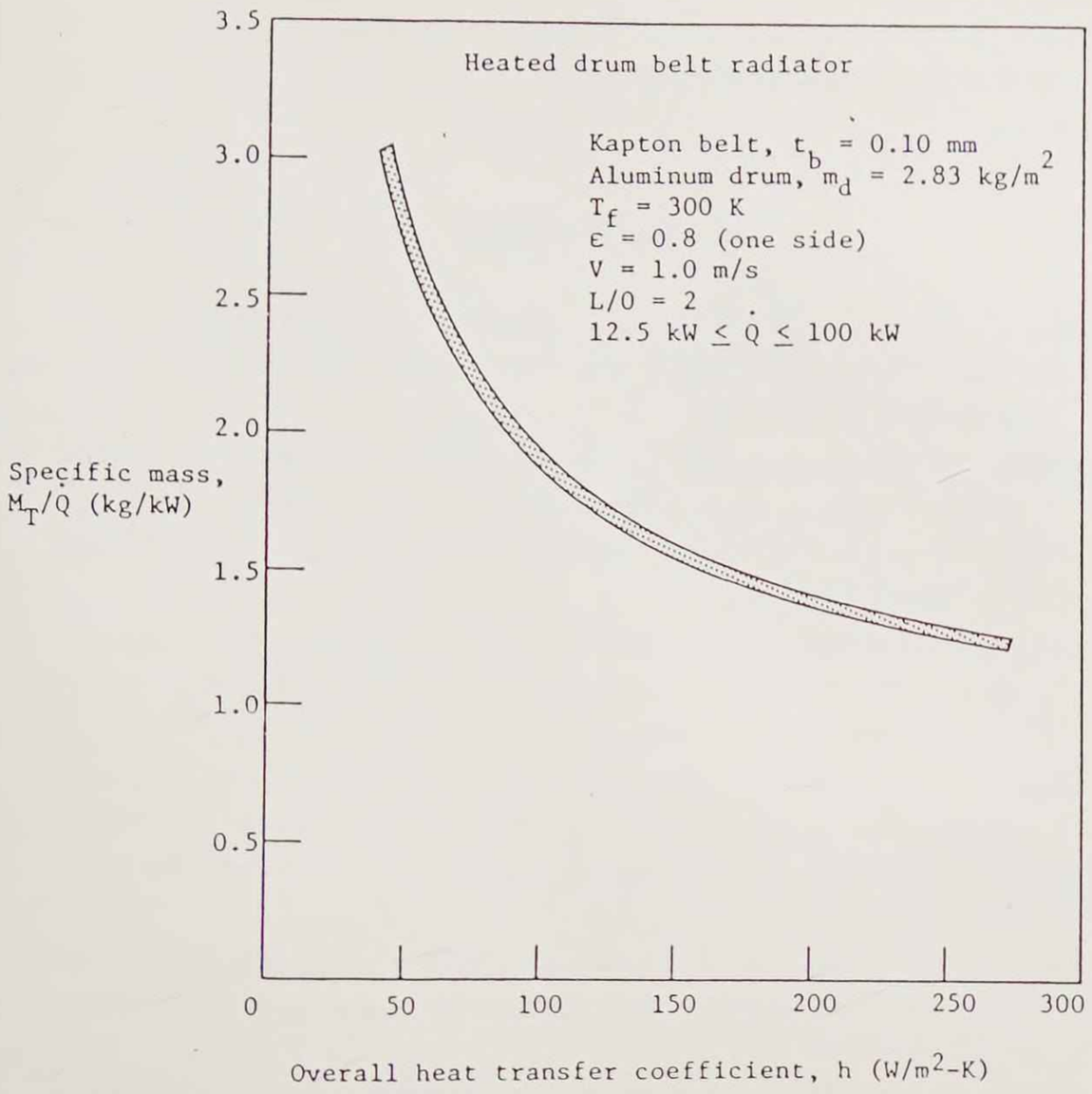


Figure 14 *Influence of overall Belt Radiator Heat Transfer Coefficient (from Knapp 1984).*

W/m^2-K for the overall coefficient is appropriate. This value would correspond to a specific mass of approximately 1.7 kg/kW.

Belt radiators will passively accept variations in heat rejection rates by changing the mean belt temperature. Active control is also possible by varying belt velocities. If a hydraulic drive motor were employed, the belt heat rejection capability could be controlled by the spacecraft's coolant flow rate.

Heating of the belt can also be accomplished by allowing the hot fluid to come in direct contact with the belt surface. This approach may yield even lower masses than when a drum is used. Figure 15 shows that

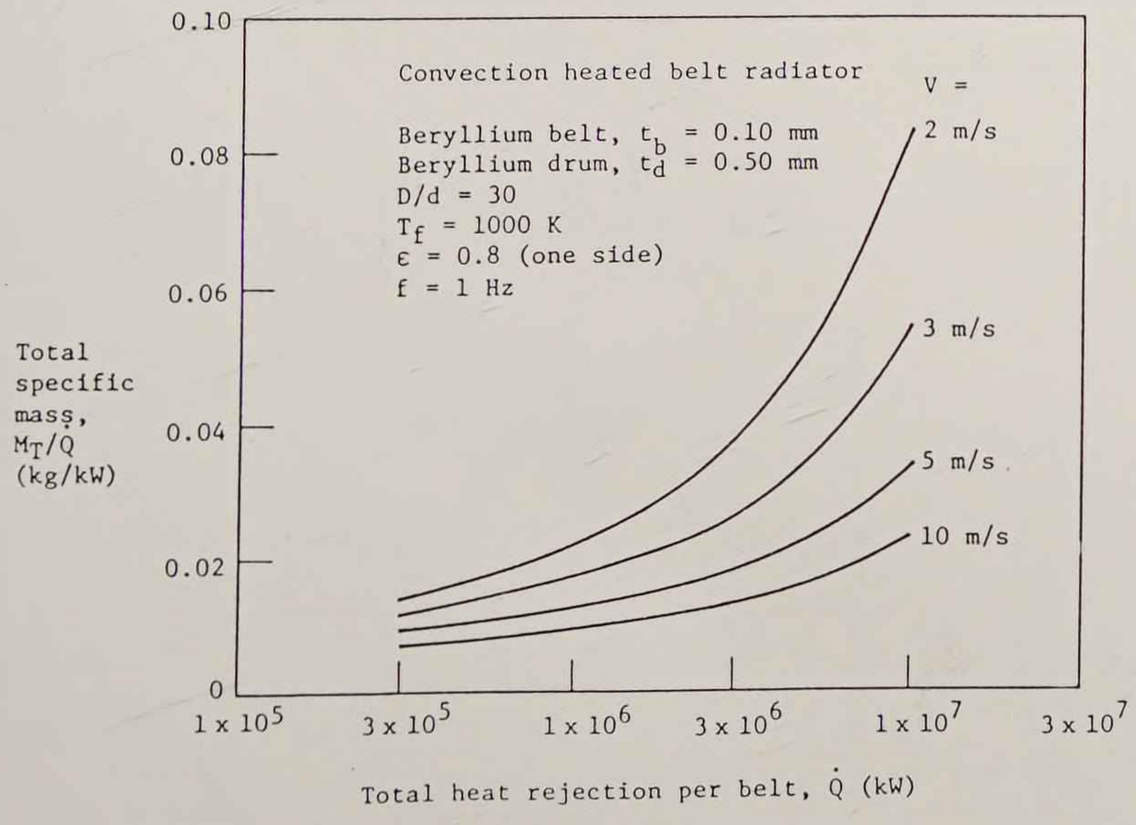


Figure 15 *Convection Heat Belt Radiator Performance (from Knapp 1984).*

when belt speeds as low as 2 m/sec are used, a total specific mass of less than 0.1 kg/kW is obtainable for high powers. Analysis has also shown that the selection of the fluid does not appear to have any influence on the system mass. The compatibility of the belt, fluid, and seal materials along with the effectiveness of the seal system are the major design challenges of this concept.

It appears obvious that the chamber should be operated at the lowest possible pressure to minimize fluid leakage. It is not clear whether or not the selection of a low vapor pressure fluid can be used to minimize such losses. In order to do so, any fluid which leaks on to the belt must be recovered, possibly by a scraper feeding a scavenging pump.

Additional Concepts

There are other concepts for advanced radiators that have yet to receive government funding for their research. This is primarily due to the fact that interest in them is now reemerging along with perceived future mission requirements, rather than a technical preference for one concept over another. One proposed variation on the LDR would collocate the generator and collector, thereby eliminating the need to return the droplets through a pipe or another LDR. The drops would be charged opposite to the collector charge, and would execute a slightly elliptical orbit.

Another interesting concept discussed by Prenger and Sullivan (1982) is the Filament Radiator. A continuous filament of a viscous material is drawn from a melting pot which receives the waste heat from the power cycle heat exchanger. The filament then traverses through space, radiates heat, and returns to the melt pot to repeat the process.

Similar in some ways to the belt concepts is the Disk Radiator. This concept utilizes fluid ejected from a manifold located at the center of the disk. Due to the rotation of the disk, the heated fluid migrates to the end, radiates heat, and is collected by a tube directed into the flow. Assuming that fluid management problems could be resolved, and high emissivity achieved, this approach appears to be limited (as with many other concepts) only by the size of the disk and structure.

Some concepts are conceived for a specific mission or power conversion system. The Rankine Cycle Supersonic Condenser-Radiator is one example. In the power conversion subsystem the working fluid would exist the power turbine as a vapor or as a wet vapor with a considerable fraction of vapor liquefied into small droplets. This fluid is then fed into the supersonic condenser where the hot vapor and liquid droplets if present are expanded through a high area ratio nozzle. These high temperature droplets are then injected into space where their heat is rejected by radiation. The cooled droplets are then collected and pumped back

through the system. Rocketdyne is currently investigating this concept.

Conclusions

There are additional concepts which exist that cannot be discussed in this paper because of their proprietary nature, because the owner of the idea did not want to have the idea appear in the open literature as yet, or because the author is simply not aware of them.

While it is true that current technology for space radiator systems do not show promise for some of the future missions currently under consideration by the U.S., we have seen here that many concepts exist that can accomplish the job when developed. Some of these concepts can be developed in the near term and actually replace state of the art radiators, while others still be considered far term (1990) technology but necessary to enable very high powers.

Acknowledgments

The author wishes to thank all of those individuals who have contributed concepts to this paper. Wide exposure of these ideas will foster constructive criticism and help improve future technology development.

References

Botts, T. E. et al. (1983) *Magnetic Focusing of Liquid Droplet Sheets for Heat Rejection in Space*, Air Force Rocket Propulsion Laboratory Report TR-83-072.

Buden, David and Joseph A. Anjelo (1982) *The Role of Nuclear Reactors in Future Military Satellites*, Los Alamos National Laboratory Paper LA-UR-82-1649, 8th DARPA Strategic Space Symposium, Monterey CA.

Knapp, Karl (1984) *Study of Moving Belt Radiators for Heat Rejection in Space*, Final Report, Air Force Rocket Propulsion Laboratory Contract F04611-83-C-0012.

Mattick, A. T. and R. T. Taussig (1982) *New Thermal Management and Heat Rejection Systems for Space Applications*, Air Force Rocket Propulsion Laboratory Contract F04611-81-K-0040, Interim Technical Report.

Prenger, F. C. and J. A. Sullivan (1982) *Conceptual Designs for 100-Mw Space Radiators*, Los Alamos National Laboratory Paper LA-UR-82-3279.

Wetherston, R. C. and W. E. Smith (1960) "A Method for Heat Rejection from Space Power Plants", *A.R.S. J.* 30: 268–269.

Part 8

SAFETY AND RELIABILITY



Space Nuclear Power Systems 1984
Edited by M. S. El-Genk and M. D. Hoover
© Orbit Book Company, Malabar, FL, 1985

Chapter 56

Space Nuclear Safety Review Process

Marvin P. Norin

U.S. Department of Energy
Washington, D.C. 20545

The space nuclear safety review process is discussed with respect to the roles of those organizations directly responsible for the safe conduct of a safe mission and the Interagency Nuclear Safety Review Panel (INSRP) which is responsible for independent evaluation of the nuclear risks associated with that mission.

Introduction

The Space Nuclear Safety Review Process includes both the activity of the Interagency Nuclear Safety Review Panel (INSRP) and the activity of the program elements, that is, those organizations directly responsible for the safe conduct of a mission. INSRP is responsible for an independent evaluation of nuclear risks associated with that mission. The launch and deployment of spacecraft must be evaluated for potential hazards to operations personnel and to local and world populations. The scope and complexity of the safety evaluation peformed for a particular mission are related to previous experience with the payloads and launch operations involved. Differences in equipment, mission, and payload characteristics influence the operational aspects which must be evaluated and the depth to which these need to be evaluated. Although missions and equipment may differ, the systematic safety evaluation of space missions and related ground activities is a practice common to all missions, nuclear and non-nuclear.

The safety evaluation for a mission when the spacecraft is equipped with a nuclear power system would generally involve all the aspects of a non-nuclear launch. Additionally, the potential risks associated with radiation exposure must be considered. My discussion is concerned with the nuclear aspects of the safety evaluation. Further, my discussion is limited to the safety considerations which apply during that period of risk starting when the nuclear power system is installed into a fueled launch vehicle through deployment of the payload vehicle or spacecraft containing the nuclear system. Bear in mind, however, that safety is also a prime consideration in the various activities involved in design, manufacture, test, and transportation of the nuclear power system and the integration of that system into the spacecraft and launch vehicle. The nuclear safety review process for these activities is internal to the operations of the responsible government agencies and their contractors. For example, such activities up to delivery of a nuclear power system to the launch site or to a spacecraft integration facility would be the responsibility of the Department of Energy (DOE). Safe ground operation with a nuclear power system at the launch site or spacecraft integration facility would also be the concern of the National Aeronautics and Space Administration (NASA) where that agency has spacecraft or launch responsibility and the Department of Defense (DOD) which is the range operator and can also have spacecraft or launch responsibility. The safety of these activities are covered by the procedures within the cognizant agencies and will not be further discussed here.

Let us return now to the period of risk which includes the installation of a nuclear power system into a payload coupled to a launch vehicle through deployment of the payload in space and, where appropriate, post mission reentry of the nuclear power system. The safety related aspects of the use of nuclear power in space are primarily concerned with this period of risk and are provided with a nuclear safety overview by an Interagency Nuclear Safety Review Panel. Before discussing the activity of the Panel, let me briefly look at the safety role of the program side of the nuclear safety process.

Safety is a Line Responsibility

I cannot overstate this. The *program* or *project* is *responsible* for the safety of a nuclear power system for space use. The terms program or project mean the responsible line elements directly responsible for safe, successful mission accomplishment. Typically, program has meant a tri-agency interactive activity. In a nuclear safety sense, the various program elements must be assured, consistent with overall mission requirements, that their areas of responsibility are compatible with the use of a nuclear power system in space. Consider, for example, Galileo, a current NASA program. For the Galileo project, DOD is responsible for range opera-

tions; NASA is responsible for the spacecraft, launch vehicle, and mission operations; DOE is responsible for the nuclear power system. The Galileo programmatic interaction paramount to nuclear safety is, in this case, between the NASA and DOE parts of the program. Under NASA cognizance are the spacecraft, the spacecraft deployment vehicle, and the conduct of the mission. The configuration, components and propellants of this equipment and their response to postulated accidents or malfunctions or aborts will determine the accident environments to which the nuclear power system can be subject.

DOE is responsible for the nuclear power supply; therefore, DOE is responsible to provide a power supply that can accommodate the external hazards which can result from those credible accident environments postulated for the various phases of the launch and mission. The degree of accommodation or conversely the severity of the hazards to the nuclear power system will then lead to a determination of the potential risks to local and world populations. Risks in the case of a radioisotope thermoelectric generator (RTG) type of nuclear power system derives from the potential accident environments which are externally caused. A reactor type of power supply would also involve considerations such as criticality and the time dependency of radioactivity for an operating reactor.

U.S. experience in the use of nuclear power systems in space has generally shown that all specific hazards to the nuclear power system in terms of quantitative requirements are not available at the outset of a program. This further demands that, as the program develops, safety be continually factored into the design process.

The program's evaluation of the safety aspects of a nuclear power system as associated with a specific space mission is provided via Safety Analysis Reports (SAR's). These reports are the responsibility of DOE and are prepared by the DOE nuclear system contractor. They contain and utilize significant input information which originates from the agencies responsible for the spacecraft, launch vehicle, launch operations, and the launch range. Briefly, an SAR includes a description of the mission and flight system including the appropriate details of the nuclear power system, the spacecraft, launch vehicle, and the flight profile and characteristics. The SAR then develops the potential accident environments and response of the nuclear power system to these environments. The SAR then proceeds to describe the resulting potential radiological risks. There is usually a Preliminary Safety Analysis Report (PSAR), an Updated Safety Analysis Report (USAR) and a Final Safety Analysis Report (FSAR).

The Interagency Nuclear Safety Review Panel

The Interagency Nuclear Safety Review Panel provides an independent evaluation of the risks associated with the launch of a nuclear power system in space. The Panel members consist of a representative from each of the Departments of Defense and Energy and from NASA. The Panel members are independent of the program and the panel is organized such that no single agency is dominant. The Panel includes an observer participant from the Nuclear Regulatory Commission. The Environmental Protection Agency and the National Oceanic and Atmospheric Administration also participate. The Panel is an ad hoc organization which is established when a mission utilizing a nuclear power system is being planned. The current Panel was established for the Galileo and the International Solar-Polar missions.

The Panel is supported by Sub-Panels sponsored by the three agencies. The Sub-Panels are currently organized in the areas of Launch-Abort (DOD), Reentry (NASA), Meteorology (DOE), Oceanography (DOE), and Biomedical/Environmental (DOE). The sub-panels are staffed by technical experts who are independent of direct responsibility for the various program activities. The Panel meets with the program elements to review the nuclear safety aspects of a proposed mission after issuance of the PSAR, the USAR, and the FSAR. The Panel and/or the Sub-Panels meet with the program elements on an ad-hoc basis during the course of the program as determined by the status of the program activity and the nature of the safety issues at hand. The continuing interaction between the Panel and Sub-Panels with the program assures that the Panel and Sub-Panel personnel are informed of the program events important to nuclear safety while the program is in progress.

After review of the FSAR and any other germane documents such as test reports and additional analyses provided by the program, the Panel prepares a Safety Evaluation Report. This report summarizes the Panel's risk evaluation and is provided to DOD, NASA, and DOE management. Assuming the acceptance of the risk and with the concurrence of the other two agencies the user agency proposes launch approval to the Office of Science and Technology Policy. Thus for Galileo, NASA will propose launch approval having obtained concurrence from DOD and DOE.

The independent safety review process conducted by the Panel has been in place since the mid 60's. The process has been used for review of diverse missions where spacecraft deployment has included earth orbit, lunar surface, Jupiter fly-by/deep space, Mars lander, and Jupiter/Saturn fly-by. The current missions include Jupiter orbit (NASA's Galileo Program), and solar exploration (the NASA/ESA International Solar Polar Program).

Conclusion

In conclusion, what I have tried to show is that the process for the safe launch of nuclear power systems in space is predicated on programmatic responsibility for

safe design and operations, independent review by an Interagency Nuclear Safety Review Panel, and decision making at the agency level and within the Office of the President.

Acknowledgments

Marvin Norin is the Deputy Director, Division of Safety, Quality Assurance, and Safeguards within the U.S. Department of Energy's Office of the Assistant Secretary for Nuclear Energy. He is also the DOE coordinator for the Interagency Nuclear Safety Review Panel.

References

Bennett, G. L. (1981) "Overview of the U.S. Flight Safety Process for Space Nuclear Power," *Nuclear Safety* 22:423–434.

Bennett, G. L., J. J. Lombardo, and B. J. Rock (1983) "U.S. Radioisotope Thermoelectric Generator Space Operating Experience (June 1981–December 1982)," 18th Intersociety Energy Conversion Engineering Conference, August 1983.

Kerr, T. B. (1983) "Procedures for Securing Clearance to Launch Reactors," in *Proc. of the Symposium on Advanced Compact Reactor System*, National Academy of Sciences, National Academy Press, Washington, D.C.

Space Nuclear Power Systems 1984
Edited by M. S. El-Genk and M. D. Hoover
© Orbit Book Company, Malabar, FL, 1985

Chapter 57

Mechanics of Space Nuclear Safety

Richard W. Englehart

NUS Corporation
910 Clopper Road
Gaithersburg, MD 20878

This paper uses current activities for the space shuttle launches of the Galileo Mission to Jupiter and the Ulysses Mission to describe the mechanics of nuclear safety. Both missions use the new General Purpose Heat Source in a Radioisotope Thermoelectric Generator. The paper includes failure mode and probability analyses for the launch vehicle, determination of accident environments in the vicinity of the nuclear system, testing of the response of the nuclear system in the various environments, and calculation of the radiological impact of any releases of radioactivity from accidents. These assessments are reviewed by the Interagency Nuclear Safety Review Panel and provide a basis for emergency planning and launch safety operations at the launch site. Such an approach has provided assurance of the safe application of nuclear power in space for the United States. Extension of these activities to missions using nuclear reactors is discussed.

Introduction

The conduct of a safety analysis for a space mission using nuclear power requires:

- Definition of potential mission accidents and probabilities;
- Determination of the types and severity of the resulting accident environments or stresses on the nuclear system;
- Testing of the nuclear system to obtain data on responses to the various accident environments;
- Organization of the information on accidents, probabilities, and system responses into event trees for each mission phase (phases oriented to human risk potential);
- Analysis of radiological risk using radionuclide environmental pathway and dose models and world wide data bases; and finally
- Appropriate emergency planning, launch safety preparations, and real time accident analysis and recovery capability.

The Interagency Nuclear Safety Review Panel (INSRP) reviews the status of information available on each of these areas during the Preliminary Safety Analysis Report review and initiates efforts on the part of subpanels to review test data and analyses as they develop. Later, updated and then final safety analyses are performed. This paper discusses each of these components of safety analysis and launch safety activities and reflects current efforts for the next launches of Radioisotope Thermoelectric Generators (RTGs) aboard the Galileo and Ulysses Missions.

Overview of Technical Aspects of Preparation of a Space Nuclear Safety Analysis Report

When an agency of the U.S. Government identifies and proposes a space mission utilizing a nuclear power source, the INSRP activities are initiated. INSRP requires the preparation of a safety analysis report by the Project (mission) and also performs its own independent safety evaluation.

There are three stages of safety analyses required, preliminary, updated, and final. These are usually characterized by increasing amounts of technical data supplied and also by feedback from one stage to the next reflecting safety concerns identified and design changes and analyses required to address them.

In the case of missions utilizing RTGs, DOE's Office of Special Nuclear Projects (OSNP) has the responsibility of design, production, and supply of the RTG and also of providing safety testing and analyses to INSRP for their consideration. OSNP has published Safety Guidelines for RTG heat sources which define safety objectives, test requirements, design goals relating to potential accident environments, and documentation required.

Present plans call for future launches of spacecraft containing nuclear power supplies to make use of the Space Transportation System (STS) or Space Shuttle. The safety analysis is directed to consideration of the possibilities and potential consequences of the various abnormal interaction modes among the launch vehicle, other propulsion systems aboard, and the nuclear power system. Therefore, one of the first tasks required in

developing the data base for a safety analysis is the identification of accident scenarios with associated probabilities and the determination of the associated environments to which the nuclear power supply may be subjected.

This work is being accomplished in support of Galileo and Ulysses by the NASA Project offices and working groups. These organizations are made up of experts from the member agencies and are supported by additional expertise from their contractors.

The Vehicle Level Working Group (VLWG) has complied data on the Shuttle and has performed failure mode and probability analyses for the STS and other boosters involved in Galileo and Ulysses (Backer 1981, Vedder and Brown 1982, J. H. Wiggins Company 1979, Kaukonen 1983, Batand 1983, and Makela 1983). These reports have been provided to INSRP, which independently evaluates them. Since the STS has little flight history, INSRP balances the theoretical failure rate analyses with practical experience with other vehicles to arrive at their own judgment of appropriate accident probabilities.

The Shuttle Blast Hazards Analysis Subcomittee has adapted its work in support of range safety to the estimation of explosion severity for accidents on or near the launch pad (Ullian 1983) for the STS. This effort makes use of the Project PYRO (Willoughby et al. 1968) and Project SOPHY (Elwell et al. 1967) work and applies extensive conservatisms. Their recommendations were presented to INSRP in a special briefing.

The Jet Propulsion Laboratory and the Air Force Weapons Laboratory have analyzed the various orientations of misoriented burn for trajectory insertion once in orbit as well as an orbital decay case and have carried those analyses through reentry breakup of the spacecraft and the time-altitude-temperature-velocity histories prior to impact on earth of the nuclear heat source.

The data provided by NASA (VLWG) form the basis for planning the Safety Verification Test (SVT) series test conditions for the new General Purpose Heat Source (GPHS) (Bronisz et al. 1983). These tests encompass the types of accident conditions which have been identified as possible and are for the purpose of compiling data on the behavior of the nuclear system in those environments. The primary objective is to learn if releases of radioactive material can occur, to determine under what conditions (thresholds) they might occur, and to characterize those releases for the parameters important to radiological consequences evaluation. Because the nuclear system (GPHS) is a new design, these tests have not yet been completed.

Whenever possible, flight quality production modules of the GPHS are used in the testing. One of the objectives of the GPHS design was to produce a modular system which could be tested in a full up configuration. The system is made up of identical modules. This is important for two reasons. First, the cost per module is significant, so testing one module instead of a complete system is more cost effective. Second, some test facilities such as a hypersonic wind tunnel have size limitations for the tested object. Where release of radioactive materials is possible, testing must be done under controlled and contained conditions. This is obviously not possible when conducting large-scale fire tests, explosion tests, and fragment tests. In these cases a fuel simulant is used, but the balance of the module is flight quality.

Testing philosophy is an important issue in compiling safety data. Because the test items are expensive and the tests and their evaluations are time consuming, it is not possible to run large numbers of repetitive tests to build statistics or to closely identify failure thresholds. Since the data are being used to provide the best estimates of radiological risk associated with proposed missions, an attempt is being made to conform test conditions to nominal accident environments where risk is likely. In some cases, the severity of an accident environment has a large range of uncertainty associated with it. An example of this is liquid and solid rocket propellant explosion overpressure and impulse. These parameters are highly susceptible to variations resulting from the nature of mixing of liquid propellants or the amount of damage to solid propellants before ignition. In these cases, it is important to attempt to identify failure thresholds. It is also important to get some estimate of the probability distribution of explosion severity.

The investigations discussed in the preceding paragraphs provide the basic system data to perform a risk assessment. In this context, risk is defined as the summation over all mission phases and accidents of the probabilities multiplied by the consequences of the accidents.

$$R = \sum_{f,a} P_{f,a} C_{f,a}$$

R = risk

f = mission phase

a = accident type

$P_{f,a}$ = probability of accident type a in mission phase f

$C_{f,a}$ = consequence of accident type a in mission phase f.

The analyses of accident consequences requires an additional data base (environmental) and various models to (1) describe the behavior of radioactive materials in the environment following accidental release and (2) calculate radiological impact.

Description of the Risk Analysis Process

The first step in the systematic analysis of mission risk is to define mission phases. It is convenient to define the phases relating to the radiological pathway

models to be applied in accident consequence analyses. For example, one phase is logically related to accidents on the launch pad or very nearby, including that time period when the launch vehicle is still over land and would impact on land if a failure occurred. The next, for the STS, would be the period during which a failure would lead to impact on near shore water, prior to the time the Shuttle Orbiter could separate and return to the launch site. Subsequent phases would be ascent to orbit, orbit, and trajectory insertion.

Next, for each mission phase, the sequence of operations is examined to identify and order potential failures and their consequences to build an "event tree." The data provided by NASA are used as input to this process for the initiating events for accidents, the potential resulting accident environments, and the associated probabilities. The event trees are carried through all the way to the branches resulting in a release of radioactivity to the environment (or to the first branch where it is clear that there would be no subsequent release). The safety test program results provide basic data to identify those branches of the event tree which would result in releases (source terms).

In the case of radioisotope systems, source terms may be postulated for some accidents in the form of vapor and/or particulate releases to the atmosphere at or near the launch pad and also if the system reenters the atmosphere and impacts on a hard surface under some conditions. The radioisotope systems are designed to survive reentry, so that no high altitude burnup is expected. For some accidents it may be postulated that some contamination of the near shore coastal environment at the launch site could result. Finally, it can be postulated that some accidents could result in intact modules in shallow or deep ocean waters, not recoverable.

For reactor systems, assuming that the reactor is not started up until the orbital phase of a mission, launch pad and ascent accidents would have minimal radiological consequences except for the case of accidental criticality. Depending on the design, this may be postulated to occur from explosion overpressure compression, impact on ground or immersion in water.

After a reactor has operated at design power even for a short time, the direct radiation field from the core would pose an acute radiation exposure hazard to persons in its vicinity. (Short zero power criticality tests prior to launch would not create significant amounts of fission products.) Therefore, one option which is considered a safety feature would be a core design which would disintegrate upon reentry (DOE 1982).

In general, space nuclear safety models are needed for upper atmospheric burnup, and dispersion of small and larger particulates, lower atmosphere dispersion, and shallow and deep ocean dispersion as well as pathway models leading to uptake and dose to man. These models are discussed in the next section.

Radiological consequences of accidents which may be postulated include

(1) Acute radiation syndrome from short-term exposure to radiation in the immediate vicinity of an accident,

(2) Somatic and genetic effects from lower level exposure in the vicinity surrounding an accident, and

(3) Longer term exposure-related somatic and genetic effects resulting from radioactivity which remains in the environment (not cleaned up).

The first category can generally be controlled by design and safety precautions. The second category can be addressed by emergency procedures and precautions in the area of the launch site and by prompt action in the case of other sites. The third category can be controlled by decontamination in the case of a localized accident, but not in the case of a widespread contaminating event such as upper atmospheric burnup.

Current radiation protection philosophy regards these categories as equivalent, even though the third category may imply extremely small individual radiation doses and unmeasurable effects, while the first two could result in measurable effects to specific population groups. Indeed, the third category can dominate mission risk calculations while the real concerns are the first two categories. It appears that there may be some movement toward the concept of deminimus radiation dose levels, which could resolve this incongruity.

Description of Technical Models

The Department of Energy Office of Special Nuclear Projects sponsors the development and maintenance by NUS Corporation of a series of volumes called the Overall Safety Manual (OSM), (NUS 1982). The OSM contains the models and data which have been used to perform the radiological consequence analyses for space nuclear missions in conjunction with risk assessments by NUS and others over the past twenty years. The OSM is continuously being updated with new data and models as the need arises. Most of the dispersion models are directly applicable to reactors, but reactor fission product and activation product generation and decay models, coupled with environmental pathway, dose, and health effect models are different from those used for RTGs. The reactor models which have been used are consistent with the Nuclear Regulatory Commission's guidance. The OSM has also been undergoing peer review by appropriate INSRP subpanels, whose comments will be used as guidance in the continuing update effort.

The Risk II Model

The models and data described in the OSM are linked together in a computer program called RISK II. With appropriate probabilities, source terms, and release types specified as input, RISK II performs the risk analyses for the launch area and worldwide reentry

RISK II COMPUTER PROGRAM

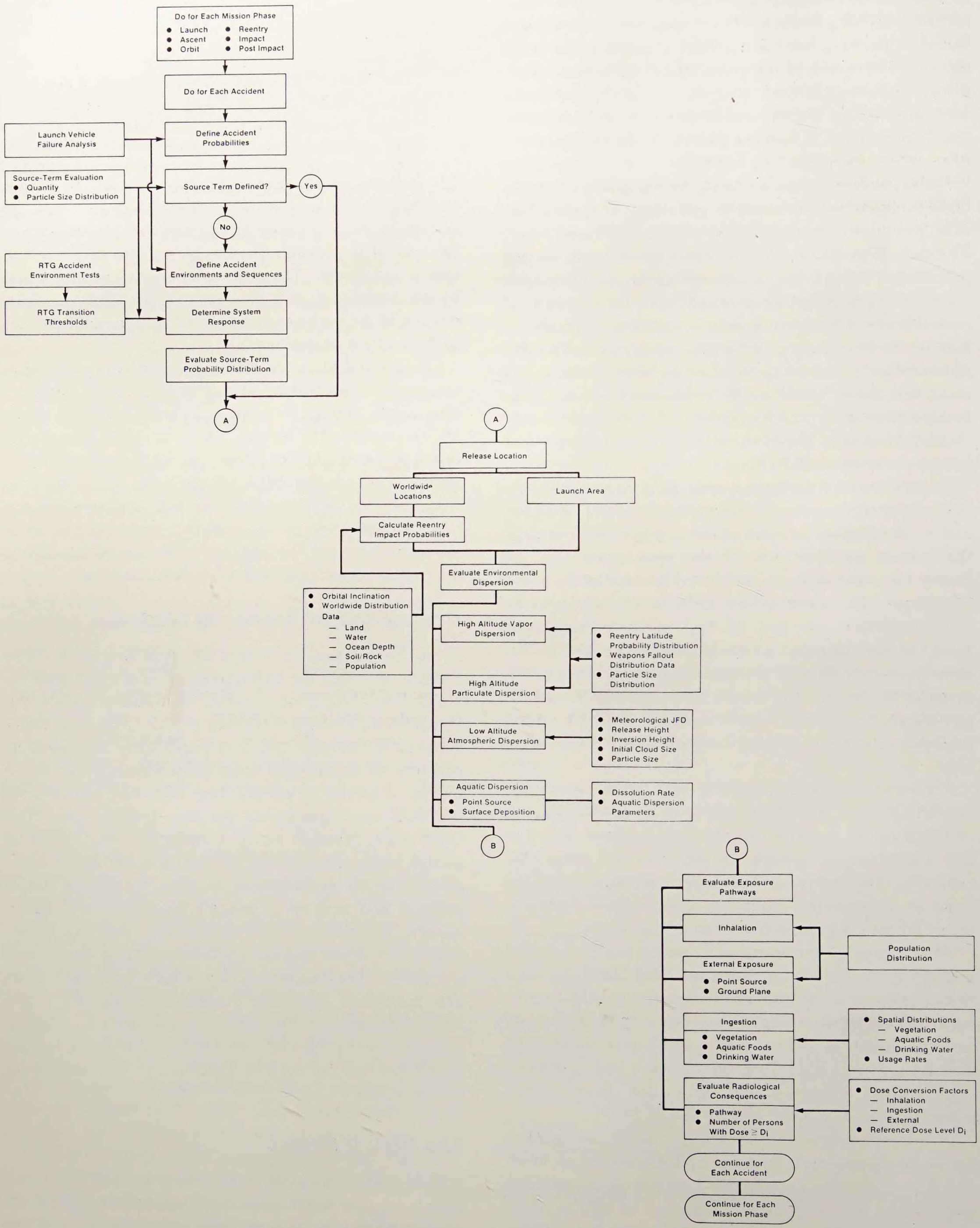


Figure 1 *Flow Chart for the RISK II Computer Program.*

related accidents consistent with the generalized flow diagram for risk analyses shown on Figure 1. For the purpose of these analyses worldwide data on populations, food production, meteorology, and oceanography have been compiled. The world's surface has been divided into 720 equal areas and data descriptive of each area are included in the OSM. During 1983, demographic and agricultural data within 20 miles of the Kennedy Space Center (KSC) shuttle launch pads have been updated (NUS 1983). These data are on a 2 acre resolution and show day- and nighttime worker, launch spectator, and general population distributions typical of shuttle launches. Also during 1983, the worldwide population density, elevation, and hard surface distributions have been compiled and correlated on a much finer grid.

The severity of impact conditions (impact speed and temperature) is dependent on the elevation of the impact. It is planned, in the near future, to refine the worldwide data base to a maximum cell size of approximately 4000 square miles and to incorporate software so that data under a particular orbital track can be called up. This is important for the ascent phase and also under real reentry conditions such as for Skylab or the COSMOS reactors when projections can be made for the time of reentry.

In the case of a postulated launch pad accident which releases radioactive vapor or particulates to the atmosphere, a Gaussian plume dispersion model, modified to include particle fall velocity, is used in conjunction with historical KSC meteorological data and demographic data to produce a probability distribution of the number of people exposed to several critical time integrated air concentration levels and the areas of several ground contamination levels. These concentration calculations are coupled to appropriate radiation dose models, the most significant of which (for plutonium) is an inhalation dose model. This model is a mathematical representation of the ICRP Task Group Lung Model with an extension to treat transfer of material from the lung to other organs of the body. Ingestion doses are calculated through vegetation contamination from deposition, edible vegetation crop density data, and consumption data, compiled worldwide and for the KSC area in the OSM. Other dose pathways treated are resuspension inhalation and direct radiation dose.

These models also apply in the case of worldwide random reentry and impact on a hard surface, resulting in a surface level atmospheric release. The exceptions are that worldwide population density data are used as well as atmospheric dispersion parameters for the worldwide data base which are related to the Koppen climatic system. In order to use these data, the probability of impacting a given worldwide meteorological, demographic, or surface type, knowing the orbital inclination, is calculated in the OSM using a random orbital decay probability model which relates the 720 equal area data base to time spent over the areas as a function of the latitude band covered. In the case of high altitude burnup, there is an upper atmospheric model based on measurements of weapons test debris and also a model for larger particulate fallout which can be coupled to an ocean dispersion model.

All of these models are coupled in RISK II. For a specific mission risk analysis, the analyst specifies the accidents, probabilities, source terms, and radiological pathways to be included in the run. The code handles all release types (high altitude, surface, and aquatic) at launch area and worldwide random locations. It considers all exposure pathways (inhalation, ingestion, and external) and cycles through each accident and mission phase. The output of RISK II includes the probability and number of persons calculated to receive radiation doses above specified levels for each postulated accident of the mission. An overall mission risk index is computed by summing the product of accident probabilities and the number of person-rem from each accident over all mission phases.

The RISK III Model

During the period of 1975 to 1980, the scientific community began to focus attention on the long-term health effects of radiation. This was due in part to attention that WASH-1400, the *Reactor Safety Study* (NRC 1975), received during this period. A review of DOE programs by the Mitre Corporation recommended that risk analyses of plutonium-fueled space nuclear systems consider the long-term behavior of plutonium in the environment and associated health effects following postulated accidents.

In response to this need, NUS began development in 1980 of an overall mission risk model that specifically addressed long-term health effects. This effort resulted in a model called RISK III. The approach to risk and the sub-models incorporated into RISK III differed entirely from those in RISK II. The reason for this vast difference is due to a single assumption made in RISK III that a linear dose response model (without a threshold level) was appropriate for use in calculating health effects. This assumption had also been adopted by the U.S. Nuclear Regulatory Commission, Environmental Protection Agency, and the International Commission on Radiological Protection. However, a linear dose response model implies that very low doses to large population groups could be as important as high doses to small population groups in terms of health effects and risk. This required that RISK III consider many more exposure pathways, larger segments of the exposed population, and longer time periods than considered in RISK II.

Other differences in RISK II and RISK III are evident when the distribution of dose versus number of persons exposed resulting from a given postulated acci-

dent is considered. RISK II requires evaluating the actual distribution curve in the region of high doses in order to determine the number of persons receiving doses above specified levels. This is accomplished using dispersion models to determine the relative spatial distribution of people (or food supplies) and plutonium concentrations. RISK III requires an integration of the entire dose distribution curve to calculate population dose which is then converted to health effects in terms of excess cancer fatalities. A second critical assumption is made in RISK III that considerably simplifies the integration of the dose distribution curve. It is assumed that the population density and food sources are uniformly distributed throughout the contaminated region. The resulting population exposure then becomes directly proportional to the plutonium source term, and independent of the distribution of plutonium within the contaminated region. Dispersion models required in RISK II are no longer necessary in RISK III.

The problem with performing risk analyses for space reactors is the large number of fission radionuclides that must be handled and the time variation associated with the source terms following reactor shutdown and disassembly. NUS recognized that RISK III would be ideally suited for such analyses because these problems could be accommodated in the RISK III structure. Therefore, a development effort took various features of the RISK III model and incorporated them into an interim computer code that considers long-term intercompartment transfer of released radioactivity only for certain situations, such as those associated with high altitude releases, ground contamination, and fuel dissolution in aquatic environments. Secondary environmental transfers, such as the transport of radioactivity in contaminated watersheds by erosion to rivers and then to shallow and deep ocean, were not incorporated. This development effort resulted in an interim version of the RISK III model suitable for use in risk analyses of both plutonium-fueled and fission-reactor space nuclear systems in terms of long term health effects (Bartram and Dougherty 1981 and Bartram et al. 1981).

Launch Safety

The safety analysis activities described in the earlier parts of this paper provide a basis for the INSRP risk assessment which is sent forward in the launch approval decision process. The capability for real-time launch accident assessment and accident response should also be an important ingredient in the decision process, especially in cases where accidents could have radiological consequences which extend beyond the immediate area of the launch pad. For example, if the safety analyses include postulated accidents in which an airborne puff of radioactive vapor or particulates could be transported by winds into the viewing area, nearby populated areas, and agricultural areas, then the capability should exist to make use of current meteorological data and the safety analysis estimates of radioactivity releases from the various postulated launch pad accidents to estimate radiation doses and contamination levels as a function of location and time as the puff release disperses.

This capability exists and has been provided by NUS, making use of the Kennedy Space Center WINDS (meteorological data) network, for past launches for RTGs from KSC. This capability is currently being upgraded, making use of a system developed by NUS for the nuclear electric utility industry in response to post-Three Mile Island emergency response capability requirements of the Nuclear Regulatory Commission. The new model is a three-dimensional model which will provide, on a near-real-time basis (in minutes), plume dimensions and location, and isopleth displays of time integrated air concentrations. It accounts for meteorological variability, multiple met station inputs, and the possibility of a sea or land breeze condition, among other factors.

The system will be installed on a KSC computer and run from the Radiological Control Center (RADCC) established for these launches at KSC. Back-up capability exists at NUS Corporate Headquarters using a separate more simple model developed by the DOE Savannah River Laboratory.

Information from the running of these models prior to a launch provides guidance to those responsible for positioning of radiation monitoring teams and would also provide projections which would be useful to make decisions for appropriate emergency response in the case of an actual accident resulting in the release of radioactive material. The demographic and land use data (NUS Corporation 1983) includes the numbers and location of residential, occupational, and observer populations for both day time and night time launches of the Space Shuttle at KSC.

Conclusions

The mechanics of space nuclear safety include failure mode and probability analyses for the launch vehicle, determination of accident environments in the vicinity of the nuclear system, testing of the response of the nuclear system in the various environments, and calculation of the radiological impact of any releases of radioactivity from accidents. These assessments are reviewed by the Interagency Nuclear Safety Review Panel and provide a basis for assuring the safe application of nuclear power in space.

Acknowledgments

This work was performed at the NUS Corporation under contract to the U.S. Department of Energy.

References

Backer, J. B. (1981) *Space Shuttle Range Safety Hazards Analysis*, Technical Report No. 81–1329.

Bartram, B. and D. Dougherty (1981) *A Long Term Radiological Risk Model for Plutonium Fueled and Fission Reactor Space Nuclear Systems*, NUS 3845.

Bartram, B., D. Dougherty, and S. Tammara (1981) *TDOS Computer Code Users' Manual*, NUS 3851.

Batand, B. U. (1983) *Identified Shuttle/Centaur Airborne Hazards for the Radioisotope Thermoelectric Generator Safety Study*, General Dynamics Report GDC-SP-83-005.

Bronisz, S. E., R. W. Zocher, and C. M. Seabourn (1983) *General Purpose Heat Source Safety Verification Test Plan*, Los Alamos National Laboratory, MST-5-C-83-18.

DOE (1982) *Nuclear Safety Criteria and Specifications for Space Nuclear Reactors*, OSNP-1.

Elwell, R. B., O. R. Irwin, and R. W. Vail, Jr. (1967) *Project SOPHY—Solid Propellant Hazards Program*, AFRPL-TR-67-211.

Kaukonen, E. K. (1983) *Centaur G Prime Vehicle Description for the Radioisotope Thermoelectric Generator Safety Study*, General Dynamics Report GDC-SP-83-024.

Makela, E. (1983) *Galileo Mission Centaur G Prime Reliability Analysis for the Radioisotope Thermoelectric Generator Safety Study*, General Dynamics Report GDC-SP-83-005.

Makela, E. (1983) *International Solar Polar Mission Centaur G Prime Reliability Analysis for the Radioisotope Thermoelectric Generator Safety Study*, General Dynamics Report GDC-SP-83-005.

NUS Corporation (1982) *Overall Safety Manual*, U.S. Department of Energy (4 Volumes).

NUS Corporation (1983) *Kennedy Space Center Demographic and Land Use Study*, U.S. Department of Energy.

Ullian, L. J. (1983) *Activities of the Launch Abort Subpanel for the Galileo and Solar/Polar Mission*, Meeting Minutes, Feb., May, June 1983.

U.S. Nuclear Regulatory Commission (1975) *Reactor Safety Study*, WASH 1400.

Vedder, J. D. and R. H. Brown (1982) *Space Shuttle Data for Nuclear Safety Analysis*, JSC-16087, Revision 1.

J. H. Wiggins Company (1979) *Development of STS Failure Probabilities, MECO to Payload Separation*, Technical Report No. 79-1359.

Willoughby, A. B., C. Wilton, and J. Mansfield (1968) *Liquid Propellant Explosive Hazards*, AFRPL-TR-68-92.

Space Nuclear Power Systems 1984
Edited by M. S. El-Genk and M. D. Hoover
© Orbit Book Company, Malabar, FL, 1985

Chapter 58

SNAP-10A Aerospace Nuclear Safety A Good Foundation for the SP-100 Program

R. B. Harty and J. A. Hartung

Energy Systems Group
Rockwell International
Post Office Box 309
Conoga Park, CA 91304

As part of the SNAP-10A flight test program, a comprehensive aerospace nuclear safety program was conducted. The objectives of this program were to evaluate and control the nuclear hazards associated with the transportation, launch, operation, and disposal of space nuclear reactor power systems, and to develop methods and designs to assure their radiological safety. The program consisted of several analytical and experimental activities that included reactor disintegration, fuel rod reentry burnup, critical configurations, reactor transient behavior, mechanical and thermochemical incidents, end-of-life shutdown, and disposal mode studies. This paper reviews the analytical and experimental activities performed in each of these areas as a helpful basis, or stepping stone, for the SP-100 Aerospace Nuclear Safety Program.

Introduction

In April 1965, the SNAP-10A with a reactor heat source and SiGe thermo-electric power conversion system was successfully launched and operated in space. In support of this program, an Aerospace Nuclear Safety Program was conducted to assure public and worker safety. This program provided valuable information to support analyses performed for the Preliminary and Final Safety Analysis Reports. This paper summarizes that Aerospace Nuclear Safety Program as a helpful basis, or stepping stone, for the SP-100 Aerospace Nuclear Safety Program.

Aerospace Nuclear Safety Program

The objectives of the SNAP-10A Safety Program were to evaluate and control the nuclear hazards associated with the transportation, launch, operation, and disposal of SNAP systems, and to develop methods and designs to assure radiological safety. The program consisted of several analytical and experimental activities:

- Reactor disintegration,
- Fuel rod reentry burnup,
- Critical configurations,
- Reactor transient behavior,
- Mechanical and thermochemical incidents,
- End-of-life shutdown, and
- Disposal mode studies.

The activities performed in each category are summarized below.

Reactor Disintegration

Safe disposal of a reentering reactor is accomplished if the reactor structure disintegrates and releases the fuel at a sufficiently high altitude for it to melt and disperse. Thermal analyses of SNAP designs supported by experiments were conducted at Energy Systems Group to determine if this disposal mode was operative.

Preliminary Theoretical Analyses

Preliminary analytic studies described the general characteristics of a SNAP reactor reentering the atmosphere and helped define and design experiments for improving the characterization and for substantiating analytical techniques. The system considered was primarily the SNAP-10A-Agena D reactor and vehicle. The aerodynamic and inertial characteristics of the system, reentering satellite trajectory, reentry attitude and oscillation, stagnation and local aerodynamic heat rates, flow regimes, and failure modes were studied.

Initial Wind Tunnel Tests

To predict the disintegration of space reactor systems along their reentry trajectories required establishing the magnitude of the hypersonic heat transfer rates. This task could not be done by theoretical work alone, since the available hypersonic boundary layer theory was limited mainly to relatively clean aerodynamic shapes.

Wind tunnel tests generated comparative laminar, hypersonic boundary layer heat transfer data for the irregularly shaped envelope of the SNAP-10A reactor for various altitudes and angles of attack. The results were used in predicting the disintegration and ablation of SNAP-type reactors during reentry.

The tunnel tests produced a simulated reentry environment for periods of 1 to 10 ms. Scale model SNAP-10 reactors coated with thermopaint were tested at simulated flight environments; relative surface heat transfer rates were indicated by the discoloration of the paint. Two models were 1/50 scale for the SNAP-10A-Agena vehicle and full scale and 1/4 scale for the components. The heat transfer data from the tunnel tests were in the form of color number contours for several components of the reactor.

Reactor Flight Demonstration

A full-size, nonradioactive model of the SNAP-10A reactor was high-altitude flight tested to investigate aerodynamic heating effects and to demonstrate that space reactors can be designed to break apart and disintegrate during reentry. The flight test, called Reentry Flight Demonstration 1 (RFD-1), was conducted in May 1963 using a NASA Scout booster to carry the payload, which consisted of the reactor model and a reentry vehicle that contained telemetry and recovery equipment. The suborbital flight path had an apogee of 490,000 ft and a range of 800 n.mi. Valuable telemetry data were obtained during the descent.

Figure 1 summarizes the flight. Telemetry reception was good until ~350 s after liftoff, when the ionized gas layer that normally surrounds reentry bodies caused loss of the radio signals. The data received before rf blackout indicated significant temperature rises at the instrumented locations and separation of the reflectors as predicted. The instrumented test model was a full-scale replica of the SNAP-10A reactor, but without fuel inside the core vessel.

Heating rates for the various components calculated from the thermocouple (T/C) data when compared to equilibrium flow theory showed the theory to not be well founded. An intensive study of aerodynamic heating in nonequilibrium flow and in the transition regimes between free-molecule and equilibrium flow was initiated because of the results of this test.

Improved Reentry Analysis

The analysis of the disintegration of the SNAP-10A-Agena during reentry was improved by using more refined data and methods for calculating aerodynamic heating rates and their effects on structural components of the reactor and vehicle. Aerodynamic heating rates obtained from the measured temperature histories of the instrumented components of RFD-1 were applied to the SNAP-10A reactor in an orbital decay trajectory, with basic corrections for differences in velocity and time of descent through various altitudes. The exact altitude of reflector ejection was shown to have little influence on the altitude of vessel melting provided the NaK was released soon enough.

A detailed thermal model was devised to calculate the altitude at which the reactor would separate from the power system. Local heating rates were based on the results of the wind tunnel tests. A similar analysis was made for the disintegration of the reactor vessel.

Based on new data and the improved analysis, the following conclusions were drawn:

- During reentry, the Agena vehicle will oscillate about

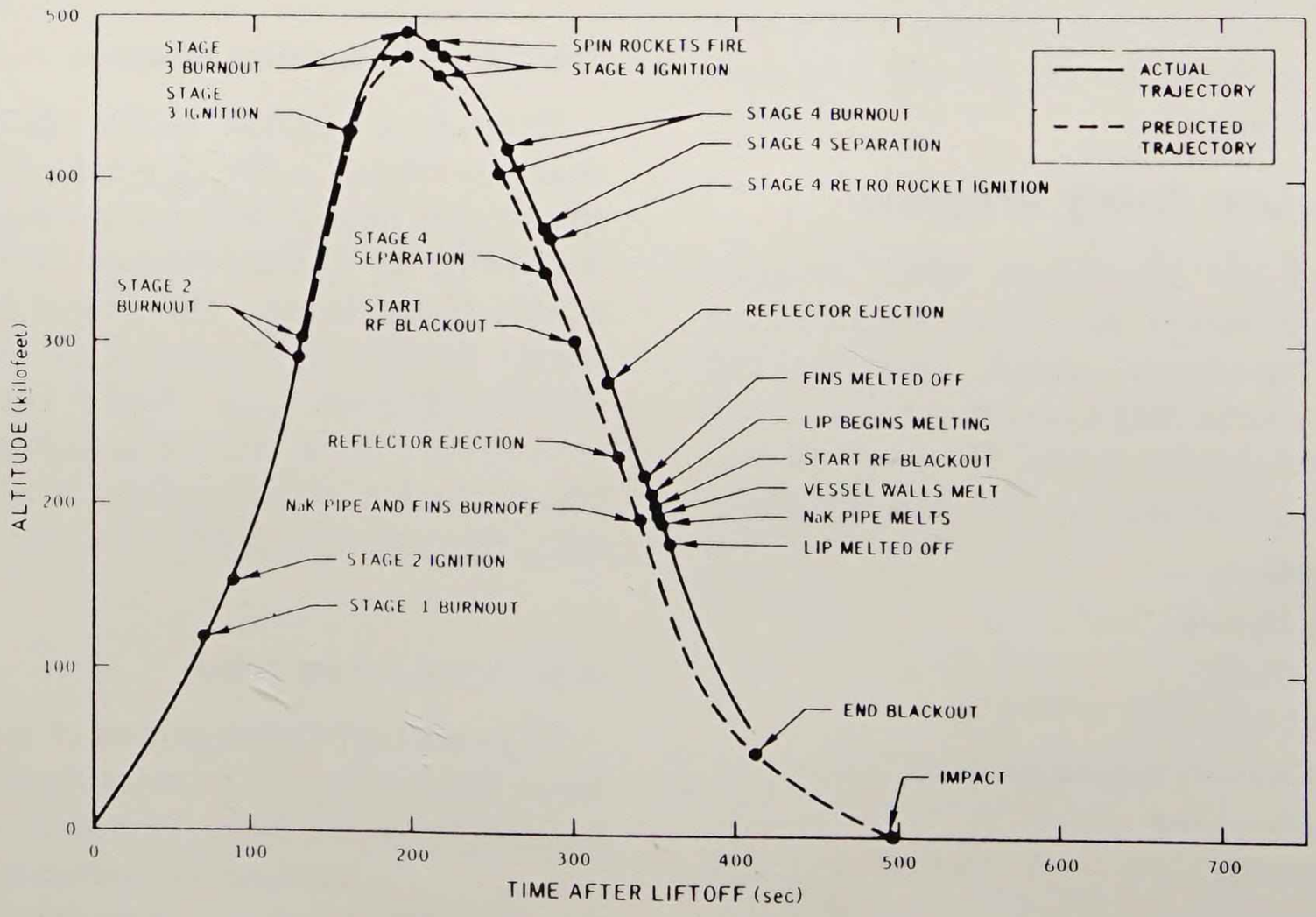


Figure 1 *Reactor Flight Demonstration Trajectory.*

an approximately nose-first attitude, with the amplitude of the oscillations tending toward smaller values as the vehicle descends. Tail-first reentry is impossible because the vehicle is aerodynamically unstable in a tail-first attitude.

- The external components of the SNAP-10A system will begin to disintegrate by melting at altitudes above 300,000 ft. Portions of the vehicle will fail at altitudes above 280,000 ft, and the reactor will separate from the vehicle at an altitude above 260,000 ft.
- The walls of the reactor vessel will melt away, releasing the partially melted remains of the top and bottom heads and allowing the core assembly to fall free at an altitude above 237,000 ft.

Self-Welding Experiments

Final shutdown of the SNAP reactor requires that the external beryllium reflector be ejected away from the core vessel. This might occur before reentry or the reflector might act as an ablative shield to the core and prevent the disintegration of the nuclear fuel rods. Although designed to separate from the core vessel and reactor assembly, thermal growth might cause the reflector assembly to be in contact with the core vessel during full-power operation of the reactor. This condition, in the combined environments of space vacuum, high temperature, and radiation, could cause the reflector to adhere or "self-weld" to the core vessel.

A special test program was conducted to determine the adhesion that could occur between the Type 316 stainless steel vessel and the beryllium reflector when subjected to the worst-case enviromental conditions. Evaluations were also made of the effect of coating the contacting surfaces with a thin film of colloidal graphite to prevent adhesion. Eight tests between Type 316 stainless steel and beryllium were conducted: four for 10,000 h and four for 5,000 h. In each group of four, two were coated with the colloidal graphite and two were base metal. Each test combination was tested under vacuums of 10^{-7} and 10^{-9} Torr with the samples at 1000°F and 100 psi continuous load on the contact surface. In each case where the contacting surfaces had been coated, adhesion was very small or immeasurable. But the bare, uncoated surfaces grossly adhered to each other from contact welding.

Extensive screening of over 200 material combinations established that adhesion will be absent or minimal if dry film lubricants, such as MoS_2 plus graphite, are used as one of the contact surfaces or between metal contact surfaces. But if bare metals are allowed in contact, a five-fold increase in adhesion forces can be expected.

Reactor Ablation Disintegration Experiment (RADE)

RADE was conducted to measure the aerodynamic heat flux to the complicated geometry of SNAP reactors and to demonstrate the capacity and accuracy of the analytical techniques used in the reactor disintegration analysis. Half-scale models of the SNAP-10A (RADE-A) and SNAP-8 (RADE-B) nuclear reactor configurations were tested in the NASA Ames hyperthermal wind tunnel under simulated atmospheric reentry conditions. Surface heat flux measurements were made with calorimeter models employing asymptotic calorimeter heat sensors. The experimental RADE models were ablated at both 0° and 30° angles of attack in the flow stream. The temperature response of the models to the aerodynamic heating was obtained using strategically mounted T/C's.

High-speed motion picture film coverage during each test provided a detailed visual description of the sequences of events during reactor ablation disintegration. These events clearly defined the meltdown and mode of disintegration of the reactor components under simulated reentry conditions. Post-test analysis showed that considerable welding between the upper grid plate and the fuel element bundle and between fuel elements probably would occur during reentry.

A computer code, the Thermal Analyzer Program (TAP), was developed to represent a 180° portion of each RADE experimental model configuration for both the head-on (0°) and 30° angle-of-attack test positions. The good agreement between the test data and the analytical code demonstrated that the preablation temperature response of SNAP reactors reentering the Earth's atmosphere could be accurately predicted.

Aerodynamic Heating Experiment

Reentry aerodynamic heating distributions for the SNAP-8 configuration were obtained based on hypersonic shock tunnel experiments conducted in Cornell's 48-in. hypersonic shock tunnel. The heat transfer correlations were determined as a function of angle of attack from 0° to 70°. The local aerodynamic heating factors for the 0°, 30°, and 70° angle-of-attack cases obtained in this experiment formed the basis of the heating distributions used in analytical calculations in which the shadow shield was attached to the reactor.

The aeroheating model was 1/5 scale. Test conditions were set to a simulated altitude of 250,000 ft and a free-stream Mach number of 18.4 in a hypersonic, continuum flow regime. In general, all heat transfer trends were substantiated by theory.

SNAP-8 Analysis

An analysis to simulate the thermal behavior of a SNAP-8 reactor system during reentry was performed to determine whether sufficient ablation would occur to release the reactor core at an altitude sufficient to ensure the complete burnup of the fuel elements in the upper atmosphere. Unfortunately, the analysis concluded that it would not.

Fuel Rod Reentry Burnup

Arc-Jet Tests and Analysis

Arc-heated, hyperthermal wind tunnel (arc-jet) tests were performed at Rockwell to provide experimental support for formulating an analytical description of the SNAP fuel rod reentry behavior. Fuel rod meltdown calculations were made for orbital reentry.

Examination of test specimens involved microstructural analysis with conventional metallographic techniques and spot chemical analyses. After preparation, the sections were examined, and photomicrographs and macrographs of significant structures were taken. Chemical sampling was then used to provide information on the distribution of elements within the section.

The effort led to the following general observations and conclusions:

- In the sectioned specimens, the concentration of hydrogen increased with the distance from the heated surface and from cracks within the specimen.
- The hydrogen was lost so that discrete interfaces were formed between the phases present.
- The zirconium-oxygen reaction at the surface was apparently preferential to the reaction of zirconium with nitrogen.
- The material in the vicinity of a molten surface was always devoid of hydrogen.

Rod Burnup Analysis

The transient behavior of $UZrH_x$ SNAP reactor fuel elements under atmospheric reentry conditions was analyzed to describe the conditions necessary for burnup and dispersal of the radioactive fuel material. Trajectory transient calculations were made for SNAP-10A reactor fuel elements released from the reactor vehicle at selected altitudes between 200,000 and 400,000 ft. The aerodynamic heating, transpiration cooling, and chemical reactions of the fuel with air were analyzed to determine the net surface heat flux to the elements. An analytical model was developed with which simultaneous solutions of the heat and hydrogen transport equations were obtained, including variable material properties and material phase changes. Data from experimental tests on the transient heating and burnup of the fuel material in a hyperthermal wind tunnel were used to correlate the analytical description. Given the uncertainties in parameters, the agreement was found to be good.

Measurements of Thermophysical Properties

The thermal properties of SNAP fuel were systematically investigated to obtain the reliable thermophysical properties data needed to describe its behavior during reactor operation and reentry. Heat capacity, thermal diffusivity, electrical resistivity, and thermal conductivity measurements were made on the SNAP fuel alloy, Zr-10U, as well as on this alloy hydrided to H/Zr atom ratios of 0.50, 1.26, 1.58, 1.81, and 1.90.

Advanced Arc-Jet Tests

Experimental support for SNAP fuel element reentry burnup analytical programs and associated fuel particle disintegration studies was provided by a series of ablation tests on actual fuel material (nonenriched uranium) in a partially simulated reentry environment. Data were obtained on the transient temperature and hydrogen diffusion behavior, surface catalytic effects on heat flux, and ablating particle size distributions and compositions.

The test series evolved from the results of previous experimental programs and from the development of analytical descriptions of the thermochemical behavior of the fuel material. The testing was necessary to provide data for the use in, and verification of, a complete description of SNAP fuel behavior during reentry.

The test series was important for the large number of specimens tested and the flow conditions and configurations used. The abundant data gave confidence to the conclusions. The arc-jet test series was performed in a Rockwell hyperthermal, electric-arc wind tunnel capable of producing nominal Mach-3 gas flows at extremely high temperatures. Valuable data on fuel behavior during reentry were obtained.

Particle Ablation Model

A digital computer program was written to describe the behavior of liquid metal particles in both reentry and laboratory environments. Heat, mass, and momentum transfer mechanisms were described. The program provided a means of studying particles formed from the reentry ablation of SNAP reactor fuel elements and for providing analytical support to SNAP fuel particle disintegration experiments. The code determined the temperature, radius, and velocity of a particle as functions of time.

The given particle was assumed to be initially at a temperature high enough for oxidation by a limited oxygen supply (linear oxidation). The particle was heated by aerodynamic and oxidation heating and cooled by convection, radiation, and evaporation. The oxide of the particle was assumed to form as a coating, which was assumed to evaporate, followed by evaporation of the unoxidized material, if exposed. Fission products were assumed to evaporate directly with the oxide, followed by fractional distillation from the unoxidized material, if exposed.

Particle Ablation Analysis

The behavior of reentering fuel particles from ablating SNAP-10A and SNAP-8 fuel rods was analyzed statistically, using the program described above. Sensi-

tivity coefficients and uncertainties in the final radius resulting from variations in individual parameters were calculated. A parametric study was performed to indicate the sensitivity of particle dimension and release conditions to the percent of total aerodynamic heating received in the transition regime.

Critical Configurations

Water Immersion Experiments

The water immersion experiments were performed to determine the reactivities of SNAP-10A and SNAP-8 reactor cores immersed in water and to test the effectiveness of devices designed to maintain subcriticality. Initial experiments determined the excess reactivity of a water-reflected, bare SNAP-10A core to be $\$6.4 \pm 0.6$. The additional worth of internal water was estimated to be $\$7.2 \pm 0.7$. Simple poison sleeves surrounding the core were found to render the water-reflected dry core subcritical, but not to prevent criticality in the water-flooded-and-reflected case.

Subsequent tests showed that:

- A combination voids and poison sleeve (designated a shipping sleeve) surrounding the bare core was capable of maintaining SNAP-10A and SNAP-8 reactor cores subcritical when they were immersed in and internally flooded by water.
- Combination void and poison filler blocks that fill the four control drum void and cover two radial beryllium faces of the reactor are capable of maintaining a beryllium-reflected SNAP-10A reactor subcritical when it is immersed in, but not internally flooded by, water. Such a device was used when working around the reactor during erection on the Agena launch vehicle. It was removed before launch.

Intrinsic Subcriticality Experiments and Analysis

The water critical experiments demonstrated the feasibility of using void-poison sleeves and void-poison filler blocks to preclude accidental criticality of SNAP reactors due to water immersion and/or human body reflection during reactor shipment, ground handling, and prelaunch checkout operations. But such devices did not preclude accidental criticality during a launch abort into water. Consequently, the concept of intrinsic water subcriticality (IWS) was developed to effectively safeguard against accidental criticality during the launch phase and to simplify core shipment.

The IWS concept provided safety in a water environment, yet maintained adequate core performance under normal operating conditions. Two methods were investigated in detail:

- Use of highly spectrum-dependent thermal-resonance neutron absorbers in the fuel elements and in the core reflector interface region and
- Use of modified core and reflection geometries.

The first method takes advantage of the shape of the low-thermal-energy neutron cross-section characteristic of gadolinium and other rare-earth elements. The special shape of this cross section increases the poison effectiveness of the material in a water-immersed SNAP reactor relative to that in the operational mode. This occurs because the water softens the thermal neutron spectrum. The reactivity change that results from increasing the poison effectiveness can be sufficient to render a reactor subcritical in water while maintaining operational capabilities. In addition, burnout of the poison in the operational mode provides compensation for normal reactivity losses. Thus, prepoisoning a SNAP system produces two desired results: (1) an engineered safeguard against launch aborts and (2) a burnable poison for normal operation.

A second method exploits the high neutron leakage characteristic of SNAP reactors and the superior neutron-reflecting properties of beryllium relative to water. In general, the core geometry is designed to make the reactor configuration subcritical in water yet supercritical when beryllium reflected. This has the advantage of permanent water immersion safety (the reactor is subcritical in water whether the reactor is clean or has been operated). It has the disadvantages of higher system mass and lower power lifetime capabilities.

Initial experiments were performed to provide data for evaluating the use of natural gadolinium poison and core geometry changes as potential techniques for the design of SNAP reactors that would be subcritical when immersed in water, yet retain their operational capabilities. Reactivity worths of various concentrations of gadolinium, applied to the surface of the fuel elements and separately to the surface of the core vessel, were measured in both the water-immersed and the operational environments. Critical dimensions in water, as a function of core geometry, were also determined.

Analytical studies to evaluate the system weight and power lifetime penalties associated with each IWS technique showed the penalties to be significantly more severe for core geometry changes than for a prepoison. They also showed that the dominating isotope, ^{157}Gd, had a burnout rate too rapid for use as a prepoison. Subsequent experiments to evaluate the effectiveness of ^{155}Gd, ^{149}Sm, and ^{151}Eu as prepoison materials, which included tests to determine the effect of the prepoison on the reactor prompt-temperature coefficient of reactivity, showed that the negative magnitude of the coefficient was reduced by gadolinium and samarium and increased by europium.

It was concluded that none of the prepoison materials should be used alone in the quantity (approximately \$8) required for sustained (20,000 h) SNAP reactor operation. The preferred approach would be to use combinations of two or three of the rare earths.

Reactor Transient Behavior

SNAPTRAN-3 Experiment

The SNAPTRAN-3 destructive experiment was conducted at the National Reactor Testing Station (NRTS) as one of the major projects in the Aerospace Safety Program. In this test, a NaK-filled SNAP-10A reactor was submerged in water and subjected to a \$3.60 step transient above critical, which was terminated by core disassembly.

The SNAPTRAN-3 reactor consisted of a standard SNAP-10A core containing 37 fuel-moderator ($UZrH_x$) elements. The elements were positioned within the core vessel with upper and lower grid plates. The reactor vessel was positioned in an environmental tank constructed of steel-reinforced concrete, 14 ft in diameter by 10 ft deep. Since the reactor vessel lacked external beryllium reflectors and control drums, reactor power was controlled with a cylindrical binal (B_4C) sleeve. The binal control sleeve was provided with two in-line drive systems: (1) motor drive for low-speed movement (2.3 in./min) and precise positioning and (2) a pyrotechnic actuator for rapid removal of the sleeve (approximately 90 ft/s) for the destructive testing.

Reactivity as a function of time was obtained from power history (energy probe) data by solving the reactor-kinetics equations. Continuous energy deposition was indicated up to fuel disintegration or massive mechanical disassembly. Temperatures measured at disassembly ranged from 1800 to 2000°F. Photographs showed the vessel to bulge at the center, becoming circular as expansion proceeded (Figure 2). Radial and axial temperature distributions obtained from fitted energy probe data were integrated to obtain the total core energy release of 32.5 ± 3.6 MW · s. A fuel-moderator temperature coefficient of $-0.22¢/°F$ up to about 1400°F was derived from the data. A reactivity feedback coefficient of expansion was derived using expansion photographs. The value was $-\$6.65$/in. up to 0.12-in. expansion, and $-\$11.05$/in. thereafter.

Specific results calculated using theoretical models gave good agreements for power, energy, inverse period, reactivity, and maximum radial expansion as functions of time. Improved analytical models based on SNAPTRAN-1 and -2 experimental results (described below) gave a temperature coefficient of $-0.24¢/°F$, in good agreement with the experiment. An anlysis made of the remains of intact fuel elements showed that fuel disintegration was caused by the generation of hydrogen pressure.

Electrical Pulse-Heating Experiments

The specific heat, thermal expansion, and hydrogen evolution rates for $UZrH_x$ fuel material were determined using electrically induced heating rates. Composition of the fuel was varied from an H/Zr ratio of 0.50 to 1.81. Heating rates to be studied ranged from 7000 to 100,000°C/s. Twenty-one specimens were pulse heated during the tests. The experiments were grouped according to the initial heating rate: rates greater than 80,000°C/s were in group I, from 20,000 to 80,000°C/s were in group II, and below 20,000°C/s were in group III. Specimens in group I exploded between 20 and 30 ms without evolving hydrogen; the specimens in groups II exploded before 40 ms and began evolving hydrogen just before failure; specimens in group III evolved hydrogen over a longer period and exhibited characteristics in three time regions due to phase changes.

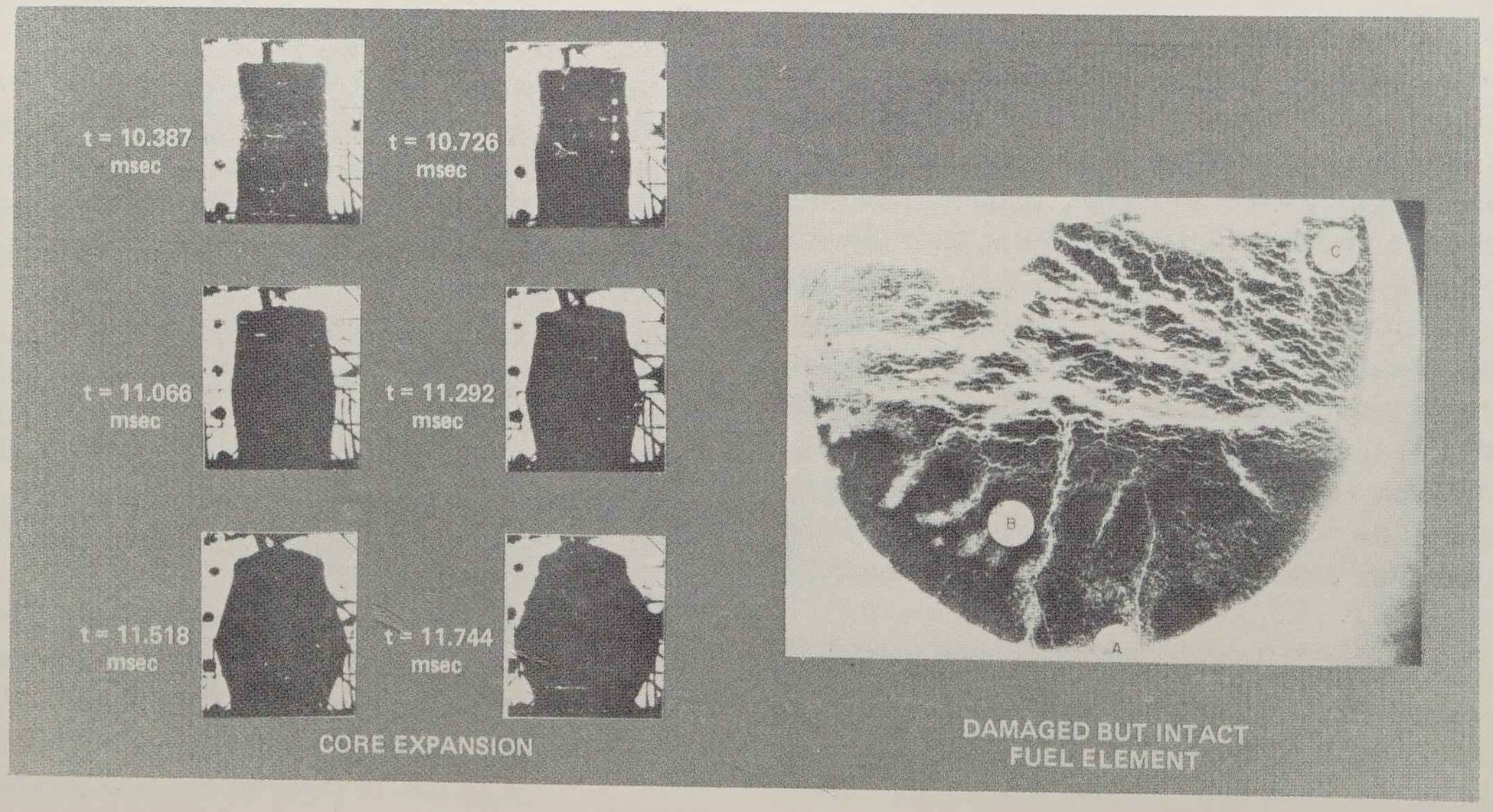


Figure 2 *Core Vessel during Expansion.*

Transient Reactor Test (TREAT) Nuclear Test Capsule Experiment

The TREAT experiment was performed to measure the hydrogen diffusion coefficient, thermal expansion, and burnup of $ZrUH_x$ fuel at high temperatures. This was done using a series of neutron bursts obtained in the TREAT reactor at NRTS.

Each of the 17 capsules prepared for this test series consisted of a 3-in.-OD by 5-in.-long by 0.188-in.-thick stainless steel shell with an internal tantalum foil used as a heat shield. These capsules were instrumented for temperature and pressure. Suspended inside each capsule was a 1.212-in.-diameter by 0.100-in.-thick wafer of $ZrUH_x$ that contained 10 wt. % ^{235}U. Mounted against the edge of the fuel wafer was a linear displacement tranducer for measuring thermal expansion of the fuel. These prepared capsules received from 1 to 5 bursts in the TREAT reactor.

The fuel varied from intact to powdered and granulated form after irradiation. For those capsules that yielded temperature data, values ranged from 1100 to $>$ 1500°C. Postirradiation hydrogen analysis was made on each of the fuel wafers. Final values ranged from 0.14 to 1.50 wt. % for all samples originally containing 1.8 wt. %. The burnup analysis was obtained by counting and integrating over the 1.60-MeV Ba-La 140 photo peak. Samples receiving a single TREAT burst showed $6.7\ (\pm 0.6) \times 10^{-6}$ at. % burnup.

Fission Product Release Tests

Experiments were performed to determine the fission product release from SNAP-10A $UZrH_x$ fuel samples. No prior experimental data were available for this material, and extrapolation from other materials was not possible because of the complex solid-state processes involved.

Twelve tests were run using six samples with standard SNAP-10A Hasteloy-N clad fuel and six samples with no cladding. Samples were irradiated in the materials testing reactor (MTR) of NRTS for the equivalent of one year of operation at 60 kW. Later, each sample was heated in a closed induction furance to temperatures from 2000 to 3500°F. Temperatures were maintained from a few minutes (for melts) to eight hours (for nonmelts). All fission products were collected in specially designed particulate collectors, iodine traps, and gas traps. The entire system was closed to the atmosphere and contained helium gas as a carrier.

Activities of isotopes of interest were determined for the fuel residue and evolved material through radiochemical analyses. Since decay times between irradiation and testing were on the order of three to eight weeks, short-lived isotopes were not studied.

SNAPTRAN-3 tests had indicated that, during a maximum excursion, the maximum fuel temperature in a SNAP-10A reactor was 2000°F. If this were followed by a rocket fuel fire during launch, the temperature could be maintained for about ten minutes. Results from these tests indicate release for clad samples would be small (0.002 to 0.2%). Had these release experiments and the SNAPTRAN-3 tests not been performed, the radiation hazard from fission product release, based on conservative assumptions, would have been overestimated by several orders of magnitude.

SNAPTRAN-1 Experiment

The SNAPTRAN-1 test series included several nondestructive power transients to enable studying the prompt neutron kinetics of the SNAP core with a beryllium reflector. Extensive analyses of these tests extracted basic kinetics data over a wide range of variables.

The SNAPTRAN-1 reactor consisted of a SNAP-10A core and reflector. The four reflector control drums were controlled using special drive assemblies. Two diametrically opposed drive assemblies were provided with pneumatically driven rack-and-pinion operation through a 45° arc, allowing step reactivity insertions ($14/s single drum) to be made. The other two control drums were provided with impulse control (that is, a 450° drum rotation from the least reactive position through the most reactive position, then to rest at the least reactive position).

Twenty-nine step transients were initiated from ambient starting temperatures. Reactivity inputs ranging from $0.27 to $1.50 produced reactor periods ranging from 6670 to 1.7 ms. During the initial tests, where the reactor period was greater than 500 ms, the transient was terminated with a manual scram. All other transients were terminated by a programmed scram.

One SNAPTRAN-1 objective was to extend the average core temperature as high as possible to determine the magnitude of the temperature feedback mechanisms. The previous test series was extended until maximum core temperatures were raised to ~1300°F as a result of a single $1.70 coupled-drum transient. To accomplish this, transients were run in which the average core temperature was raised above ambient temperature using nuclear heat. The first transient involved higher reactivity inputs ($1.50 to $1.68). After thermal equilibrium in the core had been established, the reactor was subjected to a second transient, then a third and fourth of lesser reactivity inputs ($1.40 to $1.10). Five step-tests were run, and temperature feedback mechanisms and reactor characteristics were determined over that elevated temperature range.

Single-drum impulse transient tests were preformed to extend reactivity inputs from the maximum obtained in the step-transient series ($1.70) to $2.34. The impulse mode of reactivity insertion provided a well-defined 28-ms reactivity pulse from −135 to 0 to +135° drum rotation. Kinetic behavior of the reactor was determined by using a single reactivity insertion starting from various subcritical and critical power levels.

A series of transients was performed using the highest

reactivity insertion mode of the SNAPTRAN-1 test series. Reactivities ranging from \$2.00 to \$4.15 were inserted by means of coupled-drum impulse tests. The influence of reflector neutron delay on dynamic behavior was observed, and the prompt-temperature coefficient of reactivity was measured in transients where significant nuclear heat was developed.

SNAPTRAN-2 Experiment

The analytical model refined during the nondestructive SNAPTRAN-1 tests was used to predict the results of the planned SNAPTRAN-2 destruction test. Input parameters to the analytical model were based on the capabilities of the stepper and impulse drive mechanism. The mode of reactivity insertion for the destruct test was to first insert as much reactivity as possible with the stepper drums to bring the reactor slightly supercritical and then to insert the remaining reactivity with the impulse drums. Programming these reactivity values into the analytical model showed that the SNAPTRAN-2 reactor would undergo complete destruction with a stepwise reactivity insertion of ~\$5. By performing a destructive transient of this magnitude, knowledge of the neutronic behavior of the reactor was extended from the range observed during the nondestructive transients. Also, the mechanical and fission-product-release behaviors of this type of reactor were determined. The foregoing results and consequences were then factored into the analytical model for determining maximum reactivity accidents in SNAP-10A reactors.

The SNAPTRAN-2 destruct machine was essentially the same as the SNAPTRAN-1 reactor described above. The impulse drum drive mechanisms were modified to allow rapid (~12-ms) step reactivity insertion. To accomplish this, the impulse drums were stopped at their full-in position (0°), using pneumatic shock absorbers. A new core was used for the destructive test. Instrumentation for the SNAPTRAN-2 reactor included: (1) reactor power; (2) temperature (energy probe); (3) radial and axial fuel element, vessel, and reflector strains; (4) acoustics; (5) motion detectors; and (6) motion pictures.

The destruct test was initiated by the full insertion of the four reflector control drums. The drum position data and slow-motion pictures showed that all drums were fully inserted before the time interval considered in these analyses. The total drum-inserted reactivity was determined to be \$5.05. Energy probe data were used to reconstruct power and energy release from the destructive test. The maximum reactor power calculated from energy probes was 7.31×10^4 MW released compared to 7.24×10^4 MW obtained from the nuclear detectors. The released energy total was 47.25 MW · s (energy probe) compared to 46.78 MW · s (nuclear detectors). The temperature coefficient calculated from the energy probes was constant over the entire range of calculations and was determined to be $-0.208¢/°F$ compared to $-0.207¢/°F$ from the nuclear detectors.

Analysis of the fuel debris found after the SNAPTRAN-2 destruct test showed that a significant portion of the fuel material had undergone sufficient heating to melt. Electron microscope data showed that the spheroids contained only uranium and zirconium. Other identifiable fuel fragments (fuel element and pieces) showed little more than mechanical damage and minor peripheral dehydriding.

Mechanical and Thermochemical Incidents

A Phase I mechanical and thermochemical test series was conducted, in conjunction with the Air Force Special Weapons Center, to obtain data for evaluating the hazards that might occur before, during, and after the flight of the SNAP-10A reactor.

From the factory to orbit, the SNAP-10A system would be subjected to various handling, transportation, and launch conditions. From these conditions, potential accidents, such as impacts, chemical interactions, explosions, and fires could be postulated. To provide adequate nuclear safeguards, the potential radiological hazards from the postulated thermochemical and mechanical incidents were evaluated.

The selection of the individual tests was quite critical because the number of accident conditions, attitudes, and geometries that could be postulated was large. The 14 tests selected to give a statistically representative sampling of the credible conditions and to develop the most meaningful information are discussed below. Where possible, limiting conditions were selected in each test.

Liquid Oxygen Spray Tests

This test simulated the reactor being exposed to a liquid oxygen (LOX) spray from a ruptured Atlas fuel tank to measure the effects of the thermal shock on the reactor vessel, grid plates, and fuel element array and to observe the reactor for evidence of structural failure. For 40 s, a dense spray of LOX enveloped the reactor. There was no external or internal physical damage to the reactor. A similar test was made with NaK also exposed to the LOX spray. The NaK solidified at the nozzles and no damage resulted.

Explosion Test

The purpose of this test was to measure the geometric changes of the fuel element array and to observe structural failure of the reactor and fuel element dispersal resulting from an explosion. This test simulated prelaunch or postlaunch Atlas abort and subsequent propellant explosion.

The suspended reactor was subjected to an overpressure of 400 psi for 2.8 ms caused by an explosion of

156 lb of TNT 13 ft below it. The reflectors were blown off and the bottom of the reactor vessel deformed inwardly.

NaK-Water Interaction Immersion Test

The purpose of this test was to observe the NaK-H_2O chemical reaction and its effect on the reactor. The reactor was placed in a 36-ft^3 tank filled with water. The exposure of NaK to water caused an explosion that reptured the tank. The core vessel was slightly ballooned by pressure buildup inside.

Drop Tests from 100 ft

These tests determined the mode of failure of the reactor assembly when subjected to impact with concrete at an impact velocity of 70 ft/s. These tests simulated a reactor being dropped from the top of the launch vehicle during the mating operation. To simulate various modes of impact, test articles were dropped: (1) side-on, (2) tail-on, and (3) nose-on. In the side-on drop test, the impact velocity was at 68.8 ft/s. The reflectors were knocked off and the vessel sustained a small puncture. All the support legs failed. One reflector rotated inward before the reflectors separated. In tail-on impact, the reactor fell into the converter conical structure. All reflector drum brackets were severed, and all top pins were bent outward. The core vessel buckled circumferentially. In the nose-on, the impact velocity was 64.4 ft/s. The impact caused complete failure of the pump radiators and severed all of the reflector drums. After the vessel support legs failed, the reflector blocks were pushed into the converter structure and were held around the reactor vessel by the structure. Examination indicated that no nuclear hazard would result except for water immersion.

Fire Test

The purpose of this test was to measure differential expansion and to observe evidence of structural failure of the reactor when subjected to a high thermal flux environment. It simulated a prelaunch or postlaunch abort and subsequent propellant fire. The reactor was surrounded by a burning cycle of 400°F flames for 2.2 s and 1500°F flames for 15 min based on launch-abort fire information. The reflector separated during the initial high-temperature burn. A local deflection inversion occurred in the lower vessel head.

Water Impact Tests

The purpose of these tests was to observe the reactor assembly during and after water impact. These tests simulated an abort after launch of 10,000 ft or above, including a free fall from the apogee. Three reactor assemblies and one unit, including the converter shield, were impacted at different attitudes into an 8- by 8- by 16-ft deep water tank.

A side-on water test was performed at 500 ft/s; the reactor passed through the water tank. The fixed reflector blocks and the reflector dums were completely separated from the reactor vessel in the water. The vessel was found intact. The nose-on water impact test was performed at 573 ft/s; the reactor passed through the water tank. The reflector assembly separated completely from the reactor vessel in the water. Also, the NaK pump, the upper head, and the upper grid plate were severed from the test article. Fuel elements were displaced longitudinally in such a manner as to form a spherical pattern at the ends. Sufficient disassembly of the core did not occur to prevent its criticality in the water. The tail-on water impact test was performed at 596 ft/s. The reflector assembly was separated, and the core vessel split open axially. Fuel elements were displaced longitudinally through the bottom of the vessel, and two elements were completely ejected from the array. A fueled core would have gone critical in water.

The unit with converter cone structure and shield was impacted at 428 ft/s. The reflector assembly, NaK pump, shield, converter structure, bottom grid plate, and bottom head separated from the core vessel. Fuel elements were displaced through the open end of the vessel. Core disassembly was not sufficient to prevent criticality in water.

Concrete Impact Test

The purpose of this test was to observe the reactor assembly during and after a high-speed concrete impact. This test simulated an abort after launch at 10,000 ft or higher, including a free fall from the apogee.

A concrete-faced monorail sled was impacted at 560 ft/s onto the pump end of the test article. The impact completely destroyed the reactor. The vessel was in three parts: the upper head, lower head, and the shell. The shell was completely flattened and had many local failures.

A Phase II test series was conducted as a rerun of the Phase I test series under improved conditions.

NaK-Water Interaction Immersion Test

An accident in which the reactor is dropped into water with subsequent rupture of the NaK nozzles was simulated. Two explosive pulses were followed by a gradual pressure buildup ending at 15 s. Strain measurements showed that the stresses were generally below the yield stress of the Type 316 stainless steel vessel. The core vessel was not damaged during the test. The measured time of the initial pressure pulse was slower than the calculated time to peak power of a water-immersed core.

Fire Test on Squibs

A test was performed to evaluate the possibility of a missile abort fireball causing ignition of the SNAP-10A drum lockout pin puller squibs during a free fall of the

reactor to the pad. To simulate the abort environment, the squibs were subjected to an incident heat flux of greater than 360 Btu/s · ft^2 for 3 s. Three sets of two squibs each were tested. At the end of the 3-s period, the temperature of the actuator assembly had risen to ~600°F, but none of the squibs tested had ignited. Squib ignition took place at 8.7 s.

Soil Impact Tests

A terminal-velocity soil impact test was performed to establish the condition of the SNAP-10A core vessel and fuel element array after a terminal-velocity head-on impact on compacted soil. The test article, consisting of the core vessel with internals, reflector assembly, pump and fins, shield, and the top part of the converter structure, was impacted into a rectangular parallelopiped of compacted soil that was 126 ft wide, 8 ft high, and 8 ft deep.

The reflector assembly separated from the core vessel. Very little damage was incurred by the vessel, the most noticeable being a 1-in.-long opening in the vicinity of the top head weld. The fuel element array was not appreciably changed. The test indicated that the core vessel would survive a terminal-velocity land impact.

End-of-Life Shutdown

Although not incorporated in the SNAP-10A, an extensive analytical and experimental program was conducted to investigate the use of tritium for end-of-life shutdown. Radioactive tritium decays with a half-life of 12.26 yr to ^{3}He, which is a strong neutron adsorber. Such an additive to SNAP fuels was found to be very effective in eliminating radiological hazards from reactor missions greater than 400 yr.

Disposal Mode Studies

Methods for safely disposing of SNAP reactors after space operation were evaluated. Three principles were employed: decay, dilution, and recovery. Three basic methods had evolved for implementing the disposal principles: (1) boost to a long-lived orbit, (2) destruct, and (3) controlled reentry. The value of each of the methods depended on the characteristics of the reactor.

Boost to a sufficiently long-lived orbit would allow fission products to decay until no reentry hazard existed. If a reliable end-of-life shutdown device were used, orbit lifetimes as short as 50 yr could be adequate. For shorter-lived orbits, reentry radiation hazards are functions of the reactor power history, shutdown mechanism, and orbit lifetime.

The hazards associated with the radiation field produced by large particles from the ablation of a SNAP-10A core reentering the atmosphere were evaluated. Fallout calculations were made using conservative assumptions. The equivalent residual dose limit would not be exceeded unless the activity concentration was at least one core per square mile. It was concluded that reentry burnup would virtually eliminate SNAP-10A radiological hazards.

A study was directed toward the disposal problems associated with orbits of short duration (< 50 yr). Combinations of disposal methods and system failures were considered. The study showed that reentry burnup, as a backup to orbital boost or controlled reentry, may provide a two-order-of-magnitude improvement over all other disposal methods. Development of an effective destruct device was recommended.

Acknowledgments

This work was performed at the Energy Systems Group of Rockwell International.

Space Nuclear Power Systems 1984
Edited by M. S. El-Genk and M. D. Hoover
© Orbit Book Company, Malabar, FL, 1985

Chapter 59

Space Nuclear Safety From A User's Viewpoint

Robert W. Campbell

Jet Propulsion Laboratory
California Institute of Technology
4800 Oak Grove Dr.
Pasadena, CA 91109

The National Aeronautics and Space Administration (NASA) launched the Jet Propulsion Laboratory's (JPL) two Voyager spacecraft to Jupiter in 1977, each using three radioisotope thermoelectric generators (RTGs) supplied by the Department of Energy (DOE) for onboard electric power. In 1986 NASA will launch JPL's Galileo spacecraft to Jupiter equipped with two DOE supplied RTGs of an improved design. NASA and JPL are also responsible for obtaining a single RTG of this type from DOE and supplying it to the European Space Agency as part of its participation in the International Solar Polar Mission. As a result of these missions, JPL has been deeply involved in space nuclear safety as a user. This paper will give a brief review of the user contributions by JPL—and NASA in general— to the nuclear safety processes and relate them to the overall nuclear safety program necessary for the launch of an RTG. The two major safety areas requiring user support are the ground operations involving RTGs at the launch site and the failure modes and probabilities associated with launch accidents.

Introduction

The National Aeronautics and Space Administration (NASA) launched the Jet Propulsion Laboratory's (JPL) Voyager I and II spacecraft on missions to the planet Jupiter and beyond in August and September of 1977. Each of the spacecraft used three multihundred watt (MHW) radioisotope thermoelectric generators (RTGs) obtained from the Department of Energy (DOE) to supply all of the onboard electric power for the mission (Figure 1). JPL is currently preparing for a 1986 launch of the Galileo spacecraft (Orbiter plus Probe) to Jupiter. This spacecraft incorporates two newly designed, DOE supplied General Purpose Heat Source (GPHS) RTGs for onboard power (Figure 2). In addition, JPL is participating with the European Space Agency (ESA) in the International Solar Polar Mission (ISPM) which will launch a European built spacecraft into a polar orbit around the sun using a gravity assist trajectory around Jupiter. This spacecraft uses a single GPHS RTG (Figure 3). JPL is responsible for developing the requirements and environmental specifications for the RTG and is responsible for the overall operational activities at the launch site which involve the RTG. Both the MHW and GPHS generators are fueled with $^{238}PuO_2$. The total plutonium activity flown on a Voyager spacecraft was approximately 231,000 Curies and that for Galileo is to be approximately 270,000 Curies with one half of this latter value for ISPM. As a result of these missions, JPL has been intimately involved with space nuclear safety as a user for a number of years. Under a NASA/DOE Interagency Agreement, DOE has the overall safety responsibility for the RTGs.

In this paper the term "user" is not limited to JPL but also encompasses NASA because both the supplier(s) of the launch vehicle and the launch complex at Kennedy Space Center develop input that plays a vital role in determining the nuclear safety of the mission. A major difference between the Voyager mission and those currently under way is the launch vehicle itself. The Voyager spacecraft were launched using the Titan III-E/Centaur (Lewis Research Center/General Dynamics-Convair) while the current missions will be launched from the man rated Space Shuttle (Johnson Space Center/Rockwell International) using the newly developed wide-bodied Centaur *G* as an upper stage.

The user contributions to nuclear safety can be separated into two major activity areas. One of these areas involves support to the DOE analysis of the nuclear risks that may be incurred as a result of anomalies, malfunctions, or failures of the launch vehicle and/or the spacecraft. These risks must be evaluated not only for the launch complex personnel but for the Earth's population as well. This area will be identified in this report as the nuclear safety analysis. The second area of support involves the RTG operational activities at the launch site, including the efforts necessary to meet the DOE and KSC radiological and safeguards/security requirements.

In order to better understand the details of the nu-

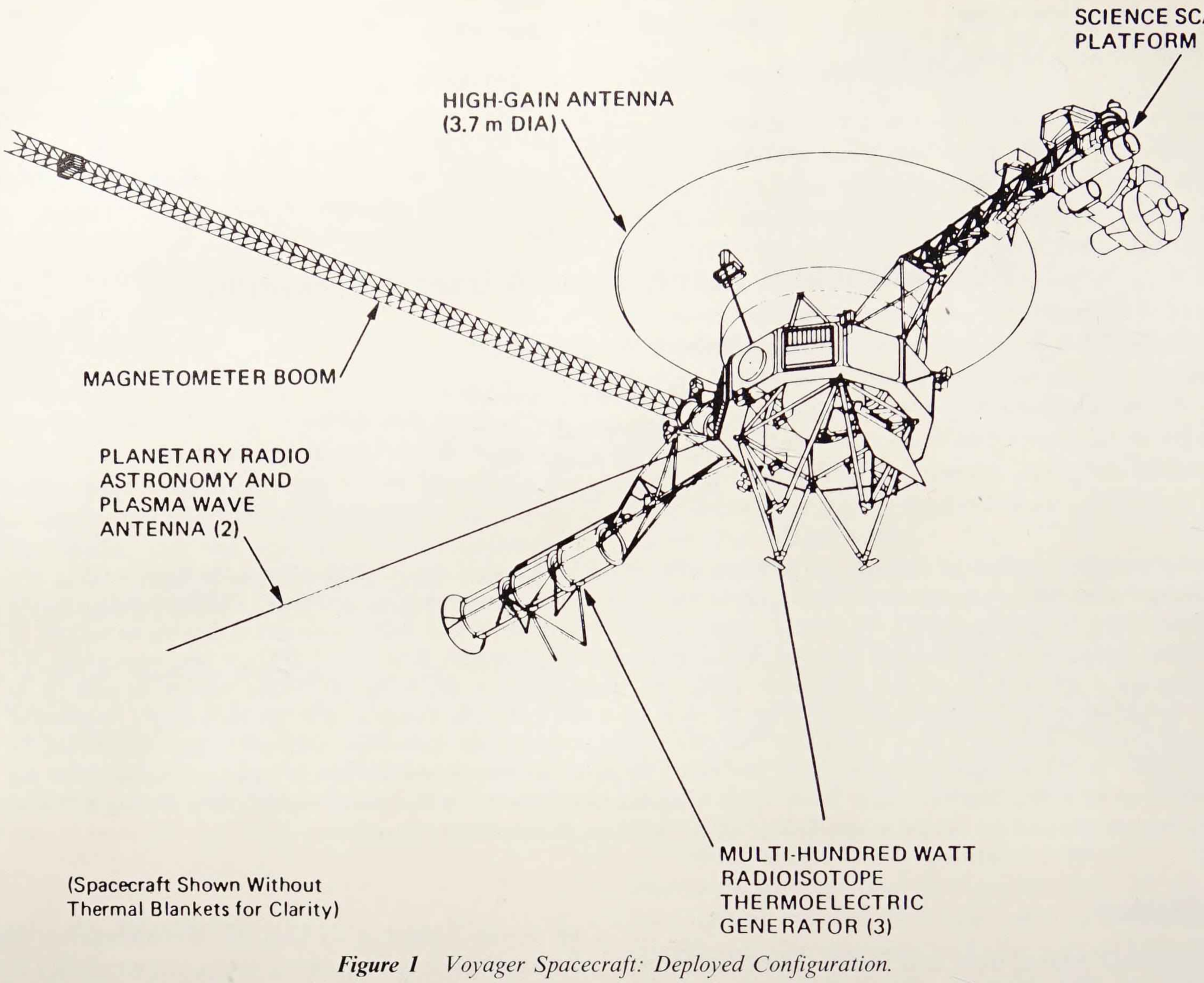


Figure 1 *Voyager Spacecraft: Deployed Configuration.*

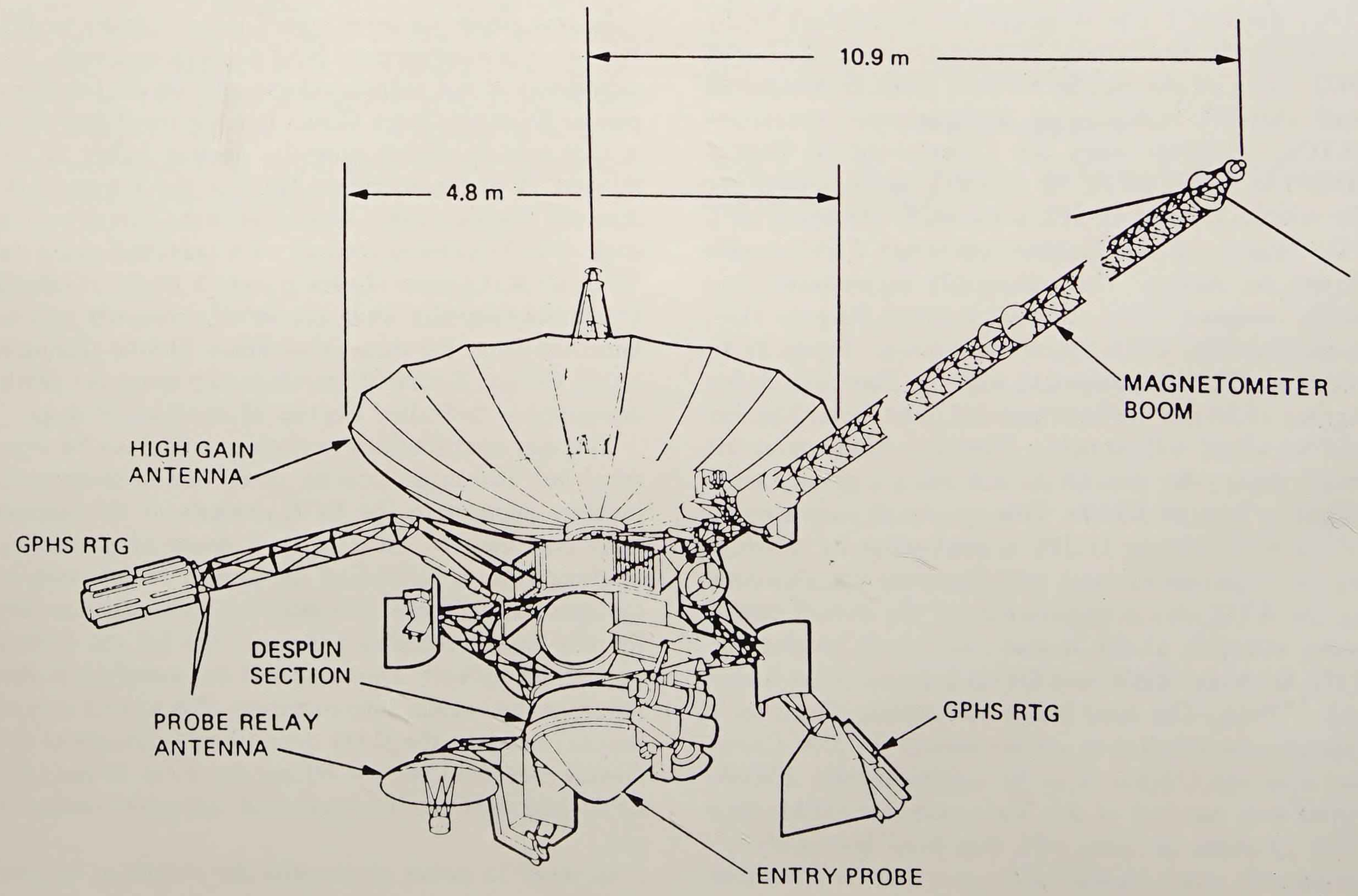


Figure 2 *Galileo Spacecraft: Deployed Configuration.*

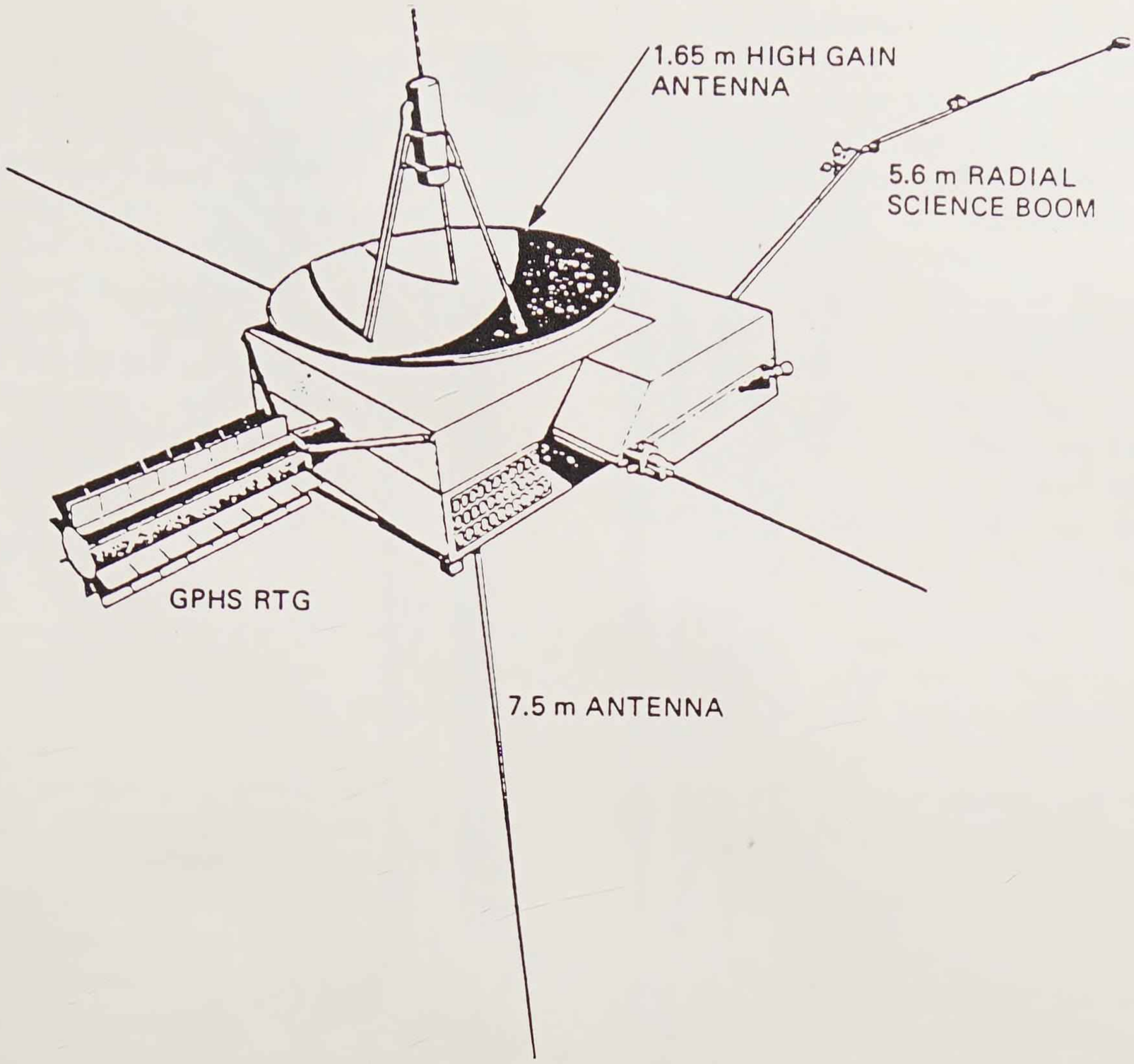


Figure 3 *European Space Agency (ESA) Spacecraft: International Solar Polar Mission.*

clear safety issues to be presented in this paper, they will be preceded by a brief description of the RTGs and how the RTGs are mechanically integrated onto the spacecraft.

RTG Description/Spacecraft Attachment

The design philosophy used by DOE for both the MHW and GPHS RTGs was to immobilize the plutonium fuel to the maximum extent possible under accident conditions occurring during all phases of the mission, including atmospheric reentry and earth impact. The RTGs consist of two major components—the radioisotope heat source and a thermoelectric converter.

The MHW RTG had a 2400 watt thermal loading and an electric output of approximately 155 watts at the beginning of mission. It is approximately 24 inches long, and 15 inches in diameter and weighs about 80 pounds (Figure 4). The thermoelectric converter case is made of beryllium. Cantilevered from the inside of the case are 312 thermocouples which in turn support a multifoil thermal insulation package between the thermocouples. Centrally located in the RTG is the heat source (Figure 5). It is supported at each end and is under compressional preload. This support is such that the heat source becomes a free body in the event that the RTG would break up under a postulated reentry. The cylindrical containment shell of the heat source is made up of two components. The outermost of these is a thin ablative sleeve made from a composite. The inner component is a graphite aeroshell that protects the remainder of the heat source from severe aerothermodynamic environments and also acts as the primary heat source structural member. Within this cylindrical containment shell are 24 fuel sphere assemblies arranged in six layers of four spheres each. Each sphere contains 100 thermal watts of $^{238}PuO_2$. Surrounding the fuel is a post impact containment shell of iridium and surrounding this a graphite impact shell. These shells absorb the shock of earth impact to prevent the release of fuel.

The three MHW RTGs required for each Voyager spacecraft were mounted in tandem with each other on a deployable boom. Three self-aligning ball joints are provided at the aft end of the outer case for attachment to the spacecraft and three opposing attachment locations are provided at its forward end for tandem attachment of the RTGs.

The GPHS RTGs have a thermal loading of approximately 4400 thermal watts and an output of 285 watts electrical at the beginning of mission. They are approximately 48 inches long, 18 inches fin-tip to fin-tip and weigh 123 pounds (Figure 6). The converter case was changed to aluminum because of its lower melting point to allow additional margin for release of the heat source during reentry. Five hundred and seventy two thermo-

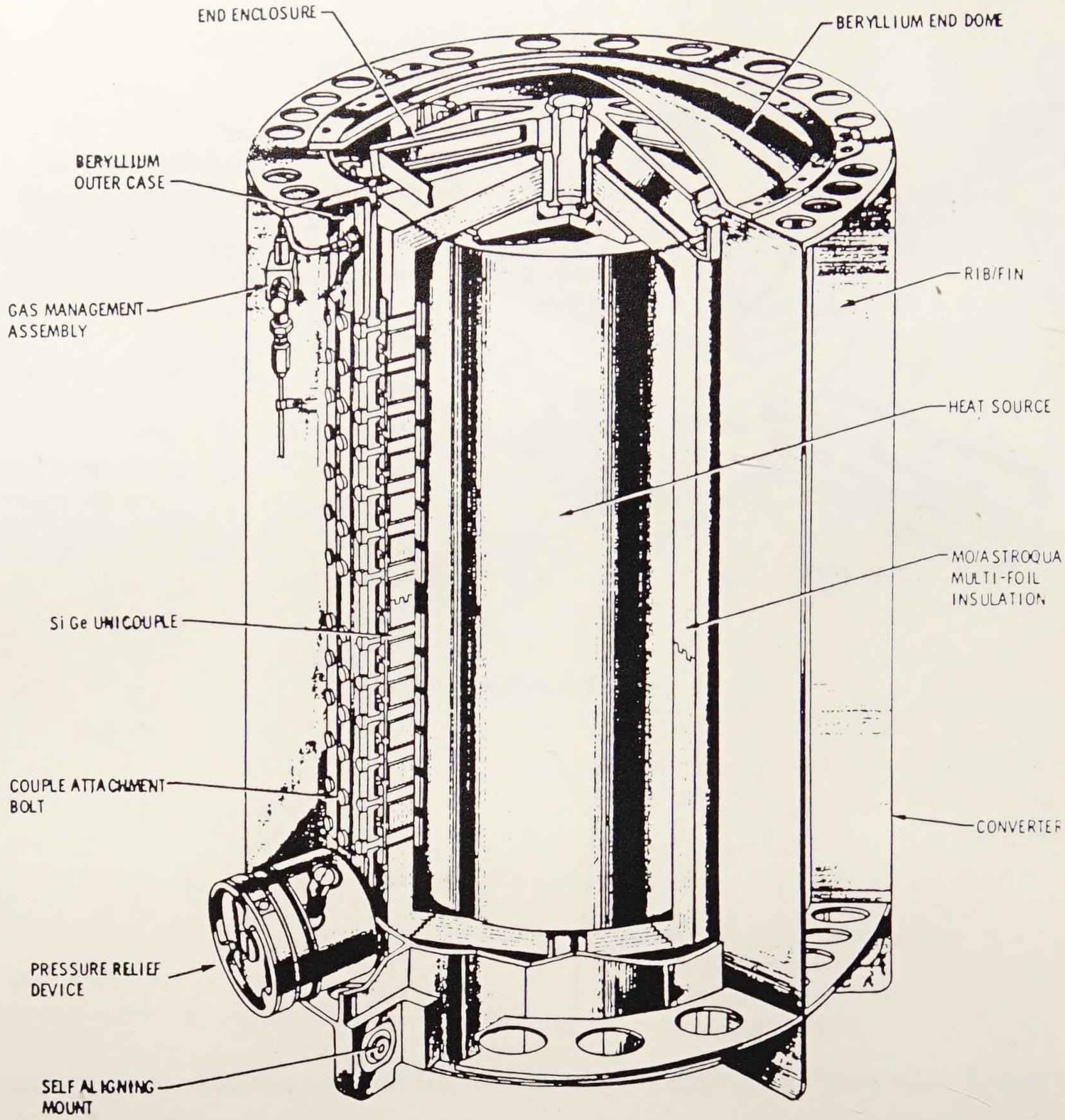


Figure 4 *Multihundred Watt Radioisotope Thermoelectric Generator.*

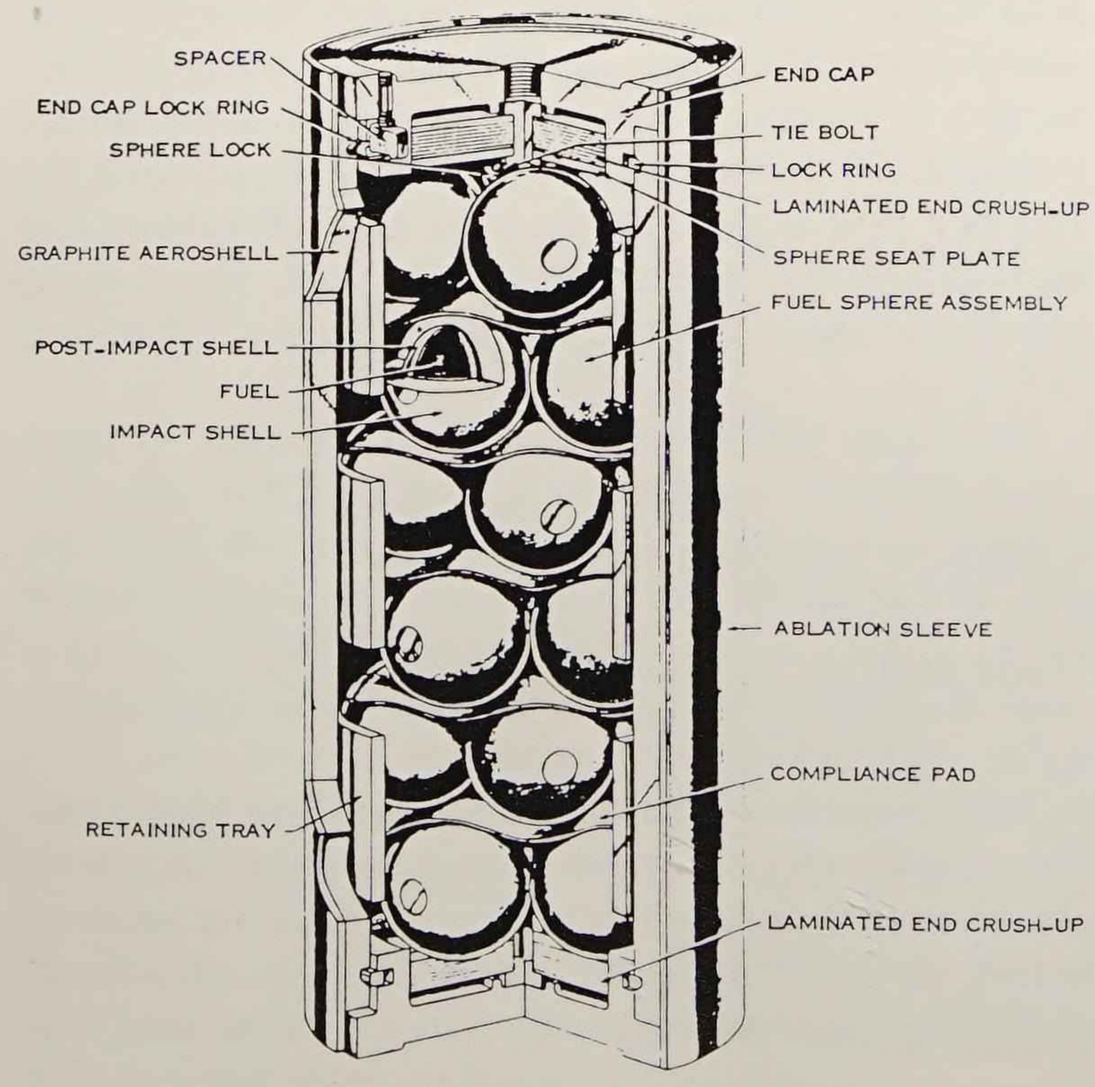


Figure 5 *Multihundred Watt Heat Source.*

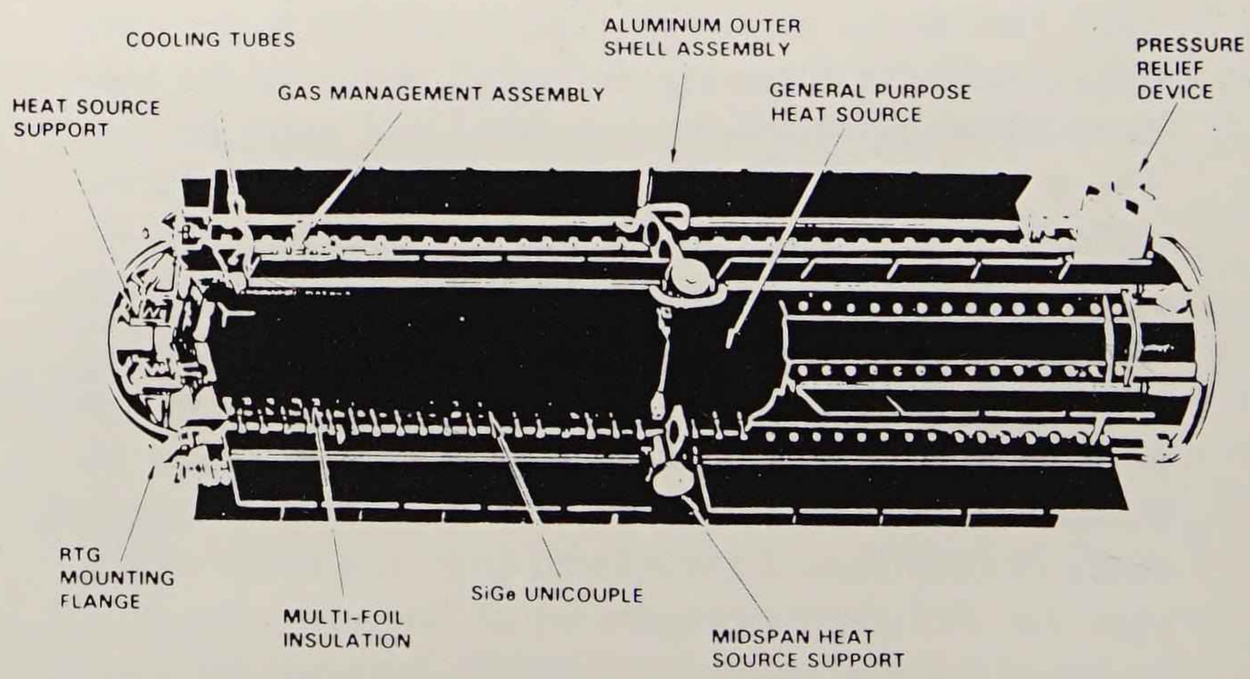


Figure 6 *General Purpose Heat Source Radioisotope Thermoelectric Generator.*

couples plus multifoil insulation are cantilevered from it. The heat source represents a major departure from that used in the MHW RTGs. It consists of 18 separate modules designed to individually survive a postulated reentry through the atmosphere and earth impact (Figure 7). The outer aeroshell is a hexahedron approximately 3.5 inches by 3.5 inches by 2 inches made of fine-weave-pierced fabric graphite as protection from the aerothermodynamic reentry environment. Within this aeroshell are two cylindrical graphite impact shells each containing two fueled clads. The fueled clad consists of a 62.5 watt pellet of $^{238}PuO_2$ clad with a post impact shell of iridium. The 18 heat source modules are supported at each end under compressional preload and at the mid-span of the RTG.

The GPHS RTG has four bolt holes and captive nuts on the inboard mounting flange and two pairs of bolt holes 180° apart at the mid-span. The mechanical interface differs between the Galileo and ISPM spacecraft. Galileo mounts each RTG to a deployable boom at the inboard mounting location and further supports it at the mid-span with a *W*-truss attached to the spacecraft-to-Centaur adapter. The *W*-truss is pyrotechnically released at the RTG mid-span to allow boom deployment. In the case of the ISPM spacecraft, the RTG is fixed mounted to a spacecraft adapter flange by the inboard mounting locations only.

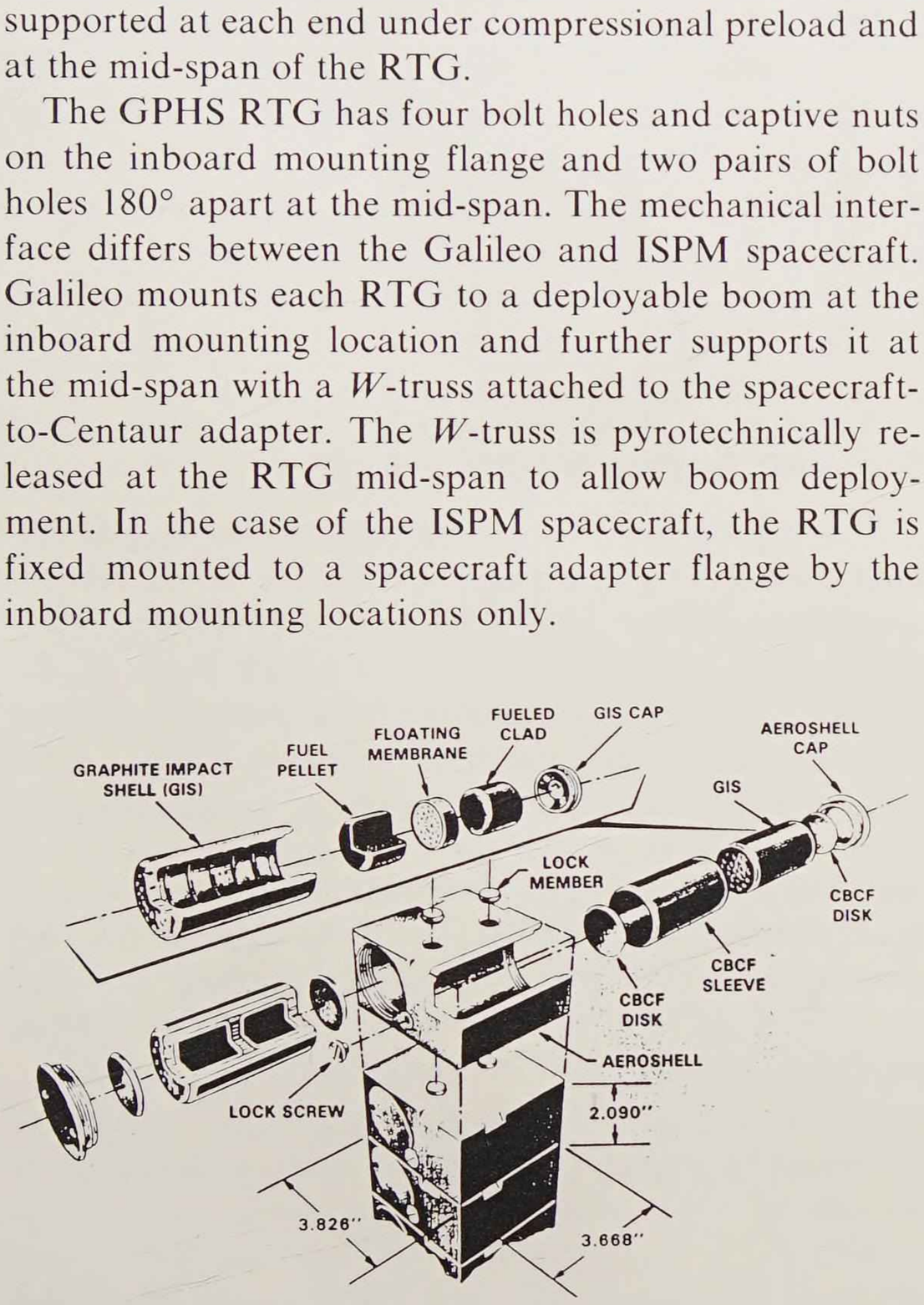


Figure 7 *General Purpose Heat Source.*

Nuclear Safety Analysis

Requirements/Implementation

To better understand the user's activities in nuclear safety analysis for missions flying RTGs, it is necessary to first understand the overall nuclear safety activity requirements. The United States Government requires that each space mission using a nuclear power source be analyzed to determine its potential radiological risk to the world's population. Such risks must be shown to be commensurate with the benefits derived from the mission. The results of this analysis must be reviewed and approved by the Office of the President of the United States before launch of the spacecraft.

The coordination and review of the nuclear safety analysis is carried out by the Interagency Nuclear Safety Review Panel (INSRP). The panel is chaired by three coordinators, one each from the Department of Defense (DOD), Department of Energy (DOE) and the National Aeronautics and Space Administration (NASA). The Nuclear Regulatory Commission, the Environmental Protection Agency and the National Oceanic and Atmospheric Administration may also participate on the panel. To insure adequate expertise in the technical areas of concern, five subpanels of INSRP have been established. They are the Launch Abort, Reentry, Meteorology, Oceanographic, and Biomedical and Environmental Effects Subpanels. INSRP reviews the safety analysis performed for the mission and issues an independent risk analysis in the form of a Safety Evaluation Report (SER). This information is then passed on to DOE, DOD, NASA and other government agencies for approval before it is sent to the Office of the President of the United States for approval.

Safety Analysis Reports

The Department of Energy, which is responsible for the safety of the nuclear power sources it builds, requires that the documentation of the analyses takes the form of three reports, a Preliminary, Updated and Final Safety Analysis Report (PSAR, USAR, and FSAR, respectively). The PSAR consists of two volumes, a Reference Design Document and an Accident Model Document. The USAR and FSAR contain these volumes plus a third called the Nuclear Risk Analysis Document. This last volume is normally classified. The analysis studies begin in the early design phases of both the power source and mission and continues on through the launch safety approval process. The FSAR should be issued about one year before launch to allow adequate review and approval time. These SARs are submitted by the DOE systems contractor for the RTGs. For the missions discussed in this paper, this has been the General Electric Company. Contributions to these documents are made by both the RTG supplier and user agencies as well as by a large number of their contractors representing a broad spectrum of the space nuclear safety community.

User Inputs to Safety Analysis Reports

The user makes major contributions to both the Reference Design Document and the Accident Model Document of the Safety Analysis Reports. To better coordinate the many user organizations contributing to these documents a Vehicle Level Working Group has been established. The group is chaired by a representative from Johnson Space Center and has members from the DOE, European Space Agency, JPL, Kennedy Space

Center, Langley Research Center, Lewis Research Center, Marshall Space Flight Center, and the United States Air Force. It meets several times a year to assure timely availability and proper dissemination of information to concerned organizations.

Johnson Space Center has developed a document entitled, "Space Shuttle Data for Nuclear Safety Analysis" (Vedder and Brown 1982) that is intended to support, as background information, these Safety Analysis Reports for all missions that contain nuclear material as part of the payload. Most of the information contained in the following two subsections are discussed in great detail in this document.

Reference Design Document

The user inputs to the Reference Design Document include detailed descriptions of the spacecraft, launch vehicle and launch site, reference trajectory and flight characteristics, and flight contingency modes. These descriptions must include safety planes for the launch pad, range, Orbiter and Centaur.

Accident Model Document

User contributions to the Accident Model Document include a definition of possible accidents, a determination of the failure probabilities leading to those accidents, and a description of those accident environments. The accidents can be categorized by mission phase as prelaunch, launch (or lift off) through payload (Centaur plus spacecraft) deployment from the Shuttle, Centaur flight, and spacecraft trajectory events. These latter events include the results of the spacecraft breakup analysis which treats the accidental condition of spacecraft reentry into the atmosphere. The objective is to determine the reentry parameters of the radioisotope heat source at the point it is freed from the spacecraft. The RTG contractor then uses this information to study the behavior of the heat source upon earth impact.

The failure probabilities and the quantification of the Shuttle vehicle environments must be calculated for a number of possible accidents from prelaunch through payload separation. Important accidents include

- Liquid propellant fire,
- Solid propellant fire,
- Combination liquid and solid propellant fire,
- Explosion overpressure,
- Projectile impact,
- Tipover on launch pad,
- High velocity ground or water impact, and
- Sequential combinations of the above.

Involved in these calculations are identification of which particular item failed, its failure rates, the number of items involved, critical time periods and the subsystems affected. Since information was developed before actual Shuttle flight data existed, the failure probabilities are based on failure rates of components and systems having similar characteristics to those in the Shuttle. "The Reactor Safety Study" (WASH-1400) database was used for components where applicable.

After deployment from the Shuttle Orbiter, the failure probabilities are the responsibility of General Dynamics (Convair)/Lewis Research Center. In this case, old reliability data from the Voyager Safety Study has been updated and used as much a possible with current industry-wide generic data used for the fluid systems.

All of these accidents will be analyzed by the DOE systems contractor and independently reviewed by DOE space nuclear personnel and by INSRP. They will use the data predicted from the fires, explosion overpressures, and fragmentation models in both analytic and experimental determination of the resulting response of the heat source modules.

Spacecraft Breakup Analysis

This reentry analysis can be broken into several distinct phases. The first phase sets up the initial reentry conditions that occur as a result of a postulated misaligned burn and/or an abnormal length burn of the Centaur. Trajectories resulting from these postulated malfunctions are calculated to be either elliptic, parabolic or hyperbolic. Reentry is defined as occurring for those trajectories where the spacecraft or spacecraft plus Centaur encounters the sensible atmosphere at a geodetic altitude of 400,000 feet. If the Centaur has fuel remaining when it plus the spacecraft reach this altitude, it is defined as a powered reentry. The other trajectory options result in orbital capture or escape.

For the Voyager Mission, the misoriented burns were evaluated by trajectory simulation using a Monte Carlo analysis of 1000 randomly oriented cases (General Dynamics 1975). Approximately 800 separate burns were analyzed for both Galileo and ISPM by the Air Force Weapons Lab (Martens 1983). The results of these analyses are summarized in the form of V-Gamma maps which present envelopes of possible reentry velocity and angle combinations. A typical map is shown in Figure 8 for the ISPM space craft.

The second phase of the reentry analysis begins with the V-Gamma map. From this map the Reentry Subpanel of INSRP chooses a number of cases for which JPL must determine the reentry response of the spacecraft up to the point at which the RTG breaks away from the spacecraft or the heat source (or heat source module) is released from the RTG still attached to the spacecraft. The major cases generally chosen are given below with a brief description of their characteristics

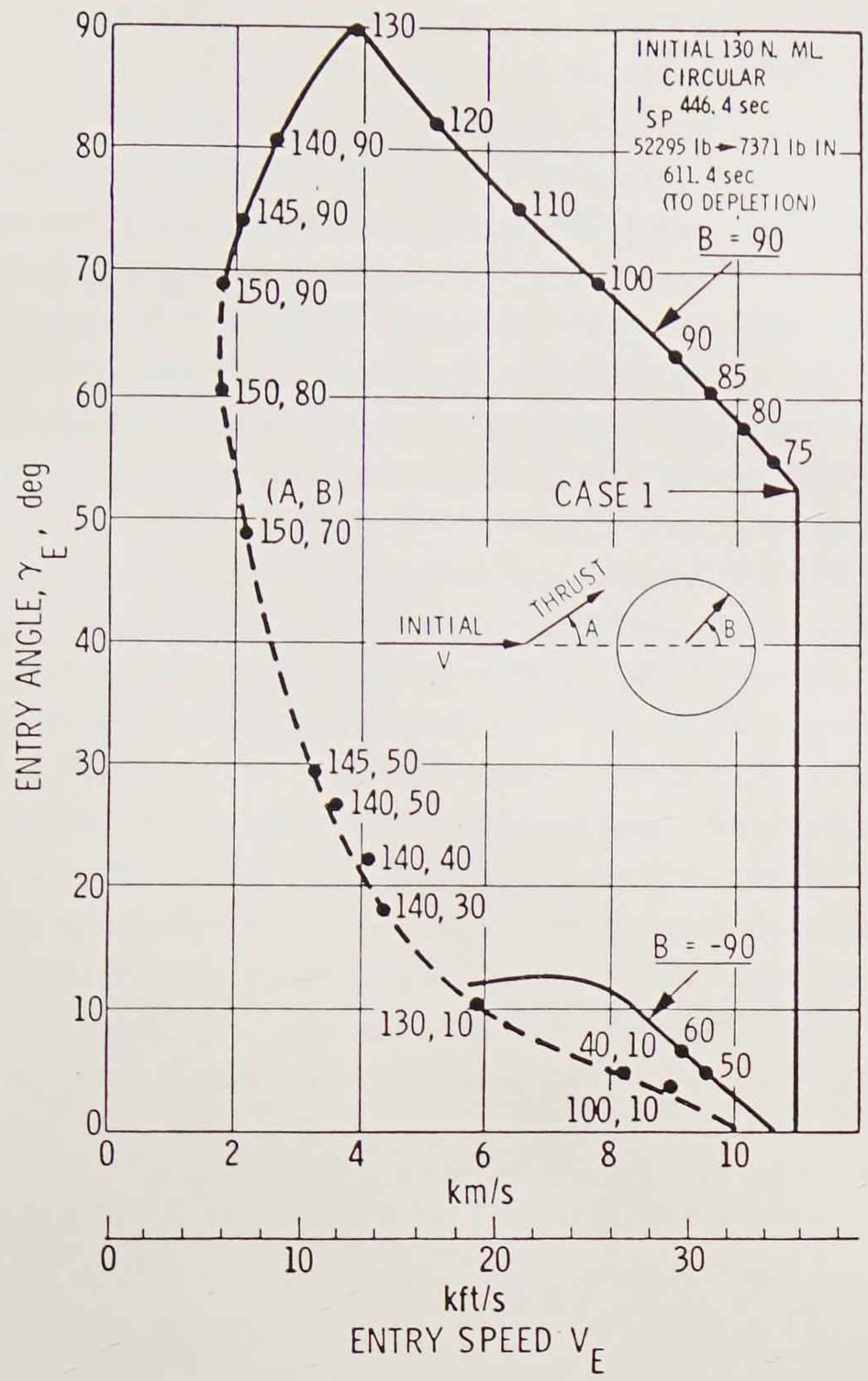


Figure 8 *V-Gamma Map for the ISPM Spacecraft.*

(Jaffe and McRonald 1983):

Orbital Decay (corresponds to lower right hand portion of V-Gamma map). After approximately a month in orbit, free-molecular drag reduces the altitude of the spacecraft to 400,000 feet and reentry begins. Breakup of the ISPM spacecraft for this case is predominantly by aerodynamic heating and in approximately one half an hour the heat source modules are released from the RTG while it is still attached to the spacecraft (S/C).

High Speed, Steep Angle (corresponds to the upper right hand corner of the V-Gamma map). This case has a high probability of producing the maximum heating and structural loads on the GPHS modules. Several hours after the Centaur burn, the 400,000 feet altitude is reached. Approximately seven seconds later the ISPM RTG has released the heat source modules. For the same case, Galileo enters with the RTG booms pointing into the flow. Thermal erosion plus aerodynamic loads on the RTGs cause the boom longerons to fail. The RTGs then rotate backwards in the flow plain held only by the power and instrument cables. After about 5.8 seconds, the cable connector pins pull out of the insulator; then with increasing aerodynamic force on the RTGs, the cable mesh braiding breaks loose from its mechanical attachment at 6 seconds, freeing the RTGs.

Minimum Gamma. This case combines a shallow entry angle (< 1 degree) with the relatively low entry speed (i.e., near 25K ft/sec rather than near the maximum of 36K ft/sec). Because of this, the breakup of the spacecraft occurs over a considerable length of time and results predominantly from thermal failure. The slow descent also means that breakup can actually begin in the free-molecular flow and then continue in the atmospheric continuum. The assumptions used in the transition between the free molecular flow region and continuum become important here. Times for RTG release can be in the 8 to 10 minute range.

Powered Reentry. This case results from a postulated misaligned burn of the Centaur in such a manner that the Centaur with spacecraft attached reenters the atmosphere with the engines still burning. A combined Galileo/ISPM case has been run with an entry angle of 10.5 degrees, velocity of 21K ft/sec and 50% of its propellant remaining. Because of the liquid oxygen mass near the engine nozzle it trims nozzle first, overcoming the vehicle's gimbaling capability. The propellant tank walls heat up and rupture, releasing the engines and part of the tank from the vehicle. The vehicle then trims side-on for ISPM and spacecraft-forward for Galileo. During this reorientation, the Galileo RTGs are released to free flight; and about 60 seconds after entry, the heat source modules are released. In the ISPM case the RTG remains on the spacecraft and 67 seconds after entry releases the modules due to aeroheating erosion.

Once the RTGs or heat source modules are separated from the spacecraft, it is the responsibility of the RTG contractor rather than the user, to follow its reentry to earth impact and determine the resulting radioactive source term, if any. In the Voyager spacecraft analyses for orbital decay, high speed and steep angle, and minimum gamma, the stack of three RTGs was found to be in a near end-on trim attitude at the time of release from the *S/C* and would remain that way until the RTGs broke up. The RTG Contractor continued the analysis and for the steep angle, high velocity case (maximum stress), the end dome and heat source support structure of the leading RTG would melt away exposing the end cap of the heat source to excessive stresses. This could lead to failure of the end cap and result in an excessive source turn for the release of radioactive material. As a result JPL redesigned the interstitial monoball connection between the three RTGs to include a thermally activated pin puller for releasing the RTGs individually from the stacked configuration prior to peak heating. This eliminated the postulated failure mode.

RTG Launch Operations Safety

The second important area of contribution to space nuclear safety involves the RTG launch operations activities at the Kennedy Space Center and Cape Canaveral Air Force Station. These activities include all oper-

ations involving the RTGs from receipt at the site, testing and check out, matchmate and pathfinder operations with the spacecraft, to installation onto the spacecraft. The safety issues of concern here include radiological safety of personnel, hardware safety, Space Shuttle safety and launch site safety. Each of these will be discussed below.

Radiological Safety

The first step in approaching radiological safety for launch operations is to clearly identify the agencies that control the radiation activities and what regulations they levy on the user. Because DOE has the overall safety responsibility for the RTGs the user is required to comply with certain parts of the DOE's Environmental, Safety and Health program. The current guiding document to the applicable DOE regulations is the "Minimum Radiological Health and Criticality Safety Criteria," originally issued by the Operational Safety Division but now under the auspices of the Emergency Preparedness Staff of the Department of Energy/Albuquerque Operations Office (DOE/AL). It addresses such issues as organization and personnel, documentation, personnel dosimetry, radiation monitoring, contamination control, instrumentation, facilities and equipment, training, packaging and transportation, and incidents or accidents. The document's position with respect to exposure of personnel is as follows:

> Maintaining personnel exposures ALARA (as low as reasonably achievable) shall be a primary consideration during the development of ground handling equipment and operational sequences. Special emphasis shall be placed on minimizing exposure to personnel who have no direct involvement with the nuclear power system(s).

All JPL employees who are residents of California, whether working in California or Florida at the launch site, must abide by the California Radiation Control Regulations, Title 17, California Administrative Code, Chapter 5, Subchapter 4. These regulations as far as pertaining to the activities discussed here are basically the same as those of the Federal Government. In addition, the state regulations require that JPL establish a Radiation Safety Committee to regulate the use of radioactivity and ionizing machines by its employees. This committee has set as a goal dose allowances for JPL personnel that are one tenth the doses allowable under the Federal and state regulations.

Finally, since the prelaunch operations will take place at the Kennedy Space Center, all personnel must meet the regulations of both the Biomedical and Safety Offices of the Kennedy Space Center. From a radiological standpoint the two top level documents to be complied with are KMI 1860.1A "Radiation Protection Program —Policies and General Provisions for Ionizing and Non-Ionizing Radiation" and KHB 1860.1 "Radiation Protection Handbook."

The achievement of the ALARA approach to radiation exposure as called out by the DOE/AL Minimum Radiological Health and Criticality Safety Criteria is made possible through an adequate combination of design, analyses and training. Initially all operations that involve the RTG's are defined and then fitted into the overall flow plan of launch activities at the site. Care must be taken to select location and times of the operations consistent with ALARA.

For the Voyager mission the RTGs were installed on the spacecraft in the Spacecraft Assembly and Encapsulation Facility, the combined spacecraft plus RTG was then moved to the launch pad and installed on the launch vehicle. This meant that the RTGs stayed with the spacecraft and/or launch vehicle for a period of about 20 days. Some statistics from the health physics activities point out the difficulty in maintaining radiation exposure ALARA and also minimizing exposure to indirectly involved persons (casuals). A total of 238 people wore dosimetry to determine whole body exposure. The total dose to these people was 21.6 person Rem or an average of 90 mRem per person. The RTG and spacecraft workers (i.e. radiation workers) consisted of 75 people who received a total dose of 10.4 person Rem. This left 163 other people (the casuals) who received 11.2 person Rem which is about 1 person Rem more than the radiation workers. It is also interesting to note that the 238 people represented 32 different companies or organizations. For the Galileo and ISPM launches the decision was made to delay installing the RTGs on the launch pad until as short a time as possible before shuttle door closing. This approach represents a significant savings in exposure time to personnel on the launch pad.

Once the times and locations of various operations that will take place have been defined, then appropriate ground handling equipment and tools to safely carry them out can be designed. This often means adding extension handles so that movement of the RTG can be performed at a suitable distance and making certain that tools are equipped with extenders and/or operated automatically so that time and/or distance may be minimized in the immediate vicinity of the RTG. This type of implementation as well as the step by step procedures must then be iterated with time and distance studies to insure maximum safety without compromising the quality of the operation being performed.

The training of personnel to carry out the RTG operations with due regard to radiation safety is a significant factor in meeting ALARA. JPL has many engineers and technicians with experience in *S/C* launch operations but few of them had any radiation experience before the Voyager mission. Initially, all involved personnel are given lectures in basic radiation safety. Topics include the nature of the radiation, its

effect on the human body, and understanding of the regulations and the approach to be used in meeting them. Following this, specific procedures are reviewed and walk-throughs performed using actual ground handling equipment and tools in conjunction with simulated RTGs. During one procedures walk-through for Voyager, a low-level radioactive source was enclosed in the simulated RTG and operations personnel were equipped with audible dose rate meters. This gave them a real time sense of the advantage of using distance to reduce exposure levels. The walk-throughs were also performed for the JPL Radiation Safety Committee as part of the review and approval process.

The Galileo project has established a Nuclear Safety Coordinating Group whose activities are concerned with the safe control of all nuclear radiation sources associated with the project when those sources are under direct control of JPL. Its chartered tasks are as follows:

1. Determine what radiation sources the project plans to use.
2. Outline the set of requirements to be met by activities involving the use of isotopes.
3. Distribute appropriate information (to various project areas) for radiation safety.
4. Maintain an overview of activities to assure that all nuclear safety requirements are fulfilled and advise the project of any concerns in meeting the requirements or the schedules involving the requirements.
5. Review activities and requirements periodically to assure that an understanding commensurate with needs is occurring.
6. Examine technical, schedule and budgeting ramifications of new requirements or newly planned activities and advise project management.
7. Coordinate the training of personnel needed to fulfill project radiation worker requirements.
8. Coordinate procedure and facility review as necessary to obtain JPL Radiation Safety Committee approval.

The approval cycle for the ground operations begins with the JPL Radiation Safety Committee. Following their approval these procedures are passed on to the DOE/Albuquerque Operations Office and KSC. In addition to these procedure, dose assessments to JPL personnel are submitted to KSC for incorporation into an overall personnel dose assessment for the entire operation. This is then reviewed by DOE/AL. This will not be their first exposure to the planned operations. Ground Operations Working Group meetings are held several times a year at KSC throughout the flight program and discussions of RTG handling represents a significant portion of the agenda. As an adjunct to this working group, a Radiological Subworking Group has been established whose work is dedicated to the special requirements concerning radiological health, contingency support and security control. The group is cochaired by persons from the Cargo Projects Office and the Biomedical Office at Kennedy Space Center. Several JPL and DOE people belong to this group.

The DOE/AL Minimum Radiological Health and criticality Safety Criteria also levies a requirement directly on the launch site organization to develop both a Radiation Protection Plan and an Emergency Preparedness Plan. A single set of these plans is developed that is applicable to all ground nuclear power system operations. This plan is developed by the Biomedical Office of KSC. Also required are plans and procedures to deal with launch and post-launch contingencies. The contingency concepts must be identified and the management and responsibilities for onsite and offsite contingencies as well as source recovery must be established. An example of an offsite contingency activity would be that at a secondary or contingency landing site of the Shuttle or a touch down in the public domain. The contingency procedures are very complex and may involve NASA, DOE and DOD. JPL is required to contribute in this area because of the interface of the RTG with the spacecraft.

STS Payloads Systems Safety Requirements

Safety reviews are conducted at Johnson Space Center and Kennedy Space Center to assess the overall safety of each STS payload and its associated ground support equipment and ground operations to determine compliance with the requirements of STS payload and ground safety requirements documents. These reviews consider the RTGs as only one of the many payload elements that may present a hazard to the STS and look at all postulated hazards that it may present rather than just those of a nuclear nature. Hazards that are covered by the safety analyses required by INSRP are cited but nuclear safety issues not addressed by INSRP must also be covered.

There are four safety reviews each at Johnson Space Center and Kennedy Space Center phased over the time period from conceptual design definition to completion of payload fabrication and testing. The payload organization's responsibility to these reviews is to perform a safety analysis of the hardware and ground operations (for KSC). It is necessary to initially define potential hazards and causes. Actions must then be developed for either reducing or controlling these hazards. It is then necessary to identify and develop an approach to verify the safety of that hardware, event or operation. By the time of the last review all safety verification tests, analyses or inspections must be completed and a safety assessment report written. Typical of a nuclear hazard not addressed elsewhere was the potential release of radioactive radon from plutonium decay in the event that the RTG cover gas was released into the Shuttle bay.

Operations Analysis

The Department of Energy conducts an Operations Analysis of the RTG handling, test, storage and installation on the spacecraft for both matchmate tests and launch. The emphasis is on radiological safety and secruity/safeguards of the special nuclear material as well as operations and environments involving the RTGs. This is part of an overall evaluation that DOE conducts of the factory-to-flight operations involving the RTGs. The review is conducted at a time when the plans and procedures at the launch site are nearing finalization. Both JPL and KSC are required to support this effort.

DOE will also conduct a preoperational survey of safety and security/safeguards readiness at the launch site for the receipt, handling and protection of the RTG and special nuclear material. This survey is conducted shortly before the receipt of the RTGs at KSC and also requires both JPL and KSC participation.

Summary

The above discussion has been an attempt to present a broad overview of a user's activities in support of the nuclear safety effort associated with the launch of RTGs. To address the wide range of issues that must be covered the term user must be expanded to include both launch site and launch vehicle organizations rather than just the immediate user of the nuclear device. It then becomes a combined effort of user, supplier and regulatory agencies to determine the risks involved and to verify that the launch is carried out in a manner consistent with those risk levels. Although it has not been possible to acknowledge the many organizations throughout the space nuclear safety community that contribute to this effort through the supplier or user agencies, their work is nevertheless invaluable. It is the close cooperation of individuals from all these organizations, overriding organizational and disciplinary boundaries, that is necessary to insure the safety of nuclear activities in space.

Acknowledgments

The writing and publication of this paper was supported by the Jet Propulsion Laboratory, California Institute of Technology, under contract with the National Aeronautics and Space Administration.

References

General Dynamics (1975) *MJS '77 RTG Safety Study. Phase II. Range Safety Equipment, Launch Pad Hazards, Launch Vehicle Failure Probabilities, and Re-entry Environment*, CASD/LVP76-004, San Diego, CA.

Jaffe, P. and McRonald (1983) *Private Communication*, Jet Propulsion Laboratory, Pasadena, CA.

Martens, J. D. (1983) *Galileo/International Solar Polar Orbital Malfunction Analysis*, AFWL-TR-83-11, Kirtland Air Force Base, NM.

U.S. Nuclear Regulatory Commission (1975) *Reactor Safety Study*, WASH-1400, Washington, D.C.

Vedder, J. D. and R. H. Brown (1982) *Space Shuttle Data for Nuclear Safety Analysis*, JSC-16087: RI, Johnson Space Center, TX.

Space Nuclear Power Systems 1984
Edited by M. S. El-Genk and M. D. Hoover
© Orbit Book Company, Malabar, FL, 1985

Chapter 60

Fission Gas and Volatile Release-Venting Model for Space Nuclear Reactors

David L. Y. Louie and Mohamed S. El-Genk
Department of Chemical and Nuclear Engineering
University of New Mexico
Albuquerque, NM 87131

Steven Wright
Sandia National Laboratories
P. O. Box 5800
Albuquerque, NM 87185

This paper discusses the development of a fission gas and volatile release-venting model for space nuclear reactors. The model is applied to the heat pipe space nuclear reactor (HPSNR) design of Los Alamos National Laboratory in order to investigate the consequences of a partial or complete plugging of its venting system. Calculations show that if the venting system were plugged, the pressure buildup in the core due to the accumulation of fission gases could fail the core can and/or partially damage the multifoil thermal insulation wrapped around the can. Such damage could cause overheating of the reflector, or perhaps the control drums and the radiation shield. However, adequate venting of fission gases into space can be sustained with only one vent channel (~2.5 mm in diameter) open.

Introduction

A concern in the development of space nuclear reactors is venting the fission gases and volatile fission products from the reactor core while minimizing the mass and size of the system as much as practically possible. Even with the recent advancements in the space transportation system, excess mass would not only increase the transportation cost, but might also require special arrangements for launching. Venting the fission gases and volatile fission products reduces neutron losses due to capture by non-fuel materials in the core, thus increasing the maximum fuel burnup and extending the core's lifetime. Gaseous and volatile fission products could be vented directly into space (JPL 1982, Los Alamos 1982, El-Genk et al. 1985, and Louie 1984) or to a storage tank outside the reactor core region (Katucki et al. 1985). The former method was suggested in the Los Alamos HPSNR design that employs unclad fuel. The latter method is being considered in the General Electric design which employs clad fuel (Katucki et al. 1985).

Each of the above core designs will require an adequate venting system for gaseous and volatile fission products, an area which deserves particular attention. In general, there are three distinct processes for venting fission gases and volatiles from the reactor core, namely: molecular flow at very low partial pressure of the gas in the core, transitional flow at intermediate pressure, and viscous flow at high partial pressure of the gas in the core. When fission products are vented directly into space, as the molecules of volatile fission products (for example, Cs, Rb, and Sr) approach the exit of the venting passage, they are subjected to steep declines in temperature and pressure. For example, the reference operating temperature of the fuel in the HPSNR core is 1700 K and the temperature of the vent walls could be several hundred degrees less. Thus, it is possible that some of these volatiles may condense on the vent walls or may even solidify. (See Figure 1.) Continuous deposition of volatiles on the walls of the venting passages may eventually plug the venting system. Subsequently, pressurization of the core containment could occur due to the accumulation of gaseous fission products in the core. Such pressure buildup in the core may either fail the core containment and/or partially damage the multifoil thermal insulation wrapped around the core containment walls.

The objectives of this work were to develop a fission gas release-venting model for space nuclear reactors and apply the model to the HPSNR in order to assess the effects of either partial or total plugging of the venting system.

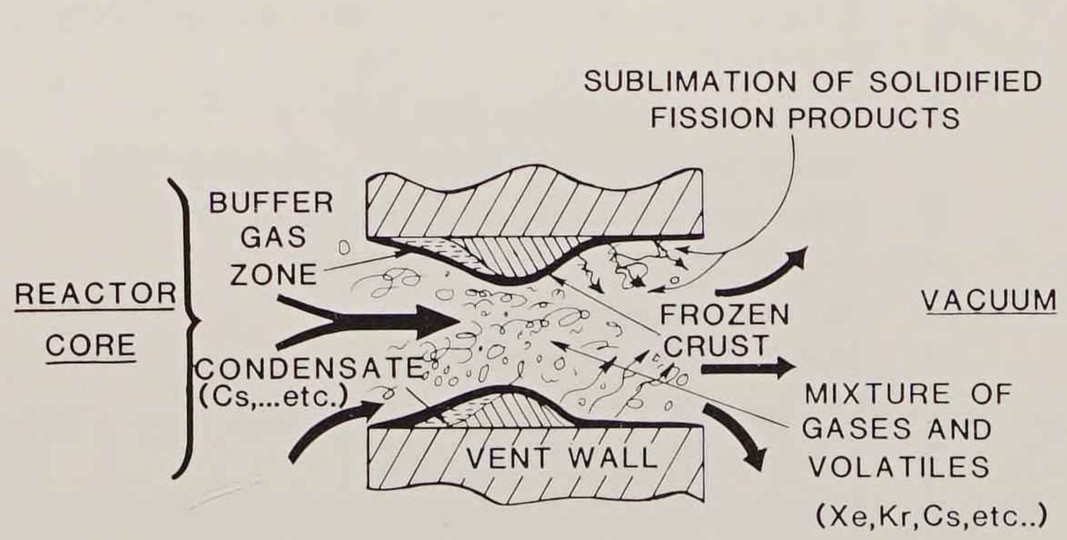


Figure 1 *Schematic of a Channel for Venting Gaseous and Volatile Fission Products into Space.*

Analysis and Model Development

The analysis of fission gas and volatile release from UO_2 fuel is performed as a function of the fuel operating temperature and fuel burnup by using an intragranular fission gas release model (Wood and Matthews 1980; Booth 1957; and Speight 1969). This model coupled with another model for venting fission gases can estimate the pressure buildup in the core as a function of the temperature of the venting passage walls as well as the number of open passages. The following sections present a description of the fission gas and volatiles release and venting models and of the governing equations as well as the results of calculations and conclusions.

Heat Pipe Space Nuclear Reactor

The HPSNR, though it is not currently considered for future development, is an advanced system design for space power applications. The HPSNR is a 100 kWe, high temperature, UO_2 fueled, heat pipe cooled, fast reactor with a thermoelectric conversion system. Figure 2 shows a cutaway view of the HPSNR core. In this design (JPL 1982, Los Alamos 1982, El-Genk et al. 1985, and Louie 1984), the reactor core has 120 fuel modules arranged in five concentric rings around a central plug region. Each fuel module is comprised of a central molybdenum-13 wt% rhenium alloy heat pipe with integrated fins. Fuel wafers of 93.1 percent enriched UO_2 are placed between the fins. The reasons for using unclad fuel were to save mass and extend the lifetime of the core since fission gases are readily released from the fuel into the core cavity and in turn vented directly into space.

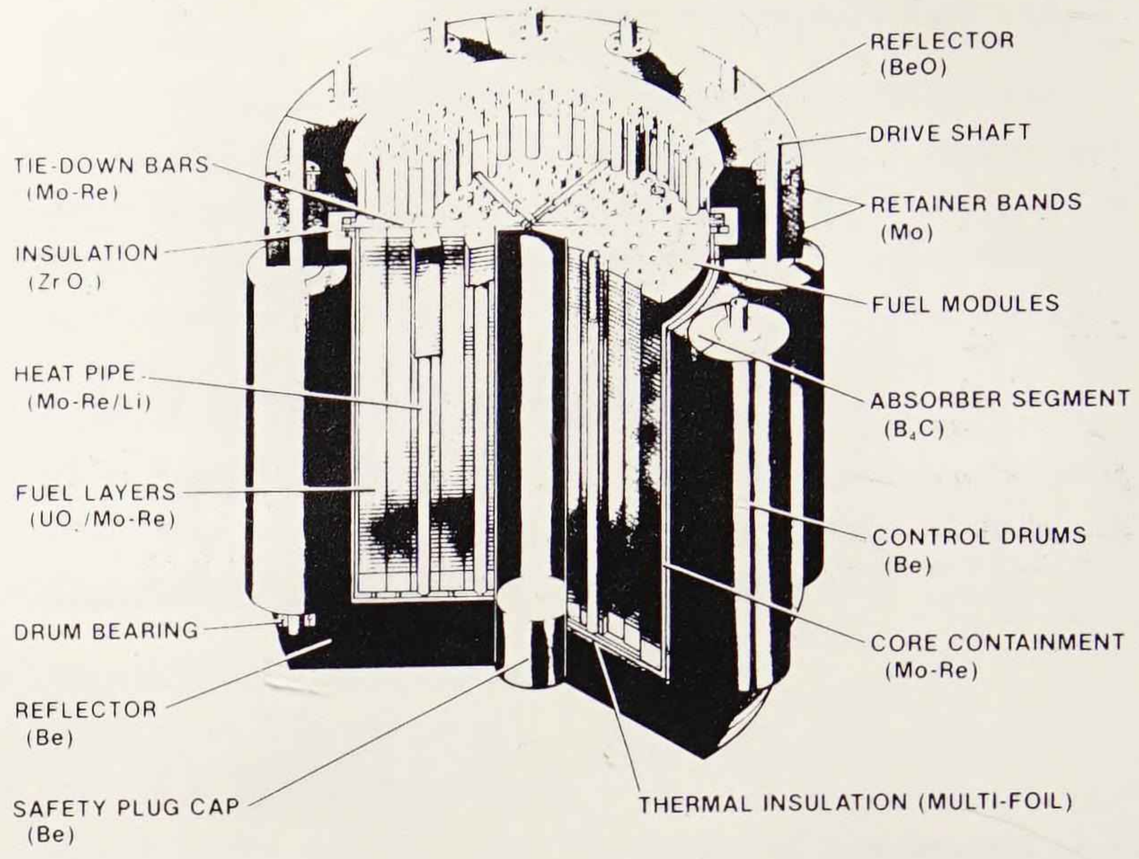


Figure 2 *Cutaway Drawing of the Heat Pipe Space Nuclear Reactor Core.*

The fins and fuel wafers in the HPSNR account for 42 and 27 percent of the reactor core mass, respectively. Adding a 1 mm thick cladding of the same fin material (Mo-13 wt% Re) would increase the mass of the core by as much as 10 percent (Louie 1984). The fuel mass would also have to be increased to make up for the absorption of neutrons in the cladding. In addition to increasing the size of the core, the size of the reflector and the number of control drums, the radiation shield would also need to be increased, thus further increasing the size and mass of the whole system.

NOMENCLATURE

English

C: Total concentration of fission gas (atoms/cm^3)
C_g: Concentration of dissolved gas atoms in fuel grain (atoms/cm^3)
C_b: Concentration of gas atoms in bubbles in fuel grain (atoms/cm^3)
$\overline{C}$: Average gas concentration in fuel grain (atoms/cm^3)
D_g: Effective gas diffusion constant within fuel grain (cm^2/s)
F: Fission rate (fissions $\cdot$ cm$^{-3} \cdot$ s^{-1})
k: Boltzmann constant (ergs/K), Equation (15)
$\overline{K}$: Dimensionless coefficient, Equation (12)
l: Length of venting channel (cm)
m: Molecular weight (g)
M: Molar weight (g/mole)
n: Design safety factor, Equation (1)
P: Pressure (Pa), Equation (8)
Q: Flow of fission gas vented into space (cm^3/s)
r: Radial coordinate
r_{in}: Inner radius of core can (cm), Equation (1)
r_c: Equivalent radius of venting channel (cm)
r_g: Radius of equivalent spherical grain (cm)
RF: Release fraction of fission gas from fuel grain, Equation (7)
t: Time (s)
t^*: Wall thickness (cm), Equation (1)
T: Temperature (K)
V: Volume (cm^3)
X: Empirical constant, Equation (8)
Y: Fission yield (%)
Z: Dimensionless coefficient, Equation (14)

Greek

δ: Diameter of gas molecules (cm), Equation (8)
η: Volumetric fission rate (atoms $\cdot$ cm$^{-3} \cdot$ s^{-1}), Equation (4)
λ_i: Eigenvalue, Equation (1)
σ_{yp}: Ultimate tensile strength of the wall material (Mo-13 wt% Re) of the core can (MPa), Equation (1)
μ: Dynamic viscosity (g $\cdot$ cm$^{-1} \cdot$ s^{-1})

Subscripts

av: Average
c: Core cavity
F: Fuel
s: Outer space

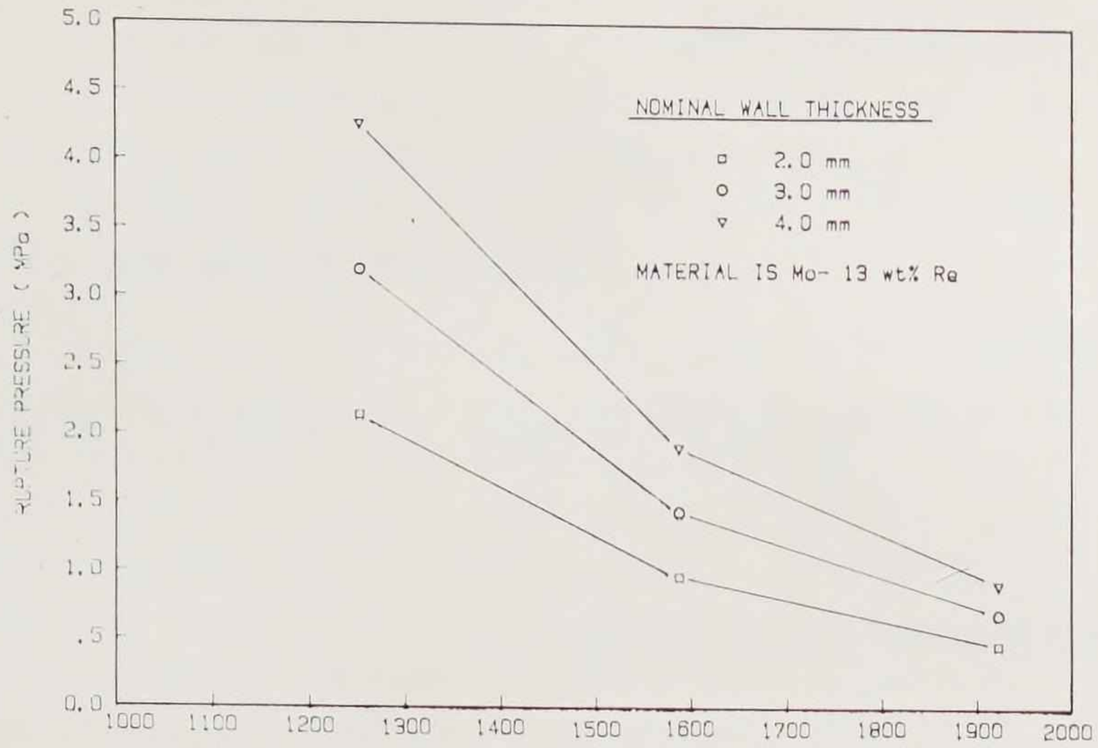


Figure 3 *Calculated Rupture Pressure of the Heat Pipe Space Nuclear Reactor Core Can.*

The core can for the HPSNR is made of 3 mm thick Mo-13 wt% Re alloy and is wrapped in a 5 mm thick multifoil (approximately 60 foils) thermal insulation. The type of the multifoil insulation (high temperature multifoil furnaces, ThermoElectron Corporation) was not determined; however, the use of zirconia coated stainless steel was assumed for the purpose of the present analysis. Applying a small differential pressure (a few kPa) on the multifoil around the core can could effectively increase the heat losses from the core, causing overheating of the reflector and possibly the radiation shield and control drums.

The failure criterion for the core can is

$$\frac{\sqrt{3}\, P_c r_{in}}{2t^*} \geqslant \frac{\sigma_{yp}}{n} . \tag{1}$$

The ultimate tensile stress for the Mo-13 wt% Re is 49.63 and 103.09 MPa at 1923 and 1588 K, respectively. The calculated failure pressure for the core can (inner radius is 16.55 cm), based on a stress analysis of a thin walled cylinder with a safety factor of 1.5, is 0.6925 and 1.439 MPa at 1923 and 1588 K, respectively (Louie 1984). Figure 3 shows the effect of varying the fuel temperature and wall thickness on the failure pressure of the core can. As indicated, the effect of temperature on reducing the failure pressure of the core can is more pronounced than the effect of reducing the wall thickness.

The HPSNR design calls for the fission gases and volatiles to be vented into space by traveling through numerous structural clearances (Meier 1983). Because the venting passages are not well defined, it is difficult to accurately estimate the venting rate of fission gases from the core into space.

Fission Gas Release Model

An intragranular fission gas release model (Wood and Matthews 1980, Booth 1957, and Speight 1969) was used to calculate the release fraction of noble gases (Xe and Kr) and volatile (Cs) fission products from the UO_2 fuel into the core cavity. The gas pressure within the core was calculated as a function of fuel burnup, fuel temperature, and the venting fraction of fission gases into space.

Based on the original idea of Booth (1957) and the modification of Speight (1969), Wood and Matthews (1980) have developed a modified version of intragranular fission gas release model based on random diffusion. They have taken into account the knock-on resolution process and the nucleation of gas bubbles within a spherical grain. The governing equation for the fission gas release from an equivalent spherical grain to the grain boundary can be given as:

$$\frac{\partial C}{\partial t} = \frac{1}{r^2}\,\frac{\partial}{\partial r}\left[D_g r^2 \frac{\partial C}{\partial r} \right] + \eta \tag{2}$$

where $C = C_g + C_b$.

The initial and boundary conditions are

$$C(r, 0) = 0, \tag{3a}$$

$$\frac{\partial C}{\partial r}(0, t) = 0, \tag{3b}$$

$$C(r_g, t) = 0. \tag{3c}$$

The effect on the diffusion process of the resolution and nucleation of gas bubbles within the grain is considered in determining the effective gas diffusion coefficient, D_g, (Wood and Matthews 1980). The effects on the biased diffusion of gas atoms of temperature have been neglected in the present model because of the small spatial temperature variation in the HPSNR fuel wafers (~300°C/cm). The fission gas production rate within the grain, η, is defined as:

$$\eta = F \cdot Y \tag{4}$$

where η can be taken as a constant or a function of time for steady-state and transient operation of the reactor core, respectively.

The solution of Equation (1), using the given initial and boundary conditions and assuming a constant fission gas production rate is

$$C(r, t) = \frac{\eta r_g^2}{6Dg}\left[1 - \frac{r^2}{r_g^2} \right] + \sum_{i=1}^{\infty} \frac{2\eta(-1)^i}{r_g D_g \lambda_i^3} \sin(\lambda_i r_g) e^{-\lambda_i^2 D_g t} \tag{5}$$

where λ_i is the eigenvalue of ith term and it is defined as:

$$\lambda_i = \frac{i\pi}{r_g} . \tag{6}$$

The release fraction, RF, of a fission gas species is

calculated using the following equation:

$$RF = 1 - \frac{\bar{C}(t)}{\eta t} . \quad (7)$$

For more details on the model development, see Louie (1984), Wood and Matthews (1980), Booth (1957), and Speight (1969).

Fission Gas Venting Model

The gas flow in vacuum can be classified either as molecular flow, transitional flow or viscous flow. For viscous flow, the Knudsen number (that is, the ratio of the mean free path of the gas molecules to the radius of the venting channel), Kn, is less than 0.01; for molecular flow, Kn is larger than 1; and for transitional flow, Kn is between 0.01 and 1.

Molecular flow occurs if the gas partial pressure in the core satisfies the following criterion:

$$P_i < \frac{\left[1 + \frac{X}{T_{av}}\right] kT_{av}}{10\sqrt{2}\,\pi\delta^2 r_c} . \quad (8)$$

The gas flow through the venting channel will become viscous flow when the partial pressure of the gas in the core becomes more than two orders of magnitudes higher than the pressure given by Equation (8).

If there is more than one species of gas present in the core cavity, the total pressure in the core, P_c, can be calculated as:

$$P_c = \sum_{i=1}^{n} P_i \quad (9)$$

where P_i is the partial pressure of the ith species in the core and is given as:

$$P_i(t) = \frac{kT_c}{10V_c}\left[\eta_i t R F_i V_F - N_i\right]. \quad (10)$$

In the HPSNR, the fission gas temperature in the core is approximately the same as that of the fuel (~1700 K). Because the temperature in space is about ~10 K, the number density of the gas would change along the venting channel. The vented rate of fission gas, Q (cm^3/s), from the core to outer space can be given as (Louie 1984):

For Molecular Flow

$$Q = 3.64 \times 10^3 \bar{k}\pi r_c^2 \left[\frac{T_{av}}{M}\right]^{1/2}, \quad (11)$$

and the coefficient $\bar{k}$ is given by:

$$\bar{k} = \left(1 + \frac{3}{8}\frac{l}{r_c}\right)^{-1}. \quad (12)$$

For Transitional Flow

$$Q = 30.43 \times 10^3 \frac{r_c^3}{l}\left[\frac{T_{av}}{M}\right]\left[(0.1472/\mathrm{Kn}) + Z\right] \quad (13)$$

where

$$Z = (1 + (2.507/\mathrm{Kn}))/(1 + 3.095/\mathrm{Kn}). \quad (14)$$

For Viscous Flow (Laminar)

$$Q = \frac{\sqrt{kT_{av}}}{45.6 m P_c}\left\{-167l + \sqrt{kT_{av}(16\mu l)^2 + 456 r_c^4 P_c^2 m}\right\}. \quad (15)$$

Cesium Release Model

Unlike noble gases Xe and Kr, volatile fission products (for example, Cs and Rb) exhibit strong chemical reaction with UO_2 fuel as well as with other fission products such as iodine. Only cesium release was considered in this analysis. According to the cesium release model by Schumacher and Wright (1982), the cesium release fraction can be calculated in terms of the cesium's partial pressure in the fuel. The latter is calculated as a function of the oxygen-to-metal ratio (O/M) in the fuel and the fuel temperature. The model assumes that only the more stable of the two cesium uranate compounds, Cs_2UO_4 and $Cs_2UO_{3.56}$, and elemental cesium will contribute to the release of cesium.

To determine which cesium compound (Cs_2UO_4 or $Cs_2UO_{3.56}$) is the more stable, the oxygen potential in the fuel is compared with the oxygen potential of a molar balanced Cs_2UO_4-$Cs_2UO_{3.56}$-UO_2 system. This oxygen potential determines the phase boundary changing from Cs_2UO_4 to $Cs_2UO_{3.56}$. Then the cesium vapor pressure in the fuel is calculated as a function of the oxygen partial pressure and compared with the vapor pressure of elemental liquid cesium at the fuel operating temperature. The cesium pressure is taken from the species with the lowest vapor pressure because it is the most stable. After the cesium pressure in the fuel is determined, the model (Schumacher and Wright 1982) assumes that if the cesium vapor pressure is less than the xenon gas pressure in the fuel, the release fraction of Cs would equal the ratio of Cs vapor pressure to the Xe pressure in the fission gas bubbles in the fuel, multiplied by the release fraction of xenon. When the cesium pressure is greater than the xenon pressure in the fuel, the release fraction of Cs is assumed to be the same as that of Xe. For more details, see Louie (1984) and Schumacher and Wright (1982).

Equations (7) and (9) are solved simultaneously to calculate the release fractions as well as the partial

pressures of Xe, Kr, and Cs in the HPSNR core as functions of fuel temperature and fuel burnup, with the core vents either partially or completely plugged.

Results and Discussion

To predict the effect of either partial or complete plugging of the core venting system on the potential failure of the core containment of the HPSNR, calculations were conducted for the release fractions of noble gases (Xe and Kr) as well as of cesium. Both xenon and krypton possess the same release characteristics (Wood and Matthews 1980). Table 1 presents the data used in calculating these release fractions (Louie 1984).

Figure 4 shows the predicted weighted release fractions of fission gases Xe, Kr, and Cs as functions of fuel burnup for a fuel temperature of 1700 K, the operating fuel temperature in the reference design of the HPSNR. In Figure 4, the weighted release fraction of cesium is the same as the cesium release fraction given by Equation (7). However, the weighted release fractions for Xe and Kr are equal to the release fraction from Equation (7) multiplied by $(Y_{Xe}/(Y_{Xe} + Y_{Kr}))$ and $Y_{Kr}/(Y_{Xe} + Y_{Kr}))$, respectively. As shown in Figure 4, the release fraction initially increases rapidly with fuel burnup up to 2.0 at.%; then it increases slowly with fuel burnup. More than 90 percent of the Cs, approximately 80 percent of Xe, and only 15 percent of Kr would be released into the core at the end of life (3 to 7 years) or approximately 3 to 5 at.% burnup.

To examine closely the effect of fractional venting of the reactor core on the core can pressurization, the

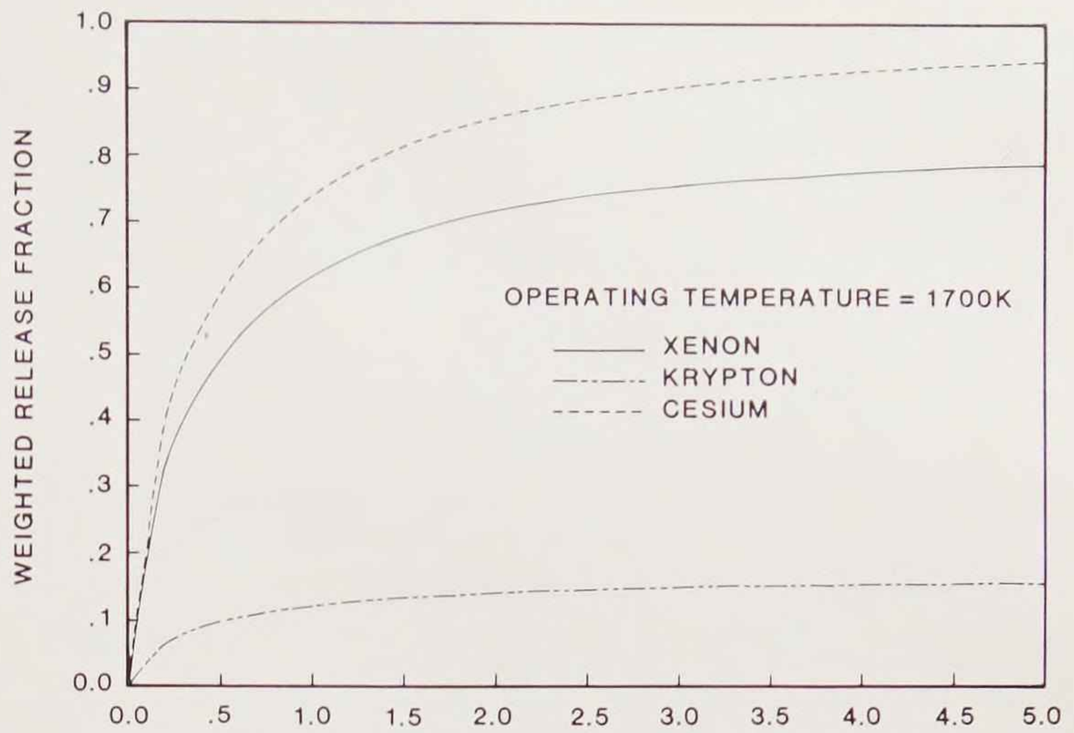


Figure 4 *Predicted Release Fractions of Xe, Kr, and Cs from UO_2 Fuel at 1700 K.*

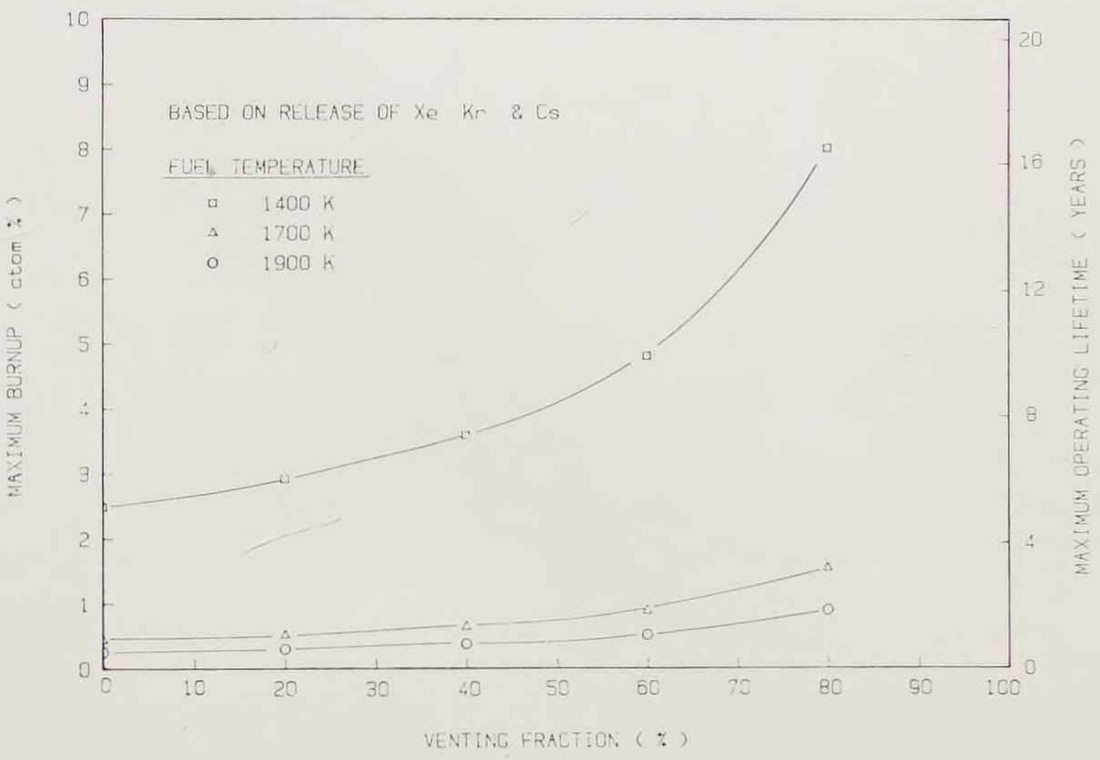


Figure 5 *Maximum Fuel Burnup in the Heat Pipe Space Nuclear Reactor Core to Avoid Rupturing the Core Can.*

Table 1 *Parameters for Fission Gas Release Calculations.*

Effective Diffusion Coefficient:

$D_g = 9.281 \times 10^{-17} \text{cm}^2/\text{s}$, at 1400 K

$D_g = 8.459 \times 10^{-15} \text{cm}^2/\text{s}$, at 1700 K

$D_g = 2.140 \times 10^{-14} \text{cm}^2/\text{s}$, at 1900 K

Fuel Grain Radius:

$r_g = 6.0\ \mu\text{m}$, at 1400 K

$r_g = 15.5\ \mu\text{m}$, at 1700 K

$r_g = 20.0\ \mu\text{m}$, at 1900 K

Fission Rate:

$F = 3.624 \times 10^{12}$ fission/cm^3/S

Fission Product Yield:

$y = 21.6\%$ for xenon

$y = 4.2\%$ for krypton

$y = 16.4\%$ for cesium

Venting Channel Dimensions:

$l = 10$ cm, $r = 254\ \mu\text{m}$

Average Temperature in Venting Channel:

$T_{av} = T_c - 200$ K, at heat pipe exit

$T_{av} = \dfrac{T_c + T_s}{2}$, at bottom reflector exit

Core Dimensions:

$V_c = 6265.6\ \text{cm}^3$,

$V_F = (133.26 \times 10^3/(\text{density of } UO_2))\ \text{cm}^3$

$t^* = 0.3$ cm

maximum fuel burnup needed to avoid rupturing the HPSNR core can is plotted in Figure 5 as a function of the venting fraction for varying fuel temperatures. As indicated in Figure 5, there is an increase in the maximum fuel burnup (at.%) (or the maximum operating lifetime) as the venting fraction of the noble gases (Xe and Kr) and Cs increases.

When the fuel operating temperature is as low as 1400 K, a maximum fuel burnup of ~2.5 at.% (or an operating lifetime of 5 years) is attainable, even if the reactor core is completely plugged. As the fuel temperature increases from 1400 to 1700 K, more fission gases are released from the fuel matrix into the core cavity causing pressurization of the core can, and in turn, reducing the operational lifetime of the core. However, the HPSNR design requirement of 3 to 5 at.% fuel burnup or 3 to 7 years lifetime of the core can easily be attained with only 30 percent of the released gases vented into space.

As the previous discussion indicates the complete plugging of the venting system in the reference design

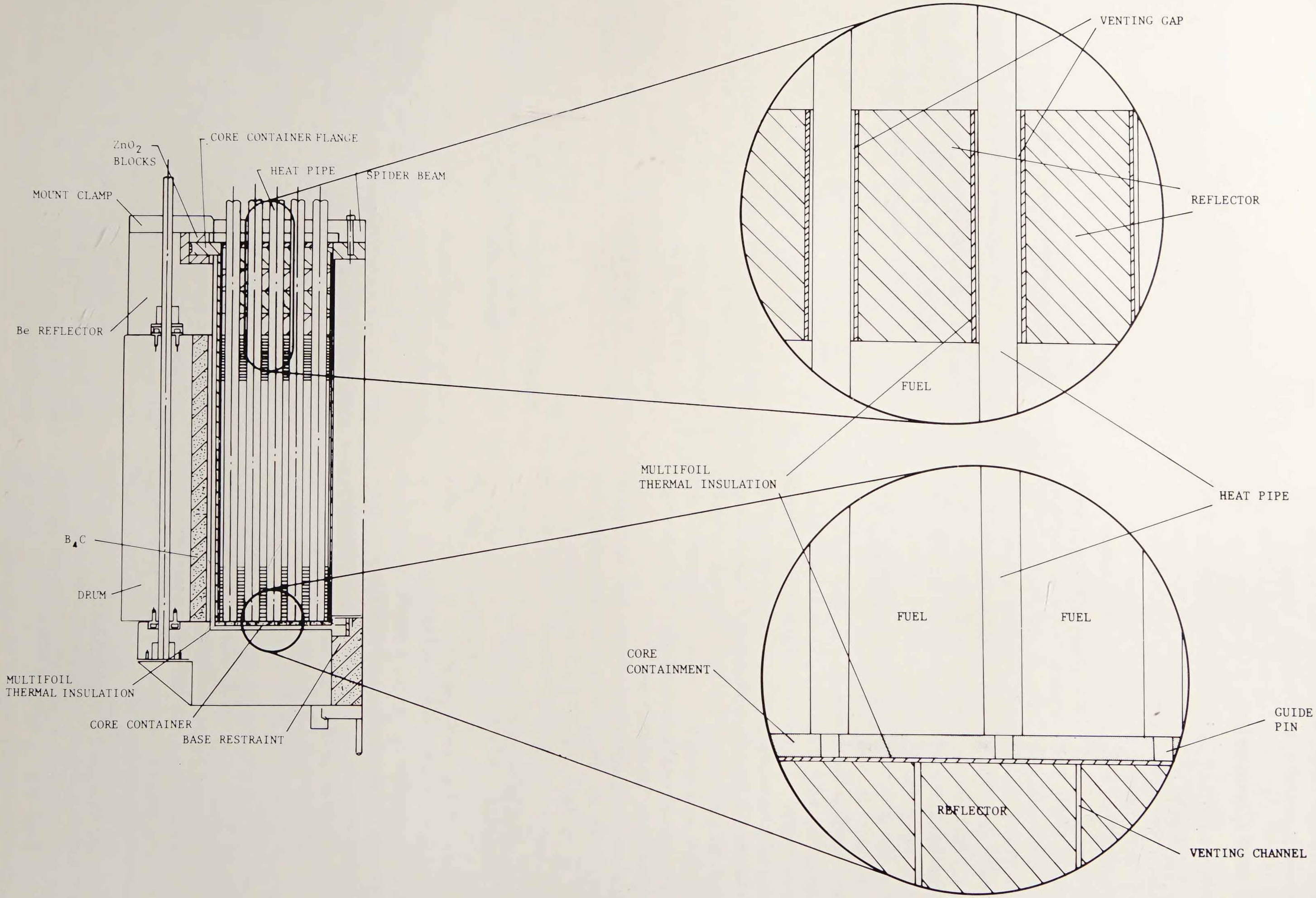


Figure 6 *Venting Channels at the Top and the Bottom Structures of the Heat Pipe Space Nuclear Reactor Core.*

of HPSNR would not cause immediate failure of the core can; however, it would reduce the maximum fuel burnup and subsequently the core's lifetime. Operating the fuel at 1400 K, instead of 1700 K stipulated by the reference design, would not affect the operation of the core even if the core becomes completely plugged. Although operating at this low temperature would reduce fuel swelling, such low operating temperature would concomitantly increase the size and mass of the radiator in addition to reducing the conversion efficiency of the thermoelectric converters.

In the HPSNR, the fission gases may be vented from the core through the structure clearance around the heat pipes that exit through the top BeO reflector. To prevent heat pipes from making contact with and in turn overheating the reflector, a multifoil thermal insulation is wrapped around a segment of the heat pipe. Between each heat pipe and the multifoil insulation, there is a narrow gap (few millimeters in size) which can be used to vent the fission product (both the noble gases and volatiles) into space. (See Figure 6.) The other possible location for venting the HPSNR core design (Meier 1983) is at the bottom reflector as shown in Figure 6. Unlike exiting through the heat pipe and thermal insulation gap at the top reflector where the venting temperature is 1500 K, exiting at the bottom reflector would allow an average venting temperature of ~855 K.

Even well before the rupturing of the core can, applying an external pressure (in the order of a few kPa) on the multifoil insulation wrapped around the core can could cause overheating of the Be reflector. A major contributor is the thermal multifoil insulation wrapped around the core can; this multifoil does not insulate effectively. As shown in Figure 7, 100 foils would provide almost perfect insulation if all the released noble gases are readily vented to space. However, partial venting of these gases would reduce the insulating capability of the multifoils due to the pressure applied on the multifoils by the core can walls. For instance, at a fuel burnup of only 0.10 at.%, the heat flux through a 100 foil insulation would increase from 0 to 110 W/m^2, if only 80 percent of fission gas were vented out. With the venting system completely plugged, the heat losses from the core will almost double to about 260 W/m^2.

As delineated in Figure 8, applying a pressure on the multifoil insulation significantly reduces its insulation capability and subsequently overheats the Be reflector. The calculation presented in Figure 8 assumed adiabatic heating condition. The temperature of 900 K is an upper limit value for the proper operation of Be reflector (Los Alamos 1982).

If the initial temperature of Be reflector were 900 K and the applied pressure were 10 KPa, in a system using the 25 foil insulation the Be reflector would reach its melting point after 10 days of continuous operation. In a system using the 100 foil insulation it would take 39 days for Be reflector to reach the melting point. Increasing the applied pressure to 40 KPa reduces the time for the reflector to reach its melting point; 4 days with the 25 foil insulation and 19 days with 100 foil insulation. It is also shown in Figure 8 that decreasing the initial temperature of Be reflector from 900 to 600 K effectively increases the time required for Be reflector to reach its melting point. Similar arguments could also be made for the effect of any overheating of the control

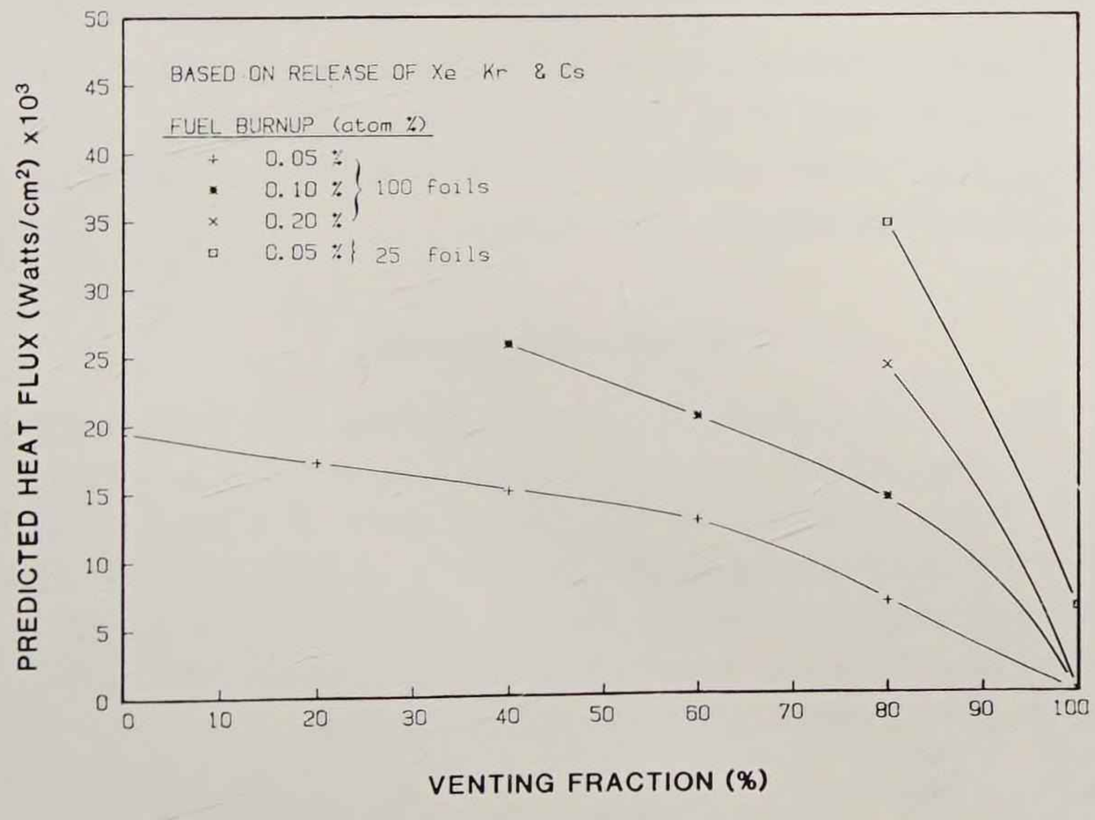


Figure 7 *Predicted Heat Flux Loss through the Multifoil Thermal Insulation as a Function of the Vented Fraction.*

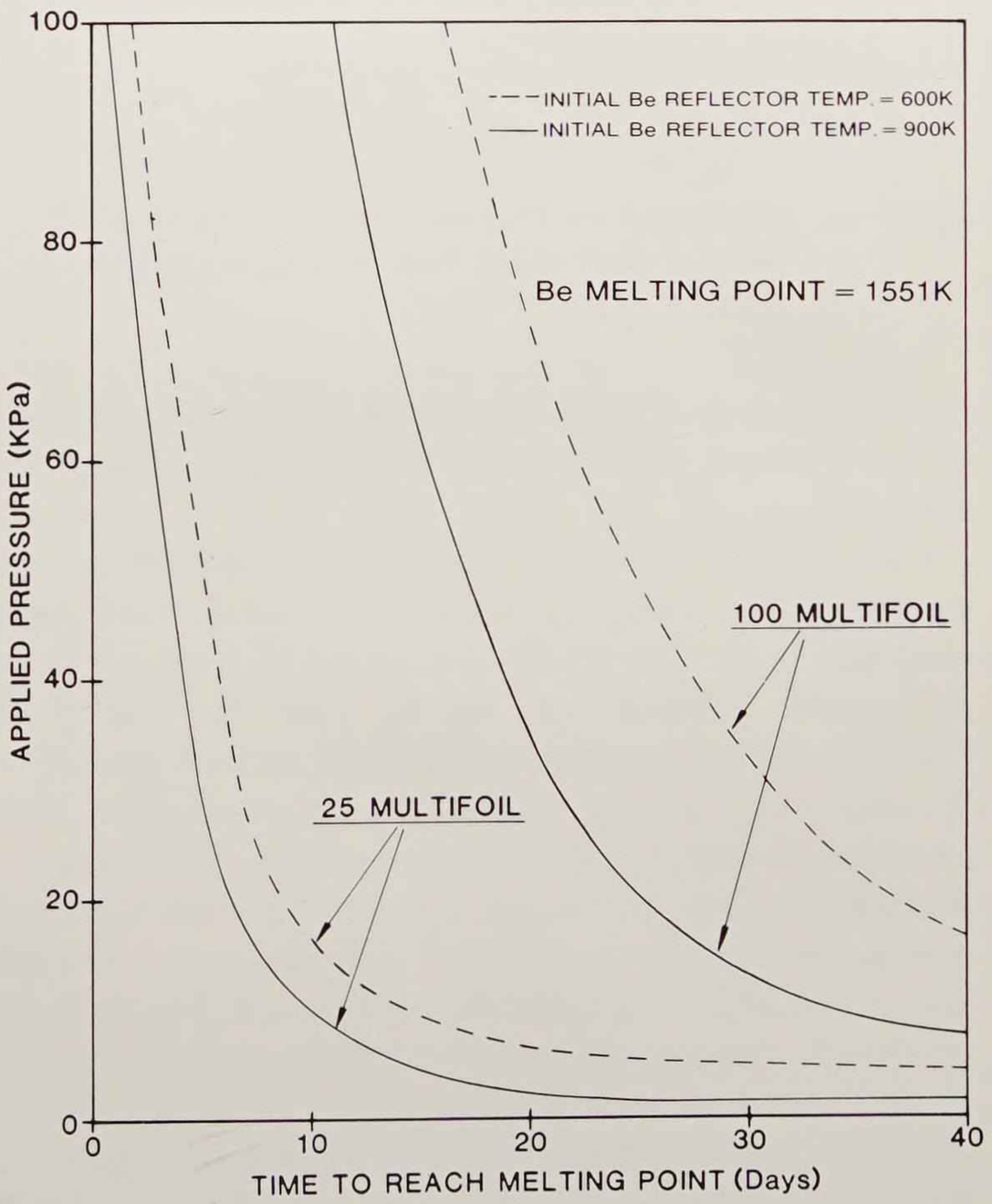


Figure 8 *Overheating of Be Reflector due to Partial Damage of the Multifoil Insulator.*

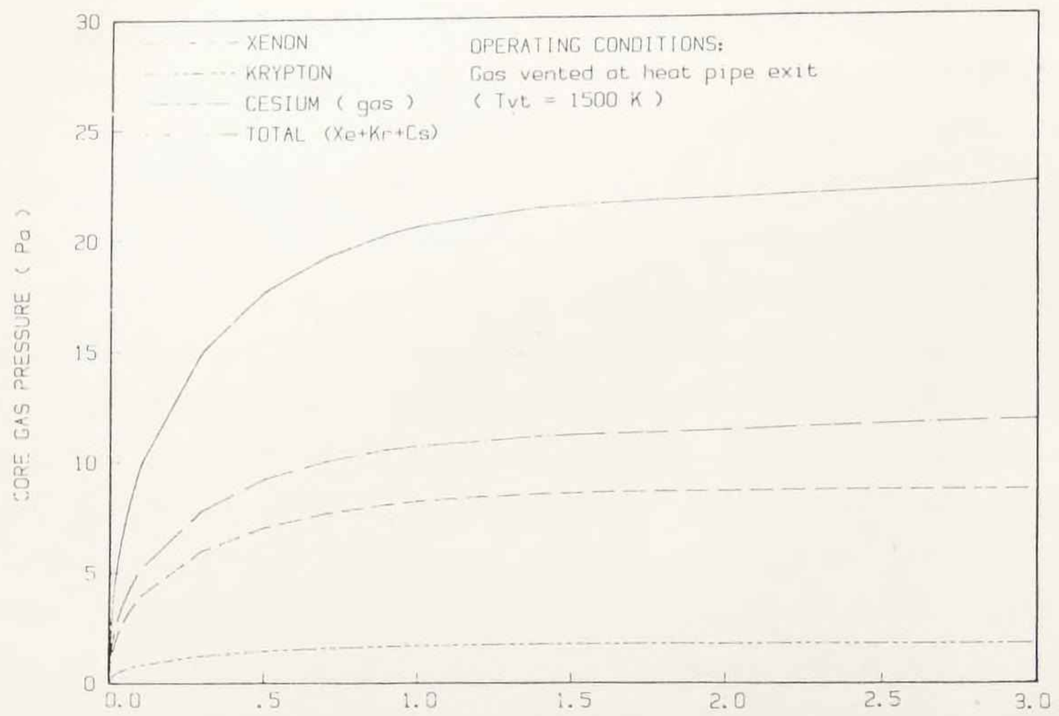


Figure 9 *Predicted Core Pressure with Only One Venting Channel Open in the Top Structure of the Core.*

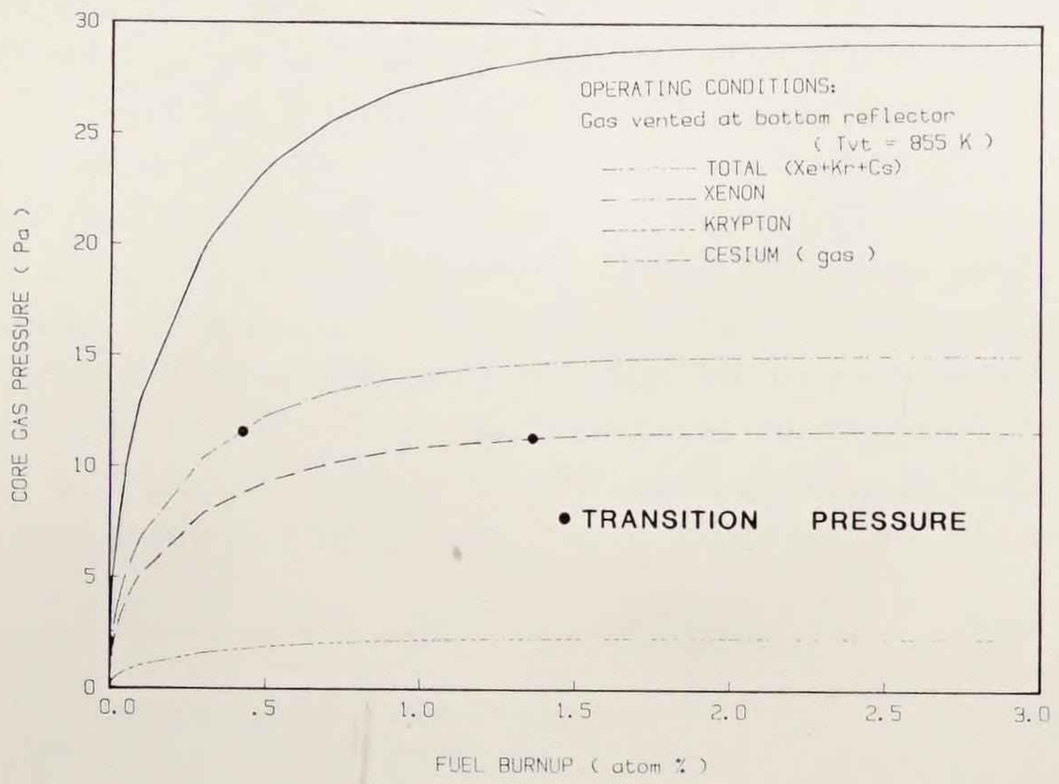


Figure 10 *Predicted Core Pressure with Only One Venting Channel Open in the Bottom Structure of the HPSNR Core.*

drums and radiation shield caused by the partial failure of the multifoil thermal insulation wrapped around the core can.

Calculations were also conducted based on the assumption that only one venting gap at the heat pipe exist was open. The results delineated in Figure 9 show the partial pressures of Xe, Kr, and Cs plotted as functions of fuel burnup. Initially the vented gases flow through the venting channel as a molecular flow (Knudsen number < 0.1); subsequently, it becomes a transitional flow as the pressure in the core increases due to the partial accumulation of fission gases. For the gas exiting at the top reflector, as shown in Figure 9, the maximum pressure in the core is predicted to be only 23 Pa at 3 at.% fuel burnup. On the other hand, for the gas exiting at the bottom reflector as shown in Figure 10, the maximum pressure in the core is predicted to be 29 Pa at 3 at.% fuel burnup. The higher pressure for the latter case is due to the lower venting temperature (855 K) which would decrease the flow through the channel. (See Equations 11–15.) For both venting temperatures (1700 and 855 K), the pressure buildup in the core is well below the predicted rupture pressure of the HPSNR core can. (In Figure 10, the transition pressure is the core pressure at which the flow in the venting channel changes from molecular flow to transitional flow.)

Conclusions

This study explored the consequences of either partial or complete plugging of the venting system in the HPSNR by developing a coupled fission gas and volatile release-venting model. The release fractions of Xe, Kr, and Cs were calculated by using an intragranular fission gas release model based on an equivalent spherical grain. This model is coupled with a venting model of fission gases into space to assess the pressure buildup in the core caused by the accumulation of noble gases (Xe and Kr), as well as cesium. Preliminary calculations showed that complete plugging of the venting system in the HPSNR would neither influence the core's performance nor its lifetime as long as the temperature of the fuel is kept at about 1400 K. However, operating the fuel at the specified operating temperature of 1700 K for the reference design of the HPSNR would encourage fission gas release from the fuel into the core cavity; such a release could cause the core can to fail prematurely. In either case, moderate pressurization of the core without a concomitant failure of the core can could damage the multifoil insulation wrapped around the core can and cause overheating of the Be reflector, control drums, and radiation shield. However, it is highly unlikely that the venting system of the HPSNR would be completely plugged early in its life.

Although the models presented in this paper were applied to a specific design (HPSNR), it could easily be applied to other space nuclear reactor designs. For example, these models could aid in designing a core venting system and could augment the study of the effects of fission gas and volatile venting on the performance of thermionic fuel design.

Acknowledgments

The authors gratefully acknowledge the help provided by Dr. Jeffery Rest at Argonne National Laboratory, and Professor Norm Roderick in the Department of Chemical and Nuclear Engineering at the University of New Mexico. This work is supported by the Nuclear Technology Office of the Air Force Weapons Laboratory, under Contract No. F29601-82-K-0055 to the University of New Mexico.

References

Booth, A. H. (1957) *A Method of Calculating Fission Gas Diffusion from UO_2 Fuel*, Chalk River Report CRDC-721.

El-Genk, M., D. Woodall, V. Dean, and D. Louie (1985) "Design Status of the SP-100 Nuclear Reactor System," in *Space Nuclear Power Systems 1984*, M. S. El-Genk and M. D. Hoover eds., Vol. 1, Orbit Book Co., Malabar, FL.

JPL, *SP-100 Conceptual Design Description*, Jet Propulsion Laboratory, Pasadena, CA, June, 1982.

Katucki, R. J., A. Josloff, A. Kirpich, and A. Florio (1985) "Evaluation of System Concepts for the 100 kWe Class Space Nuclear Power System," in *Space Nuclear Power Systems 1984*, M. S. El-Genk and M. D. Hoover, eds., Vol. 1, Orbit Book Co., Malabar, FL.

Los Alamos (1982) *SP-100 Project Semi-Annual Technical Progress Review*, Los Alamos National Laboratory, Los Alamos, NM, October, 1982.

Louie, D. L. Y. (1984) *Effects of Venting System Failure on Operation of SP-100 Space Nuclear Reactors*, M.S. Thesis, Department of Chemical and Nuclear Engineering, University of New Mexico, Albuquerque, NM.

Meier, K. (1983) *Private Communication*, Los Alamos National Laboratory, Los Alamos, NM.

Speight, M. V. (1969) "A Calculation on the Migration of Fission Gas in Material Exhibiting Precipitation and Resolution of Gas Atoms Under Irradiation," *Nucl. Sci. Engr.*, **37**:180–185.

Schumacher, G. and S. A. Wright (1982) *Advanced Reactor Safety Research Quarterly Report, April–June, 1982*, Sandia National Laboratories, Albuquerque, NM, Vol. 22 pp. 352–375.

Wood, M. H. and J. R. Matthews (1980) "A Simple Operational Gas Release and Swelling Model," *J. Nucl. Mater.* **91**:34–40.

Space Nuclear Power Systems 1984
Edited by M. S. El-Genk and M. D. Hoover
© Orbit Book Company, Malabar, FL, 1985

Chapter 61

Overview of the Hazards of Using Lithium in Space Nuclear Reactor Systems

Mark D. Hoover, Michael D. Allen, Bernard J. Greenspan, Simon J. Rothenberg, and Fritz A. Seiler

Lovelace Inhalation Toxicology Research Institute
Albuquerque, New Mexico 87185-5890

Lithium and lithium compounds are being considered for use in space nuclear systems. Lithium metal is an excellent heat transfer fluid and lithium hydride forms an effective neutron shield. However, there are safety concerns associated with the use of lithium because it is highly chemically reactive. Reactions of lithium with containment materials can cause corrosion and structural degradation. If molten lithium metal is exposed to air, it will react exothermically and form a dense, white aerosol. Lithium aerosols are caustic and can damage the respiratory tract if inhaled. Information in the literature on the toxicity of inhaled lithium is limited to studies of lithium hydride. Additional studies are needed on the products of lithium combustion in air, specifically lithium monoxide, lithium hydroxide, and lithium carbonate. Such studies are important in evaluating the consequences of a potential accident during production and handling of lithium on the ground, during a launch pad accident, or during atmospheric reentry of the lithium components of space nuclear systems.

Introduction

Safety is a major concern in developing space nuclear reactor systems. Design criteria have been focused on developing cost effective systems with high reliability and on minimizing the hazards to ground personnel and the public. Design concepts attempt to minimize the probability of accidental releases of toxic materials to the workplace or general environment. Lithium is one of the materials that could present a safety hazard. This paper highlights the potential uses of lithium in space nuclear systems, describes the biological properties of lithium, considers possible releases of lithium during accidents involving a space nuclear system, and discusses areas where additional work is needed.

Lithium in Space Nuclear Systems

Two chemical forms of lithium will probably be used in space nuclear systems: lithium metal as a heat transfer fluid and lithium hydride as a neutron shield (see for example, Figure 1). In the late 1950s through the early 1970s, significant work was done with these uses of lithium in projects such as the Airplane Nuclear Propulsion (ANP) Program, the Lithium Cooled Reactor Experiment (LCRE), and the Advanced Power Reactor (APR) Program (Voss 1984). In the Systems for Nuclear Auxiliary Power Program, the SNAP 8 and SNAP 10A designs used lithium hydride shields (Staub 1973).

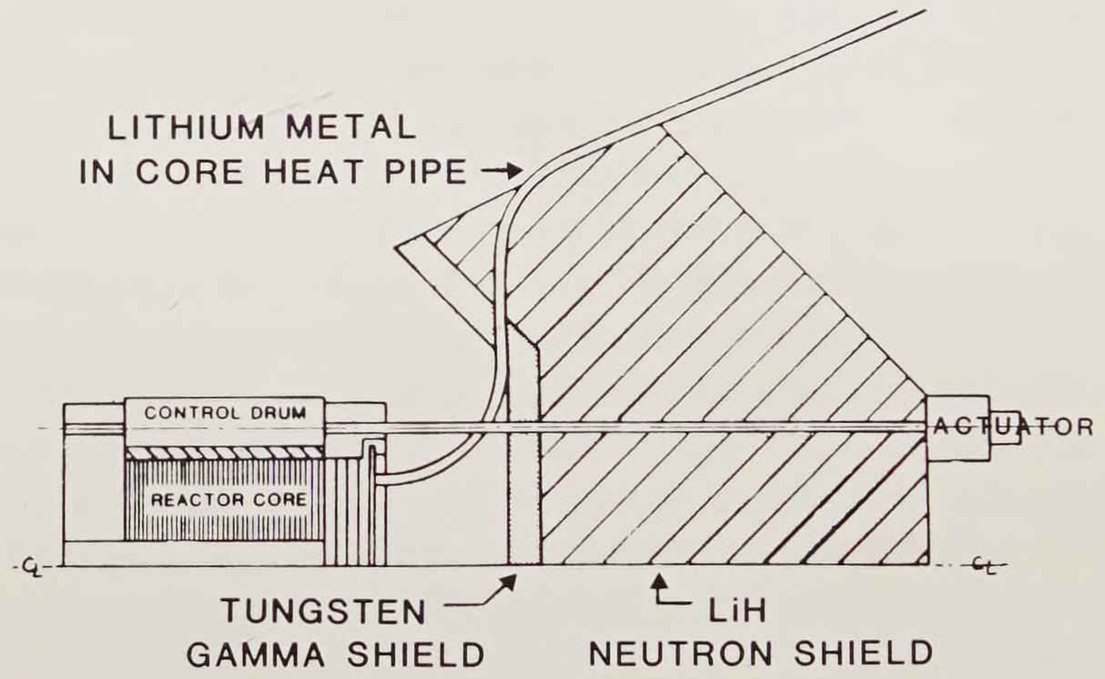


Figure 1 *Schematic of a Reactor Configuration Using Lithium Metal as a Coolant and Lithium Hydride as a Neutron Shield (adapted from Los Alamos 1982).*

Lithium as a Coolant

Lithium is a soft, grey-colored metal that melts at a relatively low temperature (454 K). Along with sodium, potassium, rubidium, and cesium, it is one of the alkali metals. It has excellent thermal transport properties such as thermal conductivity, heat capacity, and high boiling point (1620 K). It is electrically conductive and can be pumped electromagnetically.

Liquid metal cooling is especially suitable for space nuclear reactors with high power density, compact size, and low mass. Liquid metal systems can achieve the high thermal efficiencies associated with high operating

temperatures. Lithium, in particular, because of its high boiling point and low vapor pressure at relatively high temperatures, allows for design of systems with lower mass since thinner walled components can be used in lower pressure systems. Lithium's high heat transfer coefficient enables higher heat fluxes which also allow smaller systems. Smaller systems require smaller shields leading to additional savings in mass.

Liquid metal cooling can be coupled to a number of power conversion designs including thermoelectric systems (Bankston 1985), thermionic systems (Holland, Horner, and Yang 1985), and systems using Stirling (Katucki et al. 1985), Rankine (Jones, MacPherson, and Nichols 1985), or Brayton (Anderson et al. 1983) cycles.

In some power conversion designs, liquid metal will comprise only a portion of the heat transfer system. For example, a system concept involving the Brayton cycle (Anderson et al. 1983) is lithium-cooled, with lithium-to-gas heat exchangers. There are 16 kg of lithium metal in this system: 7 kg in the reactor subsystem and an additional 9 kg in the primary heat transport subsystem. Lithium coolant is circulated by electromagnetic pumps. A combination of helium and xenon is the working fluid for Brayton turboelectric converters.

Lithium could be used in a number of radiator configurations. In a heat pipe radiator, lithium in the hot end of the pipe is evaporated by absorbing heat from the reactor. It travels as a vapor to the cold end of the heat pipe where it gives up heat by condensing. The condensed lithium is drawn back to the hot end by capillary action through a screen wick lining the heat pipe. In the design shown in Figure 2 (Los Alamos 1982), heat pipes are used to transfer heat from a space nuclear reactor to the hot side (inside) of a thermoelectric power conversion system. Heat is radiated to space by the cold side (outside) of the thermoelectric converter. The temperature gradient across the converter induces a voltage drop that can be incorporated into an electric circuit.

Liquid droplet radiator (LDR) systems (Mattick and Hertzberg 1984) use a vibrating orifice plate to create a

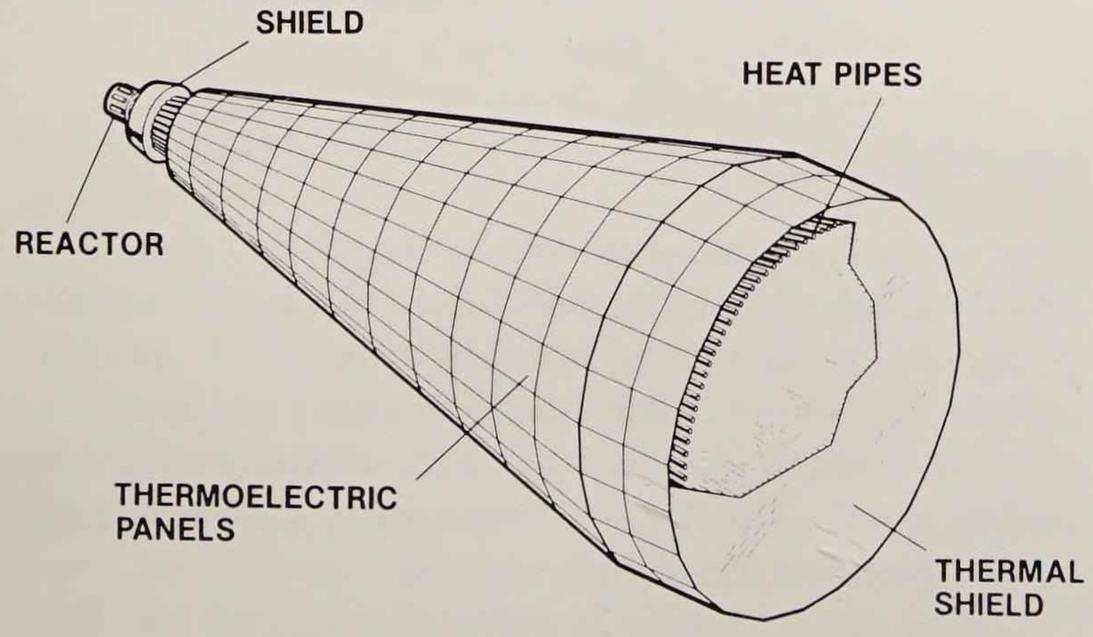


Figure 2 *Schematic of Lithium Heat Pipes coupled to a Thermoelectric Power Conversion System (adapted from Los Alamos 1982).*

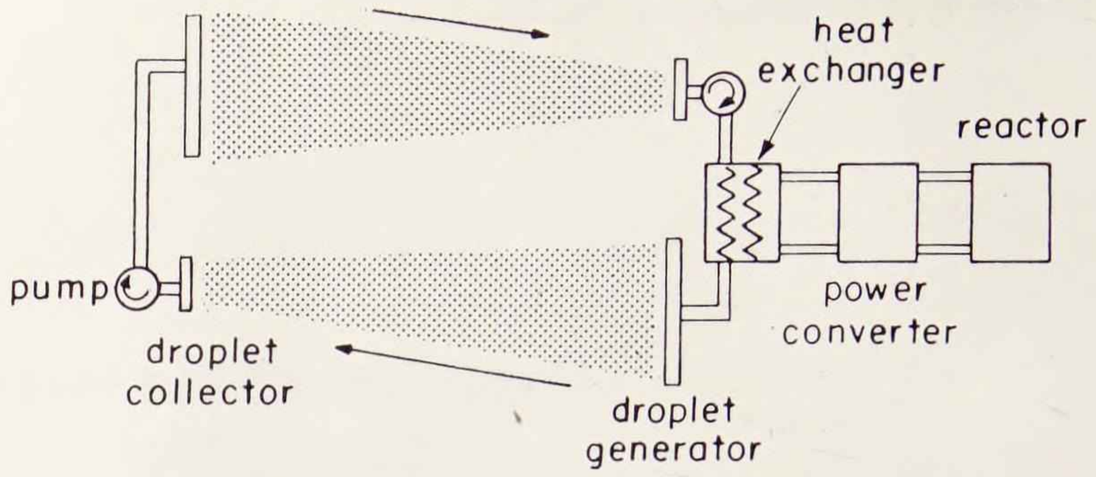


Figure 3 *Schematic of a Liquid Droplet Radiator Concept that could use Lithium Metal as the Heat Transfer Medium (from Mattick and Hertzberg 1982).*

sheet of liquid droplets (Figure 3). The droplets are exposed to space where they can radiate heat effectively. They are collected and returned to the reactor. LDR systems using lithium may be several times lighter than heat pipes. The total radiator system mass could be on the order of 2000 kg with lithium comprising about half of this mass (Mattick and Taussig 1984).

Direct condensing radiators (for example, Miller 1962 and Korsmeyer 1963) operate by condensing the working heat transfer fluid directly on the inside of the radiating surfaces. This results in a higher radiating surface temperature which leads to a higher radiator efficiency, reduced radiator surface area, and reduced radiator mass (Hoffman and Yoder 1985).

Lithium Hydride as Shielding

The second major use of lithium in space nuclear reactor systems is lithium hydride (LiH) as the neutron attenuation component of the radiation shield. The lithium hydride would most likely be surrounded by a shell of stainless steel to protect it from damage (for example, by meteorites) and to help maintain the shield if the lithium hydride suffered melting, swelling, cracking, or thermal dissociation. In order to minimize internal heating within the shield, designs will probably incorporate lithium hydride enriched in ^{7}Li. Naturally occurring lithium is about 92.5% ^{7}Li and 7.5% ^{6}Li (Lederer and Shirley 1978). Lithium-6 readily absorbs a thermal neutron to produce a tritium nucleus and an alpha particle (Figure 4). Lithium-7 has a smaller absorption cross section for thermal neutrons, but will react with fast neutrons. The SNAP 8 design used a lithium hydride shield to spread the internal heating over the shield (Masora 1973).

Lithium hydride would be used in conjunction with a gamma-attenuating material such as shown schematically in Figure 1. Tungsten is a prime candidate because of its high gamma attenuation and good structural properties, although materials such as depleted uranium, borated stainless steel, or Pb-W-LiH are also being considered (Barattino, El-Genk and Voss 1984). The primary neutron shield could have a mass on the order of 350 kg to cover the area between the reactor

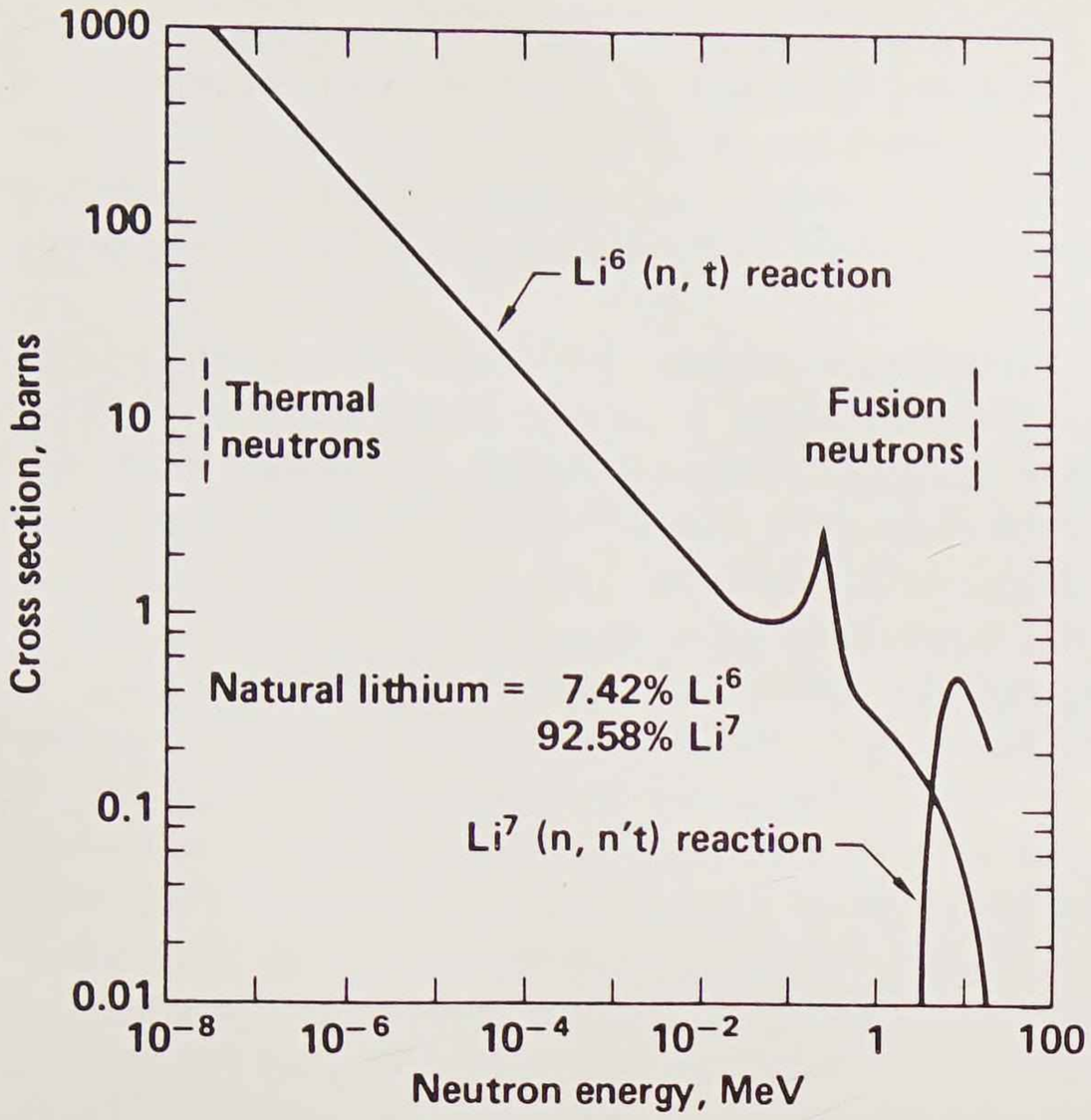


Figure 4 *Neutron Absorption Cross Sections for Lithium-6 and Lithium-7 as a Function of Neutron Energy (from Blink, Krikorian, and Hoffman 1981).*

and the rest of the system. The lithium hydride shield might have a thickness of about 0.8 m (Los Alamos 1982).

One disadvantage of using lithium hydride as a neutron shield is that it must be maintained in a relatively narrow temperature range, probably by some active means (Keshishian et al. 1973). The lithium hydride shield will need to be insulated from any external heat sources to maintain a temperature well below the melting point of lithium hydride (960 K). The operating range of the lithium hydride shield may be as narrow as 600–680 K (El-Genk et al. 1985). At temperatures below about 600 K, there may be significant swelling of lithium hydride exposed to high neutron fluences because radiolytically dissociated lithium hydride does not recombine efficiently at lower temperatures (Welch 1967). The operating range of 600–680 K is also below the temperature at which significant thermal dissociation of lithium hydride might result in hydrogen loss if the shield were punctured by meteoroids.

Biological Properties of Lithium

This section gives an overview of the history of medical use and the biological properties of lithium in order to clarify why there are health and safety concerns related to its use in space systems.

Lithium Ion Toxicity

Lithium salts have an interesting history of use in medicine. In the 19th century, they were prescribed as a sedative and as an anticonvulsant. They were popular for the treatment of gout until this therapy was shown to be of little value (Good 1903). In the 1940s, lithium chloride was used for a relatively brief period as a dietary salt substitute for cardiac and other chronically ill patients. This was soon discontinued following numerous reports of severe intoxication and death (for example, Hanlon et al. 1949). Toxic responses reported by Hammond and Beliles (1980) include a spectrum of effects such as tremors, muscle hyperirritability, and other neuromuscular changes; apathy, mental confusion, blurred vision, seizures, blackouts, comas, and other central nervous changes; hypertension, cardiac arythmia, circulatory collapse, and other cardiovascular changes; loss of appetite, nausea, vomiting, and other gastrointestinal changes; and kidney damage.

Lithium is neither mutagenic nor carcinogenic, but lithium ingested by a mother early in pregnancy may result in an increased frequency of birth defects (Schon 1976) and lithium ingested by a mother late in pregnancy may be chemically toxic to the fetus, causing cyanosis (oxygen deficiency) or flaccidity (poor muscle tone) (Harbison 1980). There is no specific antidote for lithium poisoning. In severe cases, dialysis is sometimes used to remove lithium ions from the body (Gilman et al. 1980).

Lithium salts were introduced in psychiatry in 1949 for the treatment of severe depression, but until 1970 there was a reluctance of American physicians to accept the safety of this treatment (Gilman et al. 1980). One difficulty in this type of therapy is the low safety margin for the concentration of lithium ions in the body. The objective in treatment is to establish and maintain an effective but safe concentration of lithium ions in the body. This is usually done by prescribing a small dose of a lithium compound (for example, one 300 mg tablet of lithium carbonate) to be taken several times a day. Although there is now a large body of information on the determination of safe dosages in the treatment of severe depression (for example, Jefferson and Greist 1977), the mechanism of action of lithium as a mood stabilizing agent remains unknown (Gilman et al. 1980).

The mechanisms of lithium ion toxicity in the body are also not well understood. Lithium ions are readily absorbed from the gastrointestinal tract and become distributed uniformly in human organs. Excretion is mainly through the kidneys. Although trace amounts of lithium ions occur naturally in body tissues, they have no known physiological role. They are smaller in size but chemically similar to the biologically important alkali metal cations sodium and potassium. They also share some of the chemical properties of the divalent cations magnesium and calcium. The average human daily intake of lithium of 2 mg can be compared to 500 mg for magnesium and to gram amounts of dietary calcium, sodium, and potassium (Hammond and Beliles 1980). According to Cox and Singer (1981), a high lithium ion concentration may cause a biological response in two related ways: by upsetting the body's

normal electrochemical and osmotic gradient when lithium ions act as imperfect substitutes for the usually biologically important cations, and by altering the physicochemical properties of proteins, enzymes, and other biological macromolecules.

Lithium Burns

Lithium and lithium compounds can be intensely corrosive and irritating to body tissues. Oral ingestion of substances like lithium hydride has effects similar to those caused by unslaked lime, drain cleaners, and other caustic agents. These alkaline compounds may cause severe chemical burns (Rumack and Peterson 1980). Upon contact with the eyes, they can cause irritation and even permanent eye injury. An individual accidentally burned on the face and upper chest by approximately 500 g of LiH died as a result of his injuries (AIHA 1964).

Apparently, the nature of the cation has relatively little bearing on the severity and consequences of alkali burns (Potts and Gonasun 1980). The extent and duration of the locally altered pH appear to be the critical factors. These local changes in pH are undoubtedly due in part to the production of anions (for example, OH^-) when materials like lithium hydride are hydrolized in body fluids. It is these anions that denature proteins, destroy cell membranes, and affect other critical biological molecules.

Lithium Inhalation Exposure Limits

At present, lithium hydride is the only lithium compound specifically addressed in occupational exposure standards (ACGIH 1982). The Threshold Limit Value (TLV) for lithium hydride is 0.025 mg/m^3 for an 8-hour average exposure and the maximum concentration of lithium hydride in the air must not exceed 0.5 mg/m^3 for even a brief period (ACGIH 1982). There is some evidence that workers readily adapt to exposures to low levels of lithium hydride in air (0.05 mg/m^3), but that such levels are found objectionable by unadapted individuals (AIHA 1964).

Although lithium hydride, lithium oxide, lithium hydroxide, and lithium carbonate are also expected to be damaging when inhaled, they are not specifically addressed in an occupational exposure standard. The only publication on the inhalation toxicity of lithium describes a study of lithium hydride in rats, mice, rabbits, and guinea pigs (Spiegl et al. 1957). Inhaled lithium hydride causes irritation and damage to the cells lining the respiratory tract. Reddening (erythema) or swelling (edema) of tissues occurs. Lung effects, such as pulmonary edema, may result in severe respiratory distress. These effects on the respiratory tract are similar to those resulting from inhalation of other caustic aerosols such as sodium compounds (for example, Zwicker et al. 1979 and Busch et al. 1983).

Information on the effects of inhaled lithium aerosols in humans is limited to personal experiences resulting from small leaks or spills of lithium. Even in the absence of a visible white cloud, reaction to airborne lithium is rapid and characterized by a choking sensation.

Inhalation exposures of people to lithium aerosols are expected to result in caustic damage to tissue rather than systemic effects. Although the human body can accumulate toxic concentrations of lithium ions when lithium is administered orally, it is extremely unlikely that a person could accumulate such a body burden of lithium by inhalation. The normal concentration of lithium ions in the blood of people is about 17 μg per liter blood (Hammond and Beliles 1980). This can be contrasted to a therapeutic, steady-state blood concentration of about 7 mg lithium ions per liter blood (Cox and Singer 1981), achieved by continuous, daily ingestion of a standard lithium therapeutic formulation. Toxic levels of lithium ions in blood are on the order of 14 mg lithium ions per liter blood (Criado et al. 1981).

If we assume that the absorption of lithium ions into the blood from lithium inhaled and deposited in the respiratory tract is similar to the absorption of lithium ions into the blood from lithium in the gut, then we can calculate how much airborne lithium a person might have to be exposed to in order to accumulate a given concentration of lithium ions in the body. The therapeutic blood level of lithium ions is usually maintained by ingesting about 200 mg of lithium ions per day (usually contained in about 1 g of lithium carbonate) (Cox and Singer 1981). Let us assume that a person is breathing at a rate of 7.5 L/min (ICRP 1974) and that 30% of the lithium inhaled is deposited in the respiratory tract (Morrow 1966). In order to deposit 200 mg of lithium ions in the lungs in a 24-hr period, a person would have to be exposed continuously to an air concentration of 70 mg lithium hydride per cubic meter of air. This is nearly 3000 times the TLV for lithium hydride. To accumulate a toxic level of lithium ions in the body, a person would have to remain continuously exposed to an airborne concentration of lithium hydride nearly 6000 times the TLV. No person could tolerate such high exposures.

Concerns for Lithium in Space Systems

This section describes a sequence of generic events in the application of a space nuclear power system during which lithium could be released. These events are shown in Figure 5.

Materials Extraction and Processing

Extraction and processing of lithium and lithium compounds needed for space applications will not cause new hazards to workers in the lithium industry. Standard operating procedures and engineered safety sys-

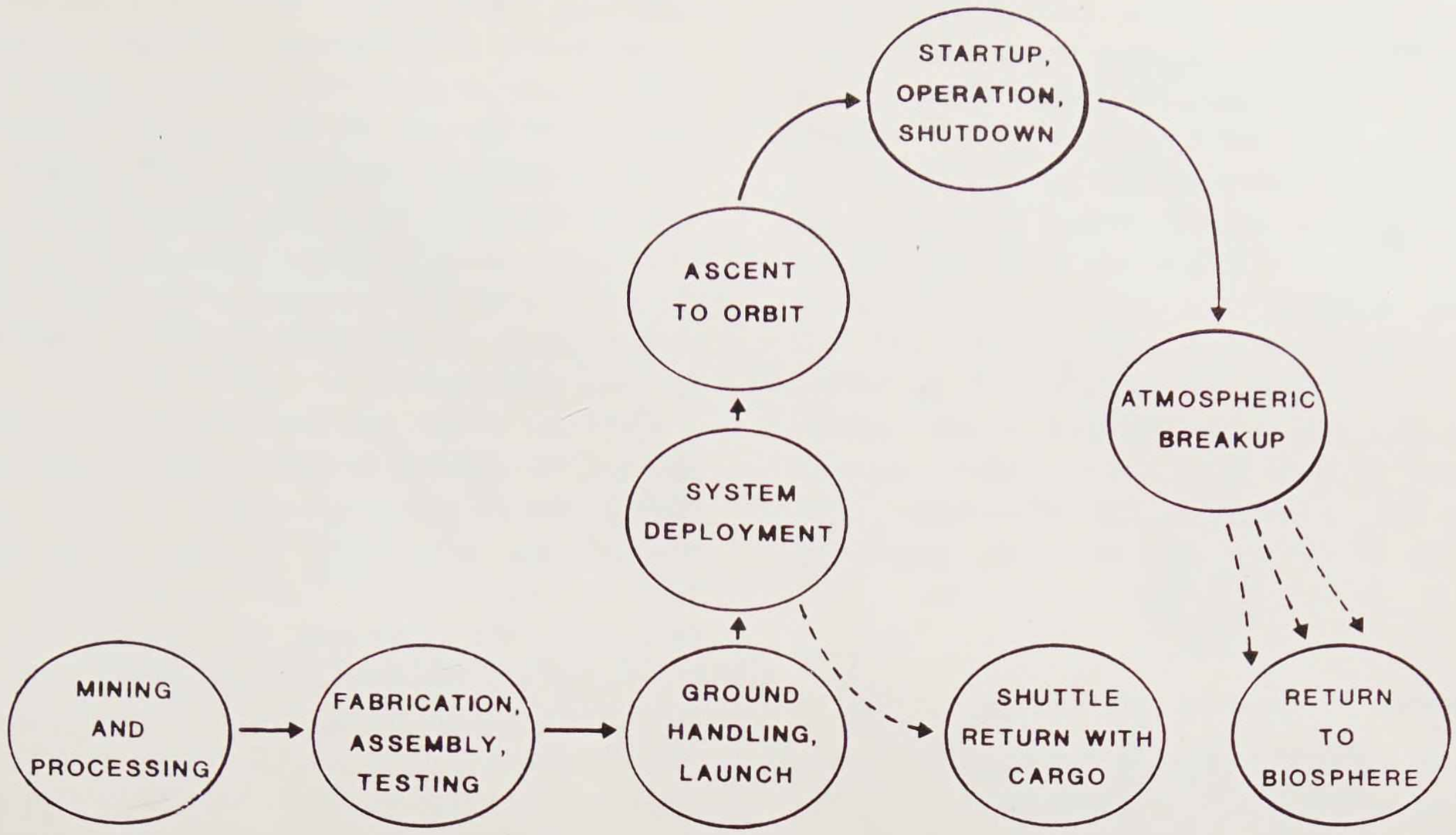


Figure 5 *Events in the Life of a Space Nuclear System during which Release of Toxic Materials could occur.*

tems have attempted to minimize the exposures of workers. Recommendations for the safe handling of lithium are available from a number of sources (for example, from Foote Mineral Company, Lithium Corporation of America, and the Liquid Metals Safety Committee of the U.S. Atomic Energy Commission). Lithium hydride is specifically addressed in the American Industrial Hygiene Association Hygienic Guide Series (1964) and in the National Safety Council Data Sheets (1978). However, no specific information is provided for other chemical forms of lithium.

Because of its reactivity, lithium is generally stored under inert conditions. The metal is usually submerged in a refined, white mineral oil and stored in metal drums coated heavily with petroleum or stored under kerosene or other light petroleum fractions. Storage under high purity argon or helium is also effective (Lithium Corporation of America 1976).

At room temperature, chemical reactions between lithium and air proceed slowly and involve the formation of a soft, white hydroxide and carbonate layer. Water vapor catalyzes the reaction of lithium with atmospheric gases to form lithium nitrides, oxides, carbonates and secondary products (Foote Mineral Co. 1976). Without adequate CO_2 and O_2 in air, lithium metal forms a dense, brittle, reddish-brown coating that

Table 1 *Properties of Lithium and Several Lithium Compounds.*

	Lithium Metal	Lithium Hydride	Lithium Hydroxide	Lithium Oxide	Lithium Carbonate
Chemical Symbol	Li	LiH	LiOH	Li_2O	Li_2CO_3
Molecular Mass (g/mole)	6.94	7.95	23.95	29.88	73.89
Density (g/cm^3)	0.53	0.82	1.46	2.01	2.11
Heat of Formation (kcal/g · mole)	0	−21.6	−116.5	−142.4	−290.5
Melting Point (K)	454	960	723	> 1970	996
Boiling Point (K)	1620	1270[a]	1197[a]	1473[b]	1583
Threshold Limit Value (mg/m^3)	–[c]	0.025	–[c]	–[c]	–[c]

[a] Decomposes.
[b] Sublimes.
[c] No Threshold Limit Value (TLV) has been established for these forms of lithium.

is probably largely lithium nitride (Lithium Corporation of America 1976). These reactions are not sufficiently exothermic to melt or ignite the metal. However, the reactivity of the metal increases rapidly as its melting point is approached. Once lithium metal is ignited, its temperature increases rapidly and it burns with an intense flame. Molten lithium can react with CO_2 to form lithium carbonate (Li_2CO_3), with water or water vapor to form lithium hydroxide (LiOH), and with oxygen to form lithium monoxide (Li_2O) or lithium peroxide (Li_2O_2). Any aerosol formed by the combustion of lithium in air is likely to be a mixture of these compounds. Table 1 gives a number of important physical properties of lithium and its major combustion products.

System Fabrication, Assembly, and Testing

Fabrication, assembly, and testing of components or the integrated reactor system may provide opportunities for lithium leaks, spills, fires, or explosions. Primary concern is for inhalation exposures to lithium that may occur in confined spaces where dilution is limited and escape may be difficult. In addition to inhalation hazards, there are dangers from thermal burns and corrosion of exposed areas of skin.

Safety precautions should include maintaining adequate ventilation and respiratory protection, handling lithium metal with tongs or rubber gloves, and wearing eye protection, protective shoes, gloves, and flame retardant clothing. Caution is recommended, however, when relying on protective clothing. Blink and Hoffman (1981) have reported the results of placing 2–4 g of ignited lithium in contact with various materials. It burned holes in gloves made of PVC and asbestos. Leather gloves burst into flames. It melted holes in aluminum foil, aluminized fire suit material, and face goggles. It reacted violently with vinyl asbestos floor tile, with concrete, and with calcium silicate and other insulations.

For accidents involving leaks and spills, lithium aerosol production may be minimized by flooding with inert gas or smothering with nonreactive powders. Special powders like LITH-X (The Ansul Company, Marinette, WI) and carbon microspheres are effective in extinguishing shallow lithium pool fires. It requires about 5 kg of LITH-X or 3.5 kg of carbon microspheres per kg of liquid lithium to adequately extinguish the reactions (Jeppson 1979a). This type of control is only effective if the powder can form a crust on the top of the liquid or saturate the entire pool. Releases of aerosol from enclosed doors can be reduced by HEPA filters, wet scrubbers, or sand and gravel filter beds (Muhlestein 1980).

Experiments on lithium combustion and control of the combustion products have been performed in connection with fission and fusion research programs (for example, Jeppson 1979a, 1979b, and 1982, Muhlestein 1980, and Hoover et al. 1984). Lithium has been allowed to burn in air and other atmospheres and to react with concrete or water. Since there is water in concrete (about 140 kg/m^3), hydrogen gas is released in the highly exothermic reaction of hot lithium with concrete. The resulting heat keeps the reaction going by forcing more water to the surface. Steel liners or catch pans should be used over concrete in the reactor test area to prevent spills of liquid lithium from contacting and reacting with concrete.

The temperatures produced from an air-lithium reaction are not dependent on the initial temperature of the molten lithium and temperatures can rise to over 1250 K during the course of the reaction (Muhlestein 1980). However, the results of such experiments are very dependent on the combustion atmosphere. Bagnall et al. (1980) studied the formation of lithium aerosol under helium and argon atmospheres at reduced pressures and found aerosol concentrations of up to 10 mg/m^3 at temperatures between 650 K and 850 K. Jeppson (1982) reported that aerosol concentrations of up to 16 g/m^3 can result when a pool of lithium burns in an enclosed area at atmospheric pressure in air and that aerosol concentrations of up to 34 g/m^3 can result when steam is injected into a vessel containing a molten lithium pool. Thus, the concentrations of lithium aerosol that may result from fires or other accidents can be orders of magnitude higher than the airborne concentrations of lithium hydride which are known to cause discomfort and injury in people (see Table 2). (Unfortunately, the entries in Table 2 refer to different chemical forms of lithium and there are no studies in the literature relating the toxicity of these various chemical forms.)

Testing of systems containing lithium also involves concerns for the corrosion and degradation of materials that are in contact with lithium. Whitlow et al. (1979) and Bagnall et al. (1980) have reported the corrosion of austenitic and ferritic steels in an experimental lithium facility. Corrosion rates at 800 K were on the order of $mg/m^2/sec$. The measured weight losses were shown to be due to loss of iron from the ferritic alloys and from the loss of alloying elements from the near surface regions of the austenitic steels. In terms of weight loss, the corrosion by lithium of austenitic alloys was a factor of 3 times more severe than the corrosion of the ferritic materials. Bagnall et al. (1980) also reported that materials like zirconium suffer embrittlement as a result of exposure to molten lithium.

Lithium can also react with nuclear fuel materials. Uranium dioxide (UO_2) has been shown (Kangilaski et al. 1965) to react with lithium at elevated temperatures (1400–1500 K) to form U_3O_8 and free U. The lithium can provide a diffusion path between fuel and cladding and allow atoms of fuel material to react with the cladding (Gluyas and Watson 1975). The free uranium will be molten at temperatures above 1400 K and can degrade the fuel cladding and other structures by forming lower melting point eutectics. Excess carbon in

Table 2 *Comparison of a Range of Lithium Aerosol Concentrations and Their Significance.*

Concentration	Significance
25 $\mu g/m^3$	This is the threshold limit value for an 8 hr average exposure of workers to lithium hydride.[a]
50 $\mu g/m^3$	People initially find this concentration of lithium hydride objectionable, but workers can adapt to it.[b]
100 $\mu g/m^3$	Eye and nose irritation result at this concentration of lithium hydride, even in people with some adaptation.[b]
200 $\mu g/m^3$	Itching of exposed areas of skin results above this concentration of lithium hydride.[b]
500 $\mu g/m^3$	This is the maximum tolerable concentration for even brief exposures of workers to lithium hydride.[a]
10 mg/m^3	This lithium aerosol concentration was measured during handling of molten lithium metal under argon and helium atmospheres at reduced pressures.[c]
5–55 mg/m^3	Laboratory animals exposed to lithium hydride at these concentrations developed ulcers of the nose and forepaws and had damage to the tissues lining the upper respiratory tract.[d]
16 g/m^3	This lithium aerosol concentration was measured when molten lithium metal was combusted in air in an enclosed area. This aerosol was approximately 70% Li_2O, 15% LiOH, 3% Li_2CO_3, 0.2% Li_2O_2, and the balance unidentified.[e]
34 g/m^3	This lithium aerosol concentration was measured when molten lithium metal reacted with injected steam in an enclosed area. This aerosol was primarily $LiOH \cdot H_2O$.[e]

[a] From ACGIH 1982.
[b] From AIHA 1964.
[c] From Bagnall, Down, and Kardos 1980.
[d] From Spiegl et al. 1956.
[e] From Jeppson 1982.

uranium carbide is readily soluble in liquid lithium and can also react with cladding and structure (Cox et al. 1984). Uranium nitride, however, appears to have little reaction with liquid lithium (Weaver and Scott 1965 and Gluyas 1975).

Muhlestein et al. (1980) found that lithium-air reactions that occur in contact with neutron activated stainless steel can volatilize and release radioactive species such as cobalt, iron, and manganese. Figure 6 gives examples of inhalable lithium aerosols formed by the reaction of lithium metal with water, by burning lithium metal in air, and by vaporizing lithium together with stainless steel (Hoover et al. 1984). Whatever the reactor design, it is likely to involve high temperature alloys of the refractory metals niobium, tantalum, molybdenum, and tungsten. Their advantages include high melting points and high elastic moduli. The resistance of refractory alloys to corrosion by liquid metals depends on temperature and the availability of oxygen (Klopp 1984). The presence of nitrogen at concentrations of over 2000 ppm greatly enhances the corrosive interac-

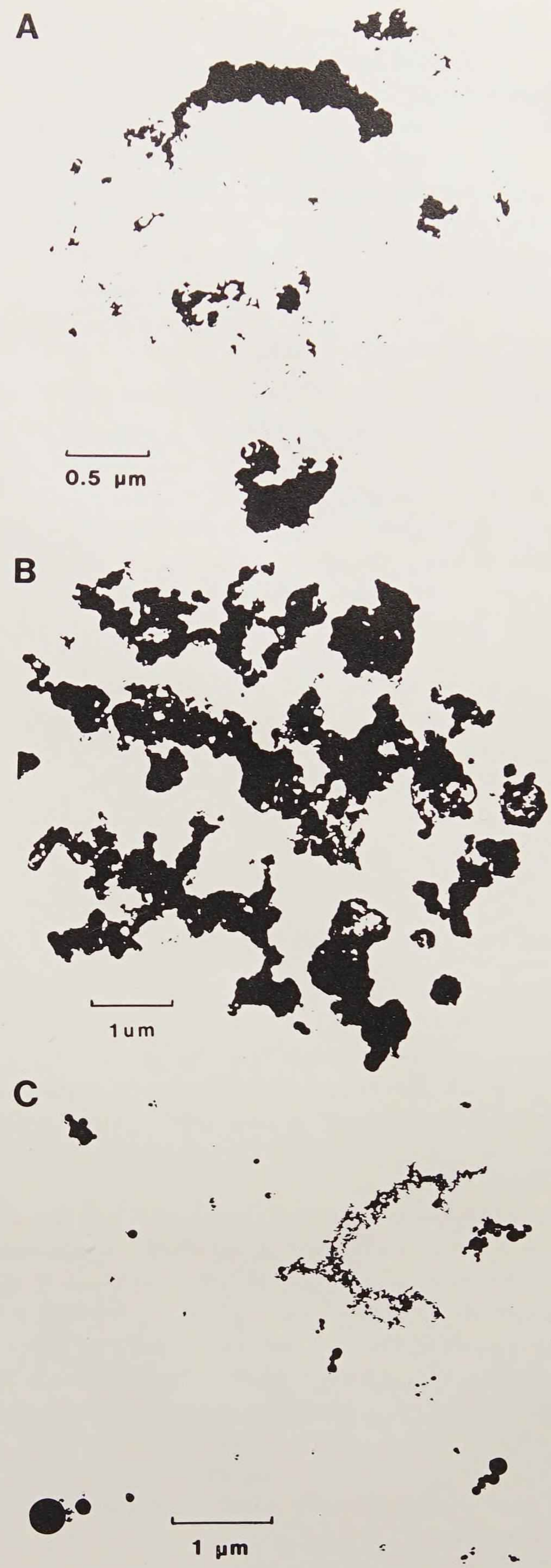


Figure 6 *Transmission Electron Photomicrographs of Lithium Combustion Aerosols produced by (a) Reaction of Lithium Metal with Water, (b) Burning Lithium Metal Heated to 850 K in Air, and (c) Vaporizing Lithium in a Stainless Steel Tube with a Plasma Torch. The Ultrafine, Branched-chain Aggregates in (c) are Stainless Steel and the Attached Larger Spheres (which can be evaporated under the Electron Beam) appear to be Lithium (from Hoover* et al. *1984).*

tion of lithium with stainless steel (Muhlestein 1980). Thus, for demonstration reactor systems undergoing full power testing on the ground, there will be concern for accidental dispersion of fuel material, fission products, and neutron activation product radionuclides. These can be transported and inhaled with the lithium aerosols. At this time there are no data on the health consequences of inhaling lithium in conjunction with other toxic materials such as radionuclides.

Ground Handling and Launch

It is not clear whether the lithium coolant should be molten and in circulation prior to launch, or whether the system should be designed so that the coolant can be solid during launch but melted after the reactor is in orbit. The lithium could also be protected during ground handling and launch by a secondary containment, but this might have to be removed after the system is launched. Minimal fission products and neutron activation products from zero power ground testing will be associated with reactor systems scheduled for launch, but fire or explosion during ground handling, preparation for launch of the space shuttle, or launch could release other airborne contaminants. Lithium would be one component of a complex cloud that could expose ground personnel, visitors at the launch site, and people in offsite areas.

Shuttle Ascent and System Deployment

In the event that the space shuttle is successfully launched but the reactor cannot be deployed, it may be necessary to land the shuttle with the reactor system still in the shuttle bay. Any lithium spills in the cargo bay may cause damage to the shuttle and its cargo. Respiratory protection may be needed for the ground crew after landing.

Accidents during ascent to orbit, start up, operation, and shutdown of the system are more of concern for reliability than for safety. Corrosion product contamination of the coolant could lead to degradation of the thermal performance of the reactor system (Hoffman and Yoder 1985). Leaks during operation could contaminate other parts of the space system with lithium. If the reactor system were deployed in support of a manned operation, such as a space station, it is not clear how accidents could affect the crew, beyond the loss of power.

Atmospheric Reentry of the System

At the end of its mission, the system is expected to be in an orbit with a time to atmospheric reentry (for example, 400 years) adequate to allow for decay of the fission products. Current plans call for dispersion of the reactor system during reentry. This is likely to lead to a fine particle mixture of uranium fuel material, refractory metals, lithium, fission products, neutron activation products, and other structural materials. Since the

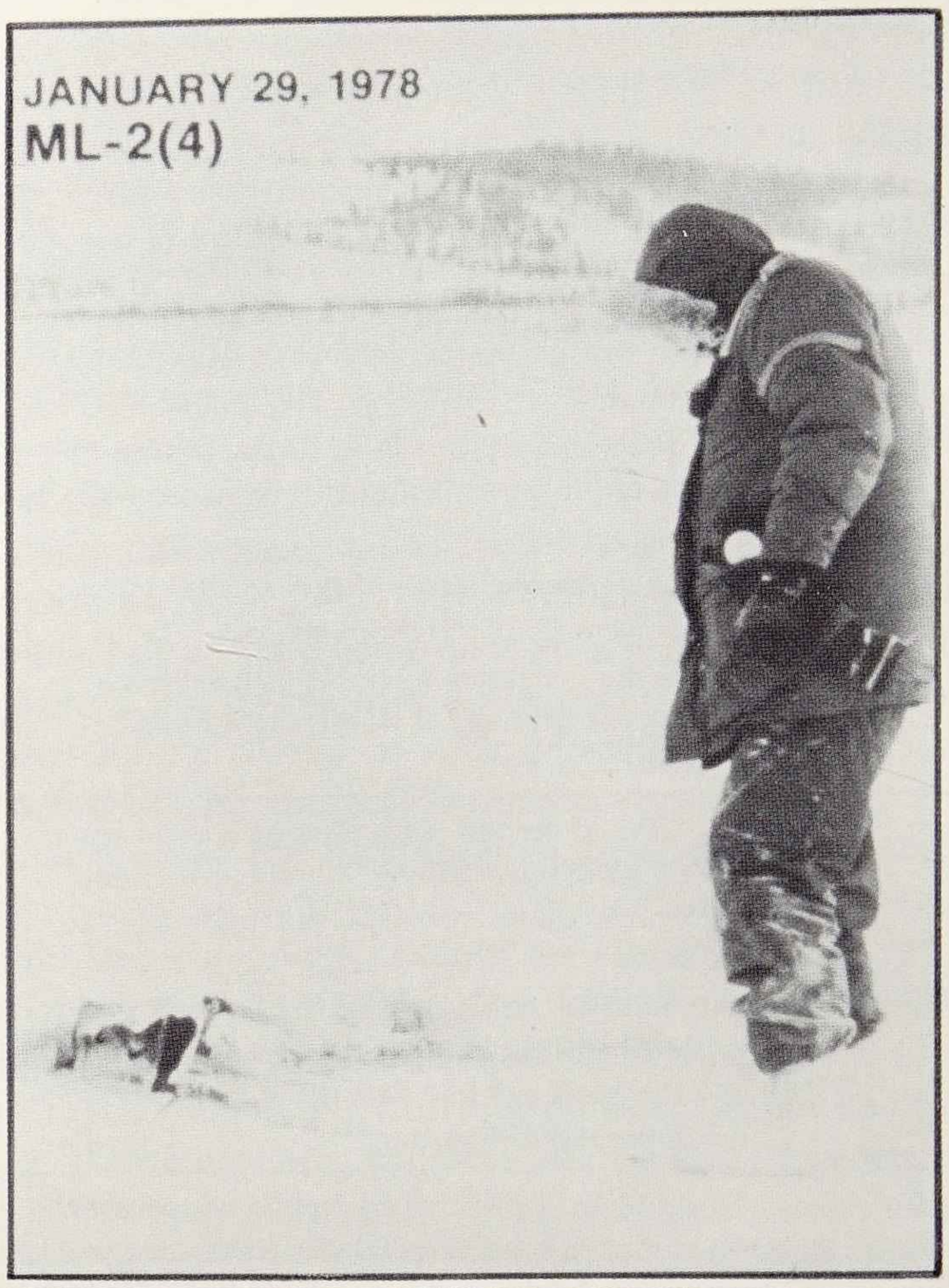


Figure 7 *Photographs of a Lithium Hydride-Containing Portion of the Cosmos-954 Reactor Control System as It was found in the Snow, with Areas of Melting and Dispersed Debris indicating that Combustion had occurred. The Melted Area in the Snow is Approximately 6 m in Diameter. (Photographs courtesy of R. S. Eaton, Health and Welfare, Canada.)*

amount of lithium in most space systems is small, there would probably be no inhalation hazard if lithium were dispersed in the atmosphere during reentry. Some local hazard may result if a component containing lithium, such as an individual heat pipe, reached the earth.

The Cosmos-954 incident provided some information on the reentry and combustion of lithium and other components (for example, Hanafee 1978, Landingham and Casey 1978, Wikjord et al. 1980, and Eaton 1984). Figure 7 shows photographs of a lithium hydride-containing portion of the reactor control system as it was found in the snow by the recovery team (Eaton 1984). It appeared that the lithium hydride had reacted with the snow, melting an area around it and dispersing debris.

Conclusions

Liquid lithium metal is likely to be used for heat transfer and lithium hydride for neutron shielding in space nuclear reactor systems. However, lithium's chemical reactivity makes its use a concern from a safety and reliability perspective. Special procedures and precautions will be necessary to ensure its reliable and safe application. Questions of safety include the risks to ground personnel and possibly members of the public from fire, explosion, and inhalation of lithium aerosol. Although combustion of lithium metal or lithium hydride is likely to result in a respirable aerosol consisting of lithium monoxide, lithium hydroxide, and lithium carbonate, information in the literature on the inhalation toxicology of lithium is limited to studies of lithium hydride. There is no information on the health effects of inhalation exposures to lithium combustion aerosols or on the health effects of inhaling lithium aerosols in conjunction with other toxic materials such as radionuclides. Studies should be conducted to provide this information.

Acknowledgments

This research was performed under U.S. Department of Energy Contract Number DE-AC04-76EV01013. We gratefully acknowledge the useful discussions held with many individuals including W. J. Barattino of the University of New Mexico, J. A. Blink of Lawrence Livermore National Laboratory, J. H. Devan of Oak Ridge National Laboratory, R. S. Eaton of Health and Welfare Canada, H. R. Grady of Foote Mineral Co., D. W. Jeppson and L. D. Muhlestein of Hanford Engineering Development Laboratory, and P. J. McDaniel of Sandia National Laboratories. The useful discussion and critical review of Drs. R. G. Cuddihy, A. R. Dahl, H. C. Yeh, B. B. Boecker, and R. O. McClellan of the Inhalation Toxicology Research Institute are also gratefully acknowledged.

References

ACGIH (1982) *Supplemental Documentation of the Threshold Limit Values*, Fourth Edition, American Conference of Governmental Industrial Hygienists, Cincinnati, OH.

AIHA (1964) "Lithium Hydride," in the *Hygienic Guide Series*, American Industrial Hygiene Association, July–August 1964.

Anderson, R. V. et al. (1983) *SP-100 Program Space Reactor Investigations, Power Plant System Final Report*, Report ESG-DOE-13413, Rockwell International, Canoga Park, CA.

Bagnall, C., M. G. Down, and Z. L. Kardos (1980) *Lithium Studies*, Report WARD-LI-1570-2, Westinghouse Electric Corporation, Madison, PA, August 1980.

Bankston, C. P., T. Cole, S. K. Khanna, and A. P. Thakoor (1985) "Alkali Metal Thermoelectric Conversion (AMTEC) for Space Power Systems," in *Space Nuclear Power Systems 1984*, M. S. El-Genk and M. D. Hoover, eds., Vol. 2, Orbit Book Co., Malabar, FL.

Barattino, W. J., M. S. El-Genk, and S. S. Voss (1985) "Review of Previous Shield Analysis for Space Reactors," in *Space Nuclear Power Systems 1984*, M. S. El-Genk and M. D. Hoover, eds., Vol. 2, Orbit Book Co., Malabar, FL.

Blink J. A. and N. J. Hoffman (1982) "Lithium Safety Considerations," in *1981 Laser Program Annual Report*, Report UCRL-50021-81, Lawrence Livermore National Laboratory, CA.

Blink, J. A., D. H. Krikorian, and N. J. Hoffman (1981) *The Use of Lithium in Fusion Reactors*, Report UCRL-85145, Lawrence Livermore National Laboratory, CA.

Busch, R. H., K. E. McDonald, J. K. Briant, J. E. Morris, and T. M. Graham (1983) "Pathologic Effects in Rodents Exposed to Sodium Combustion Products," *Environ. Res. 31*:138–147.

Cox, C. M., D. S. Dutt, and R. A. Karnesky (1985) "Fuel Systems for Compact Fast Space Reactors," in *Space Nuclear Power Systems 1984*, M. S. El-Genk and M. D. Hoover, eds., Vol. 2, Orbit Book Co., Malabar, FL.

Cox, M. and I. Singer (1981) "Lithium," in *Disorders of Mineral Metabolism*, Vol. 1, Academic Press, New York.

Criado, A., J. Gomez-Arnau, C. Luengo, F. Gilsanz, E. Dominguez, and F. Avello (1981) "Acute Pulmonary Oedema due to Lithium Intoxication," *Resuscitation 9*:353–357.

Eaton, R. S. (1984) *Personal Communication*, Health and Welfare Canada, Ottawa, Canada.

El-Genk, M. S., D. M. Woodall, V. F. Dean, and D. L. Y. Louie (1985) "Review of the Design Status of the SP-100 Space Nuclear Power System," in *Space Nuclear Power Systems 1984*, M. S. El-Genk and M. D. Hoover, eds., Vol. 1, Orbit Book Co., Malabar, FL.

Foote Mineral Company (1976) *Safe Handling of Lithium*, Technical Data Bulletin, Foote Mineral Co., Exton, PA.

Gilman, A. G., L. S. Goodman, A. Gilman, S. E. Mayer, and K. L. Melmon (1980) *The Pharmacological Basis of Therapeutics*, MacMillan Publishing Co., New York.

Gluyas, R. E. and G. K. Watson (1975) *Materials Technology for an Advanced Space Power Nuclear Reactor Concept: Program Summary*, Report NASA-TN-D-7909, National Aeronautics and Space Administration, March 1975.

Good, C. A. (1903) "An Experimental Study of Lithium," *Am. J. M. Sci. 125*:273.

Hammond, P. B. and R. P. Beliles (1980) "Metals," in *Casarett and Doull's Toxicology: The Basic Science of Poisons*, J. Doull, C. D. Klaassen, and M. O. Amdur, eds., Macmillan Publishing Co., New York.

Hanafee, J. E. (1978) *Analysis of Beryllium Parts for Cosmos 954*, Report UCRL-52597, Lawrence Livermore Laboratory.

Hanlon, L. W., M. Romaine III, F. J. Gilroy, and J. E. Deitrick (1949) "Lithium Chloride as a Substitute for Sodium Chloride in the Diet—Observations on Toxicity," *JAMA 139*(11):688–692.

Harbison, R. D. (1980) "Teratogens," in *Casarett and Doull's Toxicology: The Basic Science of Poisons*, J. Doull, C. D. Klaassen, and M. O. Amdur, eds., Macmillan Publishing Co., New York.

Hill, P. L. (no date) *Alkali Metals Safety Guide*, Y-12 Alkali and Liquid Metals Safety Committee, U.S. Atomic Energy Commission, Oak Ridge, TN.

Hoffman, H. W. and G. L. Yoder (1985) "Liquid Metal Heat Transfer Issues," in *Space Nuclear Power Systems 1984*, M. S. El-Genk and M. D. Hoover, eds., Vol. 2, Orbit Book Co., Malabar, FL.

Holland, J. W., M. H. Horner, and L. Yang (1985) "Thermionic Fuel Element Technology Status," in *Space Nuclear Power Systems 1984*, M. S. El-Genk and M. D. Hoover, eds., Vol. 2, Orbit Book Co., Malabar, FL.

Hoover, M. D., F. A. Seiler, G. J. Newton, and S. J. Rothenberg (1984) "Characterization of Potential Aerosols from Fusion Energy Systems," *J. Nucl. Matl. 122 & 123*:827–832.

ICRP (1974) *Report of the Task Group on Reference Man*, International Commission on Radiological Protection Report 23, Pergamon Press, Oxford.

Jefferson, J. W. and J. H. Greist (1977) *Primer for Lithium Therapy*, Williams and Wilkins Co., Baltimore.

Jeppson, D. W., J. L. Ballif, W. W. Wuan, and B. E. Chou (1978) *Lithium Literature Review: Lithium's Properties and Interactions*, Report HEDL-TME-78-15, Hanford Engineering Development Laboratory, Richland, WA.

Jeppson, D. W. (1979a) *Liquid Lithium Behavior and Control*, Report HEDL-SA-1877, Hanford Engineering Development Laboratory, Richland, WA.

Jeppson, D. W. (1979b) *Interactions of Liquid Lithium with Various Atmospheres, Concretes, and Insulating Materials, and Filtration of Lithium Aerosols*, Report HEDL-TME-79-7, Hanford Engineering Development Laboratory, Richland, WA.

Jeppson, D. W. (1982) *Scoping Studies—Behavior and Control of Lithium and Lithium Aerosols*, Report HEDL-TME-80-79, Hanford Engineering Development Laboratory, Richland, WA.

Jones, J. E., R. E. MacPherson, and J. P. Nichols (1985) "Multimegawatt Space Nuclear Power Concept," in *Space Nuclear Power Systems 1984*, M. S. El-Genk and M. D. Hoover, eds., Vol. 1, Orbit Book Co., Malabar, FL.

Kangilaski, M., E. O. Fromm, D. H. Lozier, V. W. Storhok, and J. E. Gates (1965) *High Temperature Irradiation of Niobium—1 w/o Zirconium Clad UO_2*, Report BMI-1730, Battelle Memorial Institute, Columbus, OH.

Katucki, R., A. Josloff, A. Kirpich, and F. Florio (1985) "Evolution of Systems Concepts for a 100 kWe Class Space Nuclear Power System," in *Space Nuclear Power Systems 1984*, M. S. El-Genk and M. D. Hoover, eds., Vol. 1, Orbit Book Co., Malabar, FL.

Keshishian, F. et al. (1973) *Radiation Shielding for Zirconium Hydride Reactor Systems*, Report AI-AEC-13081, Atomics International, Canoga Park, CA, June 1973.

Klopp, W. D. (1985) "Technology Status of Molybdenum and Tungsten Alloys," in *Space Nuclear Power Systems 1984*, M. S. El-Genk and M. D. Hoover, eds., Vol. 1, Orbit Book Co., Malabar, FL.

Korsmeyer, R. B. (1963) *Notes on the Liquid Metal Boiling Phenomena*, Report ORNL/TM-534, Oak Ridge National Laboratory, TN.

Landingham, R. L. and A. W. Casey (1978) *Morning Light Cleanup and Recovery Operation: Simulation Studies of Possible Reactor Fuels*, Report UCRL-52543, Lawrence Livermore Laboratory.

Lederer, C. M. and V. S. Shirley (1978) *Table of Isotopes*, Seventh Edition, John Wiley and Sons, New York.

Lithium Corporation of America (1976) *Lithium Metal Handling, Storage, and Safety Precautions*, Product Bulletin, Lithium Corporation of America, New York, NY.

Los Alamos (1982) *Semi-Annual SP-100 Technical Progress Review*, Los Alamos National Laboratory, Los Alamos, NM, October 1982.

Mason, D. G. (1963) *SNAP 8 Design Description*, NAA-SR-MEMO-8740, Atomics International, Canoga Park, CA, August 1963.

Mattick, A. T. and R. T. Taussig (1984) *New Thermal Management and Heat Rejection Systems for Space Applications*, Final Report, Air Force Rocket Propulsion Laboratory Contract F04611-81-K-0040.

Mattick, A. T. and A. Hertzberg (1985) "Liquid Droplet Radiator Technology Issues," in *Space Nuclear Power Systems 1984*, M. S. El-Genk and M. D. Hoover, eds., Vol. 2, Orbit Book Co., Malabar, FL.

Miller, A. J. (1962) *Space Power Program Semi-Annual Progress Report for Period Ending December 31, 1961*, USAEC Report ORNL-3270, Oak Ridge National Laboratory, TN.

Morrow, P. E., D. V. Bates, B. R. Fish, T. F. Hatch, and T. T. Mercer (1966) "Deposition and Retention Models for Internal Dosimetry of the Human Respiratory Tract," *Health Phys. 12*:173 – 207.

Muhlestein, L. D. (1980) *Liquid Metal Reactions Under Postulated Accident Conditions for Fission and Fusion Reactors*, Report HEDL-FP-2131, Hanford Engineering Development Laboratory, Richland, WA.

Muhlestein, L. D., D. W. Jeppson, and J. R. Barreca (1980) *Summary of HEDL Fusion Reactor Safety Support Studies*, Report HEDL-SA-2360, Hanford Engineering Development Laboratory, Richland, WA.

National Safety Council (1978) *Lithium Data Sheet*, Document I-566-78, Revised 1978, National Safety Council, Chicago, IL.

Potts, A. M. and L. M. Gonasun (1980) "Toxic Responses of the Eye," in *Casarett and Doull's Toxicology: The Basic Science of Poisons*, J. Doull, C. D. Klaassen, and M. O. Amdur, eds., Macmillan Publishing Co., New York.

Rumack, B. H. and R. G. Peterson (1980) "Clinical Toxicology," in *Casarett and Doull's Toxicology: The Basic Science of Poisons*, J. Doull, C. D. Klaassen, and M. O. Amdur, eds., Macmillan Publishing Co., New York.

Shou, M. (1976) "Pharmacology and Toxicology of Lithium," in *Annual Review of Pharmacology and Toxicology*, H. W. Elliott, ed., Vol. 16, Annual Reviews Inc., Palo Alto, CA.

Spiegl, C. J., J. K. Scott, H. Steinhardt, L. J. Leach, and H. C. Hodge (1956) "Acute Inhalation Toxicity of Lithium Hydride," *Arch. Indust. Health 14*:468–470.

Staub, W. D. (ed.) (1973) *SNAP Programs Summary Report*, Report AI-AEC-13067, Atomics International, Canoga Park, CA, July 1973.

Voss, S. S. (1984) *SNAP Reactor Overview*, Report AFWL-TN-84-14, Air Force Weapons Laboratory, Kirtland, NM.

Weaver, S. C. and J. L. Scott (1965) *Comparison of Reactor Fuels for High Temperature Applications*, Report ORNL-TM-1360, Oak Ridge National Laboratory, December 1965.

Welch, F. H. (1967) *Lithium Hydride Technology*, Report NAA-SR-9400, Atomics International, Canoga Park, CA.

Whitlow, G. A., W. L. Wilson, W. E. Roy, and M. G. Down (1979) "Materials Behavior in Lithium Systems for Fusion Reactor Applications," *J. Nucl. Matl. 85 & 86*:283–287.

Wikjord, A. G., F. E. Doern, L. Hachkowski, and J. Baird (1980) "Electron Beam Microanalysis of Radioactive Particulates from the Disintegration of Russian Satellite Cosmos 954," *Scanning Electron Microscopy 1980*, Vol. I, SEM Inc., AMF O'Hare, Chicago, IL.

Zwicker, G. M., M. D. Allen, and D. L. Stevens (1979) "Toxicity of Aerosols of Sodium Reaction Products," *J. Environ. Path. and Toxic. 2*:1139–1150.

Space Nuclear Power Systems 1984
Edited by M. S. El-Genk and M. D. Hoover
© Orbit Book Company, Malabar, FL, 1985

Chapter 62

State Variable Method of Fault Tree Analysis

Robert J. Bartholomew

Los Alamos National Laboratory
MS C948, Los Alamos, NM 87545

Harold K. Knudsen

Dept. Of Electrical Engineering and Computer Science
University of New Mexico
Albuquerque, NM 87131

Glenn A. Whan

Department of Chemical and Nuclear Engineering
University of New Mexico
Albuquerque, NM 87131

The current technique of Fault Tree Analysis (FTA) generally employs computer codes that calculate the minimal cut sets of the Boolean function, where each cut set comprises basic "initiator" events (roots) whose intersection implies the occurrence of a TOP (system failure) event. Because the number of calculations can be very large for typical fault trees, the importance of any given cut set is assessed by qualitative algorithms that may include the number of basic events in the cut set, and quantitative importance algorithms that involve probabilistic upper and lower bound estimates. The sets are culled before quantitative probability calculations are made. The assumption of statistical independence of all events is often imposed as a requirement for quantitative analysis. The question addressed in this paper is: Can a tractable mathematical model be found that can perform quantatitive calculations without the need of upper or lower bound simplifications and include within its structure the capability of handling common cause/common mode statistical dependence, failure mode coupling interdependence, and sequential failure time dependence? The Failure Mode State Variable (FMSV) model developed here is the affirmative answer to this question. The model is applied to simplified fault trees representing some nuclear power system components and subsystems considered for space electric power generation.

Introduction

This paper deals with the problem of developing probabilistic reliability and risk analysis methodology. Such methodology lends insight into safety determinations when applied to the analysis of engineered systems whose failure entails potential hazardous consequences in terms of injury, loss of life, economic loss, or environmental degradation. We will focus attention on the requirements of mathematical framework needed in order to formulate probabilistic failure prediction models that are realistic (in probabilistic sense) as well as practical and useful (in an engineering analysis sense).

In the analysis of complex systems for safety, reliability, and risk, the fault tree technique has enjoyed great favor recently because of its versatility and utility in expressing, mathematically, the inherent engineering logic found in very detailed engineered systems. The technique was originated by H. A. Watson of Bell Telephone Laboratories to analyze the Minuteman Launch Control System. It was further refined in studies by a team at the Bell Telephone Laboratories.

The fault tree is a graphical illustration of logic that employs mathematical symbols to describe "decision gates" that have "input events" (lower branches or roots) and outputs (higher branch events) that converge through fewer and fewer gates to a single "TOP" event that represents failure of the system described by the fault tree. The lowest initiating points of the tree have symbols that represent basic failure events or "causes" and are the roots of the tree.

The fault analysis of an engineered component, subsystem, or complete system using the fault tree technique is called Fault Tree Analysis (FTA). FTA is used for safety, reliability, and risk assessment, and to design engineered safety systems for nuclear power plants. The FTA method is a pivotal analysis methodology in the

Reactor Safety Study WASH-1400 (1975) and has been computer codified by many analysts, such as Vesely and Narum (1970), Worrell and Stack (1978), and Caldarola and Wickenhauser (1977).

FTA has many advantages as listed by Dhillon and Singh (1981) in that the technique:

1. provides insight into the behavior of an operating component or system,
2. requires that the analyst gain a thorough understanding of the component or system,
3. helps the analyst to deduce failure points,
4. is a very good visual aid in tracking system fault circuits to provide needed engineered safety measures,
5. can describe very complex systems involving multitudes of interactions, and
6. allows performance of both qualitative and quantitative reliability analyses.

The above list of advantages is not necessarily complete, and Dhillon and Singh go on to list some of the disadvantages that include but are not limited to the following:

1. FTA is costly and time consuming,
2. FTA results are difficult to check,
3. FTA is designed for only dual state components making partial failure states difficult to handle, and
4. common cause or common mode failures require considerable effort to include.

Another, perhaps more important disadvantage in FTA is its unsuitability in describing sequentially based (time based) dependence and time rate interdependencies between failure modes. The method described in this paper resolves this problem.

Approach

We deal primarily with the problem of formulating a probabilistic model using stochastic process theory as described, for example, by Karlin and Taylor (1975), that is in a mathematical form that (1) retains the failure mode structure of the fault tree and (2) allows a differential equation modeling method to handle common cause/common mode dependencies, sequential dependencies, and rate interdependencies between failure producing mechanisms. Such an approach is considered new, and has not appeared in the literature previously. The failure mode events and TOP gate events can be statistically dependent (s-dependent) and their occurrence probabilities in $[0, t]$ are the state variables for the system.

The new modeling procedure is called the Failure Mode State Variable (FMSV) method developed as the mathematical modeling framework for time dependent, quantitative probabilistic FTA. The FMSV modeling procedure utilizes a transformation of the classical Markov model used in stochastic process theory. We define the transformed model to be called the "Adjoint model," where the model describes the probability densities of failure in $[0, t]$ of the failure modes and TOP events of fault trees. The FMSV model is a subset of inhomogeneous differential equations embedded in the homogeneous complete Markov Adjoint model and is implemented using techniques of modern control system analysis using state variable theory as described, for example, by Brogan (1974). Models for two, three, and four component Markov models (or intiators in a fault tree) have been developed, and computer programs for their solution by deterministic methods and by Monte Carlo simulation with time as the continuous random variable have been developed. The solutions are in the form of lifetime cumulative distribution functions (lcdf's) representing the probabilities of occurrence of the failure modes and the TOP events (for both an AND gate and an OR gate at the TOP) for "generic" fault trees having two failure modes. A method of least squares curve fitting of these lcdf's by single term exponential functions over any arbitrary time period of interest is incorporated in the computer programs. Methods of modularizing given fault trees to include the generic trees as subsystems have been devised, and some practical sample problems have been solved. A reliability assessment of a space nuclear electric power system comprising core heat pipes for heat transport and external thermoelectric converters is reported here.

Methods

From stochastic process theory, a system of n components each having a binary "good" or "failed" description of possible condition states will comprise 2^n possible states S_i; $i = 0, 1, \ldots, 2^n - 1$ involving all n components. The events of being in any of these states in which none, one or more, or all components are failed constitute a complete event space where all possibilities are exhausted. These events are called mutually exclusive or disjoint because the system can be in one and only one state at any given time t. We consider a Markov stochastic process model involving the discrete probabilities of being in any given state S_j at some time t and moving to another state S_i during an arbitrarily small continuous time interval Δt. The Markov model consists of the first order differential equations in the vector form

$$\dot{\mathbf{P}}(t) \equiv d\mathbf{P}/dt = \mathbf{A}\mathbf{P}(t), \tag{1}$$

where $\mathbf{P}(t)$ is the vector of elements describing the probability of being in any one of the possible states, and $\mathbf{A}$ is the "infinitesimal generator" matrix. (See, for example, Karlin and Taylor (1975)).

We now consider a state ordering process. We begin S_0 with the condition that all components are "good,"

depicted by the binary indicator variable

$$X = \begin{cases} 0 \rightarrow \text{failed} \\ 1 \rightarrow \text{good}, \end{cases} \tag{2}$$

as the set (11 . . . 11) for n components. The last state S_m; $m = 2^n - 1$, we choose to be the state wherein all components are failed, depicted as the set (00 . . . 00) for all n components. As our second group of states we arbitrarily choose the $\binom{n}{1} = n$ combinations of sets ordered so that S_1 is the set (11 . . . 10), S_2 is the set (11 . . . 01), and so on, until S_n is the set (01 . . . 11). In words, the states S_1 through S_n are ordered with the last component only failed, then the next to last only failed, and so on, until S_n has the first component only failed. The third group of sets has the $\binom{n}{2} = n(n-1)/2$ combinations where two components are failed. These, too, are ordered in such a way that the last two components are failed in the first state of the third group and in the last state, the first two components are failed. If there is a fourth group of $\binom{n}{3} = n(n-1)(n-2)/6$ combinations where three components have failed, these are also ordered similarly. The ordering process is continued to the last state S_m; $m = 2^n - 1$, in which all components have failed.

As an example of the ordering process, we consider the case where $n = 3$. The following tabulation illustrates the ordering of the $2^3 = 8$ states beginning with S_0 and ending with S_7.

State	Component Number 1 2 3	Group Number
S_0	1 1 1	1
S_1	1 1 0	
S_2	1 0 1	2
S_3	0 1 1	
S_4	1 0 0	
S_5	0 1 0	3
S_6	0 0 1	
S_7	0 0 0	4

We note from the locations of the zero's in our tabulation that component 1 is failed in states S_3, S_5, S_6, and S_7.

Similarly, component 2 is failed in S_2, S_4, S_6, and S_7, and component 3 is failed in S_1, S_4, S_5, and S_7. Components 1 and 2 are failed in S_6 and S_7; components 2 and 3 are failed in S_4 and S_7; and components 1 and 3 are failed in S_5 and S_7. Finally, all components are failed in only S_7.

We can formalize the ordering process for n components by defining a set of Adjoint model states $\hat{S}_i$; $i = 0, 1, \ldots, 2^n - 2$ each of which comprises the unions of the disjoint Markov states wherein a particular component or group of components is failed. The last Adjoint state $\hat{S}_m$; $m = 2^n - 1$, is chosen to be Ω, or all possibilities. In Table 1 we tabulate the procedure for three components. We note that the last Adjoint "state" being Ω, or all possibilities, is the union of all of the disjoint Markov states, which exhausts all possibilities. Its probability $\hat{P}_7(t) = P_\Omega(t) = 1$, for all $t \geqslant 0$. We have used the (+) symbol to signify the union operator. We also will use the (·) symbol to signify the intersection operator.

Table 1 *Tabulation of the Procedure for Ordering Three Components by Defining a Set of Adjoint Model States.*

Markov State	Component Number 1 2 3	Adjoint State	Component(s) Failed 1 2 3	Equivalent Unions of Markov States
S_0	1 1 1	$\hat{S}_0$	0 0 0	S_7
S_1	1 1 0	$\hat{S}_1$	0 0 1	$S_6 + S_7$
S_2	1 0 1	$\hat{S}_2$	0 1 0	$S_5 + S_7$
S_3	0 1 1	$\hat{S}_3$	1 0 0	$S_4 + S_7$
S_4	1 0 0	$\hat{S}_4$	0 1 1	$S_3 + S_5 + S_6 + S_7$
S_5	0 1 0	$\hat{S}_5$	1 0 1	$S_2 + S_4 + S_6 + S_7$
S_6	0 0 1	$\hat{S}_6$	1 1 0	$S_1 + S_4 + S_5 + S_7$
S_7	0 0 0	$\hat{S}_7$	Ω	$\bigcup_{i=0}^{7} S_i$

The Adjoint state description is a formulation wherein the probability of failure of one or more components is the exclusive phenomenon that is described. In the Markov model $P_0(t)$ represents the system reliability—the opposite of unreliability or failure, and $P_7(t)$ is the only probability of failure, exclusively, that is depicted. For FTA (which almost always represents a failure model) we desire a probabilistic model that depicts failure exclusively, and the Adjoint state representation has this desired property. It is natural to search for a transformation such that the Markov model of the form $d\mathbf{P}/dt = \mathbf{AP}$ can be transformed into an Adjoint model of the form $d\hat{\mathbf{P}}/dt = \hat{\mathbf{A}}\hat{\mathbf{P}}$. It turns out that a fairly simple nonsingular transformation matrix $\mathbf{E}$ exists, and is easily formulated from our state ordering process. We will now describe the properties of $\mathbf{E}$ for the reasonably simple two component model.

In Table 2 we tabulate the procedure for two components. From the equivalent unions of Markov states it is

Table 2 *Tabulation of the Procedure for Ordering Two Components by Defining a Set of Adjoint Model States.*

Markov State	Component Number 1 2	Adjoint State	Component(s) Failed 1 2	Equivalent Unions of Markov States
S_0	1 1	$\hat{S}_0$	0 0	S_3
S_1	1 0	$\hat{S}_1$	0 1	$S_2 + S_3$
S_2	0 1	$\hat{S}_2$	1 0	$S_1 + S_3$
S_3	0 0	$\hat{S}_3$	Ω	$\bigcup_{i=0}^{3} S_i$

easy to formulate $\hat{\mathbf{P}}(t) = \mathbf{E}\mathbf{P}(t)$:

$$\begin{bmatrix} \hat{P}_0 \\ \hat{P}_1 \\ \hat{P}_2 \\ \hat{P}_3 \end{bmatrix} = \begin{bmatrix} 0 & 0 & 0 & 1 \\ 0 & 0 & 1 & 1 \\ 0 & 1 & 0 & 1 \\ 1 & 1 & 1 & 1 \end{bmatrix} \begin{bmatrix} P_0 \\ P_1 \\ P_2 \\ P_3 \end{bmatrix}. \tag{3}$$

The inverse transformation $\mathbf{P}(t) = \mathbf{E}^{-1}\hat{\mathbf{P}}(t)$ is also easy to obtain from

$$\begin{aligned} P_3(t) &= \hat{P}_0(t) \\ P_2(t) &= \hat{P}_1(t) - \hat{P}_0(t) \\ P_1(t) &= \hat{P}_2(t) - \hat{P}_0(t) \\ P_0(t) &= \hat{P}_3(t) - \hat{P}_2(t) - \hat{P}_1(t) + \hat{P}_0(t), \end{aligned} \tag{4}$$

or, in matrix form,

$$\begin{bmatrix} P_0 \\ P_1 \\ P_2 \\ P_3 \end{bmatrix} = \begin{bmatrix} 1 & -1 & -1 & 1 \\ -1 & 0 & 1 & 0 \\ -1 & 1 & 0 & 0 \\ 1 & 0 & 0 & 0 \end{bmatrix} \begin{bmatrix} \hat{P}_0 \\ \hat{P}_1 \\ \hat{P}_2 \\ \hat{P}_3 \end{bmatrix}. \tag{5}$$

Given a Markov model $d\mathbf{P}/dt = \mathbf{A}\mathbf{P}$ with initial condition $\mathbf{P}(0) = [P_0(0)P_1(0)P_2(0)P_3(0)]^T$, we can transform the model into an Adjoint model by the similarity transformation:

$$\begin{aligned} \hat{d}\mathbf{P}/dt &= \mathbf{E}\mathbf{A}\mathbf{E}^{-1}\hat{\mathbf{P}} \\ \hat{\mathbf{P}}(0) &= \mathbf{E}\mathbf{P}(0), \end{aligned} \tag{6}$$

where the matrices $\mathbf{E}$ and $\mathbf{E}^{-1}$ are as defined in Eq. (3) and (5), respectively, for the two component case. We are especially interested in matrices $\mathbf{A}$ such that $\mathbf{E}\mathbf{A}\mathbf{E}^{-1} = \mathbf{A}^T$, the transpose of our Markov infinitesimal generator matrix. It turns out that for systems that have common cause/common mode s-dependencies that can be depicted in fault trees and that can be modeled by a Marshall–Olkin (1967) multivariate exponential distribution for the waiting times between such events, the transpose $\mathbf{A}^T$ results, and we say that the $\mathbf{A}$ matrix is self-adjoint. (The exponential waiting time distribution follows from a Poisson process assumption regarding the occurrence of each initiator in a fault tree.) If there are repair rates or internal synergistic failure-repair rates, in general, the matrix $\mathbf{A}$ is not self-adjoint. However, the similarity transformation $\mathbf{E}\mathbf{A}\mathbf{E}^{-1} = \hat{\mathbf{A}}$ is valid for matrices that are not self-adjoint. The Adjoint model expresses all of the probability densities for failure in $[0, t]$ (failure densities) of every single component (or initiator) and every binomial combination of components (AND gate combinations) possible in the system. Using these concepts we formulate generic fault trees for two, three, and four component systems for which FMSV inhomogeneous differential equation models are contained as a subset of the Adjoint models, and which yield solutions that give the lifetime cumulative distribution functions (lcdf's) for each of two failure modes (E_1, E_2) and the TOP "AND" event.

Specifically, for the two component system, we have

$$\begin{aligned} &\left[\hat{P}_0(t)\hat{P}_1(t)\hat{P}_2(t)\hat{P}_3(t)\right]^T \\ &\equiv \left[T_{\text{AND}}(t)F_1(t)F_2(t)1\right]^T. \end{aligned} \tag{7}$$

If lcdf's for the two failure modes are called $F_1(t)$ and $F_2(t)$, for $\Pr(E_1$ occurs in $[0, t])$ and $\Pr(E_2$ occurs in $[0, t])$, respectively, and $T_{\text{AND}}(t)$ is the lcdf for Pr(TOP "AND" occurs in $[0, t]$), we can calculate the lcdf for the TOP "OR" event $T_{\text{OR}}(t)$ by:

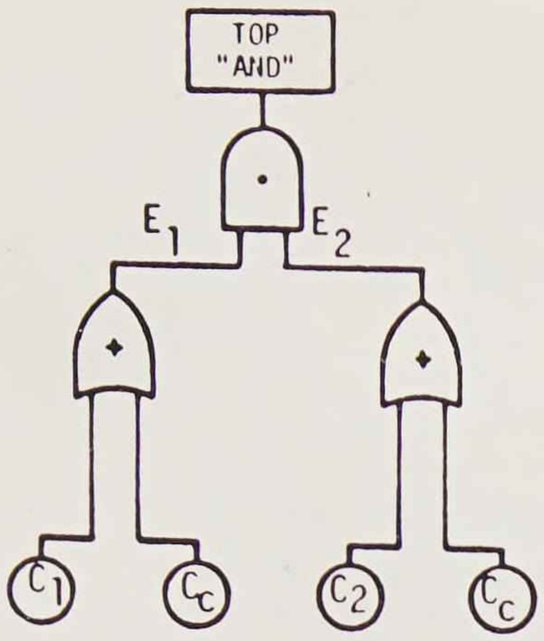
$$T_{\text{OR}}(t) = F_1(t) + F_2(t) - T_{\text{AND}}(t). \tag{8}$$

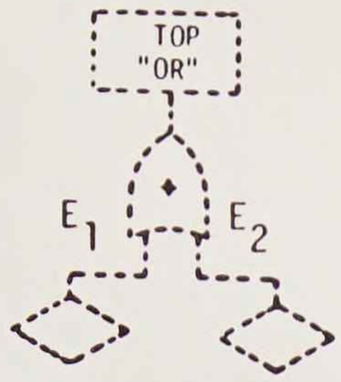
The FMSV two component model is formulated as in modern control theory to have the form:

$$\begin{aligned} \dot{\mathbf{F}} \equiv d\mathbf{F}/dt &= \mathbf{A}'\mathbf{F} + \mathbf{B}\mathbf{u}(t) \\ \mathbf{F}(0) &= \left[F_1(0)F_2(0)T_{\text{AND}}(0)\right]^T \\ \mathbf{u}(t) &= \left[1u_1(t)u_2(t)\right]^T \\ \mathbf{T}_{\text{OR}}(t) &= \mathbf{C}\mathbf{F}(t), \end{aligned} \tag{9}$$

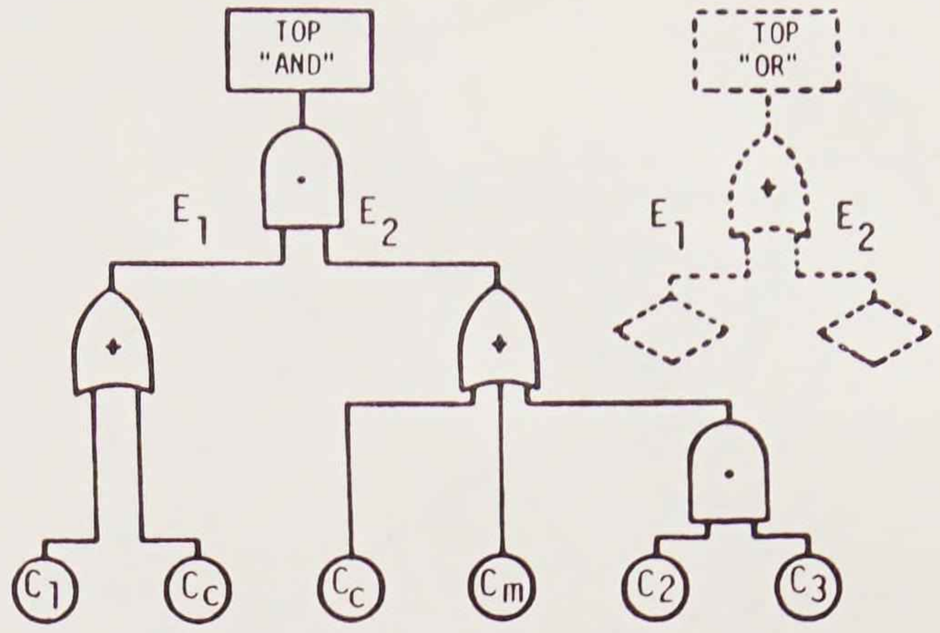
where $\mathbf{C}$ is an "output" transformation matrix that the analyst uses to choose what he deems represents system failure probabilities among the combinations of the $F_i(t)$; $i = 1, 2$, and $T_{\text{AND}}(t)$. The output is often $T_{\text{OR}}(t)$, Equation (8), which gives $\mathbf{C} = [1\ 1\ -1]$. The $u_1(t), u_2(t)$ are Pr (initiator 1 occurs in $[0, t]$), Pr (initiator 2 occurs in $[0, t]$), respectively, and are assumed to be known (or separately calculated) constant probabilities or exponential functions of time. $\mathbf{A}'$ is a "failure (repair) rate" matrix that may "couple" the two failure modes and the TOP "AND" event. This rate coupling is defined as "intermodal coupling." Common cause coupling between the two components is automatically included in the formulation.

The generic fault trees for two components with both TOP "AND" and TOP "OR" events are depicted in Figure 1(a) and their Markov model transition diagrams for three of four types of coupling mechanisms are shown in Figure 2. The generic fault trees for three and four component systems are shown in Figure 1(b) and (c), respectively. Common mode s-dependency, defined as suggested by Fussell and Burdick (1977) to represent common cause failure of components in redundancy is included in the three and four components systems. For example, in the three initiator fault tree of Figure 1(b), occurrence of the common mode (C_m) will



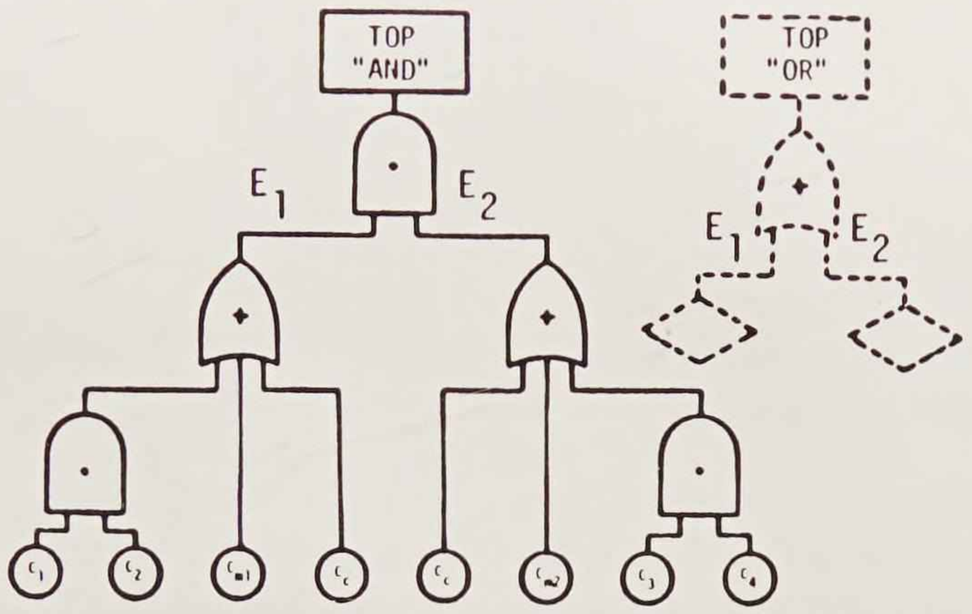


(a) Generic fault trees for two s-independent initiators with common cause s-dependency



(b) Generic fault trees for three s-independent initiators with common cause and common mode s-dependency

$C_i \equiv$ ith CAUSE,
$C_c \equiv$ COMMON CAUSE,
$C_{mi} \equiv$ ith COMMON MODE,
$E_i \equiv$ ith EFFECT



(c) Generic fault trees for four s-independent initiators with common cause and common mode s-dependency

Figure 1 *Generic Fault Trees for Two, Three, and Four Statistically Independent Initiators with Common Cause and Common Mode Statistical Dependencies.*

fail the parallel component module comprising components 2 and 3, but component 1 is unaffected. In contrast, the occurrence of the common cause (C_c) will fail all three components and cause the TOP event system failure.

A complete analysis of the two component system transformation $\hat{\mathbf{A}} = \mathbf{EAE}^{-1}$ was performed for two component systems having *s*-dependencies in addition to common cause and involving:

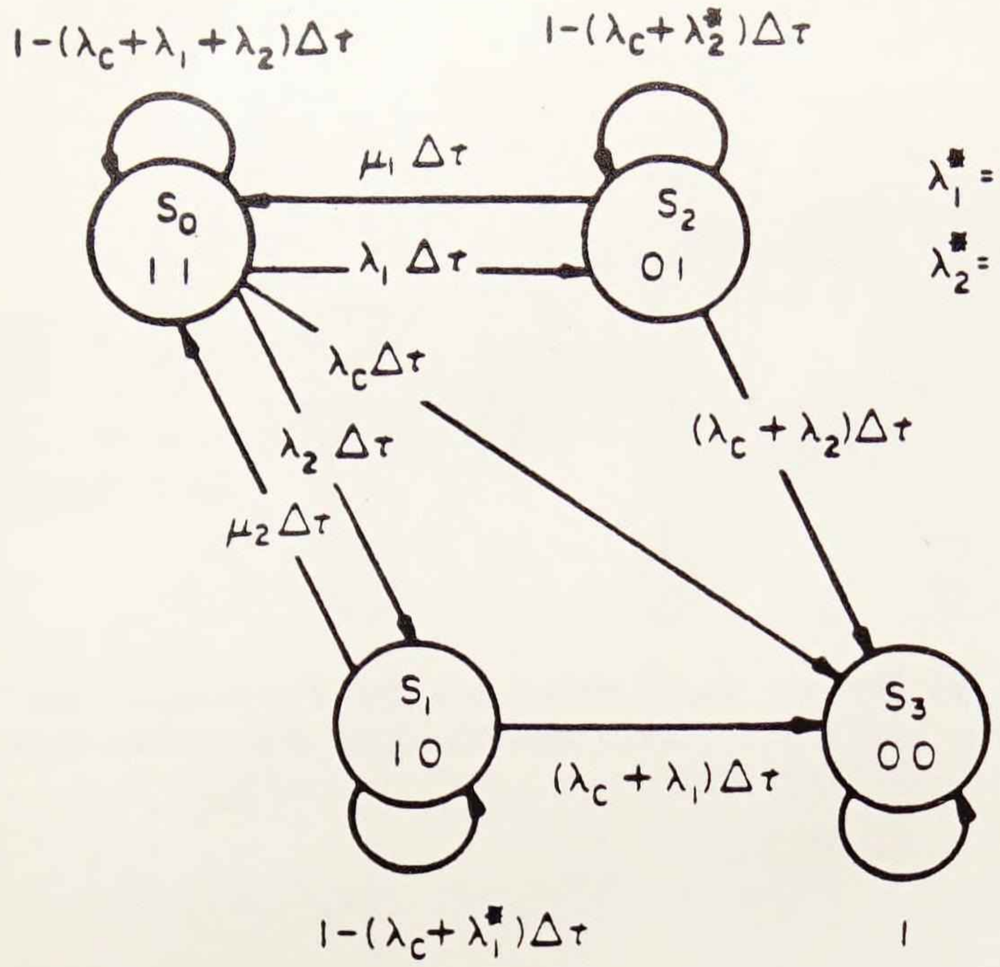
1. external repair mechanisms,
2. internal synergistic failure-repair mechanisms,
3. combined external repair and internal synergistic failure-repair mechanisms.

We also include, without common cause *s*-dependency:

4. sequential "jump" dependencies in failure rates of three identical components.

Item (4) is an eight state Markov model reducible to a four state Markov model by state merging as suggested by Papazoglou and Gyftopoulous (1977) because the components are identical. These authors have shown that failure states of identical components in Markov models can be merged, resulting in a reduced order Markov model. The Markov state transition diagrams for items (1) through (3) of these systems are shown in Figures 2(1), (2), and (3). Figure 3 depicts the item (4) *s*-dependency transition diagram. For all four systems the FMSV model is the inhomogeneous third order system expressed as a general state space analog simulation depicted in Figure 4 and described by the vector model Equation (9). Such vector simulation diagrams are standard in modern control theory, for example, Brogan (1974). The constraints on the initial condition vector $\mathbf{F}(0)$ are obtained from the Markov model constraints $\mathbf{0} \leqslant \mathbf{P}(t) \leqslant \mathbf{1}$ and $P_0(t) + P_1(t) + P_2(t) + P_3(t) = 1$, in accordance with the definition of the Adjoint model state vector Equation (7).

Similar models for the three and four component generic fault trees (Figures 1(b), (c)) with common cause/common mode and internal synergistic failure-repair mechanisms were also developed. Digital computer programs for obtaining the lcdf's for these models as well as the corresponding two component model were written, utilizing not only deterministic explicit integration methods, but also Monte Carlo analog simulation as described by Carter and Cashwell (1975) and Spanier and Gelbard (1969). These authors apply this technique to particle transport in nuclear physics. Lewis and Bohm (1983) apply the technique to Markov processes allowing *s*-dependencies and utilizing variance



$\lambda_1^* = \lambda_1 + \mu_2$

$\lambda_2^* = \lambda_2 + \mu_1$

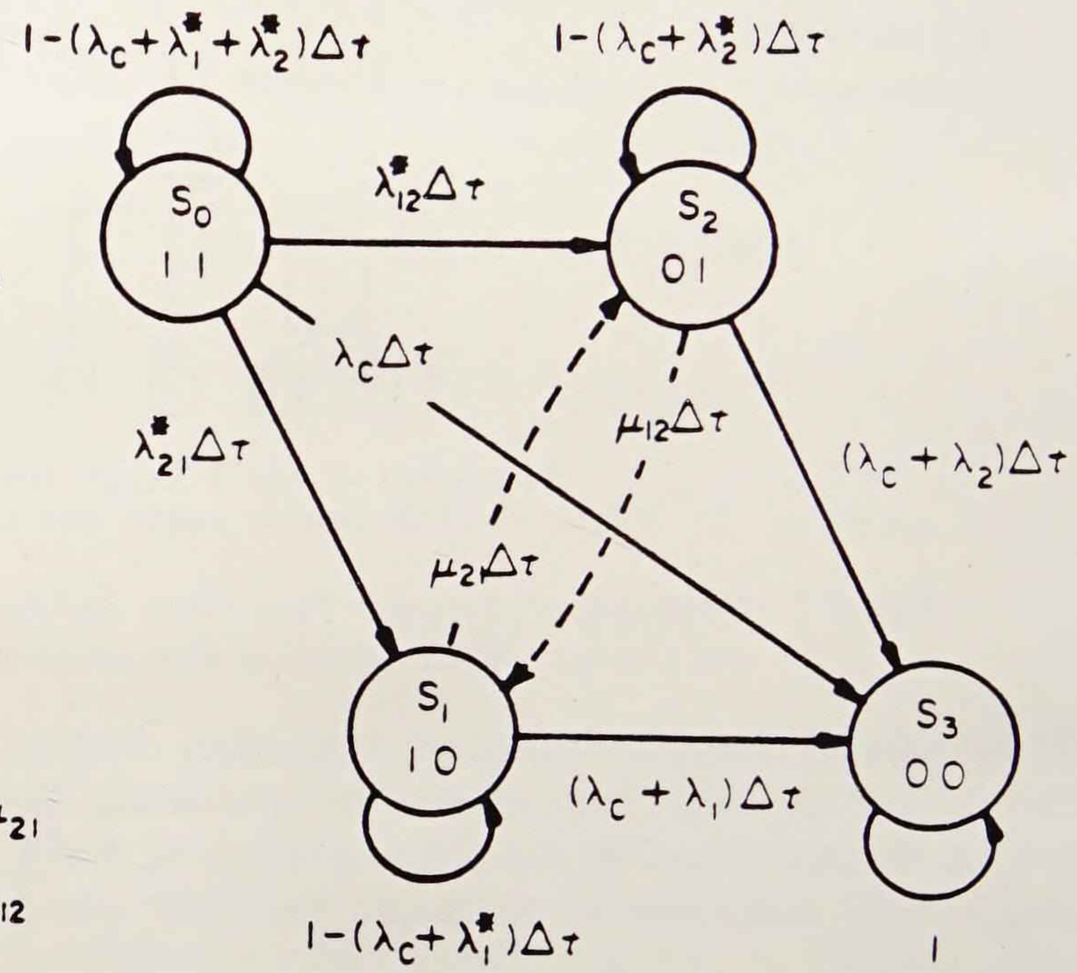
$\lambda_c \equiv$ Common cause occurrence rate

$\lambda_i; i=1,2 \equiv$ Occurrence rates of initiators 1 and 2, respectively

$\mu_i; i=1,2 \equiv$ Repair occurrence rates of components failed by initiators 1 and 2, respectively (external renewal)

$\mu_{ij}; i,j=1,2; i\neq j \equiv$ Synergistic failure-repair occurrence rate involving repair of component failed by initiator (i) at the expense of failure of still functioning component that can be failed by initiator (j) (internal loss-renewal)

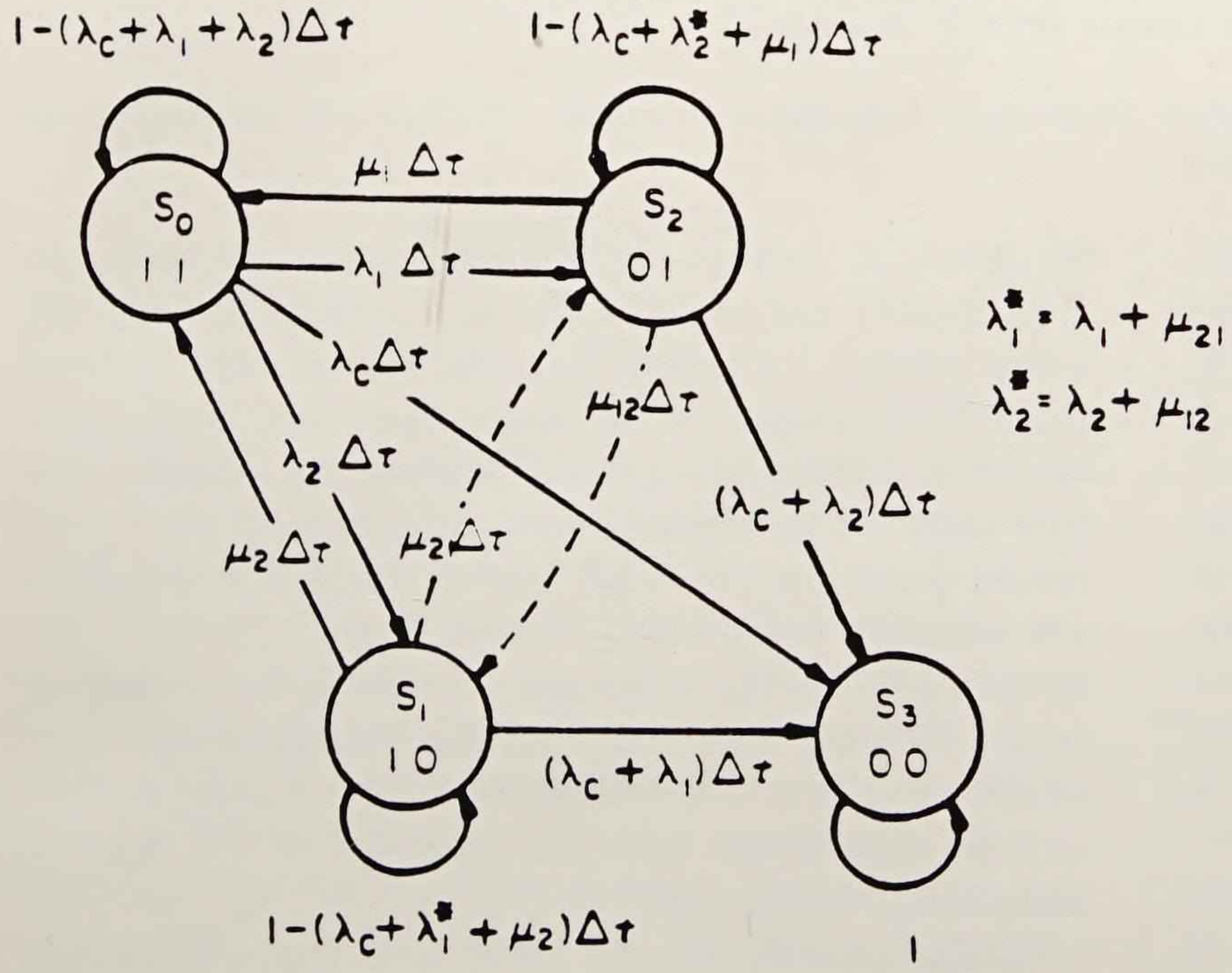
(1) External repair



$\lambda_1^* = \lambda_1 + \mu_{21} = \lambda_{12}^*$

$\lambda_2^* = \lambda_2 + \mu_{12} = \lambda_{21}^*$

(2) Internal synergistic failure-repair



$\lambda_1^* = \lambda_1 + \mu_{21}$

$\lambda_2^* = \lambda_2 + \mu_{12}$

(3) Combined (1) and (2)

Figure 2 *Two Component Generic Fault Tree Markov State Transition Diagrams for Three Kinds of Intermodel Coupling s-Dependencies in Addition to Common Cause s-Dependency.*

reduction with bias sampling. Transition among the Markov states in accordance with the transition diagrams of Figures 2 and 3 for the two component system, and similar Markov model transition diagrams for the three and four component systems formed the basis for the Monte Carlo simulations of this paper. Shooman (1968) describes a Monte Carlo simulation to calculate the reliability of a system comprising three parallel elements. Arley and Buch (1950) describe probability in terms of a mass flow process as a Brownian motion. Following population dynamics (birth and death) processes as described by Karlin and Taylor

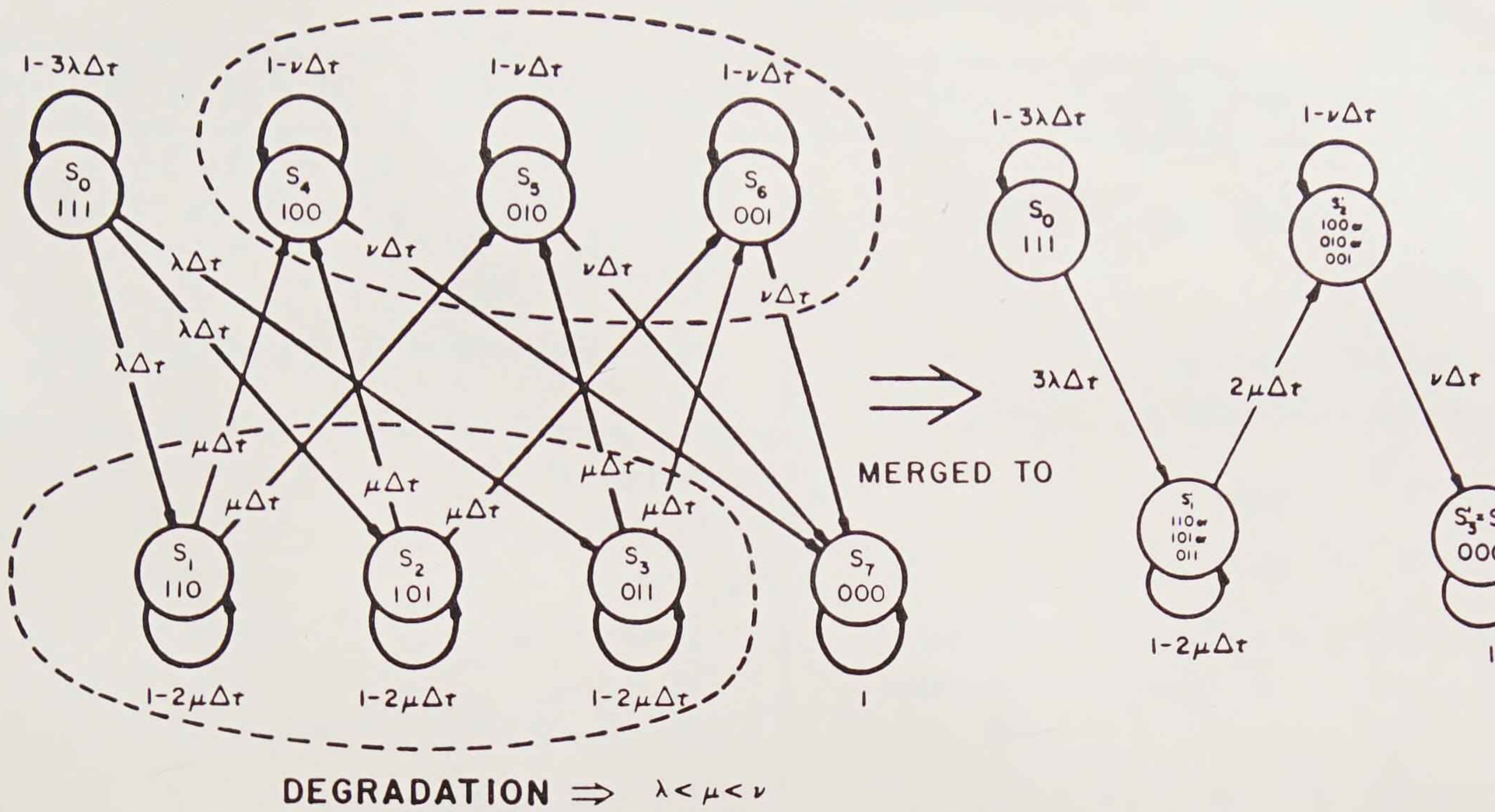
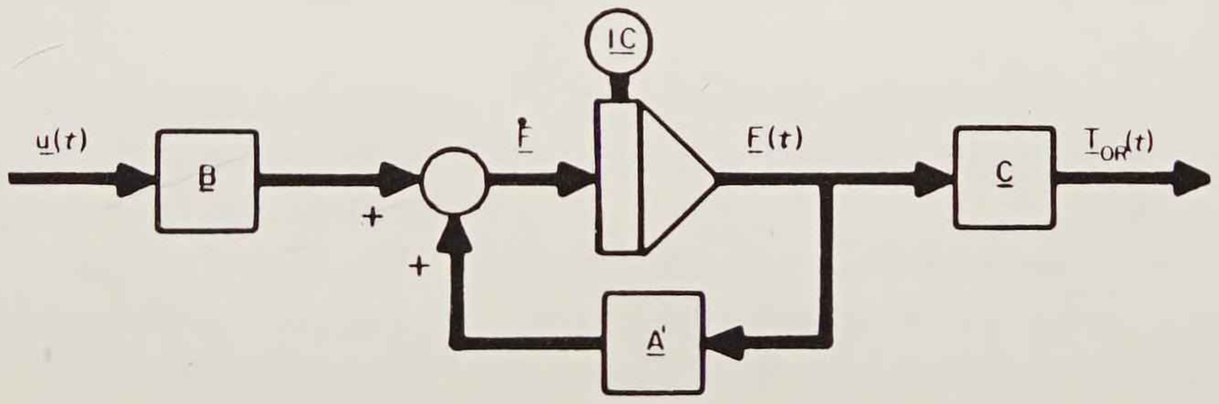


Figure 3 *Sequentially Increasing "Jump" Failure Rate s-Dependency Markov Model Merged State Transition Diagram for a Three Identical Component System. Common Cause / Common Mode s-Dependencies not Included.*

(1975), in our simulation of Markov models probability is represented as a population of particles that make transitions among the Markov states. The Monte Carlo sampling is from the uniform distribution on (0, 1) determined by taking the inverse of a discrete transition event space constructed as a cumulative distribution function to randomly select one of the disjoint events occurring in a small time interval Δt. The random time interval between successive events is tracked by sampling the uniform distribution on (0, 1) determined from



(1) External repair

$$\underline{A}' = \begin{bmatrix} -(\lambda_C+\lambda_1') & 0 & \mu_1 \\ 0 & -(\lambda_C+\lambda_2') & \mu_2 \\ \lambda_2 & \lambda_1 & -(\lambda_C+\lambda_1+\lambda_2) \end{bmatrix}$$

$$\underline{F}(t) = \begin{bmatrix} F_1(t) & F_2(t) & T_{AND}(t) \end{bmatrix}^T, \quad \underline{IC} = \begin{bmatrix} F_1(0) & F_2(0) & T_{AND}(0) \end{bmatrix}^T, \quad \underline{u}(t) = \begin{bmatrix} 1 & 1-e^{-\lambda_1 t} & 1-e^{-\lambda_2 t} \end{bmatrix}^T$$

$$\underline{B} = \begin{bmatrix} (\lambda_C+\lambda_1) & 0 & 0 \\ (\lambda_C+\lambda_2) & 0 & 0 \\ \lambda_C & 0 & 0 \end{bmatrix}$$

$$\underline{C} = \begin{bmatrix} 1 & 1 & -1 \end{bmatrix}$$

$$\lambda_1' = \lambda_1+\mu_1, \quad \lambda_2' = \lambda_2+\mu_2$$

(2) Internal synergistic failure-repair

$$\underline{A}' = \begin{bmatrix} -(\lambda_C+\lambda_1^*+\mu_{12}) & 0 & \mu_{12} \\ 0 & -(\lambda_C+\lambda_2^*+\mu_{21}) & \mu_{21} \\ \lambda_2 & \lambda_1 & -(\lambda_C+\lambda_1+\lambda_2) \end{bmatrix}$$

$$\underline{F}(t) = \begin{bmatrix} F_1(t) & F_2(t) & T_{AND}(t) \end{bmatrix}^T, \quad \underline{IC} = \begin{bmatrix} F_1(0) & F_2(0) & T_{AND}(0) \end{bmatrix}^T, \quad \underline{u}(t) = \begin{bmatrix} 1 & 1-e^{-\lambda_1 t} & 1-e^{-\lambda_2 t} \end{bmatrix}^T$$

$$\underline{B} = \begin{bmatrix} (\lambda_C+\lambda_1^*) & 0 & 0 \\ (\lambda_C+\lambda_2^*) & 0 & 0 \\ \lambda_C & 0 & 0 \end{bmatrix}$$

$$\underline{C} = \begin{bmatrix} 1 & 1 & -1 \end{bmatrix}$$

$$\lambda_1^* = \lambda_1+\mu_{21}, \quad \lambda_2^* = \lambda_2+\mu_{12}$$

(3) Combined (1) and (2)

$$\underline{A}' = \begin{bmatrix} -(\lambda_C+\lambda_1'+\mu_{12}) & \mu_{21} & (\mu_1+\mu_{12}-\mu_{21}) \\ \mu_{12} & -(\lambda_C+\lambda_2'+\mu_{21}) & (\mu_2+\mu_{21}-\mu_{12}) \\ \lambda_2 & \lambda_1 & -(\lambda_C+\lambda_1+\lambda_2) \end{bmatrix}$$

$$\underline{F}(t) = \begin{bmatrix} F_1(t) & F_2(t) & T_{AND}(t) \end{bmatrix}^T, \quad \underline{IC} = \begin{bmatrix} F_1(0) & F_2(0) & T_{AND}(0) \end{bmatrix}^T, \quad \underline{u}(t) = \begin{bmatrix} 1 & 1-e^{-\lambda_1 t} & 1-e^{-\lambda_2 t} \end{bmatrix}^T$$

$$\underline{B} = \begin{bmatrix} (\lambda_C+\lambda_1) & 0 & 0 \\ (\lambda_C+\lambda_2) & 0 & 0 \\ \lambda_C & 0 & 0 \end{bmatrix}$$

$$\underline{C} = \begin{bmatrix} 1 & 1 & -1 \end{bmatrix}$$

$$\lambda_1' = \lambda_1+\mu_1, \quad \lambda_2' = \lambda_2+\mu_2$$

(4) Sequential "jump" failure rate dependency among three identical components

$$\underline{A}' = \begin{bmatrix} -3\lambda & 0 & 0 \\ 2\mu & -2\mu & 0 \\ 0 & \nu & -\nu \end{bmatrix}$$

$$\underline{F}(t) = \begin{bmatrix} F_1'(t) & F_2'(t) & F_3'(t) \end{bmatrix}^T,$$

$$\underline{IC} = \begin{bmatrix} F_1'(0) & F_2'(0) & F_3'(0) \end{bmatrix}^T,$$

$$\underline{u}(t) = \begin{bmatrix} 1 & 0 & 0 \end{bmatrix}^T$$

$$\underline{B} = \begin{bmatrix} 3\lambda & 0 & 0 \\ 0 & 0 & 0 \\ 0 & 0 & 0 \end{bmatrix}$$

$$\underline{C} = \begin{bmatrix} 1 & -1 & 0 \\ 0 & 1 & -1 \\ 0 & 0 & 1 \end{bmatrix}$$

Figure 4 *General State Variable Analog Simulation for Two Component, Two Failure Mode FMSV Models with Several Kinds of Failure Mode Coupling With Common Cause s-Dependency, and for Sequential Failure s-Dependency.*

Table 3 *Comparison of FMSV Model Solutions with Fault Tree Minimal Cut Set Expansion Solutions to Generic Two Component (Initiator) Fault Tree With Common Cause S-Dependency*

FMSV MODEL SOLUTIONS

$u_C(t) = 1 - e^{-\lambda_C t}$
$u_1(t) = 1 - e^{-\lambda_1 t}$
$u_2(t) = 1 - e^{-\lambda_2 t}$
} input lcdf's

Initial condition: $\underline{E}(0) = \underline{0}$

Rate coupling condition: $\mu_{12} = \mu_{21} = 0$

$F_1(t) = 1 - e^{-(\lambda_C + \lambda_1)t} = \hat{P}_1(t)$

$F_2(t) = 1 - e^{-(\lambda_C + \lambda_2)t} = \hat{P}_2(t)$

$T_{AND}(t) = 1 - e^{-\lambda_C t}\left[e^{-\lambda_1 t} + e^{-\lambda_2 t} - e^{-(\lambda_1+\lambda_2)t}\right] = \hat{P}_0(t)$

$\neq F_1(t) \bullet F_2(t) \Longrightarrow$ system is s-dependent.

$T_{OR}(t) = F_1(t) + F_2(t) - T_{AND}(t)$

$= 1 - e^{-(\lambda_C + \lambda_1 + \lambda_2)t}$

MINIMAL CUT SET EXPANSION

$P(C_C) = 1 - e^{-\lambda_C t}$
$P(C_1) = 1 - e^{-\lambda_1 t}$
$P(C_2) = 1 - e^{-\lambda_2 t}$
} initiator lcdf's

$\bar{C}_i \equiv$ complement of C_i ; $i = 1,2,C$

Boolean reduction (+ denotes union ; • denotes intersection)

A. AND gate at TOP

$E_1 = C_C + C_1$

$E_2 = C_C + C_2$

$TOPAND = E_1 \bullet E_2$

$= C_C + C_1 \bullet C_2$

B. OR gate at TOP

$E_1 = C_C + C_1$

$E_2 = C_C + C_2$

$TOPOR = E_1 + E_2$

$= C_C + C_1 + C_2$

$Pr(E_1 \text{ occurs in } [0,t]) \equiv F_1(t) = P(C_C + C_1)$

$= 1 - P(\bar{C}_C) \bullet P(\bar{C}_1) = 1 - e^{-(\lambda_C + \lambda_1)t}$

$Pr(E_2 \text{ occurs in } [0,t]) \equiv F_2(t) = P(C_C + C_2)$

$= 1 - P(\bar{C}_C) \bullet P(\bar{C}_2) = 1 - e^{-(\lambda_C + \lambda_2)t}$

$Pr(\text{TOPAND occurs in } [0,t]) \equiv T_{AND}(t) = P(C_C + C_1 \bullet C_2)$

$= 1 - P(\bar{C}_C) \bullet \left[P(\bar{C}_1) + P(\bar{C}_2) - P(\bar{C}_1) \bullet P(\bar{C}_2)\right]$

$= 1 - e^{-\lambda_C t}\left[e^{-\lambda_1 t} + e^{-\lambda_2 t} - e^{-(\lambda_1+\lambda_2)t}\right]$

$Pr(\text{TOPOR occurs in } [0,t]) \equiv T_{OR}(t) = P(C_C + C_i + C_2)$

$= 1 - P(\bar{C}_C) \bullet P(\bar{C}_1) \bullet P(\bar{C}_2) = 1 - e^{-(\lambda_C + \lambda_1 + \lambda_2)t}$

the inverse of the exponential distribution representing the random waiting time Δt between successive failure events or initiator occurrences.

The FMSV models for three and four component systems were formulated using an **E** transformation matrix based on the same principle of unions of Markov states that the two component model illustrates. Because three components require $2^3 = 8$ states, and four components require $2^4 = 16$ states, the Markov transition diagrams and matrices become complicated, and are not included for the sake of brevity. However, the form of the analog simulation state variable diagram of Figure 4 still applies, but with a seventh order inhomogeneous system describing three components, and a fifteenth order inhomogeneous system describing four components. Note that the inclusion of common cause/common mode initiators in the generic fault trees does not increase the order of the Markov models.

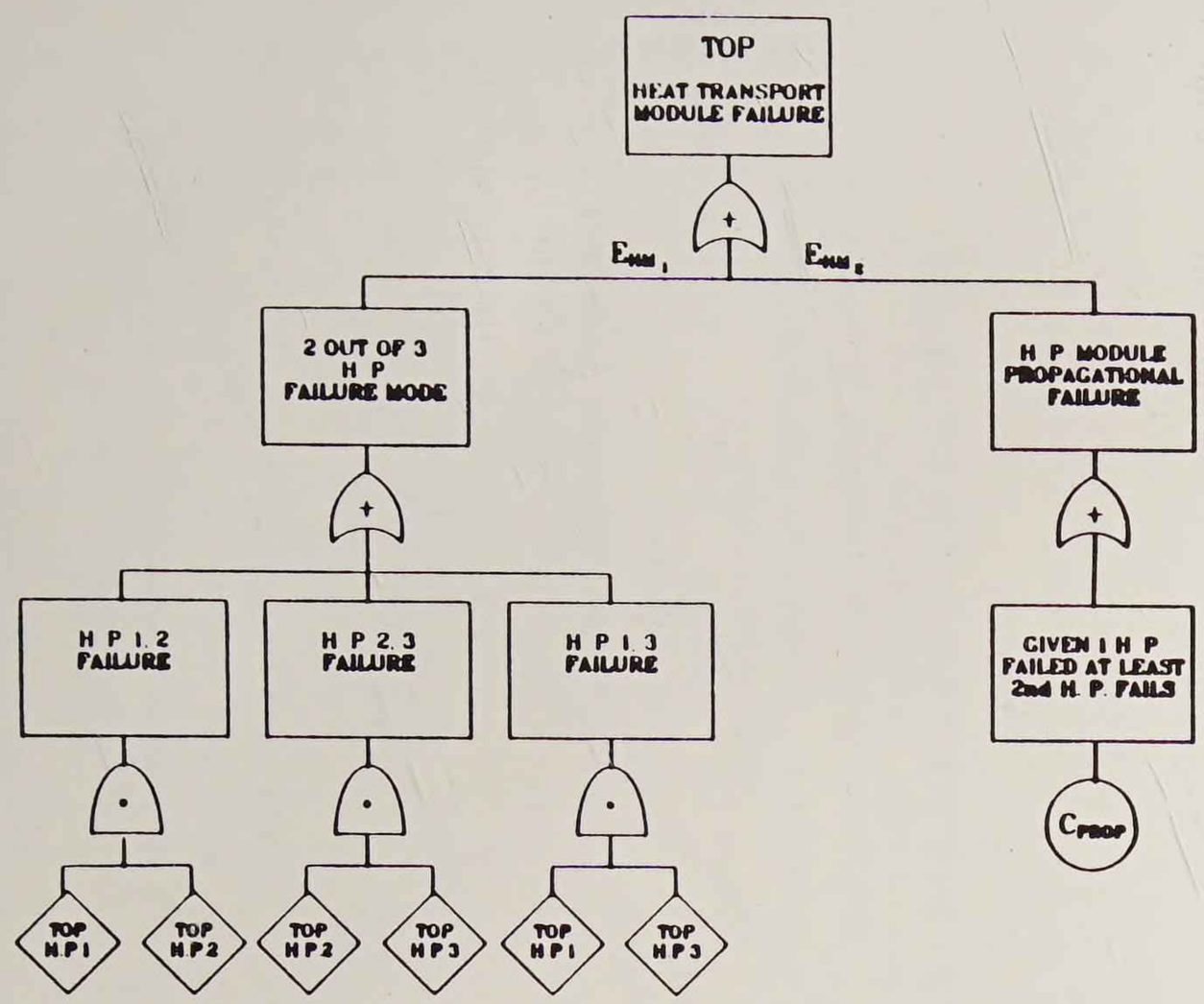
It is noted that when no intermodal coupling repair rates or failure-repair rates exist, $\hat{\mathbf{A}} = \mathbf{A}^T$, and a far simpler FMSV representation can be formulated; in fact, closed form solutions are easily obtained. In Table 3 we compare the FMSV solutions with those obtained from taking the probability of the Boolean functions describing the failure modes and TOP events for the two component system. The two methods yield identical results, and it can also be shown that this is also true for the three and four component models.

We apply a least squares, single exponential curve fitting procedure to the TOP lcdfs to determine effective failure rates ($\hat{\lambda}$'s) of components. These approximations are then used to synthesize fault tree modules in larger systems. This modularization and synthesis is used in our application example that follows.

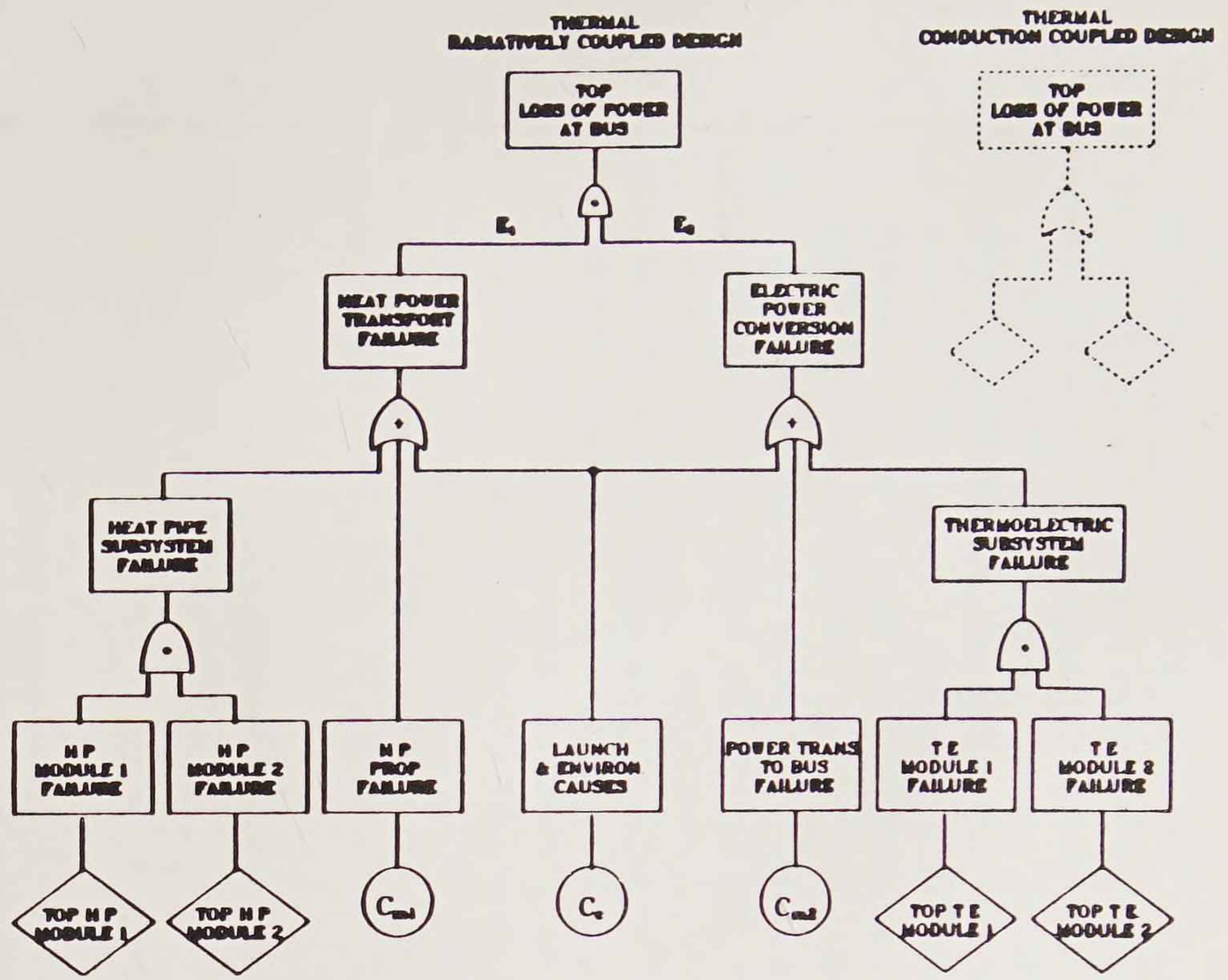
Application to a Space Nuclear Electric Power System

A space nuclear electric power generation system conceptual design employing thermal coupling between heat pipes for heat transport from a nuclear core to thermoelectric converters has been studied by several authors, for example, Buden, Ranken, and Koenig (1980). Bartholomew (1981, 1982) developed some early reliability models for such a system. Basically, two reliability concepts are compared in this paper:

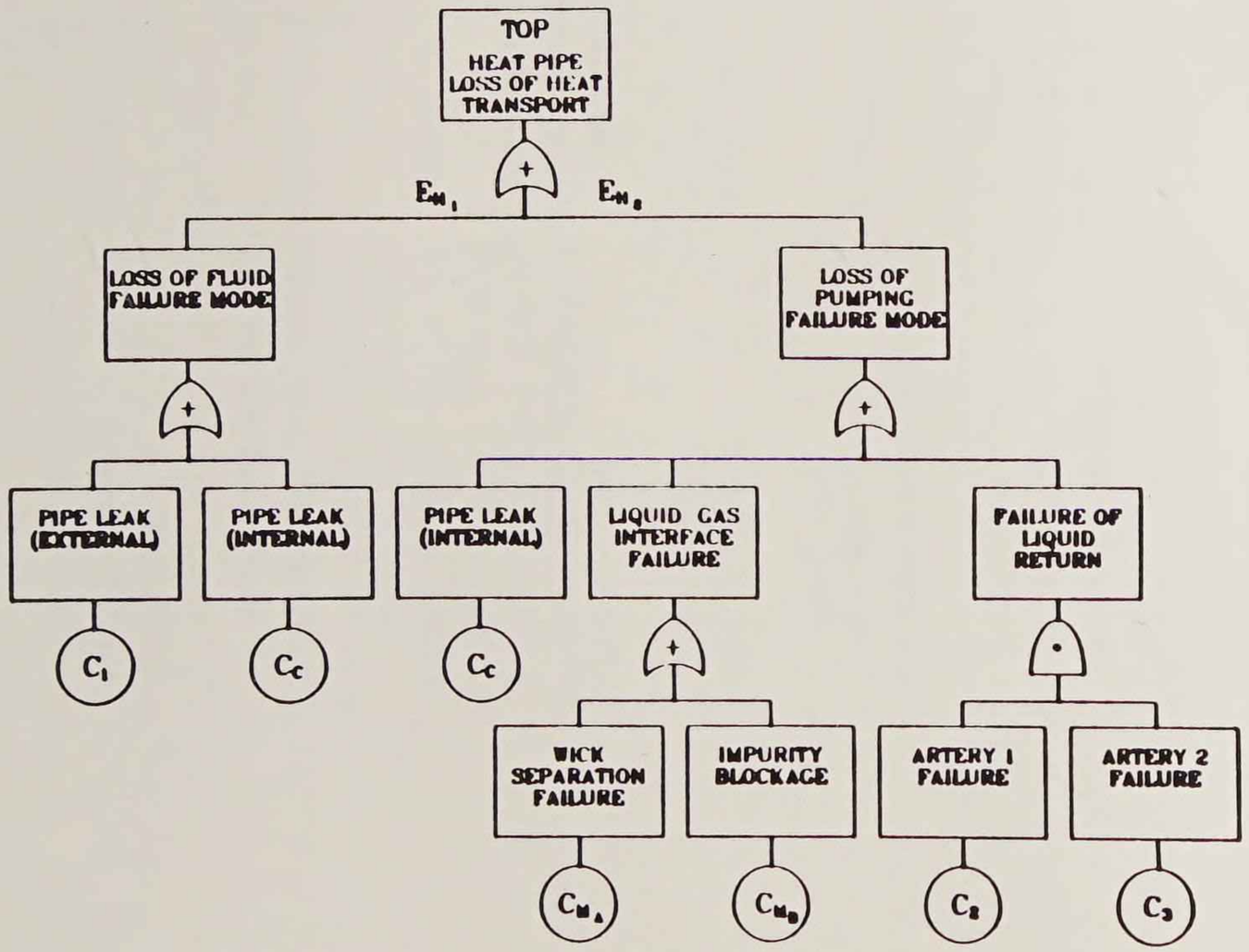
1. direct thermal conduction coupling (series reliability model), and
2. radiation thermal coupling (parallel reliability model).



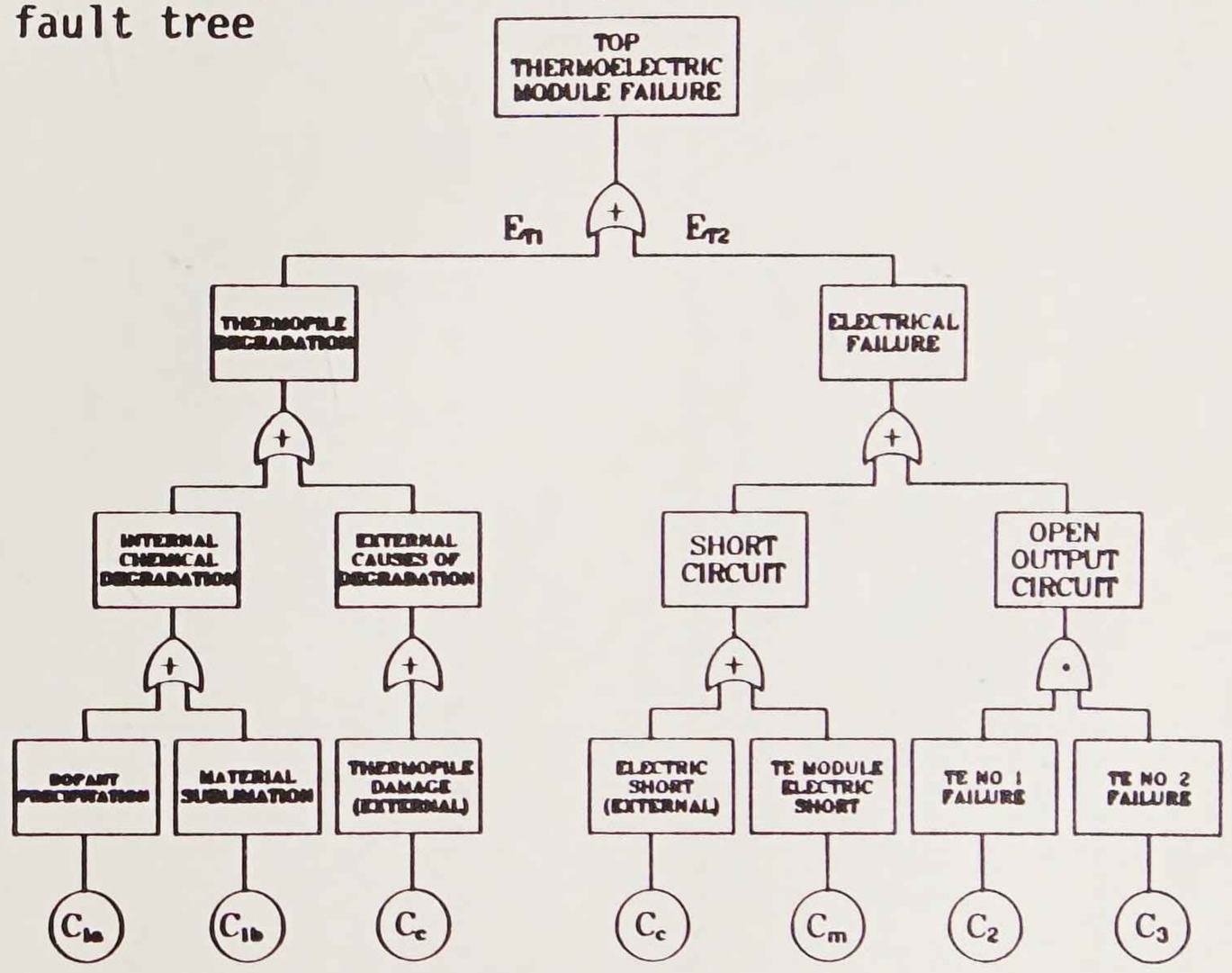
(c) Heat transport subsystem fault tree



(d) Heat transport-electric power conversion system fault tree



(a) Single heat pipe fault tree



(b) Single thermoelectric converter fault tree

Figure 5 *Modularized Fault Trees for System Failure Sensitivity Comparisons between Two Space Based Nuclear Electric Power Generating System Designs.*

The failure analysis of this system employed the following steps:

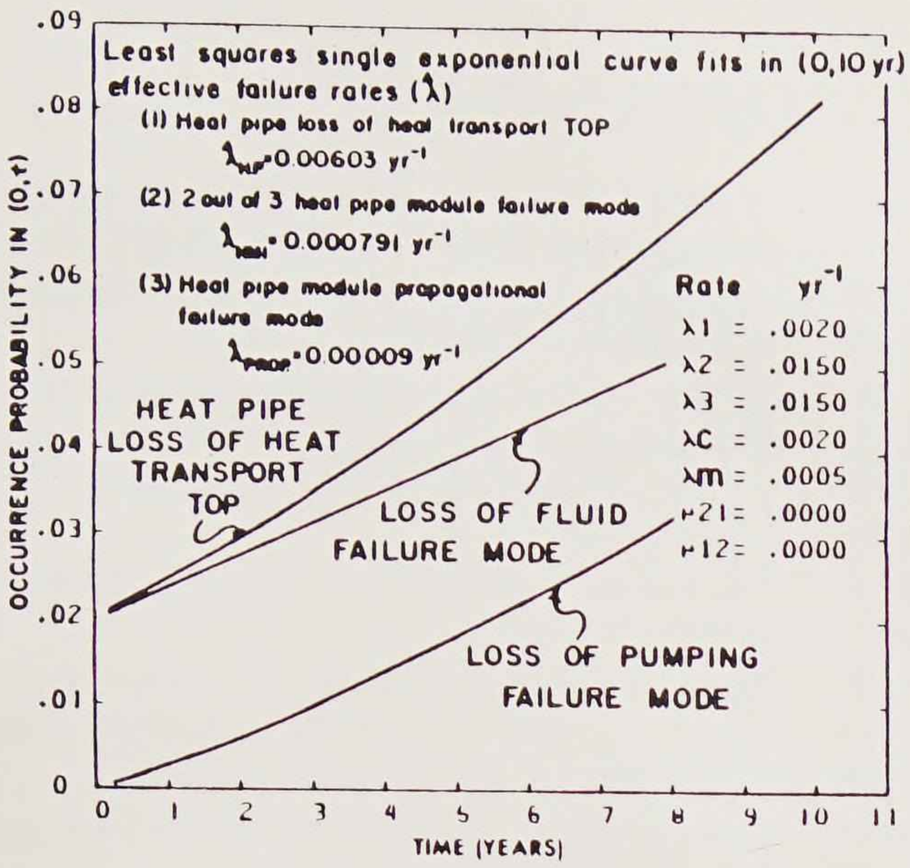
1. a failure modes and effects analysis of both components (FMEA),
2. fault tree construction and analysis (FTA),
3. estimation of the kind and magnitude of failure rates to achieve reliability goals,
4. identification of common cause/common mode initiators,
5. formulation of FMSV models, and
6. determination of expected lifetime cumulative distribution functions (lcdf's).

The generic system models that were developed were utilized to form modularized blocks beginning at the component level and employing least squares single exponential $(1 - e^{-\hat{\lambda}t})$ curve fitting techniques to calculate TOP event probabilities in $[0, T]$, where T is the range of time of interest. The component TOP event lcdf data generated at discrete time points in the computer models are curve fit. The fault trees of Figure 5 illustrate this modularization concept. Because of the presence of common cause/common mode initiators, our modularization and curve fitting techniques were employed so that such initiators were only counted once (as required) in our final calculation of the loss of power TOP event. This procedure of exclusion of these dependencies until the final calculation is similar to the Olmos–Wolf (1978) modularization procedure for fault trees. It does not reduce the required number of calculations, but ensures that repeated initiators in a fault tree are only counted once.

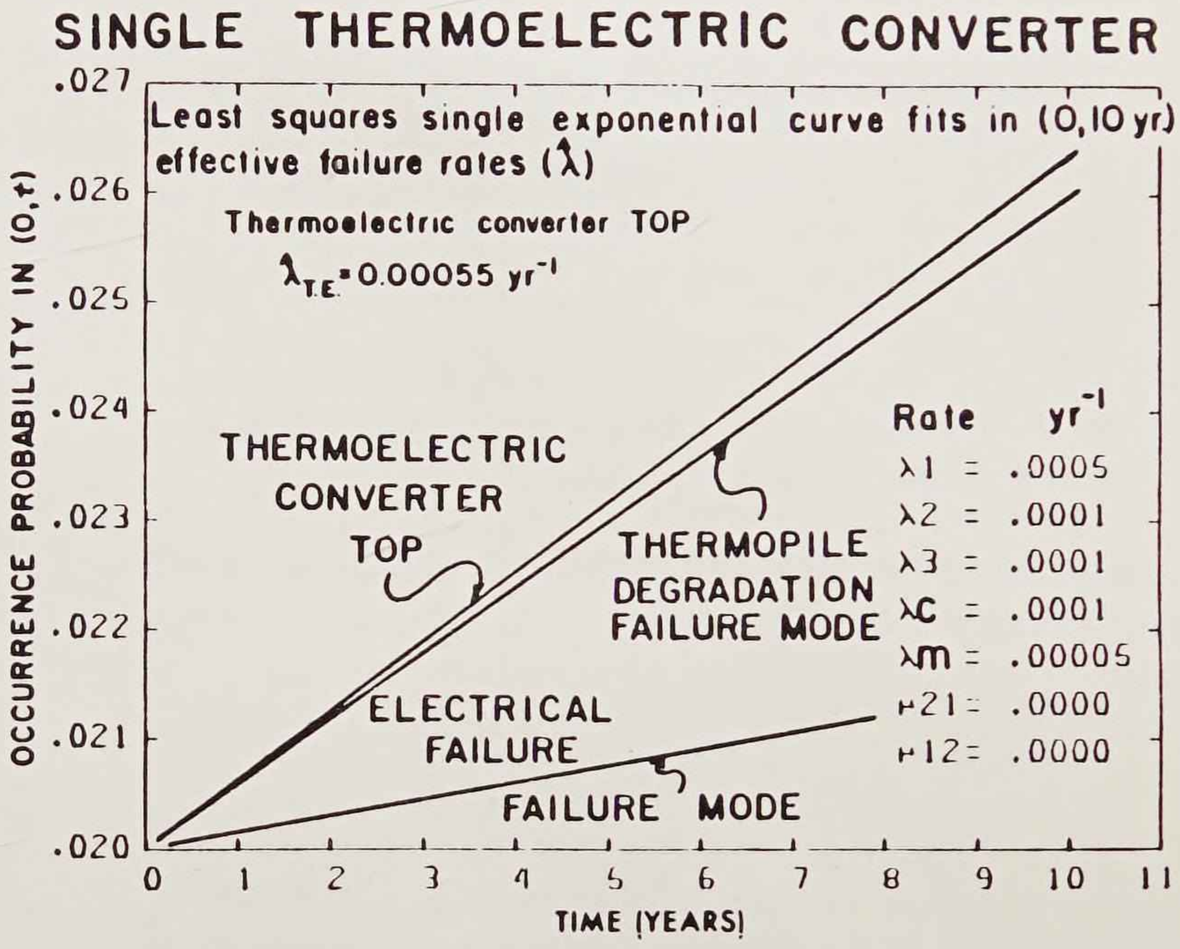
Table 4 presents the estimated/goal failure rates and the reliability estimate for shuttle launch load payload isolation. These numbers are not from any data base, and are considered as goals that are currently thought by experts to be achievable during a comprehensive program of component hardware development. Figure 6 presents the lcdf's for the heat pipe failure modes and

Table 4 *Estimated/Goal Failure Rates and Event Occurrence Frequencies.*

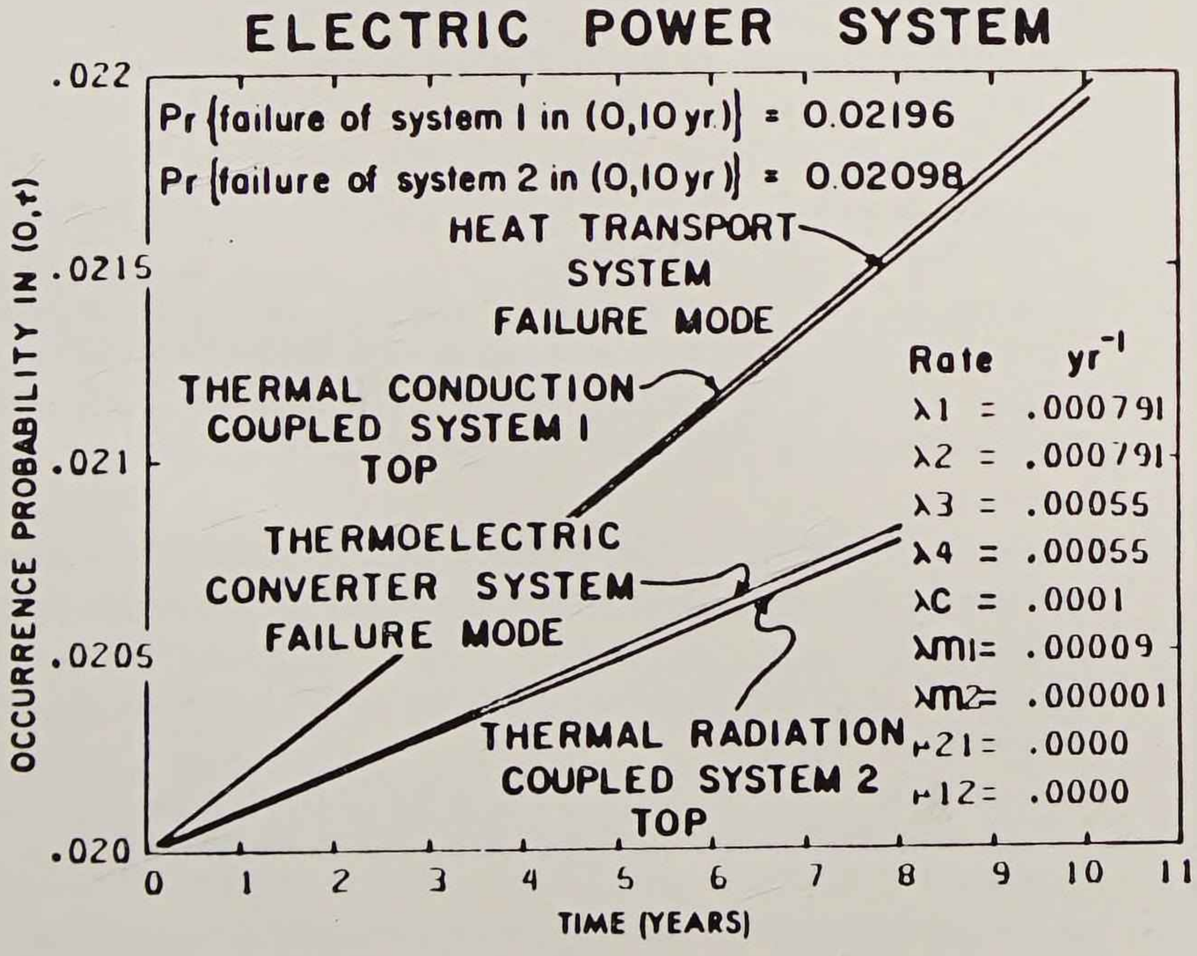
Component or Event	Probability of Failure, Failure Rate, or Occurrence Rate	Source
Heat Pipe		
(1) C_1, externally caused leak	launch failure prob. = 0.02 induced degradation failure rate = 0.002 yr^{-1}	Expected launch load isolation reliability estimated at 0.98. Other failure rates are goals believed to be achievable with vigorous heat pipe development program
(2) C_c, internally caused leak	0.002 yr^{-1}	
(3) C_m, wick separation blockage	0.0005 yr^{-1}	
(4) C_2, C_3 artery separation	0.015 yr^{-1}	
Thermoelectric Converter		
(1) C_{1a}, dopant precipitation	0.0003 yr^{-1}	Total based on D. Buden and J. Stocky (1982) and budgeted by R. Bartholomew
(2) C_{1b}, material sublimation	0.0002 yr^{-1}	
(3) C_c, external damage, degradation	launch failure prob. = 0.02 induced degradation failure rate = 0.0001 yr^{-1}	
(4) C_m, electric short	0.00005 yr^{-1}	
(5) C_2, C_3 open circuit failure	0.0001 yr^{-1}	
Power Loss		
(1) C_m1, heat pipe propagational failure	0.00009 yr^{-1}	Calculated by FMSV sequential model using heat pipe estimates
(2) C_m2, power transmission failure	0.000001 yr^{-1}	Estimated by R. Bartholomew (very dependent on circuitry and component quality)



(a) Lifetime distribution for single heat pipe TOP event and two failure modes.



(b) Lifetime distribution for single thermoelectric converter TOP event and two failure modes.



(c) Lifetime distribution comparison between a thermal conduction coupled system and a thermal radiation coupled system of heat pipes and thermoelectric converters.

Figure 6 *Lifetime Cumulative Distribution Functions (LCDF's) for Reliability Comparison Between Two Space Based Nuclear Electric Power Generating System Designs.*

TOP event, the thermoelectric module failure modes and TOP event, and the system TOP event loss of deliverable electric power for (1) the thermal conduction coupled design, and (2) the thermal radiation coupled design.

Conclusions and Further Work

The major conclusions of the research reported here are

1. A useful matrix similarity transformation $\hat{\mathbf{A}} = \mathbf{EAE}^{-1}$ has been discovered that allows formulation of stochastic process FMSV models based on the classical Markov model. This transformation provides for more efficient and direct calculation of failure densities and lcdf's for generic fault trees, which include time dependent *s*-dependency coupling mechanisms not currently allowed from standard FTA.
2. A modularization technique for approximating effective failure rates of components and subsystems by least squares curve fits is suggested as a way of reducing the enormous computational requirements (2^n for n components in a Markov model and $2^n - 1$ for n minimal cut sets in a fault tree) for large systems.
3. The methods developed have been practically applied to compare two possible space based electric power system designs.

Further work suggested along the lines formulated in this paper are

1. Expand the analysis procedure beyond the four component level by a digital computer code capable of implementing the complicated state combinational process algorithm. To accomplish this, a higher level programming architecture that employs an artificial intelligence language such as LISP as described by Winston (1979) is suggested.
2. Account for failure rate uncertainty by utilizing the FMSV models as state variable coordinates in a Fokker–Planck formulation to calculate probability densities of failure (repair) rates in highly coupled systems.
3. Expand the Markov model and FMSV model now utilizing only two condition states ("good"-"failed") to include an intermediate state ("good," "degraded," "failed") yielding 3^n differential equations.

Acknowledgments

This paper is a result of research by the principal author in partial fulfillment of Ph.D. dissertation requirements at the University of New Mexico. The research was Co-Sponsored by the US Department of Energy—Office of Space Nuclear Projects (1981–1982) and Los Alamos National Laboratory—Independently Supported R&D Project (1982–1983).

References

Arley, N. and K. R. Buch (1950) *Introduction to the Theory of Probability and Statistics*, John Wiley and Sons, New York, pp. 48–54.

Bartholomew, R. J. (1981) "Failure Mode Analysis Using State Variables Derived from Fault Trees with Applications," in *Proc. ANS/ENS Intl. Topical Meeting on Probabilistic Risk Assessment*, September 20–24, 1981, Port Chester, New York.

Bartholomew, R. J. (1982) "Failure Modes and Effects Critical Analysis (FMECA) and Reliability Studies," in *Space Reactors Progress Report April–June 1981*, prepared by W. A. Ranken, LA-9106-PR or UL-33, issued January 1982.

Brogan, W. L. (1974) *Modern Control Theory*, Quantum Publishers, New York, Chap. 9, pp. 148–170.

Buden, D., W. A. Ranken, and D. R. Koenig (1980) *Space Nuclear Reactor Power Plants*, Los Alamos Scientific Laboratory report LA-8223-MS, January 1980.

Buden, D. and J. Stocky (1982) *SP-100 Conceptual Design Description No. 1*, Jet Propulsion Laboratory, June 1982, pp. 21–33.

Caldarola, L. and A. Wickenhauser (1977) "Recent Advancements in Fault Tree Methodology at Karlsruhe," in *Nuclear Systems Reliability and Risk Assessment*, eds. J. B. Fussell and G. R. Burdick, SIAM, pp. 518–542.

Carter, L. L. and E. D. Cashwell (1975) *Particle-Transport Simulation with the Monte Carlo Method*, TID-26607, Technical Information Center, ERDA, Washington, D.C.

Dhillon, B. S. and C. Singh (1981) *Engineering Reliability—New Techniques and Applications*, John Wiley and Sons, New York, Chap. 4, p. 48, p. 93.

Fussell, J. B. and G. R. Burdick, Eds. (1977) *Nuclear Systems Reliability and Risk Assessment*, SIAM, pp. 265–268.

Karlin, S. and H. M. Taylor (1975) *A First Course in Stochastic Processes*, 2nd edition, Academic Press, New York, Chap. 4, pp. 123–125.

Lewis, E. E. and F. Bohm (1983) "Monte Carlo Simulation of Markov Unreliability Models," submitted to *Nucl. Eng. Design*, June 1983.

Marshall, A. W. and I. Olkin (1967) "A Multivariate Exponential Distribution," JASA 62:30–44.

Olmos, J. and L. Wolf (1978) "A Modular Representation and Analysis of Fault Trees," *Nuclear Engineering and Design* 48: 531–561.

Papazoglou, I. A. and E. P. Gyftopoulos (1978) "Automated Merging of Markov Processes of Large Reactor Systems," in *Proc. of the ANS/ENS International Topical Meeting on Probabilistic Analysis of Nuclear Reactor Safety*, May 8–10, 1978, pp. VIII.3-1–VIII.3-12.

Reactor Safety Study (1975) WASH-1400, NUREG 75/014, October 1975, Appendix II, "Fault Trees."

Shooman, M. L. (1968) *Probabilistic Reliability: an Engineering Approach*, McGraw-Hill, New York, pp. 61–67; 96–115; 156–263.

Spanier, J. and E. M. Gelbard (1969) *Monte Carlo Principles and Neutron Transport Problems*, Addison-Wesley, Massachusetts, pp. 1–82.

Vesely, W. E. and R. E. Narum (1970) *PREP and KITT: Computer Codes for the Automatic Evaluation of the Fault Tree*, IN-1349, August 1970.

Winston, P. H. (1979) *Artificial Intelligence*, Addison-Wesley, Massachusetts, pp. 257–286.

Worrell, R. B. and D. W. Stack (1978) *A SETS User's Manual for the Fault Tree Analyst*, NUREG/CR-0465, SAND 77-2051, November 1978.

Space Nuclear Power Systems 1984
Edited by M. S. El-Genk and M. D. Hoover
© Orbit Book Company, Malabar, FL, 1985

Chapter 63

Reliability Analysis Using Network Simulation

Dennis Engi

Sandia National Laboratories
P. O. Box 5800
Albuquerque, NM 87185

The models that can be used to provide estimates of the reliability of nuclear power systems operate at many different levels of sophistication. The least-sophisticated models treat failure processes that entail only time-independent phenomena (such as demand failure). More advanced models treat processes that also include time-dependent phenomena such as run failure and possibly repair. However, many of these dynamic models are deficient in some respects because they either disregard the time-dependent phenomena that cannot be expressed in closed-form analytic terms or because they treat these phenomena in quasi-static terms. The next level of modeling requires a dynamic approach that incorporates not only procedures for treating all significant time-dependent phenomena but also procedures for treating these phenomena when they are conditionally linked or characterized by arbitrarily selected probability distributions. The level of sophistication that is required is provided by a dynamic, Monte Carlo modeling approach. A computer code that uses a dynamic, Monte Carlo modeling approach is Q-GERT (Graphical Evaluation and Review Technique—with Queueing), and the present study has demonstrated the feasibility of using Q-GERT for modeling time-dependent, unconditionally and conditionally linked phenomena that are characterized by arbitrarily selected probability distributions.

Introduction

The choice of the model to be used in the analysis of the reliability of a space nuclear power system depends on the failure process that is assumed and on the availability of suitable models for treating this process. The process by which a system can fail consists of a sequence of potentially realizable events such as component, subsystem, and system failures. An event such as a component failure depends upon the phenomena that can cause the event and affect the time at which the event occurs. Examples of such phenomena are demand failure (failure of a component to operate when it is first turned on), run failure (failure that occurs after the component has been operating for some period of time), and component repair (an activity that, if completed within a certain period of time after a failure, can be regarded as restoring the component to operational status without imperiling the operation of the subsystem of which it is a part).

Each of these phenomena—demand failure, run failure, and repair—may be manifested in more than one way. For example, a component run failure may occur, depending upon the complexity of the component, because a fuse blows, a shorted circuit develops, or a bearing fails. If a particular phenomenon can be manifested in only one mode, no choice of mode is possible: The choice is deterministic. If more than one mode is possible and these modes can be unconditionally manifested, a choice can be made, and the choice can be made probabilistically. This is not, however, the case when more than one mode is possible and these modes are conditionally determined, that is, when the choice of mode is dependent on the mode of a phenomenon manifested in a previous event (for example, the mode of repair of a component is determined by the mode of failure). In this situation, no choice is possible because the choice is predetermined.

In reliability analyses of nuclear reactor safety systems, time-dependent phenomena (such as component failure during operation and the ensuing repair activity) are often disregarded or treated quasi-statically because the time dependencies involved are not amenable to closed-form analytic formulation. In addition, conditional phenomena (such as a failure mode that depends on the failure mode in a previous event) and phenomena that must be characterized by arbitrary probability distributions are often ignored. This paper reports the initial application of the computer program Q-GERT (Graphical Evaluation and Review Technique—with Queueing) (Pritsker 1979), an existing code that uses dynamic Monte Carlo modeling, to reactor safety-system simulation and analysis. Using Q-GERT with its Monte Carlo techniques, the above shortcomings can, in principle, be dealt with, and the analysis can be elevated from the level of a reliability analysis to that of a maintainability analysis.

The Maintainability Analysis Procedure (MAP)

The new application of Q-GERT, called the Maintainability Analysis Procedure (MAP), is illustrated by simulating and evaluating the behavior of a simple safety system as this system is subjected to each of four possible failure processes. These processes are distinguished by the number of complexity of the included phenomena, and the effects on estimates of the probability of system failure are shown to be significant as the processes become more complex.

As is shown in Figure 1, MAP is better suited to situations requiring a dynamic, Monte Carlo approach than are the models SETS (Worrell and Stacks 1978), PREP (Vesely and Narum 1970), and KITT (Vesely and Narum 1970 and Vesely 1969). These models have previously been used in reliability analyses of reactor safety systems. The potential usefulness of MAP is made apparent by comparing MAP with the other dynamic model, KITT. Time dependencies that are amenable to description by exponential probability functions can be treated by KITT but, unlike MAP, KITT cannot readily model arbitrary probability distributions or, more importantly, conditional dependencies such as conditional failure and conditional repair.

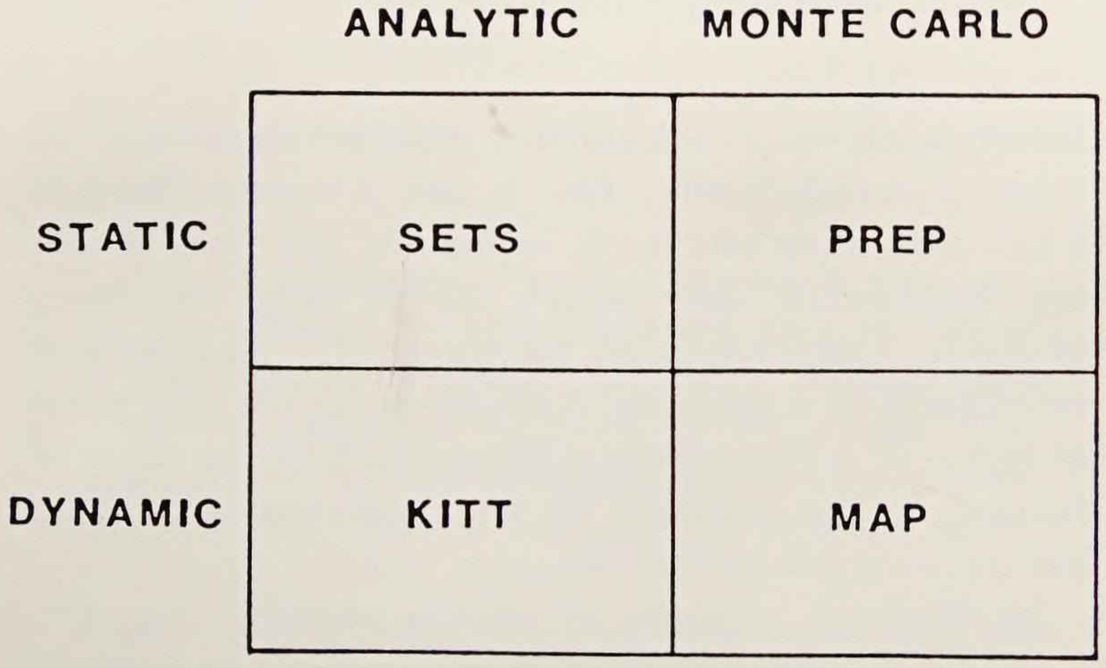


Figure 1 *Models for Analyses of Reactor Safety-System Performance.*

MAP Simulations of a Simplified Safety System

A Safety System and Failure Processes

The application of Q-GERT in the form of MAP and the types of simulations and analyses that can be done with MAP can be illustrated through the description of a simple reactor safety system and of four possible failure processes that determine the behavior of the system. Consider the safety system that is shown in Figure 2 along with the fault tree that portrays the logic of the system's operation. The Boolean statement of system failure that is made just below the fault tree shows that system S fails if either subsystem X or subsystem Y fails, because these two subsystems are in series. Components C and D of subsystem Y are also in series, so Y fails if either C or D fails; however, components A and B of subsystem X are in parallel, so X fails only if both A and B fail. The individual components of this system must be specified so that the assumed probability distributions for the time intervals for failure and repair can be based upon available data. Thus, components A and B are assumed to be diesel generators, C is assumed to be a pump, and D is an electric motor.

The three standard phenomena previously discussed (demand failure, run failure, and repair) and the two advanced phenomena (conditional run failure and conditional repair) can be incorporated in the simulation of the operation of this safety system. In the present study, these phenomena are variously combined into four processes that are labeled according to the phenomena they include

Process 1: Demand Failures Only,
Process 2: Demand and Run Failures,
Process 3: Demand and Run Failures with Repair, and
Process 4: Demand and Conditional/Unconditional Run Failures with Conditional/Unconditional Repair.

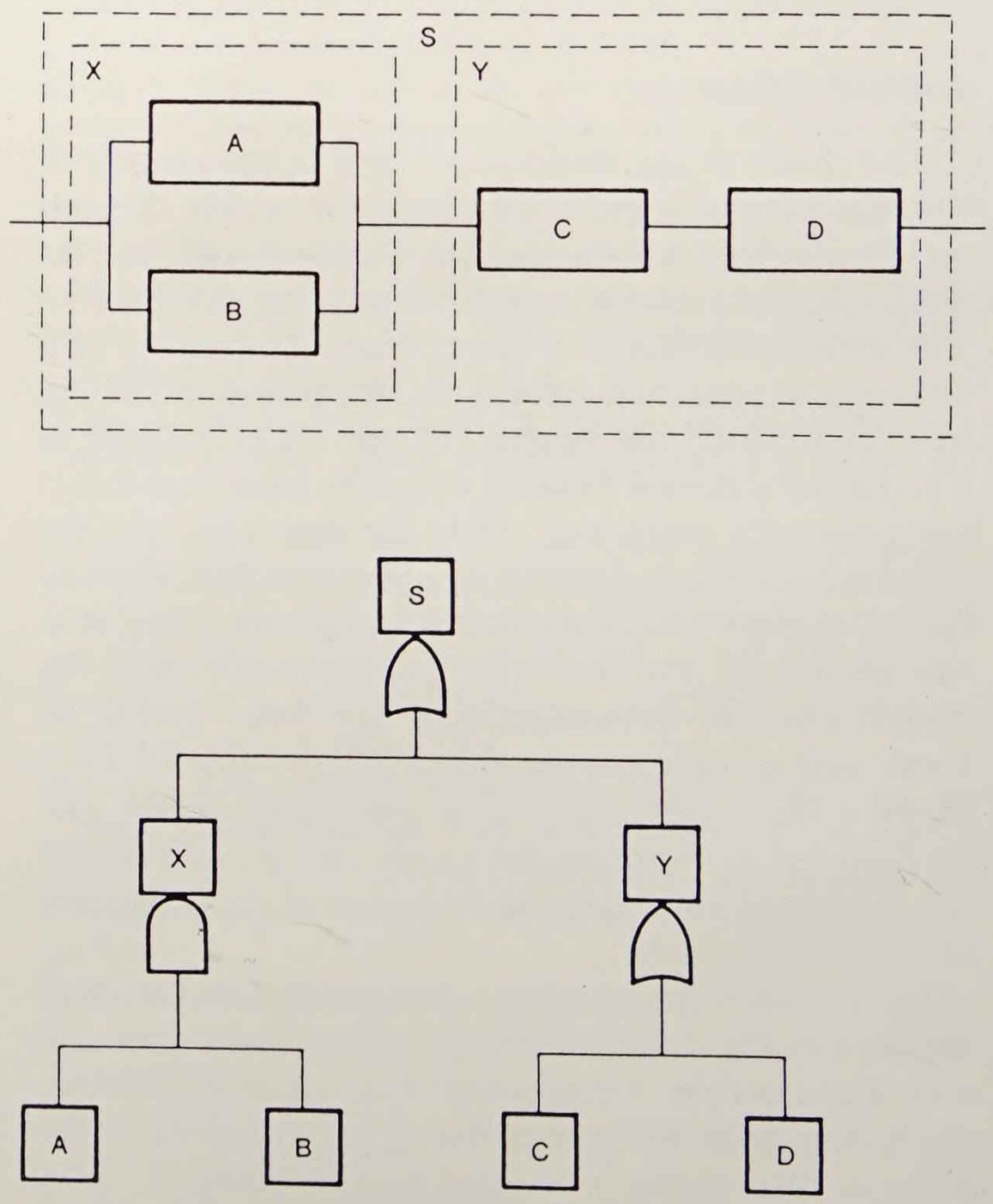


Figure 2 *A Reactor Safety System and Its Logic (Fault) Tree.*

Note that Processes 2, 3, and 4 each build upon the previous process by including an additional level of complexity. Thus, the investigation of these four processes can serve to illustrate that MAP has the capability to (1) model increasing levels of complexity and (2) to demonstrate the effects of including increasingly complex phenomena on estimates of system reliability.

Q-GERT Networks

The key to using MAP lies in understanding the Q-GERT networks that are used to represent the system as it is subjected to the four processes being considered. The fault tree for the safety system (Figure 2) shows the topology of the system (the set of logical relationships among the components of the system). This topology is then combined with the appropriate phenomena (from the five phenomena listed previously) to construct the Q-GERT networks for Processes 1 through 4 that are shown in Figures 3 through 6. It is a simple matter then to translate each network into a series of computer input cards that describe the network and the parameters that apply to the network. A complete discussion of the construction of networks and the translation of these networks into appropriate computer inputs is given in Pritsker (1979).

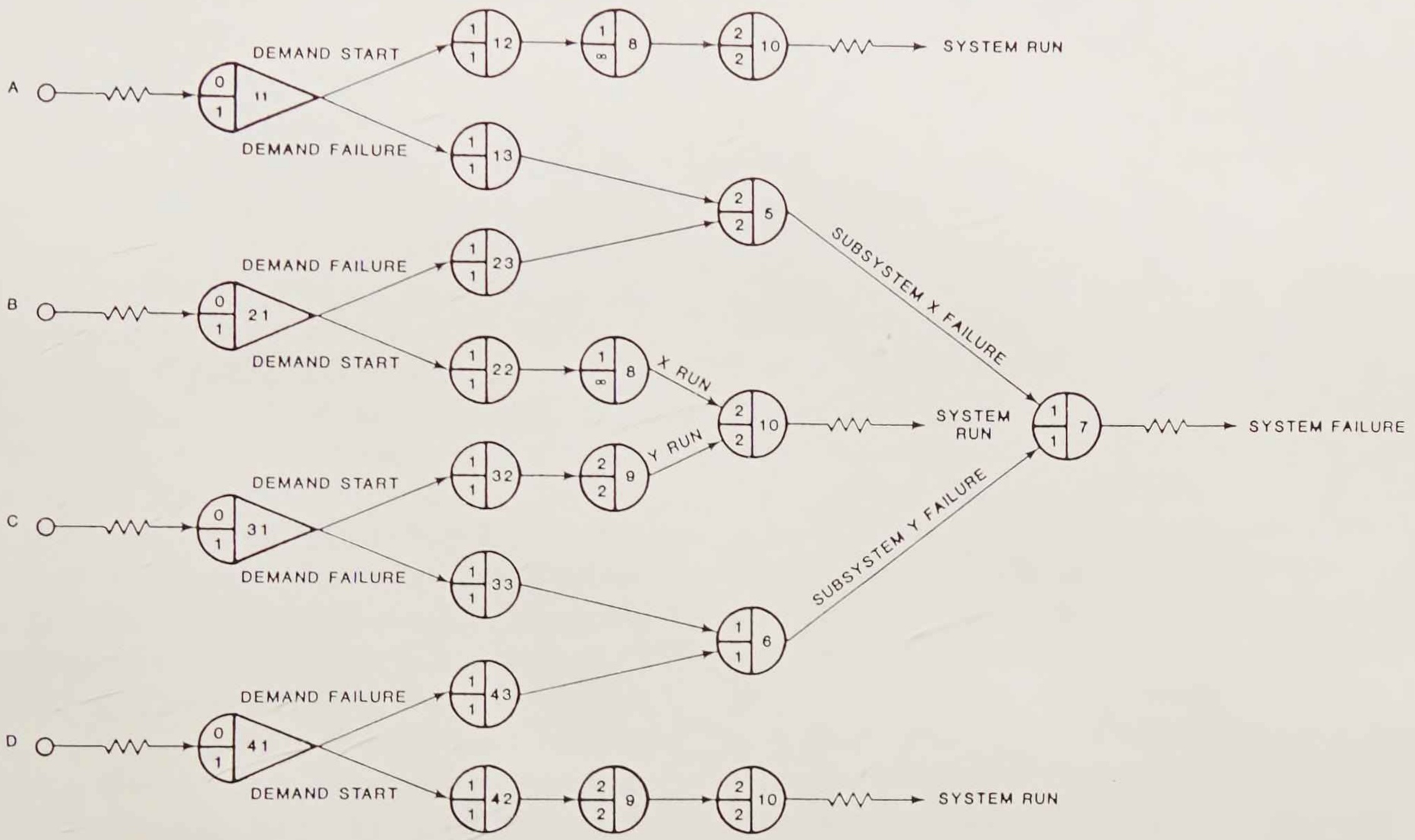


Figure 3 *Process 1 Network—Demand Failures Only.*

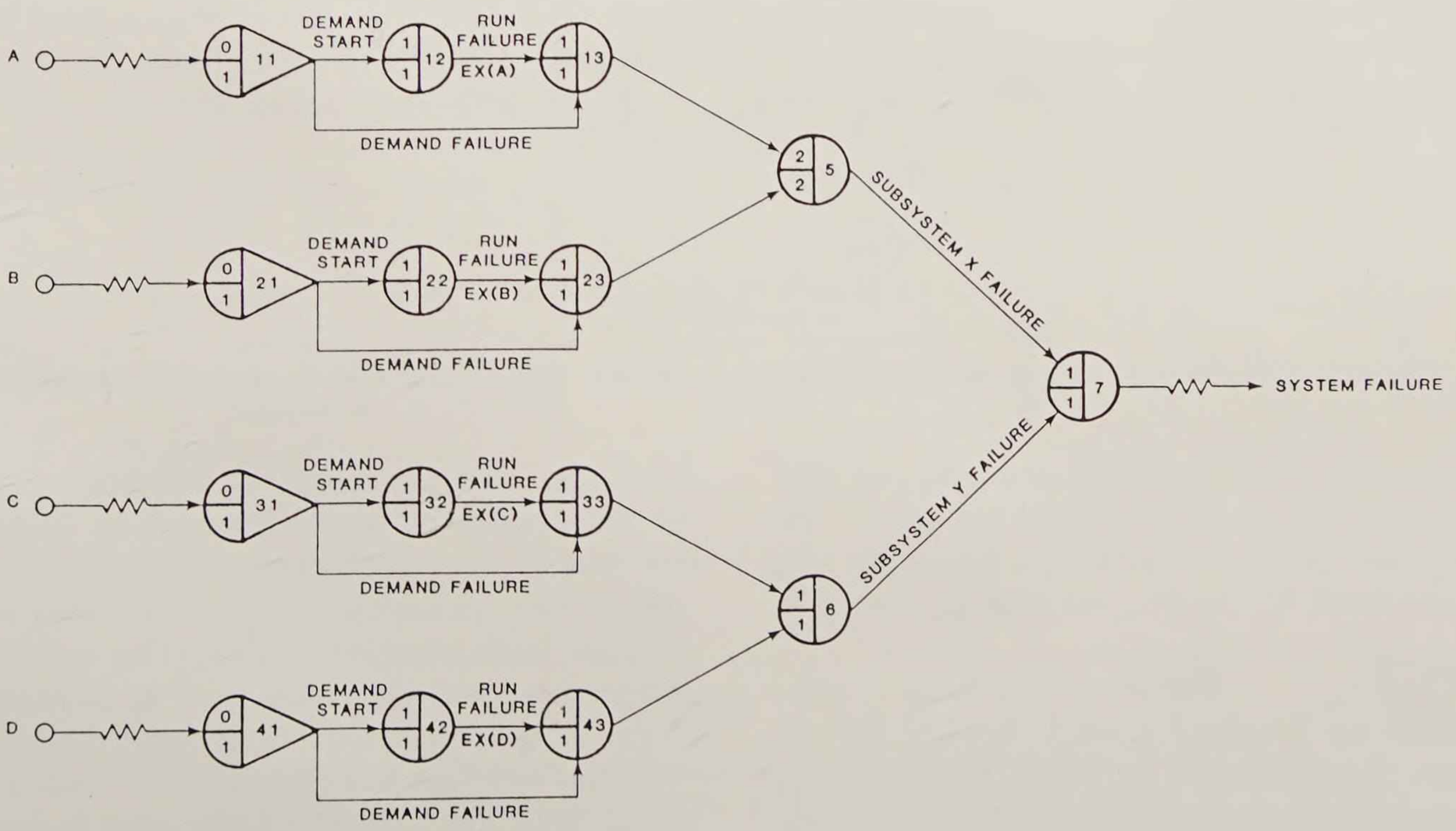


Figure 4 *Process 2 Network—Demand and Run Failures.*

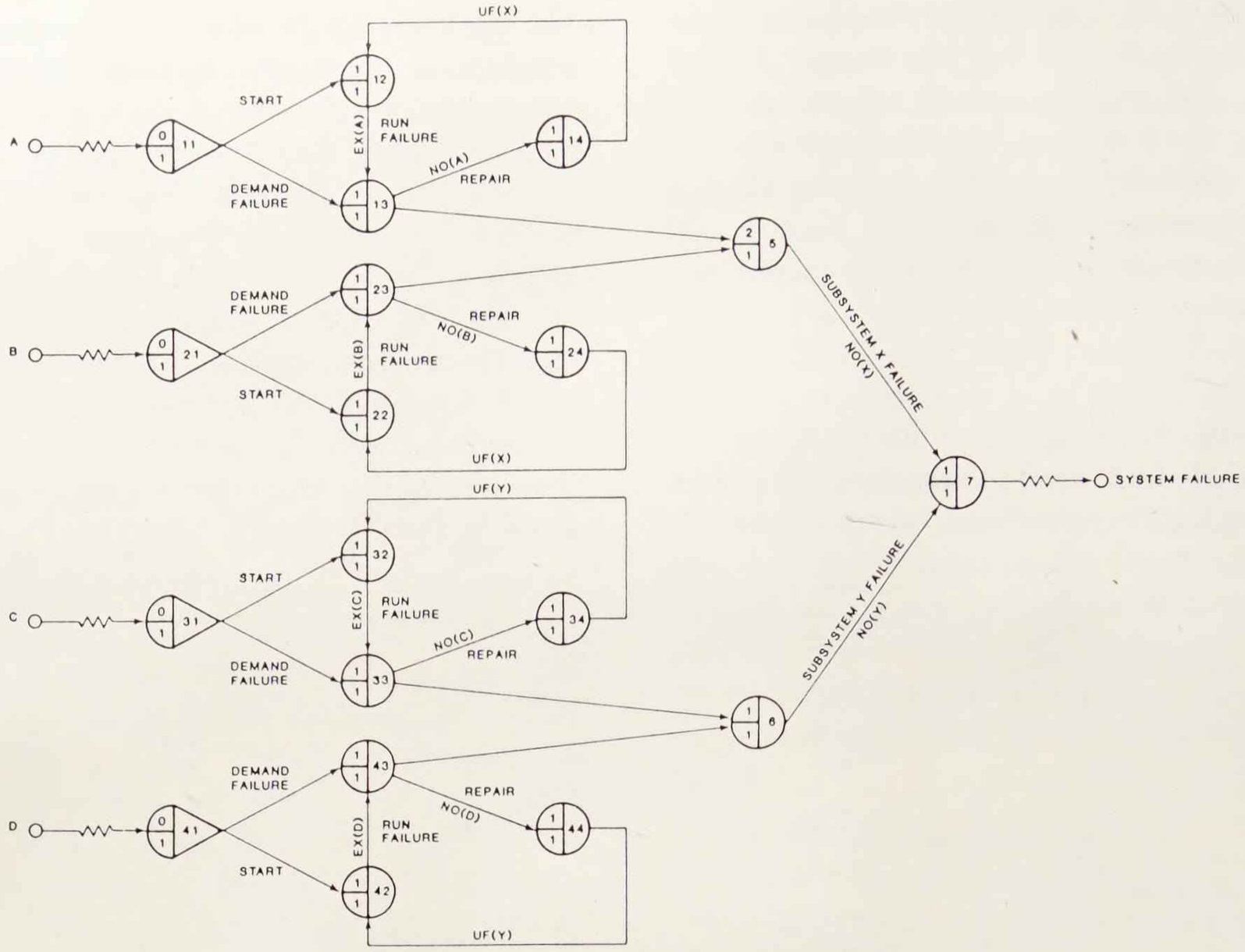


Figure 5 *Process 3 Network—Demand and Run Failures with Repair.*

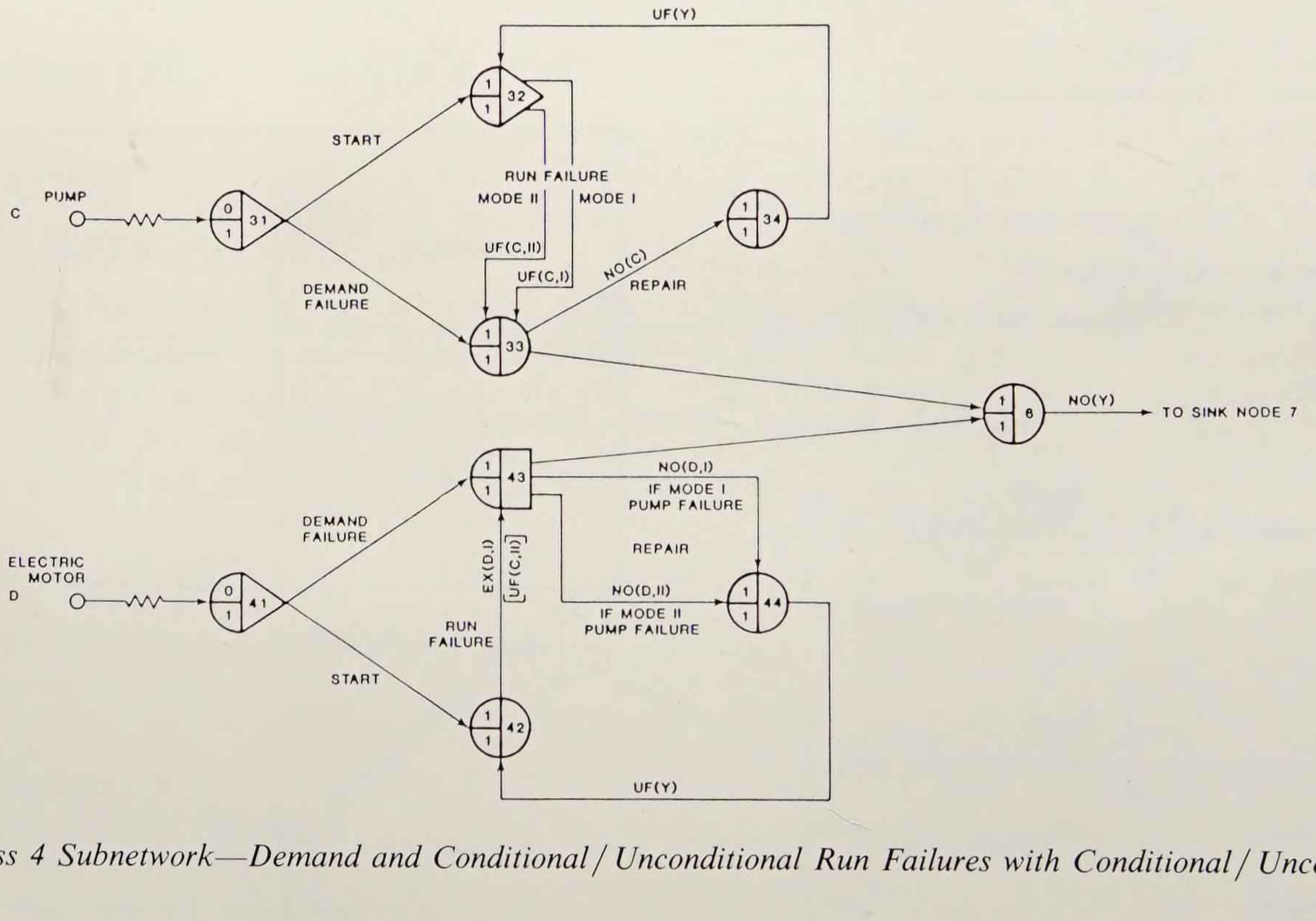


Figure 6 *Process 4 Subnetwork—Demand and Conditional / Unconditional Run Failures with Conditional / Unconditional Repair.*

The functioning of the Q-GERT networks can best be illustrated by examining the salient features of the networks for each of the four processes, beginning with those of the network for the simplest process, Process 1.

Process 1 Network

The network for Process 1 exhibits most of the primary features of all Q-GERT networks (Figure 3). The network constitutes a graphical representation of a process consisting of a time-varying sequence of events, activities, and decisions. It consists of nodes and branches through which transactions (indicators that the constitutive components are operating or have failed) flow. Branches represent activities such as run and, in later processes, repair. The nodes of various shapes represent (1) events such as component failure (and, in later processes, component repair completed) that end activities and (2) points at which decisions are made regarding further routing of a transaction. The key to understanding the operation of the network lies

Table 1 *Values for Input Parameters for Processes 1, 2, and 3.*[a,b]

Component	Q Demand	$1/\lambda$ Run	$1/\mu$[c] Repair
Diesel *A*	3×10^{-2}	3×10^{-3}/hr	1/hr
Diesel *B*	3×10^{-2}	3×10^{-3}/hr	1/hr
Pump *C*	1×10^{-3}	1×10^{-3}/hr	1/hr
Electric Motor *D*	3×10^{-4}	1×10^{-3}/hr	0.5/hr

[a] From U.S. NRC (1975) Appendix III, pp. 45 and 47.
[b] Assumes subsystem *X* (*A* and *B*) must be down for an average of 1 hour or subsystem *Y* (*C* and *D*) for an average of 2 hours for system *S* to fail.
[c] Coefficient of variation = 1/3.

in understanding what is symbolized by the various shapes of the nodes and what is represented by the numbers or symbols on the lefthand sides of the nodes. The numbers on the righthand sides of the nodes are simply the designation numbers of the nodes; for example, the node in the upper lefthand corner of Figure 3 is node 11. Also note that the same node (for example, nodes 8, 9, and 10 in Figure 3) may appear more than once in a single network because of the limitations of representing the network in two dimensions; it is the same node no matter how often in appears.

To initiate a simulation in Figure 3, four simultaneous transactions for Process 1 are generated at source nodes 11, 21, 31, and 41 (designated as source nodes by the sawtooth lines on the input side). The numbers on the lefthand side of these nodes show that they require zero incoming transactions to release the node initially and one incoming transaction to release the node subsequent to a previous release. (Release of a node causes a transaction to be passed on from the node.) The shape of these source nodes (triangular on the right side) indicates that branching from them is probabilistic; that is, a transaction is routed along one branch (demand start) or the other (demand failure) depending upon the result of comparing a random number (drawn from a uniform distribution) between zero and one to a probability Q. The values of Q (probability of failure per demand) for all four components and the source of these values are listed in Tables 1 and 2 for all four processes. All activities in Process 1 take zero time; system *S* either starts or fails to start. To end a simulation, either failure or success must be determined and noted.

At the end of the demand-start activity (zero duration), transactions arrive at regular nodes 12, 22, 32, and 42, which are released initially and subsequently by "1" incoming transaction (see Figure 3). The shape of these nodes (semicircle on the right) indicates that branching is deterministic (transactions are passed on along all branches emanating from these nodes). The start transactions of subsystem *X* (*A* and *B*) are passed on to regular node 8, and those of subsystem *Y* (*C* or *D*) are passed on to regular node 9. Nodes 8 and 9 are placed in the network to reflect the logic of the fault tree. Whereas a single transaction, arriving at node 8 from either node 12 or node 22, will release node 8 initially (indicating that at least one diesel is operating), subsequent transactions from nodes 12 or 22 will not be passed on to sink node 10 because they must be infinite in number (as indicated in Figure 3) to cause a subsequent release. Sink node 10 (designated by the sawtooth lines exiting the node) is released, signaling system success, when a pair of transactions arrives. Were it possible for the pair to come from the subsystem *X*, sink node 10 would be released, but this release would not necessarily indicate that the system is operating. (Subsystem *Y* might have failed.)

Node 9 serves as an AND gate and is released only with the arrival, initially and subsequently, of a pair of transactions. Release of node 9, then, corresponds to the running of both pump and motor. The arrival of a pair of transactions—one from node 8 and one from node 9—releases node 10, thereby signaling the end of one complete simulation of Process 1 during which both pump and motor and at least one diesel do not fail.

At the end of the demand-failure activity (zero duration) shown in Figure 3, transactions arrive at regular

Table 2 *Values for Input Parameters for Process 4.*[a]

Component	Q Demand	$1/\lambda$ Run		$1/\mu$ Repair	
		Mode I[b]	Mode II[b]	Mode I[c]	Mode II[c]
Pump *C*	Table 1	10^{-3}/hr	5×10^{-4}/hr	Table 1	
Electric Motor *D*	Table 1	10^{-3}/hr	5×10^{-3}/hr	1/hr	5×10^{-1}/hr
Diesel A			Table 1		
Diesel B			Table 1		

[a] Assumes either subsystem *X* or subsystem *Y* must be down for an average of 2 hours for system *S* to fail.
[b] Assumes that the pump run-failure modes I and II are equally probable. Motor run-failure modes I and II are contingent on pump run-failure modes I and II.
[c] Mode I motor repair is conditional on mode I pump failure; mode II motor repair on mode II pump failure.

nodes 13, 23, 33, and 43. Branching is deterministic, and transactions are routed to regular nodes 5 and 6. Node 6 is released by the arrival of at least one transaction both initially and at all subsequent times. Thus, in consonance with the logic of the system, node 6 acts as an OR gate for fail transactions that originate with the pump and motor. Node 5, however, acts as an AND gate, requiring two transactions initially and subsequently in order to be released. Consequently, only when node 5 receives a pair of fail transactions, indicating failure of both diesels, will a fail transaction be passed on to node 7. Node 7 is also a sink node, and only one fail transaction, from either subsystem X or subsystem Y, is required to release it. Consequently, the release of sink node 7 signals system failure.

For Process 1, the release of either node 7 or node 10 completes each simulation, and data (the cumulative count of the number of system successes and system failures) for multiple simulations, or runs, are gathered at these two nodes. For this purpose, nodes 7 and 10 act not only as sink nodes but also as statistics nodes. With the completion of the specified number of runs, the output summary will display the number of system successes (from node 10) and system failures (from node 7).

Process 2 Network

Figure 4 shows the Process 2 Q-GERT network, which incorporates both demand and run failures. This network reflects a simple modification of the Process 1 network to incorporate the dependence of the system upon the operating times of the components.

The modification of the network to include the possibility of run failure has two important aspects:

- First, for each component, it introduces into the network an activity (labeled run failure) that is associated with a nonzero time interval. As a result, an expanded criterion is used for ending a simulation. A simulation will be ended when either of the following conditions occurs: (1) node 7 is released, indicating system failure, or (2) the time of arrival of a transaction at a node equals or exceeds a user-specified total simulation time, (a maximum allowable operating time for the system). (In this study a total simulation time of 20 hours was deemed as sufficient to allow adequate development of the trends represented by the cumulative failure probability curves for Processes 2, 3, and 4.)
- Second, because of the time-dependent activity, the release of a node is contingent not only upon a count of the arriving transactions but also upon the expected (scheduled) arrival times of the transactions at the node.

For each transaction, the scheduled arrival time is the sum of (1) the time interval required for the completion of the last activity that the transaction encountered and (2) the accumulated time for all previous activities to which the transaction was subjected. An accumulated time is one of the possible attributes of a transaction (initially this time attribute was the start time); this attribute is updated when the last activity is completed and the node at which the transaction arrives is released.

Assuming all components start, the expected times of arrival for the four transactions at nodes 12, 22, 32, and 42 are all zero (see Figure 4). The time intervals for the run-failure activities (42, 43), (32, 33), (22, 23), and (12, 13) are obtained by Monte Carlo sampling of exponential probability distributions that are characterized by the values of $1/\lambda$ listed in Table 1. In this sampling procedure, the probability of run failure for a component is determined by the generation of a random number (drawn from a uniform distribution) between zero and one. The time interval to failure is then the time, as determined from the exponential distribution, that corresponds to this probability. (The explicit form of the exponential probability distribution used here is $(e^{-t/\lambda})/\lambda$ with mean λ and variance λ^2.) Use of an exponential distribution to determine the time interval to (first) run failure is based on the assumption that the probability of failure is proportional to the duration of operation. There is no compelling requirement for using the exponential in preference to any other particular distribution. With different assumptions, different distributions might be used. Within Q-GERT a wide variety of probability distribution functions are available, and, if need be, the user can construct and use his own empirical distributions.

The event calendar now contains four expected arrival times corresponding to the four time-to-run-failure intervals. The current cumulative simulation time, t_c, is equated to the least of these four expected arrival times (the simulation time is advanced from zero to the earliest scheduled event). If t_c is equal to or greater than the user-specified total simulation time (for example, 20 hours), the system operating time is greater than the time of interest, and the simulation ends. If t_c is less than 20 hours, and if the node to which the transaction is directed can be released, then the event is removed from the calendar upon release of the node. The tasks associated with node release are performed, and the end-of-activity event for the ensuing activity is scheduled. As long as the earliest scheduled time on the event calendar is less than the user-specified total simulation time, the system can fail only by the release of either node 6 (by a single transaction) or node 5 (by a pair of transactions). When either of these events occurs, a transaction is routed to sink node 7, the node is released, and the time of system failure is marked.

The output summary for Process 2 will display the statistics for component failure (from statistics nodes 13, 23, 33, and 43), those for subsystem failure (from statistics nodes 5 and 6), and those for system failure (from sink node 7).

Process 3 Network

The maintainability network for Process 3 is shown in Figure 5. Because Process 3 may be regarded as Process 2 with repair added, demand failures and run failures are characterized exactly as they are in Process 2, with the same values of Q and $1/\lambda$ (listed in Table 1). By adding the possibility of repair in Process 3, an additional node and two activities (branches) are added to the Q-GERT network for each component in the system. In addition, the activities associated with the branches from the subsystems (from nodes 5 and 6) to sink node 7 are no longer regarded as zero-time activities. These activities determine the length of time that a subsystem may be inoperative without jeopardizing the entire system.

Each of the activities, (5, 7) or (6, 7), is assumed to be characterized by a normal probability distribution $NO(X)$ or $NO(Y)$ of the time interval, Δt_F, for the activity. The normal probability distribution $NO(X)$ characterizing activity (5, 7) has a mean of 1 hour and a "window" (maximum allowable minus minimum time interval) of 1 hour; the distribution $NO(Y)$ characterizing activity (6, 7) has a mean of 2 hours and a window of 2 hours. Assigning these values to the parameters of the distributions is equivalent to specifying the average repair times and the ranges for the repair times that can be tolerated in subsystems X and Y without causing the system to fail. For example, subsystem Y may be "down" for an average of 2 hours (for as little as 1 hour to as much as 3 hours) without causing system failure.

A repair time interval Δt_R is obtained by sampling the appropriate distribution in the manner previously described for sampling an exponential distribution to determine a particular run-failure time interval. Repair activities are assumed to be characterized by normal probability distributions $NO(A), \ldots, NO(D)$ of the repair time intervals. Values of the parameters $1/\mu$ for these distributions are given in Table 1.

A single transaction can release node 14, 24, 34, or 44, and therefore an event representing completion of repair is scheduled at one of these nodes when its antecedent node is released. This event is scheduled at time $t_c + \Delta t_R$. If node 5 or 6 can be released, a transaction is routed to node 7. Because a single transaction releases node 7, the time interval Δt_F for the activity (5, 7) or (6, 7) is obtained, and the system failure event at node 7 is scheduled at $t_c + \Delta t_F$.

The next event to be removed from the event calendar is determined by whichever is less, the time $t_c + \Delta t_R$ or the time $t_c + \Delta t_F$. Thus, if $t_c + \Delta t_F$ is less than $t_c + \Delta t_R$, the system fails: The event is removed (sink node 7 is released) from the calendar, and the simulation ends because the time for repair of subsystem X or Y is too great. On the other hand, if $t_c + \Delta t_F$ is greater than $t_c + \Delta t_R$, the subsystem is still operational, and the event for node 14, 24, 34, or 44 (repair complete) is removed from the calendar.

When subsystem repair is timely, the event at node 7 must also be removed from the event calendar, but without causing system failure, and this is done by stopping ongoing activity (5, 7) or (6, 7). Otherwise, the system can be failed (erroneously) when all components are running, simply because the event scheduled at node 7 is the earliest event on the calendar. To avert an erroneous failure, the user function $UF(X)$ or $UF(Y)$ is used to stop the activity (5, 7) or (6, 7) and to thereby permit the scheduling of an event at node 12, 22, 32, or 42. Functions such as $UF(X)$ and $UF(Y)$ can be written by the user, making use of subroutines that exist within the Q-GERT library.

If the simulation time, which is equated to the earliest (next) scheduled event on the network calendar (it could be the scheduled time for system failure), equals or exceeds the user-specified simulation time, the simulation ends without a system failure. Data are collected at sink node 7 and at specified statistics nodes for all simulations, as in Process 2. In addition, nodes 14, 24, 34, and 44 (the end-of-repair-event nodes) provide data on the time intervals for repair whether these repairs are successful or not.

Process 4 Network

By the inclusion of conditional run failures and contitional repairs in the subsystem Y portion of the Process 3 network, the maintainability subnetwork shown in Figure 6 results. The Process 4 network consists of this subnetwork plus the subsystem X portion from Process 3. In Process 4, all the features of Process 3 are retained except those that are modified by the inclusion of conditional run failures and conditional repairs, as noted in the following.

In the subnetwork of Figure 6, unconditional run failure and repair (of the pump) and conditional run failure and repair (of the motor) are possible. Unconditional run failure of the pump can be manifested in two different failure modes, each of which is characterized by an exponential distribution but with different parameters (mean times to failure). The fun-failure mode for the pump is determined probabilistically. Unconditional repair of the pump can be carried out in but one mode.

Conditional run failure and conditional repair of the electric motor are each manifested in two different modes. The two failure modes are characterized by two exponential distributions; the two repair modes are characterized by two normal distributions. Unlike the unconditional phenomena, however, the mode of run failure and the mode of repair of the motor are conditionally linked to the mode of failure of the pump. Consequently, these modes are predetermined stochastically. When the pump exhibits an unconditional mode I run failure, then conditional modes of motor failure and repair (designated mode I failure and mode I repair) are invoked, and the time-dependent run failure and repair probabilities for the motor take the form of

an exponential distribution with $\lambda = \lambda_I$ and a normal distribution with $\mu = \mu_I$, respectively. If the pump fails by another mechanism (designated unconditional mode II failure), then conditional motor failure and repair (designated mode II failure and mode II repair) are called for, and $\lambda = \lambda_{II}$ and $\mu = \mu_{II}$.

Based on the foregoing considerations, the following modifications of the subsystem Y portion of Figure 5 (Process 3) are made to produce Figure 6 (Process 4):

1. The pump run-failure activity of Process 3 is replaced by two run-failure activities. These activities are characterized by exponential probability distributions (values for the $1/\lambda$ parameter are in Table 2) that are accessed by user functions $UF(C, \text{I})$ and $UF(C, \text{II})$. To accommodate this modification, deterministic node 32 is replaced by probabilistic node 32.
2. For the motor, provision is made to replace the normal mode I run-failure activity with the mode II run-failure activity if mode II pump failure is selected. User function $UF(C, \text{II})$ brings about this replacement at the time mode II pump failure is selected. The appropriate values of the parameter $1/\lambda$ that are used to determine the time intervals to mode I and mode II motor failure are shown in Table 2.
3. Motor-repair activity is carried out in mode II if the pump (and hence the motor) fails in mode II; otherwise, motor repair is carried out in mode I. The values of $1/\mu$ for the respective normal distributions are listed in Table 2. This modification is brought about by replacing deterministic node 43 with conditional take-all node 43. Release of this node always routes transactions to nodes 6 and 44, but the branch that is selected for sending a transaction to node 44 is determined by a numeric attribute of the transaction. In addition to the standard accumulated-time attribute, each transaction from node 42 carries a numeric attribute, the value of which is determined by the pump failure mode. (The value of this numeric attribute for each transaction generated at source node 41 is one.) This value is set equal to two whenever user function $UF(C, \text{II})$ is invoked (whenever mode II pump failure is selected). It is set equal to one by $UF(C, \text{I})$ when mode I pump failure is selected.

With the exception of the parameters for $NO(X)$ and $NO(Y)$, all other user functions and distributions are unchanged from Process 3. In Process 4, the mean for both distributions is 2 hours. The window for $NO(X)$ is 4 hours, and the window for $NO(Y)$ is 2 hours. As with the other processes considered, the output summary provides data from each statistics node and the sink node.

Process 4 illustrates the flexibility that can be achieved through the use of user functions that can be tailored to handle conditional phenomena. More complex networks that include additional dependencies can be handled by essentially the same techniques.

MAP Simulation Results

A summary of the results for the four processes is shown in Figure 7. For each selected time value on the graph, the corresponding cumulative probability of system failure represented by each individual plot was obtained by averaging the mean cumulative system-failure probabilities that were obtained from each set of 1000 or more simulations (runs). (Using a CDC 6600, a set of 1000 simulations of a single process required an average of 10 seconds of CPU time.)

Figure 7 shows that significantly different results are obtained by including different time-dependent phenomena in the maintainability analyses. The differences in the results are clear cut, notwithstanding the effects due to sample size. The primary goal of these analyses was to show and compare the general trends in the results for the four processes. Therefore, no special effort was made to determine the sample size needed to ensure statistical convergence of the results for each process. (For example, the difference between the exact solution (0.0022 using the value of Q from Table 1) and the MAP solution (.002) for Process 1 is due to the sample size used in MAP; running additional sets of simulations would bring the MAP value closer to the theoretical value.) For the analysis of real systems, however, the sample size providing stability in the results would need to be determined for each process because the proper sample size will depend on the complexity of the process considered.

The curve for demand failures only (Process 1) overestimates safety-system reliability, whereas the curve for demand and run failures (Process 2) is probably too pessimistic. The maintainability estimates that fall on intermediate curves (Process 3 and particularly Process 4) can be expected to be more realistic and therefore represent better estimates of system reliability. The confidence with such estimates can be regarded, however, will depend upon future analyses of the sensitivity of the results to changes in the nature and number of included phenomena and to the nature and extent of the conditional dependencies that may exist among these phenomena.

The most important aspect of Figure 7 is the fact that the differences between the probability for the time-independent process and the probabilities for the time-dependent processes (and, indeed, the differences among the probabilities for the time-dependent processes) are nontrivial for operating times up to 20 hours. At the end of the simulations, the failure probabilities for the time-dependent processes are 4 to 20 times as great as the failure probability for the time-dependent process. Furthermore, the time-dependent process with the greatest failure probability (Process 2) is approximately five times more probable than the time-dependent process with the least failure probability (Process 3).

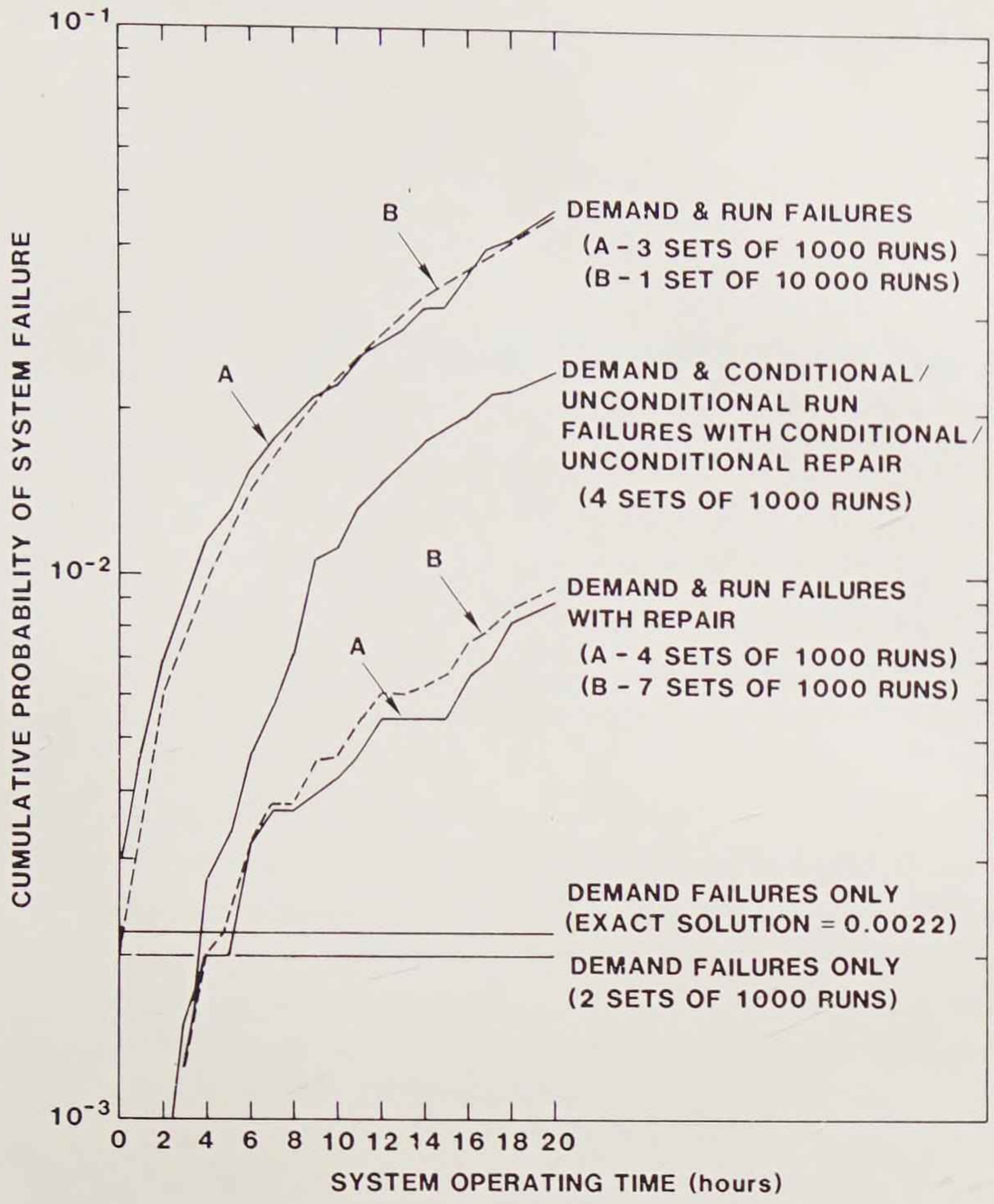


Figure 7 *The Cumulative Probability of System Failure vs. System Operating Time for the Four Processes.*

Conclusions and Recommendations

The analyses of the simple four-component safety system have been carried out at levels of increasingly greater complexity (Process 1 through Process 4) by successively including additional time-dependent phenomena and by including conditional dependencies. At the last level (Process 4), the maintainability estimates for the safety system can be regarded as reasonably realistic although the analysis, even for such a simple system, is by no means exhaustive. For example, it would be quite reasonable to include the possibility for demand failure after each repair with, as a result, the additional conditional dependencies that might pertain. Doing so, however, would contribute little additional support to the demonstration of the capabilities of MAP. Indeed, the very act of generating the results by which the four processes can be compared has demonstrated, in principle, that the capabilities of MAP are sufficient to treat the phenomena of interest.

There are, however, at least three areas in which the capabilities of MAP could be extended. First, treatment of the statistical aspects of MAP could be improved. Because MAP uses a Monte Carlo approach, an investigation of variance-reduction techniques could lead to improvement in the statistical aspects of the procedure and, therefore, to the reduction of the time and costs associated with the analysis.

Second, a software interface for translating safety-system fault trees into maintainability networks could be developed. By making use of computerized descriptions of the topologies of fault trees that are currently used for reactor reliability analyses, the "bounding" maintainability networks for MAP could be obtained directly by supplying the appropriate interface. Thus, the curves (typified by those for Processes 2 and 3 on Figure 7) that provide bounds to best-estimate curves can be obtained directly with little or no network preparation effort on the part of the analyst. This would result in significant cost savings, since the preparation of the networks is by far the most time-consuming task in the maintainability analysis.

Third, a computer "language" could be developed that is specifically tailored to the application of MAP to reactor safety-system analyses. By tailoring the language to the problem (that of reactor safety-system analysis), considerable savings could be expected particularly in regard to analyst time and to computer resources such as storage space and execution time.

These enhancements to the basic capabilities of MAP would make it even more useful for modeling the reliability of space nuclear power systems.

Acknowledgments

Research performed at Sandia National Laboratories, Albuquerque, NM.

References

Pritsker, A. Alan B. (1979) *Modeling and Analysis Using Q-QERT Networks*, John Wiley & Sons, New York.

U.S. NRC (1975) *Reactor Safety Study, An Assessment of Accident Risks in US Commercial Nuclear Power Plants*, Appendices III and IV, WASH-1400, NUREG-75/014, U.S. Nuclear Regulatory Commission, October 1975.

Vesely, W. E. and R. E. Narum (1970) *PREP and KITT: Computer Codes for the Automatic Evaluation of a Fault Tree*, USAEC Report IN-1349, Idaho Nuclear Corporation, August 1970.

Worrell, R. B. and D. W. Stack (1978) *A SETS User's Manual for the Fault Tree Analyst*, NUREG/CR-0465, SAND77-2051, Sandia National Laboratories, Alburquerque, NM, November 1978.

Space Nuclear Power Systems 1984
Edited by M. S. El-Genk and M. D. Hoover
© Orbit Book Company, Malabar, FL, 1985

Chapter 64

Artificial Intelligence Applications to Design Validation and Sneak Function Analysis

R. C. Stratton

EBR-II Project
Argonne National Laboratory
P.O. Box 2528
Idaho Falls, Idaho 83401

An objective of the U.S. space reactor program is to design systems with high reliability and safety of control over long operating lifetimes. Argonne National Laboratory (ANL) is a participant in the National Man-Machine Integration (MMI) program for Liquid Metal Fast Breeder Reactors (LMFBR). A purpose of this program is to promote the development of concepts and technologies that enhance the operational safety and reliability of fast-breeder reactors. Much of the work is directly applicable to the space reactor program. This paper reports on one of the MMI projects being developed by ANL. The project reported pertains to an automated system that demonstrates the use of artificial intelligence (AI) for design validation (DA) and sneak function analysis (SFA). The AI system models the design specification and the physical design of the cooling process assigned to the Argon Cooling System (ACS) at Experimental Breeder Reactor II (EBR-II). The models are developed using heuristic knowledge and natural laws.

Introduction

Argonne National Laboratory (ANL) is actively involved in the Liquid Metal Fast Breeder Reactor (LMFBR) Man-Machine Integration (MMI) Safety Program. This program should enhance the operational safety and reliability of fast-breeder reactors by optimum integration of men and machines through the application of human factors principles and control engineering to the design, operation, and control environment (Vaurio et al. 1982). However, similar methods can be applied to other nuclear systems including space nuclear plants. Significant technology being developed at Argonne for the LMFBR-MMI program is directly applicable to the space reactor program, since many of the concerns associated with high reliability and safety of control systems over long operating lifetimes are common to both. One aspect of the MMI work at ANL, and its implications, is reported in this paper.

This paper demonstrates the potential application of artificial intelligence (AI) to certain aspects of design. An AI system is described that performs design validation (DV) and sneak function analysis (SFA) of the fuel-subassembly cooling process provided by the Argon Cooling System (ACS) at Experimental Breeder Reactor II (EBR-II). The AI system models the design specification and the physical product of the design (the design incarnation or physical design) and compares the models for agreement. Validation of the process described in the design specification is satisfied if the models agree. If validation is not satisfied, the AI system compares the design-incarnation model to engineering process models to determine if process functions exist in the incarnation that are not defined in the design specification; these process functions are classified as sneak functions. In other words, sneak functions are those which occur in the process, but which were not planned by the engineers.

Validation is the act or process of assuring the compliance of an object to a standard. As used here, validation is that process which can verify that the incarnation of a design functionally complies with its specification. SFA involves reasoning about the physical product of design in order to determine unplanned functions resulting from a specific incarnation. DV and SFA are part of the necessary criteria for ensuring that a system satisfies reliability requirements (Wojcik 1983 and Ehrlich and Gabriel 1983).

There are two basic requirements that must be satisfied in order to develop an AI system that performs DV and SFA. First, the design specification, its incarnation, and the engineering processes must be modeled so that the AI system can reason about the models and their comparison. Second, rules and methodologies in the form of AI algorithms that provide for analysis of the design must be defined. This project utilizes hierarchical structure for modeling and establishes element definitions and relations that enable the reasoning about DV and SFA (Stratton and Lusk 1983 and Gabriel 1983). The modeling, relationships, and definitions are developed in Prolog (Clocksin and Mellish 1981 and Pereira

1983) an AI programming language which uses logical problem-solving concepts (Kowalski 1982).

The advantages of performing DV and SFA by use of AI principles lie in the ability to perform exhaustive path searches, and the ability to develop rules and knowledge bases that are interactive and easily maintained. Exhaustive path searches are performed as a function of the path criteria, and the search is unencumbered by tedium and clerical errors. That is, given the start path segment and the end path segment (which can be the same) of a physical design (a piping and instrument diagram), the AI system will search and catalog all paths that include these boundary segments. In addition, the determination of paths can be controlled by defining specific states of components in the physical design.

In developing an artificial intelligence system, system rules and knowledge are represented in Horn clauses. Because of the Horn clause logic, information can be modified, deleted and added interactively during program execution. Also because of this form of information representation, system rules and knowledge can be edited with minimal impact on nonedited clauses. The architecture of the AI rules and knowledge bases is discussed further in the following section.

Artificial Intelligence

As stated in Jackson (1976), AI is the ability of machines to do things that people would say require intelligence. AI research is an attempt to discover and describe aspects of human intelligence that can be simulated by machines. Alternatively, AI research may be viewed as an attempt to develop a mathematical theory to describe the abilities and actions of things exhibiting intelligent behavior, and to serve as a calculus for the design of intelligent machines. As yet there is no "mathematical theory of intelligence," and researchers dispute whether there ever will be. The definition given by Jackson summarizes the initial point of view and potential for success of the AI goal to produce a general model of human intelligence.

Present trends in AI research are directed towards domain-specific applications. These types of application provide for domain modeling of human knowledge. This view is expressed well by Vamos (1983). The philosophical issue is the problem of the definition of intelligence, and closely connected with it the question whether a machine can be more intelligent than its creator. We shall not submerge ourselves in this scholastic mood, but cannot miss the opportunity to indicate that recent results and more practical trends in AI are directed precisely towards circumventing this human-intelligence-imitating mechanization problem. Two major areas can be classified as those AI applications which are now in the focus of practical interest: the man-machine interface, and the inclusion of human knowledge and experience in a machine system. It should be understood that the main trend of AI is not to replace the human element but rather to elevate the humans value and role. This paper is focused on the second AI application expressed by Vamos, that is, the inclusion of human knowledge and experience in a machine system.

Knowledge in AI

Knowledge in an AI system can be modeled as either heuristic knowledge or as natural laws. Heuristic knowledge is the understanding of a phenomenon gained by experience and is usually manifested as rules of thumb. This type of knowledge does not have a clear proof as to its existence and application to a phenomenon. Natural laws are derived from structural and behavioral models and basic laws of nature (for example, the known biological and physics laws). These laws have well founded proofs and are understood in direct relation to the phenomena to which they are applied.

The AI system in this paper contains both heuristic knowledge and knowledge of natural laws. Heuristic knowledge along with natural laws are represented in the component functional models, engineering process models, and engineers' component state models. Natural laws are also represented in the structure, functions, and behavior of elements in the physical design.

Relationships and Definitions

In order to perform DV and SFA, element relationships and definitions are required to define the system model and rules. Elements are the physical entities that build the process and are defined as components, subsystems, and systems. The relationships and definitions are manifested as element functional definitions, state relationship to functions, function relationship to direction, element connectivity, and functional hierarchical configuration. "State" defines the element's condition of existence (Seeman, Colley and Stratton 1983 and Colley 1982). These relationships and definitions are further defined below.

The justification for elements in a system is that the elements perform functions. Each element, therefore, represents single or multiple functions, as shown by the turbines and heat exchanger in Figure 1. These functions exist in a hierarchical network that satisfies a design function. The elements can be characterized as providing functions at required design capacity or limits. This paper deals with the functional aspect of the elements. This functional aspect can best be understood by examples such as pumps, valves, and filters. As a component element, a pump develops a driving force (a pressure differential), a filter purifies a medium, and a valve regulates flow. As a subsystem element, however, the combined functions of a pump, filter, and valve can

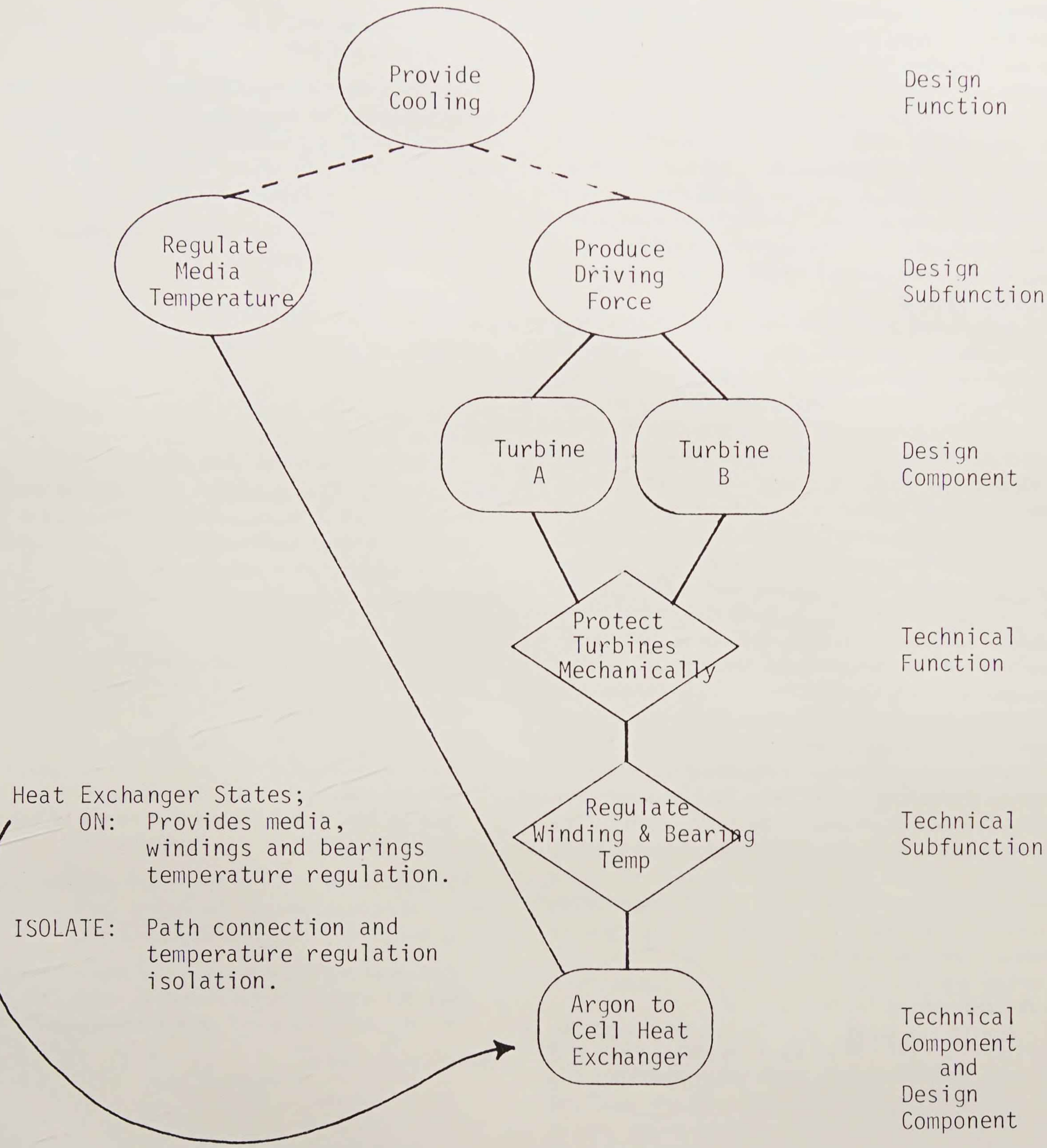


Figure 1 *Element Hierarchical Relationships for an Artificial Intelligence System applied to the Argon Cooling System.*

be to prevent damage to a related subsystem or component by purification of the medium.

Element state is directly related to element function; therefore, the element state further defines the element function. An element with multiple functions provides a defined function only when it resides in a specific state (for example, on, off, variable), and the element may provide certain functions when in one state but different functions in yet another state. A valve, for example, can provide the functions of isolation, path connection, and regulation. The isolation function exists only when the valve is in the "off" state (shut), whereas the path

and regulation functions exist only when the valve is in either the "on" or "variable" state.

In addition to being related to state, the functions are also impacted by flow direction of the medium. The direction of flow through an element can alter the element's functional characteristics. Depending on the element's function, the alteration can either be neutral, negative, or positive. For example, a check valve provides flow in one direction and isolation in the opposite direction, whereas a gate valve in the "open" state will provide "path" in both directions. However, a radioactive particulate filter can provide filtration in one direction and contamination in the other direction. Obviously, the filtration function is a desired (positive) function, whereas the contamination is an undesirable (negative) function.

Element connectivity characterizes the physical connection between elements. Connectivity associates the serial and parallel functions of the process as well as the function integration. In addition, connectivity provides the mechanism that allows functional evaluation of the integrated elements for comparison with the design specification.

The functional relationships necessary for furnishing the overall (top-level) design function are described by a "functional hierarchical configuration." The top function is the highest node in the functional hierarchy. Each successively lower level of the hierarchy defines functions required to achieve the top-level function. Functions are classified either as design functions or as technical functions. Design functions are independent of physical incarnation and express the physics and engineering functions necessary to satisfy the design process. Technical functions, however, directly depend on physical incarnation. The design functions and components are present because of the requirements of the process in question. In contrast, technical functions are present to support the design component. In some cases, though, a component can provide both design and technical considerations, for example, the argon-to-cell heat exchanger in Figure 1.

AI Architecture

The basic architecture of an AI system consists of a reasoning mechanism, rules about the phenomenon and facts that provide knowledge defining structure, and state of the phenomenon. The reasoning system used in this project is Prolog. Prolog means programming in logic (see Clocksin and Mellish 1981). Prolog is a Horn clause problem-solving system that reasons using top-down logic. Horn clauses are logic statements of the form: "if X then Z," where X is described as the condition and Z is the conclusion. A Horn clause contains only one conclusion. An example of a Horn clause would be

> If the AC turbine is connected to valve C and valve C is connected to the gas purifier then the AC turbine is connected to the gas purifier.

The same Horn clause in a more generic form would be expressed as

> X is connected to Z if there exists a path XY where Y is connected to Z.

Top-down logic is a problem-solving scheme whereby the conclusion is the initiation point and the objective is to determine if the conditions exist to support the conclusion. In the AI system using DV and SFA, top-down logic can be shown as follows:

> Path X is validated with the design specification if the following are true:
>
> - The function of path X is a design specification function, and
> - Path X conforms to the engineer's designed state criteria.

The rules for this system define the requirements for validation and sneak function analysis as well as defining the relation between element state, function, and function models. The validation rules or criteria can be seen in the path X validation example; a path is validated if it satisfies both condition one and condition two. An example of a relation rule is shown by the determination of the state and function of a path segment.

> If X is a valve and X is open, then X provides the function of path; however if X is closed it provides the function of isolation.
>
> If X is a filter and X is on and the flow direction is from inlet to outlet, then X provides the function of filtration. However, if the flow direction is from outlet to inlet then X provides the function of contamination.

The physical structure of the system and the existing state of the components in the system are contained in the system facts. Structure is expressed as:

> Path segment n is connected to path segment $n + 1$ and $m + 1$, where the components in segment $n + 1$ and $m + 1$ are valve c and valve d respectively.

State is expressed as:

> Valve c is open.
> Turbine AC is on.
> Valve d is shut.

Performing DV and SFA

To perform DV and SFA of an actual design, the design specification is modeled as a functional hierarchy based on physics, engineering principles, objectives, and constraints. Each element of the design incarnation is modeled with respect to its functional attributes and

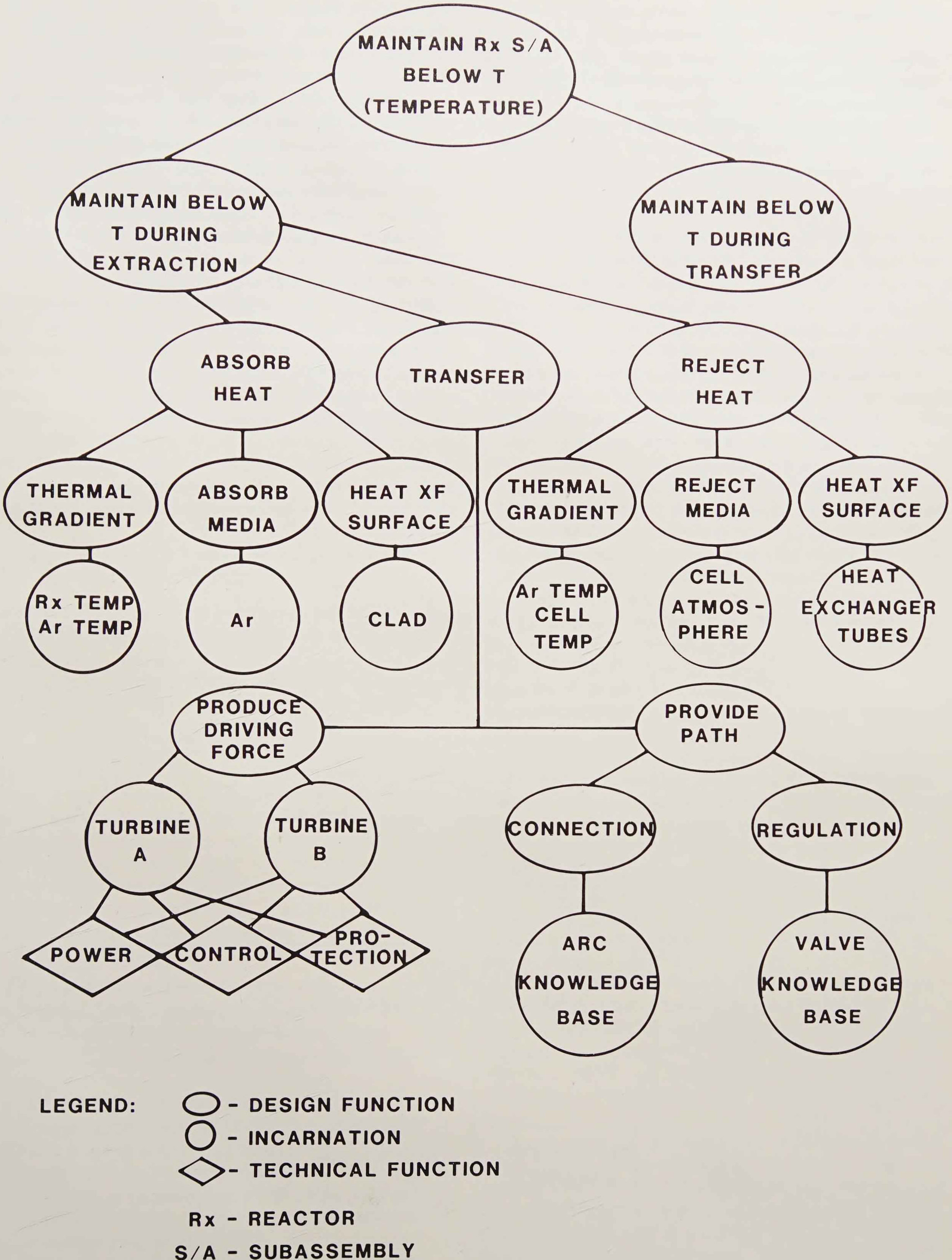


Figure 2 *Functional Hierarchy for the Argon Cooling System.*

interelement relationships. The design-incarnation models are then built from the component models. And finally, analysis and comparison of the design-incarnation models with the design-specification model are performed.

The basic difference in these models should be specifically noted. The design-specification model is constructed using top-down logic beginning with the desired process and ending with the component level. A process can have more than one model solution; however, the design specification will define a specific set of models as a function of the process, objectives, and constraints. The design-incarnation models are constructed using bottom-up logic beginning with the components of the system and ending with a process.

A design function of the ACS, for example, is to maintain the temperature of an irradiated reactor subassembly below a specified temperature when the subassembly is not immersed in sodium. In order to provide a cooling process, the design must specify a heat-transfer surface, a heat-absorbing medium, a temperature gradient between the heat-rejecting medium and the heat-absorbing medium, and a function that will replace the heated absorbing medium with a cool (relative to the temperature-gradient requirement) absorbing medium. In addition, objectives and constraints are placed on the ACS. The cooling medium is required to be a gas (because of economics and corrosion consideration), the cooling system is to be a recirculation type with redundant delta (flow)-pressure producers, and environmental integrity must be maintained. The design specification of the cooling process is modeled in Figure 2 using the above requirements. This model also includes the defined component states according to the engineers' intent. The design-incarnation models are constructed using the specified components, component functional models, engineering process models, and physical paths of the physical design.

The AI system constructs the design-incarnation models by the following procedure: Given the path limits (a start path segment and a stop path segment as shown in Figure 3), all paths in the system are determined. The path sets are then categorized according to the engineers' classification criteria. Classification criteria are defined by element function and/or state. The functions of selected path sets are determined using the component functional models and the engineering process models. These functional models define the design-incarnation models.

Next the AI system performs DV and SFA using the

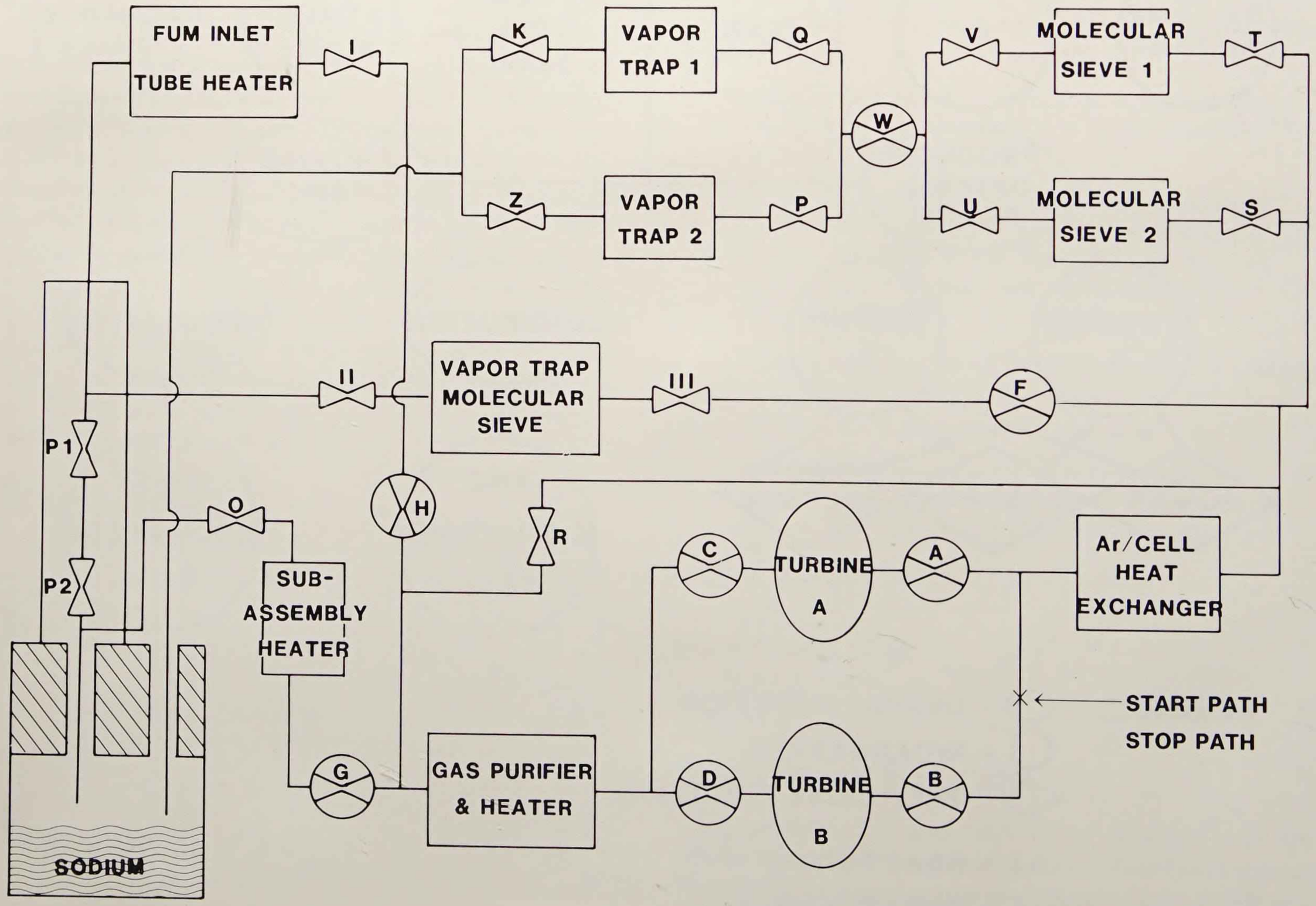


Figure 3 *Configuration of the Fuel Unloading Machine (FUM) and the Argon Cooling System.*

design-specification models, design-incarnation models, engineering process models, and the engineers' defined component state. An incarnation model validates a specification model if their process hierarchies are the same and the component states in the incarnation model are the same as the engineers' defined component states. If the path is not validated, then it is analyzed as a sneak function. The path model is compared against the engineering process models to determine definable sneak functions. If there is no agreement, then the path model is classified as an undefined sneak function.

The path from turbine A through valve C, valve H, valve I, valve F, valve A and back to the turbine is an example of a validated incarnation model, Figure 3. The path performs the process of reactor subassembly cooling and conforms to the engineer's defined element state criteria. The path from turbine A through valve C, valve G, valve F, valve A and back to the turbine is an example of a definable sneak function. The path performs the process of reactor subassembly cooling, however, the path state does not conform to any of the engineer's defined element state criteria.

ACS System Description

This section contains more detailed information on the Argon cooling system (ACS) to which the AI system was applied.

The Argon Cooling System performs a subfunction for the Fuel Handling System (FHS). The FHS functions to transfer nonirradiated fuel into the reactor core and irradiated fuel from the core to the fuel-subassembly shipping cask. The ACS principally functions to provide thermodynamic integrity of the subassembly when it is outside the reactor pool. The ACS circulates argon gas through fuel subassemblies for preheating (during transfers into the primary tank) or cooling (during transfers out of the primary tank).

The functional considerations and constraints that must be understood and accounted for in the design of the ACS are as follows:

- Subassemblies are either irradiated or nonirradiated.
- Irradiated subassemblies are radioactive, generate decay heat, and contain radioactive sodium residue.
- Nonirradiated subassemblies require preheating prior to immersion in the reactor pool sodium.
- The refueling environment contains sodium which is radioactive and will plate out on system components.
- After components have been removed from a sodium environment, the sodium residue must be removed.
- The purity of the primary-pool argon cover gas must be maintained, and argon must not be released to the atmosphere external to the FHS.
- The integrity of all interfacing processes must also be maintained.

These functions and constraints must be included in any design specification, which will of course express the essential functions required to provide the process. The functions will be design functions and/or technical functions. The manifestations of the design specification are the physical components and structure of the ACS.

As Figure 4 shows, the ACS has three principal flow paths:

1. Fuel Transfer Port (FTP);
2. Fuel Unloading Machine (FUM); and
3. Interbuilding Coffin (IBC).

Each path should allow the argon gas to flow to a subassembly for heating or cooling and should also provide the necessary ACS support functions. The ACS consists of the following: control console, turbines, heat exchanger, heaters, vapor traps, molecular sieves, gas purifier bed, oxygen monitor, moisture monitor, and pressure control.

The control console regulates the ACS and provides visual displays of the ACS flow paths and instruments. The console also supplies the operator with the information necessary for his remote operation of the system.

The ACS delta pressure (flow pressure) is provided via the ac or dc turbine. The ac turbine supplies flow during normal operation, and the dc turbine can be used as backup during ac-turbine or ac-power off-normal events. On loss of normal power, the dc turbine starts automatically and is supplied by the ACS batteries until the 400-kW diesel generator assumes the emergency loads. At this time, the dc turbine automatically switches to the rectified ac power supply. Vibration monitors are mounted on the ac and dc turbine flanges. These monitors will provide warning of abnormal vibration to permit turbine switchover or ACS shutdown prior to actual turbine failure. A multiple-tube argon-to-air heat exchanger located upstream of the turbines cools the argon to below 100°F. The inlet-gas-temperature rating to both turbines is 150°F (maximum) to prevent overheating of the turbine windings and bearings.

The heat exchanger rejects ACS heat to the reactor containment atmosphere. The heat exchanger is a natural-convection air-cooled horizontal multitube type with a design capacity for cooling 70 cfm of argon from 700°F to 100°F. In actual operation, the outlet gas temperature is reduced to nearly ambient room temperature.

Four heaters are provided in the ACS for argon and component preheat: gas-purifier-bed heaters, fuel unloading machine (FUM) inlet-line heaters, fuel transfer port (FTP) pipeline heaters, and subassembly heaters. The gas-purifier bed is equipped with nine resistance heaters rated at 1000 W each. These heaters are left "off" to prevent high interbuilding coffin (IBC) outlet

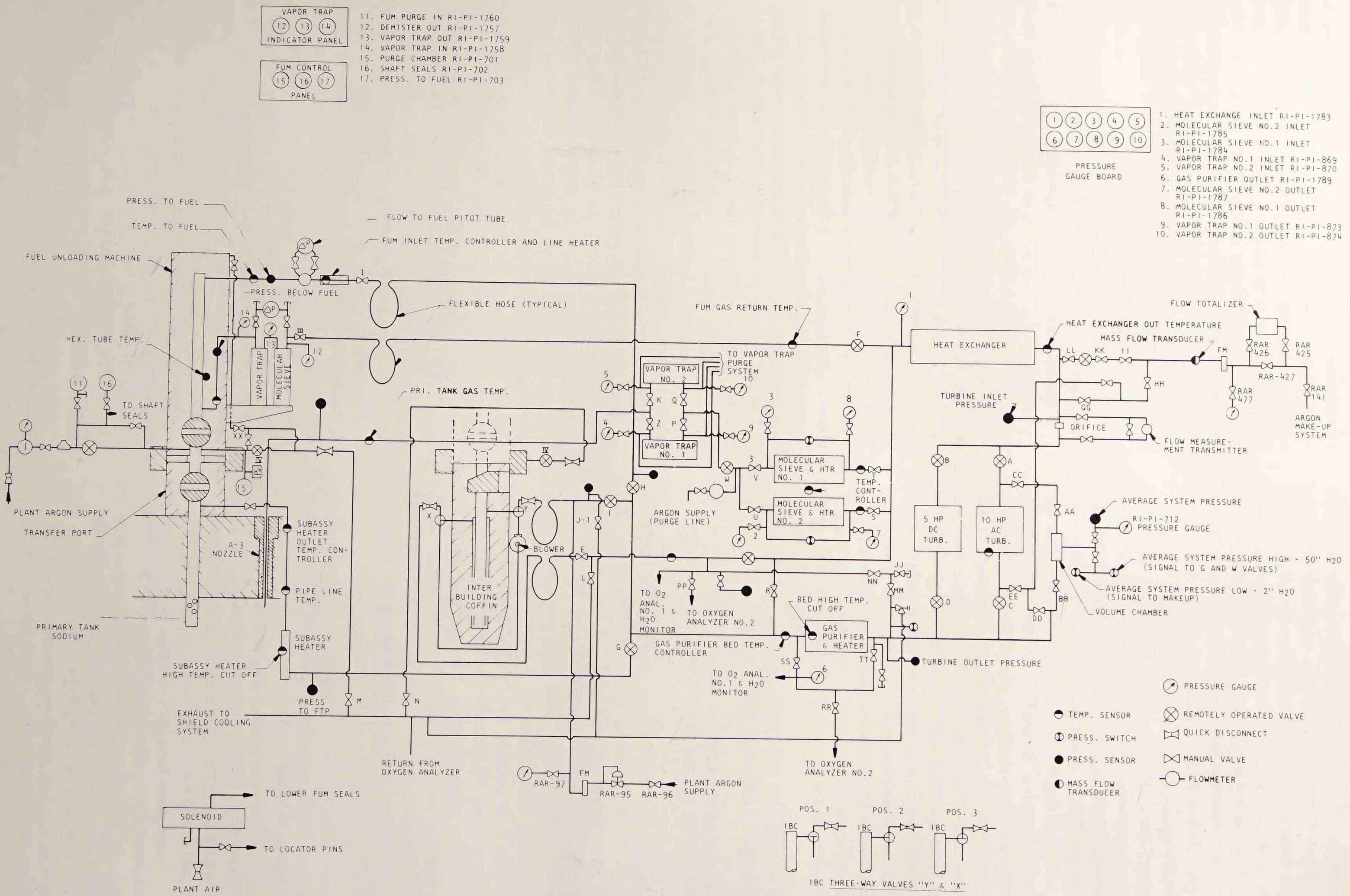


Figure 4 *Argon Cooling System Piping and Instrument Diagram.*

temperature when the ACS flow is routed through an IBC. The FUM-inlet line heater is an immersion-type heater rated at 9 kW. This heater warms argon entering the FUM and ensures that the subassembly bond sodium is melted from the top down. The FTP path of the ACS has two separate heaters. The pipe line heater consists of two resistance wire-wrapped heaters wrapped around the pipe leading to the FTP. This heater is used to preheat the argon piping. The subassembly heater, an immersion-type heater rated at 12 kW, is located in the piping leading directly to the FTP. Both these heaters heat argon gas to approximately 650°F before it enters the FTP for subassembly blowing and heating sequences. These heaters serve to heat the subassembly to a minimum of 450°F before it is lowered into the primary tank, to limit thermal shock to the subassembly.

The ACS utilizes two vapor traps and two molecular sieves that remove radioactive sodium aerosol from the argon gas, preventing accumulations of sodium or its oxide. As the vapor trap in service becomes plugged, the standby unit can be put in service and the plugged one removed for cleaning. However, both molecular sieves are required on-line simultaneously. If either of the molecular sieves becomes plugged, the ACS must be shut down to replace the plugged component. The FUM exhaust line also contains a vapor trap in series with a molecular sieve. These components are similar in construction but physically smaller than the ones described above. The gas-purifier bed is filled with stainless steel mesh. The mesh removes particles that would otherwise be circulated through the system.

The oxygen content of the argon must be monitored continuously during fuel-handling operations. Oxygen inleakage will cause sodium oxide formation in the subassembly being cooled. This can block cooling circulation and cause fuel-pin melting. Also, oxide formation on the FUM gripper will hinder operation of the jaws and the sensor rod. Two oxygen analyzers are provided to monitor the oxygen content of either the IBC or the ACS. A moisture monitor is provided to sample ACS flow for moisture content. Moisture in the system has the same effect as oxygen. The primary sources of moisture are the IBC's when they are returned from the Hot Fuel Examination Facility.

To ensure that oxygen inleakage in the ACS is held to a minimum, the system pressure is maintained positive when flow is through the FUM only and is therefore assumed positive for all other flow paths. This is accomplished by maintaining the turbine inlet pressure slightly positive, which results in a turbine discharge pressure of approximately 3.5 to 4.5 psig. A turbine delta-pressure signal is used to control the turbine inlet pressure. This is done by adjusting the throttle valves, which lead to a pressure-balance chamber between the turbine inlet and discharge lines. An argon makeup arrangement automatically feeds argon into the ACS when pressure in the chamber decreases to less than 2 in. of water. It stops supplying argon to the system when the chamber pressure reaches 6 in. of water. The argon makeup and vent subsystem is also used to prevent system damage during ACS heatup and cooldown.

Discussion

The relations, definitions, and methodologies developed in this project potentially have wide application in addition to validation and sneak function analysis. These relations, definitions, and methodologies can be applied to design, operation, and training. Transformation of a design concept for a process into a design specification is defined and bounded by laws of physics, engineering principles, objectives, constraints, and technology. When presented in a functional hierarchical construction, the functions tend to layer themselves from top to bottom in the order of laws and principles, objectives, constraints, and technology. That is, the hierarchy tends to place the essential function toward the top and the physical functions towards the bottom.

These hierarchies can be developed for specific processes by experts in that process field. The resulting process hierarchy can then be utilized by less experienced engineers as consultant aides in future design of same or similar processes. These hierarchies can also be utilized to document the physical incarnation functionally and to analyze the effect of future design changes. The hierarchy and path characteristics can be used to help develop normal and off-normal operating procedures for the process and can be used to analyze and process off-normal situations both diagnostically and prognostically.

As a training aid, the functional hierarchy would explain and reinforce the functional aspects of the components and higher elements to the trainee. The path and path function characteristics will help develop the trainee's ability to functionally analyze physical paths within the design incarnation, piping and instrument diagram (P&ID). That is, it will allow the trainee (either operator or engineer) to learn, review, and test the system concept of function and incarnation relationships.

Two other areas of potential application of these methodologies are fault-tree analysis and alarm handling. Fault-tree analysis requires the determination of all singular and integrated faults derived from electrical and mechanical designs. The design can be transformed into a graph consisting of arcs that represent the design elements, where each element has a defined number of states. Algorithms would then determine paths and path combinations associated with faulted element states and conclude with a fault tree for the design in question.

Alarms represent states of process elements (systems, subsystems, and components). The matrix of alarms

that result from a process fault is a function of the fault and the process elements associated with the fault. By defining the fault/component/function relationship, alarm states can be mapped into a graph representing alarm relations and hierarchy. These graphs can then be analyzed by "path" and "path function" algorithms to determine the hierarchical fault relationships during a given alarm situation.

Conclusion

This paper discusses a project that demonstrates the potential application of AI to DV and SFA. The project concerns an AI system that performs design-specification validation and determines sneak functions pertaining to the subassembly cooling process provided by the Argon Cooling System at EBR-II. The advantages of applying AI technology to the problem of DV and SFA is that of complete and exhaustive path-search capabilities and the development of an interactively operated and maintained logic system composed of engineering heuristics and natural laws.

It should be noted that if such a system is to be employed as a practical engineering tool, then several aspects must be further developed. Heuristic and natural-law knowledge bases of components and engineering process models need to be defined and built. The AI algorithms must be expanded so that they are capable of dealing with parallel-path segments of same or different functions. The design capacity of elements and their relationship to the process need to be incorporated. And finally, computing hardware and software systems must be available that provide for the operating and storage requirements needed for exhaustive path searches of a complex physical design, and the search must be performed in a timely manner.

Acknowledgments

I would like to thank those at Argonne National Laboratory who provided advice and support in this work. I would also like to thank Allen Christie at Westinghouse Advance Energy Systems for his comments. Work supported by the U.S. Department of Energy under Contract W-31-109-38.

References

Clocksin, W. F. and C. S. Mellish (1981) *Programming in Prolog*, Springer-Verlag, Berlin.

Colley, R. W. (1982) "A Transition Control System for Procedure Prompting," in *Transactions of the American Nuclear Society 1982 Summer Meeting* 41:529.

Ehrlich, S. M. and J. R. Gabriel (1983) *Cutsets With Required Arcs: A Prolog-Based Approach*, ANL/MCS-TM-11, U.S. Department of Energy.

Gabriel, J. R. (1983) *Algorithms for Automated Diagnosis of Faults in Physical Plant*, ANL-83-70, U.S. Department of Energy.

Jackson, P. C. (1976) *Introduction to Artificial Intelligence*, Petrocelli, New York.

Kowalski, R. (1982) *Logic for Problem Solving*, Elsevier North Holland, Amsterdam.

Lusk, E. L. and R. O. Overbeek (1982) *An LMA-Based Theorem Prover*, ANL-82-75, U.S. Department of Energy.

Pereira, E. F. (1983) *E-Prolog User's Manual*, University of Edinburgh, England.

Seeman, S. E., R. W. Colley, and R. C. Stratton (1983) "Optimization of the Man-Machine Interface for LMFBRs," *Nuclear Safety* 24(4): 506–512.

Stratton, R. C. and E. L. Lusk (1983) "Automated Reasoning in Man/Machine Control Systems," in *Transactions of the American Nuclear Society 1983 Winter Meeting* 45:204.

Vamos, T. (1983) "AI As a Tool For Flexible Manufacturing," in *Proceedings of the Ninth Annual Control Conference*, held in West Lafayette, Indiana, Sept. 19–21, 1983, pp. 1–16.

Vaurio, J. K. et al. (1982) *Man-Machine Interface Program Plan*, LMFBR Safety Program, U.S. Department of Energy.

Wojcik, A. S. (1983) "Formal Design Verification of Digital Systems," *20th Design Automation Conference*, IEEE, pp. 228–231.

Space Nuclear Power Systems 1984
Edited by M. S. El-Genk and M. D. Hoover
© Orbit Book Company, Malabar, FL, 1985

Chapter 65

Transference of Advanced Liquid Metal Fast Breeder Reactor Control Technology to the Aerospace Power System Program

Gregory H. Chisholm

EBR-II Project
Argonne National Laboratory
P.O. Box 2528
Idaho Falls, Idaho 83401

The next generation of nuclear power-generating stations will be designed to optimize operation of the plant without sacrificing overall safety. Attaining this optimization will require applying sophisticated control technology that will provide a highly reliable control system which has authority for the safe control of the plant. Such a control system would ensure plant safety with enough reliability so that safety credit could be taken for it during the licensing process. To alleviate the vulnerability of the control system to component failures, the controller should be fault-tolerant. A complex control system, the reactor control system, for example, is made fault-tolerant by providing duplicates of critical components (both physically or analytically), by providing as complete as practical analysis of the design (verification and validation), by providing diverse methods of operation when non-redundant components fail, and finally by providing for on-line detection/identification of failures and automatic or manual compensation.

Introduction

Much recent research has been devoted to the safety of Liquid Metal Fast Breeder Reactors. Part of the resulting technology, especially advanced control systems, appears to be directly transferable to the space nuclear power program. Some of the ideas described in this paper have already culminated in successful products available for application, such as analytical redundancy and fault-tolerant computers. Other applications are currently being developed as elements to support the design goals outlined in the following section: automated software verification, automated hardware verification, and system validation.

Background and Philosophy of Reactor Safety

Argonne National Laboratory (ANL) has been involved in conceptualizing designs for the next generation of Liquid Metal Fast Breeder Reactors. As part of this task, existing successful reactor designs were reviewed to determine which features should be emulated. Economic factors were considered as well as technical issues. This paper concentrates only on the conclusions drawn regarding continuity of power generation and overall plant safety.

Control Design Example

Two classes of reactors were judged to have the best operational record in both continuity of power generation and overall plant safety: (a) the pool-type Liquid Metal Fast Breeder Reactor of which the sole U.S. example is Experimental Breeder Reactor II (EBR II), and (b) the smaller, pressurized water reactors, of which the naval power plants are examples.

From the standpoint of continuity of power, both classes of reactors have impressive records. A decisive factor is their simplicity of design. The control philosophy for naval plants places a significant amount of responsibility upon the operator. To guard against operator error, all reactor safety functions are implemented in fail-safe hardware. The control system for which the operator is responsible is kept simple, enabling the operator to carry a model of the plant in his head and to diagnose off-normal transients in a quick and sure manner.

The EBR-II design philosophy parallels these concepts for operator involvement, but emphasizes an additional concept—inherent safety— which is vital to the premise of this paper. The features of EBR-II that promote inherent safety are worth a brief digression, as a prelude to the discussion of control systems.

The inherent safety of EBR-II centers around two choices made by the designers. In contrast to either a Pressurized Water Reactor or Boiling Water Reactor, the system pressure in an Liquid Metal Fast Breeder Reactor is very low. The water-cooled reactors require pressurizing the coolant to approximately 2000 psi in order to obtain the high temperatures necessary for reasonable thermal efficiency. But this, in turn, raises the concerns of decay-heat removal during a loss-of-

pressure accident. The choice of sodium, a liquid-metal coolant, permits very low system pressure of the order of two atmospheres, and reduces the design constraints that must be included for anticipation of a loss-of-pressure accident.

The second choice was the use of a pool-type design at EBR-II. This also reduces the design constraints imposed for anticipation of a loss-of-coolant accident which is a classic accident scenario for reactor safety evaluation. The reactor is located inside a pool of liquid sodium. Should the primary-heat-exchange function be lost for any reason, this large pool will absorb the energy produced during the power-decay period.

Discussion of the design of EBR-II has been essential to establish the concept of an inherently safe system. This paper concentrates on the design of a control system for application to a reactor that is inherently safe.

Design Philosophy for Control

The extant design philosphy for control of power-producing nuclear reactors is based upon ensuring safe operation with respect to radiation releases to the environment. The authority for this assurance is usually placed upon the safety systems. The underlying rationale is that the control systems responsible for continuous operation of plant subsystems are the first line of defense for mitigating radiation releases. Safety systems are the last line of defense and are designed to ensure that reactivity is reduced to subcritical levels and that decay heat is adequately dissipated.

"Inherently safe" reactors rely on passive system features to mitigate radiation release. The advent of these reactors permits restructuring of the present control system design philosophy. This restructuring is based upon the fact that authority for safety is placed upon the passive features of the system instead of the traditional placement upon the plant protection system.

We have postulated that if the control system is kept simple and if the reactor system is forgiving, the plant can be demonstrably more safe and maintain continuity of power. However, the two designs discussed above maintain a separation between the control system and the reactor shutdown system, based on the philosophy that the control system may fail and that the shutdown system must be available to mitigate the impact of this failure. It is postulated here that adherence to this philosophy is the reason that control systems at commercial reactors are so complex. The Liquid Metal Fast Breeder Reactor community is currently involved in research efforts which, if successful, will permit adoption of simpler control schemes. It is also postulated that these simpler schemes will lead to inherently safe designs for nuclear power stations—whether located on earth or in space.

Argonne National Laboratory believes that the plant-protective and plant-contol functions can be integrated into a system capable of performing the combined functions in an active control manner. This is in contrast to the combination of an active control system and a passive plant-protection system typical of systems installed at nuclear plants today. An example of an integrated control philosophy is that used during the design of fly-by-wire aircraft. The difference in mission between aircraft and nuclear reactors places different contraints upon the design criteria. The aircraft is designed for short missions predicated by availability of fuel while the power-producing reactor is designed for extended periods of operation. However, the success of fly-by-wire aircraft control systems is strong evidence that this integrated philosophy is valid and should be considered for reactor control.

Application of Philosophy

The application of this philosophy to reactors will depend on the successful completion of some basic research and development. Argonne National Laboratory is currently identifying the research requirements to implement this philosophy and is defining a program that will investigate those problems that they have expertise in solving. This will center on developing a methodology for automated verification and validation of the control system. Preliminary results indicate that the intended approach will be fruitful. However, the reader is cautioned that much remains to be done.

The Liquid Metal Fast Breeder Reactor safety community has recognized that control-system reliability can be enhanced by incorporating computational ability in the controller. The flexibility of a computer-based controller to reconfigure upon sensing subcomponent failures is very powerful in comparison to existing analog systems. Qualification of computers for use in highly reliable control systems is the primary subject for the remainder of this paper.

Simplicity and control-system integrity are the central ideas presented within the context of whole-plant design and are coupled to the choices made for design of the hydraulic system. These arguments (and those following) are predicted on a reactor that is inherently safe. This perspective is basic to the following arguments.

Current Design Practices for Reliable Reactor Systems

A reliable system is defined here as a system that is the last line of defense for mitigation of an occurrence that would result in loss of life or a large investment. An example would be the plant protection system at a nuclear power station. The design elements that contribute to reliable operation of this system are

1. Redundancy of like components,
2. Diversity of sensed parameters for identification of off-normal transients,
3. Coincidence of actuating signals,

4. Design verification and validation, and
5. Selection of proven components.

Each of these elements is discussed in more detail, but first, it should be noted that these elements are based on discrete implementation of functions. This means that most parameters are sensed by a complete subsystem, which typically consists of a transducer, amplifier/converter, and actuator. Figure 1 shows a typical implementation of the system input for sensing a reactor overpower condition. From this simple figure, it is easy to visualize the immense number of components required to implement a modern reactor control/protection system.

Identifying the elements of a reliable system as implemented today, and then the techniques that would permit the design of reliable systems with significantly fewer components, is essential to demonstrate that available technology supported by impending research will lead to plant designs which are safer and more dependable. These two qualities should be characterisitic of a power system in remote locations.

The first design element to be considered is redundancy. In Figure 1, there are three redundant nuclear-power channels and three redundant temperature-sensing channels. Each channel is an exact duplicate of the other two, demonstrating redundancy. The philosophy underlying the requirement for redundancy is based on single-failure analysis. Analysis of a system design must be able to demonstrate that non-simultaneous, single failures will not degrade performance of the system. This analysis is qualitative in nature and presupposes the use of highly reliable components. Redundancy of and by itself would result in

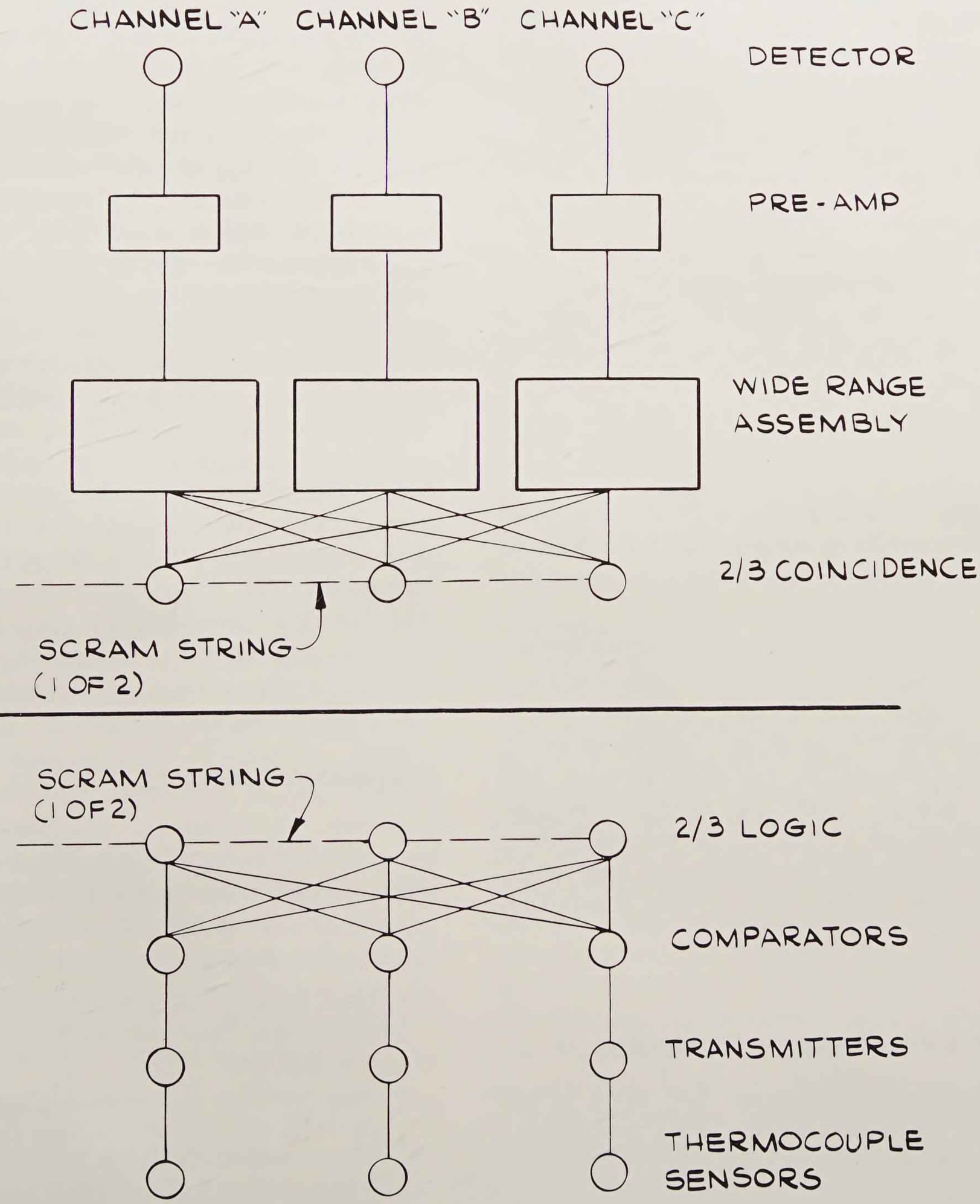


Figure 1 *Plant Instrumentation for Diverse / Redundant Over-power Reactor Trip Strategy.*

the need for only two channels. The third channel results from satisfying the coincidence requirement.

Coincidence is the element of system design that requires x out of n channels to be in agreement before a protective action is taken. In the subsystems shown in Figure 1, two out of the three must indicate that a parameter has exceeded a predetermined limit before protective action is taken. As mentioned above, the single failure analysis postulates single component failures, and without coincidence the plant would spuriously shut down during the accepted failure. Coincidence is a method of maintaining the plant in a safe manner without unnecessary disruptions of power. Other factors must also be considered when determining the number of channels and the required coincidence. These factors, such as reliability of the individual channels based on equipment failure data and the period between tests, are beyond the scope of this paper.

Figure 1 also demonstrates diversity, in that the temperature parameter is a diverse method of monitoring reactor power. This diverse method of sensing reactor power assures that, if some major oversight in design could result in the nuclear detectors failing to sense an overpower transient, the diverse sensor would provide the necessary protection.

One method of design verification and validation mentioned above is the single-failure analysis which is an example of qualitative system analysis. System reliability is ascertained by quantitative analyses such as success diagrams, fault-tree analysis, or Markovian analysis. The result of quantitative analysis is a reliability number which predicts failure rates. The failure rate coupled with risk determines the acceptability of the design.

Another method of design verification and validation is to implement a rigid test program. Usually this program attempts to duplicate anticipated conditions and verify minimal impact upon the system.

The implementation of imbedded computers has led to a number of methods of verification and validation. Among these are diverse design and verification teams, and rigid acceptance tests. A recent installation at Argonne National Laboratory's Transient Reactor Test Facility has a monitor system that runs inverse algorithms of those run on the three-part control system. The one common factor in the verification and validation efforts to date is that each is very manpower-intensive.

Transference Technology Strategies

There are technologies available that, upon proper implementation, would enhance the safety posture of a nuclear power station. These technologies are described, and advantages and disadvantages listed in this section. However, there are open questions that must be addressed before we can implement these technologies. The following section identifies proposed solutions to these questions and describe a potential program for demonstration of proven results.

Analytical Redundancy

Analytical redundancy techniques were developed at the Charles Stark Draper Laboratory and have been applied at EBR-II. The specific application at EBR-II has been to analytically derive flow measurements from related plant parameters. The Draper work is based on use of analytic tools available to the design engineer in a real-time analysis of plant parameters (Deutsch et al. 1982). These techniques account for calibration and temperature errors and have proven to be within 1% of actual plant parameters at EBR-II.

The specific application at EBR-II was predicated on the loss of seven out of the original ten primary flowmeters. The transducers for primary flow are inaccessible and repair impossible. The methods developed by Draper are being analyzed for installation as flowmetering.

Experience has shown that the analytical redundancy system at EBR-II provides valid on-line detection of plant instrumentation failures, isolation of the failed instruments, and derivation of the correct information. The application of this technique to control systems would reduce the physical redundancy or diversity or coincidence requirements. Less instrumentation would have to be installed, since the system would be capable of deriving the redundant parameter from analysis of related parameters.

To exploit the advantages of this technique, a number of questions must be addressed, such as reconciling current design practices with the new technology. The main impediment to using the analytical redundancy technique is that of proper verification and validation. The licensing community for reactor systems is accustomed to quantitative analysis. The question then becomes one of providing an analogous form of analysis for a computer-based system.

Fault-tolerant Computers

Within the context of this paper, a fault-tolerant computer is one that will execute prescribed software in the presence of any single conceivable hardware failure. A number of available systems meet this definition, and fall into two general classifications:

1. Fault tolerance implemented via software, of which the Tandem Corp. and August computer system are examples, and
2. Fault tolerance implemented in hardware, of which the Intel 432 and Charles Stark Draper Laboratory Multi-Processor Computer are examples.

A decided advantage to using fault-tolerant computers in reactor-control-system designs is that they sup-

port implementation of versatile techniques such as analytical redundancy. Exploiting the flexibility of computers in reactor control systems could result in a reduction of the number of instruments, resulting in a initial cost saving to the buyer. More importantly, it would result in a less complicated design. The EBR-II/Navy experience is conclusive that the less complex systems are operationally superior, both for a continuity of power and for safety.

However, application of computers in reactor safety systems needs to comply with the current design practices mentioned above. Current methods for verification and validation of programmable components are quite manpower-intensive.

Man-machine Interaction

Man-machine interaction is defined here as encompassing the breadth of current research and development of the interaction between man and machine and include the following major areas of concentration.

Procedure prompting consists of on-line computer generation of procedures that guide the operator. Some of the target systems will be repositories of existing procedures, and the computerized system will act as a procedure-base manager. This type of system is intended to replace the manual system on a one-for-one basis. Other computerized systems will be driven by real-time data and, when the plant is sensed as being in an off-normal situation, will automatically generate a procedure to prompt the operator in returning the plant to a safe situation. This second type of system uses established procedures but is intelligent to the extent of recognizing off-normal conditions and of prompting with the correct procedure for return to normal. A third type of system, which is under development, is intended to identify an off-normal situation, evaluate what would be the most appropriate next state, and generate a unique procedure to attain the result.

Procedure-prompting systems share the advantage of improving the operator's response. Current methods have allowed up to 30 minutes for an operator to respond to an off-normal situation. A significant reduction in this time should be realized from the application of procedure prompting.

Most procedure-prompting systems are large software systems. The verification and validation effort for application of a procedure-prompting system where it may affect plant safety is manpower-intensive. Therefore, procedure prompting is currently limited to the task of automating administrative functions, such as maintaining red-tag loss of isolated plant components.

Automatic Plant Diagnosis

A recent study completed for the Fast Reactor Safety Technical Management Center (a DOE-sponsored organization) concluded that a large percentage of Licensee Event Reports (LER's) were the the result of poorly controlled maintenance activities. This has been further substantiated by a report from Oak Ridge (Siegel et al. 1983). Based on Diagnostic Automation (Gabriel 1983) developed at ANL, research is in progress to develop a system to address these problems. Automated plant diagnosis will initially focus on providing computer-generated prompting of a technician through the troubleshooting phase of diagnosing a complex and failure-prone system.

The main advantage is that of providing on-line monitoring of maintenance activities. This monitoring is in essence an on-line automated quality-assurance mechanism. Additional benefit should be gained in reducing the duration of the troubleshooting phase of maintenance. Experience with complex systems dictates that the problem may be found within a short period of time (especially if the problem is traceable to a board-level failure); however, less obvious failures take significantly longer to locate and correct. If the failure perturbs the generation of power, automated diagnosis provides a direct monetary advantage.

The completed research and development indicates the potential benefits of automating diagnosis, but significant work remains to be completed before a system will be installed. In addition, the present automated system was written in the logic programming language Prolog, for which only one compiler exists. A number of software houses are currently working on developing compilers for the size of machine that would be required to support automatic diagnosis as presently conceived. The scheduled release dates would support a program as presently envisioned.

Technology Transference via Demonstration

The previous sections have presented a strategy for the design of nuclear power stations that provide an optimum system from the standpoints of safety and continuity of power. The underlying basis for this strategy are: (1) an inherently safe thermal-hydraulic design, and (2) a simple control scheme. Granted, a benign thermal-hydraulic system allows a simple control scheme, but incorporation of technological advances into the control system design would allow further simplification. Specifically, the plant protection system functions could be incorporated into a highly reliable control system. We recognize that this would require the control system to be designed to the reliability standards imposed on current reactor-safety-system designs. We further recognize that the concepts identified are dependent on the computational power and flexibility of programmable computers. The remainder of this paper describes current developments at Argonne National Laboratory that may provide a methodology for automated verification of computer-based control-system designs.

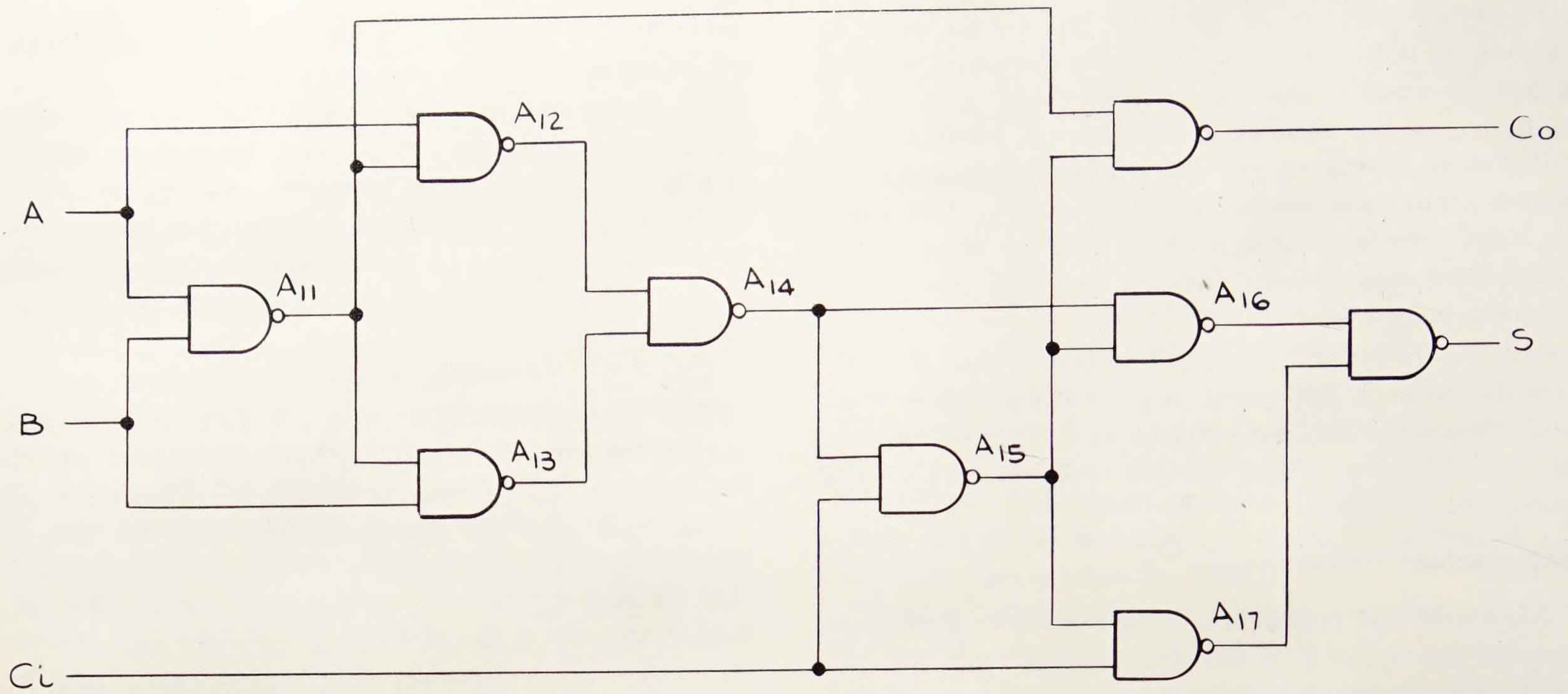


Figure 2 *One Bit Adder Circuit Inputs: A, B & Ci Output: Co & S NAND GATE Implementation.*

System Verification and Validation

The techniques presented are visualized as improving current practices from both a reduction in total manpower required and an improvement in final product. It cannot be overstressed that the following concepts are based on preliminary results, and that research is required to demonstrate complete confidence in the application.

The principal tools to be used in these investigations will be an automated reasoning (AR) system developed within the Mathematics and Computer Science Division of ANL (Lusk et al. 1983). This system is an interactive-clause-based theorem-proving program currently running on a VAX computer. This general-purpose system incorporates the features found in the theorem-proving program AURA, and offers many additional features as well. It is the most powerful system of its kind in the world, having recently answered open questions in mathematics and logic. A second tool that may be utilized is the logic programming language Prolog. The impetus for using this tool is work completed in proof of hardware designs (Barrow 1983).

The intended methodology is to first verify the software and hardware components of the system. (Hardware includes the fault-tolerant computer, the input output appurtenances of the computer, the system sensors, and the system actuators.)

Second, the verified software and hardware will be integrated and thoroughly tested to validate the integrated design. The ultimate proof is intended to be a demonstration of a highly reliable control system that has been designed, verified, and validated by the techniques described herein. The target system is the automated reactivity controller at EBR-II.

Hardware Verification

As noted above, the computer for this application should be demonstrably "fault-tolerant." It has been argued that this demonstration should be analogous to fault-tree analysis, which is the accepted method for proof of reliability in commercial reactor safety systems. The method of hardware verification that was developed at ANL is demonstrated in Figure 2 and Appendix A showing the circuit that was verified, and the clausal description that was used by the automated reasoning program in developing the verification.

The underlying theory (Wojcik 1983) is that register-transfer statements are used to specify the design. This results in a bit-level description of the logic circuit, which is then transformed into clausal form and presented to the reasoner system. The function that is being verified is presented to the system as a theorem, along with demodulators that allow the system to transit between the two levels of definition (that is, the clausal description for the circuit definition and the theorem). The desired theorem is then denied, and the proof is declared when a contradiction is encountered. Once a subcircuit (such as that shown in Figure 1) is verified, it may be used in conjunction with other subcircuits to build more complex circuits. In this fashion, a number of one-bit adders may be combined to form a four-bit adder. In representing the four-bit adder to the reasoning system, each subcircuit is treated as a generic module with specific input(s) and output(s), which ensures that each subcircuit is described in clausal form only once. The point here is that the effort involved in defining a complex circuit in clause form increases linearly with the complexity, in contrast to the expected factorial increase.

Hardware verification work at ANL is a hierarchical process in that a design is defined at several levels of detail, starting at the integrated chip layout at the bottom to a high-level system description. Looking at adjacent levels in this hierarchy verifies that functional integrity has been preserved as one transcends the design hierarchy. Our work has concentrated on the verification between the gate (or bit) level and the register level. Verification of the fault to tolerance of a computer is a quantum leap for this technology. For this reason, the most important criterion for selection of the appropriate fault-tolerant computer will be ease of verification.

Software Verification

ANL has developed techniques for software verification that are very complex. Because of time-space limitations, the following exerpt (Wos et al. 1984) must suffice for the purposes of this paper. " . . . the general approach to proving a program correct consists of the following steps:

1. Obtain or formulate the specification and input assumptions for the program.
2. Use invariants to divide the program into segments of straightline code, possibly containing conditional statements, and to cut loop bodies so that they consist of sequences of straight-line and possibly conditional code.
3. Formulate and prove the relevant theorems for each code segment and the inductions for the loops.
4. Verify that the conclusions and hypothesis of adjacent subtheorems match along all possible execution paths, identifying hypotheses added to force termination (or confirming that termination has been proved).
5. Conclude that the program has been proved partially (or totally) correct."

This process is developmental in nature, but ANL is optimistic that the code for the control function of the demonstration is verifiable.

The intent of this project is to demonstrate the validity of the above verification techniques for development of a highly reliable control system. This demonstration will consist of installation of such a system at EBR-II as the controller element of the automatic control-rod-drive system. Successful testing of the control-rod-drive system will confirm the process for automated verification and validation of a reliable controller. An extension of this work would be to tackle a more sophisticated software system. The analytical redundancy system discussed above is an ideal target program. ANL is currently determining the improvement to the safety posture of the plant provided by application of analytical redundancy techniques. The essential elements of this application would be to verify the program, implement it to verified fault-tolerant hardware, and validate its operation.

An additional demonstration planned by ANL is that of the automatic diagnostic system. Though this demonstration is not tied directly to the verification and validation effort, it is visualized as showing a method for improving the maintenance of complex critical systems.

Conclusion

The Liquid Metal Fast Breeder Reactor Base Program community is currently analyzing reactor designs to determine what contributes to a superior system design. The findings should benefit the designers of nuclear power systems for space applications. Specifically, the thermal hydraulic system design should encompass the design criteria of simplicity and inherent safety. Current research and development in the areas of reliable control-system design, analytical redundancy, and automated diagnosis should allow designers to maintain the design precepts of simplicity and safety. Design of power-generating stations for use in remote locations should benefit from this work.

Acknowledgments

I am grateful to the Math and Computer Science Division of Argonne National Laboratory for their assistance in using the automated reasoning system, in learning logic programming and for many helpful discussions and suggestions. Specifically I'd like to thank John Gabriel, Brian Smith, and Tony Wojcik of Illinois Institute of Technology. Work supported by the U.S. Department of Energy under contract W-31-109-38.

References

Barrow, H. G. (1983) "Proving the Correctness of Digital Hardware Designs," in *Proceedings of AAAI-83*, held in Washington, D.C., August 1983.

Deutsch, O. L., R. S. Ornedo, J. C. Deckert, A. Ray and D. B. Laning (1982) *Development and Testing of A Real-Time Measurement Validation Program for Sodium Flowrate in the EBR-II*, the Charles Stark Draper Laboratory, Inc., CSDL-R-1592.

Gabriel, J. R. (1983) *Algorithms for Automated Diagnosis of Faults in Physical Plant*, Argonne National Laboratory, ANL-83-70.

Lusk, E. L. and R. A. Overbeek (1982) *An LMA-Based Theorem Prover*, Argonne National Laboratory, ANL-82-75.

Siegel, A. I., W. D. Bartter, J. J. Wolf, H. E. Knee, and P. M. Hass (1983) *Front-End Analysis for the Nuclear Power Plant Maintenance Personnel Reliability Model*, Oak Ridge National Laboratory, NUREG/CR-2669, ORNL/TM-8300.

Wojcik, A. S. (1983) "Formal Design Verification of Digital Systems," in *Proceedings of the 20th Design Automation Conference*, held in Miami Beach, Florida, June 1983.

Wos, L. T., R. A. Overbeek, E. L. Lusk, and J. M. Boyle (1984) *Automated Reasoning, Introduction and Applications*, Prentice Hall, New Jersey.

Appendix A
Clauses for AR Proof of One-Bit Adder

Clause representing the circuit that is being validated:

CKT(sl, cl)

Deny that this satisfies the specifications for a one-bit adder:

$-$CKT(sum(a, b, carryin), carryout(a, b, carryin))

Where the specifications are expressed by the given demodulators:

EQUAL(sum(x, y, z, eor, eor(x, y), z))
EQUAL(carryout(x, y, z), or(and(x, or(y, z)),
and(not(x), and(y, z))))

Demodulators that defines eor:

EQUAL(eor(x, y), or(and(x, not(y)), and(y, not(x))))

Here are the clauses that describe the adder as it built using NAND gates:

EQUAL(and, not(and(a, b)))
EQUAL(a12, not(and(all, a)))
EQUAL(a13, not(and(all, b)))
EQUAL(a14, not(and(a12, a13)))
EQUAL(a15, not(and(a14, carryin)))
EQUAL(a16, not(and(a14, a15)))
EQUAL(a17, not(and(a15, carryin)))
EQUAL(s1, not(and(a16, a17)))
EQUAL(c1, not(and(all, a15)))

These demodulators move not symbols inside, simplify not (not(x))to x, and do no other processing:

EQUAL(not(and(x, y)), or(not(x), not(y)))
EQUAL(not(or(x, y)), and(not(x), not(y)))
EQUAL(not(not(x)), x)

This set of demodulators commutes and/or arguments and moves ands inside ors:

EQUAL(and(x, y)and(y, x))
EQUAL(or(x, y), or(y, x))
EQUAL(and(or(x, y), z), or(and)x, z), and(y, z)))
EQUAL(or(or(x, y), z), or(or(x, z), y))
EQUAL(and(and(x, y), z)and(and(x, z), y))

Evaluators of pairs of terms:

EQUAL(and(x, 0), 0)
EQUAL(and(x, 1), 1)
EQUAL(and(x, not(x)), 0)
EQUAL(or(x, 0), x)
EQUAL(or(x, 1), 1)
EQUAL(or(x, not(x)), 1)
EQUAL(not(0), 1)
EQUAL(not(1), 0)
EQUAL(and(x, x), x)
EQUAL(or(x, x), x)

Evaluators of lists of three terms:

EQUAL(and(and(x, y), not(y)), 0)
EQUAL(and(and(x, y), not(x)), 0)
EQUAL(or(or(x, y), not(y)), 1)
EQUAL(or(or(x, y), not(x)), 1)
EQUAL(and(and(x, y), y), and(x, y))
EQUAL(or(or(x, y), y), or(x, y))

Simplifiers for products of four terms:

EQUAL(and(and(and(x1, x2), x3), not(x1)), 0)
EQUAL(and(and(and(x1, x2), x3), not(x2)), 0)

Subsumption-type demodulators:

EQUAL(or(and(x, y), y), y)
EQUAL(or(and(x, y), x), x)
EQUAL(or(or(and(x, y), z), y), or(z, y))
EQUAL(or(or(x, and(y, z)), z), or(x, z))

Karnaugh simplifiers:

EQUAL(or(and(x, not(y)), y)or(x, y))
EQUAL(or(and(not(x), not(y)), y), or(y, not(x)))

Karnaugh simplifier inside a product:

EQUAL(or(and(and(x, y), not(z)), and(x, z)),
or(and(x, y), and)x, z)))

AUTHOR INDEX

(Bold chapter numbers indicate senior authorship.)

Allen, D. T. 25
Allen, Michael D. 61
Ambrus, Judith H. **10**
Anderson, John L. **17**
Anderson, R. V. **22**

Bailey, Sterling **26**
Bankston, C. Perry **45**
Barattino, William J. **39**, **52**
Bartholomew, Robert J. **62**
Beatty, Richard G. 10
Becker, M. 33
Botts, T. E. 29, **31**, **50**
Brandon, D. I. 28
Britt, Edward J. 16
Buden, David **20**
Bunch, Delbert F. **11**

Campbell, Robert W. **59**
Chipman, Gordon L., Jr. **4**
Chisholm, Gregory H. **65**
Cole, T. 45
Cox, C. M. **36**
Cronenberg, August W. **37**

Dean, Virginia F. 23
Determan, William R. **12**
Diaz, N. J. 35
Dix, George P. **6**
Dugan, Edward T. **35**
Dutt, Dale S. 36

El-Genk, Mohamed S. **23**, 39, 52, 60
Elliott, David G. **51**
Elms, Richard V. **19**
Engi, Dennis **63**
Englehart, Richard W. **57**
Ewell, Richard **44**

Feig, Jason R. **55**
Fenske, George R. **38**
Ferrigno, Dennis **13**
Fisher, C. R. 25
Florio, F. 21
Fornoles, Efren V. 9

Gido, R. G. 28
Greenspan, Bernard J. 61

Hartung, J. A. 58
Harty, Richard B. 12, **58**
Hertzberg, A. 49
Hoffman, Eugene E. **41**
Hoffman, H. W. **47**
Hofman, G. L. 38
Holland, John W. 25, **43**
Homeyer, William G. **25**
Hoover, Mark D. **61**
Horn, F. L. 29, 31, 50
Horner, M. H. 43
Hwangbo, Han **53**

Imamura, M. S. **18**

Johnson, Ernest W. **40**
Jones, John E. Jr. **30**
Jones, Owen C. Jr. **32**, 33, 34
Josloff, A. 21

Karnesky, R. A. 36
Katucki, Richard J. **21**
Khanna, S. K. 45
Kirpich, A. 21
Klein, Gale 16
Klopp, William D. **42**
Knudsen, Harold K. 62
Koenig, Daniel R. **27**, **28**

Lazareth, O. W. 29, 31
Lee, C. C. **33**
Lee, James H. Jr. 20
Lillie, A. F. 12, **14**
Lin, Jen-Tai **34**
Louie, David L. Y. 23, **60**
Lujan, Manuel Jr. **2**

Mahefkey, Tom **46**
Major, Arthur L. **15**
Masson, James H. 18
Mattick, Arthur T. **49**
May, Gerald M. **5**
May, Gerald W. **1**
McEver, W. S. 53
MacPherson, Robert E. 30
Merrigan, Michael A. **48**
Merrill, M. H. 25
Mondt, Jack F. 44

Neimark, L. A. 38
Nelin, C. J. 16
Norin, Marvin P. **56**
Nichols, J. P. 30

Oakes, L. C. 17

Patrick, J. W. 14
Pierce, Bill L. **24**
Poeppel, R. B. 38
Powell, James R. **29**, 31, 50

Ranken, William A. 37
Redd, Frank J. **9**
Rothenberg, Simon J. 61

Seiler, Fritz A. 61
Sewell, Duane C. **7**
Shin, Tai Sung 32
Stratton, Rex C. **64**

Taussig, Robert T. **54**
Thakoor, A. P. 45

Usher, J. L. 29

Vachon, Larry J. 13
Vaidyanathan, Sam 26
Van Hoomissen, John 26
Vivona, Alexander A. Jr. 15
Voss, Susan S. 6, 39

Wetch, Joseph R. **16**
Whan, Glenn A. 62
Woodall, David M. 23
Wright, Steven 60
Wright, William E. **8**

Yang, L. 43
Yoder, Graydon L. Jr. 47
Young, Robert A. **3**

KEY WORD LIST

(Numbers indicate chapters covering these subjects.)

Artificial intelligence 64, 65
Automation 18, 65

Brayton cycle 22, 29, 31

Civil applications 2, 3, 6, 10
Costs 6, 12, 16
Compact reactors 24, 29, 36

Decision theory 20
Design validation 64

Energy storage, flywheel 30

Fission gas release 36, 37, 38, 60
Fluidized bed reactors 32, 33, 34
Fuel behavior 36, 37, 38, 43, 60

Gas cooled reactors 24, 29, 31
Gas core reactors 35

Hauck engine 35
Heat pipe reactor 23, 27, 60
Heat pipes 23, 48
History 2, 3, 4, 5, 6, 12, 13, 27, 59

Inhalation hazards 61
Interagency Nuclear Safety
Review Panel 7, 11, 56, 57, 59
Instrumentation and control 17, 65

Liquid metal technology 26, 30, 41, 42, 47, 48
Lithium toxicology 61

Military applications 2, 3, 5, 9, 46, 54
Megawatt class systems 13, 30, 54
Meteoroid punctures 39, 51
Molybdenum alloys 42, 45, 48
Multi-kilowatt class systems 21

Particle bed reactors 29, 31
Power conversion 21, 25, 44
Probabilistic risk assessment 62

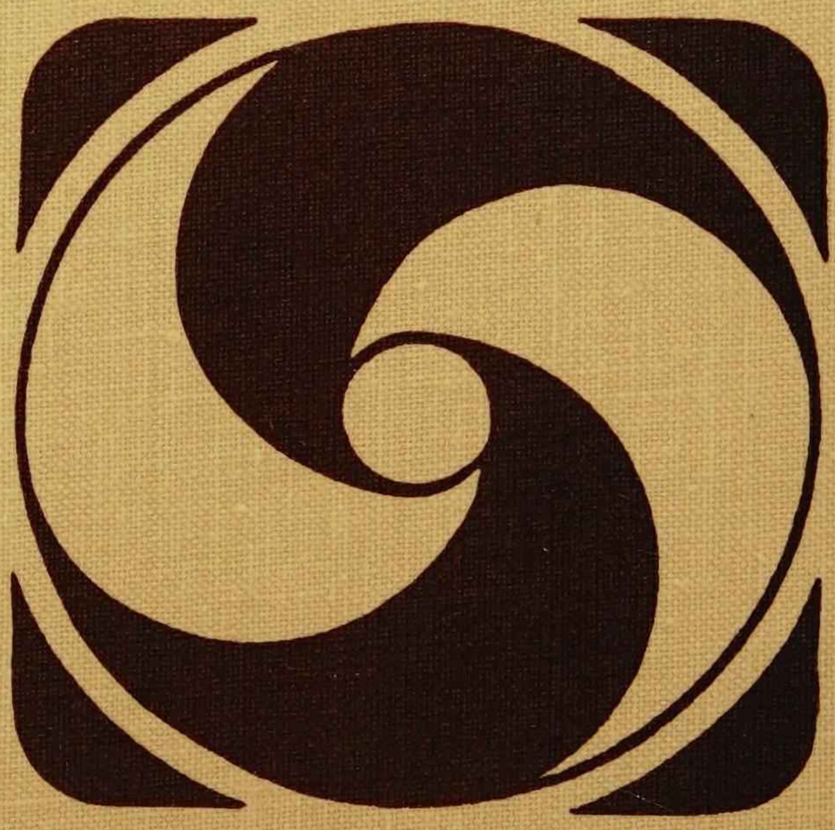
Radiation shield 39, 52
Radiator concepts 55
Radiators, direct condensing 53
Radiators, liquid droplet 49, 50
Radiators, rotary 51
Radioisotope heat sources 4, 40, 59
Rankine cycle 30, 47
Reactor startup 16
Refractory alloys 41, 42, 43
Reliability analysis 63, 64
Rover Nuclear Rocket Program 27, 28

SP-100 4, 8, 10, 11, 21, 22, 23
Safety 7, 11, 16, 23, 56, 57, 58, 59, 61
Space Transportation System 15
Stirling engine 21
Systems concepts 8, 18, 20, 21, 24
Systems integration 14, 15, 19
Systems requirements 9, 11, 26
Systems selection 20

Tantalum alloys 41
Technology transfer 1
Test requirements 13
Thermal analysis 28, 34, 52
Thermal management 46, 53, 54
Thermionics 25, 43, 44
Thermoelectrics 21, 44, 45
Thermophotovoltaic 44
Titanium alloys 45
Tungsten alloys 42, 52

U.S. House of Representatives
Committee on Science and
Technology 2, 3
Universities, role of 1

ABOUT THE SYMPOSIUM LOGO



The four corners of the logo represent the points of a compass and symbolize the role space nuclear power can play in the exploration of new frontiers; the large and small circles represent the integrated space system with a nuclear power plant at its center; the radiating spirals, also resembling a stylized atomic nucleus, symbolize the transfer of thermal and electric energy to support the space mission; and the logo's overall appearance of simplicity reflects the emphasis on space nuclear power systems that can operate without failure and provide reliable power.

ISBN 0-89464-004-6